Chemically tuning dynamic networks and supramolecular assemblies to enable synthetic extracellular matrices for tissue engineering

Chemically tuning dynamic networks and supramolecular assemblies to enable synthetic extracellular matrices for tissue engineering

Shahzad Hafeez (MSc with Honors)

The research described in this thesis has received funding from the province of Limburg and the European Research Council (ERC) under the European Union's Horizons 2020 research and innovation program (grant agreement No. 694801).

Chemically tuning dynamic networks and supramolecular assemblies to enable synthetic extracellular matrices for tissue engineering
Ph.D. Thesis, Maastricht University, Maastricht, the Netherlands
ISBN: 978-94-6419-950-5
Cover design: The prompt was provided by Shahzad Hafeez, and the cover art was created by Bing Image Creator.
Printed By: Gildeprint

Chemically tuning dynamic networks and supramolecular assemblies to enable synthetic extracellular matrices for tissue engineering

To obtain the degree of Doctor at the Maastricht University,
on the authority of the Rector Magnificus, Prof. Dr. Pamela Habibovic
following the decision of the Board of Deans, to be defended in public on
on Tuesday, 14th of November 2023 at 16:00 hours

by

Shahzad Hafeez

Promotors:
Prof. Dr. Clemens van Blitterswijk
Prof. Dr. Lorenzo Moroni

Co-promotor:
Asst. Prof. Dr. Matthew B. Baker

Defense committee:
Prof. Dr. Tilman Hackeng, Maastricht University
Prof. Dr. Bert Meijer, Eindhoven University of Technology
Prof. Dr. Roman Truckenmüller, Maastricht University
Prof. Dr. Romano Orru, Maastricht University
Assoc. Prof. Dr. Sabine van Rijt, Maastricht University
Prof. Dr. Sarah Heilshorn, Stanford University

Table of contents

Chapter 1

General introduction

Shahzad Hafeez [1] Clemens van Blitterswijk [1] Lorenzo Moroni [1], Matthew B. Baker [1]

[1] Department of Complex Tissue Regeneration, MERLN Institute for Technology Inspired Regenerative Medicine, Maastricht University, P.O. Box 616, 6200 MD Maastricht, The Netherlands.

General introduction

The extracellular matrix (ECM) is an outer part of a cell that is made up of supramolecular fibrous assemblies and exhibits controlled dynamicity and viscoelasticity.[1] The ECM is mainly composed of proteins, glycoproteins, and polysaccharides.[2,3] Self-assembly of proteins in ECM is driven by non-covalent supramolecular interactions.[1] ECM typically contains more than 80% water, with various biopolymers making up the rest. This essentially makes ECM a hydrogel. Dynamicity and viscoelasticity within ECM have mainly been associated with water, degradation of biopolymers, and non-covalent transient interactions. Unlike the ECM's dynamicity and remodelability, traditional hydrogels are static. Scientists have addressed this by developing dynamic hydrogels, which are enzymatically degradable. Enzymatically degradable hydrogels were essential in understanding the role of dynamicity for cellular behavior; however, decoupling degradation dynamics from material dynamics has proven difficult. In order to create dynamic hydrogels that can be tuned rationally to emulate the dynamicity and viscoelasticity of the ECM, researchers investigated dynamic covalent chemistry (DCvC) and supramolecular chemistry.[1,4,5–9]

The research presented in this thesis mainly focuses on tuning chemical network dynamics in hydrogels for controlled dynamicity and viscoelasticity towards cell culture and 3D bioprinting applications. In addition, the research presented in this thesis teaches supramolecular strategies for engineering fibrillar morphology in dynamic hydrogels with controlled viscoelasticity and toughness.

In **chapter II**, we introduced the field of research with a focus on the rational design of hydrogels responsive to cell stimuli. We divided cell-based stimuli into three categories, 1) enzyme 2) mechanical force, and 3) small molecule/metabolites. In this review, we also discussed dynamic covalent chemistry and supramolecular chemistries developed for creating responsive, dynamic, and viscoelastic hydrogels. Additionally, we discussed the influence of viscoelastic time scales on cellular behavior.

The author of this thesis has focused on developing hydrogels with controlled viscoelasticity and developing advanced bioinks utilizing DCvC and supramolecular chemistry. Therefore, in **chapter III**, we have provided a literature update on chemical strategies used for tuning viscoelasticity and viscoelasticity's influence on cell behavior. A large portion of the thesis also investigates dynamic chemistries for the creation of advanced bioinks. Therefore, we have provided a review of chemical strategies used for designing advanced bioinks.

Engineering dynamics in networks for controlling viscoelasticity and bioprinting properties are challenging.[5,9,10] In **chapter IV**, we utilized imine-type cross-linkers (oxime, semicarbazone, and hydrazone) with distinct equilibrium constants (K_{eqs}) and investigated the viscoelasticity, self-healing, and bioprinting of hydrogels. As reported in the literature, imine-type cross-linkers are reversible with K_{eq} of 10^8 for oxime and 10^4–10^6 for semicarbazone and hydrazone. The storage moduli decreased from 3000 Pa for oxime to 500 Pa for semicarbazone to 200 Pa for hydrazone. All hydrogels showed viscoelasticity with hydrazone exhibiting the highest viscoelasticity.

Storage modulus and viscoelasticity trends observed followed the rational trend of increasing K_{eq} values reported for these imine-type cross-linkers in the literature. Storage modulus and viscoelasticity values also indicate that the rate constants (k_1 and k_{-1}) are highest for oxime and hydrazone, respectively. Chondrocytes showed high viability within bulk and bioprinted hydrogels. Fibroblasts exhibited round morphology in oxime hydrogels in contrast to spreading morphology in hydrazone hydrogels.

The ECM is a supramolecular fibrous structure with controlled viscoelasticity and dynamicity.[1] We were interested to tune viscoelasticity in the supramolecular fibrous structure. Benzene-1,3,5-tricarboxamide (BTA) is one of the well-studied supramolecular units and self-assembles to form 1D nanofibers.[11] Our collaborators recently showed that BTAs modular mixing is possible and that modular mixing of two different BTA architectures allowed tuning mechanical properties in synthetic fibrous hydrogels.[12] In **chapter V**, we looked into the modular mixing of two BTA architectures at a higher concentration to adjust viscoelasticity and stress relaxation in the range necessary for cell culture and tissue engineering applications. A symmetrical small molecule with slow exchange dynamics and a telechelic BTA (BTA-PEG-BTA, which is a BTA connected to telechelic PEG20K on both ends) with fast exchange dynamics were copolymerized. We revealed that copolymerized BTA architectures formed stable hydrogels with tunable viscoelasticity and stress relaxation. Fibroblasts and chondrocytes showed high viability within these hydrogels (>80%). Neuronal cells PC12 and dorsal root ganglion (DRG) showed outgrowth in BTA-PEG-BTA hydrogels. Chondrocytes ATDC5 and human MSCs (hMSCs) showed cell-dependent aggregation with more compact hMSCs spheroids formation. While all formulations allowed hMSCs spheroids formation, we discovered that hMSCs spheroids formation ability was dictated by the dynamic properties of BTA hydrogel with the largest spheroids formation in the most dynamic hydrogel. Such supramolecular materials are essential for the development of spheroids in three-dimensional biomimetic space, which is essential for the successful development of large-scale tissues.

The ECM is a multifunctional and multicomponent supramolecular fibrous structure.[1,13] Creating multifunctional and multicomponent structures for emulating the complexity of ECM remains desired. The BTA supramolecular moiety offers the potential to mimic the complexity and multifunctionality of the ECM in the fibrous structure. A bottleneck is a synthetic method for upscaling the synthesis of complex and multifunctional BTAs. Usually, desymmetrization strategies are employed for the creation of multifunctional BTAs; however, existing desymmetrization strategies offered limited flexibility in upscaling the synthesis and purification of complex and multifunctional BTA structures. To address this challenge, in **chapter VI**, we developed a desymmetrization strategy that utilizes activated ester coupling of a symmetric synthon. We synthesized a small library of benzene-1,3,5-tricarboxyl activated esters and discovered that benzene-1,3,5-pentafluorophenol tri-ester (BTE-F_5Ph) undergoes effective desymmetrization and enabled the creation of multifunctional BTAs in reasonably higher yields than statistically expected. With this new methodology, we were able to create BTA monomers with hydrophobic spacers and reactive handles. We expanded this new methodology for the

creation of polymeric supramolecular hydrogelators. Under dilute aqueous conditions, polymeric BTA macromolecules self-assembled in water and created fiber and fibrous sheet-like structures. We discovered that polymeric macromolecules form hydrogels and mechanical properties can be tuned by adjusting the length of the aliphatic spacer on the BTA hydrogelators. Chondrocytes showed high cell viability within these hydrogels, extending the polymeric BTA hydrogelator's potential as biomaterials for cell culture applications. This newly developed desymmetrization strategy offers a way forward for creating multifunctional hydrogelators with controlled biophysical properties for mimicking ECM complexity in the synthetic hydrogel.

Engineering a broad range of viscoelasticity in a fibrous hydrogel remains has a long-standing challenge for recapitulating both the ECM fibrous morphology and viscoelasticity. In this chapter, we developed a series of telechelic BTA hydrogelators for molecular tuning of the fibrous structure and controlling viscoelasticity. We employed a desymmetrization strategy developed in the previous chapter and in chapter **VII** created a library of BTA macromonomers by altering carbon atoms from twelve, sixteen, eighteen, twenty, and twenty-four atoms on the exterior of the BTA. All macromonomers self-assembled into fibrous assemblies and resulted in fibrous hydrogels. While all hydrogelators showed similar storage moduli, changing the hydrophobic length on the BTA from twelve to twenty-four carbons resulted in hydrogels with controlled viscoelasticity over 5 orders of magnitude. We found that the BTA supramolecular hydrogels showed excellent extrudability, and injectability, and can be 3D bio-printed into multiple layered structures without any extra cross-links. Chondrocytes showed high cell viability when in contact with dilute solutions or encapsulated within these hydrogelators. Bioprinted chondrocytes also showed high cell viability within these hydrogels. This simple technique shows that by just adding or deleting a few carbon atoms on the supramolecular BTA macromonomer, we can leverage viscoelasticity across five orders of magnitude in fibrous hydrogels.

Load-bearing tissues are tough yet dynamic. In contrast, not only do conventional hydrogels lack the load-bearing capacity and mechanical strength of biopolymers such as cartilage and muscle but also are composed of static networks. When looking closely at nature's design of tough biopolymers such as collagen, nature utilizes non-covalent interactions for supramolecular self-assembly of fibrous structures and then stabilizes fibril assemblies with covalent bonds.[14] Synthetically speaking, combining fibrous assemblies with covalent bonds in a single network polymer remains challenging to engineer. Additionally, bioprinting of a synthetic tough hydrogel remains desirable. In **chapter VIII**, we took on the challenge of designing a synthetic mimic of the collagen biopolymer with extraordinary mechanical and bioprinting properties. To address this challenge, we proposed a biomimetic synthetic supramolecular/covalent strategy with the aim that supramolecular assemblies can self-assemble resulting in a fibrous hydrogel that then can be cross-linked for stability and tuning toughness and mechanical properties. We developed a BTA based macromonomer with norbornene handles on BTA (NB BTA). This macromonomer is self-assembled across multiple lengths scales to form a fibrillar and viscoelastic hydrogel. Taking inspiration from collagen's covalent cross-linking of fibrils, mechanical properties including strength toughness, and stiffness was tuned by covalent inter-

and intra- fiber cross-links. Without rupturing, hydrogel endured 90% compressive strain and 550% tensile strain. Hydrogel efficiently dissipated energy during cyclic loading and demonstrated recoverable hysteresis. In addition, we found that Nb BTA hydrogel was shear-thinning and could be 3D bioprinted into a cartilage tissue-like structure. Chondrocytes demonstrated good cell viability in bioprinted, injected, and bulk hydrogels. hMSCs spheroids bioprinted in Nb BTA hydrogels generated collagen II, strongly indicating the creation of chondrogenic tissue within the hydrogels.

In C**hapter IX,** we discussed why dynamic hydrogels are needed for biomaterials and tissue engineering. Different chemistries including dynamic covalent chemistry and supramolecular chemistry for tuning viscoelasticity and 3D bioprinting have been discussed with the future outlook.

Chapter X gives insight into the societal impact of this thesis and the valorization work done during this PhD thesis.

References:

(1) Goor, O. J. G. M.; Hendrikse, S. I. S.; Dankers, P. Y. W.; Meijer, E. W. From Supramolecular Polymers to Multi-Component Biomaterials. *Chem. Soc. Rev.* **2017**, *46* (21), 6621–6637. https://doi.org/10.1039/C7CS00564D.

(2) Mouw, J. K.; Ou, G.; Weaver, V. M. Extracellular Matrix Assembly: A Multiscale Deconstruction. *Nat. Rev. Mol. Cell Biol.* **2014**, *15* (12), 771–785. https://doi.org/10.1038/nrm3902.

(3) Frantz, C.; Stewart, K. M.; Weaver, V. M. The Extracellular Matrix at a Glance. *J. Cell Sci.* **2010**, *123* (24), 4195–4200. https://doi.org/10.1242/jcs.023820.

(4) Webber, M. J.; Appel, E. A.; Meijer, E. W.; Langer, R. Supramolecular Biomaterials. *Nat. Mater.* **2015**, *15* (1), 13–26. https://doi.org/10.1038/nmat4474.

(5) Tang, S.; Richardson, B. M.; Anseth, K. S. Dynamic Covalent Hydrogels as Biomaterials to Mimic the Viscoelasticity of Soft Tissues. *Prog. Mater. Sci.* **2021**, *120* (July 2020), 100738. https://doi.org/10.1016/j.pmatsci.2020.100738.

(6) Wang, H.; Heilshorn, S. C. Adaptable Hydrogel Networks with Reversible Linkages for Tissue Engineering. *Adv. Mater.* **2015**, *27* (25), 3717–3736. https://doi.org/10.1002/adma.201501558.

(7) Chaudhuri, O.; Cooper-White, J.; Janmey, P. A.; Mooney, D. J.; Shenoy, V. B. Effects of Extracellular Matrix Viscoelasticity on Cellular Behaviour. *Nature*. 2020, pp 535–546. https://doi.org/10.1038/s41586-020-2612-2.

(8) Ooi, H. W.; Hafeez, S.; Van Blitterswijk, C. A.; Moroni, L.; Baker, M. B. Hydrogels That Listen to Cells: A Review of Cell-Responsive Strategies in Biomaterial Design for Tissue Regeneration. *Mater. Horizons* **2017**, *4* (6), 1020–1040. https://doi.org/10.1039/c7mh00373k.

(9) Rosales, A. M.; Anseth, K. S. The Design of Reversible Hydrogels to Capture Extracellular Matrix Dynamics. *Nat. Rev. Mater.* **2016**, *1*, 1–15. https://doi.org/10.1038/natrevmats.2015.12.

(10) Morgan, F. L. C.; Moroni, L.; Baker, M. B. Dynamic Bioinks to Advance Bioprinting. *Adv. Healthc. Mater.* **2020**, *9* (15), 1901798. https://doi.org/10.1002/adhm.201901798.

(11) Cantekin, S.; de Greef, T. F. A.; Palmans, A. R. A. Benzene-1,3,5-Tricarboxamide: A Versatile Ordering Moiety for Supramolecular Chemistry. *Chem. Soc. Rev.* **2012**, *41* (18), 6125–6137. https://doi.org/10.1039/c2cs35156k.

(12) Vereroudakis, E.; Bantawa, M.; Lafleur, R. P. M.; Parisi, D.; Matsumoto, N. M.; Peeters, J. W.; Del Gado, E.; Meijer, E. W.; Vlassopoulos, D. Competitive Supramolecular Associations Mediate the Viscoelasticity of Binary Hydrogels. *ACS Cent. Sci.* **2020**, *6*, 1401–1411. https://doi.org/10.1021/acscentsci.0c00279.

(13) Aisenbrey, E. A.; Murphy, W. L. Synthetic Alternatives to Matrigel. *Nat. Rev. Mater.* **2020**. https://doi.org/10.1038/s41578-020-0199-8.

(14) Buehler, M. J. Nature Designs Tough Collagen: Explaining the Nanostructure of Collagen Fibrils. *Proc. Natl. Acad. Sci. U. S. A.* **2006**, *103* (33), 12285–12290. https://doi.org/10.1073/pnas.0603216103.

Chapter II

Hydrogels that listen to cells: a review of cell-responsive strategies in biomaterial design for tissue regeneration

Huey Wen Ooi [1] Shahzad Hafeez [1] Clemens van Blitterswijk [1] Lorenzo Moroni [1], Matthew B. Baker [1]

[1] Department of Complex Tissue Regeneration, MERLN Institute for Technology Inspired Regenerative Medicine, Maastricht University, P.O. Box 616, 6200 MD Maastricht, The Netherlands.

Published in: **Materials Horizons** (2017)

Ooi, H. W.; Hafeez, S.; Van Blitterswijk, C. A.; Moroni, L.; Baker, M. B. Hydrogels That Listen to Cells: A Review of Cell-Responsive Strategies in Biomaterial Design for Tissue Regeneration. *Mater. Horizons* **2017**, *4* (6), 1020–1040. https://doi.org/10.1039/c7mh00373k. This chapter was heavily adapted from the publication to be included in this thesis.

Abstract:

The past decade has seen a decided move from static and passive biomaterials to biodegradable, dynamic, and stimuli-responsive materials in the laboratory and the clinic. Recent advances toward the rational design of synthetic cell-responsive hydrogels—biomaterials that respond locally to cells or tissues without the input of an artificial stimulus—have provided new strategies and insights on the use of artificial environments for tissue engineering and regenerative medicine. These materials can often approximate responsive functions of a cell's complex natural extracellular environment and must respond to the small and specific stimuli provided within the vicinity of a cell or tissue. In the current literature, three main cell-based stimuli can be harnessed to create responsive hydrogels: 1) enzymes 2) mechanical force, and 3) metabolites/small molecules. Degradable bonds, dynamic covalent bonds, and non-covalent or supramolecular interactions are used to provide responsive architectures that enable features ranging from cell selective infiltration to control of stem-cell differentiation. The growing ability to spatiotemporally control the behavior of cells and tissue with rationally designed responsive materials can allow control and autonomy to future generations of materials for tissue regeneration, in addition to providing understanding and mimicry of the dynamic and complex cellular niche.

Introduction

A cell, and its niche, represent an instructive symphony of complex interactions, feedback loops, and signals aimed at controlling cellular behavior and function in real-time. The cell's extracellular matrix (ECM) provides the cell with a physical environment, a setting, to exist and communicate within. Made predominantly of proteoglycans and fibrous assemblies of proteins, the ECM provides a multitude of functions, including mechanical and structural support, spatio-temporal growth factor presentation, traction and movement, and the ability to remodel in response to a cell or external stimuli.[1,2] Made from a few key components, the responsiveness, instructiveness, and variability of the ECM (with respect to different tissues and organs) has long been a source of emulation. The recapitulation, control, and amelioration of ECM-cell interactions all remain significant targets for rationally designed systems.

Regenerative medicine aims to create therapies to replace or regenerate cells, tissues, and organs towards the restoration of impaired function resulting from genetic defects, disease, trauma, or aging; tissue engineering focuses a bit more to apply materials, cell biology, fabrication, and bioengineering strategies to control the growth or regrowth of tissues from basic cellular units, often progenitor cells.[3,4] In both regenerative medicine and tissue engineering, there is a large need to develop controllable materials that recapitulate functions of the natural ECM including cell signaling, delivery of bioactive compounds at controlled rates, tunable and responsive mechanical properties, yet can still allow for regeneration and growth of the nascent tissue. Viewing Nature as a source of inspiration, the materials design within these fields focuses on mimicking features of a cell's natural environment.

Various three-dimensional (3D) scaffolds that share aspects of the native ECM, including electrospun meshes,[5–7] patterned surfaces,[8,9] and 3D printed scaffolds have been investigated;[10–12] however, hydrogels remain one of the most promising ECM replacements. Hydrogels are made out of a 3D network of cross-linked hydrophilic macromolecules, which possess the ability to immobilize high amounts of water (ca 90–>99%). The natural ECM, itself, is a hydrogel. Many of the individual components of the ECM can form hydrogels (e.g., collagen, elastin). Synthetic hydrogels are a natural choice for the creation of artificial environments around cells.

The utilization of hydrogels for biomedical applications started approximately 60 years ago, with the invention of contact lenses from cross-linked poly(hydroxyethyl methacrylate) (PHEMA) networks.[13] Henceforth, hydrogels have played an increasingly important role in the design of biomaterials for drug delivery,[14–16] tissue engineering,[15,17–20], and regenerative medicine.[17,21] Although a wide array of hydrogels have been investigated, ranging from purely natural to purely synthetic polymers, each hydrogel holds its advantages and limitations. For example, naturally derived hydrogels often provide desirable performance, but are difficult to standardize and modify; synthetic hydrogels are highly customizable, yet can be difficult to impart complex mechanical properties and the correct bioactivity. Consequently, the search for hydrogel systems that can best provide cells with a designed and controllable alternative microenvironment remains an active area of research.

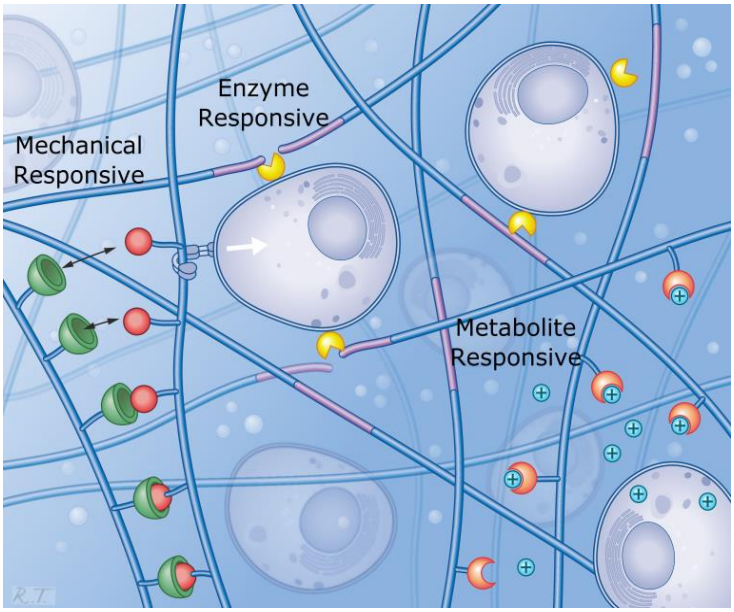

Figure 1. Shown schematically are the three main strategies for the creation of cell-responsive materials. Enzymatic catalysis (top center) of hydrogel breakdown has been extensively used in tissue engineering to allow matrix remodelability. By incorporating enzyme cleavable units into the hydrogel structure (e.g. MMP cleavage sites, depicted in purple), cells are able to infiltrate and migrate through the material via the action of enzymes (depicted in yellow) cleaving the hydrogel network (blue fibers). Most recently, mechanically responsive hydrogels (bottom left) have been developed to allow for response based on a cell's traction forces. Shown schematically, a cell transfers traction forces to the matrix via integrins (light blue), with can remodel or rearrange dynamic interactions in the hydrogel, illustrated as the binding between a green cup and a red ball. Still in their infancy, such materials heavily rely on dynamic covalent and supramolecular interactions. Metabolite and small molecule responsive (bottom right) hydrogels represent a broad-class of materials that sense and respond to small molecules, proteins, and metabolic by-products around a cell or tissue. As an example, depicted are pH sensitive receptors (orange) that become charged (light blue spheres). Such metabolite responsive materials often rely on highly specific non-covalent interactions, and are largely biohybrid type materials.

With significant progress in the field of polymer chemistry, synthetic chemistry, and supramolecular chemistry, the capacity to design and tailor polymer architecture and hydrogel networks have advanced.[22–24] No longer confined to synthesizing covalent and static networks from conventional radical cross-linking methods, current reports of instructive, stimuli-responsive, and biodegradable hydrogels bring closer the realization of complex and dynamic systems that mimic ECM functions. Aligned with these efforts, the focus has been shifted to exploring different chemistries to form dynamic hydrogels. Properties like cell-mediated remodeling, cell vitality, growth factor release, strain-stiffening, and viscoelasticity are being introduced through the incorporation of cleavable bonds, reversible bonds, supramolecular bonds/polymers, self-assembly, or flexible polymer backbones. Several excellent reviews on this current trend have come out in the last few years.[25–30]

Dynamic hydrogel architectures have found success as responsive materials to large external stimuli, yet they also have the potential to produce responsive materials that act biomimetically upon cues from a cell.[31] For example, the ability of a material to release growth factors in response to enzymes from a nearby cell can be viewed as a significant advance over a material relying entirely on external light irradiation. Consequently, current efforts to sense and respond to cells have quickly gained steam. As we obtain greater skill in rational design and more insight into cellular behavior, we are on the cusp of a new biomaterials revolution. Fully autonomous hydrogels that can sense, respond, and influence cells aim to become truly smart biomaterials of the future.

This review will delineate and focus attention on the growing trend of cell responsiveness within the hydrogel and biomaterials community. We have chosen to focus on systems designed for tissue engineering and regenerative medicine; however, significant advances from other fields (e.g. drug delivery) will also be presented with an eye toward their applications in regenerative medicine. First, we will quickly introduce the main behaviors of a cell (inputs) that can be utilized to engineer such responsive hydrogels. Secondly, we will briefly introduce the prevalent chemistries used in the construction of such materials. In the main body of this review, successful examples will be broken down into three sections, namely enzyme-responsive, mechanical-responsive, and metabolite/small-molecule responsive hydrogels (**Figure 1**). In conclusion, we will look forward at the potential of cell-responsive hydrogels and entertain the idea that dynamic and responsive synthetic environments can bring us close to the creation of an artificial ECM.

Cell outputs

The chemical makeup and manner in which the multicomponent ECM is assembled direct cellular behavior. Reciprocally, the responsive and weak interactions between the ECM components create a dynamic environment that can respond to and influence the activities of a nearby cell.[32] For example, the spatio-temporal control of growth factors is a major role of the ECM and regulates many *in vivo* processes. The ECM can sequester transforming growth factor-β (TGFβ) in an inactive form, and release its active form in response to cellular traction forces during tissue remodeling.[33] Additionally, laminin cleavage via matrix-metalloproteases (MMPs) has been shown to release fragments capable of regulating stem cell differentiation.[34] Numerous ECM components are released or presented in response to cellular cues, such as mechanical force or protease activity.[35]

When designing materials aimed at mimicking such responsive functions, it is crucial to understand what cues are both produced by a living cell and have been shown to trigger responsive materials. Shown schematically in **Figure 1**, three main cell outputs have been employed as stimuli in responsive hydrogels: 1) enzymes, 2) mechanical force, and 3) metabolites/small molecules.

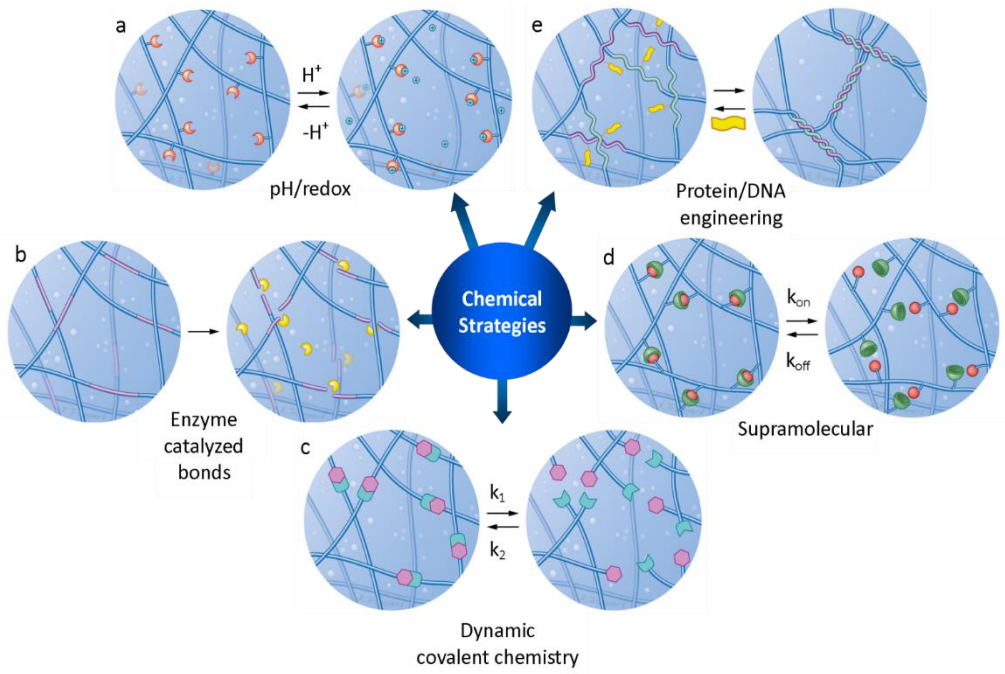

Figure 2. Chemical strategies commonly utilized for cell-responsive hydrogels. a) pH (redox) sensitive units (orange) can change protonation (oxidation) state, often becoming charged (blue positive charges), leading to changes in binding constants or the osmotic pressure within the hydrogel; e.g. amine or acid protonation, disulphide reduction b) enzyme (yellow) catalyzed irreversible bond breakage of specific peptide sites (purple) in the hydrogel network (or precursor); e.g. MMP specific cleavage, enzymatic cleavage of supramolecular hydrogelator precursor c) dynamic covalent chemistry whereby two units (green and pink) can dynamically, and reversibly, form covalent bonds depending on their reaction rates k_1 and k_2 and equilibrium constant (K_{eq}); e.g. hydrazone exchange/hydrolysis and disulphide formation, d) supramolecular chemistry shown as the reversible binding and unbinding of a red ball and a green cup based on the binding constants k_{on}, k_{off}, and equilibrium (K_{eq}); e.g. polymer aggregation, host-guest interactions, H-bonding units, and protein-small molecule binding, and e) protein/DNA engineering as shown by two engineered biomolecules in the network (light green and purple) reversibly bind and undergo conformational changes in response to the presence of an signal (yellow); e.g. incorporation of shape changing proteins (calmodulin, adenylate kinase) and RNA aptamer binding.

Enzymes

The fundamental role of enzymes as catalysts is to increase the rate of biochemical reactions. Enzymes are ubiquitous in living systems,[36] have high specificity for chemical transformations, and maintain high activity under physiologic conditions, making them ideal triggers for the chemical design of responsive hydrogel systems. Furthermore, *in vivo* cells highly rely on enzymes for the regulated remodeling of the natural ECM, a process crucial for the maintenance of normal biological functions.[2] Differences in enzyme expression is associated with many events including stem-cell differentiation, tissue repair, and pathological disorders. The altered expression level of specific enzymes can be used to catalyze a reaction in hydrogels for controlled release or degradation at desired sites or under certain events.[37,38]

Mechanical Force

In the last decade, extensive research has been carried out to investigate the influence of mechanical forces generated between cells and their environment. Researchers now have developed an understanding of the forces generated by cells in tissue remodeling and cellular functions ranging from cell adhesion, migration, proliferation, differentiation, and morphogenesis.[39–42] Generally, cells first sense the matrix and pull to deform the matrix. These contractile forces are generated by actomyosin contraction and are transmitted to the ECM via focal adhesions—an integrin-containing multi-protein complex connecting the cytoskeleton to the ECM. Cellular traction forces are in the range of piconewtons to nanonewtons and occur at the nanometer to micrometer length scale,[43] yet the mechanical feedback a cell receives from its environment can activate specific signaling pathways or alter gene expression in a surprisingly quick fashion.[44] There are numerous reviews on the complex interplay between a cell's mechanical sensing framework and its ECM environment.[37,45–48] Only in the past few years has this understanding been translated to materials that can also alter their properties in response to the small mechanical forces generated by a cell.

Metabolites and small molecules

Metabolites and small molecules produced (or consumed) by a cell also offer the possibility to be used as a trigger for cell-responsive systems. Metabolism (a set of chemical reactions taking place within a cell) is very important for a cell to regulate pathways and maintain critical concentrations of important building blocks (and byproducts) within and outside of a cell. Any up and down-regulation of these pathways leads to a change in the extracellular environment. For example, changes in the reductive power[49] and pH around cancerous cells[50], higher glucose levels in diabetic patients[51], and higher levels of reactive oxygen species under stress[52] have all been successfully utilized to create responsive hydrogel systems. In natural systems, cell metabolites are extensively used in signaling pathways, can initiate very specific interactions, and can maintain integrity and activity over long ranges. However, the difficulty and challenge lies in translating the sensitivity, specificity, and amplification, of these sometimes small differences to synthetic hydrogel systems.

Chemistries developed

The range of chemical structures and systems available to engineer cell-responsive hydrogels is a limited, but growing, set. Such chemistry must be reversible (or degradable), both stable and responsive under physiologic conditions, synthetically accessible, and ultimately, cytocompatible. Although all the systems described rely on water-soluble macromolecules, it is the incorporation of dynamic chemical units that provide responsive function. To highlight the characteristics of available systems, employed approaches can be categorized into five main chemical strategies. Shown schematically in **Figure 2**, cell-responsive materials mainly rely on pH responsiveness, enzyme-catalyzed bond breakage, dynamic covalent chemistry, supramolecular interactions, and protein or DNA engineering. One should note that often, more than one category is

implemented in more complex systems; the illustrative examples herein have been classified according to the main strategy employed.

pH responsive

The earliest hydrogel architectures to allow for responsive biomaterials were pH-responsive matrices. Such pH-responsive hydrogels normally contain amines (pKa 8–10) or acids (pKa 4–6) that are protonated/deprotonated to form charges within the hydrogel network. This change in the protonation state introduces swelling/deswelling due to changes in the ionic character of the network. In a classic example, poly(acrylic acid) hydrogels swell at higher pHs via the formation of the ionic carboxylate. General acid or base-catalyzed hydrolysis of polymer backbones can also be utilized for the creation of pH-responsive materials.

Such pH-responsive approaches have been extensively studied for drug delivery,[53] but often lack the sensitivity or specificity needed for fine control in more complex applications. To overcome this limitation, often pH-responsive hydrogels are coupled with enzymes that catalyze the conversion of a signal into an acidic (or basic) product and lowering (or rising) the local pH. An example is the glucose/glucose oxidase (Glu/GOx) system that produces gluconic acid. This type of pH-responsive hydrogel has been used extensively for glucose-responsive and insulin-releasing hydrogel systems.[54]

Enzyme-catalyzed bond breakage

One of the most visible cell-responsive strategies in tissue engineering has been enzyme-catalyzed lysis of bonds. In such a strategy, specific peptide sequences, or enzymatically cleavable bonds (e.g. phosphates, esters) are engineered into the hydrogel network or into hydrogel precursors. These systems are fairly stable in the absence of enzyme activity, but readily degraded, or activated, in the presence of a cell secreting the correct enzyme. Various enzymes including MMPs, elastase, alkaline phosphatase (ALP), esterases, thrombin, plasmin, and cathepsin K have already been utilized to create functionally responsive hydrogels.[55] One will notice an absence of enzyme-catalyzed bond formation in this area of responsive hydrogels.

Dynamic covalent chemistry

Dynamic covalent chemistry (DCvC)[56] has played a significant role in the current trend toward dynamic hydrogels. Sometimes classified as covalent adaptable networks, hydrogels based on DCvC are characterized by the breaking and reforming of covalent bonds based on their equilibrium (K_{eq}) and rate constants (k_{off} and k_{on}). These networks generally maintain the number of linkages or cross-links based on the K_{eq} value, and the time of the bond is generally governed by k_{off}.[57] Several DCvC systems are biocompatible and have already been used to form hydrogels, including boronic acids,[58] thioesters,[59] hydrazones,[60,61] imines,[62,63], and disulfides.[64,65] However, hydrazone/imine and disulfide systems have recently come to the forefront of use. Hydrazones remain dynamic under physiologic conditions, imines become more dynamic with drops in pH, while disulfides are responsive to local changes in sulfide concentration or reductive power of

the environment. Most DCvC systems are tunable via physical organic chemistry principles, and the adaptation of existing systems for use under physiologic conditions remains an active area of research.

Supramolecular

Supramolecular assemblies and non-covalent interactions have also been rich sources for the creation of dynamic and responsive biomaterials.[26] Nature, itself, relies heavily on the use of supramolecular assemblies. In a truly biomimetic fashion, the engineering of hydrogels designed from specific, directional, tunable, and reversible non-covalent interactions has enabled the creation of modular platforms with tunable physical, chemical, and biological information.[66,67] Supramolecular hydrogels[68] owe their properties to the binding, association, or assembly of discrete units. The assembly of these units is again governed by an equilibrium constant (K_{eq}), which is simply a ratio of association (k_a) and disassociation (k_d) kinetics. Numerous supramolecular systems are capable of creating hydrogels including host/guest interactions,[69,70] directional hydrogen bonding,[71,72] peptide amphiphiles,[73–75] metal-ligand coordination,[76] and small molecule gelators.[77] In theory, such systems built on weak and non-covalent interactions are well situated to quickly respond to changes in the environment or secreted factors. Although prolific as materials to drive tissue formation,[75] supramolecular materials are currently under-represented in the area of cell-responsive hydrogel systems. Progress in rational design, characterization, and control over the sometimes sensitive supramolecular interactions remain both a hurdle, and a promising research area.

Protein/DNA engineering

When creating bioresponsive systems, utilizing nature's own building blocks is a pragmatic approach. Numerous responsive enzymes and protein/protein complexes are known, expressible, modifiable, and purifiable from recombinant protein expression. Integrating such functional or responsive protein units within the network of a hydrogel allows a biosynthetic hybrid approach to materials that can sense, respond, and influence cellular behavior.[78–80] In addition, DNA origami and DNA aptamer technologies allow for the formation of spatially controlled materials and high specificity to the binding of specific analytes.[81,82] While such biohybrid approaches are less scalable and expensive for the production of hydrogels, their specificity and fine control can justify the high cost.

Enzyme responsive systems

Extensive research has developed enzyme-responsive hydrogels for applications in drug delivery,[83,84] imaging,[85] diagnostics,[86] tissue engineering,[87], and regenerative medicine.[21] The design of enzyme-responsive hydrogels that enable cell and/or tissue-specific responses is currently based on two types of mechanisms: 1) hydrogel networks with enzyme cleavable cross-links or tethers; 2) supramolecular assemblies generated from the enzymatic conversion of a non-self-assembling precursor. These mechanisms mimic the breakdown and the formation,

respectively, of ECM; however, enzymatically based systems to regulate both have not been developed.

Proteolytically-degradable hydrogels

Proteolytic-sensitive hydrogels, hydrogels engineered with enzyme-sensitive cross-links of customized peptide sequences, directly enable modulation of hydrogel degradation based on cell-secreted enzymes (shown schematically in **Figure 3a**). When compared to their static and non-degradable counterparts, cells can spread, migrate, and proliferate more freely within these protease-sensitive hydrogels.[88,89] Cellular infiltration, vascularization, tissue remodeling, and enhanced differentiation capacity of stem cells have all been observed in these biomimetic hydrogel systems.

One of the earliest works to utilize enzymatically degradable gels, from the 1980s, was based on cross-linked poly(2-hydroxyethyl-L-glutamine) (PHEG, a poly(α-amino acid)). This hydrogel showed significant degradation during the post-implantation inflammatory response, which was attributed to the presence of proteolytic enzymes.[90] Spurred from such initial studies, the field of proteolytically-degradable hydrogels has become widely studied in the context of cell-responsive biomaterials, as shown by several thorough reviews specifically on this topic.[91–93]

More recent approaches have relied heavily on the use of cross-links sensitive to MMPs, a large family of proteases that affect the natural breakdown of the ECM during processes such as tissue resorption and remodeling.[94] Although there is often overlap between MMPs and their substrates, MMPs can show substrate specificity,[95] and the rate of degradation between MMP cleavable sites can vary significantly.[96] Depending on the application in sight, careful choice of peptide substrates can be matched with enzymes present in targeted sites, events, or cell types.

Pioneering this approach of MMP degradable gels for tissue engineering was a 4-arm poly(ethylene glycol) (PEG) system with terminal vinyl sulfones to enable Michael-type additions for functionalization with cysteine-containing biomolecules. By cross-linking the system with MMP cleavable peptides, and functionalization with thiol-containing adhesive RGD sequences, hydrogels were created that cells could attach, degrade, and migrate through.[97] By incorporating growth factors like vascularization endothelial growth factor (VEGF) or bone morphogenic protein (BMP-2), these systems showed tissue formation with vascularization,[98] and bone regeneration,[99] respectively, in *in vivo* models while non-degradable cross-linked hydrogels were free of cellular infiltration (**Figure 3c**). The modularity and tailorability of this straightforward PEG-vinyl sulfone system have affected the creation of highly customizable cell culture environments. For example, recently a stiffness-switching hydrogel was designed to replace Matrigel in intestinal organoid expansion[100]—a previous bottleneck for organoid technologies. Of note, the most successful hydrogel was not the enzyme-responsive gel tested (collagen I sequence); a hydrolyzable ester linkage with slowed degradation provided the relevant timescale for this specific application.

Due to the synthetic accessibility of alkenes and the common presence of thiols in biomacromolecules, thiol-ene reactions like the Michael addition and photo-activated thiol-ene, are natural choices for hydrogel formation with biomolecules. Some of the commonly used alkenes for Michael addition and photo-initiated thiol-ene to form hydrogels in a biological environment are presented in **Figure 3b**. It should be noted that methacrylates can undergo Michael addition under appropriate conditions, yet these conditions are usually not cell-compatible.[101]

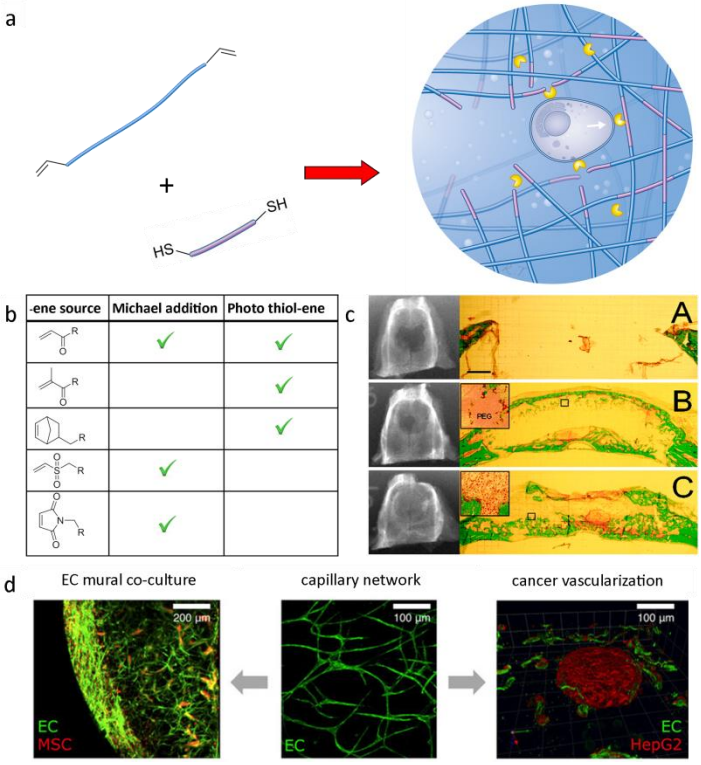

Figure 3. a) Water soluble polymers (blue) containing activated double bonds can be cross-linked with thiol terminated peptide sequences (purple) to form enzyme degradable hydrogels. A cell can remodel and migrate through these hydrogel networks via proteolytic enzymes (yellow) cutting covalently attached peptides (purple) within the network. b) Polymer chains (e.g. multi-arm PEG) are commonly functionalized with (meth)acrylates, norbornene, vinyl sulfone, and maleimides. Advantages of MMP-degradable hydrogels are shown in c) rat calvarial defects 4 weeks after implantation. Bone formation was observed within gels, which were (A) not susceptible to MMP degradation, (B) with moderate degradation by MMP, and (C) highly susceptible to MMP degradation. Assessed by radiography (left) and histology (right), gels with highly degradable MMP networks showed significantly higher bone formation than gels with less or no MMP-sensitive sites due to cellular infiltration and remodelling. d) MMP-cleavable starPEG-heparin hydrogels provides a platform for extensive *in vitro* studies of heterocellular cell-cell interactions between endothelial cells and mural cells (left), as well as heterotypic cell-cell contacts via a tumor angiogenesis model (right). (c) was reprinted from reference.[99] Copyright (2003) National Academy of Sciences. (d) was reproduced with permission.[103] Nature Publishing Group 2014.

PEG-maleimide has shown some significant improvements in cross-linking speed and efficiency over other systems (including vinyl sulfone).[102] Multicomponent PEG-maleimide hydrogels containing RGD, MMP degradable cross-links, VEGF, and hepatocyte growth factor (HGF), have been shown to increase angiogenesis in a rat infarcted myocardium.[37] Furthermore, injectable microgels based on a similar architecture have shown increased vascularization in the dorsum of mice.[38] Microgel slurries have emerged as a convenient workaround to the lack of injectability for covalently cross-linked hydrogels.

Michael-type MMP cleavable hydrogels have also proven utility as a laboratory platform to study tissue formation and the study of cell-cell interactions. For example, an MMP-cleavable biohybrid star PEG/heparin hydrogel system has been optimized to support the morphogenesis of endothelial cells.[103] Due to its susceptibility to remodeling, the hydrogel platform enabled *in vitro* studies of heterocellular cell-cell interactions between endothelial cells and other cells (**Figure 3d**: left), as well as heterotypic cell-cell contacts using a tumor angiogenesis model (**Figure 3d**: right).

Michael-type additions typically require a slightly alkaline pH to occur (p*K*a of the Michael donor), which precludes the use of some base-sensitive molecules.[104] Photo-initiated thiol-ene conjugations can overcome this limitation. Photo-initiated thiol-ene occurs quickly and in high yield at neutral pH, which can be beneficial for in-situ gelation. Furthermore, spatio-temporal control (via light) of the biomolecule conjugation and gelation has resulted in several novel materials applications in biofabrication. Recent advances include complex patterns within hydrogels[105–107] and the development of photo-crosslinkable thiol-ene hyaluronic acid[108] and polyglycidol[109]-based bioinks for 3D printing of cell-hydrogel mixtures.

An excellent example of photo-initiated thiol-ene formation is the thiol-norbornene photopolymerizable 4-arm PEG hydrogels, cross-linked with an MMP degradable sequence (KCGPQG↓IWGQCK).[110] When hMSCs were encapsulated in such hydrogels, significant increases in cell spreading were observed. Furthermore, the osteogenic, adipogenic, and chondrogenic differentiation capacity of hMSCs increased with increasing MMP-degradability of the networks, showing a clear link between differentiation capacity and the ability of a cell to remodel the synthetic ECM.

Not only for degradation, enzymes can also be used to trigger localized release through the tethering of active molecules on the cross-linker. For example, norbornene-functionalized PEG hydrogels were photo-cross-linked with MMP releasable pro-angiogenic sequences. In this design, pro-angiogenic peptides ($SPARC_{113}$ and $SPARC_{118}$) were end-capped with IPES↓LRAG sequences, which are sensitive to MMP cleavage. These hydrogels successfully promoted angiogenesis when injected subcutaneously in mice in an entirely degradation-dependent manner.[111] However, compared to other pro-angiogenic protein delivery hydrogel systems, the release profile of these enzyme-degradable systems was much shorter and would still need further optimization.

Applying such strategies to synthetically modified naturally derived polymers, MMP-cleavable hyaluronic acid (HA) hydrogels that shut down or allowed cell-mediated remodeling to have also been created. By functionalizing HA with both maleimides and methacrylates, thiol-ene cross-linking via an MMP-cleavable peptide (GCRDVPMS↓MRGGDRCG) could (or could not) be followed by a secondary non-degradable photo-initiated cross-linking of the methacrylates.[112] In these hydrogels, osteogenic/adipogenic differentiation of human mesenchymal stem cells (hMSCs) was observed to be directed mainly by degradation-mediated cellular traction. Permissive (remodelable, without secondary cross-linking) matrices gave rise to osteogenesis, while non-permissive (non-remodelable, with secondary cross-linking) matrices led to adipogenesis. Interestingly, when a stem cell's environment was switched from permissive to non-permissive via delayed secondary cross-linking, the cell also switched from an osteogenic to adipogenic phenotype. The osteogenic cell morphology remained, yet an adipogenic phenotype dominated. Recently, this same group also successfully utilized the efficiency of thiol-ene photochemistry to print fibroblast-laden HA modified with norbornene groups.[108] To highlight the versatility of the 3D printing technique, they created complex hydrogel structures comprising of MMP-degradable and non-degradable regions and observed cell spreading throughout the printed hydrogel when a degradable linker was used.

Moving towards complexity and autonomous systems, the versatility of MMP-cleavable hydrogels has been shown in the rational design of a negative feedback loop to inhibit MMP activity.[113] By loading an MMP cleavable hydrogel network with a physically-associated MMP inhibitor (TIMP-3), hydrogels were designed to buffer the local MMP activity. A significant decrease in MMP activity was observed after the delivery of these injectable hydrogels to an infarcted myocardium (MMP overexpressed region) in a pig model. Controlled delivery of MMP inhibitors is always a challenge, due to dose-limiting side effects; however, this hydrogel system is a significant example of how cell-responsive hydrogel systems can be designed for feedback loops to autonomously control pathological levels of enzyme expression.

MMP is not the only enzyme trigger used for hydrogels in tissue engineering and regenerative medicine. Hydrogels cross-linked with cathepsin K-sensitive peptide sequences have been shown to specifically degrade in the presence of osteoclasts,[114] while elastase-sensitive Ala-Ala repeat segments incorporated in PEG hydrogels have been shown to allow both in vivo degradation and cellular infiltration in mice[115] and controlled protein delivery.[116,117] Thrombin, a key enzyme of the blood coagulation cascade, has been used to trigger anti-coagulant release to prevent clotting. A modular feedback-loop PEG hydrogel system with thrombin-sensitive peptide sequences has been developed to prevent clotting through the release of heparin on demand,[118] or respond to and reverse clot formation via the release of tissue plasminogen activator.[119] Both of these thrombin-mediated hydrogels have been shown to successfully suppress critical points in the blood coagulation cascade.

The highlighted examples throughout this section only represent some of the more commonly used enzymes and some examples of their complimentary peptide. More exhaustive lists of enzymes/peptides can be found elsewhere.[36,91,95,96,120]

Enzymatic assembly of nanostructures

Enzymes can not only be used to break down hydrogels but also to induce hydrogel formation via the self-assembly of low-molecular-weight hydrogelators. This enzymatically triggered build-up of fibrous nanostructures can mimic the enzymatic remodeling and production of the ECM. The enzyme-triggered dynamic assembly, and in the future disassembly, is potentially a promising strategy to mimic the behavior of natural fibers in the cellular environment.

Most enzyme-responsive supramolecular hydrogelators are peptide-based and are converted from an inactive (non-self-assembling) to an active (self-assembling) form via hydrolysis or condensation of peptide precursors (**Figure 4a**).[77] Generally, a known self-assembling unit is conjugated to an enzymatically labile group that inhibits self-assembly. Upon cleavage of this inhibitor, hydrogelators then freely self-assemble to form nanostructures, mainly via hydrophobic interactions, hydrogen bonding, electrostatics, and π-π interactions. Through the design of the peptide sequences and the dictation of the self-assembly pathways, the morphology of the self-assembled structures can be controlled and used to direct cellular behavior.[30] A majority of the work reported to date on enzymatically triggered hydrogelation has not yet been applied to tissue regeneration but has focused on cell death and entrapment for cancer therapy.[77] Despite this, these systems carry interesting design principles, and their application towards tissue regeneration is overdue.

An illustrative example of enzyme-triggered nanostructure assembly can be seen in systems based of Naphtyl-Phe-Phe self-assembling units. Towards creating enzyme-sensitive self-assembling units, a monomer (shown in **Figure 4b**) was designed with three functional parts: a dipeptide capable of forming a hydrogen-bonding motif, a naphthyl group to provide a hydrophobic driving force to self-assembly, and an enzymatically cleavable pendant ester of the butyric diacid, which provides electrostatic repulsion to prevent self-assembly.[121] Upon exposure to esterases within HeLa cells, the anionic butyric acid is removed, and the resultant hydrogelators self-assemble to form intracellular nanofibers, leading to cell death.

Other self-assembling systems have also been created with specific MMP cleavable tails. A peptide-lipid conjugate precursor (palmitoyl-GGGHGPLGLARK-$CONH_2$) has been successfully designed with an MMP-7 cleavage site that removed a highly charged Arg-Lys sequence. The supramolecular hydrogelator self-assembles intracellularly into nanofibers upon enzymatic cleavage, leading to the death of cancer cells.[122] Importantly, this supramolecular system showed high cytotoxicity to five different cancer lines (HeLa, MIAPaCaII, SKBR3, MCF-7, A431), yet low cytotoxicity to normal cells (microvascular endothelial cells and pancreatic epithelial cells), even in co-culture situations.

Recently, the ability of the enzyme to induce self-assembly to enable both cell and organelle-specific targeting was shown by conjugating triphenyl phosphinium (TPP), a redox modulator capable of targeting cancer mitochondria, to an enzyme inducible tetra-peptide precursor capped with a fluorophore (4-nitro-2,1,3-benzoxadiazole, NBD).[123] The tetra-peptide precursor, ((NBD)-FFYpK(TTP)) undergoes dephosphorylation selectively in the environment of cancer

cells (upregulated ectophosphatases). The conjugate then self-assembles is endocytosed by cancer cells, escapes from lysosomes, and the TPP specifically targets the mitochondria.

Enzyme-responsive self-assembling systems have also been employed to image local enzymatic activity. Direct attachment of fluorophores to enzymatically self-assembling systems[85] and co-assembly strategies[124] have allowed the imaging of organelles within cells and enhanced theranostic treatments, respectively. Imaging of fluorescent nanostructures in breast cancer cells (MDA-MB-468) has even been shown via a bond-breaking bond-forming condensation to create a fluorescent monomer upon enzymatic cleavage (among other stimuli).[125]

In an advanced enzyme-responsive self-assembly system, Liang and co-workers designed a small-molecule hydrogelator that can change its self-assembled nanostructure, depending on the cellular environment (**Figure 4c**).[126] In the extracellular matrix, the 2-cyano-6-amino benzothiazole (CBT)-based precursor (C(SEt)EY(H_2PO_3)FFG-CBT) undergoes dephosphorylation, in response to ALP, forming a hydrogelator which self-assembled into nanofibers in the extracellular environment. The fibers underwent endocytosis where

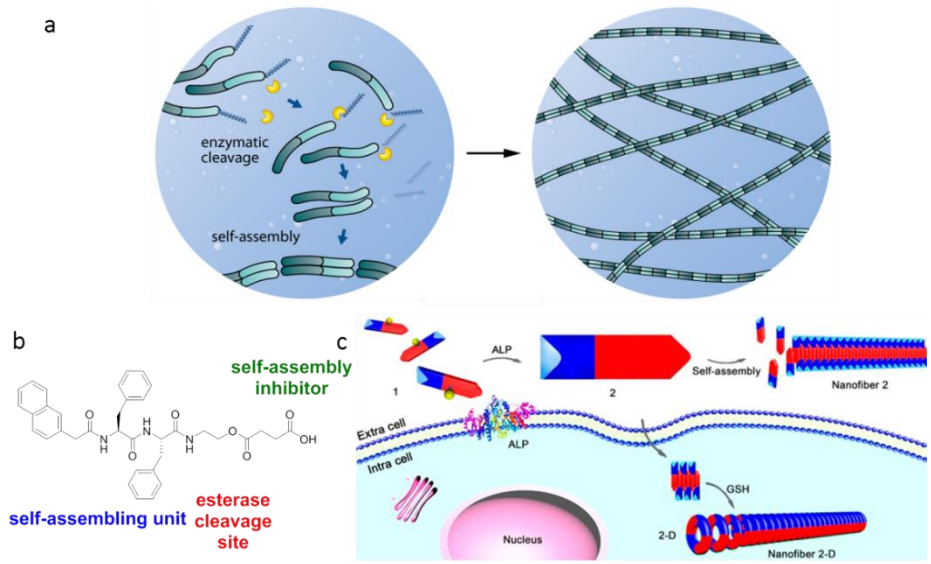

Figure 4. a) General schematic of an enzyme-triggered self-assembly mechanism. Peptide based precursors (shaded green units) are equipped with a tail (blue), that prevents self-assembly. Upon specific enzyme (yellow) cleavage, the tail is removed and the active hydrogelator is formed, assembling into a fibrous network (right). Often these hydrogelators can self-assemble into several nanostructures. b) A Nap-C(O)-FF based unit possesses all of the characteristic design elements. A self-assembling peptide with a hydrophobic moiety (naphthalene) to drive self-assembly and a dipeptide unit (Phe-Phe) as acceptor/donor of hydrogen bonds, an enzyme cleavable bond (esteraste, ester), that can remove a self-assembly inhibitor (deprotonated carboxylic acid).[121] c) Self-assembly of a cyano-6-aminobenzothazole (CBT) based precursor 1 into nanofiber 2 was catalyzed by extracellular ALP removal of a phosphate that prevented self-assembly. After cellular uptake of nanofiber 2, reduction of a protected thiol by glutathione (GSH) in the intracellular environment leads to intermolecular disulfide formation (hydrogelator 2) and the formation of the second nanofiber (2D). (c) was reprinted with permission.[126] Copyright (2016) American Chemical Society.

intracellular glutathiones (GSH) reduce the disulfide bonds of the protected cysteine residue (Cys(SEt)), allowing intermolecular cyclic dimers of the hydrogelator to form. This new molecular structure led to the formation of different morphology of nanofibers. The environmentally specific self-assembly was validated through *in vitro* studies with HeLa cells and characterization of the structures and compounds formed extra- and intracellularly when ALP or GSH was induced; however, the effects of this differential self-assembly system on the cells have not yet been fully reported.

While the majority of research on self-assembling structures has focused on homochiral molecules, in particular L-amino acids, there have also been increasing efforts to use D-amino acids and mixtures.[127] In the molecular design of enzyme-responsive supramolecular hydrogelators, simple changes in chirality can control the interactions of the self-assembled system with target cells. For example, molecules with more D-amino acid substitution were found to be more toxic than their corresponding enantiomer potentially due to their resistance toward proteolysis.[128] The accumulation of nanoscale networks in the pericellular space hindered regular cellular activities, such as migration and adhesion, and led to cell apoptosis. Based on these findings, nanoscale hydrogel networks have been developed as inhibitors of cancer cells;[129] however, inhibition of migration and adhesion can also be effectively used to control tissue formation. In future designs of chiral self-assembling structures for biomaterials, it is clear that the chirality of each amino acid is essential to control the morphology, degradation, and cell signaling behavior of the resultant nanostructures.[130]

Prospects

Several other enzyme-responsive systems present concepts that hold potential for the future design of biomaterials for use in tissue engineering and regenerative medicine. For example, Roberts et al. have developed a dynamic PEG-grafted surface with elastase-sensitive dialanine-protected RGD peptides.[131] The protected-RGD surfaces were shown to have lower, while the elastase deprotected-RGD surface had higher amounts of cell spreading and adhesion. Therefore, when MSCs were cultured on these surfaces, they showed a change from a growth state (low adhesion) to a differentiating state (high adhesion) upon elastase addition. Although this system was not shown to be cell-responsive (exogenous delivery of elastase), the use of enzyme triggers to control the phenotype of progenitor cells paves the way to develop cell culture environments that can control phenotypic changes in cells and tissue formation.

In living systems, enzymatic processes are often part of a feedback network. Mimicking such feedback loops, a hydrogel system with both enzymatically cleavable cross-links and hydrolytically activated cross-links (thioester/maleimide) has been designed.[132] In-depth studies on the reaction kinetics have led to fine control of gel transitions (gel-gel or gel-liquid-gel) based on time and enzyme concentration. The incorporation of such a design in the development of hydrogels will allow progress toward more complex materials, which have pre-programmable responses to environmental biochemical triggers.

Despite advances in using enzymes to create cell-responsive hydrogel systems, there are some limitations. A noticeable drawback is the current lack of reversibility. Hydrogel degradation, self-assembly, or phase changes are currently a one-way street, limiting some applications that may benefit from more reversible, controllable, and long-lasting systems. Studies, such as the enzymatically cleavable and hydrolytically activated cross-linking system (*vide supra*), show clues to the utility and behavior of systems that both degrade and rebuild; however, currently, these two phenomena are triggered with different mechanisms.

While enzymes are famous as highly selective catalysts, most of the cleavable peptide sequences incorporated in these hydrogels are degradable by more than one type of protease. In addition, limited studies have been conducted to tease out the changing biophysical properties of enzyme-degradable hydrogels, which play an important role in stem cell fate.[39,40] There is little control over the homogeneity of these hydrogels when cells are encapsulated, making the physical characteristics of the networks difficult to predict or measure. These systems have seen utility and good proof-of-concept in well-controlled environments, yet testing in more complex *in vivo* systems is their next hurdle, especially with respect to self-assembling systems. Studies of *in vivo* implantation of enzyme-responsive hydrogels have shown promising cellular infiltration,[99] vascularizations,[37,133] and neo-bone formation in bone defects,[99,134] yet efficient translation towards clinically relevant tissue regeneration requires more work in terms of upscaling, large animal model proofs, and clinical trial feasibility.

Mechanically responsive systems

One of the emerging areas of cell-biomaterial interactions is the interplay between the mechanical properties of a material and the mechanosensing framework of a cell. Mechanobiology is quickly becoming an active field,[135] and mechanically instructive and responsive biomaterials are advancing in a concerted fashion. In the past decade, it has become a central pillar of biomaterials that a hydrogel's stiffness can directly influence cellular behavior[136] and affect the differentiation of stem cells into different lineages.[39,137] At the most basic level, neuronal cells perform best in soft matrices, while osteoblasts perform best in hard matrices; the differentiation of progenitors is most efficient in a matrix with elasticity comparable to the mature cell's natural niche.

Natural ECM components exhibit non-linear rheological properties including strain-stiffening,[138] stress-relaxation and viscoelasticity,[139] due largely to non-covalent and reversible interactions, allowing for the matrix to respond to the presence of mechanical forces from cellular adhesion. Such materials display frequency (time) and magnitude (force) dependent relationships between the storage (G') and loss (G") moduli of the materials and many are self-healing. Efforts to mimic these behaviors in synthetic systems are uncovering elements of rational design of such properties. Nicely compared, the differences in mechanical properties of peptide-based natural and synthetic hydrogels have been topics of a comprehensive review.[140] In general, mechanically responsive networks have the potential to display different mechanical

information over time, in response to force, and even allow disruption and reformation of bonds during cell and tissue ingrowth.

Strain-stiffening

Strain stiffening is a common feature of natural physically associating hydrogels,[141] allowing for cellular traction and communication even in very soft matrices.[142] Unfortunately, biomimetic strain stiffening has been difficult to engineer in synthetic hydrogels. A breakthrough in this area was introduced in 2013 with ethylene glycol functionalized poly(isocyanides) (PICs, **Figure 5a**) that were able to recreate the magnitude and response of many ECM strain stiffening properties. Akin to collagen bundling, this biomimicry was experimentally attributed to the supramolecular bundling of the PIC polymers into a nanofibrous network.[143,144] The synthetic modularity of the system allowed engineering of the mechanical properties, including the critical stress point (the strain at which the hydrogels exhibit stiffening).[145]

Control over the differentiation of 3D encapsulated stem cells was shown via changes in the strain-stiffening behavior of the biomimetic PIC hydrogels.[41] Within a series of soft (0.2–0.4 kPa) PIC gels, moving the critical stress point from 8 Pa to 20 Pa induced a switch in hMSC differentiation from adipogenesis to osteogenesis (cultured in a 1:1 osteogenic:adipogenic culture medium). These gels all exhibit similar elasticity at rest, yet when the cells exert mechanical force on the adhesion sites (covalently attached GRGDS), the materials respond differently. To further advance this study, the authors were able to find a correlation between DCAMKL1 expression (a microtubule-associated protein) and the onset of the strain stiffening. This observation supported DCAMKL1/RUNX2 as a potentially important mechanotransduction switch in these 3D strain stiffening matrices.

More recently, a self-assembly, covalent fixation, and covalent cross-linking strategy to design strain-stiffening hydrogels were introduced.[146] Utilizing bis-urea bola-amphiphiles with internal acetylenes, covalent fixing of the self-assembled flexible fibers, followed by azide-alkyne cross-linking, led to strain stiffening hydrogels. Pre- and post-cross-linking both showed bundled fibers, and control of concentration led to control of stiffening onset. These observations give promising insights into the rational design of biomimetic strain-stiffening materials. Cell-based studies with the bis-urea materials have not been performed, yet will prove difficult due to their non-transparent nature (poly(acetylene) backbone).

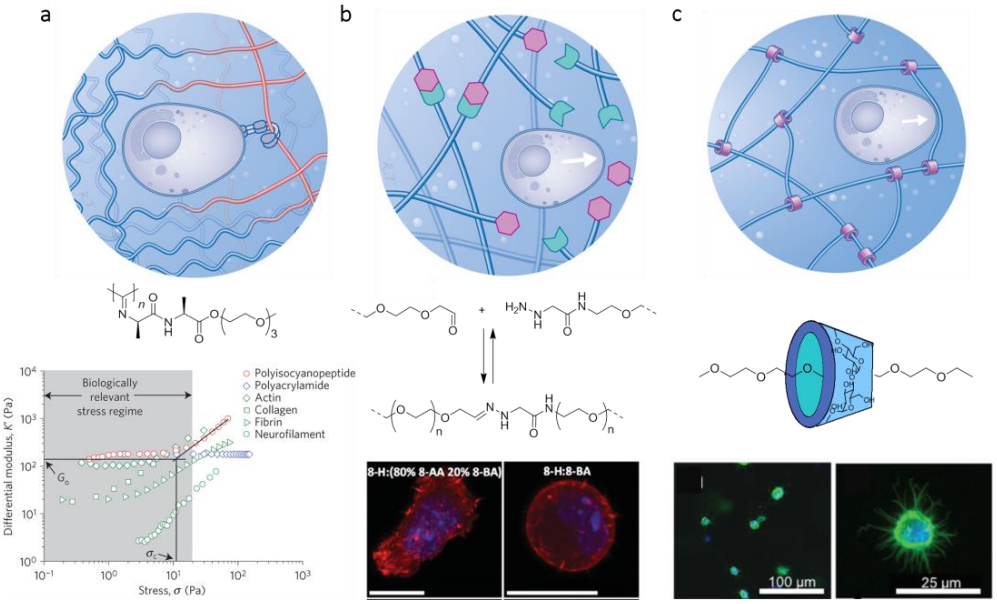

Figure 5. Significant examples of hydrogels able to respond to the mechanical forces of a cell. a) Strain-stiffening hydrogels, create a stiffer network (orange) upon applied strain from a cell, via its integrins (light blue hook), during the generation of traction forces. Poly(isocyanate) (PIC, structure shown) gels, allow for recapitulation of the strain-stiffening environment of the ECM. PIC gels showed stress stiffening behavior within the biologically relevant stress regime (see graph) in comparison to other hydrogel systems.[41] Go represents the equilibrium bulk stiffness and σc is the critical stress for the onset of stress stiffening of the polymer gel. The effect of varying these parameters through e.g. alteration in polymer chain length showed the ability to switch stem cell differentiation. b) Viscoelasticity, as in dynamic covalent hydrazone based hydrogels, allows for facile cellular remodeling of the gel. Shown both schematically (above) and chemically (middle), these dynamically interchangeable bonds create materials with different mechanical information on different time scales, and greatly affects the ability of cells to grow protrusions into the material. The dynamism of the aliphatic vs aryl aldehyde on cell viability was studied via C2C12 myoblasts encapsulated in 8-H:(80% 8-AA,20% 8-BA) (comprised of 80% aliphatic aldehyde and 20% aryl aldehyde) showed actin filaments and extend lamellipodia and filopodia, while cells encapsulated in 8-H:8-BA (100% aryl aldehyde) remained round (bottom).[60] c) Sliding hydrogels based on poly(rotaxanes) provide permanent, yet mobile cross-links (above). Shown with α-cyclodextrin threaded PEG hydrogels (middle), this atypical architecture allows for the clustering of adhesive ligands and the remodeling of the network via forces from the cell. Again here, authors see enhanced propensity for differentiation in such dynamic hydrogel architectures. hMSCs in sliding hydrogels allowed formation of protrusions (bottom), which was attributed to their ability to rearrange cross-links and ligands.[160] (a) was reproduced by permission from Macmillan Punishers Ltd: Nature[41] copyright year 2015. (b) was reproduced with permission[60] John Wiley and Sons 2013. (c) was reproduced with permission.[160] John Wiley and Sons 2016.

Viscoelasticity

Viscoelastic materials exhibit either both elastic and viscous properties that vary with the timescale of the deformation applied. Many of the natural ECM components used for cell culture are viscoelastic and stress-relaxing (e.g. collagen, basement membrane, fibrin). This plasticity of the matrix allows for cellular remodeling of the material via cellular forces[139] (combination with

enzymatic degradation). In attempts to recapitulate this dynamic nature, many of the synthetic systems rely on reversible and/or non-covalent interactions that have inherent timescales.[25,27,29]

The importance of viscosity on cell behavior was first observed within a series of 2D poly(acrylamide) hydrogels. An increase in the hydrogel's viscous behavior led to enhanced hMSCs differentiation potential to a number of lineages.[147] Later, in 3D alginate hydrogels, significant differences in cell spreading and focal adhesion formation were shown between elastic and viscoelastic 3D alginate hydrogels (covalent vs. ionic cross-linking) at a similar initial modulus.[148]

Recently it has been shown that the relaxation rate of viscoelastic hydrogels can directly influence MSC differentiation.[149] Utilizing a series of alginate hydrogels, from high molecular weight to low molecular weight with grafted PEG, stress relaxation of the gel was tuned independently of the stiffness, degradation, and adhesive ligand density (relaxation constants = 3300–70 s). Gels with a rapid rate of stress relaxation (low molecular weight alginate with grafted PEG) led to significantly higher proliferation, spreading, and osteogenic differentiation than gels with a low rate of stress relaxation (high molecular weight alginate). Clusters of adhesive ligands in the vicinity of cells were observed to a larger extent in the rapidly relaxing matrix; the force associated with this integrin-ligand clustering was previously shown to affect osteogenic differentiation.[40] The rapidly relaxing alginate gel (~1 min) was the only matrix that allowed osteogenic differentiation and the formation of an interconnected, mineralized, and collagen I-rich matrix—hallmarks of bone formation.

Viscoelasticity, and stress-relaxation, can also be engineered into hydrogels utilizing well-defined and reversible cross-links within the material. While many dynamic covalent chemistries (DCvC) are triggered by external factors, such as pH, light, and temperature, the hydrazone exchange reaction maintains a dynamic equilibrium under physiological conditions and lends itself well to the formation of biomaterials. In an instructive example, Anseth and co-workers have developed a multi-arm PEG-based hydrogel that is cross-linked via DCvC between hydrazones and aldehydes (**Figure 5b**).[60] By tuning the nature of the aldehyde (aliphatic and aromatic) and the topology of the gel (4-arm and 8-arm PEG), they report the ability to cover a wide range of elastic moduli (1.8–27 kPa) and relaxation time constants (10s–approximately hours). Within this series of dynamic gels, C2C12 myoblasts were found to fuse and demonstrate myotube-like morphology only in the dynamic hydrogels (relaxation constant 91s) (**Figure 5b**). In the more static hydrogels (slower hydrazone exchange), the cells kept mostly a rounded morphology. Less than 30% of the cells grew external protrusions into the material after 10 days of culture.

Materials made from such well-defined chemical strategies can be optimized, correlated to, and predicted based on solution phase kinetics and equilibrium constants.[150] Furthermore, these dynamic materials have the ability to maintain a constant bulk behavior, while responding acutely to the local forces from a cell. Owing to the constant bulk properties, these hydrazone-PEG hydrogels have also enabled the recording and analysis of neurite outgrowth from embryoid bodies to be translated into cellular forces involved in the remodeling of the viscoelastic

material.[151] Furthermore, recent results show that a hydrogel system based on the reversible hydrazone linkages were able to promote neural progenitor growth and have a marked increase in neural development in zebrafish when compared to a traditional alginate hydrogel.[62]

Numerous non-covalent and supramolecular hydrogels are capable of displaying viscoelastic behavior.[70,71,152–155] However, there are no known studies linking this viscoelasticity to cellular behavior. Cellular adhesion to supramolecular surfaces[156,157] and supramolecular fibers[75] has been well demonstrated, yet the correlation to viscoelasticity or timescale remains to be reported. The effect of viscoelasticity within self-assembled supramolecular matrices on 3D cell culture remains an open research question and will become crucial in the upcoming designs of a fibrous synthetic ECM.

Mechanically interlocked systems

The mechanical remodeling of a network can also be accomplished with permanent, yet mobile, cross-links within a hydrogel. Topologically interlocked networks like poly(rotaxanes)[158] have been extensively used in the toughening of materials due to their dynamic and stress-responsive network architectures.[159] Primed for a foray into biomaterials, poly(rotaxane) sliding hydrogel with mobile cross-links and adhesion ligands have recently been reported (**Figure 5c**).[160] Based on α-cyclodextrin threading PEG polymers, these hydrogels not only have enhanced toughness, but also the ability for cells to remodel the sliding cross-links and/or adhesive ligands. Key advancements were both the ability to cross-link the poly(rotaxanes) in a cell-friendly manner and prevention of cyclodextrin crystallization. As seen above, MSCs showed increased ability for differentiation to a variety of lineages in this remodelable gel, when compared to a similarly constructed statically cross-linked hydrogel.

This initial study represents a promising area of research in the future as there is a wealth of information on the unique properties of topologically interlocked networks. One can quickly imagine adding shuttling functions (e.g. in relation to transport of oxygen and removal of cellular metabolite byproducts) and off/on switches within these materials for enhanced control over cellular behavior.

Mechanochemical bond

In the cell's environment, there are several versions of mechanically sensitive bonds that provide enhanced function and responsiveness in the presence of mechanical force.[45,161] Frequently termed "soft mechanochemistry,"[162] the mechanically responsive bonds in biological systems are often based on protein conformation changes. In an ideal bond, the lifetime and/or strength of the bond or interaction is constant regardless of the applied force on the bond. However, recent research has shown that many molecular interactions involved in cell adhesion and movement deviate from this ideal relationship.[163] Catch bonds are capable of increasing in strength and lifetime under applied force, while slip bonds decrease in persistence under force. An excellent example of these phenomena exists in cadherin junctions; the presence of all three types of

bonds allows for cadherins to withstand tensile force and tune the mechanical properties of adhesive junctions.[164]

Mechanochemistry within the realm of polymer chemistry has seen a resurgence in recent years. Traditionally, these systems revolve around creating a chemical reaction (generally bond breakage) under applied force; however, recently inspired by molecular catch bonds, systems that strengthen with applied force are also being currently developed.[165] While these are covalently based systems, there is some evidence that supramolecular-based hydrogels can undergo force-mediated modulation of binding constants.[166] In addition, mechanophore research has recently allowed for the rational design of molecular sensors for mechanical force.[167,168] Currently, the mechanochemical systems developed have not been designed active on the cellular level of force generation, and only a few verified versions of synthetic catch bonds have been documented.[169] Yet, rational design and benchmarking[170] pave the way for innovation. Creating systems that are mechanochemically active to the forces of individual cells inherently will produce fragile materials that can create extreme difficulties in handling. It is likely that such systems may need an *in situ* activation step, or rely on reversible non-covalent interactions, to create functional hydrogel biomaterials.

Metabolite and small molecule responsive systems

While enzyme-responsive hydrogels have proven utility for the construction of cell-responsive materials, these protein-based catalysts are not the only molecular stimuli in the environment of a cell. In the cellular niche, there are numerous pH or reductive changes, non-catalytic proteins and small molecule metabolites, and dissolved gases that provide functions ranging from structural support to inter-cellular signaling. Creating synthetic systems that are capable of responding to these highly varied metabolic products (or fuel) of a cell can prove difficult, but can allow significant advancements in specificity, selectivity, and choice of triggers. Furthermore, these strategies can allow for reversibility of response, since many of these systems are based on binding or recognition events.

Within this section, one will find a common use of biohybrid materials relying on the synthetic integration of highly specific and bioengineered proteins and nucleic acids. Although fully synthetic materials are less prevalent, progress has been made via dynamic recognition events e.g. boronic acid sensing of glucose. Many of these metabolite/small molecule responsive systems have not yet found applications in tissue engineering or regenerative medicine; however, strategies able to respond to metabolic states or differentiation events in tissue formation can start to be entertained.

pH and redox

Hydrogels that are sensitive to pH changes[84] were among the first classes of responsive hydrogels designed to change in response to physiochemical factors,[171] while redox systems have traditionally been used intracellularly.[84] Both systems respond to local extra and intra-cellular environments and are popular with drug-delivery strategies. Easily accessible chemical motifs

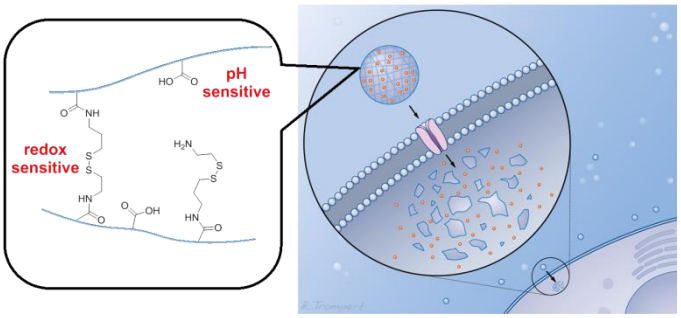

Figure 6. Many pH and redox responsive systems are engineered for drug delivery across a cell membrane. Shown schematically are hydrogel microspheres, loaded with a drug or growth factor (orange spheres), being taken up by a cell and then releasing its cargo upon breakdown of the hydrogel network. Poly(methacrylic acid) (PMAA) hydrogels with disulfide cross-links and with dual pH and redox sensitivity have been successfully created for delivery of doxyrubicin to cancer cells. These hydrogels swell at neutral pH and uptake DOX, degrade in cytosolic space due to presence of gluthatione (GSH), which reduces disulfide bonds and release DOX.. Adapted with permission.[49] Copyright (2015) American Chemical Society.

can impart pH and/or redox sensitivity; however, pH and redox changes nearby a cell are generally neither large nor specific. For these reasons, pH and redox-responsive systems are sometimes coupled with an enzyme for signal amplification (i.e. glucose-responsive hydrogels, *vide infra*).

There exist two main strategies to design hydrogel pH-responsive systems: the use of polymers with ionizable chemical groups that undergo conformational or solubility changes, and polymeric systems with acid-sensitive bonds. A major application of pH-sensitive hydrogels includes the sensing and response of hydrogel networks to the acidic environment (due to accelerated glycolysis) around cancerous cells.[50] Poly(acrylic acid) (PAA, anionic polyelectrolyte) and poly(diethylaminoethyl methacrylate) (PDEAEMA, cationic polyelectrolyte) are the most commonly studied polymers with ionizable chemical groups and can swell/deswell depending on pH changes, often releasing a drug.[14,172] As an example of bond sensitivity to pH, Schiff base hydrogel systems, including alginate-chitosan,[173] and low-molecular-weight hydrogelator (LMWG) hydrogels,[174,175] have found application in cancer therapeutics and wound healing.[63] Self-assembled hydrogelators with doxorubicin (DOX) have been reported to form injectable systems that effectively and selectively deliver DOX to breast cancer in mice and significantly inhibit tumor growth.[173,175]

Moving towards redox-sensitive systems, disulfide cross-linked hydrogels, prone to rapid cleavage by glutathione, have recently been used in effective hydrogels for gene therapy and tissue engineering. Reduction-sensitive self-assembled DNA nanogels (held together by disulfide links between the DNA building blocks) have been shown to disassemble within a cell, and were capable of effectively delivering an anti-proliferation gene.[82] In addition, Varghese and co-workers designed a disulfide cross-linked PEG hydrogel that was shown to degrade in the presence of multiple cells without external stimulus. They observed that this degradation rate

could be tuned *in vitro* via cell type, encapsulated cell density, and disulfide cross-link density. These PEG hydrogels were successfully used to deliver, and increase the retention of hMSCs in mouse dorsal muscle.[64] Various other redox-responsive systems have been employed for drug delivery, but require the input of a user-defined stimulus.[84,176]

pH and redox-sensitive hydrogels can also be combined into a functional system. Poly(methacrylic acid) (PMMA) hydrogels of micrometer-sized with dual pH and redox sensitivity have been reported by Kharlampieva and co-workers.[49] Again targeting DOX delivery to cancerous cells, the pH sensitivity facilitated DOX encapsulation, while the incorporation of disulfide cross-links triggered rapid degradation of these hydrogels in the reducing environment of a cell's cytoplasm. The concept of this system is represented in **Figure 6** where DOX (red spheres) are encapsulated in the hydrogels at neutral pH and degraded in the cytosolic space by glutathione. The authors have shown that these DOX-containing mirco-hydrogels were capable of 90% cytotoxicity when incubated with HeLa cells for 48 h.[49] Such dual responsiveness has also been effectively translated to self-assembled cyclodextrin/benzimidazole nanogels for controlled release.[177]

A newer concept to design responsive hydrogels is to use a cell or tissue's generation of reactive oxygen species (ROS). These species play important roles in cell signaling pathways and abundantly exist at sites of inflammation and tissue healing.[52] Several studies have been reported on 3D polymeric scaffolds, cross-linked with oligo(proline) ROS cleavable sites. These scaffolds showed enhanced degradation when incubated with ROS-generating macrophages, as well as improved host cell infiltration and angiogenesis when implanted subcutaneously in mice.[178,179] This concept is transferrable to hydrogels for a general degradation mechanism during tissue growth and remodeling, while also providing a potential protective effect. ROS-protective hydrogels have been shown to protect both pseudo-islets and hMSCs under high oxidative stress.[180]

Molecule specific

Molecule-specific hydrogels commonly rely on a biohybrid approach. The specificity (and amplification) of biochemical recognition, and the ability of this recognition to respond, is difficult to recreate in fully synthetic systems. However, it is this same specificity that empowers molecule-specific responsive systems to greater potential in the complex biological environment. Some of the best-known and most advanced molecule-specific hydrogels have been created for the treatment and control of Diabetes. Glucose-responsive and insulin-releasing hydrogels hold promise to replace simple insulin injection, and such hydrogel systems have been one of the few to be approximated by fully synthetic systems.

Most hydrogels designed for glucose responsiveness, utilize enzymatic conversion of glucose to gluconic acid, in the presence of glucose oxidase (GOx), to induce the swelling of pH-responsive hydrogels for insulin release (**Figure 7a**).[181] For example, glucose-responsive chitosan (protonatable amine) microgels have been designed using this approach, and their glucose-dependent insulin release showed *in vivo* efficacy in controlling glucose levels in diabetic mice.[54]

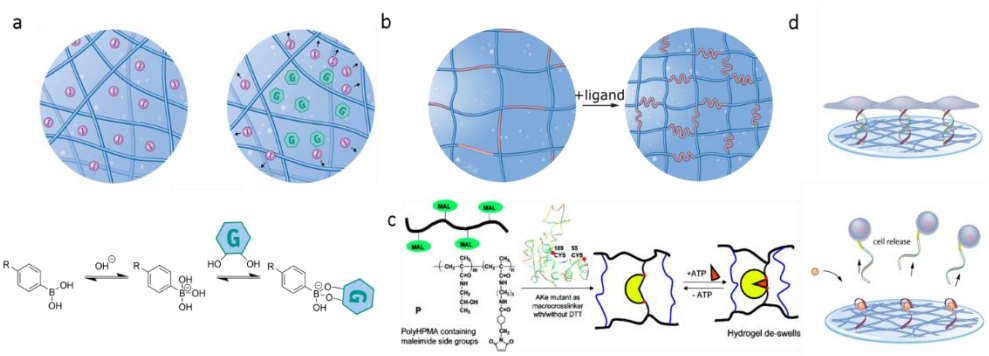

Figure 7. Selected examples of molecule specific responsive hydrogels a) Phenyl boronic acid (PBA) hydrogels for insulin (purple spheres) delivery: PBA specifically recognizes diols such as glucose. A charged PBA-glucose (G hexagons) complex is formed swelling the hydrogel network and releasing insulin as a function of glucose concentration. Due to the dynamic nature of the PBA-glucose complex, such hydrogels are often quick to respond and can be made injectable (shear-thinning).[152] b) Protein conformational changes (orange sections of hydrogel network) upon ligand binding can translate nanoscale motion into macroscale motion or materials properties. For example, calmodulin (CAM) conjugated PEG hydrogels showed volume changes upon binding to a trifluoperazine (TFP) ligand.[189] CAM goes from its extended shape (in the presence of calcium ions (left)) to a collapsed conformation (right) upon binding to TFP ligand. c) Adenylate kinase (another conformationally changing protein) hydrogels were made by cross-linking PolyHPMA (with maleimide side groups) with a thiolated mutant of adenylate kinase (AKtm). These hydrogels undergo macroscopic motion when exposed to ATP. d) DNA aptamer recognition for cell release: Apatmers (purple) sensitive to ATP (orange) are initially hybridized to complementary strands (green) with adhesive RGD attached (yellow), creating a cell-adhesive environment (top). Upon introduction of ATP (bottom, exogenous or cell-secreted), aptamers release their complementary strand and bind to ATP, thus creating a non-adhesive environment.[193] Aptamer-target interactions can be designed for virtually any target, making this a highly promising, though costly, strategy. (c) was reprinted with permission.[191] Copyright (2008) American Chemical Society. (d) was adapted from reference[193] under creative commons license (CC BY 3.0).

The production of H_2O_2 from GOx (by oxidizing glucose) has also been utilized to engineer glucose-responsive hydrogels.[182] Based on the sensitivity of ferrocene/cyclodextrin complexation to oxidation, redox-sensitive hydrogels have been created from ferrocene terminated pluronic and a polymer with cyclodextrin pendant groups. The hydrogels underwent a gel-sol transition upon exposure to glucose solutions.

While the previous examples are effective, these systems lack specificity to only glucose, due to the hydrogel response being secondary in nature. In order to increase glucose specificity, fully synthetic polymers containing phenylboronic acid (PBA) have gained much attention (**Figure 7a**).[58] Boronic acids are well known to form dynamic covalent bonds with diols, especially sugars, in aqueous media. Sakurai and co-workers were among the first to use such a system, where the creation of a charged PBA glucose complex swelled the hydrogel and allowed the release of insulin.[183] More recently, work by the Anderson group has created a series of self-healing, tunable, shear-thinning, injectable, and glucose-responsive hydrogels by incorporating both the

PBA and a competitive diol (hydrolyzed sugar) within the polymer network.[152,184] The glucose responsiveness (and insulin or IgG release) of these hydrogels were shown with hyperglycemia mimicking conditions, and these hydrogels showed a typical foreign body reaction upon implantation in mice, making them promising candidates for insulin delivery applications.

As seen by the glucose-PBA-based hydrogels, systems based on the response to a binding event from a specific small molecule are possible in many fashions. Relying on a urate-responsive protein-DNA complex, Weber and co-workers developed a hydrogel designed to provide a protective environment in patients with gout.[185] The hydrogel system was based on a urate repressor protein (HucR), conjugated to poly(acrylamide), and cross-linked via the addition of oligomeric hucO DNA ($[hucO]_n$). This system forms a cross-linking HucR▪hucO complex that dissociates at elevated urate concentrations, resulting in the dissolution of the hydrogel. By incorporating urate oxidase, the authors have shown that the hydrogel system responded protectively to uric acid pulses in a mice model.[186]

An exciting approach to designing molecule-specific dynamic hydrogels is by translating binding-induced protein conformational changes into macroscopic motion or reorganization (**Figure 7b**). For example, calmodulin (CaM) is a protein with three distinct shapes: unstructured, extended (in the presence of Ca^{2+}), and collapsed (in the presence of phenothiazine antipsychotics). CaM was first successfully incorporated into star PEG hydrogels that were shown to undergo a significant volume decrease (up to 15%) upon binding of trifluoperazine.[187] Incorporating a phenothiazine ligand into an acrylamide network containing CaM allowed for a triple-state responsive gel system that swelled and de-swelled as a function of calcium and phenothiazine concentrations.[188] These hydrogels were shown to allow active control of molecular transport across the gel and control fluid flow from a microfluidic device. CaM-based hydrogels have even found application for tissue engineering via spatio-temporal control of growth factors delivery. Murphy et al. have designed growth-factor-laden PEG-CAM-PEG acrylate-based hydrogel microspheres, using two-phase suspension polymerization that showed a maximum volume change of around 76%. The authors have shown that temporal release of VEGF and BMP-2 could be achieved by varying the timings of CaM's ligand trifluoperazine-induced volume changes.[189] CaM is just one good example of molecular motion in protein engineering for hydrogel design, as touched upon briefly in a recent review.[190] Notably, systems like adenylate kinase-ATP responsive gels (as depicted in **Figure 7c**) may see more application in the future, as they respond to a more relevant cell metabolite (adenosine triphosphate).[191]

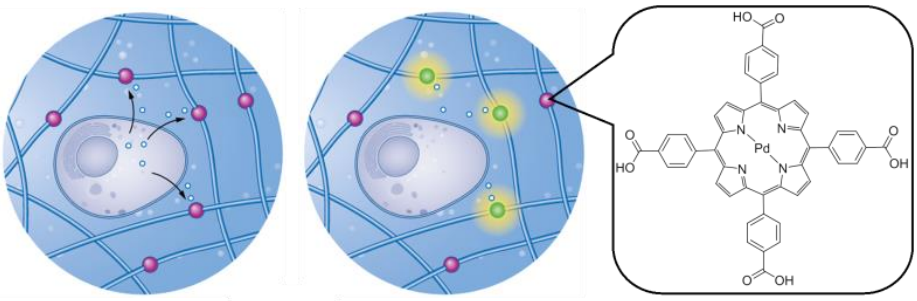

Figure 8. Gas sensitive hydrogels have mainly been designed for imaging applications. Proper concentrations of gaseous metabolites and byproducts within regenerating tissue is crucial for success, yet very difficult to measure. Incorporating gas sensitive fluorophores (purple sphere) in the hydrogel network allows the artificial environment to sense and provide this information. For example., oxygen responsive Pd-Porphyrins (left) have been used to cross-link hydrogels for monitoring of oxygen concentration subcutaneously.[206]

Although the a priori engineering of target-responsive hydrogels remains difficult, the directed evolution of DNA aptamers gives a strategy to create systems that respond to the desired target molecule. Aptamer-based hydrogels can be made responsive to specific analytes, for example, an excess of adenosine and thrombin.[192] Taking this design principle further, Qu and co-workers have recently created cell-responsive hydrogels that control 2D cellular adhesion in response to ATP concentration (**Figure 7d**). By conjugating ATP aptamers to an alginate hydrogel and hybridizing with RGD functionalized complementary DNA, a cell adhesive surface was formed. Exogenous delivery of ATP was shown to cause dehybridization of the DNA, rendering the surface non-adhesive and releasing cells. The system was demonstrated to be highly selective to ATP and even responsive to ATP signaling from cells in co-culture.[193] Such a strategy requires non-trivial aptamer generation but can be applied to a wide variety of targets and incorporated into a wide variety of systems.

Gas sensitive

The responsiveness of hydrogels to and control of gaseous metabolites is a significant need in 3D scaffolds for tissue engineering. The difficulty in maintaining oxygen partial pressures within tissue-engineered constructs and in 3D cell culture is well known but is difficult to control or to quantify/image. Ultimately, re-vascularization is desired to enable the long-term viability of an engineered tissue;[194,195] however, biomaterials that can sense and/or control the concentration of gaseous metabolites remain highly sought after. Biomaterials capable of delivering gases remain an active area of research,[196–198], and hydrogels capable of sensing gaseous metabolites are valuable research tools.

There is currently only one strategy for materials that can loosely be defined as the delivery of oxygen in response to local consumption. Perfluorocarbon (PFC) based materials, have high oxygen solubility (up to 35 times the aqueous environment) and can act as oxygen conduits when the local partial pressure drops. Hyaluronic acid hydrogels with a covalently attached polyfluorinated oxadiazole have been shown to significantly increase the viability of fibroblasts

in both normoxic and hypoxic conditions.[199] Fluorinated methacrylamide chitosan hydrogels have also shown enhanced oxygen distribution, and higher fluorine content (via conjugation of longer fluorinated chains) facilitated both the highest cell proliferation and neuronal differentiation within neural progenitor cells.[200]

While no materials are currently able to truly respond to gaseous metabolites and influence a cell, responsive hydrogels that allow the imaging of gaseous metabolites still provide significant information to tissue engineering and regenerative medicine. For example, measuring the distribution of oxygen within a tissue-engineered construct can lead to better 3D designs.[201] For biological use, oxygen-responsive probes (usually organic dyes) are physically encapsulated in a hydrophobic polymer or solid.[202] Beautiful core-shell[203] and dual-responsive[204] (to O_2 and interleukin-6) hydrogels working on this principle have already found applications for tissue engineering. Recent efforts to covalently incorporate porphyrin dyes into the hydrogel matrix have opened up the potential for hydrogel networks with immobilized (non-leachable) dyes (as depicted in **Figure 8**).[205,206] Huang et al. were even able to show the ability of a porphyrin cross-linked PEG hydrogel to perform well as an implantable oxygen sensing material,[206] showing the possibility for long-term oxygen distribution imaging of tissue-engineered constructs *in vitro* and *in vivo*.

Outlook

As we move towards more sophisticated hydrogel architectures, the progress in stimuli-responsive systems has the potential to move from large, user-generated stimuli, to smaller, locally generated biological stimuli. The ability to engineer these hydrogel systems to listen and respond to cell-based stimuli can pave the way to the creation of autonomous biomaterials to be used in tissue engineering, drug delivery, sensing, and cancer therapeutics, among other fields. With smart engineering and design, one can imagine the design of materials that can not only recapitulate the real-time response of the natural ECM, but also move towards multi-component[207] systems that provide non-natural or enhanced function,[208] controlling the growth, differentiation, and migration of cells towards the formation of regenerated tissues. For example, the design of bioresponsive hydrogels with complex logic gate functions has already been demonstrated,[209] and such logic gate architectures allow complex responses from complex inputs.

The toolbox of chemistries to use in the design of cell-responsive systems can be considered small, but more importantly, such chemistries are often poorly studied in the context of complex biological systems. For example, supramolecular biomaterials hold great promise to recreate and mimic the complex and dynamic extracellular environment.[26,66] Numerous biological systems revolve around the dynamics, specificity, responsiveness, and information richness of non-covalent interactions and self-assembly for proper function.[210] As we grow more sophisticated in our engineering of synthetic supramolecular systems, demonstration of control over molecular assembly pathways,[211,212] energetics,[213,214] consumption or dissipation of energy,[215–217] and the resultant dynamics,[218,219] clusterings,[220,221] and function in a biological setting,[66,67,222] have all been

demonstrated. Control of dynamics can enable the hydrogel to interact with different mechanosensing events, clustering can affect signal transduction or raft formation via super-selective assembly, and control over pathways can enable different environmental structures given different inputs. Of particular interest, the creation of out-of-equilibrium and dissipative self-assembled hydrogels will allow new insights into the out-of-equilibrium assembly of the natural ECM and the potential to mimic this dynamic environmental switching in biorelevant hydrogel systems.

As seen with CAM hydrogels (*vide supra*) molecular machines can generate a large output from a simple biological signal. Synthetic (supra)molecular machines, such as rotaxanes,[223] catenanes,[224], and molecular rotors[225] have all gained much recent attention due to recognition through the 2016 Nobel Prize. These systems have a long road towards functional materials in a complex environment, yet open up exciting new possibilities, directed shuttling of nutrients and growth factors in a spatio-temporal manner, and stimuli-generated mechanical forces, as already seen in rotaxane molecular muscles,[226] give scientists the potential to go above and beyond some of the complexities of natural ECM.

The use of dynamic covalent, protein/DNA engineered, and enzyme degradable gels stand to provide good benchmarks for the fundamental development of hydrogel systems in the immediate future. While dynamic covalent systems specificity, their synthetic accessibility and low cost (comparatively) render them excellent choices for the production of larger amounts of hydrogel for study. On the other hand, protein/DNA-engineered hydrogels allow ultimate levels of control and biomimicry, but come at an extremely high price. Their replacement by purely synthetic systems seems inevitable; however, it must be noted that the production of designed hydrogelators via protein expression shows promise for scalability.[227] Enzymatically responsive hydrogels are excellent at creating remodelable artificial environments and are poised to remain a valuable platform. Such systems require new enzyme-responsive motifs and orthogonality between motifs to enable complex functions such as complex signal processing and remodeling via both degradation and creation.

A major driving force for the creation of hydrogels that can respond to cellular signals or events has been the biochemical and biophysical characterization of cellular behavior in space and time. Marker identification, unraveling of signaling pathways, biochemical quantification, and high content and super-resolution microscopy techniques have all been paramount to measuring the interplay between materials and cells. When moving towards more dynamic systems, reliable cellular readouts remain an ever-present bottleneck to characterization.

Despite progress in the spatio-temporal characterization of cells and tissues, we still have a long way to go to understand the different time scales that dominate cellular behavior and decision-making. While general timescales are known (e.g. cell division normally takes 24 hours),[228] the heterogeneity of timescales within populations and in signaling pathways is less understood. Recent studies of time-dependent materials and their effect on tissue engineering reinforce this importance.[229,230] For example, the observation of stem cells containing a "memory" for a few

days for the stiffness of the substrate on which it has been previously cultured[231] clearly shows the importance of timescales for signaling pathways, adhesion formation, differentiation process, and homeostasis.

While it is the dream of many that a simple hydrogel architecture will provide an effective surrogate for the natural ECM or an instructive environment for tissue engineering, we tend to think that the replacement of such a multifunctional environmental scaffold for cells can only be accomplished effectively by multicomponent complex chemical systems. Complex, but not complicated. We support the idea that the combination of simple chemical systems to work together in a smart manner is the way forward for this, and potentially many other fields.[232]

Acknowledgments

The authors would like to acknowledge the Province of Limburg for funding. S. Hafeez and C.A. van Blitterswijk would like to acknowledge ERC-AdG-2015 "ORCHESTRATE" for funding. The authors would also like to thank Rogier Trompert for his illustrations and entertaining scientific discussion.

Contributions to the work

S. Hafeez's contribution to this review is writing the "Metabolite and small molecule responsive systems" section of the review. The enzymatically responsive section was written by H.W. Ooi and the mechanically responsive section was written by M. B. Baker. All authors reviewed each other's work and co-wrote the introduction and outlook sections.

References

(1) Mouw, J. K.; Ou, G.; Weaver, V. M. Extracellular Matrix Assembly: A Multiscale Deconstruction. *Nat. Rev. Mol. Cell Biol.* **2014**, *15* (12), 771–785. https://doi.org/10.1038/nrm3902.

(2) Frantz, C.; Stewart, K. M.; Weaver, V. M. The Extracellular Matrix at a Glance. *J. Cell Sci.* **2010**, *123*, 4195–4200. https://doi.org/10.1242/jcs.023820.

(3) Chien, K. Regenerative Medicine and Human Models of Human Disease. *Nature* **2008**, *453* (7193), 302–305. https://doi.org/10.1038/nature07037.

(4) Vacanti, J. P.; Langer, R. Tissue Engineering: The Design and Fabrication of Living Replacement Devices for Surgical Reconstruction and Transplantation. *Lancet* **1999**, *354*, SI32-I34. https://doi.org/10.1016/S0140-6736(99)90247-7.

(5) Alamein, M. A.; Liu, Q.; Stephens, S.; Skabo, S.; Warnke, F.; Bourke, R.; Heiner, P.; Warnke, P. H. Nanospiderwebs: Artificial 3D Extracellular Matrix from Nanofibers by Novel Clinical Grade Electrospinning for Stem Cell Delivery. *Adv. Healthc. Mater.* **2013**, *2* (5), 702–717. https://doi.org/10.1002/adhm.201200287.

(6) Nandakumar, A.; Truckenmüller, R.; Ahmed, M.; Damanik, F.; Santos, D. R.; Auffermann, N.; De Boer, J.; Habibovic, P.; Van Blitterswijk, C.; Moroni, L. A Fast Process for Imprinting Micro and Nano Patterns on Electrospun Fiber Meshes at Physiological Temperatures. *Small* **2013**, *9* (20), 3405–3409. https://doi.org/10.1002/smll.201300220.

(7) Gazquez, G. C.; Chen, H.; Veldhuis, S. A.; Solmaz, A.; Mota, C.; Boukamp, B. A.; Van Blitterswijk, C. A.; Elshof, J. E. Ten; Moroni, L. Flexible Yttrium-Stabilized Zirconia Nanofibers Offer Bioactive Cues for Osteogenic Differentiation of Human Mesenchymal Stromal Cells. *ACS Nano* **2016**, *10* (6), 5789–5799. https://doi.org/10.1021/acsnano.5b08005.

(8) Dalby, M. J.; Gadegaard, N.; Oreffo, R. O. C. Harnessing Nanotopography and Integrin–Matrix Interactions to Influence Stem Cell Fate. *Nat. Mater.* **2014**, *13* (6), 558–569.

https://doi.org/10.1038/nmat3980.

(9) Kim, J.; Staunton, J. R.; Tanner, K. Independent Control of Topography for 3D Patterning of the ECM Microenvironment. *Adv. Mater.* **2016**, *28* (1), 132–137. https://doi.org/10.1002/adma.201503950.

(10) Neves, S. C.; Mota, C.; Longoni, A.; Barrias, C. C.; Granja, P. L.; Moroni, L. Additive Manufactured Polymeric 3D Scaffolds with Tailored Surface Topography Influence Mesenchymal Stromal Cells Activity. *Biofabrication* **2016**, *8* (2), 025012. https://doi.org/10.1088/1758-5090/8/2/025012.

(11) Di Luca, A.; Lorenzo-Moldero, I.; Mota, C.; Lepedda, A.; Auhl, D.; Van Blitterswijk, C.; Moroni, L. Tuning Cell Differentiation into a 3D Scaffold Presenting a Pore Shape Gradient for Osteochondral Regeneration. *Adv. Healthc. Mater.* **2016**, *5* (14), 1753–1763. https://doi.org/10.1002/adhm.201600083.

(12) Di Luca, A.; Longoni, A.; Criscenti, G.; Lorenzo-Moldero, I.; Klein-Gunnewiek, M.; Vancso, J.; van Blitterswijk, C.; Mota, C.; Moroni, L. Surface Energy and Stiffness Discrete Gradients in Additive Manufactured Scaffolds for Osteochondral Regeneration. *Biofabrication* **2016**, *8* (1), 015014. https://doi.org/10.1088/1758-5090/8/1/015014.

(13) Wichterle, O.; Lím, D. Hydrophilic Gels for Biological Use. *Nature* **1960**, *185* (4706), 117–118.

(14) Qiu, Y.; Park, K. Environment-Sensitive Hydrogels for Drug Delivery. *Adv. Drug Deliv. Rev.* **2001**, *53*, 321–339. https://doi.org/10.1016/j.addr.2012.09.024.

(15) Knipe, J. M.; Peppas, N. A. Multi-Responsive Hydrogels for Drug Delivery and Tissue Engineering Applications. *Regen. Biomater.* **2014**, *1* (1), 57–65. https://doi.org/10.1093/rb/rbu006.

(16) Hoare, T. R.; Kohane, D. S. Hydrogels in Drug Delivery: Progress and Challenges. *Polymer (Guildf).* **2008**, *49* (8), 1993–2007. https://doi.org/10.1016/j.polymer.2008.01.027.

(17) Hunt, J. A.; Chen, R.; van Veen, T.; Bryan, N. Hydrogels for Tissue Engineering and Regenerative Medicine. *J. Mater. Chem. B* **2014**, *2* (33), 5319–5338. https://doi.org/10.1039/C4TB00775A.

(18) Peppas, N. A.; Hilt, J. Z.; Khademhosseini, A.; Langer, R. Hydrogels in Biology and Medicine: From Molecular Principles to Bionanotechnology. *Adv. Mater.* **2006**, *18* (11), 1345–1360. https://doi.org/10.1002/adma.200501612.

(19) Malda, J.; Visser, J.; Melchels, F. P.; Jüngst, T.; Hennink, W. E.; Dhert, W. J. A.; Groll, J.; Hutmacher, D. W. 25th Anniversary Article: Engineering Hydrogels for Biofabrication. *Advanced Materials*. 2013, pp 5011–5028.

(20) Kopeček, J. Hydrogel Biomaterials: A Smart Future? *Biomaterials* **2007**, *28* (34), 5185–5192. https://doi.org/10.1016/j.biomaterials.2007.07.044.

(21) Slaughter, B. V; Khurshid, S. S.; Fisher, O. Z.; Khademhosseini, A.; Peppas, N. A. Hydrogels in Regenerative Medicine. *Adv. Mater.* **2009**, *21* (0), 3307–3329. https://doi.org/10.1002/adma.200802106.Hydrogels.

(22) Thiele, J.; Ma, Y.; Bruekers, S. M. C.; Ma, S.; Huck, W. T. S. 25th Anniversary Article: Designer Hydrogels for Cell Cultures: A Materials Selection Guide. *Adv. Mater.* **2014**, *26* (1), 125–148. https://doi.org/10.1002/adma.201302958.

(23) Tibbitt, M. W.; Anseth, K. S. Hydrogels as Extracellular Matrix Mimics for 3D Cell Culture. *Biotechnol. Bioeng.* **2009**, *103* (4), 655–663. https://doi.org/10.1002/bit.22361.

(24) Liang, Y.; Li, L.; Scott, R. A.; Kiick, K. L. 50th Anniversary Perspective: Polymeric Biomaterials: Diverse Functions Enabled by Advances in Macromolecular Chemistry. *Macromolecules* **2017**, *50* (2), 483–502. https://doi.org/10.1021/acs.macromol.6b02389.

(25) Rosales, A. M.; Anseth, K. S. The Design of Reversible Hydrogels to Capture Extracellular Matrix Dynamics. *Nat. Rev. Mater.* **2016**, *1*, 1–15. https://doi.org/10.1038/natrevmats.2015.12.

(26) Webber, M. J. Engineering Responsive Supramolecular Biomaterials: Toward Smart Therapeutics. *Bioeng. Transl. Med.* **2016**, No. August, 1–15. https://doi.org/10.1002/btm2.10031.

(27) Burdick, J. A.; Murphy, W. L. Moving from Static to Dynamic Complexity in Hydrogel Design. *Nat. Commun.* **2012**, *3*, 1269. https://doi.org/10.1038/ncomms2271.

(28) Zhang, Y. S.; Khademhosseini, A. Advances in Engineering Hydrogels. *Science.* **2017**, *356* (6337), eaaf3627. https://doi.org/10.1126/science.aaf3627.

(29) Wang, H.; Heilshorn, S. C. Adaptable Hydrogel Networks with Reversible Linkages for Tissue Engineering. *Adv. Mater.* **2015**, *27* (25), 3717–3736. https://doi.org/10.1002/adma.201501558.

(30) Shi, J.; Xu, B. Nanoscale Assemblies of Small Molecules Control the Fate of Cells. *Nano Today* **2015**, *10* (5), 615–630. https://doi.org/10.1016/j.nantod.2015.09.001.

(31) Koetting, M. C.; Peters, J. T.; Steichen, S. D.; Peppas, N. A. Stimulus-Responsive Hydrogels: Theory, Modern Advances, and Applications. *Mater. Sci. Eng. R Reports* **2015**, *93*, 1–49. https://doi.org/10.1016/j.mser.2015.04.001.

(32) Gattazzo, F.; Urciuolo, A.; Bonaldo, P. Extracellular Matrix: A Dynamic Microenvironment for Stem Cell Niche. *Biochim. Biophys. Acta - Gen. Subj.* **2014**, *1840* (8), 2506–2519. https://doi.org/10.1016/j.bbagen.2014.01.010.

(33) Hinz, B. The Extracellular Matrix and Transforming Growth Factor-B1: Tale of a Strained Relationship. *Matrix Biol.* **2015**, *47*, 54–65. https://doi.org/10.1016/j.matbio.2015.05.006.

(34) Horejs, C. M.; Serio, A.; Purvis, A.; Gormley, A. J.; Bertazzo, S.; Poliniewicz, A.; Wang, A. J.; DiMaggio, P.; Hohenester, E.; Stevens, M. M. Biologically-Active Laminin-111 Fragment That Modulates the Epithelial-to-Mesenchymal Transition in Embryonic Stem Cells. *Proc. Natl. Acad. Sci. U. S. A.* **2014**, *111* (16), 5908–5913. https://doi.org/10.1073/pnas.1403139111.

(35) Baker, B. M.; Chen, C. S. Deconstructing the Third Dimension - How 3D Culture Microenvironments Alter Cellular Cues. *J. Cell Sci.* **2012**, *125* (13), 3015–3024. https://doi.org/10.1242/jcs.079509.

(36) Ulijn, R. V. Enzyme-Responsive Materials: A New Class of Smart Biomaterials. *J. Mater. Chem.* **2006**, *16*, 2217–2225. https://doi.org/10.1039/b601776m.

(37) Salimath, A. S.; Phelps, E. A.; Boopathy, A. V.; Che, P. lin; Brown, M.; García, A. J.; Davis, M. E. Dual Delivery of Hepatocyte and Vascular Endothelial Growth Factors via a Protease-Degradable Hydrogel Improves Cardiac Function in Rats. *PLoS One* **2012**, *7* (11), 1–12. https://doi.org/10.1371/journal.pone.0050980.

(38) Foster, G. A.; Headen, D. M.; González-García, C.; Salmerón-Sánchez, M.; Shirwan, H.; García, A. J. Protease-Degradable Microgels for Protein Delivery for Vascularization. *Biomaterials* **2017**, *113*, 170–175. https://doi.org/10.1016/j.biomaterials.2016.10.044.

(39) Engler, A. J.; Sen, S.; Sweeney, H. L.; Discher, D. E. Matrix Elasticity Directs Stem Cell Lineage Specification. *Cell* **2006**, *126* (4), 677–689. https://doi.org/10.1016/j.cell.2006.06.044.

(40) Chaudhuri, O.; Gu, L.; Klumpers, D.; Darnell, M.; Bencherif, S. A.; Weaver, J. C.; Huebsch, N.; Lee, H.-P.; Lippens, E.; Duda, G. N.; Mooney, D. J. Hydrogels with Tunable Stress Relaxation Regulate Stem Cell Fate and Activity. *Nat. Mater.* **2016**, *15* (15), 326–336. https://doi.org/10.1038/nmat4489.

(41) Das, R. K.; Gocheva, V.; Hammink, R.; Zouani, O. F.; Rowan, A. E. Stress-Stiffening-Mediated Stem-Cell Commitment Switch in Soft Responsive Hydrogels. *Nat. Mater.,* **2015**, *15* (November), 318–325. https://doi.org/10.1038/nmat4483.

(42) Huebsch, N.; Arany, P. R.; Mao, A. S.; Shvartsman, D.; Ali, O. A.; Bencherif, S. A.; Rivera-Feliciano, J.; Mooney, D. J. Harnessing Traction-Mediated Manipulation of the Cell/Matrix Interface to Control Stem-Cell Fate. *Nat. Mater.* **2010**, *9* (6), 518–526. https://doi.org/10.1038/nmat2732.

(43) Polacheck, W. J.; Chen, C. S. Measuring Cell-Generated Forces: A Guide to the Available Tools. *Nat. Methods* **2016**, *13* (5), 415–423. https://doi.org/10.1038/nmeth.3834.

(44) Tajik, A.; Zhang, Y.; Wei, F.; Sun, J.; Jia, Q.; Zhou, W.; Singh, R.; Khanna, N.; Belmont, A. S.; Wang, N. Transcription Upregulation via Force-Induced Direct Stretching of Chromatin. *Nat. Mater.,* **2016**, *15*, 1287–1296. https://doi.org/10.1038/NMAT4729.

(45) Schoen, I.; Pruitt, B. L.; Vogel, V. The Yin-Yang of Rigidity Sensing: How Forces and Mechanical Properties Regulate the Cellular Response to Materials. *Annu. Rev. Mater. Res.* **2013**, *43* (1), 589–618. https://doi.org/10.1146/annurev-matsci-062910-100407.

(46) Murphy, W. L.; McDevitt, T. C.; Engler, A. J. Materials as Stem Cell Regulators. *Nat. Mater.* **2014**, *13* (6), 547–557. https://doi.org/10.1038/nmat3937.

(47) Ivanovska, I. L.; Shin, J. W.; Swift, J.; Discher, D. E. Stem Cell Mechanobiology: Diverse Lessons from Bone Marrow. *Trends Cell Biol.* **2015**, *25* (9), 523–532. https://doi.org/10.1016/j.tcb.2015.04.003.

(48) Lutolf, M. P.; Gilbert, P. M.; Blau, H. M. Designing Materials to Direct Stem-Cell Fate. *Nature* **2009**, *462* (7272), 433–441. https://doi.org/10.1038/nature08602.

(49) Xue, B.; Kozlovskaya, V.; Liu, F.; Chen, J.; Williams, J. F.; Campos-Gomez, J.; Saeed, M.; Kharlampieva, E. Intracellular Degradable Hydrogel Cubes and Spheres for Anti-Cancer Drug Delivery. *ACS Appl. Mater. Interfaces* **2015**, *7* (24), 13633–13644.

https://doi.org/10.1021/acsami.5b03360.

(50) Norouzi, M.; Nazari, B.; Miller, D. W. Injectable Hydrogel-Based Drug Delivery Systems for Local Cancer Therapy. *Drug Discov. Today* **2016**, *21* (11), 1835–1849. https://doi.org/10.1016/j.drudis.2016.07.006.

(51) Demma, L. J.; Carlson, K. T.; Duggan, E. W.; Morrow, J. G.; Umpierrez, G. Effect of Basal Insulin Dosage on Blood Glucose Concentration in Ambulatory Surgery Patients with Type 2 Diabetes. *J. Clin. Anesth.* **2017**, *36*, 184–188. https://doi.org/10.1016/j.jclinane.2016.10.003.

(52) Xu, Q.; He, C.; Xiao, C.; Chen, X. Reactive Oxygen Species (ROS) Responsive Polymers for Biomedical Applications. *Macromol. Biosci.* **2016**, *16* (5), 635–646. https://doi.org/10.1002/mabi.201500440.

(53) Schmaljohann, D. Thermo- and PH-Responsive Polymers in Drug Delivery. *Adv. Drug Deliv. Rev.* **2006**, *58* (15), 1655–1670. https://doi.org/10.1016/j.addr.2006.09.020.

(54) Gu, Z.; Dang, T. T.; Ma, M.; Tang, B. C.; Cheng, H.; Jiang, S.; Dong, Y.; Zhang, Y.; Anderson, D. G. Glucose-Responsive Microgels Integrated with Enzyme Nanocapsules for Closed-Loop Insulin Delivery. *ACS Nano* **2013**, *7* (8), 6758–6766. https://doi.org/10.1021/nn401617u.

(55) Zelzer, M.; Todd, S. J.; Hirst, A. R.; McDonald, T. O.; Ulijn, R. V. Enzyme Responsive Materials: Design Strategies and Future Developments. *Biomater. Sci.* **2013**, *1*, 11–39. https://doi.org/10.1039/C2BM00041E.

(56) Jin, Y.; Yu, C.; Denman, R. J.; Zhang, W. Recent Advances in Dynamic Covalent Chemistry. *Chem. Soc. Rev.* **2013**, *42* (16), 6634–6654. https://doi.org/10.1039/c3cs60044k.

(57) Kloxin, C. J.; Bowman, C. N. Covalent Adaptable Networks: Smart, Reconfigurable and Responsive Network Systems. *Chem. Soc. Rev.* **2013**, *42* (17), 7161–7173. https://doi.org/10.1039/c3cs60046g.

(58) Brooks, W. L. A.; Sumerlin, B. S. Synthesis and Applications of Boronic Acid-Containing Polymers: From Materials to Medicine. *Chem. Rev.* **2016**, *116* (3), 1375–1397. https://doi.org/10.1021/acs.chemrev.5b00300.

(59) Konieczynska, M. D.; Villa-Camacho, J. C.; Ghobril, C.; Perez-Viloria, M.; Tevis, K. M.; Blessing, W. A.; Nazarian, A.; Rodriguez, E. K.; Grinstaff, M. W. On-Demand Dissolution of a Dendritic Hydrogel-Based Dressing for Second-Degree Burn Wounds through Thiol???Thioester Exchange Reaction. *Angew. Chemie - Int. Ed.* **2016**, *55* (34), 9984–9987. https://doi.org/10.1002/anie.201604827.

(60) McKinnon, D. D.; Domaille, D. W.; Cha, J. N.; Anseth, K. S. Biophysically Defined and Cytocompatible Covalently Adaptable Networks as Viscoelastic 3d Cell Culture Systems. *Adv. Mater.* **2014**, *26* (6), 865–872. https://doi.org/10.1002/adma.201303680.

(61) Dahlmann, J.; Krause, A.; Möller, L.; Kensah, G.; Möwes, M.; Diekmann, A.; Martin, U.; Kirschning, A.; Gruh, I.; Dräger, G. Fully Defined in Situ Cross-Linkable Alginate and Hyaluronic Acid Hydrogels for Myocardial Tissue Engineering. *Biomaterials* **2013**, *34* (4), 940–951. https://doi.org/10.1016/j.biomaterials.2012.10.008.

(62) Tseng, T. C.; Tao, L.; Hsieh, F. Y.; Wei, Y.; Chiu, I. M.; Hsu, S. H. An Injectable, Self-Healing Hydrogel to Repair the Central Nervous System. *Adv. Mater.* **2015**, *27* (23), 3518–3524. https://doi.org/10.1002/adma.201500762.

(63) Giano, M. C.; Ibrahim, Z.; Medina, S. H.; Sarhane, K. A.; Christensen, J. M.; Yamada, Y.; Brandacher, G.; Schneider, J. P. Injectable Bioadhesive Hydrogels with Innate Antibacterial Properties. *Nat. Commun.* **2014**, *5* (May), 1–9. https://doi.org/10.1038/ncomms5095.

(64) Kar, M.; Vernon Shih, Y. R.; Velez, D. O.; Cabrales, P.; Varghese, S. Poly(Ethylene Glycol) Hydrogels with Cell Cleavable Groups for Autonomous Cell Delivery. *Biomaterials* **2016**, *77*, 186–197. https://doi.org/10.1016/j.biomaterials.2015.11.018.

(65) Barcan, G. A.; Zhang, X.; Waymouth, R. M. Structurally Dynamic Hydrogels Derived from 1,2-Dithiolanes. *J. Am. Chem. Soc.* **2015**, *137* (17), 5650–5653. https://doi.org/10.1021/jacs.5b02161.

(66) Webber, M. J.; Appel, E. A.; Meijer, E. W.; Langer, R. Supramolecular Biomaterials. *Nat. Mater.* **2015**, *15* (1), 13–26. https://doi.org/10.1038/nmat4474.

(67) Dong, R.; Zhou, Y.; Huang, X.; Zhu, X.; Lu, Y.; Shen, J. Functional Supramolecular Polymers for Biomedical Applications. *Adv. Mater.* **2015**, *27* (3), 498–526. https://doi.org/10.1002/adma.201402975.

(68) Appel, E. A.; del Barrio, J.; Loh, X. J.; Scherman, O. A. Supramolecular Polymeric Hydrogels. *Chem.*

Soc. Rev. **2012**, *41* (18), 6195. https://doi.org/10.1039/c2cs35264h.

(69) Koopmans, C.; Ritter, H. Formation of Physical Hydrogels via Host-Guest Interactions of β-Cyclodextrin Polymers and Copolymers Bearing Adamantyl Groups. *Macromolecules* **2008**, *41* (20), 7416–7422. https://doi.org/10.1021/ma801202f.

(70) Rodell, C. B.; Kaminski, A.; Burdick, J. A. Rational Design of Network Properties in Guest-Host Assembled and Shear-Thinning Hyaluronic Acid Hydrogels. *Biomacromolecules* **2013**, *14*, 4125–4134. https://doi.org/10.1021/bm401280z.Rational.

(71) Leenders, C. M. A.; Mes, T.; Baker, M. B.; Koenigs, M. M. E.; Besenius, P.; Palmans, A. R. A.; Meijer, E. W. From Supramolecular Polymers to Hydrogel Materials. *Mater. Horizons* **2014**, *1* (1), 116–120. https://doi.org/10.1039/c3mh00103b.

(72) Dankers, P. Y. W.; Hermans, T. M.; Baughman, T. W.; Kamikawa, Y.; Kieltyka, R. E.; Bastings, M. M. C.; Janssen, H. M.; Sommerdijk, N. A. J. M.; Larsen, A.; van Luyn, M. J. A.; Bosman, A. W.; Popa, E. R.; Fytas, G.; Meijer, E. W. Hierarchical Formation of Supramolecular Transient Networks in Water: A Modular Injectable Delivery System. *Adv. Mater.* **2012**, *24* (20), 2703–2709. https://doi.org/10.1002/adma.201104072.

(73) Cui, H.; Webber, M. J.; Stupp, S. I. Self-Assembly of Peptide Amphiphiles: From Molecules to Nanostructures to Biomaterials. *Biopolymers* **2010**, *94* (1), 1–18. https://doi.org/10.1002/bip.21328.

(74) Dehsorkhi, A.; Castelletto, V.; Hamley, I. W. Self-Assembling Amphiphilic Peptides. *J. Pept. Sci.* **2014**, *20* (7), 453–467. https://doi.org/10.1002/psc.2633.

(75) Boekhoven, J.; Stupp, S. I. 25th Anniversary Article: Supramolecular Materials for Regenerative Medicine. *Adv. Mater.* **2014**, *26* (11), 1642–1659. https://doi.org/10.1002/adma.201304606.

(76) Grindy, S. C.; Learsch, R.; Mozhdehi, D.; Cheng, J.; Barrett, D. G.; Guan, Z. B.; Messersmith, P. B.; Holten-Andersen, N. Control of Hierarchical Polymer Mechanics with Bioinspired Metal-Coordination Dynamics. *Nat. Mater.* **2015**, *14* (12), 1210–1216. https://doi.org/10.1038/NMAT4401.

(77) Du, X.; Zhou, J.; Shi, J.; Xu, B. Supramolecular Hydrogelators and Hydrogels: From Soft Matter to Molecular Biomaterials. *Chem. Rev.* **2015**, *115* (24), 13165–13307. https://doi.org/10.1021/acs.chemrev.5b00299.

(78) Dooling, L. J.; Tirrell, D. A. Engineering the Dynamic Properties of Protein Networks through Sequence Variation. *ACS Cent. Sci.* **2016**, *2* (11), 812–819. https://doi.org/10.1021/acscentsci.6b00205.

(79) Maskarinec, S. A.; Tirrell, D. A. Protein Engineering Approaches to Biomaterials Design. *Curr. Opin. Biotechnol.* **2005**, *16* (4), 422–426. https://doi.org/10.1016/j.copbio.2005.06.009.

(80) Kopeček, J.; Yang, J. Smart Self-Assembled Hybrid Hydrogel Biomaterials. *Angew. Chemie - Int. Ed.* **2012**, *51* (30), 7396–7417. https://doi.org/10.1002/anie.201201040.

(81) Liu, J. Oligonucleotide-Functionalized Hydrogels as Stimuli Responsive Materials and Biosensors. *Soft Matter* **2011**, *7*, 6757. https://doi.org/10.1039/c1sm05284e.

(82) Li, J.; Zheng, C.; Cansiz, S.; Wu, C.; Xu, J.; Cui, C.; Liu, Y.; Hou, W.; Wang, Y.; Zhang, L.; Teng, I. T.; Yang, H. H.; Tan, W. Self-Assembly of DNA Nanohydrogels with Controllable Size and Stimuli-Responsive Property for Targeted Gene Regulation Therapy. *J. Am. Chem. Soc.* **2015**, *137* (4), 1412–1415. https://doi.org/10.1021/ja512293f.

(83) De La Rica, R.; Aili, D.; Stevens, M. M. Enzyme-Responsive Nanoparticles for Drug Release and Diagnostics. *Adv. Drug Deliv. Rev.* **2012**, *64*, 967–978. https://doi.org/10.1016/j.addr.2012.01.002.

(84) Mura, S.; Nicolas, J.; Couvreur, P. Stimuli-Responsive Nanocarriers for Drug Delivery. *Nat. Mater.* **2013**, *12* (11), 991–1003. https://doi.org/10.1038/NMAT3776.

(85) Gao, Y.; Shi, J.; Yuan, D.; Xu, B. Imaging Enzyme-Triggered Self-Assembly of Small Molecules inside Live Cells. *Nat. Commun.* **2012**, *3*, 1033–1038. https://doi.org/10.1038/ncomms2040.

(86) Schiffer, D.; Tegl, G.; Heinzle, A.; Sigl, E.; Metcalf, D.; Bowler, P.; Burnet, M.; Guebitz, G. M. Enzyme-Responsive Polymers for Microbial Infection Detection. *Expert Rev. Mol. Diagn.* **2015**, *15* (9), 1125–1131. https://doi.org/10.1586/14737159.2015.1061935.

(87) Moreira Teixeira, L. S.; Feijen, J.; van Blitterswijk, C. A.; Dijkstra, P. J.; Karperien, M. Enzyme-Catalyzed Crosslinkable Hydrogels: Emerging Strategies for Tissue Engineering. *Biomaterials* **2012**, *33* (5), 1281–1290. https://doi.org/10.1016/j.biomaterials.2011.10.067.

(88) Phelps, E. A.; Landázuri, N.; Thulé, P. M.; Taylor, W. R.; García, A. J. Bioartificial Matrices for Therapeutic Vascularization. *Proc. Natl. Acad. Sci. U. S. A.* **2010**, *107* (8), 3323–3328.

https://doi.org/10.1073/pnas.0905447107.
(89) Tsurkan, M. V.; Chwalek, K.; Levental, K. R.; Freudenberg, U.; Werner, C. Modular StarPEG-Heparin Gels with Bifunctional Peptide Linkers. *Macromol. Rapid Commun.* **2010**, *31* (17), 1529–1533. https://doi.org/10.1002/marc.201000155.
(90) Dickinson, H. R.; Hiltner, A.; Gibbons, D. F.; Anderson, J. M. Biodegradation of a Poly (a-Amino Acid) Hydrogel . I . In Vivo. *J. Biomed. Mater. Res.* **1981**, *15*, 577–589.
(91) Fonseca, K. B.; Granja, P. L.; Barrias, C. C. Engineering Proteolytically-Degradable Artificial Extracellular Matrices. *Prog. Polym. Sci.* **2014**, *39* (12), 2010–2029. https://doi.org/10.1016/j.progpolymsci.2014.07.003.
(92) Abul-haijarein V, Y. M.; Ulijn, R. V. Enzyme-Responsive Hydrogels for Biomedical Applications. In *Hydrogels in Cell-Based Therapies*; Connon, C. J., Hamley, I. W., Eds.; 2014; pp 112–134.
(93) Lutolf, M. P.; Hubbell, J. A. Synthetic Biomaterials as Instructive Extracellular Microenvironments for Morphogenesis in Tissue Engineering. *Nat. Biotechnol.* **2005**, *23* (1), 47–55. https://doi.org/10.1038/nbt1055.
(94) Nagase, H.; Woessner, J. Matrix Metalloproteinases. *J. Biol. Chem.* **1999**, No. 37, 1–4.
(95) Turk, B. E.; Huang, L. L.; Piro, E. T.; Cantley, L. C. Determination of Protease Cleavage Site Motifs Using Mixture-Based Oriented Peptide Libraries. *Nat. Biotechnol.* **2001**, *19* (July), 661–667. https://doi.org/10.1038/90273.
(96) Patterson, J.; Hubbell, J. A. Enhanced Proteolytic Degradation of Molecularly Engineered PEG Hydrogels in Response to MMP-1 and MMP-2. *Biomaterials* **2010**, *31* (30), 7836–7845. https://doi.org/10.1016/j.biomaterials.2010.06.061.
(97) Lutolf, M. P.; Raeber, G. P.; Zisch, A. H.; Tirelli, N.; Hubbell, J. A. Cell-Responsive Synthetic Hydrogels. *Adv. Mater.* **2003**, *15* (11), 888–892. https://doi.org/10.1002/adma.200304621.
(98) Zisch, A. H.; Lutolf, M. P.; Ehrbar, M.; Raeber, G. P.; Rizzi, S. C.; Davies, N.; Schmökel, H.; Bezuidenhout, D.; Djonov, V.; Zilla, P.; Hubbell, J. A. Cell-Demanded Release of VEGF from Synthetic, Biointeractive Cell-Ingrowth Matrices for Vascularized Tissue Growth. *FASEB J.* **2003**, *17*, 2260–2262.
(99) Lutolf, M. P.; Lauer-Fields, J. L.; Schmoekel, H. G.; Metters, A. T.; Weber, F. E.; Fields, G. B.; Hubbell, J. A. Synthetic Matrix Metalloproteinase-Sensitive Hydrogels for the Conduction of Tissue Regeneration: Engineering Cell-Invasion Characteristics. *Proc. Natl. Acad. Sci. U. S. A.* **2003**, *100* (9), 5413–5418. https://doi.org/10.1073/pnas.0737381100.
(100) Gjorevski, N.; Sachs, N.; Manfrin, A.; Giger, S.; Bragina, M. E.; Ordóñez-Morán, P.; Clevers, H.; Lutolf, M. P. Designer Matrices for Intestinal Stem Cell and Organoid Culture. *Nature* **2016**, *539* (7630), 560–564. https://doi.org/10.1038/nature20168.
(101) Nair, D. P.; Podgórski, M.; Chatani, S.; Gong, T.; Xi, W.; Fenoli, C. R.; Bowman, C. N. The Thiol-Michael Addition Click Reaction: A Powerful and Widely Used Tool in Materials Chemistry. *Chem. Mater.* **2013**, *26* (1), 724–744. https://doi.org/10.1021/cm402180t.
(102) Phelps, E. A.; Enemchukwu, N. O.; Fiore, V. F.; Sy, J. C.; Murthy, N.; Sulchek, T. A.; Barker, T. H.; García, A. J. Maleimide Cross-Linked Bioactive PEG Hydrogel Exhibits Improved Reaction Kinetics and Cross-Linking for Cell Encapsulation and in Situ Delivery. *Adv. Mater.* **2012**, *24* (1), 64–70. https://doi.org/10.1002/adma.201103574.
(103) Chwalek, K.; Tsurkan, M. V; Freudenberg, U.; Werner, C. Glycosaminoglycan-Based Hydrogels to Modulate Heterocellular Communication in in Vitro Angiogenesis Models. *Sci. Rep.* **2014**, *4*, 4414. https://doi.org/10.1038/srep04414.
(104) Mather, B. D.; Viswanathan, K.; Miller, K. M.; Long, T. E. Michael Addition Reactions in Macromolecular Design for Emerging Technologies. *Prog. Polym. Sci.* **2006**, *31* (5), 487–531. https://doi.org/10.1016/j.progpolymsci.2006.03.001.
(105) Wade, R. J.; Bassin, E. J.; Gramlich, W. M.; Burdick, J. A. Nanofibrous Hydrogels with Spatially Patterned Biochemical Signals to Control Cell Behavior. *Adv. Mater.* **2015**, *27* (8), 1356–1362. https://doi.org/10.1002/adma.201404993.
(106) Grim, J. C.; Marozas, I. A.; Anseth, K. S. Thiol-Ene and Photo-Cleavage Chemistry for Controlled Presentation of Biomolecules in Hydrogels. *J. Control. Release* **2015**, *219*, 95–106. https://doi.org/10.1016/j.jconrel.2015.08.040.
(107) Sawicki, L. A.; Kloxin, A. M. Light-Mediated Formation and Patterning of Hydrogels for Cell Culture Applications. *J. Vis. Exp.* **2016**, No. 115, 1–10. https://doi.org/10.3791/54462.

(108) Ouyang, L.; Highley, C. B.; Sun, W.; Burdick, J. A. A Generalizable Strategy for the 3D Bioprinting of Hydrogels from Nonviscous Photo-Crosslinkable Inks. *Adv. Mater.* **2017**, 1604983. https://doi.org/10.1002/adma.201604983.

(109) Stichler, S.; Bertlein, S.; Tessmar, J.; Jüngst, T.; Groll, J. Thiol-Ene Cross-Linkable Hydrogels as Bioinks for Biofabrication. *Macromol. Symp.* **2017**, *372* (1), 102–107. https://doi.org/10.1002/masy.201600173.

(110) Anderson, S. B.; Lin, C. C.; Kuntzler, D. V.; Anseth, K. S. The Performance of Human Mesenchymal Stem Cells Encapsulated in Cell-Degradable Polymer-Peptide Hydrogels. *Biomaterials* **2011**, *32* (14), 3564–3574. https://doi.org/10.1016/j.biomaterials.2011.01.064.

(111) Van Hove, A. H.; Burke, K.; Antonienko, E.; Brown, E.; Benoit, D. S. W. Enzymatically-Responsive pro-Angiogenic Peptide-Releasing Poly(Ethylene Glycol) Hydrogels Promote Vascularization in Vivo. *J. Control. Release* **2015**, *217*, 191–201. https://doi.org/10.1016/j.jconrel.2015.09.005.

(112) Khetan, S.; Guvendiren, M.; Legant, W. R.; Cohen, D. M.; Chen, C. S.; Burdick, J. A. Degradation-Mediated Cellular Traction Directs Stem Cell Fate in Covalently Crosslinked Three-Dimensional Hydrogels. *Nat. Mater.* **2013**, *12* (5), 458–465. https://doi.org/10.1038/nmat3586.

(113) Purcell, B. P.; Lobb, D.; Charati, M. B.; Dorsey, S. M.; Wade, R. J.; Zellars, K. N.; Doviak, H.; Pettaway, S.; Logdon, C. B.; Shuman, J. A.; Freels, P. D.; Gorman III, J. H.; Gorman, R. C.; Spinale, F. G.; Burdick, J. A. Injectable and Bioresponsive Hydrogels for On-Demand Matrix Metalloproteinase Inhibition. *Nat. Mater.* **2014**, *13* (6), 653–661. https://doi.org/10.1038/nmat3922.

(114) Hsu, C. W.; Olabisi, R. M.; Olmsted-Davis, E. A.; Davis, A. R.; West, J. L. Cathepsin K-Sensitive Poly(Ethylene Glycol) Hydrogels for Degradation in Response to Bone Resorption. *J. Biomed. Mater. Res. - Part A* **2011**, *98A* (1), 53–62. https://doi.org/10.1002/jbm.a.33076.

(115) Brubaker, C. E.; Messersmith, P. B. Enzymatically Degradable Mussel-Inspired Adhesive Hydrogel. *Biomacromolecules* **2011**, *12* (12), 4326–4334. https://doi.org/10.1021/bm201261d.

(116) Aimetti, A. A.; Tibbitt, M. W.; Anseth, K. S.; Aimetti, A. A.; Tibbitt, M. W.; Anseth, K. S. Human Neutrophil Elastase Responsive Delivery from Poly (Ethylene Glycol) Hydrogels. *Biomacromolecules* **2009**, *10*, 1484–1489.

(117) Aimetti, A. A.; Machen, A. J.; Anseth, K. S. Poly(Ethylene Glycol) Hydrogels Formed by Thiol-Ene Photopolymerization for Enzyme-Responsive Protein Delivery. *Biomaterials* **2009**, *30*, 6048–6054. https://doi.org/10.1016/j.biomaterials.2009.07.043.

(118) Maitz, M. F.; Freudenberg, U.; Tsurkan, M. V; Fischer, M.; Beyrich, T.; Werner, C. Bio-Responsive Polymer Hydrogels Homeostatically Regulate Blood Coagulation. *Nat. Commun* **2013**, *4*, 2168. https://doi.org/10.1038/ncomms3168.

(119) Du, H.; Li, C.; Luan, Y.; Liu, Q.; Yang, W.; Yu, Q.; Li, D.; Brash, J. L.; Chen, H. An Antithrombotic Hydrogel with Thrombin-Responsive Fibrinolytic Activity: Breaking down the Clot as It Forms. *Mater. Horiz.* **2016**, *3* (6), 556–562. https://doi.org/10.1039/C6MH00307A.

(120) Nagase, H.; Fields, G. B. Human Matrix Metalloproteinase Specificity Studies Using Collagen Sequence-Based Synthetic Peptides. *Biopolymers* **1996**, *40* (4), 399–416. https://doi.org/10.1002/(SICI)1097-0282(1996)40:4<399::AID-BIP5>3.0.CO;2-R.

(121) Yang, B. Z.; Xu, K.; Guo, Z.; Guo, Z.; Xu, B. Intracellular Enzymatic Formation of Nanofibers Results in Hydrogelation and Regulated Cell Death. *Adv. Mater.* **2007**, *19*, 3152–3156. https://doi.org/10.1002/adma.200701971.

(122) Tanaka, A.; Fukuoka, Y.; Morimoto, Y.; Honjo, T.; Koda, D.; Goto, M.; Maruyama, T. Cancer Cell Death Induced by the Intracellular Self-Assembly of an Enzyme-Responsive Supramolecular Gelator. *J. Am. Chem. Soc.* **2015**, *137*, 770–775. https://doi.org/10.1021/ja510156v.

(123) Wang, H.; Feng, Z.; Wang, Y.; Zhou, R.; Yang, Z.; Xu, B. Integrating Enzymatic Self-Assembly and Mitochondria Targeting for Selectively Killing Cancer Cells without Acquired Drug Resistance. *J. Am. Chem. Soc.* **2016**, *138*, 16046–16055. https://doi.org/10.1021/jacs.6b09783.

(124) Huang, P.; Gao, Y.; Lin, J.; Hu, H.; Liao, H.; Yan, X.; Tang, Y. Tumor-Specific Formation of Enzyme-Instructed Supramolecular Self-Assemblies as Cancer Theranostics. *ACS Nano* **2015**, *9* (10), 9517–9527.

(125) Liang, G.; Ren, H.; Rao, J. A Biocompatible Condensation Reaction for Controlled Assembly of Nanostructures in Living Cells. *Nat. Chem.* **2010**, *2* (1), 54–60. https://doi.org/10.1038/nchem.480.

(126) Zheng, Z.; Chen, P.; Xie, M.; Wu, C.; Luo, Y.; Wang, W.; Jiang, J.; Liang, G. Cell Environment-Differentiated Self-Assembly of Nanofibers. *J. Am. Chem. Soc.* **2016**, *138* (35), 11128–11131. https://doi.org/10.1021/jacs.6b06903.

(127) Luo, Z.; Yue, Y.; Zhang, Y.; Yuan, X.; Gong, J.; Wang, L.; He, B.; Liu, Z.; Sun, Y.; Liu, J.; Hu, M.; Zheng, J. Designer D-Form Self-Assembling Peptide Nanofiber Scaffolds for 3-Dimensional Cell Cultures. *Biomaterials* **2013**, *34* (21), 4902–4913. https://doi.org/10.1016/j.biomaterials.2013.03.081.

(128) Shi, J.; Du, X.; Yuan, D.; Zhou, J.; Zhou, N.; Huang, Y.; Xu, B. D-Amino Acids Modulate the Cellular Response of Enzymatic- Instructed Supramolecular Nano Fi Bers of Small Peptides. *Biomacromolecules* **2014**, *15*, 3559–3568. https://doi.org/10.1021/bm5010355.

(129) Kuang, Y.; Shi, J.; Li, J.; Yuan, D.; Alberti, K. A.; Xu, Q.; Xu, B. Pericellular Hydrogel/Nanonets Inhibit Cancer Cells. *Angew. Chemie - Int. Ed.* **2014**, *53* (31), 8104–8107. https://doi.org/10.1002/anie.201402216.

(130) Marchesan, S.; Easton, C. D.; Styan, K. E.; Waddington, L. J.; Kushkaki, F.; Goodall, L.; McLean, K. M.; Forsythe, J. S.; Hartley, P. G. Chirality Effects at Each Amino Acid Position on Tripeptide Self-Assembly into Hydrogel Biomaterials. *Nanoscale* **2014**, *6* (10), 5172. https://doi.org/10.1039/c3nr06752a.

(131) Roberts, J. N.; Sahoo, J. K.; McNamara, L. E.; Burgess, K. V.; Yang, J.; Alakpa, E. V.; Anderson, H. J.; Hay, J.; Turner, L. A.; Yarwood, S. J.; Zelzer, M.; Oreffo, R. O. C.; Ulijn, R. V.; Dalby, M. J. Dynamic Surfaces for the Study of Mesenchymal Stem Cell Growth through Adhesion Regulation. *ACS Nano* **2016**, *10* (7), 6667–6679. https://doi.org/10.1021/acsnano.6b01765.

(132) Postma, S. G. J.; Vialshin, I. N.; Gerritsen, C. Y.; Bao, M.; Huck, W. T. S. Preprogramming Complex Hydrogel Responses Using Enzymatic Reaction Networks. *Angew. Chemie Int. Ed.* **2017**, *56*, 1794–1798. https://doi.org/10.1002/anie.201610875.

(133) Vigen, M.; Ceccarelli, J.; Putnam, A. J. Protease-Sensitive PEG Hydrogels Regulate Vascularization in Vitro and in Vivo. *Macromol. Biosci.* **2014**, *14* (10), 1368–1379. https://doi.org/10.1002/mabi.201400161.

(134) Holloway, J. L.; Ma, H.; Rai, R.; Burdick, J. A. Modulating Hydrogel Crosslink Density and Degradation to Control Bone Morphogenetic Protein Delivery and in Vivo Bone Formation. *J. Control. Release* **2014**, *191*, 63–70. https://doi.org/10.1016/j.jconrel.2014.05.053.

(135) Eyckmans, J.; Boudou, T.; Yu, X.; Chen, C. S. A Hitchhiker's Guide to Mechanobiology. *Dev. Cell* **2011**, *21* (1), 35–47. https://doi.org/10.1016/j.devcel.2011.06.015.

(136) Discher, D. E.; Janmey, P.; Wang, Y. L. Tissue Cells Feel and Respond to the Stiffness of Their Substrate. *Science.* **2005**, *310* (5751), 1139–1143. https://doi.org/10.1126/science.1116995.

(137) Wen, J. H.; Vincent, L. G.; Fuhrmann, A.; Choi, Y. S.; Hribar, K. C.; Taylor-Weiner, H.; Chen, S.; Engler, A. J. Interplay of Matrix Stiffness and Protein Tethering in Stem Cell Differentiation. *Nat. Mater.* **2014**, *13*, 979–987. https://doi.org/10.1038/nmat4051.

(138) Storm, C.; Pastore, J. J.; MacKintosh, F.; Lubensky, T.; Jamney, P. A. Nonlinear Elasticity in Biological Gels. *Nature* **2005**, *435*, 191–194. https://doi.org/10.1038/nature03497.1.

(139) Nam, S.; Lee, J.; Brownfield, D. G.; Chaudhuri, O. Viscoplasticity Enables Mechanical Remodeling of Matrix by Cells. *Biophys. J.* **2016**, *111* (10), 2296–2308. https://doi.org/10.1016/j.bpj.2016.10.002.

(140) Yan, C.; Pochan, D. J. Rheological Properties of Peptide-Based Hydrogels for Biomedical and Other Applications. *Chem. Soc. Rev.* **2010**, *39* (9), 3528. https://doi.org/10.1039/b919449p.

(141) Erk, K. A.; Henderson, K. J.; Shull, K. R. Strain Stiffening in Synthetic and Biopolymer Networks. *Biomacromolecules* **2010**, *11* (5), 1358–1363. https://doi.org/10.1021/bm100136y.

(142) Winer, J. P.; Oake, S.; Janmey, P. A. Non-Linear Elasticity of Extracellular Matrices Enables Contractile Cells to Communicate Local Position and Orientation. *PLoS One* **2009**, *4* (7), 6382. https://doi.org/10.1371/journal.pone.0006382.

(143) Kouwer, P. H. J.; Koepf, M.; Le Sage, V. A. A.; Jaspers, M.; van Buul, A. M.; Eksteen-Akeroyd, Z. H.; Woltinge, T.; Schwartz, E.; Kitto, H. J.; Hoogenboom, R.; Picken, S. J.; Nolte, R. J. M.; Mendes, E.; Rowan, A. E. Responsive Biomimetic Networks from Polyisocyanopeptide Hydrogels. *Nature* **2013**, *493* (7434), 651–655. https://doi.org/10.1038/nature11839.

(144) Jaspers, M.; Pape, A. C. H.; Voets, I. K.; Rowan, A. E.; Portale, G.; Kouwer, P. H. J. Bundle Formation in Biomimetic Hydrogels. *Biomacromolecules* **2016**, *17* (8), 2642–2649.

https://doi.org/10.1021/acs.biomac.6b00703.
(145) Jaspers, M.; Dennison, M.; Mabesoone, M. F. J.; MacKintosh, F. C.; Rowan, A. E.; Kouwer, P. H. J. Ultra-Responsive Soft Matter from Strain-Stiffening Hydrogels. *Nat. Commun.* **2014**, *5*, 5808. https://doi.org/10.1038/ncomms6808.
(146) Romera, M. F.; Guibert, C.; Voets, I. K.; Storm, C.; Sijbesma, R. P. Strain Stiffening Hydrogels through Self-Assembly and Covalent Fixation of Semi-Flexible Fibers. *Angew. Chemie* **2017**. https://doi.org/10.1002/anie.201704046.
(147) Cameron, A. R.; Frith, J. E.; Cooper-White, J. J. The Influence of Substrate Creep on Mesenchymal Stem Cell Behaviour and Phenotype. *Biomaterials* **2011**, *32* (26), 5979–5993. https://doi.org/10.1016/j.biomaterials.2011.04.003.
(148) Chaudhuri, O.; Gu, L.; Darnell, M.; Klumpers, D.; Bencherif, S. A.; Weaver, J. C.; Huebsch, N.; Mooney, D. J. Substrate Stress Relaxation Regulates Cell Spreading. *Nat. Commun.* **2015**, *6*, 6364. https://doi.org/10.1038/ncomms7365.
(149) Chaudhuri, O.; Gu, L.; Klumpers, D.; Darnell, M.; Bencherif, S. A.; Weaver, J. C.; Huebsch, N.; Lee, H.-P.; Lippens, E.; Duda, G. N.; Mooney, D. J. Hydrogels with Tunable Stress Relaxation Regulate Stem Cell Fate and Activity. *Nat. Mater.* **2015**, *15* (November), 326–333. https://doi.org/10.1038/nmat4489.
(150) McKinnon, D. D.; Domaille, D. W.; Cha, J. N.; Anseth, K. S. Bis-Aliphatic Hydrazone-Linked Hydrogels Form Most Rapidly at Physiological PH: Identifying the Origin of Hydrogel Properties with Small Molecule Kinetic Studies. *Chem. Mater.* **2014**, *26* (7), 2382–2387. https://doi.org/10.1021/cm5007789.
(151) McKinnon, D. D.; Domaille, D. W.; Brown, T. E.; Kyburz, K. a; Kiyotake, E.; Cha, J. N.; Anseth, K. S. Measuring Cellular Forces Using Bis-Aliphatic Hydrazone Crosslinked Stress-Relaxing Hydrogels. *Soft Matter* **2014**, *10* (46), 9230–9236. https://doi.org/10.1039/c4sm01365d.
(152) Yesilyurt, V.; Webber, M. J.; Appel, E. A.; Godwin, C.; Langer, R.; Anderson, D. G. Injectable Self-Healing Glucose-Responsive Hydrogels with PH-Regulated Mechanical Properties. *Adv. Mater.* **2016**, *28* (1), 86–91. https://doi.org/10.1002/adma.201502902.
(153) Rowland, M. J.; Atgie, M.; Hoogland, D.; Scherman, O. A. Preparation and Supramolecular Recognition of Multivalent Peptide-Polysaccharide Conjugates by Cucurbit[8]Uril in Hydrogel Formation. *Biomacromolecules* **2015**, *16*, 2436–2443. https://doi.org/10.1021/acs.biomac.5b00680.
(154) Bastings, M. M. C.; Koudstaal, S.; Kieltyka, R. E.; Nakano, Y.; Pape, A. C. H.; Feyen, D. A. M.; van Slochteren, F. J.; Doevendans, P. A.; Sluijter, J. P. G.; Meijer, E. W.; Chamuleau, S. A. J.; Dankers, P. Y. W. A Fast PH-Switchable and Self-Healing Supramolecular Hydrogel Carrier for Guided, Local Catheter Injection in the Infarcted Myocardium. *Adv. Healthc. Mater.* **2014**, *3* (1), 70–78. https://doi.org/10.1002/adhm.201300076.
(155) Pawar, G. M.; Koenigs, M.; Fahimi, Z.; Cox, M.; Voets, I. K.; Wyss, H. M.; Sijbesma, R. P. Injectable Hydrogels from Segmented PEG-Bisurea Copolymers. *Biomacromolecules* **2012**, *13* (12), 3966–3976. https://doi.org/10.1021/bm301242v.
(156) Boekhoven, J.; Rubert pérez, C. M.; Sur, S.; Worthy, A.; Stupp, S. I. Dynamic Display of Bioactivity through Host-Guest Chemistry. *Angew. Chemie - Int. Ed.* **2013**, *52* (46), 12077–12080. https://doi.org/10.1002/anie.201306278.
(157) Neirynck, P.; Schimer, J.; Jonkheijm, P.; Milroy, L.-G.; Cigler, P.; Brunsveld, L. Carborane–β-Cyclodextrin Complexes as a Supramolecular Connector for Bioactive Surfaces. *J. Mater. Chem. B* **2015**, *3* (4), 539–545. https://doi.org/10.1039/C4TB01489H.
(158) Okumura, Y.; Ito, K. The Polyrotaxane Gel: A Topological Gel by Figure-of-Eight Cross-Links. *Adv. Mater.* **2001**, *13* (7), 485–487. https://doi.org/10.1002/1521-4095(200104)13:7<485::AID-ADMA485>3.0.CO;2-T.
(159) Ito, K. Slide-Ring Materials Using Topological Supramolecular Architecture. *Curr. Opin. Solid State Mater. Sci.* **2010**, *14* (2), 28–34. https://doi.org/10.1016/j.cossms.2009.08.005.
(160) Tong, X.; Yang, F. Sliding Hydrogels with Mobile Molecular Ligands and Crosslinks as 3D Stem Cell Niche. *Adv. Mater.* **2016**, *28* (33), 7257–7263. https://doi.org/10.1002/adma.201601484.
(161) Chen, Y.; Radford, S. E.; Brockwell, D. J. Force-Induced Remodelling of Proteins and Their Complexes. *Curr. Opin. Struct. Biol.* **2015**, *30*, 89–99. https://doi.org/10.1016/j.sbi.2015.02.001.
(162) Lavalle, P.; Boulmedais, F.; Schaaf, P.; Jierry, L. Soft-Mechanochemistry: Mechanochemistry Inspired by Nature. *Langmuir* **2016**, *32* (29), 7265–7276.

https://doi.org/10.1021/acs.langmuir.6b01768.

(163) Rakshit, S.; Sivasankar, S. Biomechanics of Cell Adhesion: How Force Regulates the Lifetime of Adhesive Bonds at the Single Molecule Level. *Phys. Chem. Chem. Phys.* **2014**, *16* (6), 2211–2223. https://doi.org/10.1039/c3cp53963f.

(164) Rakshit, S.; Zhang, Y.; Manibog, K.; Shafraz, O.; Sivasankar, S. Ideal, Catch, and Slip Bonds in Cadherin Adhesion. *Proc. Natl. Acad. Sci.* **2012**, *109* (46), 18815–18820. https://doi.org/10.1073/pnas.1208349109.

(165) Konda, S. S. M.; Brantley, J. N.; Varghese, B. T.; Wiggins, K. M.; Bielawski, C. W.; Makarov, D. E. Molecular Catch Bonds and the Anti-Hammond Effect in Polymer Mechanochemistry. *J. Am. Chem. Soc.* **2013**, *135* (34), 12722–12729. https://doi.org/10.1021/ja4051108.

(166) Izawa, H.; Kawakami, K.; Sumita, M.; Tateyama, Y.; Hill, J. P.; Ariga, K. β-Cyclodextrin-Crosslinked Alginate Gel for Patient-Controlled Drug Delivery Systems: Regulation of Host–Guest Interactions with Mechanical Stimuli. *J. Mater. Chem. B* **2013**, *1* (16), 2155. https://doi.org/10.1039/c3tb00503h.

(167) Göstl, R.; Sijbesma, R. P. Π-Extended Anthracenes As Sensitive Probes for Mechanical Stress. *Chem. Sci.* **2016**, *7* (1), 370–375. https://doi.org/10.1039/C5SC03297K.

(168) Robb, M. J.; Kim, T. A.; Halmes, A. J.; White, S. R.; Sottos, N. R.; Moore, J. S. Regioisomer-Specific Mechanochromism of Naphthopyran in Polymeric Materials. *J. Am. Chem. Soc.* **2016**, *138* (38), 12328–12331. https://doi.org/10.1021/jacs.6b07610.

(169) Groote, R.; Szyja, B. M.; Leibfarth, F. A.; Hawker, C. J.; Doltsinis, N. L.; Sijbesma, R. P. Strain-Induced Strengthening of the Weakest Link: The Importance of Intermediate Geometry for the Outcome of Mechanochemical Reactions. *Macromolecules* **2014**, *47* (3), 1187–1192. https://doi.org/10.1021/ma4022339.

(170) Lee, B.; Niu, Z.; Wang, J.; Slebodnick, C.; Craig, S. L. Relative Mechanical Strengths of Weak Bonds in Sonochemical Polymer Mechanochemistry. *J. Am. Chem. Soc.* **2015**, *137* (33), 10826–10832. https://doi.org/10.1021/jacs.5b06937.

(171) Sood, N.; Bhardwaj, A.; Mehta, S.; Mehta, A. Stimuli-Responsive Hydrogels in Drug Delivery and Tissue Engineering. *Drug Deliv.* **2016**, *23* (3), 748–770. https://doi.org/10.3109/10717544.2014.940091.

(172) Gupta, P.; Vermani, K.; Garg, S. Hydrogels: From Controlled Release to PH-Responsive Drug Delivery. *Drug Discov. Today* **2002**, *7* (10), 569–579. https://doi.org/10.1016/S1359-6446(02)02255-9.

(173) Shi, J.; Guobao, W.; Chen, H.; Zhong, W.; Qiu, X.; Xing, M. M. Q. Schiff Based Injectable Hydrogel for in Situ PH-Triggered Delivery of Doxorubicin for Breast Tumor Treatment. *Polym. Chem.* **2014**, *5* (21), 6180–6189. https://doi.org/10.1039/C4PY00631C.

(174) Milanesi, L.; Hunter, C. A.; Tzokova, N.; Waltho, J. P.; Tomas, S. Versatile Low-Molecular-Weight Hydrogelators: Achieving Multiresponsiveness through a Modular Design. *Chem. - A Eur. J.* **2011**, *17* (35), 9753–9761. https://doi.org/10.1002/chem.201100640.

(175) Singh, M.; Kundu, S.; Reddy M, A.; Sreekanth, V.; Motiani, R. K.; Sengupta, S.; Srivastava, A.; Bajaj, A. Injectable Small Molecule Hydrogel as a Potential Nanocarrier for Localized and Sustained in Vivo Delivery of Doxorubicin. *Nanoscale* **2014**, *6* (21), 12849–12855. https://doi.org/10.1039/c4nr04064c.

(176) Yan, Q.; Yuan, J.; Cai, Z.; Xin, Y.; Kang, Y.; Yin, Y. Voltage-Responsive Vesicles Based on Orthogonal Assembly of Two Homopolymers. *J. Am. Chem. Soc.* **2010**, *132* (27), 9268–9270. https://doi.org/10.1021/ja1027502.

(177) Chen, S. L.; Chen, X.; Chen, L.; Yao, X.; Zhang, Z.; He, C.; Zhang, J.; Chen, X. Dual Responsive Supramolecular Nanogels for Intracellular Drug Delivery. *Chem. Commun. Chem. Commun* **2014**, *50* (50), 3789–3791.

(178) Yu, S. S.; Koblin, R. L.; Zachman, A. L.; Perrien, D. S.; Hofmeister, L. H.; Giorgio, T. D.; Sung, H. J. Physiologically Relevant Oxidative Degradation of Oligo(Proline) Cross-Linked Polymeric Scaffolds. *Biomacromolecules* **2011**, *12* (12), 4357–4366. https://doi.org/10.1021/bm201328k.

(179) Lee, S. H.; Boire, T. C.; Lee, J. B.; Gupta, M. K.; Zachman, A. L.; Rath, R.; Sung, H. J. ROS-Cleavable Proline Oligomer Crosslinking of Polycaprolactone for pro-Angiogenic Host Response. *J. Mater. Chem. B* **2014**, *2* (41), 7109–7113. https://doi.org/10.1039/C4TB01094A.

(180) Dollinger, B. R.; Gupta, M. K.; Martin, J. R.; Duvall, C. L. Reactive Oxygen Species Shielding

Hydrogel for the Delivery of Adherent and Nonadherent Therapeutic Cell Types. *Tissue Eng. Part A* **2017**, *00* (00), 10.1089/ten.tea.2016.0495. https://doi.org/10.1089/ten.tea.2016.0495.

(181) Peppas, N. A.; Bures, C. D. Glucose-Responsive Hydrogels. *Encyclopedia of Biomaterials and Biomedical Engineering*; 2006; pp 1163–1173. https://doi.org/10.1081/E-EBBE-120042786.

(182) Zhou, Y.; Fan, X.; Zhang, W.; Xue, D.; Kong, J. Stimuli-Induced Gel-Sol Transition of Supramolecular Hydrogels Based on Beta-Cyclodextrin Polymer/Ferrocene-Containing Triblock Copolymer Inclusion Complexes. *J. Polym. Res.* **2014**, *21*, 359. https://doi.org/10.1007/s10965-014-0359-x.

(183) Kataoka, K.; Miyazaki, H.; Bunya, M.; Okano, T.; Sakurai, Y. Totally Synthetic Polymer Gels Responding to External Glucose Concentration : Their Preparation and Application to On - Off Regulation of Insulin Release. *J. Am. Chem. Soc.* **1998**, *120* (13), 12694–12695.

(184) Dong, Y.; Wang, W.; Veiseh, O.; Appel, E. A.; Xue, K.; Webber, M. J.; Tang, B. C.; Yang, X. W.; Weir, G. C.; Langer, R.; Anderson, D. G. Injectable and Glucose-Responsive Hydrogels Based on Boronic Acid-Glucose Complexation. *Langmuir* **2016**, *32* (34), 8743–8747. https://doi.org/10.1021/acs.langmuir.5b04755.

(185) Geraths, C.; Christen, E. H.; Weber, W. A Hydrogel Sensing Pathological Urate Concentrations. *Macromol. Rapid Commun.* **2012**, *33* (24), 2103–2108. https://doi.org/10.1002/marc.201200563.

(186) Geraths, C.; Baba, M. D.; Hamri, G. C.; Weber, W. A Biohybrid Hydrogel for the Urate-Responsive Release of Urate Oxidase. *J. Control. Release* **2013**, *171* (1), 57–62. https://doi.org/10.1016/j.jconrel.2013.06.037.

(187) Murphy, W. L.; Dillmore, W. S.; Modica, J.; Mrksich, M. Dynamic Hydrogels: Translating a Protein Conformational Change into Macroscopic Motion. *Angew. Chemie - Int. Ed.* **2007**, *46* (17), 3066–3069. https://doi.org/10.1002/anie.200604808.

(188) Ehrick, J. D.; Deo, S. K.; Browning, T. W.; Bachas, L. G.; Madou, M. J.; Daunert, S. Genetically Engineered Protein in Hydrogels Tailors Stimuli-Responsive Characteristics. *Nat. Mater.* **2005**, *4* (4), 298–302. https://doi.org/10.1038/nmat1352.

(189) King, W. J.; Toepke, M. W.; Murphy, W. L. Facile Formation of Dynamic Hydrogel Microspheres for Triggered Growth Factor Delivery. *Acta Biomater.* **2011**, *7* (3), 975–985. https://doi.org/10.1016/j.actbio.2010.10.026.

(190) Li, H.; Kong, N.; Laver, B.; Liu, J. Hydrogels Constructed from Engineered Proteins. *Small* **2016**, *12* (8), 973–987. https://doi.org/10.1002/smll.201502429.

(191) Yuan, W.; Yang, J.; Kopečková, P.; Kopeček, J. Smart Hydrogels Containing Adenylate Kinase: Translating Substrate Recognition into Macroscopic Motion. *J. Am. Chem. Soc.* **2008**, *130* (47), 15760–15761. https://doi.org/10.1021/ja805634x.

(192) Yang, H.; Liu, H.; Kang, H.; Tan, W. Engineering Target-Responsive Hydrogels Based on Aptamer-Target Interactions. *J. Am. Chem. Soc.* **2008**, *130*, 6320–6321. https://doi.org/10.1021/ja801339w.

(193) Li, W.; Wang, J.; Ren, J.; Qu, X. Endogenous Signalling Control of Cell Adhesion by Using Aptamer Functionalized Biocompatible Hydrogel. *Chem. Sci.* **2015**, *6* (12), 6762–6768. https://doi.org/10.1039/C5SC02565F.

(194) Rouwkema, J.; Khademhosseini, A. Vascularization and Angiogenesis in Tissue Engineering: Beyond Creating Static Networks. *Trends Biotechnol.* **2016**, *34* (9), 733–745. https://doi.org/10.1016/j.tibtech.2016.03.002.

(195) Malheiro, A.; Wieringa, P.; Mota, C.; Baker, M.; Moroni, L. Patterning Vasculature: The Role of Biofabrication to Achieve an Integrated Multicellular Ecosystem. *ACS Biomater. Sci. Eng.* **2016**, *2* (10), 1694–1709. https://doi.org/10.1021/acsbiomaterials.6b00269.

(196) Camci-Unal, G.; Alemdar, N.; Annabi, N.; Khademhosseini, A. Oxygen-Releasing Biomaterials for Tissue Engineering. *Polym. Int.* **2013**, *62* (6), 843–848. https://doi.org/10.1002/pi.4502.

(197) Qian, Y.; Matson, J. B. Gasotransmitter Delivery via Self-Assembling Peptides: Treating Diseases with Natural Signaling Gases. *Adv. Drug Deliv. Rev.* **2017**, *110–111*, 137–156. https://doi.org/10.1016/j.addr.2016.06.017.

(198) Farris, A.; Rindone, A.; Grayson, W. Oxygen Delivering Biomaterials for Tissue Engineering. *J. Mater. Chem. B* **2016**, *4*, 3422–3432. https://doi.org/10.1039/C5TB02635K.

(199) Palumbo, F. S.; Di Stefano, M.; Palumbo Piccionello, A.; Fiorica, C.; Pitarresi, G.; Pibiri, I.; Buscemi, S.; Giammona, G. Perfluorocarbon Functionalized Hyaluronic Acid Derivatives as

Oxygenating Systems for Cell Culture. *RSC Adv.* **2014**, *4* (44), 22894–22901. https://doi.org/10.1039/c4ra01502a.

(200) Li, H.; Wijekoon, A.; Leipzig, N. D. Encapsulated Neural Stem Cell Neuronal Differentiation in Fluorinated Methacrylamide Chitosan Hydrogels. *Ann. Biomed. Eng.* **2014**, *42* (7), 1456–1469. https://doi.org/10.1007/s10439-013-0925-0.

(201) Kellner, K.; Liebsch, G.; Klimant, I.; Wolfbeis, O. S.; Blunk, T.; Schulz, M. B.; Göpferich, A. Determination of Oxygen Gradients in Engineered Tissue Using a Fluorescent Sensor. *Biotechnol. Bioeng.* **2002**, *80* (1), 73–83. https://doi.org/10.1002/bit.10352.

(202) Roussakis, E.; Li, Z.; Nichols, A. J.; Evans, C. L. Oxygen-Sensing Methods in Biomedicine from the Macroscale to the Microscale. *Angew. Chemie - Int. Ed.* **2015**, *54* (29), 8340–8362. https://doi.org/10.1002/anie.201410646.

(203) Zhou, X.; Su, F.; Tian, Y.; Meldrum, D. R. Dually Fluorescent Core-Shell Microgels for Ratiometric Imaging in Live Antigen-Presenting Cells. *PLoS One* **2014**, *9* (2). https://doi.org/10.1371/journal.pone.0088185.

(204) Nagamine, K.; Okamoto, K.; Otani, S.; Kaji, H.; Kanzaki, M.; Nishizawa, M. Hydrogel-Based Bioassay Sheets for in Vitro Evaluation of Contraction-Dependent Metabolic Regulation in Skeletal Muscle Cells. *Biomater. Sci.* **2014**, *4*, 252–256. https://doi.org/10.1039/c3bm60179j.

(205) Tian, Y.; Shumway, B. R.; Meldrum, D. R. A New Cross-Linkable Oxygen Sensor Covalently Bonded into Poly(2-Hydroxyethyl Methacrylate)-Co-Polyacrylamide Thin Film for Dissolved Oxygen Sensing. *Chem. Mater.* **2010**, *22* (6), 2069–2078. https://doi.org/10.1021/cm903361y.

(206) Huang, H.; Song, W.; Chen, G.; Reynard, J. M.; Ohulchanskyy, T. Y.; Prasad, P. N.; Bright, F. V.; Lovell, J. F. Pd-Porphyrin-Cross-Linked Implantable Hydrogels with Oxygen-Responsive Phosphorescence. *Adv. Healthc. Mater.* **2014**, *3* (6), 891–896. https://doi.org/10.1002/adhm.201300483.

(207) Lau, H. K.; Kiick, K. L. Opportunities for Multicomponent Hybrid Hydrogels in Biomedical Applications. *Biomacromolecules* **2015**, *16* (1), 28–42. https://doi.org/10.1021/bm501361c.

(208) Morris, E.; Chavez, M.; Tan, C. Dynamic Biomaterials: Toward Engineering Autonomous Feedback. *Curr. Opin. Biotechnol.* **2016**, *39* (Figure 1), 97–104. https://doi.org/10.1016/j.copbio.2016.02.032.

(209) Ikeda, M.; Tanida, T.; Yoshii, T.; Kurotani, K.; Onogi, S.; Urayama, K.; Hamachi, I. Installing Logic-Gate Responses to a Variety of Biological Substances in Supramolecular Hydrogel-Enzyme Hybrids. *Nat. Chem.* **2014**, *6* (6), 511–518. https://doi.org/10.1038/nchem.1937.

(210) Pieters, B. J. G. E.; van Eldijk, M. B.; Nolte, R. J. M.; Mecinović, J. Natural Supramolecular Protein Assemblies. *Chem. Soc. Rev.* **2015**, 24–39. https://doi.org/10.1039/C5CS00157A.

(211) Korevaar, P. A.; George, S. J.; Markvoort, A. J.; Smulders, M. M. J.; Hilbers, P. a J.; Schenning, A. P. H. J.; De Greef, T. F. a; Meijer, E. W. Pathway Complexity in Supramolecular Polymerization. *Nature* **2012**, *481* (7382), 492–496. https://doi.org/10.1038/nature10720.

(212) Noteborn, W. E. M.; Zwagerman, D. N. H.; Talens, V. S.; Maity, C.; van der Mee, L.; Poolman, J. M.; Mytnyk, S.; van Esch, J. H.; Kros, A.; Eelkema, R.; Kieltyka, R. E. Crosslinker-Induced Effects on the Gelation Pathway of a Low Molecular Weight Hydrogel. *Adv. Mater.* **2017**, *29* (12), 1–7. https://doi.org/10.1002/adma.201603769.

(213) Tantakitti, F.; Boekhoven, J.; Wang, X.; Kazantsev, R. V.; Yu, T.; Li, J.; Zhuang, E.; Zandi, R.; Ortony, J. H.; Newcomb, C. J.; Palmer, L. C.; Shekhawat, G. S.; de la Cruz, M. O.; Schatz, G. C.; Stupp, S. I. Energy Landscapes and Functions of Supramolecular Systems. *Nat. Mater.* **2016**, *15* (January), 469–476. https://doi.org/10.1038/nmat4538.

(214) Ogi, S.; Sugiyasu, K.; Manna, S.; Samitsu, S.; Takeuchi, M. Living Supramolecular Polymerization Realized through a Biomimetic Approach. *Nat. Chem.* **2014**, No. 6, 188–190. https://doi.org/10.1038/nchem.1849.

(215) Boekhoven, J.; Hendriksen, W. E.; Koper, G. J. M.; Eelkema, R.; van Esch, J. H. Transient Assembly of Active Materials Fueled by a Chemical Reaction. *Science.* **2015**, *349* (6252), 1075–1079. https://doi.org/10.1126/science.aac6103.

(216) van Rossum, S. A. P.; Tena-Solsona, M.; van Esch, J. H.; Eelkema, R.; Boekhoven, J. Dissipative Out-of-Equilibrium Assembly of Man-Made Supramolecular Materials. *Chem. Soc. Rev.* **2017**. https://doi.org/10.1039/C7CS00246G.

(217) Tena-Solsona, M.; Rieß, B.; Grötsch, R. K.; Löhrer, F. C.; Wanzke, C.; Käsdorf, B.; Bausch, A. R.;

Müller-Buschbaum, P.; Lieleg, O.; Boekhoven, J. Non-Equilibrium Dissipative Supramolecular Materials with a Tunable Lifetime. *Nat. Commun.* **2017**, *8* (May), 15895. https://doi.org/10.1038/ncomms15895.

(218) Baker, M. B.; Albertazzi, L.; Voets, I. K.; Leenders, C. M. A.; Palmans, A. R. A.; Pavan, G. M.; Meijer, E. W. Consequences of Chirality on the Dynamics of a Water-Soluble Supramolecular Polymer. *Nat. Commun.* **2015**, *6*. https://doi.org/10.1038/ncomms7234.

(219) Albertazzi, L.; van der Zwaag, D.; Leenders, C. M. A.; Fitzner, R.; van der Hofstad, R. W.; Meijer, E. W. Probing Exchange Pathways in One-Dimensional Aggregates with Super-Resolution Microscopy. *Science.* **2014**, *344* (6183), 491–495. https://doi.org/10.1126/science.1250945.

(220) Albertazzi, L.; Martinez-Veracoechea, F. J.; Leenders, C. M. A.; Voets, I. K.; Frenkel, D.; Meijer, E. W. Spatiotemporal Control and Superselectivity in Supramolecular Polymers Using Multivalency. *Proc. Natl. Acad. Sci. U. S. A.* **2013**, *110* (30), 12203–12208. https://doi.org/10.1073/pnas.1303109110.

(221) Albertazzi, L.; van der Veeken, N.; Baker, M. B.; Palmans, A. R. A.; Meijer, E. W. Supramolecular Copolymers with Stimuli-Responsive Sequence Control. *Chem. Commun.* **2015**, *51* (90), 16166–16168. https://doi.org/10.1039/C5CC06951C.

(222) Newcomb, C. J.; Sur, S.; Ortony, J. H.; Lee, O.-S.; Matson, J. B.; Boekhoven, J.; Yu, J. M.; Schatz, G. C.; Stupp, S. I. Cell Death versus Cell Survival Instructed by Supramolecular Cohesion of Nanostructures. *Nat. Commun.* **2014**, *5*, 3321. https://doi.org/10.1038/ncomms4321.

(223) Stoddart, J. F. Mechanically Interlocked Molecules (MIMs)-Molecular Shuttles, Switches, and Machines (Nobel Lecture). *Angew. Chemie Int. Ed.* **2017**, 2–34. https://doi.org/10.1002/anie.201703216.

(224) Sauvage, J.-P. From Chemical Topology to Molecular Machines (Nobel Lecture). *Angew. Chemie Int. Ed.* **2017**, 347–359. https://doi.org/10.1002/anie.201702992.

(225) Feringa, B. L. The Art of Building Small: From Molecular Switches to Motors (Nobel Lecture). *Angew. Chemie Int. Ed.* **2017**. https://doi.org/10.1002/anie.201702979.

(226) Bruns, C. J.; Stoddart, J. F. Rotaxane-Based Molecular Muscles. *Acc. Chem. Res.* **2014**, *47* (7), 2186–2199. https://doi.org/10.1021/ar500138u.

(227) Sonmez, C.; Nagy, K. J.; Schneider, J. P. Design of Self-Assembling Peptide Hydrogelators Amenable to Bacterial Expression. *Biomaterials* **2015**, *37*, 62–72. https://doi.org/10.1016/j.biomaterials.2014.10.011.

(228) Shamir, M.; Bar-On, Y.; Phillips, R.; Milo, R. SnapShot: Timescales in Cell Biology. *Cell* **2016**, *164* (6), 1302-1302.e1. https://doi.org/10.1016/j.cell.2016.02.058.

(229) Parmar, P. A.; Skaalure, S. C.; Chow, L. W.; St-Pierre, J. P.; Stoichevska, V.; Peng, Y. Y.; Werkmeister, J. A.; Ramshaw, J. A. M.; Stevens, M. M. Temporally Degradable Collagen-Mimetic Hydrogels Tuned to Chondrogenesis of Human Mesenchymal Stem Cells. *Biomaterials* **2016**, *99*, 56–71. https://doi.org/10.1016/j.biomaterials.2016.05.011.

(230) Parmar, P. A.; St-Pierre, J. P.; Chow, L. W.; Spicer, C. D.; Stoichevska, V.; Peng, Y. Y.; Werkmeister, J. A.; Ramshaw, J. A. M.; Stevens, M. M. Enhanced Articular Cartilage by Human Mesenchymal Stem Cells in Enzymatically Mediated Transiently RGDS-Functionalized Collagen-Mimetic Hydrogels. *Acta Biomater.* **2017**, *51*, 75–88. https://doi.org/10.1016/j.actbio.2017.01.028.

(231) Yang, C.; Tibbitt, M. W.; Basta, L.; Anseth, K. S. Mechanical Memory and Dosing Influence Stem Cell Fate. *Nat. Mater.* **2014**, *13* (6), 645–652. https://doi.org/10.1038/nmat3889.

(232) Whitesides, G. M. Revolutions in Chemistry. *Chem. Eng. News* **2007**, *85* (13), 12–17. https://doi.org/10.1017/CBO9781107415324.

Chapter III

Tuning hydrogel viscoelasticity and dynamic bioinks for 3D bioprinting

Shahzad Hafeez [1] Clemens van Blitterswijk [1] Lorenzo Moroni [1], Matthew B. Baker [1]

[1] Department of Complex Tissue Regeneration, MERLN Institute for Technology Inspired Regenerative Medicine, Maastricht University, P.O. Box 616, 6200 MD Maastricht, The Netherlands.

Introduction

The research in biomaterials and tissue engineering has evolved over the last 5 years, since we published our comprehensive review. A huge portion of the biomaterials community has focused on developing synthetic hydrogels with tunable viscoelasticity and mechanical properties. While **chapter II** serves as an introduction to this thesis, the author feels that it is necessary to provide an update on the viscoelasticity section of the review. We will discuss the tuning of viscoelasticity in two-dimensional (2D) and three-dimensional matrices (3D) and how viscoelasticity influences cell behavior. The author has worked on developing dynamic bioinks for extrusion bioprinting and tissue engineering applications. In the second part of this chapter, we will discuss strategies to develop advanced dynamic bioinks and progress on 3D bioprinting using dynamic bioinks.

Viscoelasticity

The stiffness of the tissue plays a significant role during the development and maturation of tissues[1]. Stiffness is an elastic property of material and tissues, and the extracellular matrix (ECM) exhibits complex time-dependent viscoelasticity. Viscoelastic materials possess both elastic and viscous properties and show time-dependent behavior. The simplest example would be human skin tissue, for example, if you pinch or compress the skin, then you will notice that the skin will take some time to recover. This time dependence on the recovery of skin shows that the skin is viscoelastic. **Figure 1a** shows the storage and loss modulus values of different tissues at 1Hz indicating that skeletal tissues, soft tissues, and reconstituted ECMs are

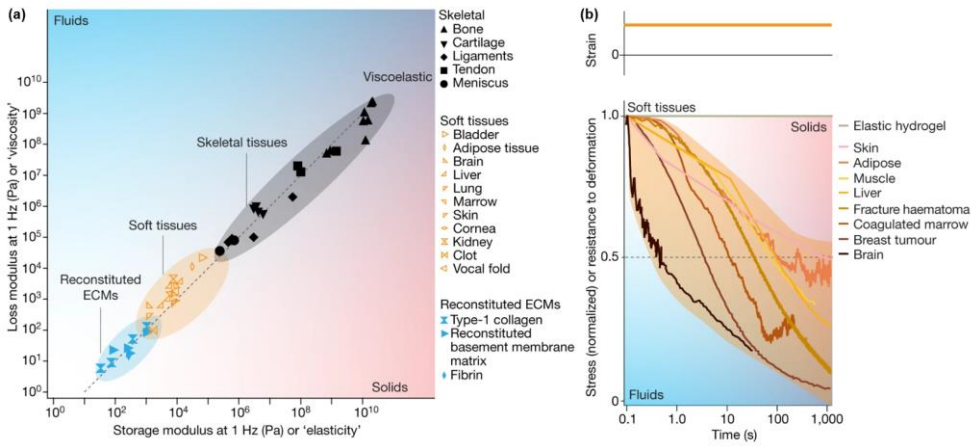

Figure 1. Biological tissues and ECM are viscoelastic and stress-relaxing. a) A graph between storage modulus and loss modulus at approximately 1Hz. Storage modulus represents the elastic component of viscoelasticity and loss modulus represents the viscous component of viscoelasticity. The data shows that skeletal tissues, soft tissues, and reconstituted ECMs are viscoelastic. The grey line indicates loss modulus values, approximately 10% of the storage modulus. b) Stress relaxation profiles of different tissue. Elastic hydrogel is in grey, with a straight horizontal line at 1.0 indicating that covalent hydrogel does not relax stress. Figure 1 was adapted with permission.[1]

viscoelastic[1]. Viscoelasticity can also be measured using a stress relaxation test and by applying a constant strain. A viscoelastic material will dissipate/relax stress as a function of time[1,2]. **Figure 1b** demonstrates the stress relaxation ability of different tissues in contrast to an elastic hydrogel indicated in grey color.

The last decade has seen increasing research in developing viscoelastic matrices and investigating cell-materials interaction on 2-dimensional (2D) and within 3-dimensional (3D) matrices. Scientists have found that, unlike elastic matrices, viscoelastic materials influence cell behavior to produce healthy tissue and influence mechanosensitive pathways differentially. Below, we provide a review of the current strategies for making viscoelastic hydrogels and discuss viscoelasticity's effect on cell behavior.

Chemical strategies for designing 2D viscoelastic hydrogels and cellular behavior on 2D hydrogels

In early studies, polyacrylamide hydrogels with varying viscoelasticity were made by adjusting the bisacrylamide cross-linker ratio (**Figure 2a**). Collagen-coated polyacrylamide hydrogels (2D) with a constant storage modulus, and varying loss moduli (**Figure 2b**) and creep responses showed that human mesenchymal stem cells (hMSCs) exhibited increased spreading (**Figure 2c**), and can differentiation towards osteogenic, adipogenic, and smooth muscle cell lineages. Differences in cellular behavior were attributed to a reduction in isometric tension by using inhibitors for Rho-Kinase and non-muscle myosin II. Reduction in cytoskeletal tension was attributed to inherent creep in substrates with high loss modulus[3]. In the follow-up study, using the same set of matrices, a mechanism for hMSCs with a particular propensity towards smooth muscle cell (SMC) lineage was disclosed on high-creep hydrogels. Rac1 signaling was found to be responsible for higher levels of SMC induction factors including N-cadherin (cell-cell adhesion molecule), increased motility, and lamellipodial protrusion of hMSCs[4]. Viscoelastic and stress-relaxing hydrogels can also be made by ionically cross-linking alginate using calcium ions (**Figure 2d**). Fibroblasts displayed spreading on soft and stress-relaxing substrates of ionically cross-linked alginate hydrogels compared to elastic substrates of the same modulus[5] (**Figure 2e&f**). Ionically cross-linked alginate hydrogels[5] and polyacrylamide hydrogels[3,4] developed above are viscoelastic; however, they also exhibit viscoplasticity (they exhibited creep and cells can induce permanent deformation), and increased cell spreading was associated with viscoplasticity on both alginate and polyacrylamide hydrogels.

To decouple the influence of viscoelasticity from viscoplasticity on cell behavior, covalent polyacrylamide hydrogels with unbound linear acrylamide chains were created (**Figure 2g & Figure 3**). These hydrogels were found to be viscoelastic and allowed independent tuning of elastic and viscous moduli (**Figure 2h**). Compared to elastic hydrogels, fibroblasts showed less spreading on the viscoelastic hydrogel[6] (**Figure 2i**). These findings were in contrast to those obtained with viscoplastic alginate substrates[5]. On a similar set of polyacrylamide viscoelastic hydrogels, normal human hepatocytes exhibited less spreading on viscoelastic substrates

compared to elastic, while the opposite was true for hepatocellular carcinoma cells.[7] We can sometimes see this duality and complex behavior in our own research.

Dynamic covalent chemistry (DCvC) can be employed to make hydrogels with reversible networks. Viscoelasticity and stress relaxation can be correlated with the reverse reaction rate constant (k_{-1}). In our lab, we developed dynamic covalent hydrogels based on imine-type dynamic covalent networks (**chapter IV**) with distinct equilibrium constants (K_{eq}).[8] Hydrazone showed higher viscoelasticity compared to semicarbazone and oxime cross-links. We observed that fibroblast cells stayed round on (2D) oxime hydrogel and showed spreading morphology on hydrazone hydrogels. In the follow-up study from our lab, Morgan et al., tuned stress relaxation time scales across two orders of magnitude by mixing slow (oxime) and fast (hydrazone) dynamic cross-links.[9] In these studies, fibroblasts exhibited round morphology on hydrazone and spreading morphology on oxime cross-linked hydrogel. In the later studies, the pH of the cross-linker solution was adjusted to 7.4 compared to earlier studies where we saw a yellow color for oxime cross-linked hydrogel. The yellow color of the cell media solution indicates low pH, which likely could be due to the acid nature of the oxime cross-linker (O, O'-1,3- propanediylbishydroxylamine dihydrochloride). The other explanation could be the viscoplastic nature of hydrazone hydrogel which allowed cell spreading[8] as cell spreading has been correlated with viscoplastic matrices[1,5]. Despite numerous attempts, we cannot yet fully uncover the mechanism for this switch in behavior.

Thioester is another type of DCvC that can be used for tuning viscoelasticity through thioester exchange. Fibroblasts exhibited increased cell spreading area and nuclear to cytoplasmic YAP/TAZ ratio on viscoelastic hydrogels compared to elastic hydrogels[10]. Using photoinitiated thiol-ene click reaction, viscoelasticity was shut off in these thioester dynamic hydrogels, cell spreading area and nuclear to cytoplasmic YAP/TAZ ratio decreased and matched controlled elastic hydrogel.[10] Interestingly, trends in cell spreading are not in agreement with the above reported viscoelastic polyacrylamide hydrogels[6] i.e., cell spreading area should increase since hydrogel behaves dominantly elastic once viscoelasticity was shut off.

In contrast to shutting off viscoelasticity using light, a hydrogel with photoinduced viscoelasticity has also been designed.[11] Photoinduced modulation of viscoelasticity could be achieved via an addition-fragmentation chain transfer reaction triggered by a photoinitiator tethered to the network. Additionally, this hydrogel system also allows spatiotemporal control of viscoelasticity. Photo-induced viscoelasticity was controlled by photoinitiation rate and chain transfer agent concentration. hMSCs cultured on the hydrogels (2D) retracted cellular protrusions instantaneously in response to photo-induced viscoelasticity.

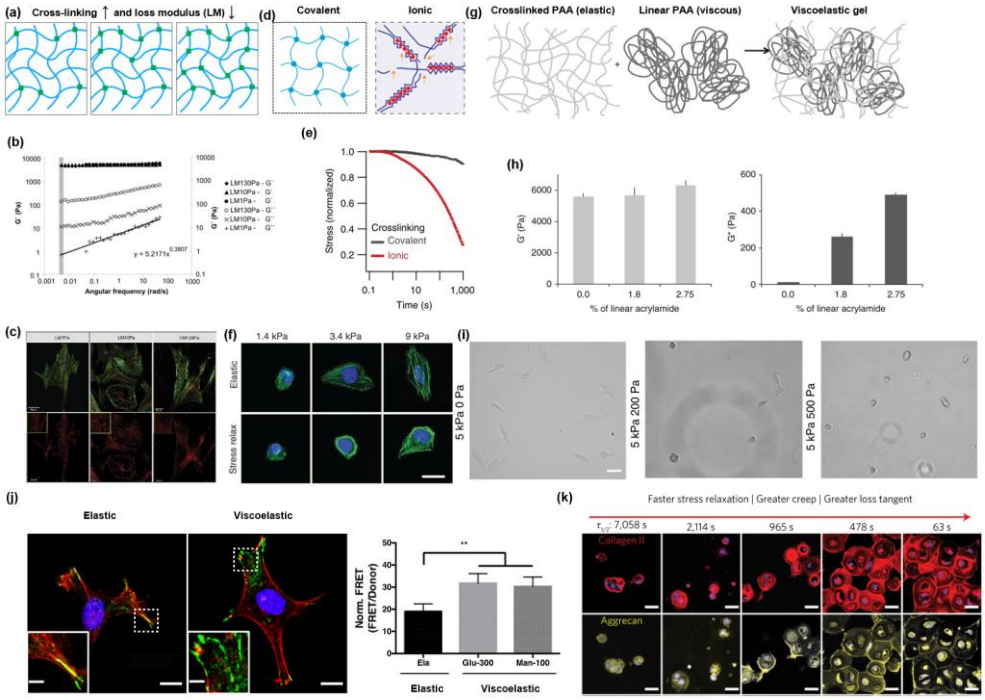

Figure 2. a) Loss modulus was tuned by varying ratios of acrylamide to bisacrylamide in polyacrylamide hydrogels. Green square dots represent cross-links, and schematics were made by the author of this thesis for clarifying the concept. b) Frequency sweep shows the evaluation of storage modulus (G') and loss modulus (G") as a function of the angular frequency sweep. All hydrogels exhibited a similar G'of around 5 kPa and a considerable difference in G" was found. G" was 130 Pa, 10 Pa and 1 Pa at 0.005 rad/s and samples are labelled with their loss modulus values. c) increase in cell spread area and a decrease in the length of vinculin focal adhesion was found. (b) and (c) was adapted from[3] d) Alginate hydrogels cross-linked either covalently or ionically. e) covalent crosslinking of alginate resulted in minimal stress relaxation while ionic cross-linking resulted in around 70% of stress relaxation in 1000 seconds. f) Cell exhibited spreading morphology on ionically cross-linked alginate hydrogel compared to covalent cross-linked alginate elastic hydrogel. (d), (e), and (f) was adapted from[5] g) schematic displaying the formation of viscoelastic polyacrylamide hydrogels by entrapping linear polyacrylamide chains into crosslinked polyacrylamide network. h) The values are plotted for storage moduli (left) and loss moduli (right). The values were taken from a frequency sweep and the plotted values are at 0.159 Hz. i) Fibroblasts exhibited spreading morphology on elastic hydrogels (left) and showed a decrease in spreading with an increase in loss modulus value to 200 Pa, and then finally further reduce in spreading morphology with an increase in loss modulus to 500 Pa. (g), (h), and (i) were adapted from[6] j) NIH 3T3s on elastic substrates exhibited clear stress fibres terminating in large vinculin focal adhesions and on viscoelastic hydrogels showed smaller stress fibres and smaller focal adhesion in the shape of dots. The graph on the left indicates that FRET signal on the left showed a higher FRET signal for viscoelastic hydrogels compared to elastic hydrogels. Adapted from[16] k) cross-linked hydrogels demonstrate more cartilage-like ECM (Collagen II in red and aggrecan in yellow) production in fast-relaxing hydrogels. (k) was adapted from[12].

Chemical strategies for designing viscoelastic 3D hydrogels and cellular responses in 3D hydrogels

In addition to previous studies (in review **chapter II**) with human mesenchymal stem cells (hMSC), utilizing a similar set of ionically cross-linked viscoelastic alginate hydrogels, Chaudhuri lab has shown that chondrocytes produced cartilage-like ECM in fast relaxing hydrogels in comparison to slow relaxing hydrogels.[12]

DCvC offers a more rational strategy for designing dynamic and viscoelastic hydrogel. Interpenetrating network (IPN) hydrogel of hyaluronic acid (HA) cross-linked with hydrazone bond and mixed with collagen I networks were created for recapitulating fibrillarity and viscoelasticity of ECM. MSCs demonstrated more cell spreading, fiber remodeling, and focal adhesion (FA) formation in faster relaxing hydrogels.[13] In **chapter IV** of this thesis, we showed that encapsulated fibroblasts exhibited spreading morphology within hydrazone hydrogels; however, fibroblasts stay rounded in more elastic oxime hydrogel.[8]

Another study reported tuning viscoelasticity by mixing alkyl-hydrazone and benzyl-hydrazone cross-links; viscoelastic loss tangents were tuned between $(9.03 \pm 0.01)10^{-4}$ to $(1.67 \pm 0.09)\ 10^{-3}$. Viscoelastic alkyl-hydrazone cross-links improve SOX9 expression (articular cartilage-specific gene expression showing) in free swelling hydrogels. When viscoelastic hydrogels were subjected to dynamic compression, hypertrophic chondrocyte markers (COL10A1, MMP13) expression was reduced. Interestingly, matrix biosynthesis was improved in elastic benzyl-hydrazone under dynamic compression and reduced in viscoelastic alkyl-hydrazone networks. Importantly, intermediate viscoelasticity was discovered to produce the highest levels of matrix biosynthesis in hydrazone networks under compression, for example on average 70 ± 4 μg of sulfated glycosaminoglycans and 31 ± 3 μg of collagen were produced per day over one month. [14] Biophysical transmission of physiologically relevant compressive strains to encapsulated chondrocytes were found to be temporally modulated by the viscoelasticity of dynamic hydrazone cross-links. While chondrocytes in viscoelastic alky-hydrazone hydrogels were able to recover $91.4 \pm 4.5\%$ rounded morphologies, only $21.2 \pm 1.4\%$ recovery was observed in benzyl-hydrazone.[15]

Dynamic covalent boronic esters also allow tuning viscoelasticity. By taking advantage of the equilibrium kinetics of the esterification of boronate esters, reversible boronate ester cross-links (pendant boronic acid and vicinal diol) were created. In comparison to elastic hydrogels, viscoelastic hydrogels demonstrated decreased focal adhesion tension and subcellular localization of YAP/TAZ.[16] Viscoelasticity of hydrogels has also been tuned by combining two phenylboronic acid derivatives with different rates of diol complexation. Viscoelastic time scales across one order of magnitude can be tuned by mixing two different phenylboronic acid derivatives. The difference in viscoelastic time scales was attributed to the phenyl boronic acid derivative pK_a difference.[17]

While DCvC continues to advance in tuning viscoelastic timescales, supramolecular chemistry also has enormous potential for tuning the dynamicity and viscoelasticity of hydrogel biomaterials. Tuning non-covalent interactions in supramolecular networks is a promising way to tune viscoelastic properties. The rate of rupture of the supramolecular complex can be directly

linked to viscoelasticity and stress relaxation time scales. Viscoelasticity could also be tuned using host-guest (β-cyclodextrin and adamantane) interactions and combining them with light-mediated thiol-ene[18] and acrylate[19] chemistries. Human hepatic stellate cells showed reduced spreading, actin stress fiber organization and nuclear localization of myocardin-related transcription factor A (MRTF-A) on viscoelastic hydrogels compared to elastic hydrogels.[18] Cell spreading was enhanced in hydrogels with higher viscous components.[19] Viscoelasticity tuning mostly has been done in non-fibrillar supramolecular hydrogels; however, supramolecular chemistry does offer the potential to design fibrous hydrogels with controlled dynamics and viscoelasticity for recapitulating ECM dynamics and fibrous structure.

Fibrous supramolecular hydrogels biomaterials are an emerging area for designing hydrogels with controlled dynamics and viscoelasticity for investigating cellular responses and tissue development in synthetic dynamic hydrogels. Owing to the specificity of supramolecular interactions, supramolecular biomaterials offer the advantage to tune mechanical properties by mix and match of supramolecular monomers. Modular mixing of supramolecular monomers offers a unique and flexible approach for adjusting viscoelasticity. Tuning of dynamics in peptide fibers[20,21,22] and peptide amphiphile[23,24,25] fibers have been explored; however, the effect of molecular dynamics on viscoelasticity remains unexplored. Recent studies showed that viscoelasticity can be tuned by modular mixing architectures with fast and slow exchange dynamics of Ureidopyrimidone (UPy)[26] and BTA hydrogels[27].

With the knowledge from our collaborators of tuning mechanical properties by mixing small molecules and telechelic BTAs, we set out to see if this could be translated into a biomaterial. We revealed in **chapter V** of this thesis that at high concentrations viscoelasticity and stress relaxation in these hydrogels can be tuned by modular mixing of small molecule BTA (slow exchange dynamics) with telechelic BTA (fast exchange dynamics).[27] We discovered that stress relaxation time scales can be tuned from a few to several thousands of seconds, which are in the range of many soft tissues. Chondrocytes and hMSCs form cell spheroids within these dynamic and stress-relaxing hydrogels. The speed of aggregation was faster in more dynamic and fast-relaxing hydrogels; this was one of the first studies to link matrix viscoelasticity to cell aggregation rates.

Using the desymmetrization strategy developed in **chapter VI** of the thesis, we created a small library of BTA hydrogels (in **chapter VII**) by changing the aliphatic spacer length on the BTA monomer. The length of the aliphatic spacers varied from 6 to 12 carbon atoms. We discovered that by simply adding or deleting a few carbon atoms on a BTA molecule, we could tune viscoelasticity in BTA hydrogels by 5 orders of magnitude. Increasing the number of carbon atoms resulted in reduced viscoelasticity and slower stress relaxation. Furthermore, all of the hydrogels exhibited an ECM mimicking hierarchical fibrous morphology.

The dynamic BTA hydrogels described in this thesis (**chapters V and VII**) not only mimic the viscoelasticity but also the fibrous structure of native ECM. Being able to tune dynamics in

synthetic BTA and correlating functional properties to nanoscale structure allowed us to mimic some of the complexity and dynamicity of natural ECM.

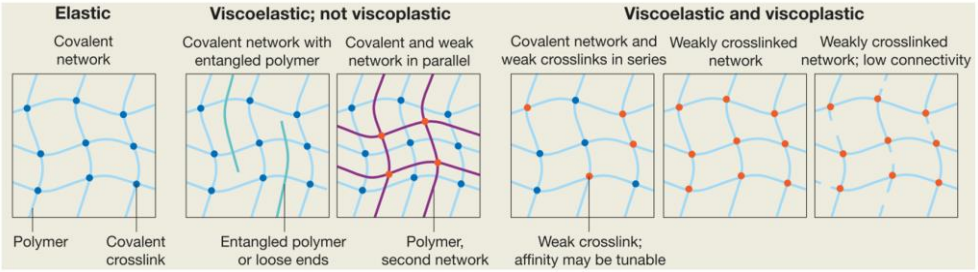

Figure 3. Generalized strategies reported by Chaudhuri et al.[1] to make hydrogels that are either elastic or viscoelastic. Hydrogels possess both viscoelasticity and viscoplasticity. Figure 3 has been adapted from[1].

Outlook

As we move towards recapitulating the viscoelasticity and structure of ECM in hydrogels, the ability to tune dynamics and structure at the molecular scale in rationally designed hydrogel systems would be crucial. Tuning of molecular dynamics can be a useful tool for designing hydrogels with controlled dynamicity which can enhance our understanding of how a cell responds and deforms the dynamic matrix.

Dynamic covalent chemistry offers a future opportunity to design dynamic and viscoelastic hydrogels where molecular information can be correlated to bulk properties. For example, the equilibrium constant (K_{eq}) and reverse reaction rate constant (k_{-1}) can be correlated to stiffness and stress relaxation ability and shear-thinning ability of hydrogels. Although great progress has been made the stability of dynamic covalent hydrogels in cell culture media remains challenging to address. Stability in dynamic hydrogel comes at the expense of losing dynamics and further exploration of tuning dynamics will be required for engineering stability without diminishing dynamics in hydrogels. Broad-range tuning of viscoelasticity and stress relaxation time scales under physiological conditions also remains difficult to engineer using DCvC and more precise tuning of dynamics is required for achieving a broad range of stress relaxation.

Supramolecular chemistry holds the potential to create biomaterials with tunable dynamics and controlled structure which recapitulate the complex environment ECM. Supramolecular interactions are specific, reversible, and responsive which can be utilized for the creation of dynamic and responsive hydrogels. Supramolecular interactions can be tuned for controlled viscoelasticity and stress relaxation time scales. While progress has been made in tuning viscoelasticity and stress relaxation using host-guest chemistry, tuning of stress relaxation and viscoelasticity remains limited in fibrous supramolecular hydrogels. Future work in fibrous hydrogels provides an opportunity to tune dynamic interactions in fibrous hydrogels for tissue-relevant stress relaxation time scales.

Dynamic bioinks for 3D bioprinting

3D bioprinting has emerged as a powerful technique, which has the potential to create complex and anatomically correct in vitro living systems. Extrusion-based bioprinting is one of the most commonly used bioprinting techniques for soft tissue fabrication. Extrusion bioprinting deposits bioink layer by layer for manufacturing customizable living tissue geometries. Many natural polymers including alginate[28,29,30,31], hyaluronic acid[32], gelatin[33,34], collagen[35], fibrin[36], agarose[37], decellularized extracellular matrices[38] and synthetic polymers including poly(vinyl alcohol)[39] and (PEG) hydrogels[40] have been employed as bioinks. Bioprinting in these materials can be adjusted by changing polymer concentration, cross-linker (calcium ions) concentration, and by adjusting pH. Usually, bioprinting utilizes low concentrations of polymer for ensuring sufficient diffusion of nutrients to the encapsulated cells. However, bioprinting of such low viscosity polymer solutions while and maintaining extruded filament shape is difficult. To address this transparent printing nozzles were developed which allowed bioinks to be partially cross-linked inside the nozzle just before extrusion. While this approach was able to print bioinks with lower viscosities, but at such low concentrations of polymers most printed constructs are not stiff enough to withstand the load of each additive layer. The other challenge is significant swelling of 3D printed constructs at such low polymer concentrations.

To overcome the difficulty of printing soft materials into the air, the freeform reversible embedding of suspended hydrogels (FRESH) printing method was developed for soft biomaterials into complex life-like structures[41,42] (**Figure 4a,b**). While FRESH has shown the potential to print arches and overhangs, the FRESH technique would require careful design of a supporting bath that can support soft biomaterial printing without exerting excessive stresses and damaging the 3D printed structure's uniformity and shape.

Other generalizable strategies include thermal and photo-triggered tandem gelation[43], 3D bioprinting using universal orthogonal network (UNION) bioinks[44] (**Figure 2c–e**), and 3D bioprinting capabilities using complementary thermo-reversible gelatin bioinks[45] (**Figure 2f–g**). These recent strategies have expanded bioinks' scope to different biomaterials, ECM dynamicity and viscoelasticity are missing in these bioinks. Additionally, encapsulated cells in static networks experience stress that could hamper essential cellular activities such as spreading, proliferation, and differentiation. Bioprinting with retention of the desired shape and maintaining dynamics of the hydrogel are mutually exclusive; this paradox has prompted scientists to look beyond static networks.

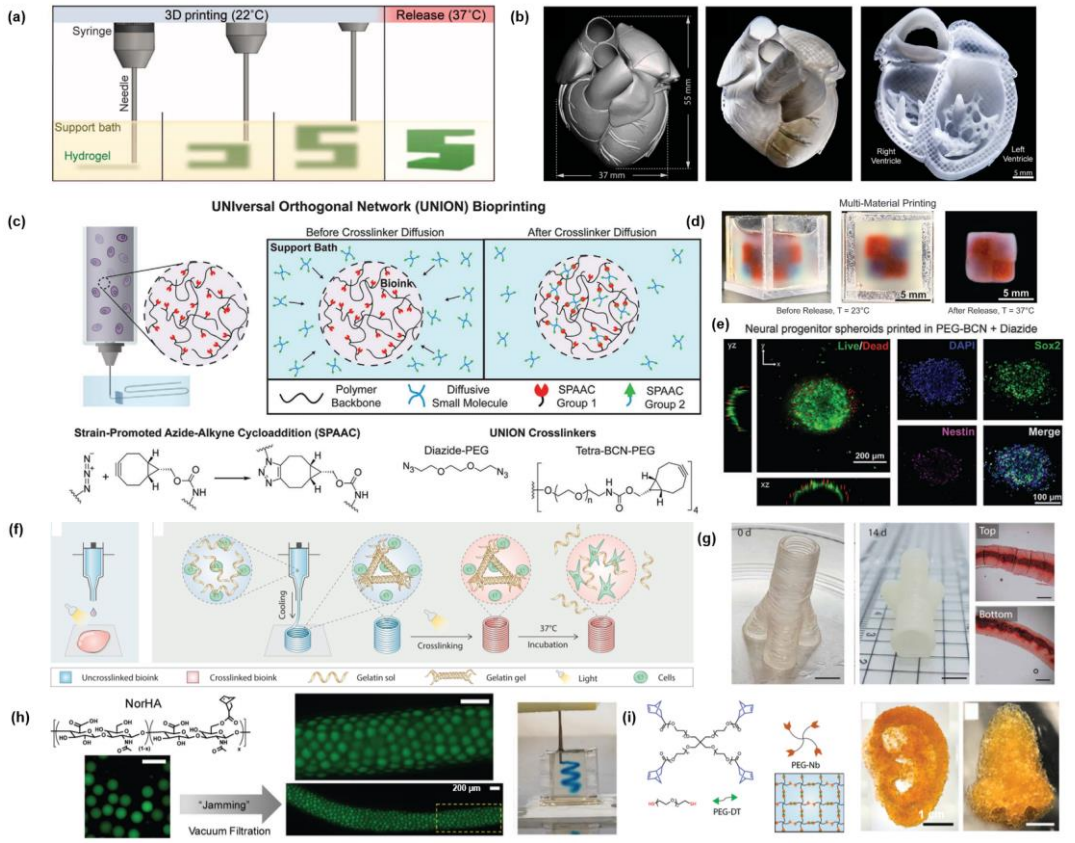

Figure 4. a) A scheme shows a FRESH process; a hydrogel (green color) is extruded in a thermoreversible gelatin-support bath. After cross-linking the support bath is melted via heating to 37°C to take out the 3D printed construct. Adapted from[41]. b) 3D MRI scan of the human heart scaled down to neonatal size (left), 3D printed collagen heart using FRESH (middle) and cross-sectional view of the left and right ventricles and interior structure of 3D printed collagen heart. Adapted from[42] .c) UNION inks mixed with cells in a syringe and extruded into a support bath (left), crosslinkers from the support bath diffuse into the ink and provided bioorthogonal stability by creating a hydrogel network (right), and union cross-linkers and copper-free strain promoted azide-alkyne cycloaddition mechanism are shown (bottom). d) Gelatin union ink (red) and PEG union ink (blue) printed into the checkerboard structure and cross-linked with the diazide-PEG crosslinker. e) Human induced pluripotent stem cell-derived neural progenitor cell spheroids printed in PEG union bioink maintained a highly viable core after 24 h (Left) and neural progenitors cell spheroids maintain a stem-cell phenotype as demonstrated by positive staining for the neural stem cell markers nestin and Sox2 after 3 days in culture in printed PEG UNION bioinks. (c), (d), and (e) have been adapted from[44]. f) Schematic shows the 3D printing of nonviscous, photocrosslinkable bioinks, which undergo spreading (left), the schematic of the 3D printing of complementary network bioinks which occur in three consecutive steps, cooling-induced gelation of gelatin which enables bioink deposition followed by photocrosslinking of the bioink, and then gelatin released via heating. g) Trifurcated tubular bioprinted construct using 5 wt% GelMA$^+$ (left, 5wt % gelatin methacryloyl mixed with 5wt% gelatin), the bioprinted construct turned opaque during 14-days of culture in osteogenic medium (middle), and alizarin red staining demonstrate calcium deposition (right). (f) and (g) have been adapted from[45]. h) Chemical structure of hyaluronic acid functionalized with norbornene and fluorescent images of microgels (left), the jammed microgel ink was extruded into a fiber using a syringe(middle). Microgels were jammed through vacuum filtration into a solid-like object. Printing of jammed microgel ink (colored with blue food dye) in a spiral shape in a shear-thinning support hydrogel. adapted from[48] .i) Thiol-ene crosslinked PEG hydrogel made of PEG microsphere 3D printed into mechanically stable ear and nose shapes. (i) was adapted from[49].

One emerging area of research for obtaining dynamic hydrogels for 3D printing is granular hydrogels. Granular hydrogels are obtained by jamming hydrogel microparticles. Granular hydrogels are dynamic structures, which possess shear-thinning and self-healing properties.[46,47] The Burdick lab has made jammed microgels using thiol-ene cross-linked hyaluronic acid[48] (HA, **Figure 2h**), photo-cross-linked poly(ethylene glycol)[49] (**Figure 2i**), thermo-sensitive agarose and shown that encapsulation of cells during jamming and extrusion of jammed microgels does not decrease 3T3 fibroblasts viability.[48] 3D printed scaffolds of hydrogel microparticles also have been shown to support mesenchymal stem cell growth and spheroid formation.[50] Granular hydrogels which are conductive have also been 3D printed[51], though cell encapsulation in conductive granular hydrogels and bioprinting of conductive granular hydrogels are yet missing. Recently, jammed micro-flake hydrogels have been developed, which were bioprinted into complex constructs. Bioprinted constructs could undergo 4D shape change while retaining high cell viability.[52] A recent study has investigated the mechanism of microparticle jamming and dissipation processes within printing nozzles which highlights the importance of hydrogel microparticle design.[53]

DCvC offers a more rational approach to designing dynamic and viscoelastic bioinks with a wide range of mechanical properties[54,55]. Mechanical properties of the hydrogel can be correlated with molecular parameters for example equilibrium constant (K_{eq}) is directly proportional to the stiffness of hydrogel, the forward rate constant (k_1) is directly linked to the kinetics of hydrogel formation, and the reverse rate constant (k_{-1}) is related to shear-thinning ability and stress relaxation time scales.

Dynamic covalent networks based on phenylboronic acid and glucose-like diol complexes showed shear-thinning and self-healing properties (**Figure 5a–c**). Phenyl boronic acids with different pKa were employed for tuning the dynamicity of hydrogels. PEG macromonomers functionalized with phenylboronic acid and glucose diol were mixed in an equimolar ratio for making dynamic hydrogels. 3T3 fibroblasts showed good viability within the bulk hydrogel; however, cell death was observed post-injection (21 gauge) likely due to high shear stresses during the injection. When injected subcutaneously (18 gauge), cells infiltrated within these materials indicating tissue biocompatibility of these hydrogels. Hydrogel networks were viscoelastic and the crossover frequency shifted to a lower critical frequency with a decrease in pK_a and an increase in pH.[56] Furthermore, by selecting the PBA used, the hydrogel storage moduli can be varied from 20 to 50 kPa. Additionally, these hydrogels demonstrated size-dependent and glucose-responsive controlled release of encapsulated proteins. Using boronic acid-glucose complexation single polymer component injectable, shear-thinning, and self-healing hydrogels were also developed. These hydrogels were discovered to be much softer (≈100 Pa); however, cell studies were not performed in these hydrogels.[57]

A shear-thinning and self-healing hyaluronic acid (HA) hydrogel has been made using dynamic covalent hydrazone cross-links (**Figure 5d,e**). Hydrazone cross-links are formed by reacting hydrazide-modified HA with aldehyde-modified HA. Hydrogels were extrudable and lattice structures were 3D printed with good shape fidelity. Encapsulated fibroblasts showed good cytocompatibility within these hydrogels. Low-concentration hydrogels (1.5 wt%) eroded 70% in two weeks compared to high-concentration hydrogels (5 wt%) which eroded only 20%. A

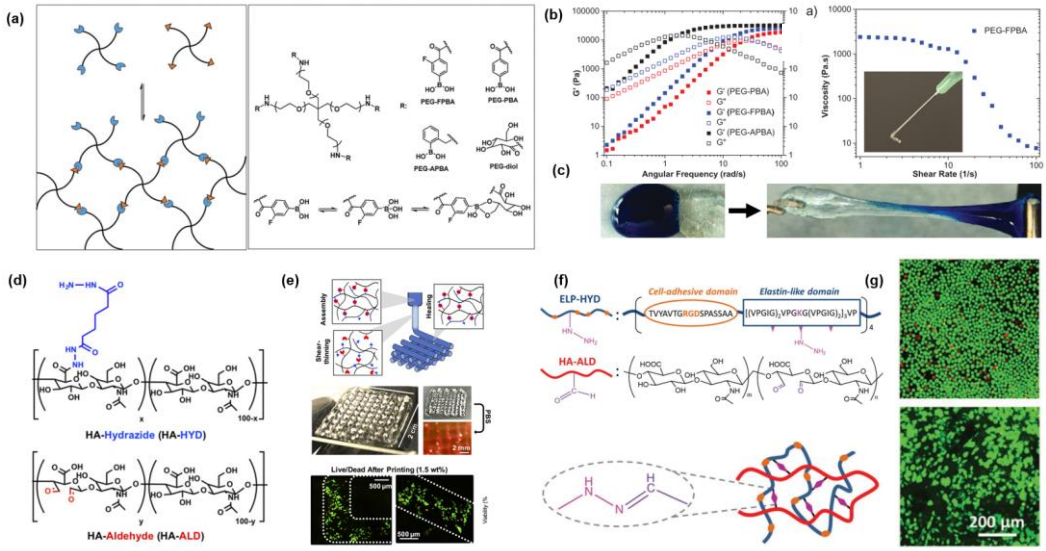

Figure 5. Dynamic covalent bioinks a) Schematic showing cross-links formation between phenylboronic acid (PBA) and diol (left) and chemical structures of diol and phenylboronic acid derivatives and mechanism of phenylboronic acid diol bond formation. b) Oscillatory frequency sweeps at 37 °C and at pH 7 demonstrate the viscoelastic nature of PBA-diol hydrogels (left) and decrease in viscosity with increasing shear rate indicating shear-thinning of FPBA-diol hydrogels. c) Self-healing of FPBA-diol hydrogel. a, b, and c adapted from[56]. d) Chemical structure of hydrazide-modified hyaluronic acid (HA-HYD) and aldehyde-modified hyaluronic acid (HA-ALD). e) schematics demonstrating 3D printing of hydrogel and shear-thinning and self-healing of hydrazone cross-links based hydrogel (top), 3D printed lattice structures (middle), and live-dead staining of 3T3 fibroblasts immediately after extrusion. (d) and (e) are adapted from[58]. f) Chemical structures of hydrazine-modified elastin-like protein (ELP-HYD, top), aldehyde-modified hyaluronic acid (HA-ALD, middle), and imine-type cross-links formation in elastin-like protein hyaluronic acid hydrogel (bottom). g) Live-dead staining shows live cells (in green) and dead (in red) MSCs extruded through 28 gauge within PBS (top) and ELP– HA hydrogel (bottom). (f) and (g) are adapted from[59].

second HA network, which is photo cross-linkable through thiol-ene chemistry, was introduced. This second network did not only reduce erosion (70%), but also allowed orthogonal photostiffening (300%) and photopatterning of these hydrogels.[58]

An injectable hydrogel using hydrazone dynamic covalent cross-linking with thermoresponsive engineered proteins has also been developed (**Figure 5f,g**).[59] Hydrogels were made by mixing hydrazine-modified elastin-like protein (ELP) with aldehyde-functionalized hyaluronic acid. The hydrogel was injectable (using 28G) and protected MSCs during the injection. MSCs maintained their differentiation potential post-extrusion. Stiffness from a few hundred pascals to around

3000 pascals for this hydrogel can be tuned by either adjusting the ELP concentration (1 to 4 wt%) or by changing the degree of HA oxidation. ELP undergoes thermal phase segregation and formed ELP aggregates which act as a physical secondary network and provide stability to the hydrogel. With a secondary ELP network, the hydrogel could last for 3 weeks of cell culture. Furthermore, hydrogel degradation was confirmed in the presence of protease elastase.

In the presence of adipic acid dihydrazide, partly oxidized hyaluronate and glycol chitosan was used to create self-healing hydrogels and 3D printable bioinks.[60] The hydrogel creates two dynamic linkages: acyl hydrazone bonds between oxidized hyaluronate and adipic acid dihydrazide and imine links through a Schiff base reaction between oxidized hyaluronate and glycol chitosan. The bioink allowed bioprinting of cell-laden constructs and ATDC5 chondrocytes retained chondrogenic phenotype. Without any secondary cross-linking after printing, this hydrogel was stable for up to 3 weeks in cell culture.

Contributing to dynamic bioinks, we have generated a small library of dynamic covalent hydrogels by cross-linking aldehyde groups on oxidized alginate with either hydrazide, semicarbazide, or aminooxy functional groups (**chapter IV**). The dynamicity, viscoelasticity, and mechanical properties of hydrogels were tuned by employing imine-type cross-links with different equilibrium constants[8]. Hydrazone and semicarbazone (K_{eq} between 10^4–10^6) hydrogels were found to be self-healing and shear-thinning. While all cross-links showed injectability, only hydrazone cross-links were bioprintable at low pressure (140 kPa and 5 mm/s). These hydrogels showed good viability for encapsulated fibroblasts, chondrocytes, and bioprinted chondrocytes. In contrast to the less dynamic oxime hydrogels, fibroblasts encapsulated within more dynamic hydrazone hydrogel displayed spreading morphology.

Our group has recently demonstrated that 3D printing can be adjusted to print dynamic and viscoelastic hydrogels by only combining dynamic cross-linkers (hydrazone and oxime)[9]. Storage moduli between 200 and 3000 Pa can be adjusted by combining oxime and hydrazone at a fixed polymer content. While oxime demonstrated the slowest stress relaxation with a relaxation half-time of 33 000 seconds, hydrazone (a more dynamical cross-linker) demonstrated the fastest stress relaxation with a relaxation half-time of 300 seconds. All hydrogels had a comparable post-rupture flow profile, but only those that contained more than 50% hydrazone were self-healing and printable. Dynamic hydrogels' capacity for self-healing also makes them recyclable. In hydrogels with higher oxime cross-link densities than hydrazone cross-link densities, the spreading morphology of fibroblasts was seen.

Recently, a new and simple formulation of a dynamic hydrogel based on thiol-functionalized HA combined with gold ions was presented.[61] This ink allows for the 3D printing of stable constructs without the usage of external stimuli. 3D constructs up to 24 layers and 10 mm in height were printed. Cell viability studies and bioprinting is yet missing.[61] While DCvC offers the potential for tuning dynamics for designing well-behaved bioinks, supramolecular chemistry also holds the potential to develop biomimetic and dynamic bioinks.

Supramolecular chemistry exploits non-covalent interactions such as hydrogen bonds, metal chelation, hydrophobic interactions, and van der Waals interactions for the creation of rationally designed hydrogel biomaterials. Supramolecular monomers formed higher ordered assemblies through specific, reversible, and directional non-covalent interactions[62]. These supramolecular interactions are dynamic and can be tuned across a broad spectrum for designing dynamic bioinks. Supramolecular hydrogels hold significant importance since they can replicate the biomimicry, self-assembly, and dynamics of native ECM and tissues. The ECM is a supramolecular self-assembled structure of proteins, glycoproteins, and polysaccharides, which provide not only structural support but also spatiotemporal signals for correct tissue formation. The specificity and dynamicity of supramolecular interaction offer the potential to emulate the spatiotemporal aspects of the ECM[63]. Additionally, shear-thinning, self-healing, and non-linear mechanical properties could be adjusted by tuning the dynamics of supramolecular interactions.

The first reported supramolecular hydrogel bioink was based on polypeptide-DNA[64]. Within a few seconds, a hybrid of polypeptide-DNA and a complementary DNA linker occurs, leading to the creation of a hydrogel. The hydrogel had a storage modulus of roughly 5000 Pa. The hydrogel was also found to be responsive to proteases and nucleases, demonstrating complete biodegradability under physiological conditions (**Figure 6a**). Using two nozzle systems and deposition of the polypeptide-DNA and DNA linker in an alternating sequence, 3D structures with uniform boundaries could be printed (**Figure 6b**). The hydrogel maintained homogeneous cell suspension and cells were highly functional in 3D bioprinted constructs (**Figure 6c**).

Using supramolecular host-guest interactions, a supramolecular printable hydrogel has also been made. Hyaluronic acid (HA) was modified with either adamantane (Ad–HA) or β-cyclodextrin (CD–HA), and supramolecular assemblies quickly formed when Ad-HA and CD-HA were combined (**Figure 6d–f**). Shear-thinning supramolecular hydrogel was 3D printed in self-healing support hydrogel. Dynamic bonds used either in ink hydrogel or support hydrogel provided shear-thinning and self-healing but lacked mechanical properties. The ink or support hydrogel was stabilized for creating free-standing 3D objects or voids. Encapsulated mesenchymal stem showed greater than 90% cell viability.[65] Next, the shear-thinning hyaluronic acid hydrogels were printed and stabilized using a secondary cross-linking. Utilization of either guest-host assembly or covalent cross-linking alone did not result in the formation of long-term stable structures because of network relaxation following printing or dispersion of the ink filaments before stabilization, respectively. Dual-cross-linked hydrogel filaments showed stability over a month. 3D printed scaffolds supported the adhesion and spreading of 3T3 fibroblasts[66]. By utilizing secondary covalent cross-linking in the host-guest hydrogels, double network tough hydrogels could be produced. These hydrogels are injectable and supported the cell viability of encapsulated mesenchymal stem cells[67].

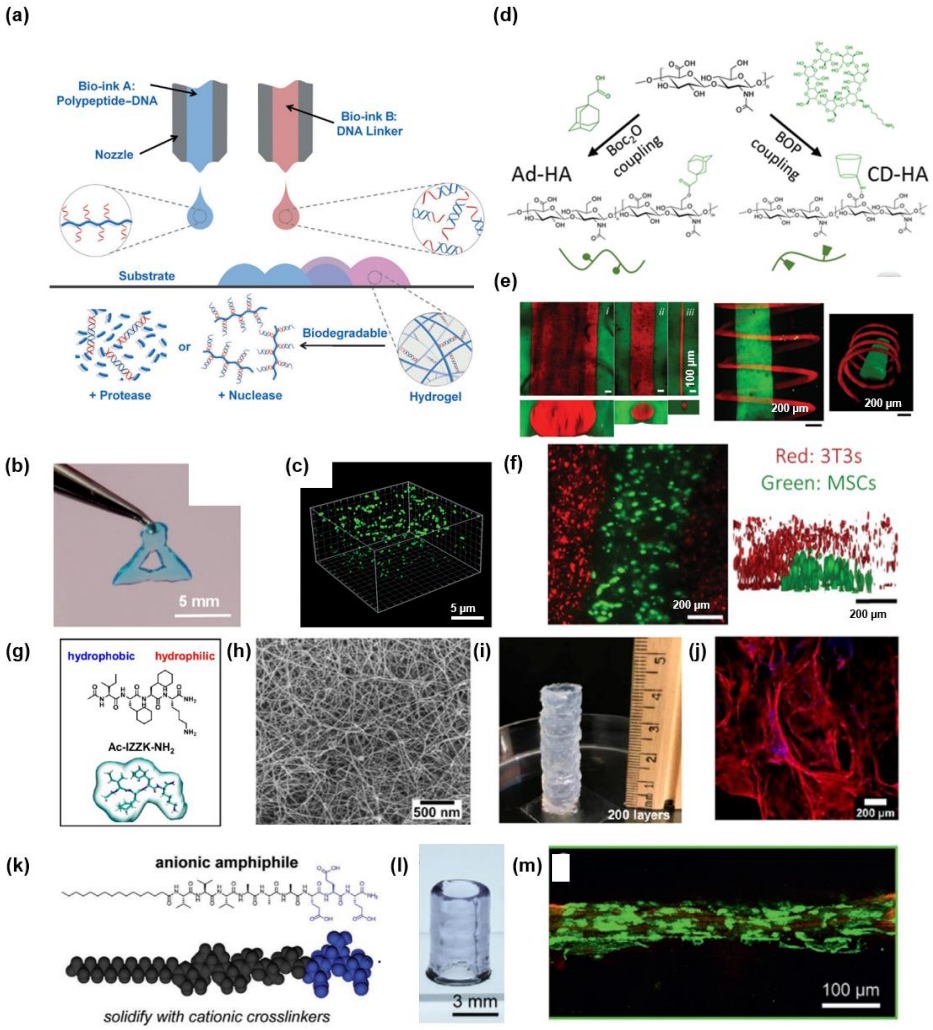

Figure 6. Supramolecular bioinks a) Schematic shows the 3D bioprinting of the polypeptide–DNA hydrogel for the fabrication of 3D structures. Bioink A (blue) is a polypeptide– DNA and bioink B (red) is a DNA linker. The DNA sequence of bioink A and bioink B are complementary, and hydrogel formation occurs via hybridization. The hydrogels were found to be sensitive to proteases and nucleases and offer on-demand control of degradation. b) 3D printed 10-layers triangle. c) T-20 cells (an anterior pituitary cell line) show around 98% live cells inside these hydrogels. (a), (b), and (c) are adapted from[64] .d) Chemical conjugation of adamantane and cyclodextrin to hyaluronic acid. e) Direct 3D printing of guest–host shear-thinning hydrogel into guest-host self-healing hydrogel either as straight fibers of different diameters or spiral shapes. f) bioprinting of MSCs (in green) in bioink into support hydrogel, which contains 3T3 fibroblasts. (d), (e), and (f) are adapted from[65] g) Chemical structures of IZZK short peptide. h) SEM micrograph of IZZK. i) 3D printed tube structure using IZZK peptide. i) human bone marrow-derived MSCs in IZZK peptide hydrogel after 30 days in culture. g, h, i, and j are adapted from[68]. k) anionic peptide amphiphile ink chemical structure, l) 3D printed tube of 9 mm height. m) encapsulated myoblasts displayed good cytocompatibility within peptide amphiphile bioink cultured for 7 days. (k), (l), and m are Adapted from[70].

Another class of supramolecular bioinks includes self-assembling short peptides. Lysine-containing hexapeptides were the first peptide-based bioink to be described. These hexapeptides self-assembled to form stable, nanofibrous three-dimensional hydrogels with a stiffness of up to 40 kPa. These hydrogels supported embryonic stem cell culture and adipogenic differentiation of hMSC in hydrogel droplets.[68] Ultrashort tetrapeptides have also been reported which enable the printing of a few centimeter scale 3D constructs using a robotic arm. Ultrashort peptides supported the growth of 3D encapsulated neuronal cells, human dermal fibroblasts, and chondrogenic differentiation of bone marrow-derived mesenchymal stem cells (**Figure 6g–j**). Cells were bioprinted into cuboids with edges that were 1 cm long and 0.26 cm high, as well as cylinders with a diameter of 1 cm and a height of 1 cm. Cell viability was maintained at above 90% for 24 days of culture[22]. The self-assembling peptides-based hydrogel (from peptide gel design) was shown to be printable into 3D constructs while maintaining good viability of mammary epithelial cells.[69]

Peptide amphiphile (PA) supramolecular inks have been investigated for fabricating structures with tunable nanoscale and bulk alignment (**Figure 6k–m**).[70] Supramolecular polymer inks were ionically cross-linked for creating a liquid crystalline hydrogel. By adjusting the pH and salt concentration, intermolecular interactions among the self-assembled structures were controlled for tuning the viscosity of the ink. By utilizing supramolecular polymers with lower charge densities and higher charge screening from the electrolyte, higher viscosity inks were obtained. Extruding higher viscosity inks through small nozzle diameters and printing at high speeds resulted in greater nanoscale alignment in the extruded macroscopic filament. C2C12 myoblasts showed high cell viability in these PA bioinks over 7 days.

Pseudo-polyrotaxane has also been used to create a bioink. Pseudo-polyrotaxane structures were created by grafting polyethylene glycol (PEG) side chains onto chitosan and then threading them with α-cyclodextrin (α-CD). Cross-linking occurs through the aggregation of the pseudo-polyrotaxane side chains. Another biopolymer physically present in this system is gelatin; however, gelatin's function in adjusting shear-thinning or mechanical properties was not investigated. The shear-thinning property of this hydrogel has been attributed to the reversibility of pseudo-polyrotaxane cross-links. Using β-glycerophosphate at different concentrations as the secondary cross-linking agent, the Young's modulus of these hydrogels can be tuned from 5 kPa to 140 kPa. Fibroblasts were bioprinted in these hydrogels and Paxillin and N-cadherin expressions were higher on day 14 compared to day 3.[71]

In pursuit of developing advanced supramolecular bioinks, we worked on developing benzene-1,3,5-tricaboxamide (BTA) supramolecular hydrogels and bioinks with fibrous structure and controlled viscoelasticity. We varied the hydrophobic length (6 to 12 carbon atoms) on BTA to tune the viscoelasticity across 5 orders of magnitude while retaining the fibrous morphology (**chapter VII**). These hydrogels exhibited shear-thinning, self-healing, and injectable properties. We discovered that the hydrophobic spacer length also dictates printability within these hydrogels; a longer hydrophobic spacer resulted in more stable and well-defined 3D printed structures started to collapse with decreasing hydrophobic length.

In **chapter VIII**, we took inspiration from Nature's ubiquitous approach of 1D supramolecular self-assembly with covalent cross-linking and created a supramolecular macromonomer with light active norbornene functionality on it. This macromonomer self-assembles to form fibrous hydrogels. Utilizing norbornene thiol-ene chemistry, we cross-linked supramolecular fibrillar assemblies for tuning stiffness, strain at break, and toughness of the hydrogels. Chondrocytes were bioprinted in these hydrogels into the cartilage-like structure and showed high viability until day 11. Bioprinted hMSCs spheroids in these bioinks produced a cartilage-specific ECM protein, collagen type II.

Outlook

Dynamic bioinks offer the unique properties of shear-thining and prevent excessive shear stresses that can result in cell death during bioprinting. Dynamic bonds enable homogeneous cell mixing and prevent cell sedimentation during the bioprinting process. The dynamic nature of bioinks have also allowed cells to remodel their microenvironment and deposit natural tissue-relevant ECM. Good progress has been made in developing dynamic hydrogels and demonstrating their unique advantages in mimicking natural tissues' dynamicity.

Granular hydrogel are the agglomeration of micrometer-sized particles that have shown potential as dynamic bioinks. Granular hydrogels possess shear-thinning and self-healing properties and enabled the bioprinting of multicellular constructs. Granular hydrogels have also successfully been used as supporting baths for extrusion bioprinting to create complex structures[72,73]. There still remain challenges to be addressed for granular hydrogel bioinks for example, tuning packing behavior with controlled non-linear mechanical properties requires in-depth investigations with a different set of materials. Some other aspects that future granular hydrogels will require are controlled degradation, long-term stability and cell culture for mature tissue formation, and tuning viscoelasticity for designing biomimetic future bioinks.

DCvC has enabled the creation of rational advanced dynamic bioinks with control on the molecular scale. For example, the equilibrium constant (K_{eq}), the forward reaction rate constant, and reverse reaction rate constants can be designed for controlled mechanical and bioprinting properties of the bioink. A range of DCvC has been employed for developing dynamic bioinks with shear-thinning and self-healing properties and has shown cytocompatibility with different cells. However, one challenge also remains with dynamic covalent hydrogel: the degradation of the hydrogel and limited stability, which provides cells with changing microenvironment. Controlling hydrogel dynamics for longer cell culture and control of hydrogel properties independent of cell culture media formulations or limited cell media interactions with dynamic chemistry will better understand cellular responses. Strategies can be envisioned to stabilize the hydrogel post-printing; for example, introducing stable crosslinks without largely compromising the dynamics of the hydrogel or by double network formation post-printing has been done[66,74]. Visible light-based reversible dynamic chemistry offers the future opportunity to understand cellular responses with control of mechanical and biological properties in space and time[75,76,77,78].

Supramolecular chemistry utilized the transient nature of supramolecular interactions and has emerged as a powerful approach for creating dynamic hydrogel and bioinks[62,63,55]. Shear-thinning supramolecular hydrogels have successfully been 3D printed into supramolecular self-healing hydrogels[74]. Supramolecular chemistry also offers the opportunity to develop ECM-mimicking fibrous bioinks[63]. Several 3D fibrous bioinks have been reported including polypeptide DNA bioinks[64], short peptides[22,68], and peptide amphiphiles[70]. All of the supramolecular bioinks have displayed good cytocompatibility (maximum for 1 week) with various cell types. Long-term cell culture studies remain absent and would be required to show added benefits of the supramolecular hydrogels. Broad-range tuning of viscoelasticity remains unreported in fibrous hydrogels which would be one of the future challenges. Future supramolecular bioinks can be designed to be multifunctional to mimic ECM proteins' multifunctionality. Multifunctional bioinks, for example, can be used to create either physical or biochemical gradients in space and time to recapitulate the ECM spatiotemporal gradients and dynamicity in synthetic bioinks.

References

(1) Chaudhuri, O.; Cooper-White, J.; Janmey, P. A.; Mooney, D. J.; Shenoy, V. B. Effects of Extracellular Matrix Viscoelasticity on Cellular Behaviour. *Nature*. 2020, pp 535–546. https://doi.org/10.1038/s41586-020-2612-2.

(2) Ooi, H. W.; Hafeez, S.; Van Blitterswijk, C. A.; Moroni, L.; Baker, M. B. Hydrogels That Listen to Cells: A Review of Cell-Responsive Strategies in Biomaterial Design for Tissue Regeneration. *Mater. Horizons* **2017**, *4* (6), 1020–1040. https://doi.org/10.1039/c7mh00373k.

(3) Cameron, A. R.; Frith, J. E.; Cooper-White, J. J. The Influence of Substrate Creep on Mesenchymal Stem Cell Behaviour and Phenotype. *Biomaterials* **2011**, *32* (26), 5979–5993. https://doi.org/10.1016/j.biomaterials.2011.04.003.

(4) Cameron, A. R.; Frith, J. E.; Gomez, G. A.; Yap, A. S.; Cooper-White, J. J. The Effect of Time-Dependent Deformation of Viscoelastic Hydrogels on Myogenic Induction and Rac1 Activity in Mesenchymal Stem Cells. *Biomaterials* **2014**, *35* (6), 1857–1868. https://doi.org/10.1016/j.biomaterials.2013.11.023.

(5) Chaudhuri, O.; Gu, L.; Darnell, M.; Klumpers, D.; Bencherif, S. A.; Weaver, J. C.; Huebsch, N.; Mooney, D. J. Substrate Stress Relaxation Regulates Cell Spreading. *Nat. Commun.* **2015**, *6*, 6364. https://doi.org/10.1038/ncomms7365.

(6) Charrier, E. E.; Pogoda, K.; Wells, R. G.; Janmey, P. A. Control of Cell Morphology and Differentiation by Substrates with Independently Tunable Elasticity and Viscous Dissipation. *Nat. Commun.* **2018**, *9* (1), 449. https://doi.org/10.1038/s41467-018-02906-9.

(7) Mandal, K.; Gong, Z.; Rylander, A.; Shenoy, V. B.; Janmey, P. A. Opposite Responses of Normal Hepatocytes and Hepatocellular Carcinoma Cells to Substrate Viscoelasticity †. *Cite this Biomater. Sci* **2020**, *8*, 1316. https://doi.org/10.1039/c9bm01339c.

(8) Hafeez, S.; Ooi, H.; Morgan, F.; Mota, C.; Dettin, M.; van Blitterswijk, C.; Moroni, L.; Baker, M. Viscoelastic Oxidized Alginates with Reversible Imine Type Crosslinks: Self-Healing, Injectable, and Bioprintable Hydrogels. *Gels* **2018**, *4* (4), 85. https://doi.org/10.3390/gels4040085.

(9) Morgan, F. L. C.; Fernández-Pérez, J.; Moroni, L.; Baker, M. B. Tuning Hydrogels by Mixing Dynamic Cross-Linkers: Enabling Cell-Instructive Hydrogels and Advanced Bioinks. *Adv. Healthc. Mater.* **2022**, *11* (1), 2101576. https://doi.org/10.1002/adhm.202101576.

(10) Carberry, B. J.; Rao, V. V; Anseth, K. S. Phototunable Viscoelasticity in Hydrogels Through Thioester Exchange. *Ann. Biomed. Eng.* **2020**, *48* (7), 2053–2063. https://doi.org/10.1007/s10439-020-02460-w.

(11) Marozas, I. A.; Cooper-White, J. J.; Anseth, K. S. Photo-Induced Viscoelasticity in Cytocompatible Hydrogel Substrates. *New J. Phys.* **2019**, *21* (4). https://doi.org/10.1088/1367-2630/ab1309.

(12) Lee, H. P.; Gu, L.; Mooney, D. J.; Levenston, M. E.; Chaudhuri, O. Mechanical Confinement

Regulates Cartilage Matrix Formation by Chondrocytes. *Nat. Mater.* **2017**, *16* (12), 1243–1251. https://doi.org/10.1038/nmat4993.

(13) Lou, J.; Stowers, R.; Nam, S.; Xia, Y.; Chaudhuri, O. Stress Relaxing Hyaluronic Acid-Collagen Hydrogels Promote Cell Spreading, Fiber Remodeling, and Focal Adhesion Formation in 3D Cell Culture. *Biomaterials* **2018**, *154*, 213–222. https://doi.org/10.1016/j.biomaterials.2017.11.004.

(14) Richardson, B. M.; Walker, C. J.; Maples, M. M.; Randolph, M. A.; Bryant, S. J.; Anseth, K. S. Mechanobiological Interactions between Dynamic Compressive Loading and Viscoelasticity on Chondrocytes in Hydrazone Covalent Adaptable Networks for Cartilage Tissue Engineering. *Adv. Healthc. Mater.* **2021**, *10* (9), 2002030. https://doi.org/10.1002/adhm.202002030.

(15) Richardson, B. M.; Walker, C. J.; MacDougall, L. J.; Hoye, J. W.; Randolph, M. A.; Bryant, S. J.; Anseth, K. S. Viscoelasticity of Hydrazone Crosslinked Poly(Ethylene Glycol) Hydrogels Directs Chondrocyte Morphology during Mechanical Deformation. *Biomater. Sci.* **2020**, *8* (14), 3804–3811. https://doi.org/10.1039/D0BM00860E.

(16) Marozas, I. A.; Anseth, K. S.; Cooper-White, J. J. Adaptable Boronate Ester Hydrogels with Tunable Viscoelastic Spectra to Probe Timescale Dependent Mechanotransduction. *Biomaterials* **2019**, *223*, 119430. https://doi.org/10.1016/j.biomaterials.2019.119430.

(17) Yesilyurt, V.; Ayoob, A. M.; Appel, E. A.; Borenstein, J. T.; Langer, R.; Anderson, D. G. Mixed Reversible Covalent Crosslink Kinetics Enable Precise, Hierarchical Mechanical Tuning of Hydrogel Networks. *Adv. Mater.* **2017**, *29* (19), 1605947–1605947. https://doi.org/10.1002/adma.201605947.

(18) Hui, E.; Gimeno, K. I.; Guan, G.; Caliari, S. R. Spatiotemporal Control of Viscoelasticity in Phototunable Hyaluronic Acid Hydrogels. **2019**. https://doi.org/10.1021/acs.biomac.9b00965.

(19) Loebel, C.; Seliktar, D.; Burdick, J. A.; Ayoub, A.; Simaan-Yameen, H.; Kossover, O.; Galarraga, J. H. Tailoring Supramolecular Guest–Host Hydrogel Viscoelasticity with Covalent Fibrinogen Double Networks. *J. Mater. Chem. B* **2019**, 17–19. https://doi.org/10.1039/c8tb02593b.

(20) Deechongkit, S.; Powers, E. T.; You, S. L.; Kelly, J. W. Controlling the Morphology of Cross β-Sheet Assemblies by Rational Design. *J. Am. Chem. Soc.* **2005**, *127* (23), 8562–8570. https://doi.org/10.1021/JA050558C/SUPPL_FILE/JA050558CSI20050418_084621.PDF.

(21) Ryadnov, M. G.; Woolfson, D. N. Engineering the Morphology of a Self-Assembling Protein Fibre. *Nat. Mater.* **2003**, *2* (5), 329–332. https://doi.org/10.1038/nmat885.

(22) Susapto, H. H.; Alhattab, D.; Abdelrahman, S.; Khan, Z.; Alshehri, S.; Kahin, K.; Ge, R.; Moretti, M.; Emwas, A. H.; Hauser, C. A. E. Ultrashort Peptide Bioinks Support Automated Printing of Large-Scale Constructs Assuring Long-Term Survival of Printed Tissue Constructs. *Nano Lett.* **2021**, *21* (7), 2719–2729. https://doi.org/10.1021/acs.nanolett.0c04426.

(23) Matson, J. B.; Stupp, S. I. Self-Assembling Peptide Scaffolds for Regenerative Medicine ChemComm. *This J. is Cite this Chem. Commun* **2012**, *48*, 12. https://doi.org/10.1039/c1cc15551b.

(24) Webber, M. J.; Newcomb, C. J.; Bitton, R.; Stupp, S. I. Switching of Self-Assembly in a Peptide Nanostructure with a Specific Enzyme. *Soft Matter* **2011**, *7* (20), 9665. https://doi.org/10.1039/c1sm05610g.

(25) Pashuck, E. T.; Cui, H.; Stupp, S. I. Tuning Supramolecular Rigidity of Peptide Fibers through Molecular Structure. *J. Am. Chem. Soc.* **2010**, *132* (17), 6041–6046. https://doi.org/10.1021/ja908560n.

(26) Diba, M.; Spaans, S.; Hendrikse, S. I. S.; Bastings, M. M. C.; Schotman, M. J. G.; van Sprang, J. F.; Wu, D. J.; Hoeben, F. J. M.; Janssen, H. M.; Dankers, P. Y. W. Engineering the Dynamics of Cell Adhesion Cues in Supramolecular Hydrogels for Facile Control over Cell Encapsulation and Behavior. *Adv. Mater.* **2021**, *33* (37), 2008111. https://doi.org/10.1002/adma.202008111.

(27) Vereroudakis, E.; Bantawa, M.; Lafleur, R. P. M.; Parisi, D.; Matsumoto, N. M.; Peeters, J. W.; Del Gado, E.; Meijer, E. W.; Vlassopoulos, D. Competitive Supramolecular Associations Mediate the Viscoelasticity of Binary Hydrogels. *ACS Cent. Sci.* **2020**, *6*, 1401–1411. https://doi.org/10.1021/acscentsci.0c00279.

(28) Ooi, H. W.; Mota, C.; Tessa Ten Cate, A.; Calore, A.; Moroni, L.; Baker, M. B. Thiol-Ene Alginate Hydrogels as Versatile Bioinks for Bioprinting. *Biomacromolecules* **2018**, *19* (8), 3390–3400. https://doi.org/10.1021/acs.biomac.8b00696.

(29) Tabriz, A. G.; Hermida, M. A.; Leslie, N. R.; Shu, W. Three-Dimensional Bioprinting of Complex Cell Laden Alginate Hydrogel Structures. *Biofabrication* **2015**, *7* (4), 045012.

https://doi.org/10.1088/1758-5090/7/4/045012.

(30) Ivanovska, J.; Zehnder, T.; Lennert, P.; Sarker, B.; Boccaccini, A. R.; Hartmann, A.; Schneider-Stock, R.; Detsch, R. Biofabrication of 3D Alginate-Based Hydrogel for Cancer Research: Comparison of Cell Spreading, Viability, and Adhesion Characteristics of Colorectal HCT116 Tumor Cells. *Tissue Eng. Part C Methods* **2016**, *22* (7), 708–715. https://doi.org/10.1089/ten.tec.2015.0452.

(31) Habib, A.; Sathish, V.; Mallik, S.; Khoda, B. 3D Printability of Alginate-Carboxymethyl Cellulose Hydrogel. *Mater. 2018, Vol. 11, Page 454* **2018**, *11* (3), 454. https://doi.org/10.3390/MA11030454.

(32) Su, W. Y.; Chen, Y. C.; Lin, F. H. Injectable Oxidized Hyaluronic Acid/Adipic Acid Dihydrazide Hydrogel for Nucleus Pulposus Regeneration. *Acta Biomater.* **2010**, *6* (8), 3044–3055. https://doi.org/10.1016/j.actbio.2010.02.037.

(33) Zehnder, T.; Boccaccini, A. R.; Detsch, R. Evaluation of an Alginate–Gelatine Crosslinked Hydrogel for Bioplotting. *Biofabrication* **2015**, *7*, 25001. https://doi.org/10.1088/1758-5090/7/2/025001.

(34) Bertassoni, L. E.; Cardoso, J. C.; Manoharan, V.; Cristino, A. L.; Bhise, N. S.; Araujo, W. A.; Zorlutuna, P.; Vrana, N. E.; Ghaemmaghami, A. M.; Dokmeci, M. R.; Khademhosseini, A. Direct-Write Bioprinting of Cell-Laden Methacrylated Gelatin Hydrogels. *Biofabrication* **2014**, *6* (2), 024105. https://doi.org/10.1088/1758-5082/6/2/024105.

(35) Diamantides, N.; Dugopolski, C.; Blahut, E.; Kennedy, S.; Bonassar, L. J. High Density Cell Seeding Affects the Rheology and Printability of Collagen Bioinks. *Biofabrication* **2019**, *11* (4). https://doi.org/10.1088/1758-5090/AB3524.

(36) Han, J.; Kim, D. S.; Jang, H.; Kim, H. R.; Kang, H. W. Bioprinting of Three-Dimensional Dentin-Pulp Complex with Local Differentiation of Human Dental Pulp Stem Cells. *J. Tissue Eng.* **2019**, *10*. https://doi.org/10.1177/2041731419845849.

(37) Daly, A. C.; Critchley, S. E.; Rencsok, E. M.; Kelly, D. J. A Comparison of Different Bioinks for 3D Bioprinting of Fibrocartilage and Hyaline Cartilage. *Biofabrication* **2016**, *8* (4). https://doi.org/10.1088/1758-5090/8/4/045002.

(38) Kim, M. K.; Jeong, W.; Lee, S. M.; Kim, J. B.; Jin, S.; Kang, H. W. Decellularized Extracellular Matrix-Based Bio-Ink with Enhanced 3D Printability and Mechanical Properties. *Biofabrication* **2020**, *12* (2). https://doi.org/10.1088/1758-5090/AB5D80.

(39) Setayeshmehr, M.; Hafeez, S.; van Blitterswijk, C.; Moroni, L.; Mota, C.; Baker, M. B. Bioprinting Via a Dual-Gel Bioink Based on Poly(Vinyl Alcohol) and Solubilized Extracellular Matrix towards Cartilage Engineering. *Int. J. Mol. Sci. 2021, Vol. 22, Page 3901* **2021**, *22* (8), 3901. https://doi.org/10.3390/IJMS22083901.

(40) Piluso, S.; Skvortsov, G. A.; Altunbek, M.; Afghah, F.; Khani, N.; Koc, B.; Patterson, J. 3D Bioprinting of Molecularly Engineered PEG-Based Hydrogels Utilizing Gelatin Fragments. *Biofabrication* **2021**, *13* (4), 045008. https://doi.org/10.1088/1758-5090/AC0FF0.

(41) Hinton, T. J.; Jallerat, Q.; Palchesko, R. N.; Park, J. H.; Grodzicki, M. S.; Shue, H. J.; Ramadan, M. H.; Hudson, A. R.; Feinberg, A. W. Three-Dimensional Printing of Complex Biological Structures by Freeform Reversible Embedding of Suspended Hydrogels. *Sci. Adv.* **2015**, *1* (9). https://doi.org/10.1126/sciadv.1500758.

(42) Lee, A.; Hudson, A. R.; Shiwarski, D. J.; Tashman, J. W.; Hinton, T. J.; Yerneni, S.; Bliley, J. M.; Campbell, P. G.; Feinberg, A. W. 3D Bioprinting of Collagen to Rebuild Components of the Human Heart. *Science (80-.).* **2019**, *365* (6452), 482–487. https://doi.org/10.1126/science.aav9051.

(43) Kesti, M.; Müller, M.; Becher, J.; Schnabelrauch, M.; D'Este, M.; Eglin, D.; Zenobi-Wong, M. A Versatile Bioink for Three-Dimensional Printing of Cellular Scaffolds Based on Thermally and Photo-Triggered Tandem Gelation. *Acta Biomater.* **2015**, *11* (1), 162–172. https://doi.org/10.1016/J.ACTBIO.2014.09.033.

(44) Hull, S. M.; Lindsay, C. D.; Brunel, L. G.; Shiwarski, D. J.; Tashman, J. W.; Roth, J. G.; Myung, D.; Feinberg, A. W.; Heilshorn, S. C. 3D Bioprinting Using UNIversal Orthogonal Network (UNION) Bioinks. *Adv. Funct. Mater.* **2020**, *2007983*, 1–11. https://doi.org/10.1002/adfm.202007983.

(45) Ouyang, L.; Armstrong, J. P. K.; Lin, Y.; Wojciechowski, J. P.; Lee-Reeves, C.; Hachim, D.; Zhou, K.; Burdick, J. A.; Stevens, M. M. Expanding and Optimizing 3D Bioprinting Capabilities Using Complementary Network Bioinks. *Sci. Adv.* **2020**, *6* (38), 1–14. https://doi.org/10.1126/sciadv.abc5529.

(46) Riley, L.; Schirmer, L.; Segura, T. Granular Hydrogels: Emergent Properties of Jammed Hydrogel Microparticles and Their Applications in Tissue Repair and Regeneration. *Current Opinion in Biotechnology*. Elsevier Current Trends December 1, 2019, pp 1–8. https://doi.org/10.1016/j.copbio.2018.11.001.

(47) Daly, A. C.; Riley, L.; Segura, T.; Burdick, J. A. Hydrogel Microparticles for Biomedical Applications. *Nat. Rev. Mater. 2019 51* **2019**, *5* (1), 20–43. https://doi.org/10.1038/s41578-019-0148-6.

(48) Highley, C. B.; Song, K. H.; Daly, A. C.; Burdick, J. A. Jammed Microgel Inks for 3D Printing Applications. *Adv. Sci.* **2019**, *6* (1), 1801076. https://doi.org/10.1002/advs.201801076.

(49) Xin, S.; Chimene, D.; Garza, J. E.; Gaharwar, A. K.; Alge, D. L. Clickable PEG Hydrogel Microspheres as Building Blocks for 3D Bioprinting. *Biomater. Sci.* **2019**, *7* (3), 1179–1187. https://doi.org/10.1039/c8bm01286e.

(50) Zhang, H.; Cong, Y.; Osi, A. R.; Zhou, Y.; Huang, F.; Zaccaria, R. P.; Chen, J.; Wang, R.; Fu, J. Direct 3D Printed Biomimetic Scaffolds Based on Hydrogel Microparticles for Cell Spheroid Growth. *Adv. Funct. Mater.* **2020**, *30* (13), 1910573. https://doi.org/10.1002/ADFM.201910573.

(51) Shin, M.; Song, K. H.; Burrell, J. C.; Cullen, D. K.; Burdick, J. A. Injectable and Conductive Granular Hydrogels for 3D Printing and Electroactive Tissue Support. *Adv. Sci.* **2019**, *6* (20), 1901229. https://doi.org/10.1002/advs.201901229.

(52) Ding, A.; Jeon, O.; Cleveland, D.; Gasvoda, K. L.; Wells, D.; Lee, S. J.; Alsberg, E. Jammed Micro-Flake Hydrogel for Four-Dimensional Living Cell Bioprinting. *Advanced Materials*. 2022, p 2109394. https://doi.org/10.1002/adma.202109394.

(53) Xin, S.; Deo, K. A.; Dai, J.; Pandian, N. K. R.; Chimene, D.; Moebius, R. M.; Jain, A.; Han, A.; Gaharwar, A. K.; Alge, D. L. Generalizing Hydrogel Microparticles into a New Class of Bioinks for Extrusion Bioprinting. *Sci. Adv.* **2021**, *7* (42), 3087–3102. https://doi.org/10.1126/SCIADV.ABK3087/SUPPL_FILE/SCIADV.ABK3087_MOVIES_S1_AND_S2.ZIP.

(54) Tang, S.; Richardson, B. M.; Anseth, K. S. Dynamic Covalent Hydrogels as Biomaterials to Mimic the Viscoelasticity of Soft Tissues. *Prog. Mater. Sci.* **2021**, *120* (July 2020), 100738. https://doi.org/10.1016/j.pmatsci.2020.100738.

(55) Morgan, F. L. C.; Moroni, L.; Baker, M. B. Dynamic Bioinks to Advance Bioprinting. *Adv. Healthc. Mater.* **2020**, *9* (15), 1901798. https://doi.org/10.1002/adhm.201901798.

(56) Yesilyurt, V.; Webber, M. J.; Appel, E. A.; Godwin, C.; Langer, R.; Anderson, D. G. Injectable Self-Healing Glucose-Responsive Hydrogels with PH-Regulated Mechanical Properties. *Adv. Mater.* **2016**, *28* (1), 86–91. https://doi.org/10.1002/adma.201502902.

(57) Dong, Y.; Wang, W.; Veiseh, O.; Appel, E. A.; Xue, K.; Webber, M. J.; Tang, B.; Yang, X.; Weir, G.; Langer, R.; Anderson, D. G. Injectable and Glucose-Responsive Hydrogels Based on Boronic Acid – Glucose Complexation. **2016**. https://doi.org/10.1021/acs.langmuir.5b04755.

(58) Wang, L. L.; Highley, C. B.; Yeh, Y. C.; Galarraga, J. H.; Uman, S.; Burdick, J. A. Three-Dimensional Extrusion Bioprinting of Single- and Double-Network Hydrogels Containing Dynamic Covalent Crosslinks. *J. Biomed. Mater. Res. - Part A* **2018**, *106* (4), 865–875. https://doi.org/10.1002/jbm.a.36323.

(59) Wang, H.; Zhu, D.; Paul, A.; Cai, L.; Enejder, A.; Yang, F.; Heilshorn, S. C. Covalently Adaptable Elastin-Like Protein–Hyaluronic Acid (ELP–HA) Hybrid Hydrogels with Secondary Thermoresponsive Crosslinking for Injectable Stem Cell Delivery. *Adv. Funct. Mater.* **2017**, *27* (28), 1–11. https://doi.org/10.1002/adfm.201605609.

(60) Kim, S. W.; Kim, D. Y.; Roh, H. H.; Kim, H. S.; Lee, J. W.; Lee, K. Y. Three-Dimensional Bioprinting of Cell-Laden Constructs Using Polysaccharide-Based Self-Healing Hydrogels. *Biomacromolecules* **2019**, *20* (5), 1860–1866. https://doi.org/10.1021/acs.biomac.8b01589.

(61) Díaz, A.; Herrada-Manchón, H.; Nunes, J.; Lopez, A.; Díaz, N.; Grande, H.-J.; Loinaz, I.; Fernández, M. A.; Dupin, D. 3D Printable Dynamic Hydrogel: As Simple as It Gets! *Macromol. Rapid Commun.* **2022**, 2200449. https://doi.org/10.1002/MARC.202200449.

(62) Webber, M. J.; Appel, E. A.; Meijer, E. W.; Langer, R. Supramolecular Biomaterials. *Nat. Mater.* **2015**, *15* (1), 13–26. https://doi.org/10.1038/nmat4474.

(63) Goor, O. J. G. M.; Hendrikse, S. I. S.; Dankers, P. Y. W.; Meijer, E. W. From Supramolecular Polymers to Multi-Component Biomaterials. *Chem. Soc. Rev.* **2017**, *46* (21), 6621–6637.

https://doi.org/10.1039/C7CS00564D.

(64) Li, C.; Faulkner-Jones, A.; Dun, A. R.; Jin, J.; Chen, P.; Xing, Y.; Yang, Z.; Li, Z.; Shu, W.; Liu, D.; Duncan, R. R. Rapid Formation of a Supramolecular Polypeptide-DNA Hydrogel for in Situ Three-Dimensional Multilayer Bioprinting. *Angew. Chemie - Int. Ed.* **2015**, *54* (13), 3957–3961. https://doi.org/10.1002/anie.201411383.

(65) Highley, C. B.; Rodell, C. B.; Burdick, J. A. Direct 3D Printing of Shear-Thinning Hydrogels into Self- Healing Hydrogels. *Adv. Mater.* **2015**, *27*, 5075–5079.

(66) Ouyang, L.; Highley, C. B.; Rodell, C. B.; Sun, W.; Burdick, J. A. 3D Printing of Shear-Thinning Hyaluronic Acid Hydrogels with Secondary Cross-Linking. *ACS Biomater. Sci. Eng.* **2016**, *2* (10), 1743–1751.

(67) Rodell, C. B.; Dusaj, N. N.; Highley, C. B.; Burdick, J. A. Injectable and Cytocompatible Tough Double-Network Hydrogels through Tandem Supramolecular and Covalent Crosslinking. *Adv. Mater.* **2016**, *28* (38), 8419–8424. https://doi.org/10.1002/adma.201602268.

(68) Susapto, H. H.; Alhattab, D.; Abdelrahman, S.; Khan, Z.; Alshehri, S.; Kahin, K.; Ge, R.; Moretti, M.; Emwas, A. H.; Hauser, C. A. E. Ultrashort Peptide Bioinks Support Automated Printing of Large-Scale Constructs Assuring Long-Term Survival of Printed Tissue Constructs. *Nano Lett.* **2021**, *21* (7), 2719–2729. https://doi.org/10.1021/acs.nanolett.0c04426

(69) Raphael, B.; Khalil, T.; Workman, V. L.; Smith, A.; Brown, C. P.; Streuli, C.; Saiani, A.; Domingos, M. 3D Cell Bioprinting of Self-Assembling Peptide-Based Hydrogels. *Mater. Lett.* **2017**, *190*, 103–106. https://doi.org/10.1016/j.matlet.2016.12.127.

(70) Sather, N. A.; Sai, H.; Sasselli, I. R.; Sato, K.; Ji, W.; Synatschke, C. V.; Zambrotta, R. T.; Edelbrock, J. F.; Kohlmeyer, R. R.; Hardin, J. O.; Berrigan, J. D.; Durstock, M. F.; Mirau, P.; Stupp, S. I. 3D Printing of Supramolecular Polymer Hydrogels with Hierarchical Structure. *Small* **2021**, *17* (5), 1–14. https://doi.org/10.1002/smll.202005743.

(71) Hu, T.; Cui, X.; Zhu, M.; Wu, M.; Tian, Y.; Yao, B.; Song, W.; Niu, Z.; Huang, S.; Fu, X. 3D-Printable Supramolecular Hydrogels with Shear-Thinning Property: Fabricating Strength Tunable Bioink via Dual Crosslinking. *Bioact. Mater.* **2020**, *5* (4), 808–818. https://doi.org/10.1016/j.bioactmat.2020.06.001.

(72) Cheng, W.; Zhang, J.; Liu, J.; Yu, Z. Granular Hydrogels for 3D Bioprinting Applications. *View* **2020**, *1* (3), 20200060. https://doi.org/10.1002/VIW.20200060.

(73) Qazi, T. H.; Blatchley, M. R.; Davidson, M. D.; Yavitt, F. M.; Cooke, M. E.; Anseth, K. S.; Burdick, J. A. Programming Hydrogels to Probe Spatiotemporal Cell Biology. *Cell Stem Cell* **2022**, *29* (5), 678–691. https://doi.org/10.1016/j.stem.2022.03.013.

(74) Loebel, C.; Rodell, C. B.; Chen, M. H.; Burdick, J. A. Shear-Thinning and Self-Healing Hydrogels as Injectable Therapeutics and for 3D-Printing. *Nat. Protoc.* **2017**, *12* (8), 1521–1541. https://doi.org/10.1038/nprot.2017.053.

(75) Accardo, J. V; Kalow, J. A. Reversibly Tuning Hydrogel Stiffness through Photocontrolled Dynamic Covalent Crosslinks. *Chem. Sci.* **2018**, *9* (27), 5987–5993. https://doi.org/10.1039/c8sc02093k.

(76) Rapp, T. L.; DeForest, C. A. Visible Light-Responsive Dynamic Biomaterials: Going Deeper and Triggering More. *Advanced Healthcare Materials*. John Wiley & Sons, Ltd April 1, 2020, p 1901553. https://doi.org/10.1002/adhm.201901553.

(77) Rapp, T. L.; DeForest, C. A. Tricolor Visible Wavelength-Selective Photodegradable Hydrogels. *ChemRxiv* **2022**, *10.26434/c.*

(78) Chung, K. Y.; Halwachs, K. N.; Lu, P.; Sun, K.; Silva, H. A.; Rosales, A. M.; Page, Z. A. Rapid Hydrogel Formation via Tandem Visible Light Photouncaging and Bioorthogonal Ligation. *Cell Reports Phys. Sci.* **2022**, *3* (12), 101185. https://doi.org/10.1016/j.xcrp.2022.101185.

Chapter IV

Viscoelastic oxidized alginates with reversible imine type cross-links: self-healing, injectable, and bioprintable hydrogels

Shahzad Hafeez [1], Huey Wen Ooi [1], Francis L. C. Morgan [1], Carlos Mota [1], Monica Dettin [2], Clemens van Blitterswijk [1], Lorenzo Moroni [1] and Matthew B. Baker [1]

[1] Department of Complex Tissue Regeneration, MERLN Institute for Technology Inspired Regenerative Medicine, Maastricht University, P.O. Box 616, 6200 MD Maastricht, The Netherlands.

[2] Department of Industrial Engineering, University of Padua, 35131 Padua, Italy.

Published in: **Gels** (2018).

Hafeez, S.; Ooi, H.; Morgan, F.; Mota, C.; Dettin, M.; van Blitterswijk, C.; Moroni, L.; Baker, M. Viscoelastic Oxidized Alginates with Reversible Imine Type Cross-links: Self-Healing, Injectable, and Bioprintable Hydrogels. *Gels* **2018**, *4* (4), 85. https://doi.org/10.3390/gels4040085.

Abstract

Bioprinting techniques allow for the recreation of 3D tissue-like structures. By deposition of hydrogels combined with cells (bioinks) in a spatially controlled way, one can create complex and multiscale structures. Despite this promise, the ability to deposit customizable cell-laden structures for soft tissues is still limited. Traditionally, bioprinting relies on hydrogels comprised of covalent or mostly static cross-links. Yet, soft tissues and the extracellular matrix (ECM) possess viscoelastic properties, which can be more appropriately mimicked with hydrogels containing reversible cross-links. In this study, we have investigated aldehyde containing oxidized alginate (ox-alg), combined with different cross-linkers, to develop a small library of viscoelastic, self-healing, and bioprintable hydrogels. By using distinctly different imine-type dynamic covalent chemistries (DCvC), (oxime, semicarbazone, and hydrazone), rational tuning of rheological and mechanical properties was possible. While all materials showed biocompatibility, we observed that the nature of imine type cross-link had a marked influence on hydrogel stiffness, viscoelasticity, self-healing, cell morphology, and printability. The semicarbazone and hydrazone cross-links were found to be viscoelastic, self-healing, and printable—without the need for additional Ca^{2+} cross-linking—while also promoting the adhesion and spreading of fibroblasts. In contrast, the oxime cross-linked hydrogels were found to be mostly elastic and showed neither self-healing, suitable printability, nor fibroblast spreading. Semicarbazone and hydrazone hydrogels hold great potential as dynamic 3D cell culture systems, for therapeutics and cell delivery, and a newer generation of smart bioinks.

Introduction

As we strive to recapitulate the complexity of native tissues and organs, bioprinting (BP) has emerged as a promising group of technologies for fields ranging from fundamental cell biology to clinically relevant tissue engineering.[1] BP allows the printing of various materials, cells, and biological molecules in a defined space. These technologies have allowed progress toward the custom 3D construction of both soft and hard tissues including skin, heart, kidney, and bone.[1,2] Bioprinting of high modulus materials (> 1 MPa range) for hard tissues, such as bone[3], has already been successfully demonstrated on a clinical scale for a wide range of polymeric materials (e.g., polyurethane, polycaprolactone, and block copolymers such as PEOT/PBT[4,5]) and printing techniques (e.g., 3D plotting[6] and fused deposition modelling[7]). However, the bioprinting of biological constructs for softer tissues with complex architecture remains limited. Though several key studies have recently shown strategies to design hydrogels with enhanced capacity to self-support bioprinted structures for soft tissues[8-10], the demand for customizable bioinks with tissue-relevant viscoelasticity and shear-thinning properties required for bioprinting remains unfulfilled.

Bioprinting of cell-laden hydrogels (bioinks) is attractive for the construction of complex soft tissue architectures, allowing for the creation of constructs with the highly defined placement of both material composition and cells[5,11]. However, printing with live cells comes with a unique set of challenges for the hydrogel system used. An ideal bioink is printable, tailorable mechanically and chemically, and maintains structural integrity—all while maintaining high cell viability and mimicking the complex mechano-chemical signals of the native extracellular matrix (ECM)[12]. Several successful material formulations have been developed with unique combinations of polymers (e.g., alginate[13,14], gelatin[15], gelatin methacrylate[16], hyaluronic acid[17], and polyglicidol[18,19]) and cross-linking strategies (ionic[13], Schiff base[15], free-radical[16,20], thiol-ene[19,21,22] and supramolecular[9]). While significant progress has been made in bioink development, only a few of these materials show viscoelasticity comparable to soft tissue[23–25].

Recent studies have shown the important effects a viscoelastic material can have on cell behavior and tissue formation. For example, a material's viscoelastic timescale can influence the spreading and proliferation of adherent cells in hydrogels[26–28] and enhance the differentiation of mesenchymal stem cells (MSCs), leading to more advanced bone tissue formation[29]. Chondrocytes in viscoelastic hydrogels have also been shown to effectively deposit the cartilage matrix[30]. A common approach to facilitate the design of viscoelastic hydrogels are networks consisting of reversible bonds. These reversible bond systems have also been shown to facilitate adherent cell spreading[27,31], myoblasts fusion[24], and MSC differentiation into multiple lineages [32]. Owing to their reversible dynamic bonds, such materials can respond to cell forces via network rearrangement, breaking and reforming the bonds, while keeping bulk biophysical properties constant[9,25,33].

In an effort to move towards smarter materials for BP, a conceptually appealing approach is to utilize hydrogels with reversible bonds and dynamic interactions. Such systems not only allow

for tunable viscoelastic properties of cell-laden constructs but also for the incorporation of shear-thinning behavior, reducing viscosity and increasing printability when shear stress is applied. Consequently, efforts have already been made to develop viscoelastic materials with shear-thinning and self-healing properties for BP. A prominent example is the hyaluronic acid hydrogels based on supramolecular host-guest complexation (adamantane and cyclodextrin). The shear-thinning and self-healing nature of this hydrogel allows for gel in gel bioprinting, yet generally requires a secondary cross-linking step to allow free-standing structures and is limited in its ability to support cell adhesion.[17,34]

Dynamic covalent chemistry (DCvC) provides a large tool-box for the construction of dynamic soft materials.[23,33] Imine-type DCvCs are particularly attractive as they possess a range of equilibrium constants (K_{eq}), and tunable hydrolysis rates at physiological pH (k_{-1}) have been widely explored for bio-conjugation strategies, and are generally chemically specific and orthogonal. With the knowledge of the K_{eq} and k_{-1} of different imine linkages, one can tune the physical properties of a hydorgel. In general, K_{eq} affects the stiffness of the hydrogel, while k_{-1} can be used to tune the rate of cross-link rearrangement and the viscoelastic response. The rate of hydrolysis (k_{-1}) for different imine type cross-links has previously been shown to decrease with increasing electronegativity of the group alpha to the primary amine: Setting oxime hydrolysis at one, semicarbazone hydrolyzes 160 times faster, and hydrazone 300 times faster under identical conditions.[35] Conveniently, imine formation and its hydrolysis is readily tunable based on the type of imine bond formed[36], and can be highly sensitive to pH[35,37,38]. Imine-type reversible covalent viscoelastic hydrogels as 3D cell culture platforms that are self-healing, shear-thinning, and injectable have also been developed.[24,25,32] However, there have been only a few studies exploring DCvC for BP.[8,10]

In light of the recent importance of reversible hydrogel networks (e.g., viscoelasticity and stress relaxation) within cell culture and tissue formation[24,29,31], we aimed to create a 3D printable bioink that better recapitulates these ECM inherent properties. We hypothesized that alginate hydrogels with different imine type cross-links (oxime, semicarbazone, and hydrazone shown in **Figure 1**) would give rise to hydrogels with different viscoelasticity, self-healing, and shear-thinning properties, resulting in different printability. Alginate, a naturally derived polysaccharide composed of β-D-mannuronic acid (M units) and α-L-guluronic acid (G units), is economically obtainable and has a long history in tissue engineering and bioprinting[39,40]. Alginate is traditionally rapidly cross-linked via divalent ions (e.g., Ca^{2+}) and has high biocompatibility, high viscosity, low gelation concentrations, and no specific interactions with cells[41,42], yet the bioprintablity of unmodified alginate provides relatively poor performance due to the stiffness and viscosity tradeoff between cell viability and printability.[12] The oxidation of alginate, via the introduction of aldehyde groups along the backbone[43], can increase its biodegradability and has been previously leveraged for tailorable hydrogel formation via imine-type cross-linking in drug delivery[44,45]. Despite the power of this system, oxidized alginate cross-linked by imine bonds has only been partially explored, and to the best of our knowledge, has never been reported in the context of bioprinting.

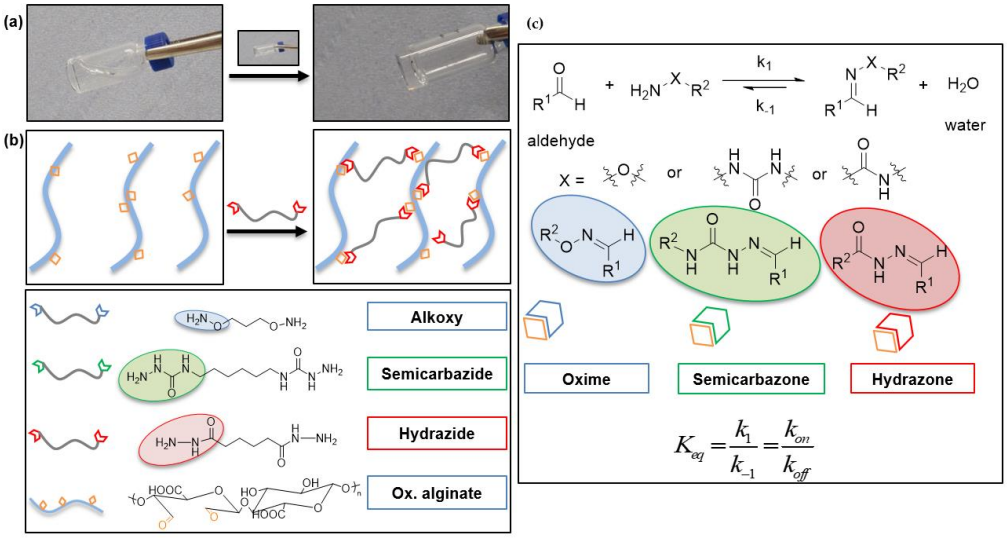

Figure 1. Scheme of hydrogel formation. a) Representative hydrogel formation for a hydrazone hydrogel. b) Schematic illustrating the cross-linking of alginate chains using dihydrazide cross-linker, the structure of oxidized alginate, and the structures of cross-linkers utilized in this study. c) A general reaction scheme for reversible imine type bonds formation and chemical structures of oxime, semicarbazone, and hydrazones.

In this study, we found that oxidized alginates cross-linked with different imine-type bonds allow an easily obtainable and modifiable bioink platform for 3D printing. The hydrogels created are mechanically tunable, biocompatible, shear-thinning, self-healing, and preserve cell viability post-extrusion. Furthermore, these hydrogels are biofunctionalizable via traditional oxime ligation strategies and show interesting changes in cell adhesion as a function of the dynamic bond used. Integrating tunable viscoelasticity into a bioink formulation brings us one step closer to the creation of synthetically modifiable ECM-mimicking hydrogels for bioprinting. Their unique material properties, along with the ability to tune the mechanochemical signals, will allow for the modular construction of more complex soft tissue mimics in the future.

Results and Discussion

Alginate Oxidation and Model Reactions

Oxidation of alginate was carried out using sodium periodate ($NaIO_4$) as an oxidizing agent, and according to literature procedures.[40] The hydroxyl groups at C-2 and C-3 of the repeating uronic acid units were oxidized resulting in the breakage of the C–C bonds to form two aldehyde groups, rapidly forming hemiacetals with neighboring alcohol groups.[46] Controlling the stoichiometric addition of $NaIO_4$, sugar monomers in alginate chains were oxidized to 5% (5% ox-alg), 10% (10% ox-alg), and 15% (15% ox-alg) theoretical degrees of oxidation (DOX) and confirmed qualitatively with the appearance of increasing hemiacetal peaks in NMR spectra (**Figure S3** in Supplementary Materials). Subsequently, model reactions with small molecules

were performed to investigate the possibility of forming hydrazone, semicarbazone, and oxime linkages (**Figure S4** in Supplementary Materials) within a reasonable time scale. At pH 7.4 and room temperature (RT), bond formation after 30 minutes—relevant conditions for the formation of cell-encapsulated hydrogels—was monitored via NMR. The appearance of imine-type bonds (oxime, semicarbazone, and hydrazone) was confirmed with ^{1}H NMR spectroscopy (**Figure S4** in Supplementary Materials). The concurrent appearance of imine-type hydrogens (6.5–8.5 ppm) and reduction in the hemiacetal hydrogens (5.15–5.75 ppm) provide evidence that the aldehydes along the oxidized alginate backbone could undergo the imine-type bond formation relatively quickly under suitable conditions.

Hydrogel Formation

Next, we evaluated the ability of three different cross-linkers designed to form imine-type cross-links (adipic acid dihydrazide, hexamethylene disemicarbazide, and aminooxy propyl hydroxyl amine dihydrochloride) to form a hydrogel at RT in phosphate-buffered saline (PBS) at pH 7.4 using 15% ox-alg, 2% (*w/v*) and an equimolar concentration of cross-linker (to the theoretical oxidation degree). All cross-linkers successfully made self-standing hydrogels (hydrazone hydrogel is shown in **Figure S8** in Supplementary Materials). However, hydrogel formation kinetics for each linker were slightly different. Monitored visually via vial inversion, the oxime cross-links were found to have the fastest kinetics (≈10 minutes stable hydrogel formation time) followed by semicarbazone (≈15 minutes stable hydrogel formation time) and then hydrazone (≈45 minutes stable hydrogel formation time). During these experiments, we also observed that oxime cross-links were non-reversible (on the time scale of our experiment), while semicarbazone and hydrazone cross-links were reversible (vide infra).

To obtain more insight into hydrogel formation kinetics, the gelation time was observed via plate-plate rheology. A time sweep was recorded to determine the gelation point, defined here as the crossover point between G' and G", after which there was a sudden increase in G'. For example, for 10% ox-alg, a 2% *(w/v)* solution was briefly mixed with an equimolar concentration of cross-linkers rheological measurements were started within four minutes. The oxime and semicarbazone hydrogels showed a G' and G" crossover point (gel point) around eight minutes, while the gel point was delayed until roughly 45 minutes for hydrazone. G' continued to increase towards a plateau after approximately 30 minutes for oxime and semicarbazone; however, hydrazone showed a continuous increase in G' even after 60 minutes (shown in **Figure 2a**). Rheological and vial inversion experiments clearly showed that imine-type chemistry has an influence on gelation kinetics, with oxime and semicarbazone gelation significantly faster than hydrazone.

Unless otherwise stated, in the remainder of this study, 10% ox-alg at 2% (*w/v*), and an equimolar amount of cross-linker (to the theoretical oxidation degree) were used to make hydrogels.

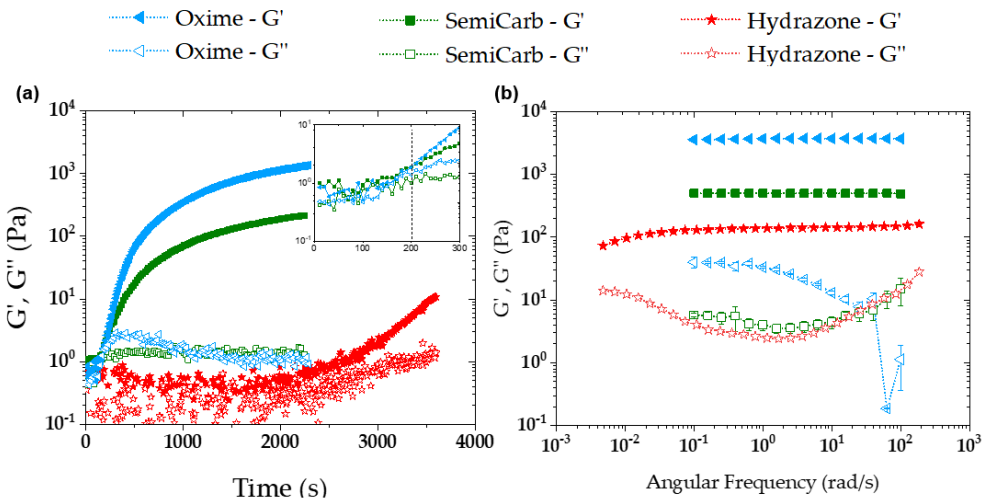

Figure 2. Hydrogel formation kinetics and viscoelasticity exhibited by a series of 2% (w/v) 10% ox-alg samples prepared with different cross-linkers (equimolar). a) Time sweep using the three different cross-linkers; aminooxy, semicarbazide, and hydrazide for evaluating hydrogel formation kinetics measured at 1% strain and 10 rad/s. b) Frequency sweep for the same three hydrogels measured at 1% strain.

Rheology

Storage and Loss Moduli

In order to determine the mechanical properties of the hydrogels, oscillatory shear rheology was performed. The mole equivalents of cross-linker, type of ox-alg, concentration % (*w/v*), and cross-linking time were kept constant to independently evaluate the effect of cross-links on stiffness and viscoelasticity. The oxime, semicarbazone (denoted by SemiCarb in **Figure 2**), and hydrazone cross-links form hydrogels whose shear moduli decrease across the series. As seen in the frequency sweep plots (**Figure 2b**), the oxime hydrogel was the stiffest (G' ≈ 4000 Pa), followed by semicarbazone (G' ≈ 500 Pa), and then hydrazone (G' ≈ 200 Pa). The oxime hydrogel was roughly eight and 20 times stiffer than semicarbazone and hydrazone, respectively for identical formulations.

For cross-linked polymer networks, the shear modulus is directly proportional to the number of elastically active cross-links[24] (Equation (1)),

$$G' = kT\frac{\nu_e}{\bar{V}} \quad (1)$$

where k is Boltzmann constant, T is the temperature, and ν_e represents the number of elastically active cross-links per unit volume ($\bar{V}$). In hydrogels with reversible cross-links, the cross-linking density depends on the ratio of formed cross-links to unbound cross-links. Assuming similar topological architecture in the system, this difference in the amount of cross-linking can be correlated with the K_{eq} of the different systems; a system with a higher modulus should be a

direct result of more cross-links indicating a higher K_{eq} of the DCvC bond[24,33]. Our results would suggest approximately one order of magnitude more cross-linking going from the hydrazone to the semicarbazone, and from the semicarbazone to the oxime. This result is nicely aligned with the trend in equilibrium constants of model systems. Oximes generally have the highest K_{eq} ($>10^8$ M^{-1}) followed by semicarbazones and then hydrazones, which are in the range of 10^4–10^6 M^{-1}.[35]

To investigate the effect of the degree of oxidation (DOX) on stiffness, 5% ox-alg, 10% ox-alg, and 15% ox-alg hydrogels were made using the dihydrazide cross-linker. Generally, an increase in storage moduli was observed with increasing DOX. Storage moduli increased by a factor of four (from ~90 to ~350 Pa) as the DOX increased from 5% to 10%; however, no considerable difference was observed between 10 and 15% ox-alg (~400 Pa) (**Figure S7** in Supplementary Materials). The observed increase in storage moduli has been correlated to the larger number of cross-linking sites available (aldehydes) with increasing DOX.[43,46] While we did not observe a significant difference between 10% and 15% ox-alg hydrogels, the NMR of the base material (**Figure S3**) indicated the presence of more aldehydes for the 15% ox-alg.

Viscoelasticity

The frequency sweep (**Figure 2b**) for both the semicarbazone and the hydrazone hydrogels showed characteristic viscoelastic behavior, with frequency-dependent loss moduli over the range explored. While the oxime hydrogel did show some frequency dependence, this appears to represent more elastic behavior. Viscoelastic materials can also show a crossover point (example in **Figure S5**) between storage (G') and loss modulus (G"), while moving from a rubbery plateau (higher frequency) to a terminal region (low frequency). However, this crossover point was not observed even during a longer-range scan of the hydrazone hydrogel down to 0.005 rad/s.

The crossover point in these reversible bond systems is largely determined by the rate at which a bond breaks (k_{-1}) which, for imine-type bonds, is directly related to the reverse rate of hydrolysis (as the rate-limiting step in the off reaction). From our observation of material behavior and moduli evolution, hydrazone should have the highest k_{-1}, among all cross-links, which is an indication that hydrazone hydrogel will show a crossover point at a higher frequency (rad/s), as compared to semicarbazone and oxime. In **Figure 2b**, a decrease in the storage modulus (G') and an increase in tanδ forecast a transition between rubbery and terminal regions and eventual convergence of G' and G". Typically, low frequencies are needed to observe a crossover point for hydrazone cross-links; Anseth and co-workers have observed a crossover point around 0.03 rad/s for methyl hydrazone cross-links on 4-arm PEG.[24] In this study, acyl hydrazone was utilized, which has half the hydrolysis rate (k_{-1}) of methyl hydrazone. Therefore, the convergence of G' and G" below 0.03 (rad/s) was expected and is not surprising for a linear alginate polymer. These results suggest that chain length, the topology of the polymer (linear versus multi-arm), and functionalities for effective cross-links are all critical factors to tune

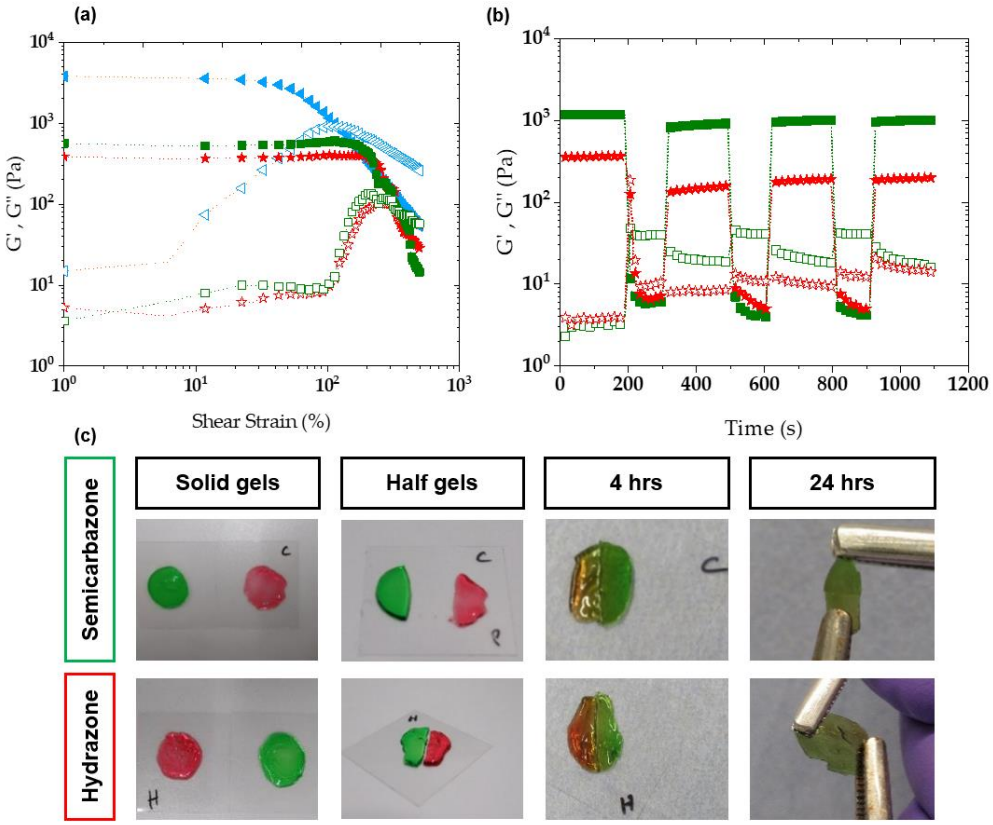

Figure 3. Demonstration of strain to rupture the network and the self-healing capacity of 10% ox-alg samples prepared with semicarbazide and hydrazide cross-linkers. a) Strain sweeps from 0% to 800% strain using oxime, semicarbazone, and hydrazone hydrogels, measured at 10 rad/s. b) Self-healing capacity with semicarbazide and hydrazide cross-linkers. The hydrogels were submitted to three strain cycles. Initially a low strain (1%) was applied, followed by three cycles of high strain (600%), to rupture the network, and low strain (1%), to allow recovery. The semicarbazone and hydrazone hydrogels rapidly self-heal. c) Macroscopic self-healing of the hydrogels. From left to right, the colored gels were formed (12 mm diameter, 2 mm thickness), cut in half, left to self-heal for four hours, and then tested at 24 hours.

viscoelasticity. However, as such, a crossover point at such small frequencies suggests that the alginate imine cross-linked hydrogels are very slow stress-relaxing networks.

Self-Healing

Self-healing was initially visualized in the lab for the 15% ox-alg hydrogel. In a glass vial, the hydrogel network was broken using a spatula, and self-healing was observed over time via the vial inversion method. The semicarbazone self-healed in ≈10 minutes, while hydrazone took ≈30 minutes to self-heal (**Figure S8** in Supplementary Materials). The oxime hydrogel did not self-heal. Oxime bonds are more stable than the semicarbazone and hydrazone bonds as the aminooxy is more electron deficient compared to the hydrazides. Presumably, the enhanced

stability (kinetically and thermodynamically) at neutral pH makes the reversibility/exchange dynamics too slow for oxime, resulting in no self-healing at room temperature and neutral pH[35,47].

In order to investigate the self-healing behavior more thoroughly, shear rupture-self-healing cycles were carried out on the rheometer. Initially, strain sweep experiments were carried out to determine the amount of strain needed for hydrogel rupture. These hydrogels proved to be surprisingly tough, with the crossover point for all hydrogels being between 100% and 400% strain (shown in **Figure 3a** and **Figure S6**). Thus, 600% strain was chosen to rupture the 10% ox-alg semicarbazone and hydrazone hydrogel cross-links, and self-healing recovery was allowed under 1% strain.

Upon rupture, the storage and loss moduli inverted (shown in **Figure 3b**), and the storage moduli dramatically decreased (<10 Pa). Upon recovery, two-phase self-healing recovery was observed: (i) Rapid bond reformation under 20 s (seconds) upon removing the rupture strain, and (ii) a slower recovery of stiffness observed during the next 160 s. The rapid bond reformation regained a majority of the network stiffness ≈70% (820 Pa out of 1160 Pa) and ≈40% (131 Pa out of 356 Pa) of their initial storage moduli compared to ≈10% and ≈5% in the slower recovery phase for semicarbazone (denoted SemiCarb in **Figure 2**) and hydrazone cross-links, respectively. Interestingly, cross-links recover ≈ 10% stronger after the 2nd and 3rd rupture cycles compared to the 1st rupture cycle. This result can partially be attributed to the inability of reactive chain ends to immediately find each other upon recovery. This kinetically traps the hydrogel in a temporarily less cross-linked state (lower modulus), which then slowly recovers towards the initial modulus after time and the rearrangement induced by subsequent self-healing cycles. The higher number of binding sites in the 15% ox-alg hydrazone hydrogel is reflected in a high moduli recovery after conformational network changes (shown in **Figure S7** in Supplementary Materials).

To visualize self-healing macroscopically, two disk shape solid hydrogels with different colors (red and green) were made. For a given linker, each pair of hydrogels was cut into two halves and then put back into contact within five minutes. We observed that the semicarbazone hydrogels self-healed faster than the hydrazone hydrogels and that the oxime hydrogels did not self-heal. After four hours, semicarbazone and hydrazone hydrogels self-healed and the hydrogel boundaries became obscured. Self-healed hydrogels could be stretched using tweezers after 24 hours: The semicarbazone hydrogel interface stayed stable under stretching force; however, upon overstretching the hydrazone hydrogel showed cracks across the interface (see in the **Figure 3c**). The oxime hydrogel did not self-heal at all, even after 24 hours (images can be seen in **Figure S8a** in Supplementary Materials).

Cell Viability

ATDC5 chondrocytes cells were used for cell viability studies (live-dead and metabolic activity) as they are known to survive in hydrogels without biochemical cues (e.g., RGD, a peptide motif required for cell adhesion to ECM)[48,49] and form multicellular aggregates[50]. ATDC5 were

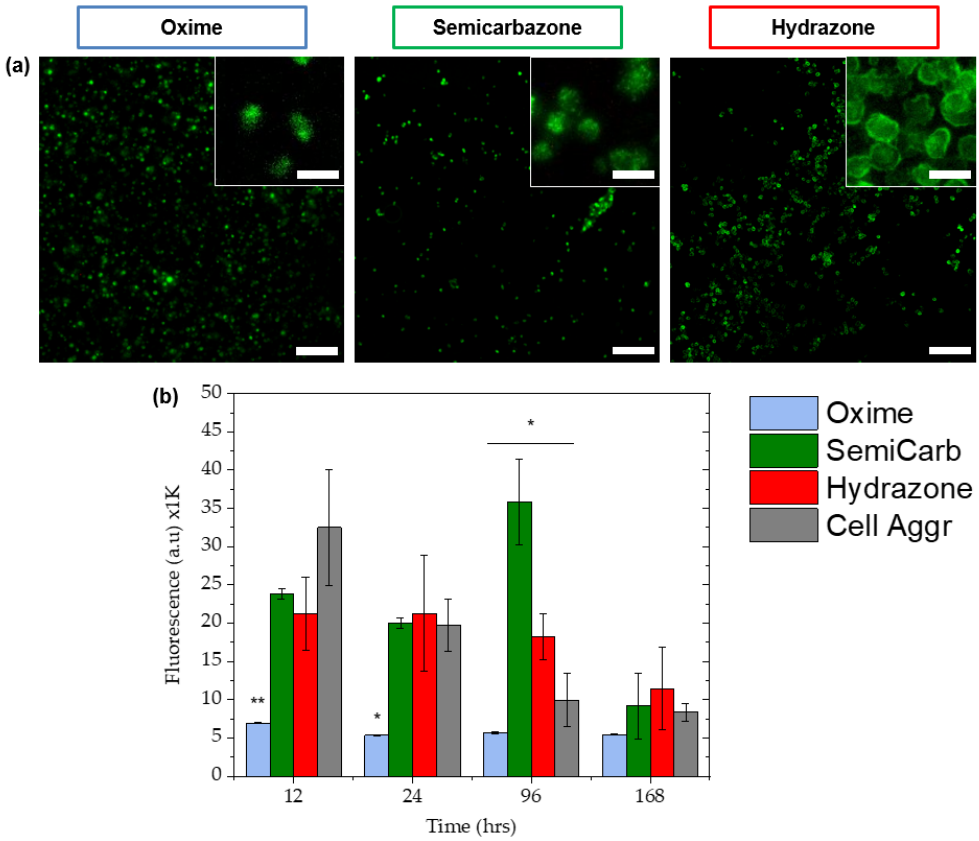

Figure 4. Cell viability. a) Image showing live cells (in green) after seven days of encapsulation in gels indicating that the great majority of cells are live and hydrogels did not cause cytotoxicity, Scale bar: 200 μm and 25 μm for inset images. b) Cell metabolic activity was recorded after 12, 24, 96, and 168 hours. For the "cell aggr" condition, cells were cultured in pellets, a standard for chondrocyte cell culture. The values reported are an average of $n = 3$, ± standard deviation.

encapsulated (3D) within 10% ox-alg hydrogels and cells were stained and imaged using an inverted fluorescence microscope to evaluate cytotoxicity after one, four, and seven days. Shown in **Figure 4a**, great majority of cells were found to be alive in all hydrogels after seven days. Live-dead images for one and four days are shown in **Figure S9** in Supplementary Materials. The oxime hydrogels were stable over seven days of culture with minimal erosion at the edges. The semicarbazone and hydrazone hydrogels swelled and eroded over time and were found to be very soft/fragile to handle on day seven. Interestingly, over time, the hydrazone hydrogels appeared to facilitate cell clustering (high magnification images are inset in **Figure 4a**). In the semicarbazone and the oxime hydrogels, this clustering of cells was noticeably less, which is hypothesized to be a result of the less dynamic reorganization of the network. The high multi-day viability of cells within these hydrogels supports future use for cell culture and bioprinting applications.

To confirm the high viability for chondrocytes seen during the live/dead assay, a prestoBlue assay was run to investigate the metabolic activity of the cells within the hydrogels over 168 hours (seven days) (Figure 4b). Within a series of 10% ox-alg, 2% (*w*/*v*), hydrogels, the oxime hydrogels maintained significantly lower metabolic activity compared to semicarbazone and the hydrazone hydrogels, which showed similar metabolic activity to the chondrocyte cell aggregate pellet—the tissue engineering standard for chondrocyte cell culture. In particular, chondrocytes showed significantly different metabolic activity in all conditions on day four. Comparing all hydrogel samples, chondrocytes in the oxime hydrogels showed a consistently low metabolic activity, while other samples started with a high metabolic activity that slowly decreased over seven days. The chondrocytes studied were able to maintain a higher metabolic flux in the more viscoelastic hydrogels (semicarbazone and hydrazone), as compared to the static (oxime) hydrogels.

Cell Spreading

Alginate possesses no active adhesion sites to interact or attach to mammalian cells, but cell adhesion and interaction can be promoted through the conjugation of cell adhesion ligands (e.g., RGD).[42] Conveniently, the oxidized alginate backbone can readily be ligated with hydroxylamine-containing biomolecules via well-established oxime ligation.[51,52] Hydrogels were bio-functionalized by incorporating aminooxy-RGD ligand (1000 μM)[53] to the 10% ox-alg hydrogel formulation. To investigate whether the cross-links with different viscoelasticity influence cell spreading, human dermal fibroblasts (HDFs) were seeded on top of hydrogels (2D) for 24 hours (see **Figure 5**). HDFs are better models for cell adhesion and spreading since they are phenotypically adherent and demonstrate an adhesion-dependent spreading morphology in 2D cell culture.

We noticed a marked effect on the amount of spreading on the different DCvC cross-linked hydrogels. Cell spreading was found to increase for networks cross-linked by bonds with a higher hydrolysis rate (k_{-1}), namely, more dynamically rearranging cross-links. HDFs seeded on the dynamic hydrogels (semicarbazone and hydrazone) showed a spindle shape, increased spreading, and an elongated morphology, with the hydrazone networks showing a more elongated morphology than the semicarbazone. For the oxime hydrogels, only rounded morphologies typical of cells in elastic hydrogels were observed (**Figure 5**). These results are in accordance with reported k_{-1} values of the cross-links: Hydrazone has the highest k_{-1}, which suggests that cross-links were permissive to changes in cell shape, while oxime has the lowest k_{-1}, resulting in elastic hydrogels where limited cell spreading was observed. As a control, cells were seeded on tissue culture plastic (TCP) and exhibited typical spreading morphology (see Figure S10 in Supplementary Materials).

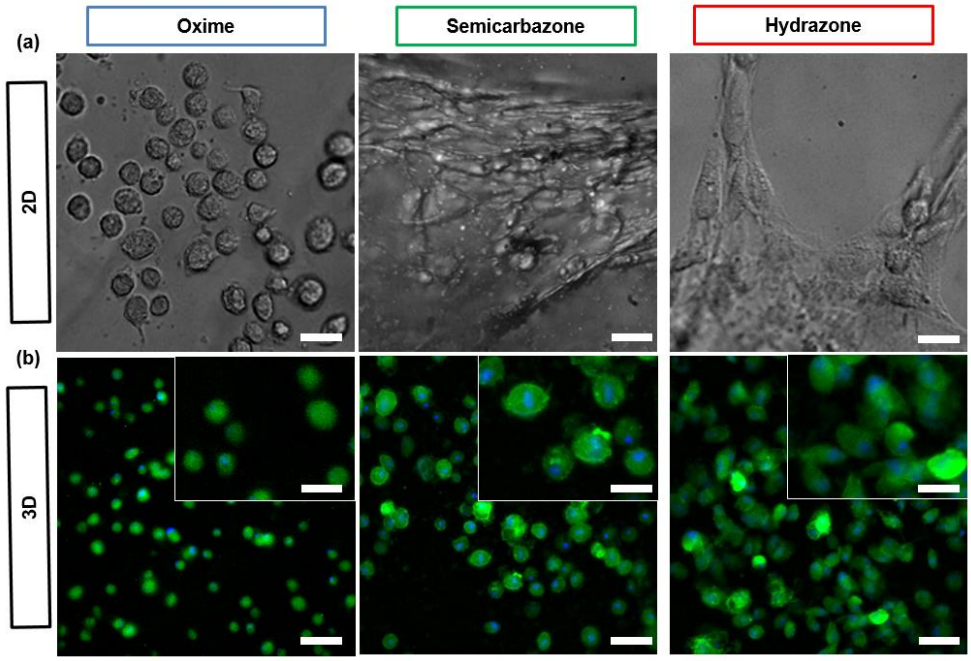

Figure 5. Fibroblasts spreading morphologies in oxime RGD ligated hydrogels, a) on top of (2D) and b) within (3D) oxime, semicarbazone and hydrazone cross-linked hydrogels, scale bar: 25 μm for 2D, 50 μm for 3D images, and 25 μm for 3D insets.

Of note, adherent cells generally increase their spreading area with an increase in substrate stiffness (2D elastic)[54]. This would suggest that cells should spread more on the oxime hydrogels (stiffest and most elastic); however, we have observed larger cell spreading on viscoelastic matrices (semicarbazone and hydrazone). A larger spreading of cells on the soft and stress-relaxing substrate (ionically cross-linked alginate) has also been reported by the Chaudhuri lab.[55] Such observation would suggest the viscoplastic nature of these hydrogels would allow cells to permanently remodel and elongate on these hydrogels. The deformable nature and degradation of hydrazone and semicarbazone would suggest the viscoplastic nature of these hydrogels. Also, important to mention, we observed that the cell does not remain exactly on top of semicarbazone and hydrazone hydrogel and rather migrates inside these hydrogels and experienced 3D environment. That might explain why cells showed spreading morphology on semicarbazone and hydrazone hydrogel. The same trend in cellular spreading was observed when HDF was cultured within hydrogels (3D). 3D encapsulation results are in accordance with recent literature finding a relationship between cellular spreading and reversible hydrogel networks[24,29,33]. Our current hypothesis is that microenvironment clustering of adhesive ligands[55] or stress relaxation[29] plays a significant role. To explain these seemingly disparate results, we would propose a more in-depth study by making a series of dynamic hydrogels with controlled stress relaxation. A few important points should be considered while making hydrogels. 1) Adjust the pH of oxime hydrogel to 7.4, 2) ensure that the hydrazone hydrogel retains sufficient thickness during cell

culture and cell did not migrate within hydrogel or on tissue culture plastic, and 3) ensure that imaged cells are on the surface of the hydrogel.

Observing more cellular spreading on hydrazone compared to oxime prompted our group to do a follow-up study in more depth[56]. Colleagues Francis and Julia made a series of dynamic hydrogels by modular mixing of oxime and dynamic cross-links. In alignment with the results presented here, more cell clustering was observed in hydrogels with a higher ratio of hydrazone cross-linker. They also found that cells exhibited more spreading morphology with an increasing oxime crosslinker ratio i.e., exhibited more elastic character which aligns with the current literature of less spreading on polyacrylamide-based viscoelastic hydrogels[57]. Interestingly, cell-dependent spreading has also been reported in polyacrylamide viscoelastic hydrogels, for example, healthy human hepatocytes showed expected less spreading compared to enhanced spreading by hepatocellular carcinoma cells[58]. We think that decoupling viscoelasticity from viscoplasticity and investigating multiple cells under healthy and diseased conditions would allow a better understanding of cellular behavior on such dynamic matrices.

Injectability and Bioprintability

With control over the material's properties, self-healing, cell viability, and bio-functionalization in these materials, we next investigated the injectability of these hydrogels. To assess the shear-thinning capability of the 10% ox-alg with different cross-linkers, we attempted to inject these materials from a syringe through a 25-gauge needle (260 μm internal diameter). The hydrazone and semicarbazone hydrogels were injectable through the needle with only the force of the hand and formed intact smooth fibers due to their self-healing capability (**Figure 6a**). Interestingly, the oxime hydrogel was also found to be injectable, but the injected fiber was a non-continuous hydrogel slurry upon injection. Hydrogels made from the 15% ox-alg with both hydrazone and semicarbazone were also observed to be injectable; however, the 15% semicarbazone hydrogels did not produce smooth fibers and required more force for injection (**Figure S11b** in Supplementary Materials). These initial experiments encouraged the exploration for use as bioinks for bioprinting and forecast their suitability as drug or cell delivery vehicles.

While both hydrazone and semicarbazone hydrogels showed some initial printability, the semicarbazone hydrogels required significantly higher pressures and larger needle diameters. Consequently, the hydrazone hydrogels were deemed more likely to support cell viability and were further optimized for bioprinting. A simple grid structure was employed to study the effects of deposition speed and extrusion pressure on printability. Using different deposition speeds and extrusion pressures, we used the 10% ox-alg 2% (*w*/*v*) hydrazone hydrogels to deposit 2-layered grid structures via a 0.25 mm diameter conical needle. Extrusion of the hydrogel at 115 and 120 kPa were observed to be more homogeneous and better-defined structures were extruded at a speed of 5 mm/s, as opposed to the partial and inhomogeneous hydrogel fibers bioprinted at 7 mm/s (**Figure S12** in Supplementary Materials). This could be expected as the bioprinting speeds employed should allow ample time for an appropriate amount of material to be deposited and placed on a substrate. Similarly, extrusion pressure was optimized to tune the

amount of deposited hydrogel and three different pressures (115, 120, and 140 kPa) were tested. A pressure of 140 kPa was found to be the optimal pressure for fiber extrusion among the tested values (**Figure S13** in Supplementary Materials).

We also tested printability with a lower concentration of the 10% ox-alg (1% (*w*/*v*)) and 5% ox-alg hydrazone hydrogels (2% (*w*/*v*)). Since these formulations form softer and less viscous gels, smaller diameter needles, and low extrusion pressures were tried for printing. Though both formulations showed promising 2-layered constructs, the integrity of the structure was compromised owing to their softer nature (printed structures are shown in **Figures S14 and S15** in Supplementary Materials).

Utilizing the optimized pressure (140 kPa) and deposition speed (5 mm/s) for the 10% ox-alg (2% (*w*/*v*)) hydrogels, we bioprinted one, two, and four-layered grid scaffolds (**Figure S16 in Supplementary Materials**). These hydrogels show printability, yet are not able to recreate high-fidelity grid formation as seen in high-viscosity and covalently cross-linked formulations. While grid formation provides good insight into the bioprinting fidelity of a grid, our aim to create soft tissue constructs prompted the exploration of either more life-like or solid structures. To investigate the ability of the 10% ox-alg hydrazone hydrogel to make more complex and self-supporting structures, we bioprinted the name of our institute "MERLN", and a vascular tree model, both with 6 mm thickness (shown as **b-2 and b-5 in Figure 6**). While the recreation of the vascular tree was found possible, the printing of sharp angels and closely spaced or parallel lines resulted in occlusion and merging as found in the MERLN name.

To increase bioprinting fidelity and print self-supporting structures with continuous deposition of material, printability was also tested by manually disrupting the hydrogel network before printing. Preprinting network disruption allowed uniform deposition of material at seven mm/s using 150 kPa, and this modification resulted in a vascular structure with better printing resolution and uniformity (shown as b-6 in Figure 6). This manual disruption method was also tested using 5% ox-alg (3 and 4% (*w*/*v*) and resulted in a similar result (shown as **b-7 and b-8 in Figure 6**). However, these higher concentrations of hydrogel (3–4% (*w*/*v*)) needed significantly higher pressure (600 kPa) compared to 2% (*w*/*v*), 10% ox-alg (150 kPa). Further exploration of printing parameters and network dynamics modifications are expected to increase the printability of these materials.

The viability of 10% ox-alg (2% (*w*/*v*)) hydrazone hydrogels with ATDC5 was evaluated 24 hours after bioprinting and compared it to the control, without bioprinting (**shown in Figure 6c**). Very few dead cells were found, which is in agreement with the cell viability experiment carried out over seven days (shown in **Figure 4a**). Cell viability decreased after 24 hours of bioprinting, which could be attributed to the shear stress suffered by cells during bioprinting (**c-2 in Figure 6**).

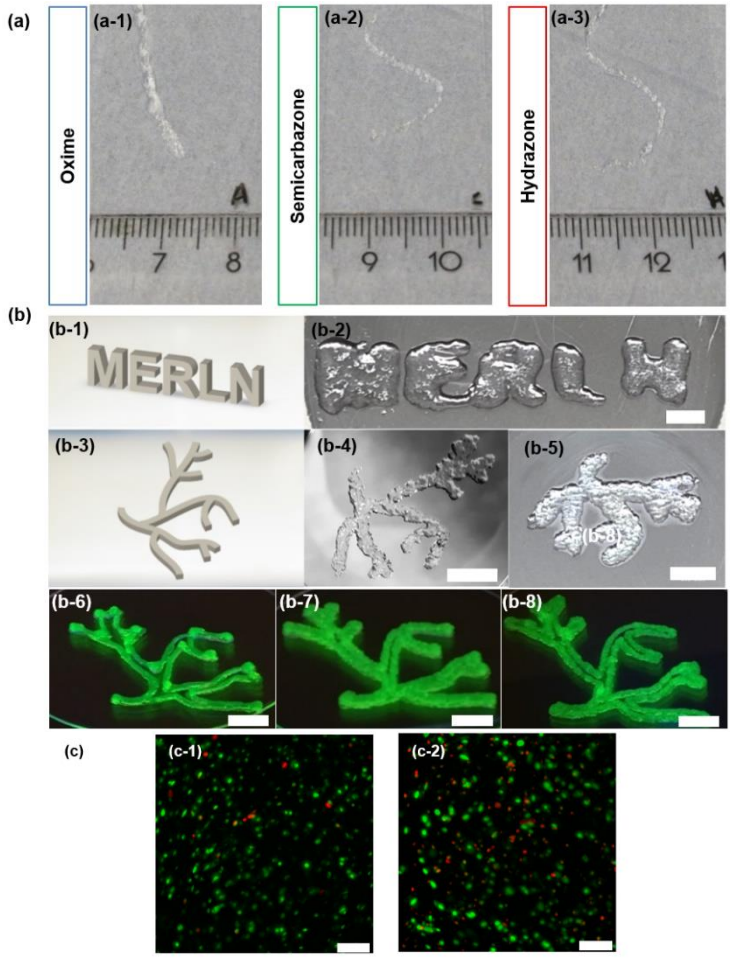

Figure 6. Injectability and bioprintability. a) 10% ox-alg gels with oxime (a-1), semicarbazone (a-2), and hydrazone (a-3) cross-linkers were extruded through a 25G needle. Semicarbazone and hydrazone showed injectability, and to our surprise oxime gels were also injectable, although they were not self-healing. b) Printed MERLN and vascular tree structures using hydrazone cross-links; 2% (*w*/*v*) of the 10% ox-alg used for (b-2–b-6) and 3% (*w*/*v*) and 4% (*w*/*v*) of 5% ox-alg used for (b-7) and (b-8), respectively. From the top left: 3D model of MERLN structure (b-1), printed MERLN structure (b-2, 6 mm thickness), 3D model of vascular tree (b-3), printed vascular tree (b-4, 2 mm thickness), printed vascular tree (b-5, 6 mm thickness), printed vascular tree (b-6–b-8) where the network was manually disrupted (fluorescein included for visibility), scale bar: 5 mm. c) 10% ox-alg hydrazone gels after 24 hours, (c-1): Without printing and (c-2): After bioprinting, Scale bar: 200 μm.

Conclusions

In this study, we have investigated the suitability of hydrogels based on oxidized alginate with imine-type cross-links as an injectable and printable biomaterials platform. The different cross-linkers had a marked effect on hydrogel formation, viscoelasticity, shear-thinning, self-healing, injectability, and printability. All explored formulations were non-cytotoxic over seven days. The

viscoelasticity could be tuned by selecting the imine type of cross-links: Oxime with the lowest off rate (k_{-1}) behaved like an elastic hydrogel and hydrazone with the highest off rate (k_{-1}) behaved like a viscoelastic hydrogel. All cross-linkers resulted in injectable hydrogels, but only the semicarbazone and hydrazone hydrogels are self-healing. Hydrazone cross-links 10% ox-alg (2% (*w*/*v*)) showed printability of self-supporting structures and high cell viability after bioprinting. HDFs cell studies showed that viscoelastic cross-links (semicarbazone and hydrazone) encouraged spreading morphology, while elastic cross-links (oxime) favored rounded morphology and were not permissive to changes in cell shape. These hydrogels represent a step towards smarter viscoelastic materials for 3D bioprinting and bioink formulations. In the future, this platform will be further explored for the effect of materials dynamics on tissue formation and for formulations with improved printability. We envision a smarter bioink that fulfills both the necessities of printability, while greatly improving upon the mimicry of the extracellular matrix.

Materials and Methods

Materials

Propanoic acid hydrazide (≥90%), O-ethylhydroxylamine hydrochloride (97%), adipic acid dihydrazide (≥98%,), O,O'-1,3-propanediylbishydroxylamine dihydrochloride (98%), propyl isocyanate, hexamethylenediisocyanate, hydrazine monohydrate, activated charcoal (Norit), sodium periodate ($NaIO_4$) and ethylene glycol were purchased from Sigma-Aldrich. Propyl semicarbazide and N,N'-(hexane-1,6-diyl)bis(hydrazinecarboxamide) (HDCA) (^{1}H NMR structures shown in **Figure S1&S2** in Supplementary Information) were synthesized according to literature.[38] Sodium alginate was purchased from FMC (Manugel GMB, Lot No. G9402001, Dialysis membrane (Spectra/Por®) with a molecular weight cut off (MWCO) 3500 Dalton (Da) from VWR, Netherlands.

Dulbecco's modified Eagle's medium (DMEM, high glucose and supplemented with GlutaMAX™ and Sodium Pyruvate), DEME-F12 (low glucose), Dulbecco's phosphate buffer saline (PBS), fetal bovine serum (FBS), penicillin/streptomycin (P/S), calcein AM, ethidium homodimer, Alexa Fluor® 488 Phalloidin, DAPI, and PrestoBlue™ cell viability reagent were purchased from Thermo Fisher Scientific.

Alginate Purification

Alginate powder was dissolved in deionized (DI) water at a concentration of 1% (*w*/*v*). Activated charcoal (1% (*w*/*v*)) was added, and the alginate solution was stirred for 24 hours at 4 °C. Subsequently, the alginate solution was filtered with 11 μm, 1.2 μm, 0.45 μm, and 0.2 μm Whatman membrane filters (Sigma-Aldrich) to remove charcoal particles. The alginate solution was then frozen and lyophilized.

Synthesis of Oxidized Alginate

To prepare 5% ox-alg, purified alginate (1.00 g, 5.68×10^{-3} mol monomer) was dissolved in 100 mL DI water. Keeping the reaction in the dark, sodium periodate (6.07×10^{-2} g, 2.84×10^{-4} mol) was added in one portion with stirring. After 17 hours in the dark (at RT), the reaction was quenched by the addition of equimolar ethylene glycol (1.76×10^{-2} g, 2.84×10^{-4} mol). The reaction solution was stirred in the dark for 1 hour to stop the reaction completely. The reaction solution was dialyzed against water (2-liter bucket) using membrane tubes with a MWCO of 3500 Da (3 days with 3× water change per day), then lyophilized (over 80% yield). The procedure was repeated to prepare 10% ox-alg and 15% ox-alg.

Preparation of Hydrogels for Rheology and Cell Culture

Oxidized alginate samples were weighed into 1.5 mL Eppendorf tubes. To prepare alginate solutions of 2.5% (*w/v*), PBS was added and the solution was mixed for 30 minutes on a thermoshaker at RT (2000 rpm). Cross-linker solution was added (prepared in PBS) to prepare hydrogels with equimolar concentrations of aldehyde/cross-linker functionalities with a final alginate concentration of 2% (*w/v*). Solutions were quickly transferred to polydimethylsiloxane (PDMS) molds with a disc geometry of 12 mm in diameter and 2.0 mm in thickness. Coverslips were placed on top of hydrogel solutions during the gelation process to ensure hydrogels have flat top surfaces and homogeneous thickness. Gelation was left to occur for 30 minutes at room temperature and then overnight at 4 °C before rheological measurements were carried out. For cell culture studies, the alginate solution was incubated at 37 °C for gelation for 45 minutes.

For cell spreading, alginate was biofunctionalized with RGD: Oxidized alginate was dissolved in PBS and aminooxy RGD[53] (see Supplementary Materials for synthesis procedure) was coupled to the network using oxime ligation[51]. The final RGD ligand concentration was set to 1000 μM and equimolar concentrations of cross-linkers (relative to aldehyde functionalities) were added and mixed uniformly to form a hydrogel with a final 2% (*w/v*) oxidized alginate.

Rheological Measurements

Rheological measurements of hydrogels were carried out using an Anton Paar MRC 702 (Graz, Austria) at 23 °C using a parallel plate geometry with bottom and top diameters of 50 mm and 12 mm, respectively. During loading, the experimental gap size was set when a threshold normal force was reached; 1 N for stiffer hydrogels and 0.1 N for softer hydrogels. This ensures good contact with the plates, prevents slippage, and increases the sensitivity of measurements by increasing the torque response. Samples were protected against evaporation by the addition of 2–3 drops of distilled water to the exposed surface after loading.

Oscillatory strain amplitude sweeps were conducted with strains from 1% to 800% at a frequency of 10 rad/s. Oscillatory frequency sweeps were performed from either 0.1 rad/s or 1 rad/s up to 100 rad/s. Step-strain measurements were undertaken to evaluate the self-healing capacity of hydrogels. Samples were subjected to three cycles, each consisting of 1% strain at 10 rad/s for 180 s, followed by 600% strain at 10 rad/s for 100 s.

*Macroscopic Self-*Healing *Experiment*

The macroscopic self-healing behavior of 10% ox-alg hydrogels was evaluated by observing hydrogel recovery at various time points (2, 4, and 24 hours without the application of any external pressure. Disc-shaped hydrogels were prepared in the presence of small amounts of food coloring (green and red). The hydrogels were cut down the middle into two pieces with a scalpel and two different colored pieces were placed in contact to determine self-healing behavior. For 15% ox-alg, hydrogels were made in glass vials, and the network was broken using a spatula, and then checked every five minutes.

Printability and Injectability

For printability, alginate solutions with hydrazone cross-linkers in PBS were loaded into 3 mL cartridges with stoppers and were left to form hydrogels for 18 to 20 hours at 4 °C before use. For printing, a conical G25 needle was used on a BioScaffolder (GeSiM–Gesellschaft für Silizium-Mikrosysteme mbH, Radeberg, Germany) controlled through proprietary software. Scaffolds with grid geometries were created with settings for a four-corner polygon, comprising 7 meandered strands placed at a distance of 1.0 mm apart. The deposition angle was rotated by 90° after each layer. The height of each layer was set to 0.2 mm and the number of layers was varied accordingly. "MERLN" and vascular tree constructs were designed and drawn in SolidWorks before being converted to .stl files. For manual disruption, 2% (*w*/*v*) of the 10% ox-alg and 3 and 4% (*w*/*v*) of 5% ox-alg with hydrazone cross-linker were left to form hydrogels for 2 to 3 hours. Manual disruption was performed by connecting the printing cartridge to a 5 mL syringe with a Luer-lock adapter. The hydrogel was forced between compartments until hydrogel disruption was observed and then extruded through a 25G needle. For injectability, 2% (*w*/*v*) hydrogels for each cross-linker were prepared and extruded through a 25G needle.

Cell Culture

ATDC5 chondrocytes cells were cultured at 37 °C under a 5% CO_2 atmosphere in Dulbecco's Modified Eagle's Medium-F12 (DMEM-F12, low glucose) supplemented with 10% (*v*/*v*) fetal bovine serum (FBS) and 1% (*v*/*v*) P/S. Cells were washed with PBS, trypsinized (0.05%), centrifuged, and then re-suspended in a 10% ox-alg solution (details in Section 4.4 above). They were subsequently mixed with a cross-linker to yield a homogenous mixture of 2% (*w*/*v*) alginate containing 4×10^6 cells/mL. The alginate mixture (50 µL) was transferred to the PDMS mold to form a hydrogel. Hydrogels were transferred to a non-adherent 24-well plate. For the cell pellet, the cell suspension was transferred to a 15 mL falcon tube with curved bottom. Media was added every two days.

HDF were cultured in Dulbecco's modified Eagle's medium (DMEM, high glucose) supplemented with GlutaMAX™, Sodium Pyruvate, 10% (*v*/*v*) fetal bovine serum (FBS), and 1% (*v*/*v*) P/S. Cells passaged at 80–85% confluence and were used after passage 6 for cell spreading experiments. For encapsulating cells within hydrogels (3D), cell suspension and cross-linker solution were mixed with alginate to yield a homogenous mixture of 2% (*w*/*v*) alginate

containing 4×10^6 cells/mL. The alginate solution (25 µL) was transferred to a PDMS mold and incubated at 37 °C for 45 minutes to form a hydrogel. Hydrogels were then transferred to a 96 flat-bottom black well plate for imaging. For 2D (cell seeded on top of hydrogels), 25 µL of the 2% (*w*/*v*) oxidized alginate mixture was transferred to a 96 flat bottom black well plate, centrifuged at 1500 RCF for five minutes to form a uniform layer on the bottom and left to cross-link at RT for 45 minutes. HDF cells were seeded on top (2D) of the hydrogel with a cell density of 0.1×10^6 cells/hydrogel. As a control, cells were seeded on TCP with 0.025×10^6 cells/well.

Viability Assays

For live-dead assays, cells were stained with calcein AM/ethidium homodimer Live/Dead solution according to the manufacturer's instructions on days 1, 4, and 7. For the metabolic assay, PrestoBlue solution (10% (*v*/*v*) in DMEM-F12, supplemented with FBS) was added and cells were incubated for 2 hours in the dark at 37 °C. At each time point, 100 µL was collected from each well and the fluorescence intensity was recorded using a microplate reader at an excitation wavelength of 530 nm and an emission wavelength of 590 nm.

Bioprintability Viability

For cell viability (live-dead) after bioprinting, 10% ox-alg hydrazone hydrogels containing an ATDC5 cell suspension were prepared, as mentioned above. A cell-laden solution was loaded into a 3 mL cartridge and placed at 37 °C for 1 hour. The cartridge with a G25 conical needle attached to it was then placed onto a BioScaffolder (GeSiM–Gesellschaft für Silizium-Mikrosysteme mbH, Germany). Bioprinting was carried out to create a four-corner polygon with a radius of 2.0 mm, comprising 2 meandered strands placed at 1.0 mm apart. Single-layer constructs with a height of 0.2 mm were created. The pressure was set to 140 kPa and extrusion was performed at 5.0 mm/s. Scaffolds were printed in 12-well non-treated cell culture plates. Live-dead viability assay was carried out after 24 hours, as mentioned above.

Cell Spreading

Cell spreading after 24 hours was visualized in 3D by staining the actin filaments in the cell body with Alexa Fluor® 488 Phalloidin and the cell nucleus with DAPI. Cells were fixed using 4% PFA for 20 minutes, washed with PBS, and membrane permeabilized with 0.1% (*v*/*v*) Triton X-100. The cells were then stained using (DAPI (1:1000) and Phalloidin (1:40)) solution in PBS for 20 minutes at room temperature. Stained cells were imaged with an inverted fluorescent microscope.

Statistics

All measurements were done in at least triplicate. Statistical significance was assessed using the two sample Student's t-test for independent sample populations in OriginLabs® Origin software. Statistical significance values were set at $p < 0.05$ (*) and $p < 0.01$ (**).

Acknowledgments

The author would like to acknowledge the Province of Limburg for funding this research. S.H. and C.A.v.B. are gracious for funding from the European Research Council (ERC) under the European Union's Horizons 2020 research and innovation program (grant agreement No. 694801). F.M., L.M., and M.B.B. are gracious for funding from the research program Innovation Fund Chemistry, which is partly financed by the Netherlands Organisation for Scientific Research (NWO) under TA grant agreement 731.016.202 ("DynAM").

Conflicts of Interest

S. Hafeez, M. B. Baker, and L. Moroni are inventors of a patent based on the findings described in this article.

Contributions to the work

This work was conceptualized by Shahzad Hafeez, Huey Wen Ooi, and Matthew. B. Baker. The author and Huey Wen Ooi decided together which model chemical reactions to perform, and Huey Wen Ooi then conducted NMR reaction investigations. Rheology studies were discussed in depth with Francis L. C. Morgan and Huey Wen Ooi, and then Francis L. C. Morgan carried out the measurements on Rheometer. 3D printing studies were done in collaboration with Huey Wen Ooi and Carlos Mota.

References

1. Moroni, L.; Burdick, J.A.; Highley, C.; Lee, S.J.; Morimoto, Y.; Takeuchi, S.; Yoo, J.J. Biofabrication strategies for 3D in vitro models and regenerative medicine. *Nat. Rev. Mater.* **2018**, *3*, 21–37, doi:10.1038/s41578-018-0006-y.
2. Moroni, L.; Boland, T.; Burdick, J.A.; De Maria, C.; Derby, B.; Forgacs, G.; Groll, J.; Li, Q.; Malda, J.; Mironov, V.A.; et al. Biofabrication: A Guide to Technology and Terminology. *Trends Biotechnol.* **2018**, *36*, 384–402, doi:10.1016/j.tibtech.2017.10.015.
3. Bose, S.; Vahabzadeh, S.; Bandyopadhyay, A.; Keck, W.M. Bone tissue engineering using 3D printing. *Biochem. Pharmacol.* **2013**, *16*, 496–504, doi:10.1016/j.mattod.2013.11.017.
4. Chia, H.N.; Wu, B.M. Recent advances in 3D printing of biomaterials. *J. Biol. Eng.* **2015**, *9*, 1–14, doi:10.1186/s13036-015-0001-4.
5. Chua, C.K.; Yeong, W.Y.; An, J. Special issue: 3D printing for biomedical engineering. *Materials* **2017**, *10*, 21–23, doi:10.3390/ma10030243.
6. Moroni, L.; De Wijn, J.R.; Van Blitterswijk, C.A. 3D Fiber-deposited scaffolds for tissue engineering: Influence of pores geometry and architecture on dynamic mechanical properties. *Biomaterials* **2006**, *27*, 974–985, doi:10.1016/j.biomaterials.2005.07.023.
7. Kalita, S.J.; Bose, S.; Hosick, H.L.; Bandyopadhyay, A. Development of controlled porosity polymer-ceramic composite scaffolds via fused deposition modeling. *Mater. Sci. Eng.* **2003**, *23*, 611–620, doi:10.1016/S0928-4931(03)00052-3.
8. Wang, L.L.; Highley, C.B.; Yeh, Y.C.; Galarraga, J.H.; Uman, S.; Burdick, J.A. Three-dimensional extrusion bioprinting of single- and double-network hydrogels containing dynamic covalent crosslinks. *J. Biomed. Mater. Res. A* **2018**, *106*, 865–875, doi:10.1002/jbm.a.36323.
9. Loebel, C.; Rodell, C.B.; Chen, M.H.; Burdick, J.A. Shear-thinning and self-healing hydrogels as injectable therapeutics and for 3D-printing. *Nat. Protoc.* **2017**, *12*, 1521–1541, doi:10.1038/nprot.2017.053.

10. Nadgorny, M.; Xiao, Z.; Connal, L.A. 2D and 3D-Printing of self-healing gels: Design and extrusion of self-rolling objects. *Mol. Syst. Des. Eng.* **2017**, *2*, 283–292, doi:10.1039/c7me00023e.
11. Malda, J.; Visser, J.; Melchels, F.P.; Jüngst, T.; Hennink, W.E.; Dhert, W.J.A.; Groll, J.; Hutmacher, D.W. 25th anniversary article: Engineering hydrogels for biofabrication. *Adv. Mater.* **2013**, *25*, 5011–5028.
12. Hölzl, K.; Lin, S.; Tytgat, L.; Van Vlierberghe, S.; Gu, L.; Ovsianikov, A. Bioink properties before, during and after 3D bioprinting. *Biofabrication* **2016**, *8*, 032002.
13. Ghanizadeh Tabriz, A.; Hermida, M.A.; Leslie, N.R.; Shu, W. Three-dimensional bioprinting of complex cell laden alginate hydrogel structures. *Biofabrication* **2015**, *7*, doi:10.1088/1758-5090/7/4/045012.
14. Ivanovska, J.; Zehnder, T.; Lennert, P.; Sarker, B.; Boccaccini, A.R.; Hartmann, A.; Schneider-Stock, R.; Detsch, R. Biofabrication of 3D Alginate-Based Hydrogel for Cancer Research: Comparison of Cell Spreading, Viability, and Adhesion Characteristics of Colorectal HCT116 Tumor Cells. *Tissue Eng. C Methods* **2016**, *22*, 708–715, doi:10.1089/ten.tec.2015.0452.
15. Zehnder, T.; Boccaccini, A.R.; Detsch, R. Evaluation of an alginate–gelatine crosslinked hydrogel for bioplotting. *Biofabrication* **2015**, *7*, 25001, doi:10.1088/1758-5090/7/2/025001.
16. Bertassoni, L.E.; Cardoso, J.C.; Manoharan, V.; Cristino, A.L.; Bhise, N.S.; Araujo, W.A.; Zorlutuna, P.; Vrana, N.E.; Ghaemmaghami, A.M.; Dokmeci, M.R.; et al. Direct-write bioprinting of cell-laden methacrylated gelatin hydrogels. *Biofabrication* **2014**, *6*, 024105, doi:10.1088/1758-5082/6/2/024105.
17. Su, W.Y.; Chen, Y.C.; Lin, F.H. Injectable oxidized hyaluronic acid/adipic acid dihydrazide hydrogel for nucleus pulposus regeneration. *Acta Biomater.* **2010**, *6*, 3044–3055, doi:10.1016/j.actbio.2010.02.037.
18. Stichler, S.; Böck, T.; Paxton, N.; Bertlein, S.; Levato, R.; Schill, V.; Smolan, W.; Malda, J.; Teßmar, J.; Blunk, T.; et al. Double printing of hyaluronic acid/poly(glycidol) hybrid hydrogels with poly(ε-caprolactone) for MSC chondrogenesis. *Biofabrication* **2017**, *9*, 044108, doi:10.1088/1758-5090/aa8cb7.
19. Stichler, S.; Jungst, T.; Schamel, M.; Zilkowski, I.; Kuhlmann, M.; Böck, T.; Blunk, T.; Teßmar, J.; Groll, J. Thiol-ene Clickable Poly(glycidol) Hydrogels for Biofabrication. *Ann. Biomed. Eng.* **2017**, *45*, 273–285, doi:10.1007/s10439-016-1633-3.
20. McBeth, C.; Lauer, J.; Ottersbach, M.; Campbell, J.; Sharon, A.; Sauer-Budge, A.F. 3D Bioprinting of GelMA scaffolds triggers mineral deposition by primary human osteoblasts. *Biofabrication* **2017**, *9*, 015009, doi:10.1088/1758-5090/aa53bd.
21. Ooi, H.W.; Mota, C.; Tessa Ten Cate, A.; Calore, A.; Moroni, L.; Baker, M.B. Thiol-Ene Alginate Hydrogels as Versatile Bioinks for Bioprinting. *Biomacromolecules* **2018**, *19*, 3390–3400, doi:10.1021/acs.biomac.8b00696.
22. Stichler, S.; Bertlein, S.; Tessmar, J.; Jüngst, T.; Groll, J. Thiol-ene Cross-Linkable Hydrogels as Bioinks for Biofabrication. *Macromol. Symp.* **2017**, *372*, 102–107, doi:10.1002/masy.201600173.
23. Ooi, H.W.; Hafeez, S.; van Blitterswijk, C.A.; Moroni, L.; Baker, M.B. Hydrogels that listen to cells: A review of cell-responsive strategies in biomaterial design for tissue regeneration. *Mater. Horiz.* **2017**, *4*, 1020, doi:10.1039/c7mh00373k.
24. McKinnon, D.D.; Domaille, D.W.; Cha, J.N.; Anseth, K.S. Biophysically defined and cytocompatible covalently adaptable networks as viscoelastic 3d cell culture systems. *Adv. Mater.* **2014**, *26*, 865–872, doi:10.1002/adma.201303680.
25. Yesilyurt, V.; Ayoob, A.M.; Appel, E.A.; Borenstein, J.T.; Langer, R.; Anderson, D.G. Mixed Reversible Covalent Crosslink Kinetics Enable Precise, Hierarchical Mechanical Tuning of Hydrogel Networks. *Adv. Mater.* **2017**, *29*, 1605947–1605947, doi:10.1002/adma.201605947.
26. Cameron, A.R.; Frith, J.E.; Cooper-White, J.J. The influence of substrate creep on mesenchymal stem cell behaviour and phenotype. *Biomaterials* **2011**, *32*, 5979–5993, doi:10.1016/j.biomaterials.2011.04.003.
27. Yeh, Y.-C.; Corbin, E.A.; Caliari, S.R.; Ouyang, L.; Vega, S.L.; Truitt, R.; Han, L.; Margulies, K.B.; Burdick, J.A. Mechanically dynamic PDMS substrates to investigate changing cell environments. *Biomaterials* **2017**, *145*, 23–32, doi:10.1016/j.biomaterials.2017.08.033.
28. Gong, Z.; Szczesny, S.E.; Caliari, S.R.; Charrier, E.E.; Chaudhuri, O.; Cao, X.; Lin, Y.; Mauck, R.L.; Janmey, P.A.; Burdick, J.A.; et al. Matching material and cellular timescales maximizes cell spreading

on viscoelastic substrates. *Proc. Natl. Acad. Sci. USA* **2018**, *115*, E2686–E2695, doi:10.1073/pnas.1716620115.
29. Chaudhuri, O.; Gu, L.; Klumpers, D.; Darnell, M.; Bencherif, S.A.; Weaver, J.C.; Huebsch, N.; Lee, H.-P.; Lippens, E.; Duda, G.N.; et al. Hydrogels with tunable stress relaxation regulate stem cell fate and activity. *Nat. Mater.* **2016**, *15*, 326, doi:10.1038/NMAT4489.
30. Lee, H.P.; Gu, L.; Mooney, D.J.; Levenston, M.E.; Chaudhuri, O. Mechanical confinement regulates cartilage matrix formation by chondrocytes. *Nat. Mater.* **2017**, *16*, 1243–1251, doi:10.1038/nmat4993.
31. Lou, J.; Stowers, R.; Nam, S.; Xia, Y.; Chaudhuri, O. Stress relaxing hyaluronic acid-collagen hydrogels promote cell spreading, fiber remodeling, and focal adhesion formation in 3D cell culture. *Biomaterials* **2018**, *154*, 213–222, doi:10.1016/j.biomaterials.2017.11.004.
32. Wang, H.; Zhu, D.; Paul, A.; Cai, L.; Enejder, A.; Yang, F.; Heilshorn, S.C. Covalently Adaptable Elastin-Like Protein–Hyaluronic Acid (ELP–HA) Hybrid Hydrogels with Secondary Thermoresponsive Crosslinking for Injectable Stem Cell Delivery. *Adv. Funct. Mater.* **2017**, *27*, 1–11, doi:10.1002/adfm.201605609.
33. Rosales, A.M.; Anseth, K.S. The design of reversible hydrogels to capture extracellular matrix dynamics. *Nat. Rev. Mater.* **2016**, *1*, 1–15, doi:10.1038/natrevmats.2015.12.
34. Highley, C.B.; Rodell, C.B.; Burdick, J.A. Direct 3D Printing of Shear-Thinning Hydrogels into Self-Healing Hydrogels. *Adv. Mater.* **2015**, *27*, 5075–5079.
35. Kölmel, D.K.; Kool, E.T. Oximes and Hydrazones in Bioconjugation: Mechanism and Catalysis. *Chem. Rev.* **2017**, *117*, 10358–10376, doi:10.1021/acs.chemrev.7b00090.
36. Lee, K.Y.; Bouhadir, K.H.; Mooney, D.J. Degradation Behavior of Covalently Cross-Linked Poly(aldehyde guluronate) Hydrogels. *Macromolecules* **2000**, *33*, 97–101, doi:10.1021/ma991286z.
37. Kalia, J.; Raines, R.T. Hydrolytic stability of hydrazones and oximes. *Angew. Chem. Int. Ed.* **2008**, *47*, 7523–7526, doi:10.1002/anie.200802651.
38. Sims, M.B.; Patel, K.Y.; Bhatta, M.; Mukherjee, S.; Sumerlin, B.S. Harnessing Imine Diversity to Tune Hyperbranched Polymer Degradation. *Macromolecules* **2018**, *51*, 356–363, doi:10.1021/acs.macromol.7b02323.
39. Andersen, T.; Auk-Emblem, P.; Dornish, M. 3D Cell Culture in Alginate Hydrogels. *Microarrays* **2015**, *4*, 133–161, doi:10.3390/microarrays4020133.
40. Jia, J.; Richards, D.J.; Pollard, S.; Tan, Y.; Rodriguez, J.; Visconti, R.P.; Trusk, T.C.; Yost, M.J.; Yao, H.; Markwald, R.R.; et al. Engineering alginate as bioink for bioprinting. *Acta Biomater.* **2014**, *10*, 4323–4331, doi:10.1016/j.actbio.2014.06.034.
41. Lee, K.Y.; Mooney, D.J. Alginate: Properties and biomedical applications. *Prog. Polym. Sci.* **2012**, *37*, 106–126, doi:10.1016/j.progpolymsci.2011.06.003.
42. Rowley, J.A.; Madlambayan, G.; Mooney, D.J. Alginate hydrogels as synthetic extracellular matrix materials. *Biomaterials* **1999**, *20*, 45–53, doi:10.1016/S0142-9612(98)00107-0.
43. Bouhadir, K.H.; Hausman, D.S.; Mooney, D.J. Synthesis of cross-linked poly(aldehyde guluronate) hydrogels. *Polymer* **1999**, *40*, 3575–3584.
44. Sarker, B.; Papageorgiou, D.G.; Silva, R.; Zehnder, T.; Gul-E-Noor, F.; Bertmer, M.; Kaschta, J.; Chrissafis, K.; Detsch, R.; Boccaccini, A.R. Fabrication of alginate–gelatin crosslinked hydrogel microcapsules and evaluation of the microstructure and physico-chemical properties. *J. Mater. Chem. B* **2014**, *2*, 1470, doi:10.1039/c3tb21509a.
45. Wei, Z.; Yang, J.H.; Liu, Z.Q.; Xu, F.; Zhou, J.X.; Zrínyi, M.; Osada, Y.; Chen, Y.M. Novel biocompatible polysaccharide-based self-healing hydrogel. *Adv. Funct. Mater.* **2015**, *25*, 1352–1359, doi:10.1002/adfm.201401502.
46. Gomez, C.G.; Rinaudo, M.; Villar, M.A. Oxidation of sodium alginate and characterization of the oxidized derivatives. *Carbohydr. Polym.* **2007**, *67*, 296–304, doi:10.1016/j.carbpol.2006.05.025.
47. Kuhl, N.; Abend, M.; Bode, S.; Schubert, U.S.; Hager, M.D. Oxime crosslinked polymer networks: Is every reversible covalent bond suitable to create self-healing polymers? *J. Appl. Polym. Sci.* **2016**, *133*, 1–9, doi:10.1002/app.44168.
48. Rocha, P.M.; Santo, V.E.; Gomes, M.E.; Reis, R.L.; Mano, J.F. Encapsulation of adipose-derived stem cells and transforming growth factor-β1 in carrageenan-based hydrogels for cartilage tissue engineering. *J. Bioact. Compat. Polym.* **2011**, *26*, 493–507, doi:10.1177/0883911511420700.
49. Sá-Lima, H.; Tuzlakoglu, K.; Mano, J.F.; Reis, R.L. Thermoresponsive poly(N-

isopropylacrylamide)-g-methylcellulose hydrogel as a three-dimensional extracellular matrix for cartilage-engineered applications. *J. Biomed. Mater. Res. A* **2011**, *98 A*, 596–603, doi:10.1002/jbm.a.33140.

50. Masuda, T.; Takei, N.; Nakano, T.; Anada, T.; Suzuki, O.; Arai, F. A microfabricated platform to form three-dimensional toroidal multicellular aggregate. *Biomed. Microdevices* **2012**, *14*, 1085–1093, doi:10.1007/s10544-012-9713-0.
51. Ulrich, S.; Boturyn, D.; Marra, A.; Renaudet, O.; Dumy, P. Oxime ligation: A chemoselective click-type reaction for accessing multifunctional biomolecular constructs. *Chem. A Eur. J.* **2014**, *20*, 34–41, doi:10.1002/chem.201302426.
52. Dirksen, A.; Hackeng, T.M.; Dawson, P.E. Nucleophilic catalysis of oxime ligation. *Angew. Chem. Int. Ed.* **2006**, *45*, 7581–7584, doi:10.1002/anie.200602877.
53. Zamuner, A.; Cavo, M.; Scaglione, S.; Messina, G.M.L.; Russo, T.; Gloria, A.; Marletta, G.; Dettin, M. Design of decorated self-assembling peptide hydrogels as architecture for mesenchymal stem cells. *Materials* **2016**, *9*, doi:10.3390/ma9090727.
54. Engler, A.J.; Sen, S.; Sweeney, H.L.; Discher, D.E. Matrix Elasticity Directs Stem Cell Lineage Specification. *Cell* **2006**, *126*, 677–689, doi:10.1016/j.cell.2006.06.044.
55. Chaudhuri, O.; Gu, L.; Darnell, M.; Klumpers, D.; Bencherif, S.A.; Weaver, J.C.; Huebsch, N.; Mooney, D.J. Substrate stress relaxation regulates cell spreading. *Nat. Commun.* **2015**, *6*, doi:10.1038/ncomms7365.
56. Morgan, F. L. C.; Fernández-Pérez, J.; Moroni, L.; Baker, M. B. Tuning Hydrogels by Mixing Dynamic Cross-Linkers: Enabling Cell-Instructive Hydrogels and Advanced Bioinks. *Adv. Healthc. Mater.* **2022**, *11* (1), 2101576. https://doi.org/10.1002/adhm.202101576
57. Charrier, E. E.; Pogoda, K.; Wells, R. G.; Janmey, P. A. Control of Cell Morphology and Differentiation by Substrates with Independently Tunable Elasticity and Viscous Dissipation. *Nat. Commun.* **2018**, *9* (1), 449. https://doi.org/10.1038/s41467-018-02906-9.
58. Mandal, K.; Gong, Z.; Rylander, A.; Shenoy, V. B.; Janmey, P. A. Opposite Responses of Normal Hepatocytes and Hepatocellular Carcinoma Cells to Substrate Viscoelasticity †. *Cite this Biomater. Sci* **2020**, *8*, 1316. https://doi.org/10.1039/c9bm01339c.

Supplementary information

Materials and Methods

Synthesis of small model reacting molecule propyl semicarbazide

A solution of propyl isocyanate (0.2 g, 2.3 x 10-3 mol) in acetonitrile (3 mL) was added dropwise to a solution of hydrazine monohydrate (0.7 g, 14.1 x 10-3 mol) in acetonitrile (2 mL) at room temperature with vigorous stirring. Following 24 hours of stirring, acetonitrile was dried in vacuo at 30 °C to yield the product as a white waxy solid. 1H NMR (600 MHz, DMSO-d6) δ 6.80-6.85 (s, 1H), 6.25 – 6.35 (s, 1H), 4.00 (s, 2H), 3.00 (q, 2H), 1.35 – 1.40 (m, 2H), 0.8 – 0.85 (t, 3H).

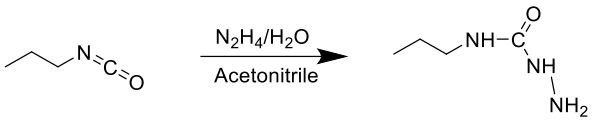

Synthesis of hexamethylene disemicarbazide linker

A solution of hexamethylenediisocyanate (0.5 g, 2.9 x 10-3 mol) in acetonitrile (4 mL) was added dropwise to a solution of hydrazine monohydrate (0.89 g, 17.8 x 10-3 mol) in acetonitrile (4 mL) at room temperature with vigorous stirring. Following 2h of additional stirring, acetonitrile was dried in vacuo at 30 °C to yield the product as a white solid.[1] 1H NMR (600 MHz, DMSO- d6) δ 6.75 – 6.85 (s, 1H), 6.29 – 6.21 (s, 1H), 4.00 (s, 2H), 3.00 (q, 2H), 1.32 – 1.40 (p, 2H), 1.26 – 1.20 (m, 2H).

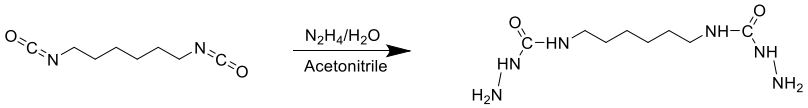

Model reaction with O-ethylhydroxylamine

Oxidized alginate (10 % ox-alg, 5.00 x 10-3 g, 5.05 x 10-6 mol of aldehyde groups) was weighed into a 1.5 mL Eppendorf tube. A 0.5 M stock solution of O-ethylhydroxylamine hydrochloride (5.00 x 10-3 g, 5.13 x 10-5 mol) in D2O (0.1025 mL) was prepared. The O-ethylhydroxylamine solution (17.70 µL, 8.85 x 10-6 mol) and D2O (0.4823 mL) was added to the tube and the reaction was carried out for 30 minutes on a thermoshaker at RT (2000 rpm). The reaction solution (0.5 mL) was transferred to an NMR tube for recording the NMR spectrum.

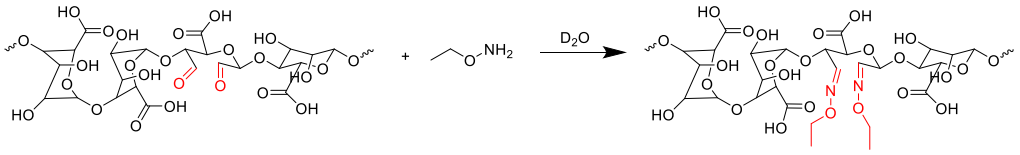

Model reaction with propyl semicarbazide

Oxidized alginate (10 % ox-alg, 5.00 x 10-3 g, 5.05 x 10-6 mol of aldehyde groups) was weighed into a 1.5 mL Eppendorf tube. A 0.5 M stock solution of propyl semicarbazide (5.00 x 10-3 g, 4.27 x 10-5 mol) in D2O (0.0854 mL) was prepared. The propyl semicarbazide solution (17.70 µL, 8.85 x 10-6 mol) and D2O (0.4823 mL) was added to the tube and the reaction was carried out for 30 minutes on a thermoshaker at RT (2000 rpm). The reaction solution (0.5 mL) was transferred to an NMR tube for recording the NMR spectrum.

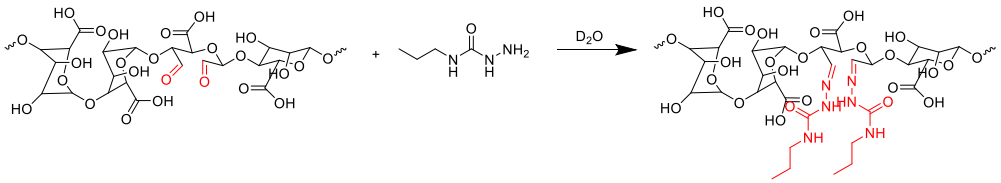

Model reaction with propanoic acid hydrazide

Oxidized alginate (10 % ox-alg, 5.00 x 10-3 g, 5.05 x 10-6 mol of aldehyde groups) was weighed into a 1.5 mL Eppendorf tube. A 0.5 M stock solution of propanoic acid hydrazide (5.00 x 10-3 g, 5.67 x 10-5 mol) in D2O (0.1135 mL) was prepared. The propanoic acid hydrazide solution (17.70 µL, 8.85 x 10-6 mol) and D2O (0.4823 mL) were added to the tube and the reaction was carried out for 30 minutes on a thermoshaker at RT (2000 rpm). The reaction solution (0.5 mL) was transferred to an NMR tube for recording the NMR spectrum.

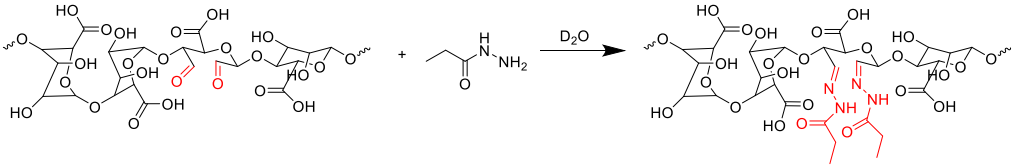

Aoa-7-GRGDSP synthesis

The peptide Aoa-7-GRGDSP (sequence: NH2-O-CH2-CO-7-aminoheptanoic acid-Gly-Arg-Gly-Asp-Ser-Pro-NH2) was synthesized on Rink Amide MBHA resin (0.60 mmol/g) using Fmoc chemistry by a Syro I synthesizer (Multisyntech, Witten, Germany). The side chain protecting groups were: OtBu, Asp; tBu, Ser; Pbf, Arg. The couplings were double for the first insertion, then single (5 equivalents of Fmoc-amino acid, 5 eq. HBTU, 5 eq. HOBt, and 10 eq. DIEA); for the last coupling 10 eq. of 2,4,6-Collidine was used instead of DIEA. The peptide was cleaved from the resin and deprotected from side chain protecting groups using the mixture 1.9 mL TFA, 0.05 mL TES, and 0.05 mL H2O, for 90 minutes. The characterization of the synthetic peptide was performed by MALDI mass spectrometry (Theoretical mass: 786.0 Da; Experimental mass: 784.8 Da; 4800 MALDI-TOF/TOF Analyzer, AB Sciex Pte Ltd, Singapore). The absence in the MALDI spectrum of different masses attributable to secondary products encouraged the use of Aoa-7-GRGDSPA without RP-HPLC purification avoiding, on the other hand, amino-oxy group reaction with acetonitrile, the RP-HPLC standard eluent.

Results and discussion

Synthesis of propyl semicarbazide

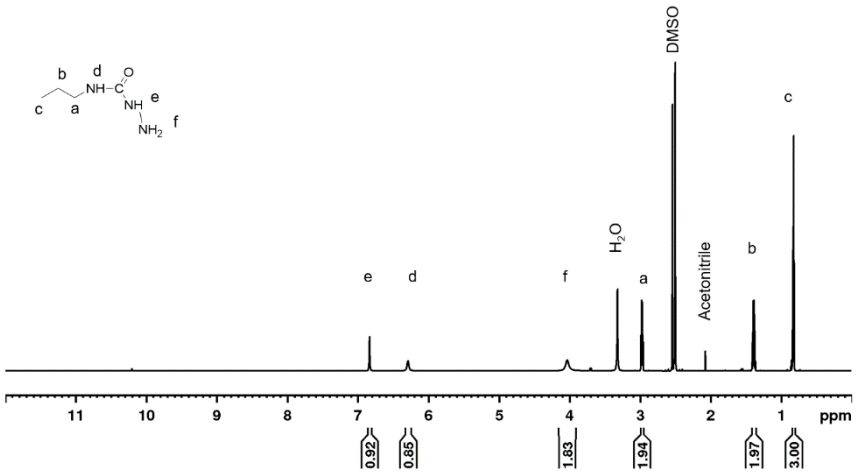

Figure S1. 1H NMR of propyl semicarbazide in DMSO.

Synthesis of hexamethylenedisemicarbazide

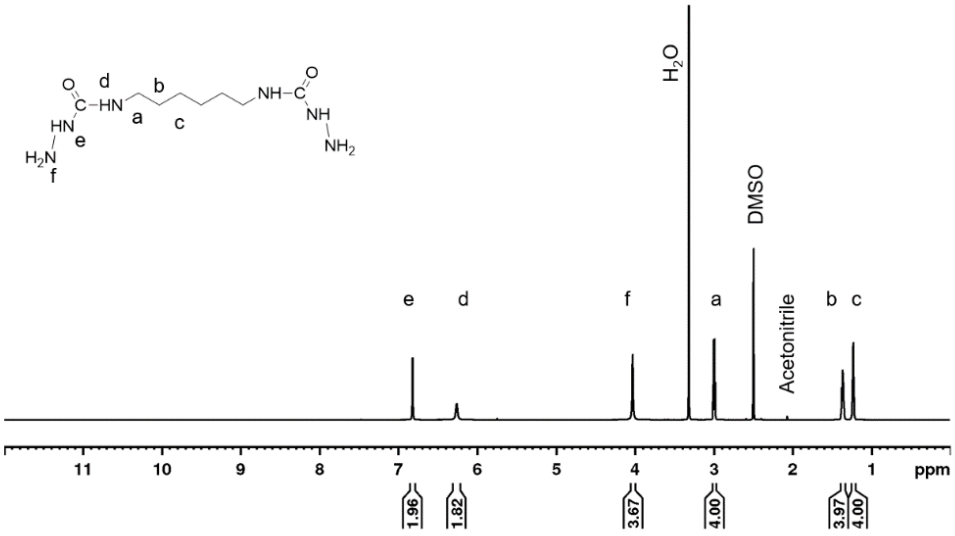

Figure S2. 1H NMR of hexamethylenedisemicarbazide in DMSO

Oxidized alginate qualitative quantification

Alginate with aldehyde groups was prepared by oxidation (5%, 10% and 15%) using NaIO4. Oxidation of alginate was confirmed by the presence of hemiacetal peaks in the NMR spectra and it was found that with an increase in the degree of oxidation, the hemiacetal peak intensity increased.

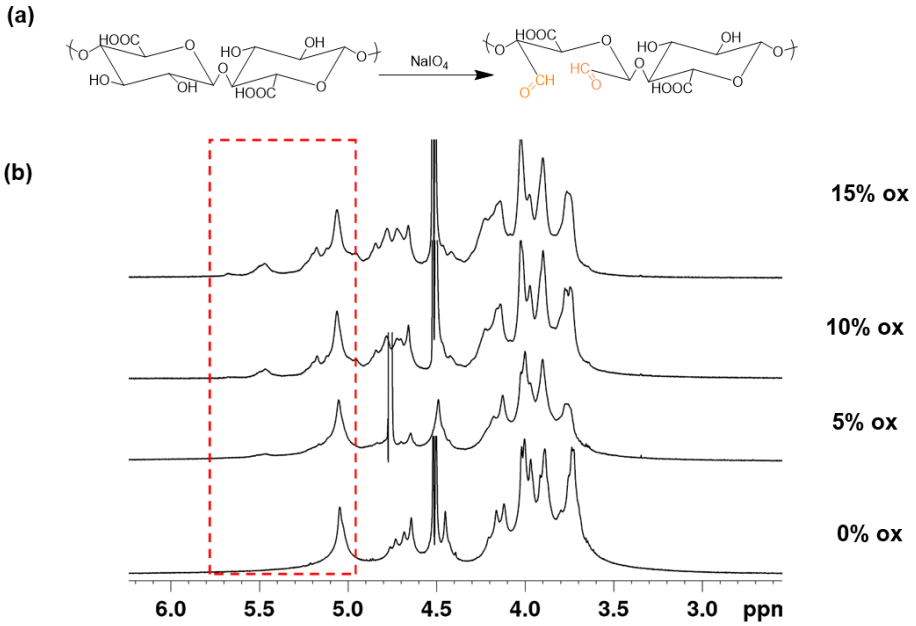

Figure S3. [1]H NMR of alginate with varying degrees of oxidation. a) 15%, b) 10%, c) 5%, and d) 0%. The appearance of protons between 5.15 - 5.75 ppm (highlighted in the red box) is attributed to the formation of hemiacetal groups upon reaction of aldehydes to neighboring hydroxyl groups. Spectra were measured at 325 K.

Small molecule model reactions

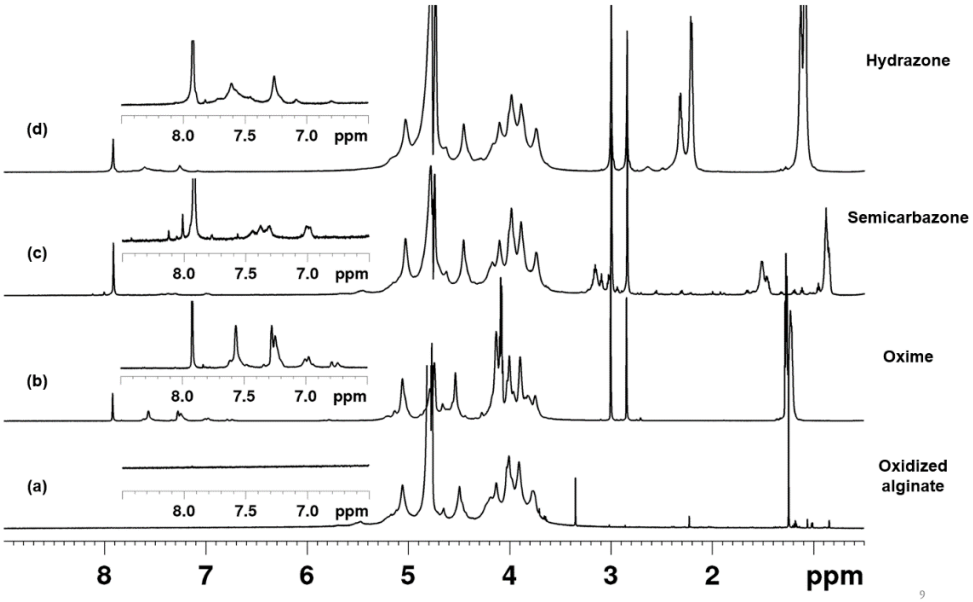

Figure S4. 1H NMR of a) 10% oxidized alginate, b) reaction solution of 10% oxidized alginate with O-ethylhydroxylamine hydrochloride, c) propyl semicarbazide and d) ethyl hydrazine in D2O. Protons attributed to the formation of oxime, semicarbazone and hydrazone appear between 6.50 - 8.50 ppm and are highlighted as zoomed in images.

Typical Viscoelastic curve for viscoelastic material

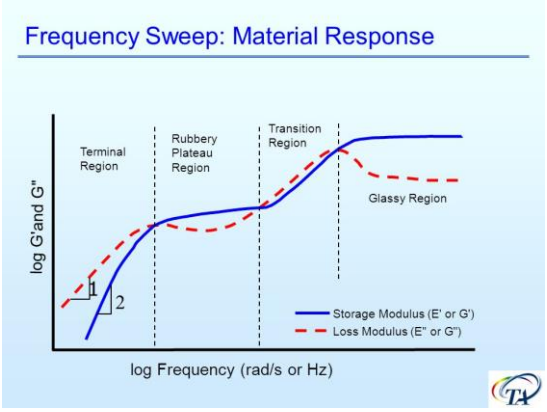

Figure S5. Typical viscoelastic material curve. Reprinted from with permission from TA instruments.

Strain sweeps

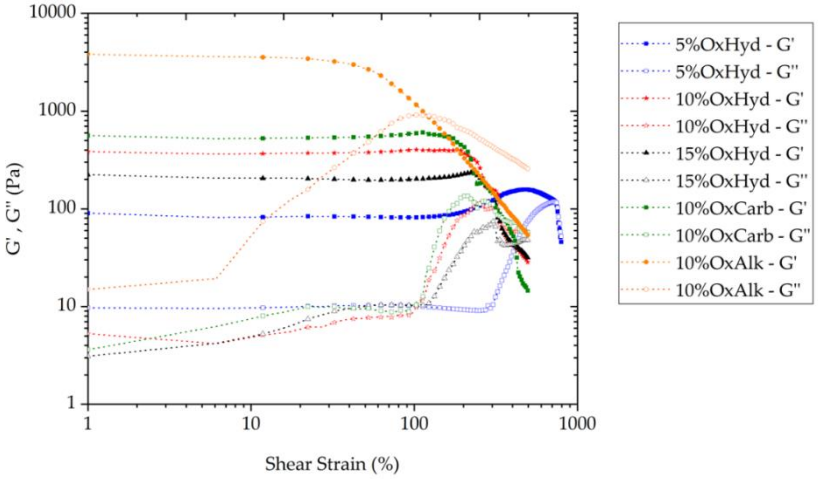

Figure S6. Strain sweeps were carried out to determine the linear viscoelastic region and the critical strain necessary for the onset of network rupture (tanδ = 1). The linear viscoelastic region was shown to be around 100% for most gels, with the exception of the oxime at 10% at 5% hydrazone at 300%. The critical strain for the onset of network rupture was determined to be around 400% with the exception of 10% oxime and 5% hydrazone showing 200% and 800% respectively. Based on these results, 600% strain was chosen for self-healing measurements to ensure network rupture, while 1% strain was chosen for frequency and time sweep measurement to remain within the linear viscoelastic region. While 600% strain does not ensure network rupture for the 5% hydrazone going beyond this point induces such large movements and sample deformation that the sample no longer remains between the parallel plates.

Effect of degree of oxidation

As it can be seen in the strain sweep in (figure S6 in SI), the 5% ox-alg network did not rupture completely at 600% strain. Therefore, 5% ox-alg did not follow the dynamics of 10% ox-alg and 15% ox-alg. Reliable measurements at a strain sufficient to rupture the 5% hydrazone network (>1200%) were not possible with our parallel plate geometry as the samples were displaced out from under the plates.

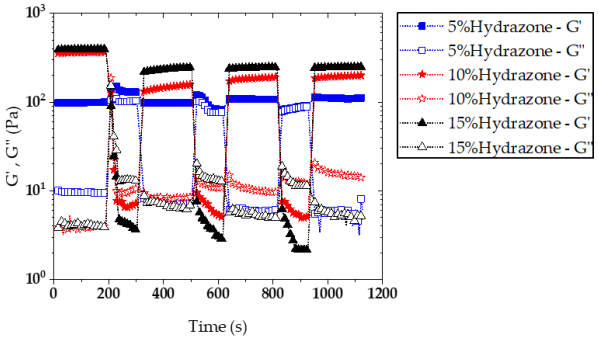

Figure S7. Effect of degree of oxidation on gel storage and loss modulus and self-healing behavior.

Self-healing

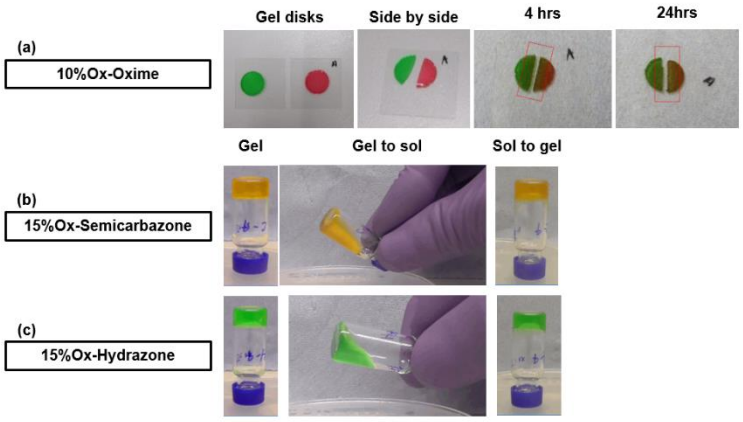

Figure S8. Macroscopic self-healing behavior of a) 10% ox alginate gel with oxime cross-links and 15% ox alginate gel with b) semicarbazone and c) hydrazone cross-links.

Cell viability

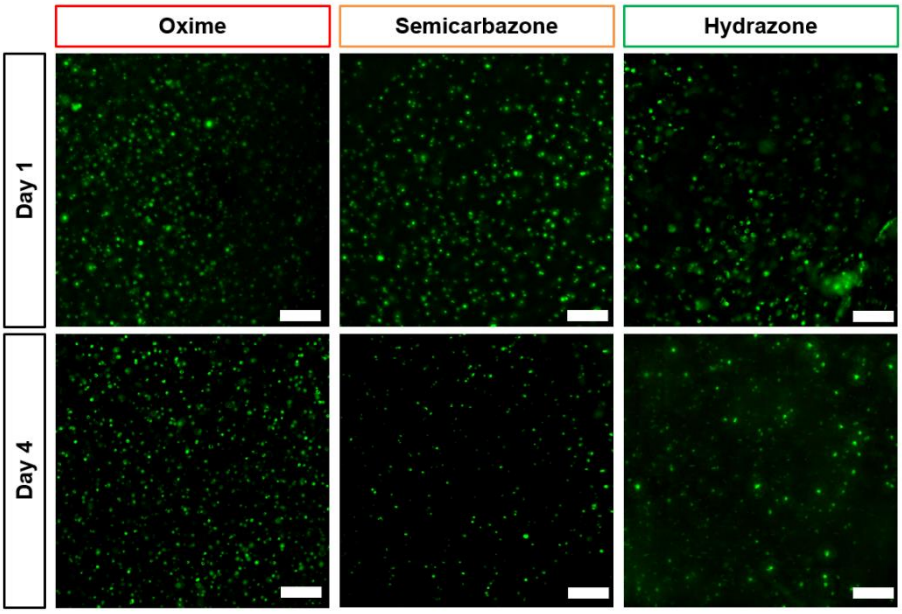

Figure S9. Live-dead staining images of chondrocytes, ATDC5, at 1 and 4 days. Scale bar: 200 μm

Cell spreading

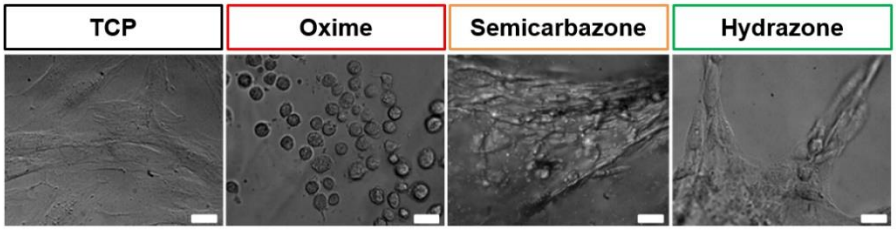

Figure S10. Cell spreading on tissue culture plastic and different imine type reversible cross-links. Scale bar: 25 μm

Injectability

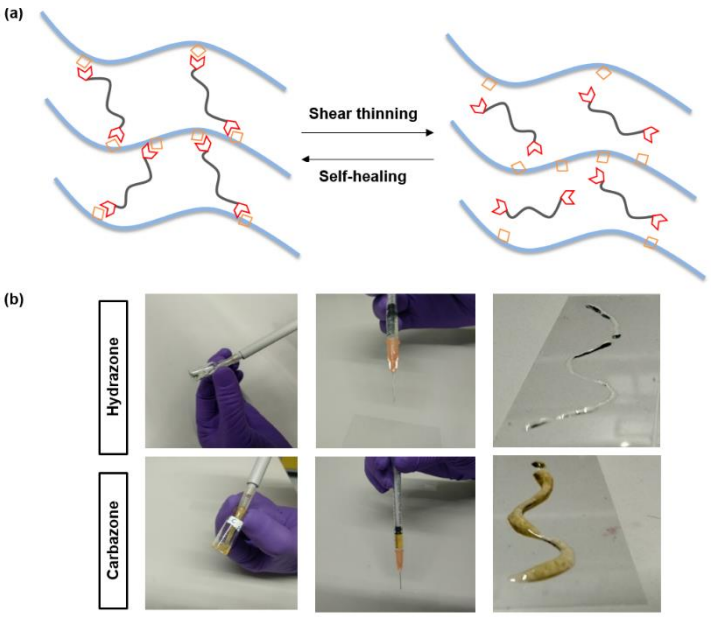

Figure S11. a) Schematics of injectability. b) 15% ox-alg gels were also injected using a 25G needle: both hydrazone and semicarbazone were found to be injectable, however semicarbazone did not produce a smooth fiber.

Printability

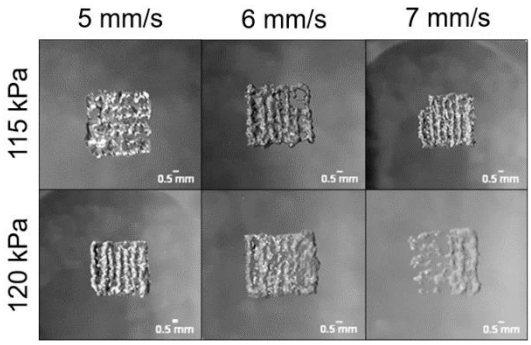

Figure S12. 2-layered scaffolds printed using 10% ox-alg (2% (w/v) alginate) with hydrazone cross-links printed at different speeds and pressures. A 0.25 mm (25G) conical needle was used.

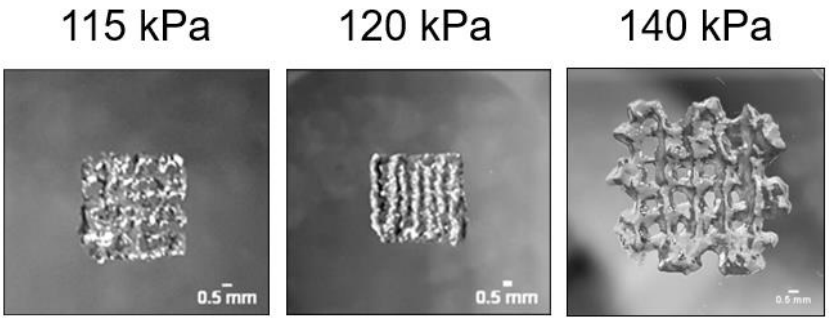

Figure S13. 2-layered scaffolds printed using 10% ox-alg (2% (w/v) alginate) with hydrazone cross-links printed at 5 mm/s using different pressure values. A 0.25 mm (25G) conical needle was used.

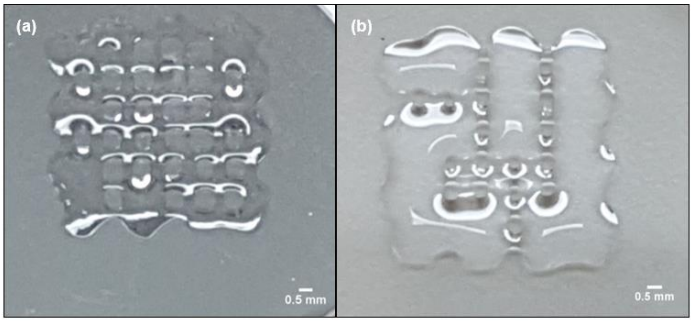

Figure S14. 10% ox-alg (1% (w/v) alginate) hydrazone cross-linked scaffolds of a) 2 layers and b) 4 layers printed at 45 kPa (30 mm/s). A 0.20 mm (27G) conical needle was used.

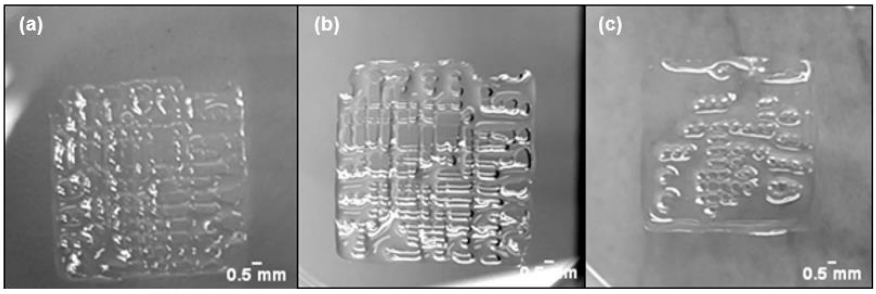

Figure S15. 2-layered scaffolds printed using 5% ox-alg (2% (w/v) alginate) with hydrazone cross-links at a) 45 kPa (10 mm/s), b) 50 kPa (10 mm/s), and c) 60 kPa (11 mm/s). A 0.20 mm (27G) conical needle was used.

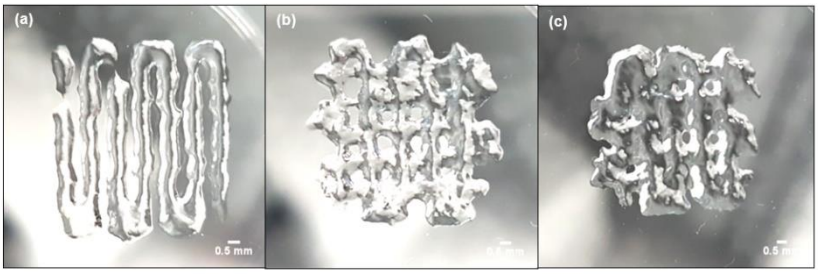

Figure S16. 10% ox-alg (2% (w/v) alginate) hydrazone cross-linked scaffolds of a) 1 layer, b) 2 layers, and c) 4 layers printed at 140 kPa (5 mm/s). A 0.25 mm (25G) conical needle was used.

References

(1) Sims, M. B.; Patel, K. Y.; Bhatta, M.; Mukherjee, S.; Sumerlin, B. S. Harnessing Imine Diversity to Tune Hyperbranched Polymer Degradation. Macromolecules 2018, 51 (2), 356–363.

Chapter V

Modular mixing of benzene-1,3,5-tricarboxamide supramolecular hydrogelators allows tunable biomimetic hydrogels for control of cell aggregation in 3D

Shahzad Hafeez [1], Fiona R. Passanha [2], Antonio J. Feliciano [1], Floor A.A. Ruiter [1,2], Afonso Malheiro [1], René P. M. Lafleur [3], Nicholas M. Matsumoto [3], Clemens van Blitterswijk [1], Lorenzo Moroni [1], Paul Wieringa [1], Vanessa L. S. LaPointe [2], Matthew B. Baker [1]

[1] Department of Complex Tissue Regeneration, MERLN Institute for Technology-Inspired Regenerative Medicine, Maastricht University, P.O. Box 616, 6200 MD Maastricht, The Netherlands;

[2] Department of Cell Biology–Inspired Tissue Engineering, MERLN Institute for Technology Inspired Regenerative Medicine, Maastricht University, P.O. Box 616, 6200 MD Maastricht, The Netherlands;

[3] Institute for Complex Molecular Systems, Eindhoven University of Technology, P.O. Box 513, 560 MB Eindhoven, The Netherlands.

This chapter was submitted to **Biomaterials Science** (2022) and the revised version with some edits was published.

Hafeez, S.; Passanha, F. R.; Feliciano, A. J.; Ruiter, F. A. A.; Malheiro, A.; Lafleur, R. P. M.; Matsumoto, N. M.; Van Blitterswijk, C.; Moroni, L.; Wieringa, P.; Lapointe, V. L. S.; Baker, M. B. Modular Mixing of Benzene-1,3,5-Tricarboxamide Supramolecular Hydrogelators Allows Tunable Biomimetic Hydrogels for Control of Cell Aggregation in 3D †. *Biomater. Sci.* **2022**. https://doi.org/10.1039/d2bm00312k.

This article also received a cover for Biomaterials Science Issue 17 2022.

Abstract:

Few synthetic hydrogels can mimic both the viscoelasticity and supramolecular fibrous structure found in the naturally occurring extracellular matrix (ECM). Furthermore, the ability to control the viscoelasticity of fibrous supramolecular hydrogel networks to influence cell culture remains a challenge. Here, we show that the modular mixing of supramolecular architectures with slow and fast exchanging dynamics can provide a suitable environment for multiple cell types, and influence cellular aggregation. We employed modular mixing of two synthetic benzene-1,3,5-tricarboxamide (BTA) architectures: a small molecule water-soluble BTA with slow exchange dynamics and telechelic polymeric BTA-PEG-BTA with fast exchange dynamics. Copolymerization of these two supramolecular architectures was observed, and all tested formulations formed stable hydrogels in water and cell culture media. We found that rational tuning of mechanical and viscoelastic properties is possible by mixing BTA with BTA-PEG-BTA. These hydrogels showed high viability for both chondrocyte (ATDC5) and human dermal fibroblasts (HDFs) encapsulation (>80%) and supported neuronal outgrowth (PC12 and dorsal root ganglion DRG). Furthermore, ATDC5s and human mesenchymal stem cells (hMSCs) were able to form spheroids within these viscoelastic hydrogels, with control over cell aggregation modulated by the dynamic properties of the material. Overall, this study shows that the modular mixing of supramolecular architectures enables tunable fibrous hydrogels, creating a biomimetic environment for cell encapsulation. These materials are suitable for the formation and culture of spheroids in 3D, critical for upscaling tissue engineering approaches towards cell densities relevant for physiological tissues.

Introduction

Unlike traditional synthetic elastic hydrogels employed for tissue regeneration, the extracellular matrix (ECM) is fibrous and possesses a range of stiffness and time-dependent viscoelastic properties.[1,2] Stiffness can be tuned in synthetic elastic hydrogels to mimic soft tissues and control cell behavior;[3,4,5,6] however, static and uniform cross-links with mesh-like structures do not mimic the dynamicity and fibrous morphology of the ECM. Fibrous proteins in the ECM such as collagen, elastin, fibronectin, and laminin self-assemble via physical interactions to form highly organized superstructures.[7,8] Furthermore, the ECM structure is highly dynamic, interacting with cells to control several functions such as growth, migration, proliferation, and differentiation[9], while undergoing continuous remodeling.[10] These physical interactions between proteins and remodelability are believed to be responsible for the dynamicity, viscoelasticity, and stress relaxation behavior of the native ECM.[2] Engineering both viscoelasticity and fibrous assembly in synthetic hydrogels remain a challenge.

Stress relaxation is a measure of viscoelasticity, which is the ability of the ECM to dissipate cell stresses by either reorganization of physical cross-links or remodeling by degradation. Stress relaxation has been shown to influence stem cell lineage and cell behavior. [1,2,11,12,13,2,14–18] Faster stress-relaxing hydrogels enhance cell spreading[11], and proliferation[18], and support the formation of actin stress fibers and focal adhesions.[16] By tuning stress relaxation, the differentiation of mesenchymal stem cells (MSCs) can be controlled towards either osteogenic[18] or adipogenic[19] lineages. Furthermore, therapeutic cells like primary chondrocytes produced more cartilage-like ECM in fast-relaxing hydrogels.[20] Myoblasts (C2C12) have also shown sensitivity to stress relaxation, spreading and forming robust actin in fast relaxing hydrogels.[14] Such stark differences are observed largely due to the viscous component (viscoelasticity) of these hydrogels, which is responsible for dissipating stresses in the materials when a cell pulls or pushes against the matrix. [1,21,22,23] While the effect of network dynamics on cell adhesion have been well documented[24], less is known about the effect these network dynamics can also have on cell aggregation.

On the molecular scale, the rate of stress relaxation in a hydrogel is inherently dictated by the dynamics of network cross-links.[1,25] An early example of tunable stress relaxation involved grafting polyethylene glycol (PEG) on alginate to affect the binding of Ca^{2+} cross-links.[18] More recent approaches use knowledge from small molecule studies including dynamic covalent chemistry and supramolecular chemistry.[1,26,27,28,29] These strategies offer a more rational way to tune the hydrogel using the equilibrium constant K_{eq}, the ratio of the rate constants of the on and off rates of binding. Exploiting dynamic covalent chemistry, stress relaxation has been tuned by utilizing differences in k_1 and k_{-1} of aliphatic (fast) versus aromatic (slow) aldehyde to form a hydrazone bond.[14] Other strategies include leveraging equilibrium kinetics of esterification of boronate esters[30], mixing two different phenylboronic acid derivatives with unique diol complexation rates[31], and employing either distinctly different imine-type dynamic cross-links (oxime versus hydrazone)[32] or modular mixing of dynamic cross-links (oxime and hydrazone).[33] Host–guest chemistry has also been applied to engineer stress relaxation by using guest

molecules with a range of affinity to host in both cucubiturils[34] and cyclodextrins.[35] Despite these advances, the control of viscoelasticity in fibrous hydrogels based on self-assembly remains elusive.[36,24]

Among hydrogels, one-dimensional (1D) synthetic supramolecular biomaterials stand out, thanks to their fibrous structure, dynamicity, and ability to create a biomimetic ECM.[37,38] Similar to the self-assembly of ECM proteins via physical interactions, building blocks in a supramolecular fiber self-assemble via non-covalent interactions such as hydrogen bonding, hydrophobic interactions, and $\pi-\pi$ stacking. Monomers in supramolecular fibers can be dynamic and can undergo exchange between fibers, which mimic the association and disassociation of physical cross-links between fibers in ECM proteins.[39,37] Supramolecular polymerization enables the creation of fibril structures with similar length scales found in native ECM proteins, tuning dynamics on the molecular scale, and building a structure-property relationship between molecular dynamics and bulk properties.[40,39,37] Molecular engineering of peptide amphiphiles[41], short peptides[42], ureido-pyrimidinone (UPy)[43], and BTAs[36,44,45] has been done to achieve fibrous structures and control the macroscale mechanical properties of hydrogels. Several recent reports have shown the ability of nanofibrillar hydrogels to support and facilitate cell aggregation[46,47]; however, the role of viscoelastic timescales (or network exchange) on the speed or amount of cell aggregation has not been investigated.

Owing to the high specificity and directionality of supramolecular interactions, modular mixing via mix-and-match of supramolecular monomers or copolymerization is a unique opportunity to create new materials on the benchtop without having to synthesize new molecules or polymers. This modular approach opens up possibilities to build generalizable platforms for the mix-and-match of supramolecular monomers for tuning material composition, mechanical properties, and bioactivity. Modular mixing has been used to create elastomeric scaffolds for tuning bioactivity in UPy polymer platforms,[48,49,50,24] and to carry different biological signals in peptide amphiphiles.[51] Recent progress has shown that modular mixing also offers the potential to tune the exchange dynamics in UPy[52] and BTA[36,45]-based supramolecular materials, which can be utilized to control hydrogel structure, dynamicity, and viscoelasticity. While both the UPy and peptide amphiphile architectures have a long history of use in hydrogel biomaterials, BTA systems have only been sparingly investigated.[53]

Here, we explore a simple and versatile supramolecular tuning strategy for cell culture applications. We build on the recently published work where BTA and BTA-PEG-BTA (a telechelic PEG functionalized with BTA on both ends) were mixed in different ratios to create 1D fibrous structures with competitive interactions.[36] By tuning the formulations at higher concentrations, we can achieve hydrogels with mechanical and viscoelastic properties in the physiological range for soft tissues. We investigated these BTA fibrous hydrogels for 3D cell culture with several different cell types. Since these BTA hydrogels are composed of non-covalent interactions, which are dynamic and can facilitate cell-cell contact and cell aggregation, we were able to employ hydrogels with different viscoelastic timescales to investigate the aggregation behavior of chondrocytes (ATDC5) and primary hMSC. To our best knowledge,

this is the first study that studies the effect of dynamic timescales on cell aggregation and spheroid formation in viscoelastic hydrogels. BTA viscoelastic hydrogels offer alternatives to typical 2D plastics and microwells for studying cell aggregation and spheroid formation, as they provide ECM mimicking 3D fibril structure with physiological stiffness ranges and controlled viscoelasticity.

Results and Discussion

Hydrogel Formation and vial inversion

In this study, we used two BTA architectures (**Figure 1A and 1B**): a small molecule BTA (slow exchange dynamics) and a telechelically functionalized PEG BTA-PEG-BTA (fast exchange dynamics). The BTA-PEG-BTA architecture was formed by connecting two BTA molecules with telechelic poly(ethylene glycol) (PEG) (PEG20K) using copper-catalyzed azide-alkyne click chemistry.[36] To start with, we investigated the ability of BTA and BTA-PEG-BTA to form hydrogels via a simple heat–cool approach. Both BTA and BTA-PEG-BTA formed hydrogels successfully at 10 wt% (**Figure 1C and 1D**). The BTA formed an optically opaque hydrogel, while the BTA-PEG-BTA formed an optically clear hydrogel. Hydrogel out of BTA-PEG-BTA can also be made by mixing BTA-PEG-BTA powder with water/DPBS/media and placing overnight at 37 °C. When subjected to a vial inversion test, we observed that the hydrogelators had markedly different behavior (**Figure S1**). After 24 hours, the BTA hydrogel stayed at the top of the vial while the BTA-PEG-BTA hydrogel flowed to the bottom of the glass vial demonstrating differences in viscoelastic properties. The flow behavior of BTA-PEG-BTA suggested greater viscoelasticity compared to BTA.

We then mixed the two hydrogelators in different ratios with a final concentration of 10 wt% (**Figure S1**). For this study, the different formulations of copolymerized hydrogels explored were 90:10, 75:25, 50:50, 25:75, and 10:90; this nomenclature indicates % of BTA:BTA-PEG-BTA. For example, 200 μL of a 100:0 hydrogel contains 20 mg of BTA and zero mg of BTA-PEG-BTA while a 75:25 hydrogel contains 15 mg of BTA and 5 mg of BTA-PEG-BTA. All tested formulations formed stable hydrogels in water and DMEM using a simple heating-cooling procedure. Transparency of the hydrogel increased with increasing % of BTA-PEG-BTA (**Figure SI**). During a cursory vial inversion test, only the 10:90 hydrogel flowed to the bottom of the vial after 24 hours and all other tested copolymerized hydrogels stayed at the top of the vial.

Storage Moduli

To investigate mechanical properties, we turned to oscillatory rheology. First, we investigated BTA and BTA-PEG-BTA with a frequency sweep at 1% strain and with a final concentration of 10 wt%. BTA (100:0, grey color **Figure 2a**) showed an equilibrium storage modulus around 300 Pa, which stayed constant over almost five decades of angular frequency. This could be attributed to the very long (several micrometers in length) and entangled fibers observed under

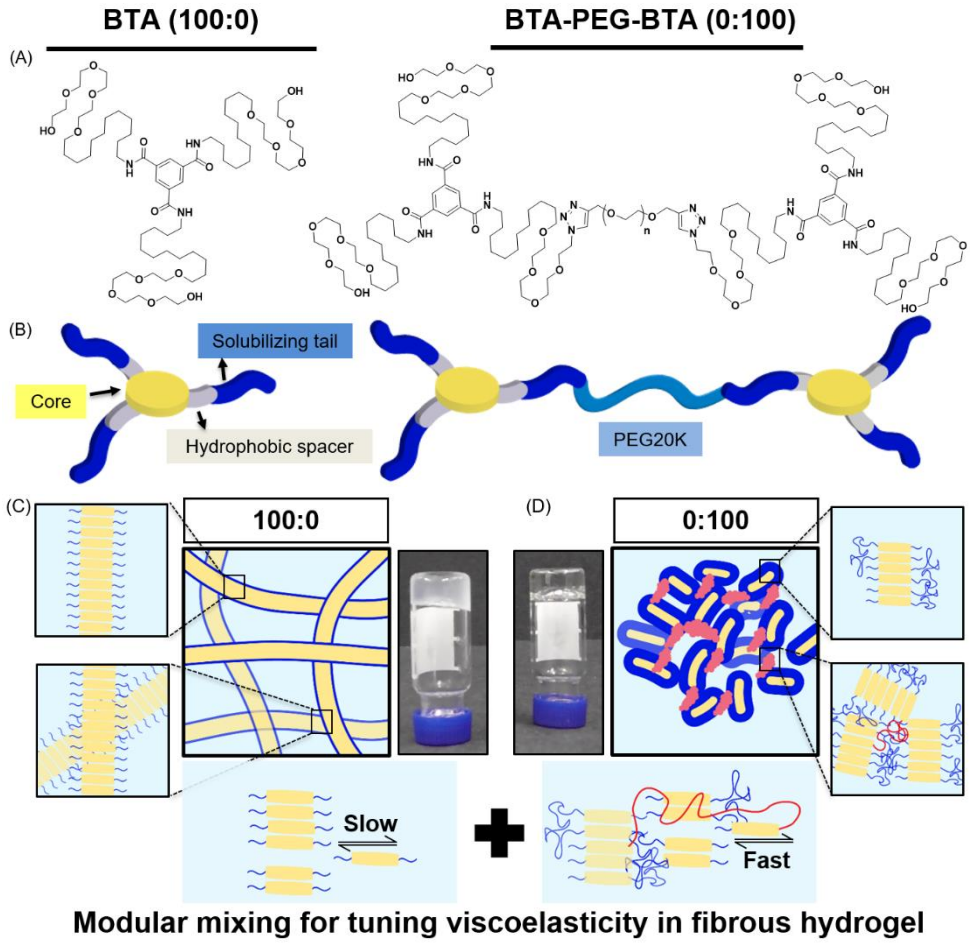

Figure 1. Chemical structures and schematic representation of BTA and BTA-PEG-BTA. A) BTA chemical structure has a benzene core covered with dodecyl hydrophobic spacer and tail of tetra-ethylene glycol units for solubilizing in water. BTA-PEG-BTA chemical structure where two BTA are connected with polyethylene glycol 20K (PEG20K) using copper-azide click chemistry. B) Schematic representations of the supramolecular networks of BTA (100:0) and BTA-PEG-BTA (0:100) hydrogelators; benzene core and hydrophobics are shown in yellow and gray, and blue represents tetra-ethylene glycol units. PEG20K is shown in light blue. C) A schematic representation of BTA units stacking over each other via 3-fold hydrogen bonding interactions, resulting in micron length long fibers. Inset images are zoomed in areas, top showing BTA stacks in single fiber and bottom demonstrates BTA fibers physical cross-links/entanglements between fibers. The image with black arrows shows slow rate of molecular exchange dynamics. D) A schematic representation of BTA-PEG-BTA forming micelles due to polyethylene glycol steric hindrance. BTAs are shown in yellow and PEG polymer in blue. Red represents bridges between micelles. Faster rate of molecular exchange dynamics is shown in image with black arrows for BTA-PEG-BTA.

cryogenic transmission electron microscopy (cryo-TEM)[44], which would result in persistent network formation. BTA-PEG-BTA (0:100, black color in **Figure 2A**) showed a plateau storage modulus of 9000 Pa. This 0:100 formulation displayed a classic viscoelastic response; decreasing storage modulus with decreasing angular frequency. The elastic plateau at a higher frequency is

believed to originate from the formation of elongated objects owing to the bridging of micelles by BTA-PEG-BTA molecules.[36]

To explore if BTA copolymerization would result in a library of hydrogels with different mechanical properties, we mixed BTA and BTA-PEG-BTA in different proportions and recorded a frequency sweep. BTA had a storage modulus of 300 Pa. When 10% BTA-PEG-BTA (90:10) was added, the storage modulus increased to ~20 kPa, indicating a surprising increase in stiffness with low amounts of the telechelic architecture. The storage moduli stayed constant upon increasing the BTA-PEG-BTA to 25% (75:25) and then decreased to 15 kPa, 9 kPa, and 6 kPa (**Figure 2B**) with increasing BTA-PEG-BTA (50:50, 25:75, and 10:90, respectively). Conveniently, these modularly mixed hydrogels have storage moduli in the range of soft tissue shear moduli such as cardiac muscle (5–50 kPa), kidney (4–8 kPa), spleen (15–20 kPa) and thyroid (1.3–1.9 kPa)[4], and can easily be tailored simply by mixing different proportions of the two components.

Non-linear dependence of storage moduli has also been observed by Vereroudakis et al[36] of BTA and BTA-PEG-BTA copolymerized binary hydrogels at low concentrations (5 wt%). Storage modulus gradually increases upon the addition of BTA-PEG-BTA to BTA and reaches a maximum of 10 kPa for 50:50 formulation. A decrease in supramolecular fiber length with increasing BTA-PEG-BTA % and the resulting changes in the connectivity of the network have been attributed to be responsible for the non-monotonic dependence of storage moduli on BTA formulation.[36]

Viscoelasticity

Previous work has shown that BTA forms largely elastic hydrogels, while BTA-PEG-BTA is viscoelastic[44]. We explored if this still holds at the higher concentration used for cell culture applications. The pure BTA largely showed frequency-independent storage and loss moduli, which is typical for a Hookean solid (see **Figure 2A**, grey color). BTA-PEG-BTA showed a complex viscoelastic behavior, with G" crossing G' at around 5 rad/s (see in **Figure 2A**, black color), which is a typical transition (rubbery plateau to terminal region, going from high to low frequency) for viscoelastic materials (**Figure S2**). These results were in agreement with previously reported studies[44] and with our visual observations during the vial inversion test.

All modularly mixed hydrogel formulations showed characteristic viscoelastic behavior as shown in **Figure S3A**. In general, we observed a shift towards more of a viscoelastic character with higher weight fractions of BTA-PEG-BTA. The formulation 90:10 showed that G', and G" remained largely independent of frequency (**Figure S3A**). The formulation 75:25 also did not show a crossover point between G' and G" within the experimental window; however, the decreasing G' as we moved to a lower frequency forecasts a convergence (**shown in Figure S3A**). This effect was more pronounced when we increased BTA-PEG-BTA to 50% (50:50) which showed the convergence point G" and G' around $\omega = 0.1$ rad/s, which is roughly 2 decades lower on the frequency axis when compared to 0:100 crossover point. Interestingly, the 25:75 hydrogel did not show any convergence or crossover point even though it has 25% more

BTA-PEG-BTA compared to the 50:50 formulation. Upon increasing BTA-PEG-BTA to 90% (10:90), the crossover point reached 3 rad/s which is close to the 0:100 formulation (5 rad/s). The shifting of crossover points to a higher frequency by adding BTA-PEG-BTA indicated that modular mixing of supramolecular BTA units allowed tuning of viscoelasticity across a relatively broad range.

Tanδ, the ratio of G"/G', provides information on viscous behavior or stress dissipation characteristic of a material. We investigated Tanδ of the different formulations as shown in **Figure 2C**. Tanδ is highest for 0:100 (BTA-PEG-BTA) across all investigated frequencies, which indicates that it has the highest viscous component in all formulations. In general, adding BTA in BTA-PEG-BTA led to a decrease in Tanδ indicating more elastic properties added to the mixture. For example, at 0.1 rad/s, 0:100 had Tanδ of 10, which decreased to 1 and 0.1 for 50:50 (50% BTA) and 90:10 (90% BTA). Interestingly, 90:10 had lower Tanδ than 100:0 (at all angular frequencies), indicating that 90:10 has more viscoelastic solid characteristics and less stress dissipation capacity compared to 100:0. Another exception to the general trend of adding BTA and decreasing Tanδ was 25:75 (75% BTA-PEG-BTA) which showed a Tanδ value lower than 50:50. Important to note, differences in the Tanδ value increased as we gradually moved to lower frequencies (from 10^2 to 10^{-2} rad/s), indicating that the hydrogels behave very different at low frequencies, which points to different exchange dynamics in BTA formulations.

Next, we investigated the stress relaxation behavior of the hydrogels for an in-depth analysis of stress relaxation modes within the hydrogels. BTA-PEG-BTA (0:100) relaxed fully under just one second, while BTA (100:0) barely relaxed to 60% after 10,000 seconds (**Figure 2D**). We found that stress relaxation time scales can be fine-tuned by mixing BTA with BTA-PEG-BTA in different ratios. While average stress relaxation times are often calculated using the Maxwell model (equation **1**), this model only contains a single characteristic relaxation mode in which a Hookean spring and a Newtonian dashpot are connected in series

$$G(t) = G_0 e^{-t/\tau_0} \qquad (1)$$

Where G(t) is the storage modulus, G_0 is the equilibrium storage modulus, and τ is the relaxation time. After the initial fitting, we realized that our supramolecular systems exhibited more complex relaxation behavior. Therefore, we use the Maxwell-Weichert model for viscoelastic fluids (equation **2**), which consists of spring-dashpot Maxwell elements in parallel. Total stress in the system would be the sum of stress in each of Maxwell's spring-dashpot elements.

$$G(t) = \sum_i G_i e^{-t/\tau_i} \qquad (2)$$

Using this approach, the average stress relaxation time can be obtained by summation of stress in each Maxwell-dashpot element over the time interval of the stress relaxation test.

$$< \tau > = \sum_i C_i \tau_i \qquad (3)$$

Using equation **3** for two Maxwell elements in parallel, the average stress relaxation time $<\tau>$ was calculated as shown in **Table 1** and **Table S1** . Increasing BTA-PEG-BTA percentages led to decreases in stress relaxation time and via modular mixing of BTA and BTA-PEG-BTA stress relaxation times can be tuned from under a few seconds to several thousand seconds. Average relaxation times ranged from several thousand to a few seconds and half relaxation times are between several hundred to a few seconds, as shown in **Table 1**. Many BTA formulations have stress relaxation half times between 0.1–100 seconds which are in a similar range of soft tissue such as brain, breast tumor, coagulated marrow, fracture hematoma, liver, and muscle[2]. In addition, our hydrogel's stress relaxation half times (below 100 seconds) are in the range of stress-relaxing hydrogels promoting osteogenic differentiation[18] and producing cartilage-like matrix formation.[20]

A general trend was observed, where increasing BTA-PEG-BTA resulted in faster-relaxing hydrogels (**Figure 2D**). This is likely due to the presence of telechelic PEG20K in BTA-PEG-BTA, which could result in less stable BTA aggregates and faster exchange dynamics. In previous studies, hydrogen/deuterium exchange (HDX) mass spectrometry (MS) experiments showed that mixing BTA-PEG-BTA with BTA weakens the association strength between BTA molecules within the assembly leading to less stable aggregates and faster exchange dynamics.[36] In a similar study with a UPy supramolecular polymer, bivalent UPy (UPy molecules connected with telechelic PEG20K) accelerated the exchange dynamics when mixed with small-molecule UPy.[52] These studies support that faster exchange dynamics in the presence of telechelic PEG are mainly responsible for the fast relaxation behavior of BTA-PEG-BTA and that different exchange dynamics, in combination with the differences in hydrogel morphology[36], are a likely source of the different relaxation behavior in these multi-component supramolecular systems.

Self-healing:

Initially, self-healing was visualized in the lab by placing two pieces of hydrogel, colored with red and green food coloring dye, side by side and compressing them. The hydrogels with ≥ 75% of BTA-PEG-BTA self-healed after 24 hours, yet the 90:10 and 100:0 formulations did not (**Figure S5**). Next, self-healing behavior was quantitatively investigated using cone-plate configuration. Initially, a strain amplitude sweep was conducted to find the critical strain needed to break the hydrogel structure. BTA (100:0) showed strain at break around 100%. Strain at break sharply decreased to ~ 2% for 90:10 (10% BTA-PEG-BTA), increased to ~ 20% for 75:25 (25% BTA-PEG-BTA), and then stayed almost constant for 50:50 and 25:75. When % of BTA-PEG-BTA increased to 90%, strain at break declined to 10% for 10:90 and ~2% for pure BTA-PEG-BTA (0:100). The data showed that modular mixing of BTA architectures allows tuning strain at break.

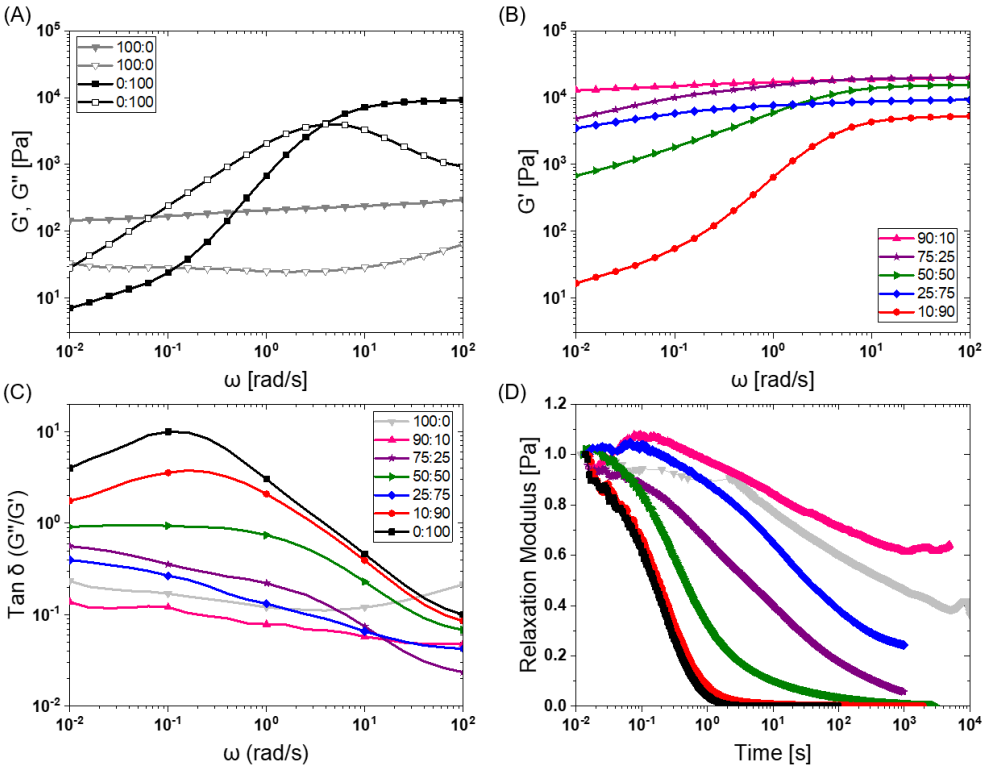

Figure 2. BTA modular mixing allows tuning viscoelastic properties of hydrogels: A) BTA (100:0, in grey) and BTA-PEG-BTA (0:100 in black) storage moduli (filled symbol) and loss moduli (empty symbol) as a function of frequency. B) Tuning of storage moduli by copolymerization of BTA and BTA-PEG-BTA. C) Tanδ (G"/G') as a function of frequency of copolymerized hydrogels. D) Stress relaxation profiles of hydrogels when subjected to constant 1% strain. Duplicates were performed for all hydrogel formulations in A, B, and C. Similar trends in viscoelasticity were found and the tanδ (G"/G') values for all runs are reported in supplementary Fig S3E. Duplicates were performed for 25:75 (BTA:BTA-PEG-BTA) in D in order to confirm the outlier and reported in Fig S4C.

We then investigated self-healing via step strain shear rupture cycles (1% to 400% strain) at a constant frequency (ω = 10 rad/s) for investigating the self-healing behavior of the hydrogels (**Figure S5**). Hydrogel rupture was observed upon applying high strain (G'>G") and quickly recovered to original values during the low strain cycle. Interestingly, 100:0 and 90:10 also showed full self-healing capacity, which we did not observe in the visual macroscopic self-healing test. This shows that shear rheology and visual self-healing test can result in contradicting results and macroscopic visual self-healing tests should be conducted for investigating macroscopic self-healing capacity. Self-healing behavior within BTA-based hydrogels can be associated with reversible and dynamic supramolecular interactions.

Table 1: Average stress relaxation times for BTA formulations.

Sample	***100:0***	***90:10***	***75:25***	***50:50***	***25:75***	***10:90***	***0:100***
τ average (seconds)	11,000	18,555	64	5	417	0.4	0.3
$\tau_{1/2}$ (seconds)	524	*N/A	4	0.4	33	0.2	0.1

*did not reach half value even after 10,000 seconds

Cell studies

BTA based Hydrogels are cytocompatible and allow cell growth

Next, we moved to determine the biological compatibility of these materials. BTAs have been used in the presence of cells before in low concentrations[53], but their cytocompatibility as hydrogels is not well explored. To investigate cytotoxicity, preliminary studies were carried out using fibroblasts with pure BTA-PEG-BTA. Fibroblasts were seeded on top (2D) and encapsulated within hydrogels (3D) utilizing the self-healing of the hydrogel. BTA-PEG-BTA hydrogel was broken into small pieces and mixed with cells. The number of dead cells determined via a live/dead assay was below 10% for both 2D and 3D conditions, indicating low cytotoxicity of the material (**Figure 3A** and **Figure S6**). This experiment also showed that the self-healing of the hydrogels can be used to encapsulate cells and 3D encapsulation did not have a negative influence on cell viability.

In initial trials, we observed aggregation of fibroblasts (**Figure S6C and video 1**) within BTA-PEG-BTA hydrogels likely due to fast exchange supramolecular dynamics. Aggregation is beneficial for many cells and multicellular aggregates en route to tissue formation; however, aggregation is usually prevented by covalently cross-linked hydrogels due to their static mesh network. For example, the aggregation of chondrocytes is desired to produce cartilage-like ECM for the creation of cartilage tissue. Correspondingly, we were interested to see if these different hydrogels could control the cell aggregation of chondrocytes in a 3D culture. First, we compared the viability of chondrocytes (ATDC5) in alginate, a standard tissue engineering hydrogel[54,55,18], to our BTA-PEG-BTA hydrogels (**Figure S7**). We determined live/dead cell area since accurate single-cell counting was misleading owing to cell aggregation. Chondrocytes cultured in both the BTA-PEG-BTA, and the alginate showed similar live/dead results; the total area for live cells was ~3x times greater than dead cells, suggesting low (15–20%) cytotoxicity (**Figure S7B**). Cytotoxicity was also monitored using an LDH assay and both BTA-PEG-BTA and alginate showed lower (8×) LDH release compared to a cell pellet negative control, suggesting again greater than 80% viability (**Figure S7C**).

Next, in order to investigate cell viability for the complete BTA series, we attempted cell encapsulation using a chemically dissolved freeze-drying method. The self-healing method for cell encapsulation was not the best choice since 100:0 and 90:10 showed poor cell encapsulation due to the non-self-healing ability of hydrogel macroscopically (**Figure S5A**). We chemically

dissolved solid polymer in dichloromethane and methanol, dried in a vacuum oven, and DPBS was added to make hydrogel. Hydrogels were frozen and freeze-dried. BTA hydrogels have a porous structure after freeze-drying. The cell suspension was added on top of the freeze-dried BTA hydrogels and incubated for ~1 hour at 37 ºC for hydrogel formation. Though we were able to encapsulate cells within freeze-dried hydrogels, not all formulations made stable hydrogels, especially those which have a larger percentage of BTA. This might be due to the fact that BTA requires heating for dissolving in water/media for self-assembly. Also, 100:0 formed a foamy lightweight structure, which was soft and most of the cells sedimented at the bottom resulting in poor cell encapsulation. This procedure of cell encapsulation was not robust and needed 4–5 days of hydrogel preparation before cell encapsulation and involved toxic agents such as dichloromethane and methanol for molecularly dissolving BTA molecules before vacuum and freeze-drying.

Using the chemically dissolved freeze-drying method, we observed greater than 80% viability (% of live cell area) in all the formulations besides 100:0 and 90:10, which showed around 40% dead cells (by cell area) relative to other formulations (**Figure S8A** and **S8B**). We hypothesized that 100:0 could retain methanol because of BTA hydrogen bonding interactions with methanol, which likely compromised the cell membrane. In a control experiment, we prepared the 100:0 hydrogel in cell culture media and encapsulated ATDC5s using the self-healing method. While this formulation did not self-heal rapidly enough for efficient cell encapsulations, live/dead staining showed almost no dead cells for both cells in the hydrogel and on the tissue culture plastic (**Figure S8C–D)**. This indicated that the hydrogel, itself, was not toxic, but likely toxicity came from residual solvent or one of the processing steps during the freeze-drying method.

Lastly, we also explored the quicker heating method for cell encapsulation for 90:10 and 0:100 BTA formulations, where we heated BTA hydrogels until they turned into liquid so that the hydrogel was pipetteable to mix with the cell suspension; however, high temperatures (minimum 60 ºC) were required (**Figure S9**), transferring the hydrogel from a glass vial to a cell culture well plate, gelation in the pipette tip, and rapid gelation (<30 s) upon mixing cell suspension prevented effective cell encapsulation. Compared to the self-healing method, relatively more dead cells were seen (**Figure S10**) and no advantages were found.

We found the self-healing method to be more reliable, applicable, and reproducible compared to the other cell encapsulation methods we tested since the hydrogel could be broken into small pieces and mixed with the cell suspension. Formulations that could not effectively self-heal and encapsulate cells were left out and not studied further. We then investigate the cytotoxicity of different formulations within our small library of BTA-PEG-BTA and BTA hydrogels. Chondrocytes were encapsulated within the different hydrogels for 7 days and a live/dead assay was performed. All hydrogels showed greater than 80% of live cell area, indicating high cell viability within modularly mixed BTA hydrogels (**Figure 3D and 3E** and **Figure S11**).

Next, we set out to investigate neurite outgrowth in BTA-based hydrogel using the PC12 cell line. Neuronal cells require dynamic and cell remodelable microenvironment[56,57]. We encapsulated PC12 as dissociated cells in most dynamic BTA-PEG-BTA hydrogel and observed that the PC12 cells aggregated in the first 48 hours and then showed neurite outgrowth in dynamic BTA-PEG-BTA hydrogel over 4 days (**Figure S12**). Then we mixed a small amount of either laminin or fibrinogen and PC12 cells exhibited more neurite projections; from a few in BTA-PEG-BTA to tens of neurites per cell aggregate in BTA-PEG-BTA hydrogel with either laminin or fibrinogen (**Figure S12**). Next, dorsal root ganglia (DRGs) were embedded within

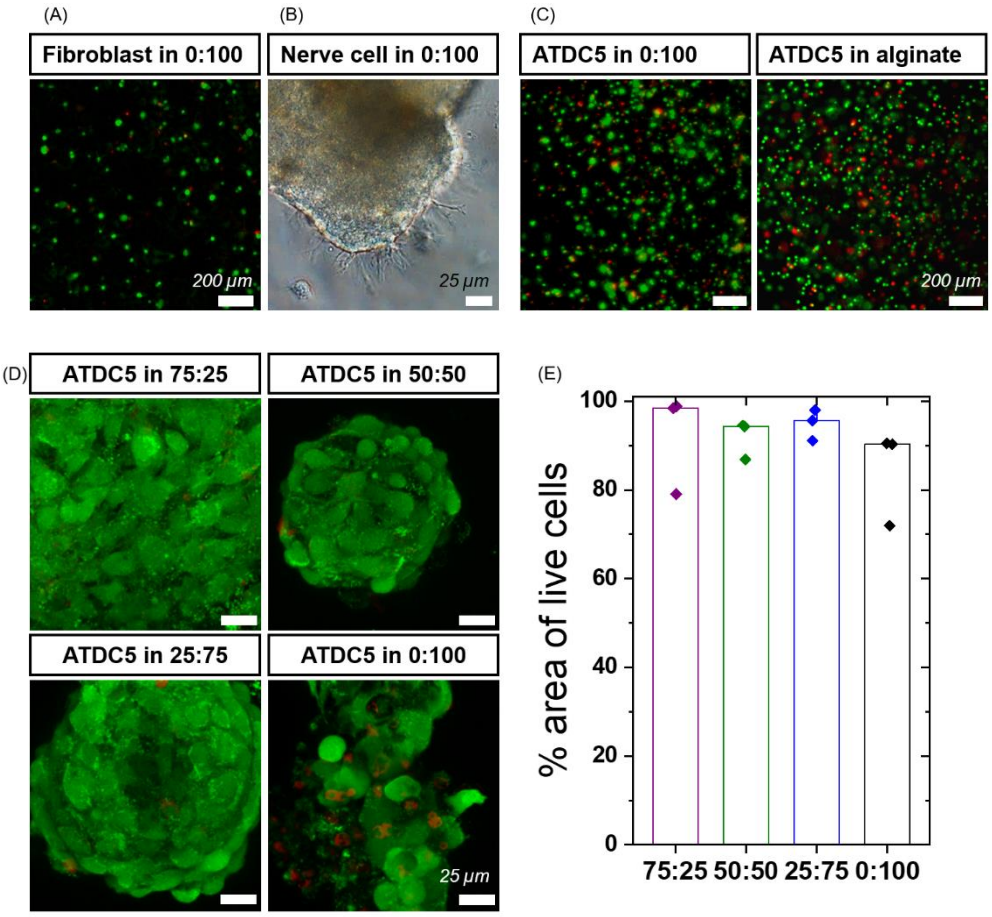

Figure 3. High cell viability in BTA formulations: A) fibroblasts showed high cell viability using a live/dead assay after 24 hours. Green represents live cells and red represents dead cells. B) Dorsal root ganglion (DRG) cells showed outgrowth in BTA-PEG-BTA (0:100) hydrogels after 48 hours. C) ATDC5 chondrocytes were around 80% viable (green) using a live/dead assay and the cell viability was comparable to alginate gels cross-linked using calcium ions. D) ATDC chondrocyte viability in BTA formulations after 7 days. Green represents live cells and red represents dead cells. E) % area of live cells calculated using the analyze particle function in Image J software for BTA formulations; the cell area for three images (top, middle, and bottom of an aggregate) was calculated. A minimum of two biological replicates were used for each experiment.

our hydrogel system and they exhibited branching neurite outgrowth when cultured in pure BTA-PEG-BTA hydrogels in just two days (**Figure 3B** and **Figure S12**). This shows that PC12 and DRGs can stay healthy and grow neurite projections in dynamic BTA-PEG-BTA hydrogels. To further understand the role of materials dynamics, exploration of the complete BTA series with neurons could be of interest to study neurite outgrowth or neuron sphere formation within BTA hydrogels utilizing aggregation properties of BTA hydrogels.

BTA dynamic and stress-relaxing hydrogels facilitate cell-dependent aggregation (ATDC5 versus hMSCs)

In the cell viability experiments, we observed that cells tended to form aggregates within the hydrogels, presumably due to the remodelability of the hydrogels. In a preliminary experiment, we observed that the material composition appeared to influence cell aggregation behavior (**Figure S13**). Slower aggregation and smaller aggregates of ATDC5 were observed in formulations with higher amounts of BTA (slow stress relaxation) compared to faster aggregation and larger aggregates with higher amounts of BTA-PEG-BTA (faster stress relaxation). While all formulations supported ATDC5 cell aggregation, we saw the best aggregation and encapsulation performance (based on the self-healing method) in the compositions from 75:25 to 0:100 and moved forward to characterize aggregate behavior in these hydrogels in more detail (**Figure 4**).

While several previous studies have shown spheroid culture[24,58], formation of spheroids in supramolecular nanofibrillar hydrogels[46,47], and pre-made spheroid fusion in the supramolecular hydrogel with viscous component[59,60], hydrogel viscoelasticity influence remains unknown on cell aggregation/spheroid formation in the 3D hydrogel. We further hypothesized that changes in the viscoelasticity/stress relaxation of the matrix could lead to control over cell aggregation – more simply, is this phenomenon a viscoelastic timescale-dependent phenomenon? We chose 75:25, 50:50, 25:75, and 0:100 for studying cell aggregation and compactness of aggregates formed when ATDC5 were encapsulated within the hydrogel (**Figure 4B**). An agarose microwell mold was used as a positive control for aggregation, which is a 2.5D cell aggregation model on a well plate, where the cells are confined by agarose, but the 3D environment is simply cell media. These agarose microwells allow for free self-assembly of cells and is the current standard for forming cell aggregates, but is limited to 2D culture platforms.[61]

Cells started to aggregate in BTA hydrogels after 6 hours and formed larger and more compact aggregates in 0:100 compared to other BTA formulations. The ATDC5 did not form uniform aggregates in the BTA hydrogels over 24 hours, yet aggregates in the 0:100 formulation were more compact, with cells aggregating more densely when compared to other BTA formulations. In other BTA formulations, single-cell boundaries could still be identified in the cell aggregates, indicative of less compactness.[62] Compared to BTA formulations, ATDC5 aggregates were more round and compact in agarose microwells after 24 hours, likely due to free assembly and the presence of only cell-growth media around the cells.

Having established the ability of these dynamic formulations to allow chondrocytes aggregation, we wanted to explore this phenomenon with hMSCs (**Figure 4C**), which have clinical potential in multiple applications. Studying the self-assembly of primary hMSCs for aggregation and spheroid formation has been linked to cadherin expression and the osteogenic, adipogenic, and chondrogenic phenotypes. [63,64] We were interested to investigate if MSCs aggregate within these hydrogels and the effect of BTA formulations on cell aggregation and compactness. MSCs started to aggregate after 6 hours; however, aggregation was slower in BTA hydrogels compared to the free self-assembly of MSCs in agarose mold control. With time, cell aggregates in the BTA hydrogels became more compact and changed their shape from elliptical to spherical after 24 hours (**Figure 4C**). MSCs formed more compact and spherical aggregates in the 0:100 hydrogel compared to the other BTA formulations in 24 hours likely due to faster supramolecular dynamics, which supported rapid MSC aggregation. In addition, a clear trend could be seen in that aggregates were more compact and roundly shaped as the percentage of BTA-PEG-BTA increased (after 24 hours). Overall, the images revealed that the dynamicity and viscoelastic/stress relaxation properties of the BTA hydrogels support cell aggregation without the presence of proteolytically degradable cross-linkers.

We hypothesized that cell aggregation can be controlled by the dynamic properties of the hydrogel (viscoelasticity/stress relaxation) and the main driving force is the exchange dynamics of the BTA molecule. However, differences in nutrient availability within the series could also influence cell aggregation. To determine if nutrient diffusion is similar across all BTA formulations, FRAP measurements were performed using fluorescently labeled dextran of 3–5 and 70 kDa. Dextran of 3–5 kDa showed a two-fold higher diffusion coefficient compared to 70 kDa likely due to differences in the hydrodynamic radii. Interestingly, no significant difference in the diffusion coefficient was observed for each molecular weight dextran (20 $\mu m^2/s$ for 3–5 kDa and around 10 $\mu m^2/s$ for 70 kDa) when comparing all BTA formulations (**Figure S14**). FRAP data indicated that, even though the diffusion coefficient is different for different sizes of dextran, diffusion of macromolecules stays constant across the BTA series. This FRAP data supports that the differences in cellular self-assembly are not likely due to differences in nutrient diffusion.

We next explored if pre-formed spheroids would fuse within the hydrogels. We continued the hMSC culture and observed the fusion of aggregates at 48 hours in all BTA formulations except 0:100 (**Figure 5A**). Fusion behavior in BTA hydrogels could be attributed to reversible supramolecular interactions and viscoelasticity of the hydrogels. Observed stable aggregate formation and MSC spheroids fusion after 48 hours is indicative of healthy and viable cells.

Overall, we have observed that hydrogel dynamicity supported ATDC5 and MSC cell aggregation without any presence of degradable cross-linkers. MSC aggregates formed well-defined spheroids compared to less defined aggregates for ATDC5 in 24 hours, which indicates cell-dependent aggregation behavior facilitated by supramolecular dynamics in stress-relaxing BTA hydrogels.

Considering the increasing need for platforms for developing 3D building blocks for tissue engineering and animal alternatives scaleable drug testing models, these dynamic and viscoelastic BTA hydrogels can be promising candidates since current technologies are limited to 2D culture. For example, by removing dimensional constraints (e.g., 2D or 2.5D), such dynamic hydrogels offer new flexibility in the scaling and size of aggregated cells and tissues which would be more physiologically relevant when compared to current 2D models. In addition, the tunable mechanical properties and controlled fibrous structures make these BTA hydrogels ideal as a biomimetic environment. In short, our results suggest that these BTA hydrogels, and potentially other dynamic hydrogels, can provide a scalable platform where cells in physiologically relevant cell densities, mechanical properties, and architectures can reorganize, assemble into desired morphologies, and develop into complex tissues.

BTA dynamic and stress-relaxing hydrogel supported hMSC spheroid fusion and affected hMSC proliferation and aggregate size and morphology

After illustrating spheroid fusion, we subsequently investigated hMSC proliferation capacity within the different BTA formulations. Previous studies have shown that proliferation rates are different in 2D and 3D, and many cell lines show reduced proliferation in 3D spheroid cultures[62] and hydrogels (synthetic and natural)[65,66,67] compared to 2D monolayer cultures. The type of matrix[66] and stress relaxation[18] also have been shown to influence proliferation rates for cells. We hypothesized that mechanical confinement would reduce proliferation as compared to 2D agarose mold (allowing free 3D self-assembly of hMSC) and the different exchange dynamics of BTA hydrogels could influence cell proliferation. To assess the influence of BTA formulations on the proliferation of cells, EdU was added in cell culture media. EdU is incorporated into newly synthesized DNA by cells and therefore can be correlated to cell proliferation. Given that the doubling time of hMSCs on tissue culture plastic was approximately 48 hours, we used a 48-hour EdU incubation to detect proliferating cells.

Free self-assembled spheroids in agarose mold showed more proliferating cells compared to BTA formulations suggesting that physical confinement in BTA hydrogels reduced proliferation (**Figure 5B and 5C**). Agarose showed a mean value for EdU-positive MSCs at around 12%. All tested BTA formulations showed proliferating cells (EdU positive) and the mean value for EdU-positive MSCs varied from 0.5 to 10%. The lowest number of proliferating cells was found in the 0:100 formulation and the highest in the 50:50, when compared to all other BTA formulations. A decrease in proliferating cells in 0:100 could also be attributed to the clumping of hMSCs. These results show that 3D confinement still allowed for significant cell proliferation, yet reduced proliferation compared to free self-assembly of cells when cultured in suspension (in agarose mold).

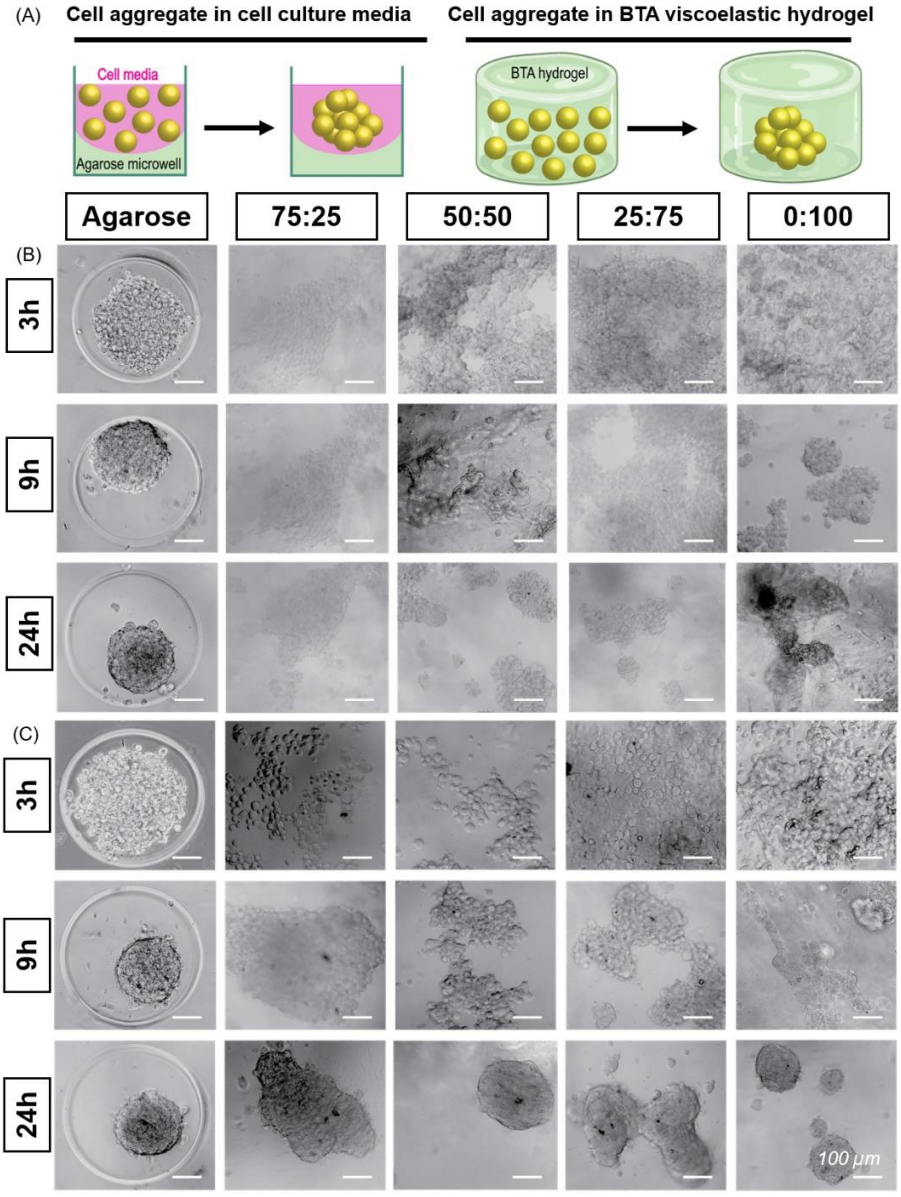

Figure 4. Self-assembly and aggregation of ATDC5 and hMSC within BTA hydrogels: A) Cell aggregate formation in cell media in agarose microwell versus cell aggregate formation in BTA viscoelastic hydrogels. B) ATDC5 form round and compact aggregate in agarose mold (positive control). ATDC5 chondrocytes tends to aggregate in all BTA formulations; however, cell aggregate are not as compact as compared to agarose mold. Among BTA formulations, 0:100 showed more compact aggregates, scale bar 100 µm, n = 2 biological replicates. C) Self-assembly and aggregation of hMSCs within BTA gels. Cell aggregates size decrease in agarose mold (positive control) showing that aggregate is getting more compact over time. All BTA formulations showed cell aggregation and spheroids formation. However, it can be seen that cells form smaller aggregates and that there is more spheroid fusion with increasing % of BTA-PG-BTA, scale bar 100 µm. n = 3 biological replicates.

We further determined shape descriptors such as spheroid size (largest length), area, and morphology of MSC spheroids in BTA hydrogels after 48 hours. Quantification revealed that the longest length of an aggregate was significantly reduced in BTA hydrogels compared to agarose, except 0:100 which was similar (**Figure 5D**). Next, we evaluated the aggregate area and observed similar trends: BTA hydrogels showed a smaller aggregate area compared to agarose (**Figure 5E**). BTA-PEG-BTA (0:100) showed a significantly higher area compared to other BTA formulations. Smaller length, reduced spheroid area, and less circularity of other BTA formulations compared to 0:100 likely could be due to slow supramolecular dynamics; for example, fewer MSCs would be able to find each other and form aggregates, resulting in smaller aggregates. In contrast, 0:100, faster supramolecular exchange dynamics would support larger aggregate formation.

Next, we determined circularity (**Figure 5F**) in order to find differences in spheroids morphology. Free self-assembled spheroids in agarose mold showed the highest circularity mean value of 0.94 and lowest was 0.86 for 75:25. Spheroids circularity mean value increased with increasing % of BTA-PEG-BTA and reached 0.94 (similar to free self-assembly in agarose mold) for 0:100. Significant differences in circularity were found between 75:25 (0.86) and 0:100 (0.94) in BTA formulations could be due to slower supramolecular dynamics of 75:25 compared to 0:100. In the cell aggregation study, we observed that 75:25 supported slower cell aggregation and the shape was relatively elliptical compared to 0:100 which is near-spherical after 24 hours, which suggests faster supramolecular dynamics supported faster aggregation into more spherical shapes.

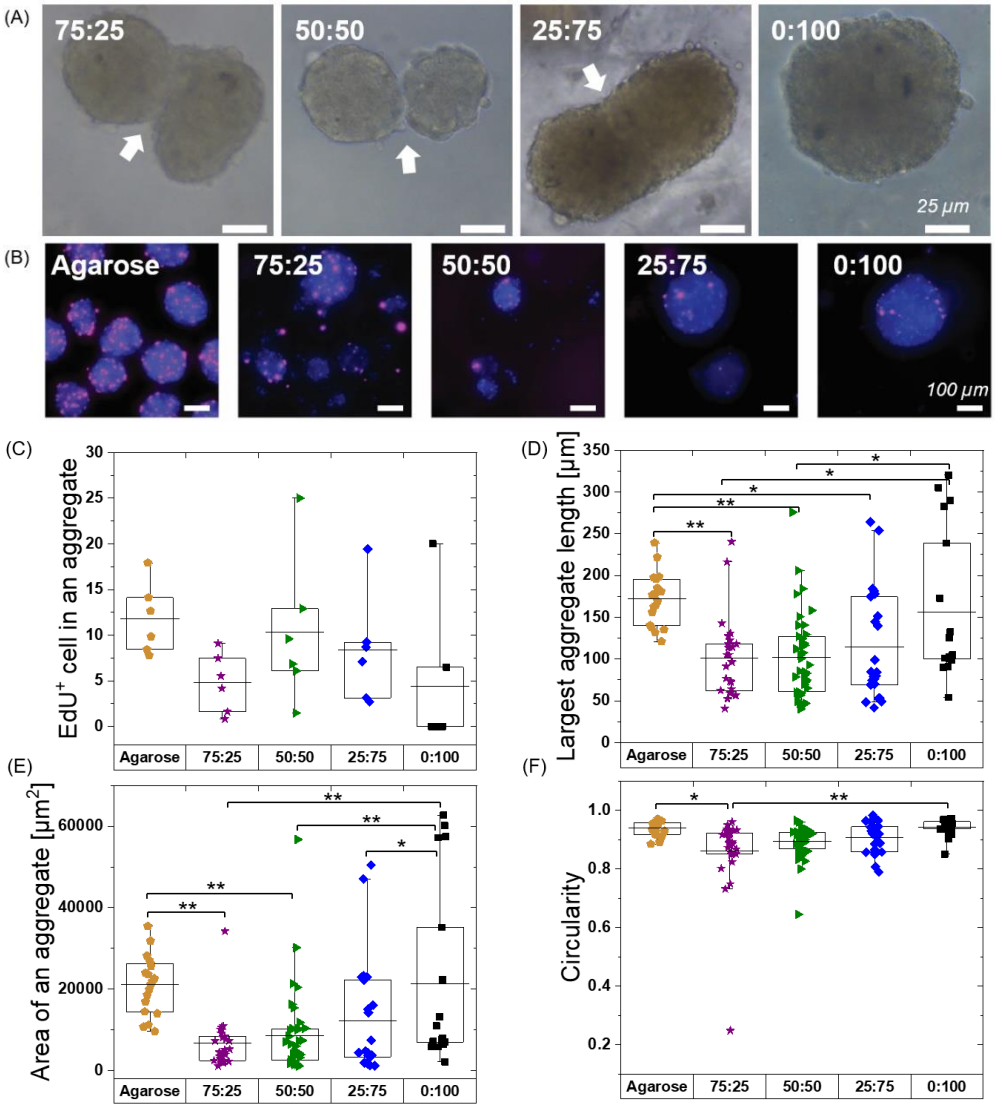

Figure 5. MSCs spheroid fusion, proliferation, and morphology after 48 hours. A) Fusion of spheroids at 48 hours in BTA hydrogels. B) Proliferating hMSCs cultured in BTA formulations stained for EdU. All formulations showed EdU poEdU-positivesitive cells in cell aggregates; however, the fewest EdU-positive cells per spheroids were seen in the 0:100 formulation. Agarose control (allow free directed self-assembly of hMSC) showed the highest number of proliferating cells (EdU positive) compared to BTA formulations. C) Quantitative analysis of EdU positive cells per aggregate in BTA BTA-basedbased hydrogel versus agarose. EdU^+ cells were counted in six aggregates. D) Largest length of an aggregate in BTA-based hydrogel versus agarose; aggregates mean length value was smaller in BTA-based hydrogels compared to agarose after 48 hours. E) Mean value of an aggregate area is smaller in BTA-based hydrogels compared to agarose. F) MSC aggregates are more circular in agarose compared to BTA-based hydrogels. n = 3 biological replicates were used for D-F and between 20–40 aggregates were randomly selected and analyzed. *$p < 0.05$, and **$p<0.005$. Statistically significant test was performed using one-way ANOVA with Tukey's post-hoc test.

Conclusions

Findings from this study show that the modular mixing of supramolecular architectures with slow and fast exchange dynamics provides quick access to tunable biomaterials. These copolymerized hydrogels resulted in materials with tunable stiffness and viscoelasticity in the physiological range of soft tissues and ECM. We were able to encapsulate cells in the hydrogels and showed that the dynamic properties of the hydrogel allowed cell aggregation, spheroid formation, and spheroid fusion—features that are not readily possible in traditional covalent hydrogels. Furthermore, the different hydrogel formulations were able to steer cell aggregation speed and aggregate fidelity, as attributed to changes in the dynamic character and viscoelasticity of the hydrogel. FRAP experiments showed that differences in diffusion were not seen in the different formulations. In the effort to find more complex and tunable ECM replacements, supramolecular systems like this offer significant advantages to rapidly increasing the materials space by leveraging modular mixing. For the creation of multi-cellular aggregates, supramolecular systems give significant advantages over 2D cell aggregate models since they recapitulate fundamental properties of ECM such as fibrous morphology and tunable viscoelastic properties. This work introduces these BTA hydrogels as promising supramolecular biomaterials for spheroid formation. Furthermore, this concept may be generalizable to other dynamic and supramolecular hydrogels. Control over viscoelastic timescales may aid in the quest to create scaleable environments for directing cell aggregation/spheroid formation and towards developing larger tissues for organ development and drug screening.

Materials and Methods

Synthesis of BTA architectures

The synthesis of BTA[44] and BTA-PEG-BTA[36] architectures was performed according to previous reports and were provided by SyMOChem B.V. Eindhoven, The, Netherlands.

Preparation of Hydrogels for Rheology and Cell Culture

A heating and cooling procedure was adopted to make BTA hydrogels. The solid polymer was weighed in a glass vial and Milli Q water/DPBS/media was added. Water was used for rheology and DPBS and Dulbecco's Modified Eagle Medium (DMEM) media with 1% penicillin/streptomycin (P/S) was used to make hydrogels for cell culture. All hydrogels were made at a final concentration of 10% (w/v). This was followed by a 2x heating to go above the lower critical solution temperature (LCST, ~80 °C) of polyethylene glycol (PEG), vortexing, and cooling. The last (3rd step) included more controlled cooling where all hydrogels were placed on a heating plate at 80 °C and slowly cooled to room temperature.

For nerve cells (PC12 and DRGs) growth, hydrogels were made by incubating pure solid BTA-PEG-BTA (0:100) overnight in DPBS with either laminin or fibrinogen at 37 ºC. The well plate was left overnight at 37 ºC for BTA-PEG-BTA to form a hydrogel. BTA-PEG-BTA formed a

transparent hydrogel after overnight incubation in DPBS. Fibrinogen's final concentration in the hydrogel is 3.5 mg/mL and laminin's final concentration in the hydrogel is 20 μg/mL.

Preparation of hydrogels by chemically dissolving and freeze-drying

BTA hydrogels were also made by chemically dissolving BTA formulations in DCM using cosolvent methanol between 10–50%. Chemically dissolved BTA was added into a well plate and solvents were removed overnight using a vacuum oven at room temperature. Upon solvent drying, the solids form a layer at the bottom of the well plate to which the required amount of DPBS was added to adjust hydrogel concentration to 10% (w/v). The well plate was left at 37 °C overnight for hydrogelators to form hydrogels. Subsequently, hydrogels were frozen and freeze-dried. After freeze-drying, a porous foam structure was obtained to which required cell suspension in cell culture media (high glucose DMEM with 1%P/S) was added and the final concentration was adjusted to 10% (w/v).

Rheological measurements

Rheological measurements were performed on a DHR-2 rheometer (TA instruments). The rheometer is equipped with an evaporation control chamber. A 20 mm 2,002° cone plate geometry was used. Samples were loaded at room temperature (RT) ~20 ºC and trimmed. The final gap was set to 53 μm.

An amplitude sweep (ω = 10 rad/s, γ = 0.01–400%) was performed on each sample to act as a pre-shear for all samples to erase any mechanical history and confirm the material's linear viscoelastic region. Afterward, a time sweep at 0.1% strain, and 10 rad/s, was run until the material's G' was stabilized which allowed the material to set before a subsequent measurement. A frequency sweep from 100 to 0.01 rad/s with 0.1% strain was performed next followed by another time sweep to ensure the material was stable before stress relaxation measurement. The relaxation modulus was recorded via a step relaxation experiment for 1000–10000s where we used 1% strain and a rise time of 0.01s.

Vial inversion and macroscopic self-Healing experiment

Hydrogels were made in Milli Q water using the standard procedure described above and vials were inverted and imaged at time zero and after 24 hours. For the self-healing test, the same formulation was colored either red or green using food color dyes for visibility. Two pieces of the hydrogels were placed side by side adjacent to each other in a petri-dish closed environment. Water was added around the hydrogel making sure that no water touched the hydrogel in order to control humidity. Self-healing of the hydrogel was tested after 24 hours by looking at how uniformly the interface had healed and then the hydrogel was lifted using a spatula and observed if the hydrogel's two pieces can fall apart under gravity.

Agarose microwell fabrication for aggregate formation

Agarose microwell arrays were prepared as previously described.[61] Briefly, 3% ultra-pure agarose solution (Invitrogen) was cast onto a poly(dimethyl siloxane) stamp with microstructures to imprint microwells, de-molded upon solidification, cut to size, and inserted into 12-well plates. Each well of the microwell array contained 450 microwells with a diameter of 400 μm.

Fluorescent recovery after photobleaching (FRAP) experiment

Hydrogels were made using the standard heating-cooling procedure described above. A volume of 200 μL of all formulations was transferred in 35 mm diameter 4-compartment cell culture disk (VWR 391-0225, Greiner bio-one), 1 mL of FITC-labelled dextran solution (3–5 or 70 kDa at 0.1 mg/mL, Sigma-Aldrich, FD4-250MG and 46945-100MG-F) was added and incubated overnight at 4°C in the dark. Fluorescent recovery after photobleaching (FRAP) imaging was performed on a Leica TCS SP8 STED using the FRAP modules of Leica Application Suite X software (LAS X FRAP). FRAP bleaching was performed on a z-height of 20 μm in each hydrogel. Parameters were set as followed: bleaching point of 60 μm diameter, bleaching laser at 100%, pre/post bleaching laser at 5%/ 488 nm/ 800 gain, and a time per frame of 0.223 sec. After 5 frames pre-bleach (1.2 sec), samples were bleached for 90 frames (21.2 sec), and fluorescent recovery was gathered for 400 frames post-bleaching (110.5 sec). 5 different areas within the hydrogels were bleached (N=5). ROI data were extracted in Fiji ImageJ-win64. Area and mean gray values were obtained for the bleach, total and background ROIs. The obtained values were imported (.cvs files) in the open-source application FrapBot[68] to obtain the $\tau_{1/2}$ (half-time) of the fluorescent recovery curve. Obtained half times ($\tau_{1/2}$) were used to calculate the diffusion coefficients by the Soumpasis equation, with D=diffusion coefficient, r=radius of the bleaching area, and $\tau_{1/2}$=the halftime of recovery (eq. 4). Statistical analysis was performed in GraphPad Prism 8.2.0, one-way ANOVA.

$$D = 0.224 * \left(\frac{r^2}{\tau_{\frac{1}{2}}}\right) \qquad \text{eq. 4}$$

Cell culture and cell encapsulation in hydrogels

Human dermal fibroblasts (HDFs) cell culture

HDFs (#R2320, ScienCell Research Laboratories) were cultured at 37 °C in 5% CO_2 atmosphere incubator and expanded using Dulbecco's modified Eagle's medium (DMEM, high glucose) supplemented with GlutaMAX, 10% (v/v) fetal bovine serum (FBS) and 1% (v/v) P/S.

ATDC5 chondrocyte cell culture

ATDC5 (RIKEN cell bank, Japan) were expanded in high glucose DMEM basal medium with 10% fetal bovine serum, 1% P/S at 37 °C in a humidified incubator with 5% CO_2. The medium was changed every 2–3 days and the cells were passaged at 80% confluence. Cells were

trypsinized using 0.05% trypsin-EDTA, washed with DPBS, and re-suspended in chondrocyte cell culture media before encapsulation in the hydrogel.

hMSCs cell culture

Bone marrow-derived hMSCs (PromoCell) were obtained at passage 1 and tested for mycoplasma using the mycoplasma detection kit from BD Biosciences. The cells were maintained in a minimal essential medium (MEM α; Gibco) supplemented with 10% (v/v) fetal bovine serum (Sigma-Aldrich). The cells were maintained at 37 °C in 5% CO_2 in a humidified incubator and the medium was changed every two days. Upon reaching 80% confluence, cells were detached by incubating with 0.05% trypsin-EDTA (Thermo Fisher Scientific) and re-plated for continuous passage. The cells were used for encapsulation experiments at passage five for all experiments. For encapsulation in the hydrogels, cells were washed with DPBS, detached using 0.05% trypsin-EDTA, and re-suspended in the media before encapsulation in the hydrogels.

Cell encapsulation (ATDC5, HDF, and hMSC) in hydrogels using the self-healing method

The hydrogels were transferred to well plates and centrifuged at 5000 × *g* for 5 mins to make a uniform layer of the gel at the bottom of the well plate. The uniform layer was broken into small pieces using a spatula and then cell suspension of either fibroblast, ATDC5, or hMSC was added and spread uniformly on the hydrogel. Then a second layer of the hydrogel was added on top of the first layer, and centrifuged at 100 × *g* for cells to get in the hydrogel and also for the second layer of the hydrogel to sandwich the cells between two layers. Next, the hydrogel was broken gently into small pieces using a spatula and mixed for uniform mixing of cells. In the last step, care was taken to be gentle and not damage the cell membrane using the spatula; however, we made sure that cells are in the hydrogel for them to be tolerant to shear stresses during the encapsulation method. After mixing, hydrogels were placed at 37 °C for 15–30 minutes for self-healing. Cell culture media was added and the experiment was continued. Cell density for live/dead studies for fibroblasts, ATDC5, and hMSCs were between 1–5 million cells/mL of the hydrogel. Cell density for ATDC5 and hMSCs for cell aggregation studies was 10 million cells/mL of the hydrogel.

Cell encapsulation in hydrogels using the chemically dissolved and freeze-dried method

Cell suspension with the required number of cells was added on top of freeze-dried hydrogels. Hydrogels were incubated for 1 hour for the freeze-drying foam to turn into a hydrogel. Though we were able to encapsulate cells within freeze-dried hydrogels, not all formulations made nice hydrogels, especially which have a larger percentage of BTA. Also, 100:0 and 90:10 formed very soft foamy structures after freeze-drying, and upon adding cell suspension most of the cell's sediment to the bottom of the hydrogel.

Encapsulation cells in hydrogels using a heating method

The hydrogel was made in chondrocyte cell culture media (high glucose DMEM basal medium with + 1% penicillin/streptomycin) by the heating-cooling method as described above.

Fabricated hydrogel (90:10 and 0:100) was maintained at 60 ºC in a clear glass vial (4 mL storage capacity, VWR, Netherlands) and then using a hydrogel pipette (Gilson, Netherlands) transferred to 24 tissue culture well plate. Cell suspension in 50 µL was added and mixed quickly using a hydrogel pipette. We noticed that 100:0 was not in solution state at 60 ºC and quickly gelled as soon as was transferred to the well plate while 90:10 was in solution state. Both formulations started to hydrogel as soon as the hydrogel pipette touch them in the glass vial and then in the 24-well tissue culture plate rendering ineffective cell encapsulation.

PC12 cell culture, expansion, and encapsulation in BTA-PEG-BTA hydrogel

PC12 cells (DSMZ, Germany) were expanded in suspension at 37 °C in a 5% CO_2 atmosphere using proliferation media composed of 85% RPMI 1640 (Thermo Fisher Scientific), 10% (v/v) Horse Serum, and 5% (v/v) FBS (Sigma-Aldrich). Cells were harvested by centrifugation (200 g) and then re-suspended in the freshly warm medium. 1000 cells in 10µL of proliferation media were added on top of hydrogel and then centrifuged at 100 g for cell encapsulation within the hydrogel. After seeding, cells were cultured in a neural differentiation medium composed of RPMI media with 1% horse serum and 200 ng/mL nerve growth factor (NGF).

DRG isolation and encapsulation in BTA-PEG-BTA hydrogel

DRGs were dissected from decapitated P7 Brown Norway rats, following the protocol previously described by Malheiro et al[69]. After dissection, one DRG was placed over the hydrogel and centrifuged at 100g to entrap the DRG. Cells were cultured with 150 µl DRG medium, composed of Neurobasal Medium, 0.5 mM Glutamax, 100 U/ml penicillin and 100 µg/ml streptomycin (all Thermo Fisher Scientific), 100 µg/ml aprotinin, 50–100 ng/ml human nerve growth factor (NGF), 50 µg/ml ascorbic acid (all Sigma-Aldrich) and N21 supplement (R&D systems). Cells were cultured for 2 days, at 37 ◦C 5% CO_2, with 150 µl medium refreshment at day 1 and day 2. All animal experiments were performed in accordance with the guidelines within the Experiments on Animals Act, and approved by the animal ethics committee at Maastricht University (DEC-UM).

Cell encapsulation in ionically alginate hydrogel

Alginate was purified as reported previously in our group.[32] Purified alginate was dissolved in DMEM media with 1% penicillin/streptomycin (P/S) at an initial concentration of 2.5 wt%. The hydrogel was made by mixing alginate stock solution at 2.5 wt% with calcium sulfate slurry of 1.22 M and ATDC5 cell suspension using Luer-lock syringes connected with a female-female connector. The mixed solution was deposited into 48 well-plate (non-adherent) and allowed to get for 45–60 minutes. Alginate final concentration was adjusted to 2wt% and calcium sulfate concentration was 25mM.

Live/dead cell viability assay

BTA hydrogelators were tested for cytotoxicity with fibroblasts, and chondrocytes. Cytotoxicity was evaluated by staining cultured cells with calcein-AM and ethidium homodimer-1, following the manufacturer's kit instructions. Chondrocyte spreading/growth within hydrogels was

evaluated using Alexa Fluor 488-Phalloidin and DAPI staining. Images were acquired using an inverted epifluorescence microscope (Nikon Eclipse Ti-e) or a confocal laser scanning microscope (Leica TCS SP8).

EdU cell proliferation detection

To assess cell proliferation, 5-ethynyl-2'-deoxyuridine (EdU) staining was conducted using the Click-iT EdU Alexa Fluor 647 Imaging Kit (Thermo Fisher Scientific), according to the manufacturer's protocol. HMSCs were incubated with 50 μM EdU for 48 h in the incubator before fixation for 30 min in 4% (v/v) formaldehyde (Sigma-Aldrich) in PBS at ambient temperature. Fixed samples were permeabilized with 0.5% (v/v) Triton X-100 (VWR) in PBS for 1 h and the incorporated EdU was labeled using a click reaction with Alexa Fluor 647 azide for 1 h according to the manufacturer's protocol. The nuclear DNA was counterstained by DAPI (0.1 μg/ml) for 1 h. The fluorescence images were acquired on a Nikon E600 inverted microscope.

Acknowledgments

SH and CvB would like to thank the European Research Council (ERC) for funding under the European Union's Horizons 2020 research and innovation program (grant agreement No. 694801). SH, PW, and MBB would like to thank the Dutch Research Council (NWO) for funding under the "Open Mind" granting scheme (grant agreement No. 18263) AJF and MBB would like to thank InSciTe for funding under the "EyeSciTe" consortium. FAAR, VLSL, and MBB would like to thank the partners of Regenerative Medicine Crossing Borders (RegMed XB), financed by the Dutch Ministry of Economic Affairs by means of the PPP Allowance made available by the Top Sector Life Sciences & Health to stimulate public-private partnerships. RPML and NMM would like to thank the Dutch Ministry of Education, Culture, and Science (Gravity program 024.001.035) and the NWO/DPI program NEWPOL (project 731.015.503) for funding. We would like to thank Prof. Egbert Willem Meijer from the Eindhoven University of Technology for supporting RPML and NMM and providing material support during this study. The hydrogel schematic was partially created using Biorender.com.

Contributions to the work

The cell work with hMSCs was carried out in collaboration with Fiona R. Passanha. Rheology measurements were run by Antonio J. Feliciano. FRAP work was done in collaboration with Floor A.A. Ruiter. Neuronal cell work was carried out in collaboration with Afonso Malheiro. The author would like to thank all the coauthors for their contribution to the work.

References

(1) Rosales, A. M.; Anseth, K. S. The Design of Reversible Hydrogels to Capture Extracellular Matrix Dynamics. *Nat. Rev. Mater.* **2016**, *1*, 1–15. https://doi.org/10.1038/natrevmats.2015.12.

(2) Chaudhuri, O.; Cooper-White, J.; Janmey, P. A.; Mooney, D. J.; Shenoy, V. B. Effects of Extracellular Matrix Viscoelasticity on Cellular Behaviour. *Nature.* **2020**, *584* (7822) 535–546.

https://doi.org/10.1038/s41586-020-2612-2.

(3) Discher, D. E. Tissue Cells Feel and Respon to the Stiffness of Their Substrate. *Science.* **2005**, *310* (5751), 1139–1143. https://doi.org/10.1126/science.1116995.

(4) Guimarães, C. F.; Gasperini, L.; Marques, A. P.; Reis, R. L. The Stiffness of Living Tissues and Its Implications for Tissue Engineering. *Nat. Rev. Mater.* **2020**, *5* (5), 351–370. https://doi.org/10.1038/s41578-019-0169-1.

(5) Engler, A. J.; Sen, S.; Sweeney, H. L.; Discher, D. E. Matrix Elasticity Directs Stem Cell Lineage Specification. *Cell* **2006**, *126* (4), 677–689. https://doi.org/10.1016/j.cell.2006.06.044.

(6) Tse, J. R.; Engler, A. J. Stiffness Gradients Mimicking in Vivo Tissue Variation Regulate Mesenchymal Stem Cell Fate. *PLoS One* **2011**, *6* (1), e15978. https://doi.org/10.1371/journal.pone.0015978.

(7) Theocharis, A. D.; Skandalis, S. S.; Gialeli, C.; Karamanos, N. K. Extracellular Matrix Structure. *Adv. Drug Deliv. Rev.* **2016**, *97*, 4–27. https://doi.org/10.1016/j.addr.2015.11.001.

(8) Frantz, C.; Stewart, K. M.; Weaver, V. M. The Extracellular Matrix at a Glance. *J. Cell Sci.* **2010**, *123* (24), 4195–4200. https://doi.org/10.1242/jcs.023820.

(9) Murphy, W. L.; McDevitt, T. C.; Engler, A. J. Materials as Stem Cell Regulators. *Nat. Mater.* **2014**, *13* (6), 547–557. https://doi.org/10.1038/nmat3937.

(10) Daley, W. P.; Peters, S. B.; Larsen, M. Extracellular Matrix Dynamics in Development and Regenerative Medicine. *J. Cell Sci.* **2008**, *121* (3), 255–264. https://doi.org/10.1242/jcs.006064.

(11) Chaudhuri, O.; Gu, L.; Darnell, M.; Klumpers, D.; Bencherif, S. A.; Weaver, J. C.; Huebsch, N.; Mooney, D. J. Substrate Stress Relaxation Regulates Cell Spreading. *Nat. Commun.* **2015**, *6*, 6364. https://doi.org/10.1038/ncomms7365.

(12) Zhao, X.; Huebsch, N.; Mooney, D. J.; Suo, Z. Stress-Relaxation Behavior in Gels with Ionic and Covalent Crosslinks. In *Journal of Applied Physics*; 2010; Vol. 107, p 063509. https://doi.org/10.1063/1.3343265.

(13) Sommerfeld, S. D.; Elisseeff, J. H. Time to Relax: Mechanical Stress Release Guides Stem Cell Responses. *Cell Stem Cell.* 2016, pp 166–167. https://doi.org/10.1016/j.stem.2016.01.020.

(14) McKinnon, D. D.; Domaille, D. W.; Cha, J. N.; Anseth, K. S. Biophysically Defined and Cytocompatible Covalently Adaptable Networks as Viscoelastic 3d Cell Culture Systems. *Adv. Mater.* **2014**, *26* (6), 865–872. https://doi.org/10.1002/adma.201303680.

(15) Richardson, B. M.; Wilcox, D. G.; Randolph, M. A.; Anseth, K. S. Hydrazone Covalent Adaptable Networks Modulate Extracellular Matrix Deposition for Cartilage Tissue Engineering. *Acta Biomater.* **2019**, *83*, 71–82. https://doi.org/10.1016/j.actbio.2018.11.014.

(16) Lou, J.; Stowers, R.; Nam, S.; Xia, Y.; Chaudhuri, O. Stress Relaxing Hyaluronic Acid-Collagen Hydrogels Promote Cell Spreading, Fiber Remodeling, and Focal Adhesion Formation in 3D Cell Culture. *Biomaterials* **2018**, *154*, 213–222. https://doi.org/10.1016/j.biomaterials.2017.11.004.

(17) Gong, Z.; Szczesny, S. E.; Caliari, S. R.; Charrier, E. E.; Chaudhuri, O.; Cao, X.; Lin, Y.; Mauck, R. L.; Janmey, P. A.; Burdick, J. A.; Shenoy, V. B. Matching Material and Cellular Timescales Maximizes Cell Spreading on Viscoelastic Substrates. *Proc. Natl. Acad. Sci.* **2018**, *115* (12), E2686–E2695 |. https://doi.org/10.1073/pnas.1716620115.

(18) Chaudhuri, O.; Gu, L.; Klumpers, D.; Darnell, M.; Bencherif, S. A.; Weaver, J. C.; Huebsch, N.; Lee, H. P.; Lippens, E.; Duda, G. N.; Mooney, D. J. Hydrogels with Tunable Stress Relaxation Regulate Stem Cell Fate and Activity. *Nat. Mater.* **2016**, *15* (3), 326–334. https://doi.org/10.1038/nmat4489.

(19) Lee, H.; Gu, L.; Mooney, D. J.; Levenston, M. E.; Chaudhuri, O. Mechanical Confinement Regulates Cartilage Matrix Formation by Chondrocytes. *Nat. Mater.* **2017**, No. October. https://doi.org/10.1038/nmat4993.

(20) Lee, H. P.; Gu, L.; Mooney, D. J.; Levenston, M. E.; Chaudhuri, O. Mechanical Confinement Regulates Cartilage Matrix Formation by Chondrocytes. *Nat. Mater.* **2017**, *16* (12), 1243–1251. https://doi.org/10.1038/nmat4993.

(21) Charrier, E. E.; Pogoda, K.; Wells, R. G.; Janmey, P. A. Control of Cell Morphology and Differentiation by Substrates with Independently Tunable Elasticity and Viscous Dissipation. *Nat. Commun.* **2018**, *9* (1), 449. https://doi.org/10.1038/s41467-018-02906-9.

(22) Yeh, Y.-C.; Corbin, E. A.; Caliari, S. R.; Ouyang, L.; Vega, S. L.; Truitt, R.; Han, L.; Margulies, K. B.; Burdick, J. A. Mechanically Dynamic PDMS Substrates to Investigate Changing Cell

Environments. *Biomaterials* **2017**, *145*, 23–32. https://doi.org/10.1016/j.biomaterials.2017.08.033.
(23) Cameron, A. R.; Frith, J. E.; Gomez, G. A.; Yap, A. S.; Cooper-White, J. J. The Effect of Time-Dependent Deformation of Viscoelastic Hydrogels on Myogenic Induction and Rac1 Activity in Mesenchymal Stem Cells. *Biomaterials* **2014**, *35* (6), 1857–1868. https://doi.org/10.1016/j.biomaterials.2013.11.023.
(24) Diba, M.; Spaans, S.; Hendrikse, S. I. S.; Bastings, M. M. C.; Schotman, M. J. G.; van Sprang, J. F.; Wu, D. J.; Hoeben, F. J. M.; Janssen, H. M.; Dankers, P. Y. W. Engineering the Dynamics of Cell Adhesion Cues in Supramolecular Hydrogels for Facile Control over Cell Encapsulation and Behavior. *Adv. Mater.* **2021**, *33* (37), 2008111. https://doi.org/10.1002/adma.202008111.
(25) Marco-Dufort, B.; Iten, R.; Tibbitt, M. W. Linking Molecular Behavior to Macroscopic Properties in Ideal Dynamic Covalent Networks. *J. Am. Chem. Soc.* **2020**, *142* (36), 15371–15385. https://doi.org/10.1021/jacs.0c06192.
(26) Ooi, H. W.; Hafeez, S.; Van Blitterswijk, C. A.; Moroni, L.; Baker, M. B. Hydrogels That Listen to Cells: A Review of Cell-Responsive Strategies in Biomaterial Design for Tissue Regeneration. *Mater. Horizons* **2017**, *4* (6), 1020–1040. https://doi.org/10.1039/c7mh00373k.
(27) Lim, J. Y. C.; Lin, Q.; Xue, K.; Loh, X. J. Recent Advances in Supramolecular Hydrogels for Biomedical Applications. *Mater. Today Adv.* **2019**, *3*, 100021. https://doi.org/10.1016/j.mtadv.2019.100021.
(28) Rizwan, M.; Baker, A. E. G.; Shoichet, M. S. Designing Hydrogels for 3D Cell Culture Using Dynamic Covalent Crosslinking. *Advanced Healthcare Materials*. 2021, pp 1–23. https://doi.org/10.1002/adhm.202100234.
(29) Feliciano, A. J.; van Blitterswijk, C.; Moroni, L.; Baker, M. B. Realizing Tissue Integration with Supramolecular Hydrogels. *Acta Biomater.* **2021**, *124*, 1–14. https://doi.org/10.1016/j.actbio.2021.01.034.
(30) Marozas, I. A.; Anseth, K. S.; Cooper-White, J. J. Adaptable Boronate Ester Hydrogels with Tunable Viscoelastic Spectra to Probe Timescale Dependent Mechanotransduction. *Biomaterials* **2019**, *223*, 119430. https://doi.org/10.1016/j.biomaterials.2019.119430.
(31) Yesilyurt, V.; Ayoob, A. M.; Appel, E. A.; Borenstein, J. T.; Langer, R.; Anderson, D. G. Mixed Reversible Covalent Crosslink Kinetics Enable Precise, Hierarchical Mechanical Tuning of Hydrogel Networks. *Adv. Mater.* **2017**, *29* (19), 1605947–1605947. https://doi.org/10.1002/adma.201605947.
(32) Hafeez, S.; Ooi, H.; Morgan, F.; Mota, C.; Dettin, M.; van Blitterswijk, C.; Moroni, L.; Baker, M. Viscoelastic Oxidized Alginates with Reversible Imine Type Crosslinks: Self-Healing, Injectable, and Bioprintable Hydrogels. *Gels* **2018**, *4* (4), 85. https://doi.org/10.3390/gels4040085.
(33) Morgan, F. L. C.; Fernández-Pérez, J.; Moroni, L.; Baker, M. B. Tuning Hydrogels by Mixing Dynamic Cross-Linkers: Enabling Cell-Instructive Hydrogels and Advanced Bioinks. *Adv. Healthc. Mater.* **2022**, *11* (1), 2101576. https://doi.org/10.1002/adhm.202101576.
(34) Zou, L.; Braegelman, A. S.; Webber, M. J. Dynamic Supramolecular Hydrogels Spanning an Unprecedented Range of Host-Guest Affinity. *ACS Appl. Mater. Interfaces* **2019**, *11* (6), 5695–5700. https://doi.org/10.1021/acsami.8b22151.
(35) Yang, B.; Wei, K.; Loebel, C.; Zhang, K.; Feng, Q.; Li, R.; Wong, S. H. D.; Xu, X.; Lau, C.; Chen, X.; Zhao, P.; Yin, C.; Burdick, J. A.; Wang, Y.; Bian, L. Enhanced Mechanosensing of Cells in Synthetic 3D Matrix with Controlled Biophysical Dynamics. *Nat. Commun.* **2021**, *12* (1), 3514. https://doi.org/10.1038/s41467-021-23120-0.
(36) Vereroudakis, E.; Bantawa, M.; Lafleur, R. P. M.; Parisi, D.; Matsumoto, N. M.; Peeters, J. W.; Del Gado, E.; Meijer, E. W.; Vlassopoulos, D. Competitive Supramolecular Associations Mediate the Viscoelasticity of Binary Hydrogels. *ACS Cent. Sci.* **2020**, *6*, 1401–1411. https://doi.org/10.1021/acscentsci.0c00279.
(37) Goor, O. J. G. M.; Hendrikse, S. I. S.; Dankers, P. Y. W.; Meijer, E. W. From Supramolecular Polymers to Multi-Component Biomaterials. *Chem. Soc. Rev.* **2017**, *46* (21), 6621–6637. https://doi.org/10.1039/C7CS00564D.
(38) Aida, T.; Meijer, E. W.; Stupp, S. I. Functional Supramolecular Polymers. *Science (80-.).* **2012**, *335* (6070), 813–817. https://doi.org/10.1126/science.1205962.
(39) Webber, M. J.; Appel, E. A.; Meijer, E. W.; Langer, R. Supramolecular Biomaterials. *Nat. Mater.* **2015**, *15* (1), 13–26. https://doi.org/10.1038/nmat4474.

(40) Boekhoven, J.; Stupp, S. I. 25th Anniversary Article: Supramolecular Materials for Regenerative Medicine. *Adv. Mater.* 2014, pp 1642–1659. https://doi.org/10.1002/adma.201304606.

(41) Pashuck, E. T.; Cui, H.; Stupp, S. I. Tuning Supramolecular Rigidity of Peptide Fibers through Molecular Structure. *J. Am. Chem. Soc.* **2010**, *132* (17), 6041–6046. https://doi.org/10.1021/ja908560n.

(42) Susapto, H. H.; Alhattab, D.; Abdelrahman, S.; Khan, Z.; Alshehri, S.; Kahin, K.; Ge, R.; Moretti, M.; Emwas, A. H.; Hauser, C. A. E. Ultrashort Peptide Bioinks Support Automated Printing of Large-Scale Constructs Assuring Long-Term Survival of Printed Tissue Constructs. *Nano Lett.* **2021**, *21* (7), 2719–2729. https://doi.org/10.1021/acs.nanolett.0c04426.

(43) Dankers, P. Y. W.; Hermans, T. M.; Baughman, T. W.; Kamikawa, Y.; Kieltyka, R. E.; Bastings, M. M. C.; Janssen, H. M.; Sommerdijk, N. A. J. M.; Larsen, A.; Van Luyn, M. J. A.; Bosman, A. W.; Popa, E. R.; Fytas, G.; Meijer, E. W. Hierarchical Formation of Supramolecular Transient Networks in Water: A Modular Injectable Delivery System. *Adv. Mater.* **2012**, *24* (20), 2703–2709. https://doi.org/10.1002/adma.201104072.

(44) Leenders, C. M. A.; Mes, T.; Baker, M. B.; Koenigs, M. M. E.; Besenius, P.; Palmans, A. R. A.; Meijer, E. W. From Supramolecular Polymers to Hydrogel Materials. *Mater. Horiz.* **2014**, *1* (1), 116–120. https://doi.org/10.1039/C3MH00103B.

(45) Hendrikse, S. I. S.; Su, L.; Hogervorst, T. P.; Lafleur, R. P. M.; Lou, X.; Van Der Marel, G. A.; Codee, J. D. C.; Meijer, E. W. Elucidating the Ordering in Self-Assembled Glycocalyx Mimicking Supramolecular Copolymers in Water. *J. Am. Chem. Soc.* **2019**, *141* (35), 13877–13886. https://doi.org/10.1021/jacs.9b06607.

(46) Tong, C.; Liu, T.; Saez Talens, V.; Noteborn, W. E. M.; Sharp, T. H.; Hendrix, M. M. R. M.; Voets, I. K.; Mummery, C. L.; Orlova, V. V; Kieltyka, R. E. Squaramide-Based Supramolecular Materials for Three-Dimensional Cell Culture of Human Induced Pluripotent Stem Cells and Their Derivatives. *Biomacromolecules* **2018**, *19* (4), 1091–1099. https://doi.org/10.1021/acs.biomac.7b01614.

(47) Chia, J. Y.; Miki, T.; Mihara, H.; Tsutsumi, H. Biofunctional Supramolecular Hydrogels Fabricated from a Short Self-Assembling Peptide Modified with Bioactive Sequences for the 3D Culture of Breast Cancer MCF-7 Cells. *Bioorganic Med. Chem.* **2021**, *46*, 116345. https://doi.org/10.1016/j.bmc.2021.116345.

(48) Dankers, P. Y. W.; Harmsen, M. C.; Brouwer, L. A.; Van Luyn, M. J. A.; Meijer, E. W. A Modular and Supramolecular Approach to Bioactive Scaffolds for Tissue Engineering. *Nat. Mater.* **2005**, *4* (7), 568–574. https://doi.org/10.1038/nmat1418.

(49) van Gaal, R. C.; Buskermolen, A. B. C.; Ippel, B. D.; Fransen, P.-P. K. H.; Zaccaria, S.; Bouten, C. V. C.; Dankers, P. Y. W. Functional Peptide Presentation on Different Hydrogen Bonding Biomaterials Using Supramolecular Additives. *Biomaterials* **2019**, *224*, 119466. https://doi.org/10.1016/j.biomaterials.2019.119466.

(50) Mollet, B. B.; Comellas-Aragonès, M.; Spiering, A. J. H.; Söntjens, S. H. M.; Meijer, E. W.; Dankers, P. Y. W. A Modular Approach to Easily Processable Supramolecular Bilayered Scaffolds with Tailorable Properties. *J. Mater. Chem. B* **2014**, *2* (17), 2483–2493. https://doi.org/10.1039/c3tb21516d.

(51) Niece, K. L.; Hartgerink, J. D.; Donners, J. J. J. M.; Stupp, S. I. Self-Assembly Combining Two Bioactive Peptide-Amphiphile Molecules into Nanofibers by Electrostatic Attraction. **2003**, 7146–7147.

(52) Hendrikse, S. I. S.; Wijnands, S. P. W.; Lafleur, R. P. M.; Pouderoijen, M. J.; Janssen, H. M.; Dankers, P. Y. W.; Meijer, E. W. Controlling and Tuning the Dynamic Nature of Supramolecular Polymers in Aqueous Solutions. *ChemComm* **2017**, *53* (14), 2279–2282. https://doi.org/10.1039/c6cc10046e.

(53) Varela-aramburu, S.; Morgese, G.; Su, L.; Schoenmakers, S. M. C.; Perrone, M.; Leanza, L.; Perego, C.; Pavan, G. M.; Palmans, A. R. A.; Meijer, E. W. Exploring the Potential of Benzene-1,3,5-Tricarboxamide Supramolecular Polymers as Biomaterials. *Biomacromolecules* **2020**, *21* (10), 4105–4115. https://doi.org/10.1021/acs.biomac.0c00904.

(54) Rowley, J. A.; Madlambayan, G.; Mooney, D. J. Alginate Hydrogels as Synthetic Extracellular Matrix Materials. *Biomaterials* **1999**, *20* (1), 45–53. https://doi.org/10.1016/S0142-9612(98)00107-0.

(55) Huebsch, N.; Lippens, E.; Lee, K.; Mehta, M.; Koshy, S. T.; Darnell, M. C.; Desai, R. M.; Madl, C. M.; Xu, M.; Zhao, X.; Chaudhuri, O.; Verbeke, C.; Kim, W. S.; Alim, K.; Mammoto, A.; Ingber, D. E.; Duda, G. N.; Mooney, D. J. Matrix Elasticity of Void-Forming Hydrogels Controls Transplanted-Stem-Cell-Mediated Bone Formation. *Nat. Mater.* **2015**, *14* (12), 1269–1277. https://doi.org/10.1038/nmat4407.

(56) Madl, C. M.; Lesavage, B. L.; Dewi, R. E.; Dinh, C. B.; Ryan, S.; Khariton, M.; Lampe, K. J.; Nguyen, D.; Chaudhuri, O.; Enejder, A.; Heilshorn, S. C. Maintenance of Neural Progenitor Cell Stemness in 3D Hydrogels Requires Matrix Remodeling. *Nat Mater.* **2018**, *16* (12), 1233–1242. https://doi.org/10.1038/nmat5020.Maintenance.

(57) Madl, C. M.; LeSavage, B. L.; Dewi, R. E.; Lampe, K. J.; Heilshorn, S. C. Matrix Remodeling Enhances the Differentiation Capacity of Neural Progenitor Cells in 3D Hydrogels. *Adv. Sci.* **2019**, *6* (4), 1801716. https://doi.org/10.1002/advs.201801716.

(58) Wojciechowski, J. P.; Martin, A. D.; Mason, A. F.; Fife, C. M.; Sagnella, S. M.; Kavallaris, M.; Thordarson, P. Choice of Capping Group in Tripeptide Hydrogels Influences Viability in the Three-Dimensional Cell Culture of Tumor Spheroids. *Chempluschem* **2017**, *82* (3), 383–389. https://doi.org/10.1002/CPLU.201600464.

(59) Daly, A. C.; Davidson, M. D.; Burdick, J. A. 3D Bioprinting of High Cell-Density Heterogeneous Tissue Models through Spheroid Fusion within Self-Healing Hydrogels. *Nat. Commun.* **2021**, *12* (1), 1–13. https://doi.org/10.1038/s41467-021-21029-2.

(60) Loebel, C.; Mauck, R. L.; Burdick, J. A. Local Nascent Protein Deposition and Remodelling Guide Mesenchymal Stromal Cell Mechanosensing and Fate in Three-Dimensional Hydrogels. *Nat. Mater.* **2019**, *18* (8), 883–891. https://doi.org/10.1038/s41563-019-0307-6.

(61) Vrij, E.; Rouwkema, J.; Lapointe, V.; Van Blitterswijk, C.; Truckenmüller, R.; Rivron, N. Directed Assembly and Development of Material-Free Tissues with Complex Architectures. *Adv. Mater.* **2016**, *28* (21), 4032–4039. https://doi.org/10.1002/adma.201505723.

(62) Edmondson, R.; Broglie, J. J.; Adcock, A. F.; Yang, L. Three-Dimensional Cell Culture Systems and Their Applications in Drug Discovery and Cell-Based Biosensors. *Assay Drug Dev. Technol.* **2014**, *12* (4), 207–218. https://doi.org/10.1089/adt.2014.573.

(63) Passanha, F. R.; Geuens, T.; Konig, S.; van Blitterswijk, C. A.; LaPointe, V. L. Cell Culture Dimensionality Influences Mesenchymal Stem Cell Fate through Cadherin-2 and Cadherin-11. *Biomaterials* **2020**, *254* (May), 120127. https://doi.org/10.1016/j.biomaterials.2020.120127.

(64) Cosgrove, B. D.; Mui, K. L.; Driscoll, T. P.; Caliari, S. R.; Mehta, K. D.; Assoian, R. K.; Burdick, J. A.; Mauck, R. L. N-Cadherin Adhesive Interactions Modulate Matrix Mechanosensing and Fate Commitment of Mesenchymal Stem Cells. *Nat. Mater.* **2016**, *15* (12), 1297–1306. https://doi.org/10.1038/nmat4725.

(65) Bott, K.; Upton, Z.; Schrobback, K.; Ehrbar, M.; Hubbell, J. A.; Lutolf, M. P.; Rizzi, S. C. The Effect of Matrix Characteristics on Fibroblast Proliferation in 3D Gels. *Biomaterials* **2010**, *31* (32), 8454–8464. https://doi.org/10.1016/j.biomaterials.2010.07.046.

(66) Hongisto, V.; Jernström, S.; Fey, V.; Mpindi, J. P.; Kleivi Sahlberg, K.; Kallioniemi, O.; Perälä, M. High-Throughput 3D Screening Reveals Differences in Drug Sensitivities between Culture Models of JIMT1 Breast Cancer Cells. *PLoS One* **2013**, *8* (10), 1–16. https://doi.org/10.1371/journal.pone.0077232.

(67) Passanha, F. R.; Gomes, D. B.; Piotrowska, J.; Moroni, L.; Baker, M. B.; LaPointe, V. L. S. A Comparative Study of Mesenchymal Stem Cells Cultured as Cell-Only Aggregates and in Encapsulated Hydrogels. *J. Tissue Eng. Regen. Med.* **2022**, *16* (1), 14–25. https://doi.org/10.1002/term.3257.

(68) Kohze, R.; Dieteren, C. E. J.; Koopman, W. J. H.; Brock, R.; Schmidt, S. Frapbot: An Open-Source Application for FRAP Data. *Cytom. Part A* **2017**, *91* (8), 810–814. https://doi.org/10.1002/cyto.a.23172.

(69) Malheiro, A.; Morgan, F.; Baker, M.; Moroni, L.; Wieringa, P. A Three-Dimensional Biomimetic Peripheral Nerve Model for Drug Testing and Disease Modelling. *Biomaterials* **2020**, *257* (June), 120230. https://doi.org/10.1016/j.biomaterials.2020.120230.

Supplementary information

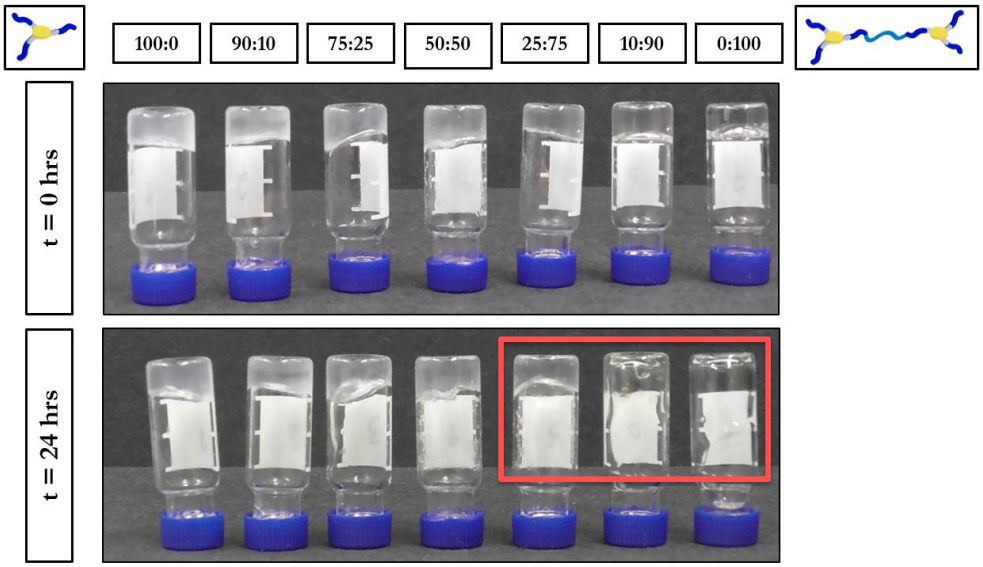

Figure S1. Tuning mechanical properties by modular mixing of BTA and BTA-PEG-BTA: Mixing of BTA and BTA-PEG-BTA allow tweaking of mechanical and viscoelastic properties of hydrogels. On the left is 100:0 BTA architecture and on the right is 0:100 BTA-PEG-BTA architecture with PEG20K connecting two BTA molecule via PEG20K polymer. Hydrogels were made with final 10 wt% and proportion or percentage of BTA and BTA-PEG-BTA were varied. BTA-PEG-BTA flowed and reached to the bottom of the glass vial after 24 hours while 100:0 did not flow at all. Mixed formulation with higher percentage of BTA-PEG-BTA such as 10:90 flowed and reached to the bottom of the glass vial but with increasing percentage of BTA no flow behavior was observed until 24 hours.

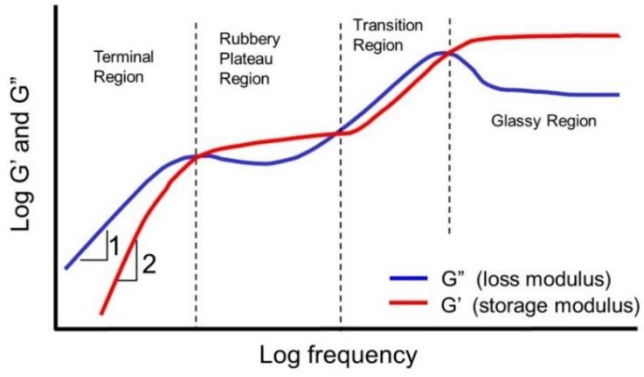

Figure S2. The typical curve for viscoelasticity materials, which shows a transition from terminal region to rubbery plateau going from lower angular frequency to higher angular frequency. In the terminal region, loss modulus (G") is dominant indicating that the material behaves dominantly liquid while in rubbery plateau storage modulus is dominant indicating materials behave dominantly as solid. Pictures obtained from: AZO MATERIALS website: https://www.azom.com/article.aspx?ArticleID=16985

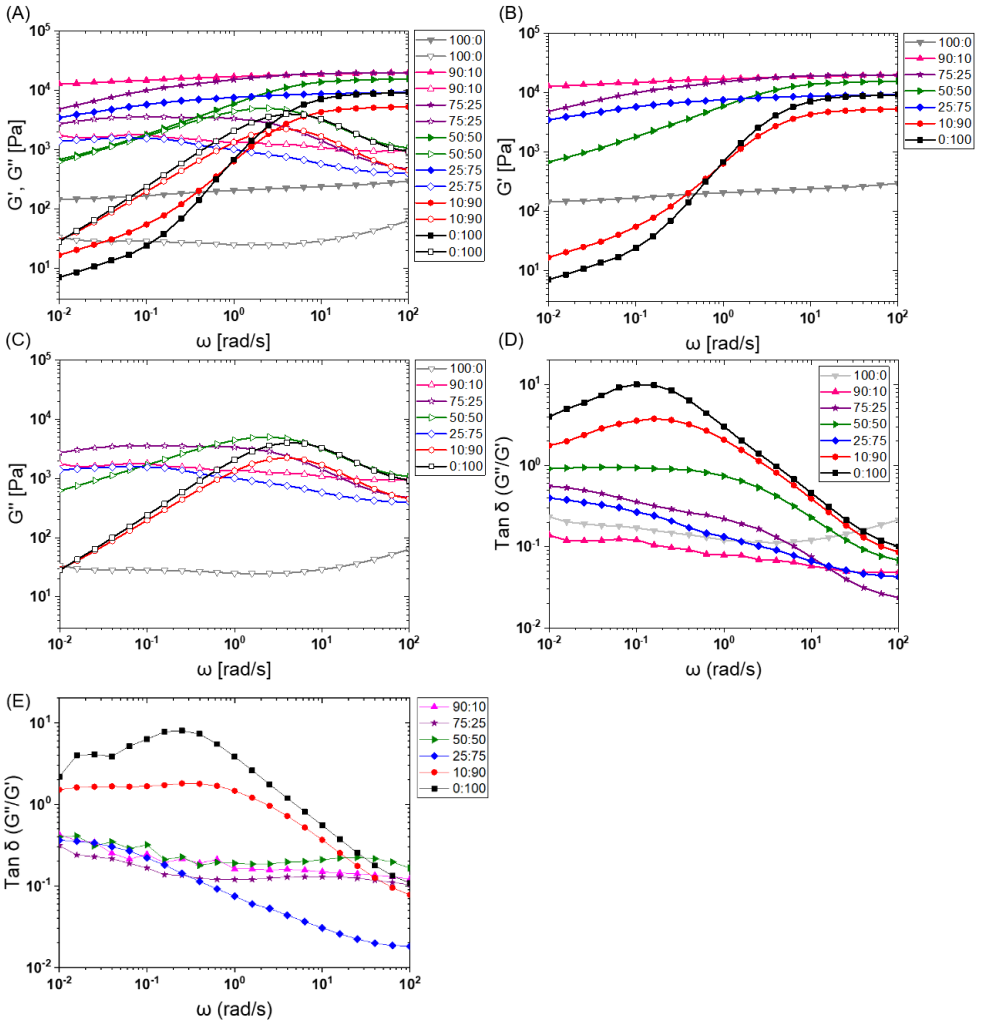

Figure S3. Mechanical and viscoelastic properties of hydrogels: A) Frequency sweep for BTA formulations, B) storage modulus (G') as a function of angular frequency, C) loss modulus (G") a function of angular frequency and D&E) Tanδ (G"/G') as a function of angular frequency of two independent samples. Tanδ (G"/G') of BTAs showed similar trends in viscoelasticity.

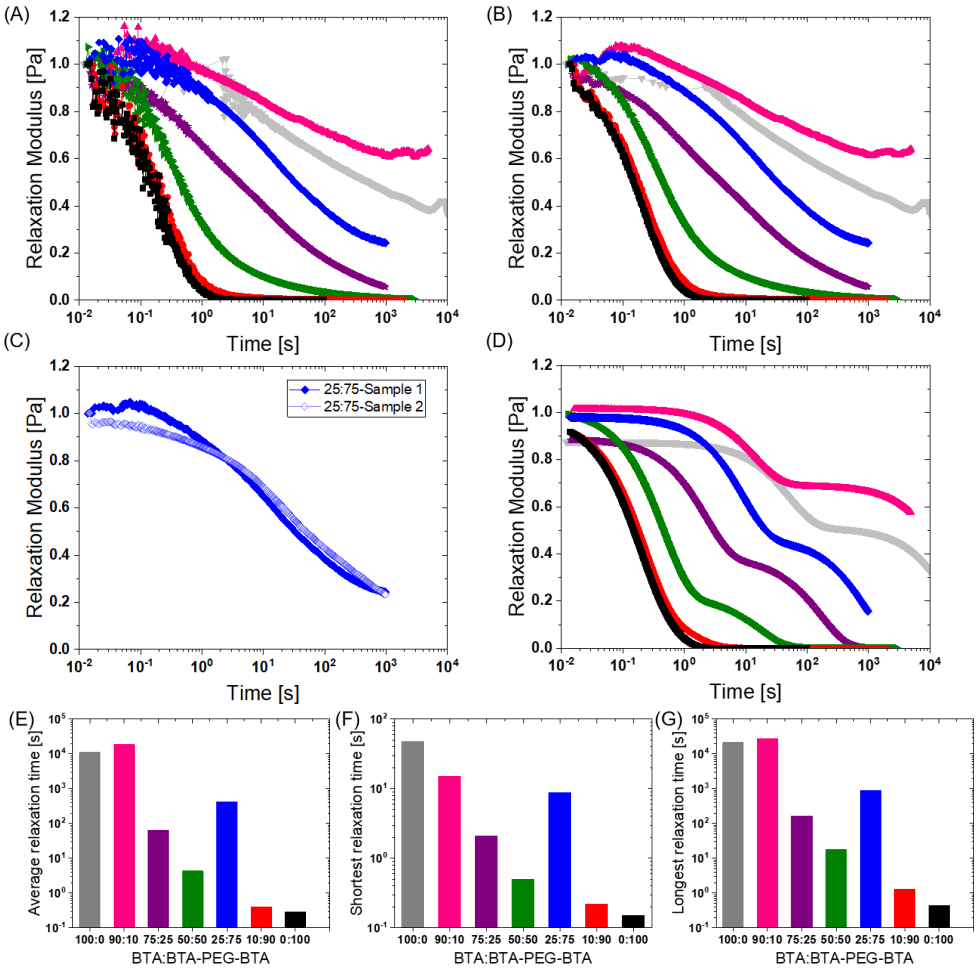

Figure S4. Relaxation modulus curves: A) Normalized relaxation modulus curve for different BTA formulations under constant 1% strain. B) Stress relaxation curves were smoothed by applying a smooth function (10-point average) using OriginLab. C) Stress relaxation curve of two independent samples for 25:75, which shows exceptional behavior, and duplicates were performed for confirming stress relaxation behavior. Both replicates showed similar stress relaxation profiles. D) Curves obtained using two Maxwell elements. D) Average stress relaxation times obtained from curve fitting using two Maxwell elements in "D". E) Shortest relaxation time for the fast mode of relaxation. F) Longest relaxation time for the slow mode of relaxation.

Table S1: Stress relaxation times for different BTA formulations. Average, longest, and smallest relaxation times are calculated by fitting two mode Maxwell element model. * indicate that the sample did not reach half relaxation time.

Formulation	Average relaxation time (seconds)	Longest relaxation time (seconds)	Smallest relaxation time (seconds)	$\tau_{1/2}$ (seconds)
100:0	11,000	21,600	48	524
90:10	**18,500**	**27,300**	15	*N/A
75:25	**64**	**165**	2.1	4
50:50	**5**	**18**	0.5	0.4
25:75	**417**	**898**	9	33
10:90	0.4	1	0.2	0.2
0:100	**0.3**	**0.4**	0.2	0.1

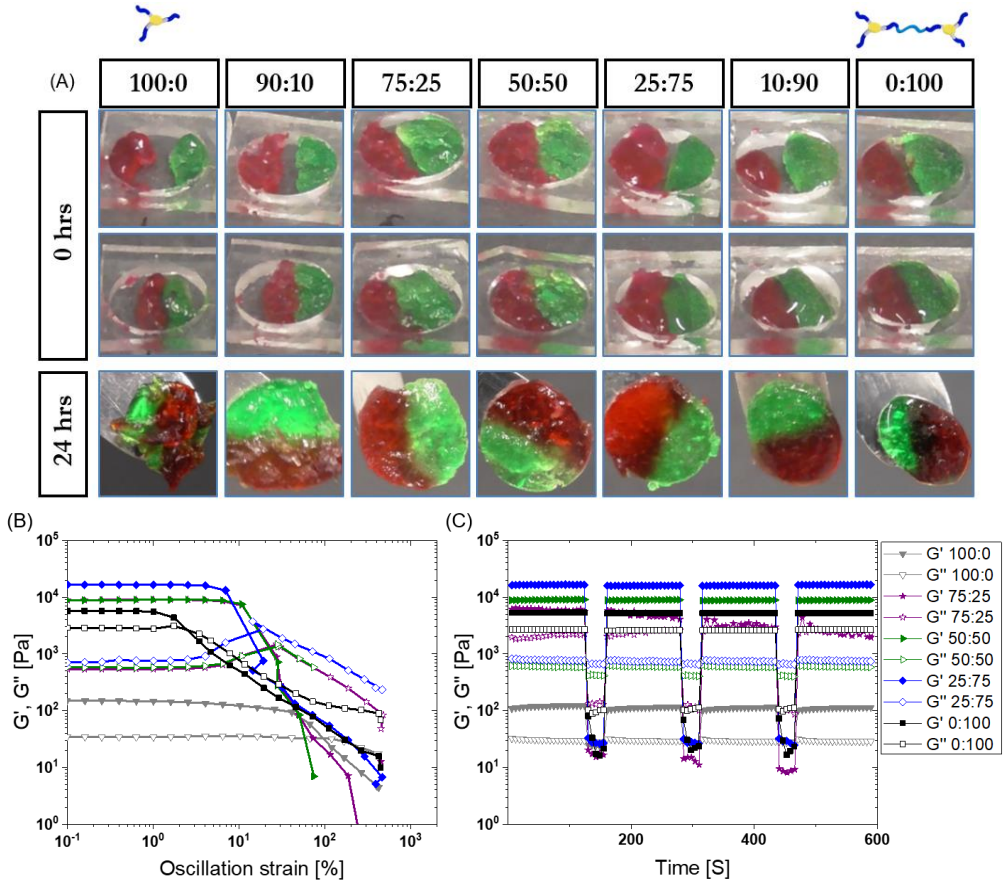

Figure S5. A) Visual demonstration of self-healing capacity of BTA hydrogel formulations, hydrogels with greater than fifty percentage of BTA-PEG-BTA show better self-healing capacity compared to other formulations. 90:10 and 100:0 showed very poor self-healing capacity. B) Amplitude sweep for BTA formulations from 0.1% to 500% strain recorded at 10 rad/sec to determine % strain required for gel to solution transition (gel point) and linear viscoelastic region of gels. C) Self-healing behavior of hydrogels under rheology. All hydrogels showed good self-healing capacity in recovery phase under 1% strain. Hydrogels were ruptured under 500% strain to destroy hydrogel network.

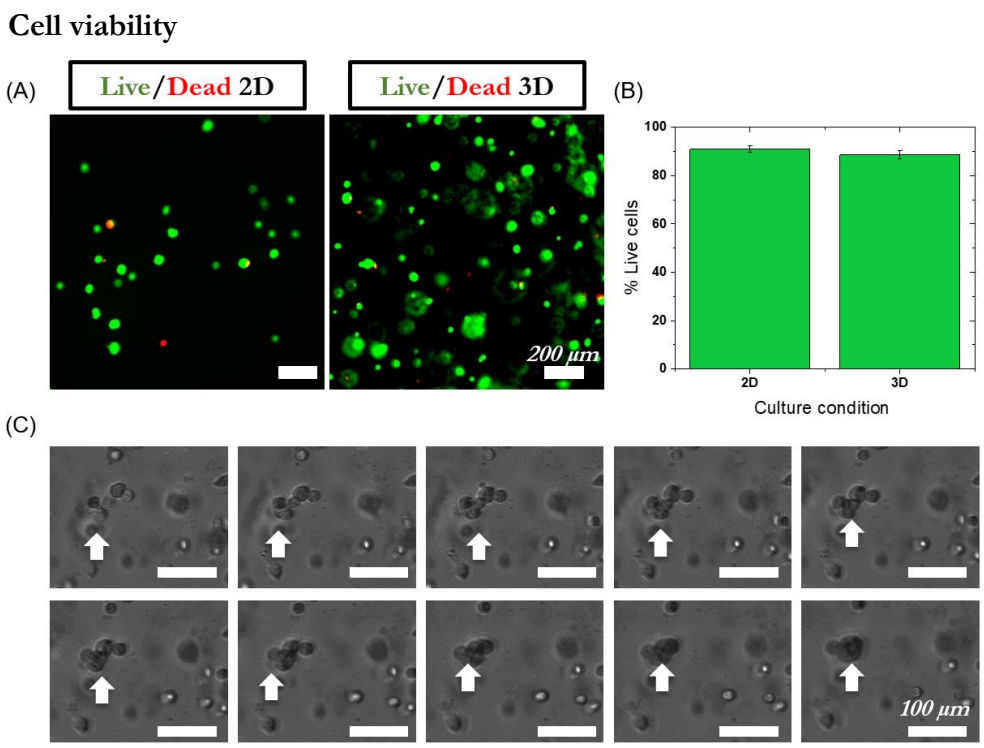

Figure S6. A) Cell viability of Human dermal fibroblasts (HDF) on top (2D) of BTA-PEG-BTA and encapsulated (3D) within BTA-PEG-BTA hydrogels. The green color represents a live cell and the red color represents a dead cell. B) % of live cells plotted for 2D and 3D culture conditions, n=2 biological replicates and imaged at multiple locations on top (for 2D) and inside (for 3D) of the hydrogel. C) Pictures from time-lapse video over 17 hours showing that HDF forming an aggregate within BTA-PEG-BTA hydrogels.

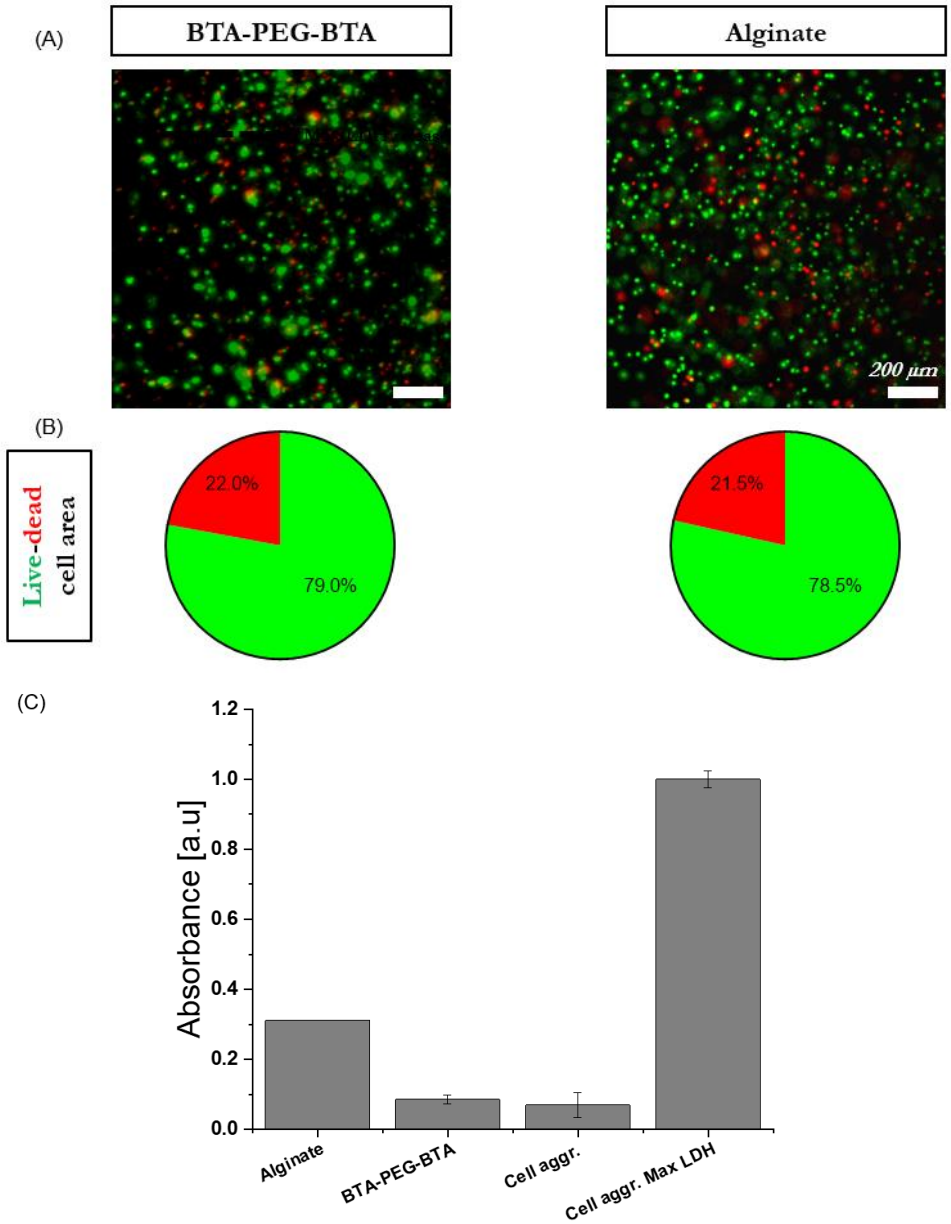

Figure S7. BTA-PEG-BTA and alginate hydrogels were equally effective for culturing chondrocytes. (a) Representative images of chondrocytes (ATDC5) encapsulated within gels after 24 h, stained for calcein (green=live cells) and ethidium homodimer (red=dead cells). The scale bar represents 200 µm. (b) Quantification of the total area of live and dead cells (n = 4 images for each hydrogel condition). (c) Quantification of LDH, a marker of cytotoxicity, after 24 hours of culture. Cell culture data was normalized to the negative control, cell aggregate Max LDH for which the LDH absorbance value is 1. For the negative control, lysis buffer was added to a cell pellet for maximum LDH release.

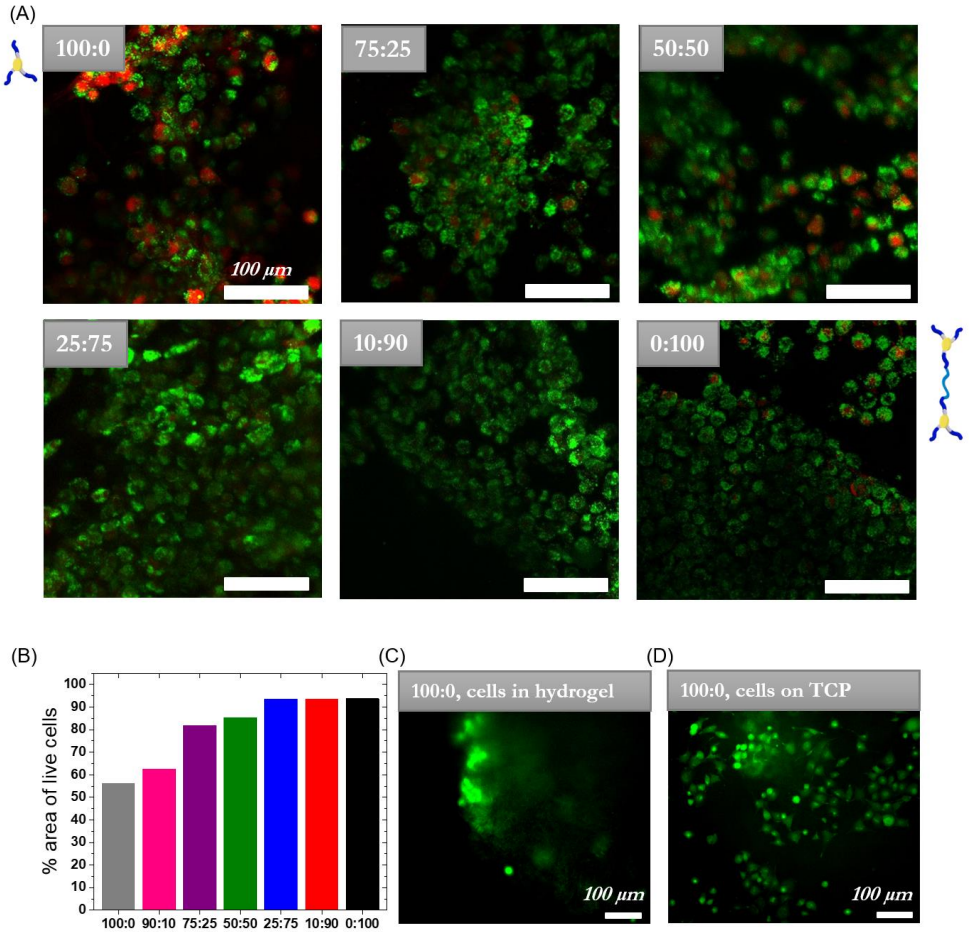

Figure S8. Chondrocytes cultured in chemically dissolved and freeze-dried hydrogels. A) Chondrocytes were cultured for 24 hours, and cells were stained for calcein (green=live cells) and ethidium homodimer (red=dead cells. More dead cells were seen in 100:0 compared to other formulations. B) Quantitative analysis of live-dead cell area. C) Chondrocytes, ATDC5, cultured in 100: using the self-healing method, the green color showed live cells within BTA100:0 hydrogel. D) Not all the cells were retained in the hydrogel due to the poor macroscopic self-healing capacity of hydrogel and chondrocytes released from 100:0 hydrogel and attached to tissue culture plastic while hydrogel sit on top (some pieces of the hydrogel were also floating). Chondrocytes attached to tissue culture plastic also stayed alive in the presence of 100:0 hydrogel demonstrating 100:0 does not kill cells.

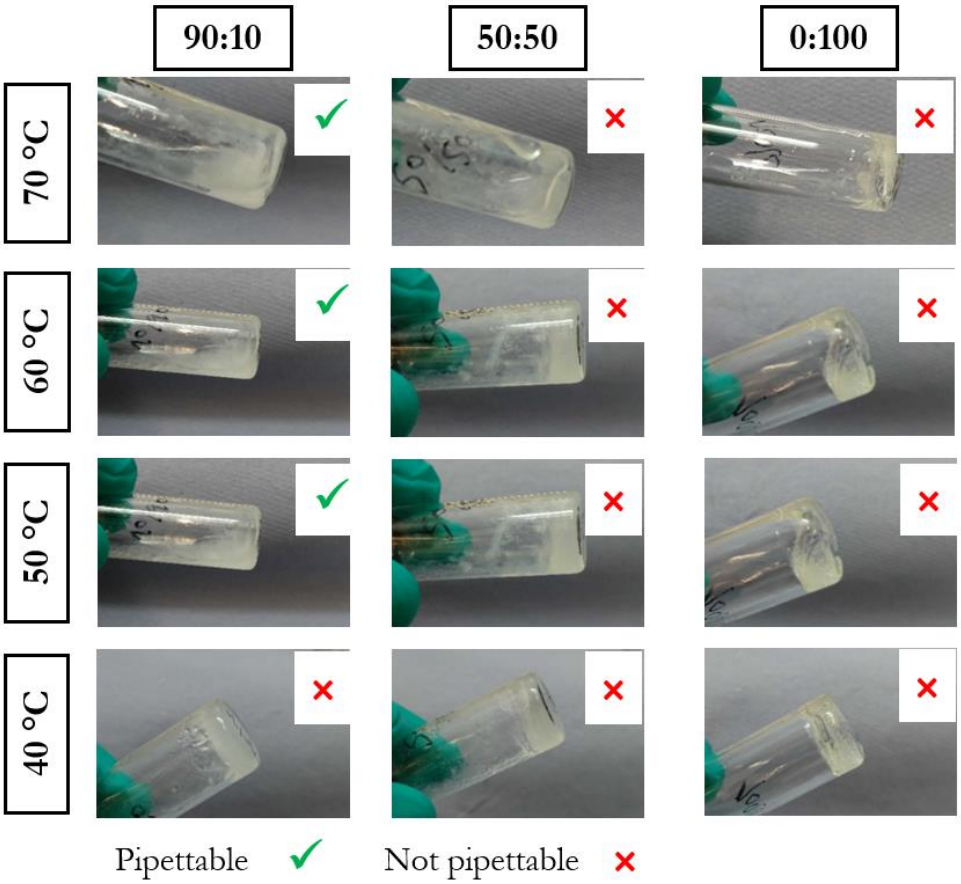

Figure S9. BTA formulation were heated to observe hydrogel to solution transition at different temperatures. We wanted to explore if cells can be encapsulated within gels when gels are in solution form.

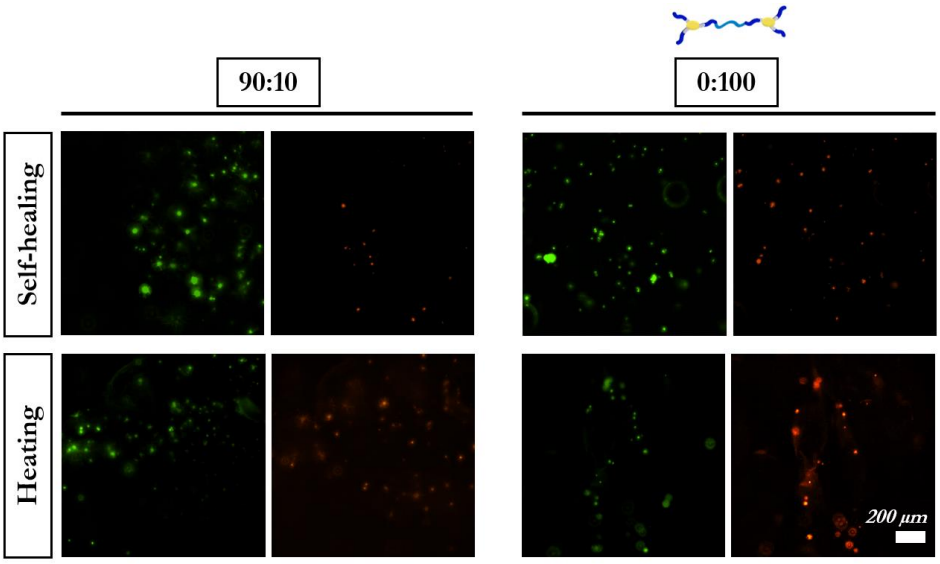

Figure S10. Comparison of the viability of cell encapsulation methods. In the mechanical method chondrocytes cells suspension was mixed with gel using a spatula. Hydrogels were divided into small pieces and then utilizing self-healing capacity cells were encapsulated within hydrogels. In the heating method, hydrogels were heated until hydrogel goes into the viscous solution (80 °C) and then cell suspension was mixed. Upon cooling, the viscous solution will again form the hydrogel. We were expecting the heating method will provide more uniform cell mixing in gels without compromising cell viability. We did not observe improved cell viability and rather it led to new challenges. Heating of the hydrogel was done in a glass vial since the plastic well plate does not support it. For 0:100 we have a very narrow window of a few seconds of mixing and pipetting gel from the glass vial into the well plate since it goes to hydrogel very quickly upon cooling. For 90:10 we have a little broad window of mixing; however, upon introducing hydrogels into the well plate and during the process of gelation, a significant number of cells settle down at the bottom of the well. The heating method did not provide any additional benefit of uniform encapsulation and we stick with mechanical mixing and utilizing the self-healing capacity of hydrogels to mix to encapsulate cells within hydrogels.

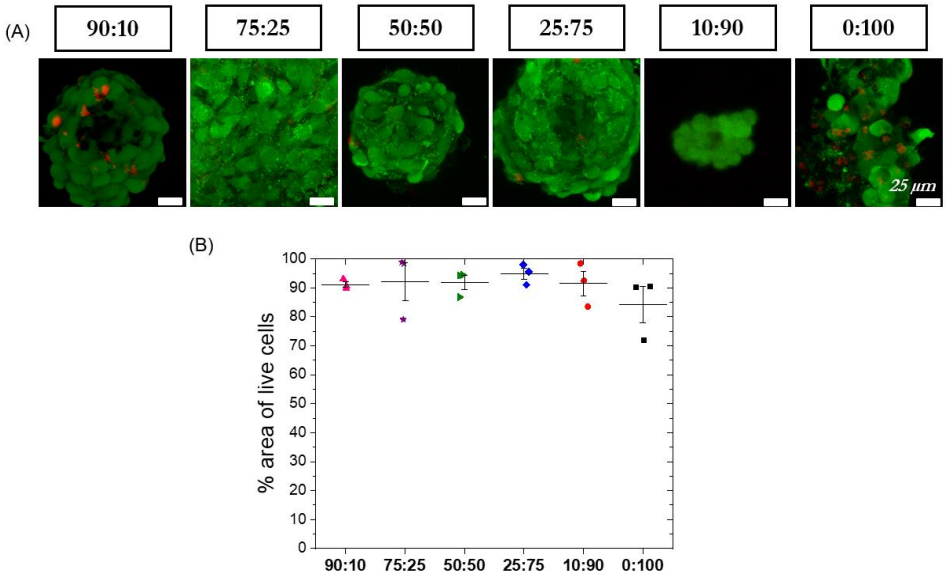

Figure S11. A) Cell viability using live-dead assay. ATDC5 chondrocytes cultured in BTA formulations for 7 days and then stained for calcein and ethidium homodimer, which stain live (green) and dead (red) cells respectively. All formulation showed high cell viability after 7 days in culture.

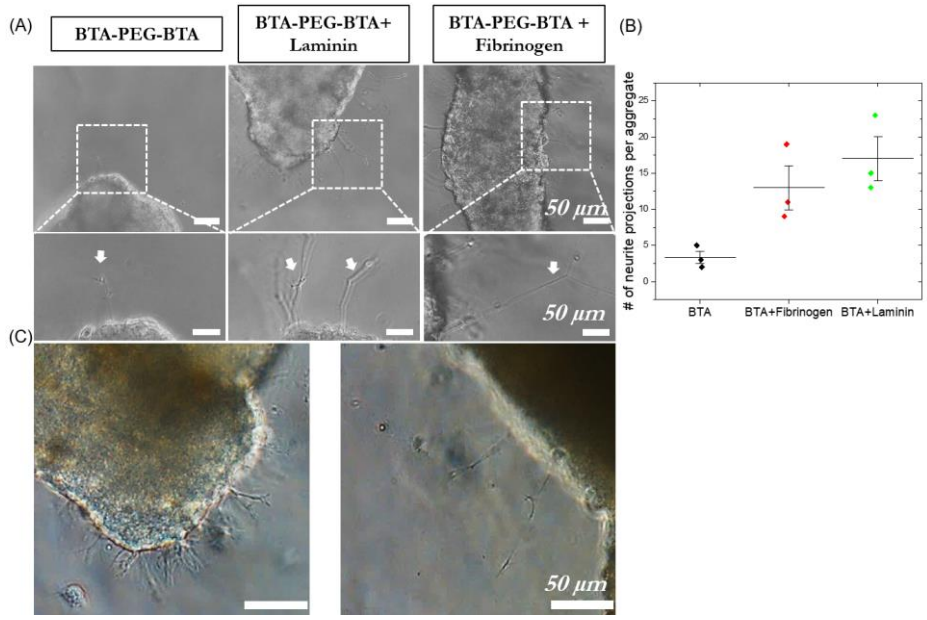

Figure S12. Nerve cell growth in BTA-PEG-BTA hydrogels. A) PC12 nerve cell growth in BTA-PEG-BTA hydrogels after 4 days in culture. Addition of laminin and fibrinogen enhanced outgrowth of nerve cells within BTA-PEG-BTA hydrogels. B) Numbers of neurite growing out of single cell aggregate, three cell aggregate were analyzed per condition, n=3 biological replicates. C) Dorsal root ganglion (DRG) cells growth in BTA-PEG-BTA hydrogel after 2 days in culture showing neurites outgrowth in BTA-PEG-BTA, n=2 biological replicates.

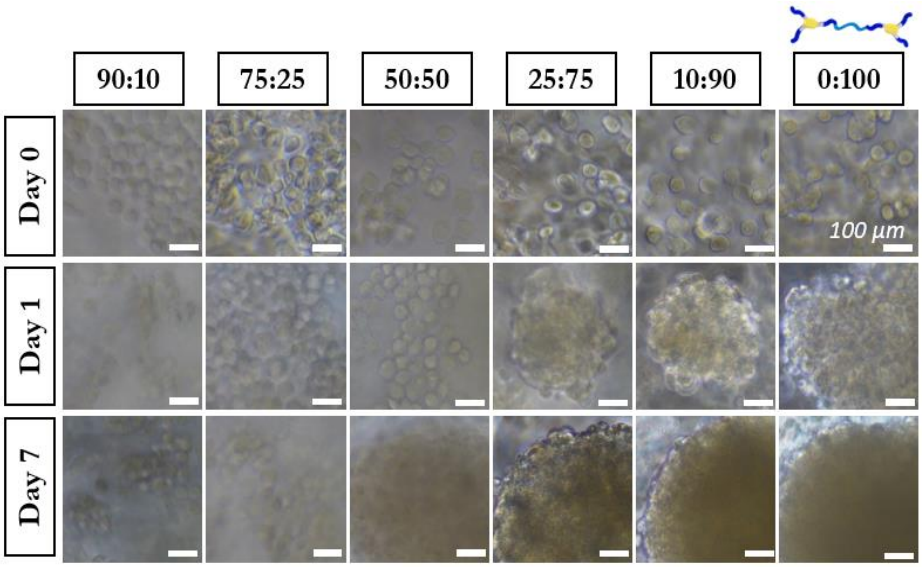

Figure S13. ATDC5 chondrocytes cultured in BTA formulations. Cell forms aggregates within all hydrogels with faster and bigger aggregates in hydrogels with greater percentage of BTA-PEG-BTA. ATDC5 chondrocytes form smaller aggregates in hydrogels with greater percentage of BTA.

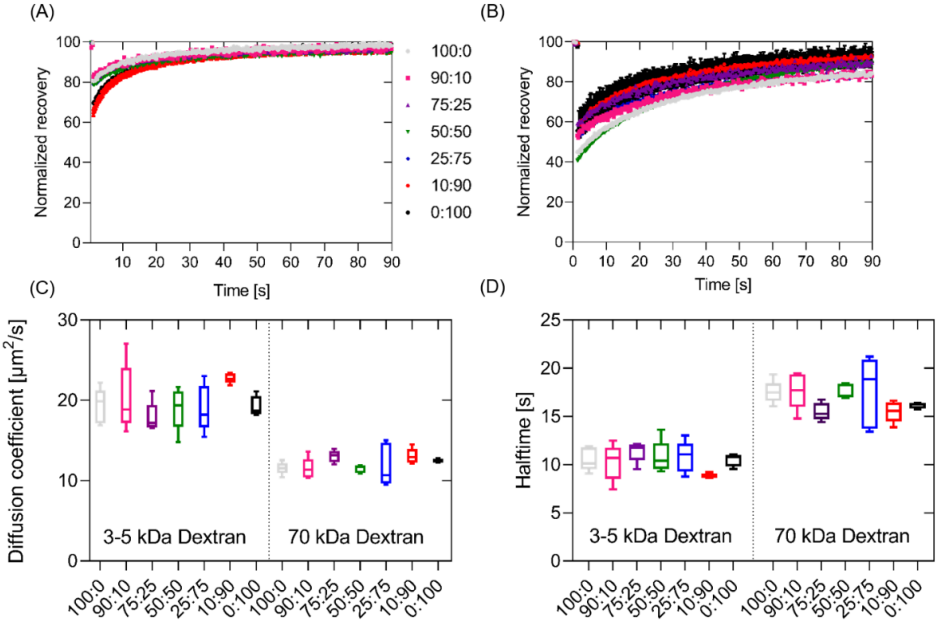

Figure S14. FRAP experiment. Recovery curves after photo bleaching were obtained for A) 3-5 kDa and B)70 kDa FITC-dextran. C) Diffusion halftimes were calculated from the normalized recovery curves and D) diffusion coefficients were calculated via the Soumpasis equation.

Chapter VI

Desymmetrization via activated esters enables rapid synthesis of multifunctional benzene-1,3,5-tricarboxamides and creation of supramolecular hydrogelators

Shahzad Hafeez,[1] Huey Wen Ooi,[1] Dennis Suylen,[2] Hans Duimel,[3] Tilman M. Hackeng,[2] Clemens van Blitterswijk,[1] and Matthew B. Baker[1]

[1] Department of Complex Tissue Regeneration, MERLN Institute for Technology Inspired Regenerative Medicine, Maastricht University, P.O. Box 616, 6200 MD Maastricht, the Netherlands;

[2] Department of Biochemistry, Cardiovascular Research Institute Maastricht (CARIM), Maastricht University, P.O. Box 616, 6200 MD Maastricht, the Netherlands;

[3] Maastricht MultiModal Molecular Imaging Institute (M4i), Maastricht University, P.O. Box 616, 6200 MD Maastricht, the Netherlands.

A revised version of this chapter with the addition of reviewers' comments was published in the **Journal of the American Chemical Society** (2022).

Hafeez, S.; Ooi, H. W.; Suylen, D.; Duimel, H.; Hackeng, T. M.; van Blitterswijk, C.; Baker, M. B. Desymmetrization via Activated Esters Enables Rapid Synthesis of Multifunctional Benzene-1,3,5-Tricarboxamides and Creation of Supramolecular Hydrogelators. *J. Am. Chem. Soc.* **2022**, *144* (9), 4057–4070. https://doi.org/10.1021/jacs.1c12685.

Abstract:

Supramolecular materials based on the self-assembly of benzene-1,3,5-tricarboxamide (BTA) offer an approach to mimic the fibrous self-assembled proteins found in numerous natural systems. Yet, synthetic methods to rapidly build complexity, scalability, and multifunctionality into BTA-based materials are needed. The creation of multifunctional and diverse BTA structures is often hampered by the limited flexibility of existing desymmetrization routes and the purification of multifunctional BTAs. To alleviate this bottleneck, we have developed a desymmetrization method based on activated ester coupling of a symmetric synthon. We created a small library of activated ester synthons and found that a pentaflurophenol (F_5Ph) benzene-1,3,5-activated triester (BTE) enabled effective desymmetrization and creation of multifunctional BTAs in good yield with high reaction fidelity. This new methodology enabled the rapid synthesis of a small library of BTA monomers with hydrophobic and/or orthogonal reactive handles and could be extended to create polymeric BTA hydrogelators. These BTA hydrogelators are self-assembled in water to create fiber and fibrous sheet-like structures as observed by cryo-TEM, and the identity of the BTA conjugated can tune the mechanical properties of the hydrogel. These hydrogelators display high cytocompatibility for chondrocytes, indicating the potential for the use of these systems in 3D cell culture and tissue engineering applications. This newly developed synthetic strategy facilitates the simple and rapid creation of chemically diverse BTA supramolecular polymers, and the newly developed and scalable hydrogels can unlock the exploration of BTA-based materials in a wider variety of tissue engineering applications.

Introduction:

Supramolecular materials offer the ability to build complex and organized materials via directional non-covalent interactions.[1] Natural systems have evolved to rely on these weak supramolecular interactions to provide complex materials functions based on the reversibility and responsiveness enabled by supramolecular interactions.[2] However, the chemical diversity of fully synthetic supramolecular molecules and assembled architectures are relatively simple when compared to the natural world. In order to continue the push toward more complex supramolecular materials, new synthetic methodology (molecular complexity) and assembly strategies (supramolecular complexity) are needed.

For example, recapitulating the complexity of the native extracellular matrix (ECM) in a controllable synthetic system is paramount for the control and guidance of cell-based therapies in applications from drug delivery to tissue engineering. Supramolecular hydrogels offer a decidedly biomimetic solution to create an artificial ECM due to their ECM mimicking fibrous structure, physical interactions, dynamics, and mechanical properties.[3,2] Such supramolecular hydrogels are designed using non-covalent interactions like hydrogen bonding, van der Waals, pi-pi, and hydrophobic interactions, which mimic the physical interactions found between proteins in the native ECM.[2] The specificity and directionality of supramolecular interactions have been used for the creation of fibrous structures similar to the ECM[3] and can enable the tuning of bioactive properties[4]. Furthermore, the self-organization and specificity of supramolecular interactions make it possible to combine different modules/monomers simply by mix and match approach to finely tune materials composition, structure, bioactivity, dynamicity, and mechanical properties on the nanoscale.[4,5,6,1,7,8,9]

Benezene-1,3,5-tricarboxamide (BTA) is a promising supramolecular synthon due to the supramolecular fibril structure in the assembled state, the potential to design multifunctional and multiarm derivatives for increased complexity, and known structure-property relationships via modular modifications.[10,11,9] BTAs can self-assemble into helical, one-dimensional supramolecular polymers via threefold hydrogen bonding and have been utilized in fundamental studies and applications[12] including catalysis[13], polymer reinforcement[14], and vaccine delivery.[15] Water-soluble versions have been shown to form long structurally complex fibers, approximately tens of microns in length and 5 nm in diameter.[16,17,18] At higher weight percentages (2–10 wt%) these water-soluble BTAs can also form hydrogels.[10] Additionally, the BTA core offers the ability to connect different sidearms and different BTA monomers (with various functionality) can be mixed to rapidly create libraries of multicomponent materials with tunable fibril structure, dynamics, and mechanical properties.[10,18,5,19,17] This modularity, fibril structure, and potential for multifunctionality make BTAs ideal candidates for biomateirals[11], especially toward 3D cell culture and tissue engineering applications.

In moving towards BTA-based materials (especially biomaterials), modular, scalable, flexible, and facile synthetic methods are necessary. For example, most BTAs are C3 symmetric, due to ease of synthesis and the symmetry of the core motif; however, non-C3-symmetric derivatives

offer the potential for increased complexity and control over the supramolecular assembly. Desymmetrization, a process to create a non-symmetrical molecule starting from a symmetrical core, is a potential strategy to create multifunctional BTA supramolecular materials. Previous approaches toward the synthesis of multifunctional/multiarm BTA derivatives involve multiple steps and protection/deprotection.[10,20,18,21,22,23] These previous synthetic strategies have enabled the creation of multifunctional BTAs; however, long linear procedures (at least seven steps) and harsh deprotections limit the approach and speed (shown in **Scheme 1**). The challenge remains to devise a strategy that provides the freedom to create multiarm and multifunctional BTA monomers in good yield, under mild conditions, and with a reduced number of steps.

Several strategies in the literature exist for the desymmetrization of a symmetric core (cyanuric chloride[24,25,26], benzene trifurnanone[27,28], and polyphenylene dendrimers[27]). With the aim to form an amide bond during the desymmetrization, we chose to use an activated ester approach, using stable benzene-activated tri-esters which are synthetically accessible and selective to aminolysis. Activated esters for amide bond formation are widely used in polymer and small molecule modifications[30–32], while the electronic coupling across the aromatic ring gave us the potential for kinetic activation/deactivation of the synthon upon reacting.

We aimed to create a simple, yet powerful, desymmetrization strategy to create multifunctional BTAs and polymeric supramolecular hydrogels. We envisioned creating a small library of activated benzene-1,3,5-tricarbonyl triester (BTE) synthons to find a BTE molecule that can 1) shorten the route to desymmetrized BTAs, 2) produce BTA derivatives with multi-functionalities via aminolysis, 3) be selective towards controllable aminolysis, and 4) be stable under common laboratory conditions. Furthermore, we aimed to expand this desymmetrization strategy to create functional macromolecular architectures to be used as hydrogels. Taken together, we hypothesized that a new desymmetrization strategy would allow us to shorten the route for the synthesis of desymmetrized BTAs, allowing the creation of multifunctionality and macromolecular BTA-hydrogels opening up further exploration of BTA-based biomaterials.

Results and discussion:

Activated Benzene-1,3,5-Tricarbonyl Triester (BTE) Library Synthesis:

In attempting to create BTAs of lower symmetry, the most convenient approach would be the desymmetrization of a commercial starting material. Benzene-1,3,5-tricarbonyl trichloride (BTCl) would be an ideal candidate, though the acid chloride functionality would not be envisioned to be stable to purification. Nevertheless, we attempted to react BTCl with one equivalent of hexylamine to investigate its suitability as a synthon (**Figure S1** in supplementary information).

In the absence of side products, the reaction would result in three product molecules (monosubstituted, disubstituted, and trisubstituted) and leftover starting material (upon workup it is expected that the acid chlorides would hydrolyze into acids). Upon ^{1}H NMR analysis of the reaction mixture, numerous peaks appeared in the aromatic region (**Figure S1B** in

supplementary information, 8–10 ppm) and we could not easily obtain useful information on the constituency of the complex mixture formed during the reaction. This result was further supported by a long continuous streak on TLC without distinct spots in the reaction mixture (**Figure S1C and D**). The reaction was run at different temperatures (20, 4, and -75 °C) to see if the temperature could clean up the product profile; however, all attempts resulted in similar peaks on the ^{1}H NMR spectrum. Testing this reaction confirmed our suspicion that desymmetrization via an activated ester approach was the best way forward.

In order to find an alternative to BTCl that can facilitate desymmetrization via aminolysis, the formation of activated esters including aromatic carboxylic esters and thioesters are appealing approaches[33] and have remained unexplored to create BTA derivatives. Aromatic carboxylate esters were determined to be a better choice since they are less susceptible to hydrolysis and more stable compared to thioesters.[34] Commonly employed phenols and N-hydroxysuccinimide, which are commercially available, were chosen for creating a library of activated BTEs (**1–4**, **Scheme 2**)**.** Phenols with differences in pKa value were chosen with pKa of 8.36[35], 7.15[36], 5.4[37], and 6.0[38,39] for 3-nitrophenol ($3NO_2Ph$), 4-nitrophenol ($4NO_2Ph$), 2,3,4,5,6-pentafluorophenol (F_5Ph), and N-hydroxy succinimide, respectively.

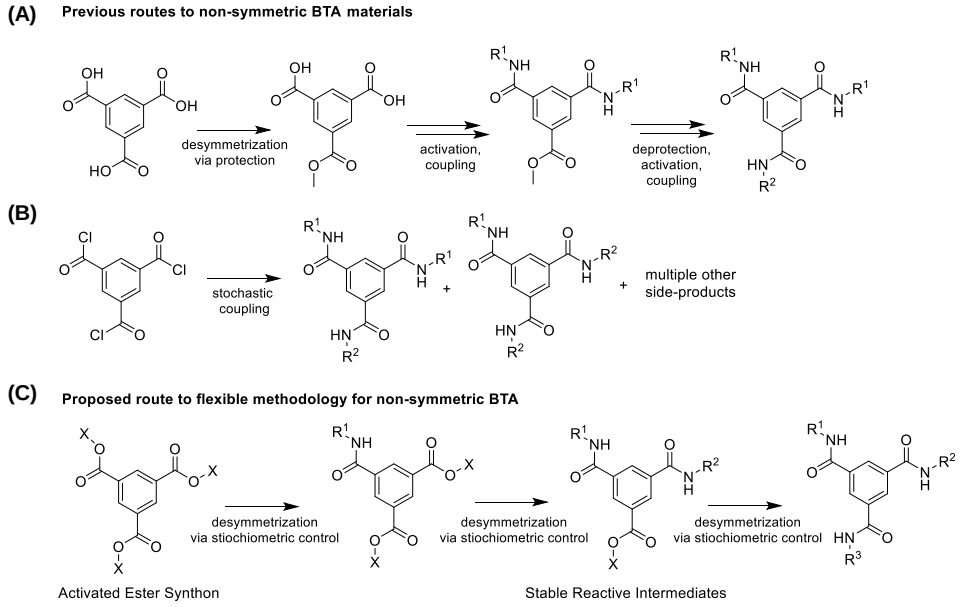

Scheme 1. Synthesis of non-symmetric BTAs are critical for creating functionally diverse supramolecular polymers. Existing routes include: A) desymmetrization via protection/deprotection and functional group conversion, B) stochastic coupling of on symmetric molecule benzene-1,3,5-tricarbonyl trichloride (BTCl) followed by extensive purification. C) A route based on activated ester stepwise coupling with stable intermediates is an attractive synthetic route with greater speed and step economy. For example, the activated ester route developed in this article allowed the creation of an ABC tri-functional BTA in fewer steps (4 steps from commercially available material) and has reduced the total synthetic procedure from weeks to days.

The aim of creating the BTE library was to investigate the ease of synthesis, stability, and desymmetrization potential via controlled aminolysis of BTEs. We started our investigation with the synthesis of nitrophenol-activated esters from BTCl (**Scheme 2**). Both the 3-NO_2Ph and 4-NO_2Ph show limited solubility in many solvents (**Table S1**), yet tetrahydrofuran (THF) was found as a suitable solvent facilitating reaction completion in <6 h. After optimization of purification (**Table S2**) **1** could be obtained in good yield (76%, **Figures S2 and S3**), and **2** could be obtained in excellent yield (92%, **Figures S4 and S5**) by recrystallization. Next, the library was expanded, and we synthesized **3** (**Scheme 2**) by coupling F_5Ph to BTCl. Due to the high solubility of F_5Ph, this reaction could be easily run in DCM in under 4 hours. The reaction was clean, and TLC showed only two spots (R_f ~0 and 0.9). The reaction mixture could be easily passed through a filter to remove the DIPEA salt and then through a bed of silica to yield **3** in 91% yield (**Figures S6 and S7**, for alternative workups see **Table S3**).

Attempting the synthesis of **4** proved problematic. NHS offered limited solubility, aside from THF and DMF (**shown in Table S4**). Running the reaction in DMF produce only non-symmetrical derivatives (based on ^{1}H NMR spectrum **Figure S8**), while running the reaction in THF produced the symmetrical target compound **4**. While TLC analysis of the reaction showed two spots (**Figure S9**), **4** was not able to be fully isolated from free NHS under numerous mobile and solid phases (**Figure S10**). Furthermore, pure **4** was not obtained via crystallization, and during numerous work-up attempts, the ^{1}H NMR evolved extra peaks suggestive of degradation. Importantly, our experiments show that production and isolation of **4** are not straightforward and appear to be very sensitive to degradation during handling.

Desymmetrization of activated BTE synthons

After a mostly successful BTE library synthesis, we moved to investigate the desymmetrization potential of the symmetrical BTEs. Via stoichiometric control, we aimed to maximize the % yield of monosubstituted and disubstituted derivatives. For reference, previous statistical simulations showed a maximum of 37% monosubstituted derivative using one equivalent of the nucleophile[27] for a triply reactive system. Using hexylamine as a model nucleophile, we set out to create a monosubstituted derivative (using one equivalent (per BTE synthon). DMF was found to be the best solvent for **1** (although not fully soluble, **Table S5**), and during the reaction, dissolution occurred (**Figure S11**).

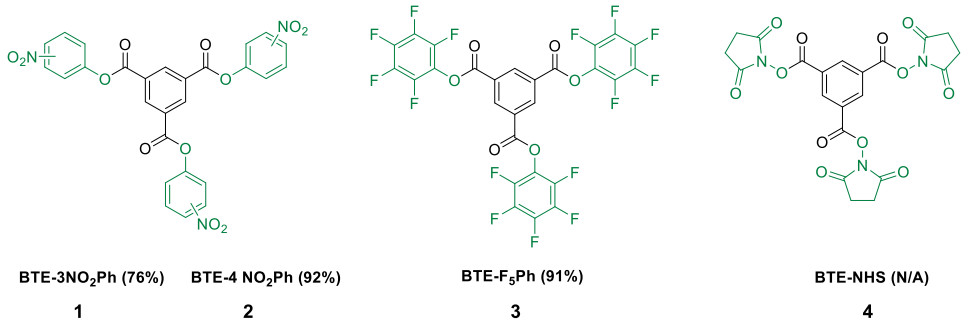

Scheme 2. Library of activated 1,3,5-benzene tricarboxyesters (BTEs) synthesized in this study. Isolated % yields are reported in parenthesis.

In the absence of any side products, desymmetrization of molecule **1** (**Scheme 3** and **Figure S11&S12**) would result in five molecules in the reaction mixture (monosubstituted, disubstituted, trisubstituted, free phenol, and remaining **1**). TLC of the reaction mixture of **1** showed three spots suggesting that some products were not formed or only formed in small amounts (**Figure S11C**).

Reaction mixtures resulting from the substitution of molecule **1** were partially soluble in DCM and the products could be isolated via column chromatography, though **7** and the trisubstituted BTA could not be fully resolved. ^{1}H NMR analysis (chemical shift, peak splitting pattern, and integration analysis of peaks) was used to identify the compounds (**Figures S13 and S14**). Most importantly, this separation allowed us to identify the complex aromatic peak splitting found in the reaction mixture and assign peak patterns to the mono-, di-, and tri-substituted derivatives (doublet and triplet at 8.95 and 8.92 ppm for **5**, doublet, and triplet at 8.70 and 8.65 ppm for **7**, and singlet at 8.34 ppm for the trisubstituted BTA).

With the knowledge of proton chemical shift and peak splitting pattern of products, we were able to analyze the crude reaction mixtures (**Figure S12** for 1 equiv) and quickly determine the relative amount of the products in the reaction mixture. Molecule **1** produced a 57% yield of **5** (monosubstituted) when treated with 1.0 equiv nucleophile. The desymmetrization of **2** behaved similarly (**Figure S15&S16**), and after separation and characterization, the crude reaction mixture produced a 38% yield of **6** (monosubstituted derivative, **Figure S16–17**). Interestingly, **1** produced the monosubstituted product significantly higher than statistically calculated, while **2** produced almost equal to statistically predicted. When the same reaction was run for two equivalents of hexylamine, **1** produced **7** (disubstituted) in 35% yield (**Figure S14**), and **2** produced **8** in 54% yield. Interestingly both produced disubstituted derivatives roughly twice than statistically predicted, which is 28% using two equivalents of the nucleophile.[27]

With promising results, we then turned to desymmetrization of the Penta-fluorophenol synthon, **3**. After running the reaction with 1 equiv of hexylamine in DCM, the crude reaction mixture showed five spots on TLC (**Figure S19**), which were isolatable via column chromatography. After ^{1}H NMR analysis, we were able to determine the ratio of substituted derivatives in the

crude reaction mixture (a similar pattern of doublet/triplets and singlets was observed as in the desymmetrization of **1**). Peak integration from the ^{1}H NMR spectrum of the crude reaction mixtures showed that **3** produced 49% of **9** (**Figures S20&S21**) and 53% of **10** (**Figures S22&S23**) using one and two equivalents of hexylamine, respectively. Both desymmetrization reactions yielded higher than statistical yields and the products were able to be readily isolated via column chromatography.

When developing a reactive synthon for desymmetrization, stability, and scalability are also important factors to consider. Both **1** and **2** were stable in a desiccator when stored for a year; however, upon handling in the lab over 2–3 months both molecules started to hydrolyze (^{1}H NMR). We did observe that **1** was more stable than **2**. In comparison, **3** showed excellent stability in the lab; it was found to be stable for more than two years, even after open handling in a humid environment (the Netherlands). Purification of **1** and **2** required a large volume of solvents owing to limited solubility (100s of mL for 10s of mg), while **3** offered a short one-step workup with good solubility.

Due to its ease of synthesis, stability, desymmetrization, and purification, **3** was determined to be the best candidate to work with moving forward. We found **3** was stable over years under an inert atmosphere, stable in the humid environment of the lab, purified in a short one-step workup, easily scaled to gram scale, showed good solubility in low boiling point solvent, and showed straightforward NMR analysis. Furthermore, the stability of the F_5Ph esters on **3** also offers easy separation of desymmetrized intermediates using flash column chromatography.

Desymmetrization of BTE-F_5Ph (3)

In order to investigate if temperature affected the product outcome in the desymmetrization of **3**, we attempted the desymmetrization at different temperatures. Using the one-mole equivalent of hexylamine, **9** was made in 50% yield at 4 °C (**Scheme 4 and Figure S20&21**), and this yield remained 50% when the reaction was run at -78 °C. Interestingly, the producing the disubstituted derivative **10** (**Scheme 4 and Figure S22&23**) from two equivalents of amine resulted in 53% and 65% yield at 4°C and -78°C (**Table S6**), respectively, showing a small temperature influence on the second aminolysis. In these test reactions, we observed only a small (5–10%) decrease in the yield after separation using a silica hydrogel flash column, resulting in an isolated yield of 40% (**9**) and 48% (**10**).

In order to test the applicability of the reaction methodology to different amine-based nucleophiles/side-arms, we attempted a few different amines. Dodecylamine resulted in a maximum 39% yield of **11** (monosubstituted derivative, 1 equiv amine, **Scheme 4 and Figure S24&S25**) and 56% yield of **12** (disubstituted derivative, 2 equiv amine, **Scheme 4 and Figure S26&S27**) at 4 °C (**Scheme 4**). There was little change in the product profile when running at -78 °C, and the isolated yields again showed the stability of the activated ester to handling and purification (e.g. 49% isolated yield for **12**). The desymmetrized synthons (**9**, **10**, **11** and **12**) were found to be stable over months under an inert and dry atmosphere in a desiccator at room

temperature, indicating the potential for storage and resumption of synthetic pathways towards multifunctional BTAs.

After successful desymmetrization using simple hydrophobic sidearms, we next explored more functional side arms. Monosubstituted and disubstituted derivatives with 5-Norbornene-2-methylamine (5Nb-2MA, **Scheme 4** and **Figure S28**) were targeted using one and two-mole

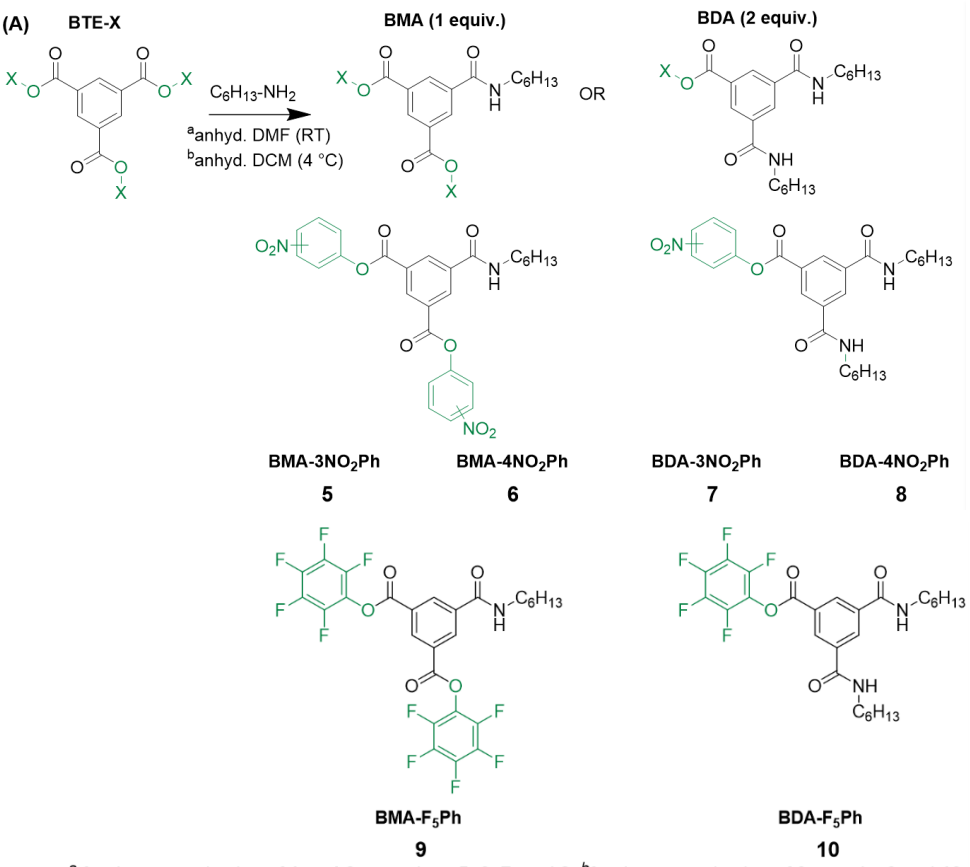

[a] for desymmetrization of **1 and 2** to produce **5**, **6**, **7**, and **8**. [b]for desymmetrization of **3** to make **9** and **10**

(B)

Activated 1,3,5-benzene tricarboxyesters **(BTE-X)**	Amine nucleophile: **Hexyl (C_6H_{13})**	
	BMA (%), 1 equiv.	**BDA (%)**, 2 equiv.
BTE-3NO_2Ph **(1)**	57 **(5)**	*35 **(7)**
BTE-4NO_2Ph **(2)**	38 **(6)**	54 **(8)**
BTE-F_5Ph **(3)**	49 **(9)**	53 **(10)**

Scheme 3. Investigating desymmetrization of activated BTEs via controlled aminolysis using hexylamine. A) All BTEs are successfully desymmetrized. B) Reaction yields are reported in the table and calculated from 1H NMR integration analysis. Molecules **7–10** could be obtained pure; however, molecule **5** and 6 were not stable to purification. *difficulty with stoichiometry control attributed to instability of **1**.

equivalents to produce **13** and **14**, respectively. Conveniently, **13** (**Figures S29&S30**) and **14** (**Figures S31&S32**) were produced in 50% and 70% yield (via ^{1}H NMR integration). Going further, we explored if an amine nucleophile would show selectivity over a hydroxyl nucleophile when in competition for the activated ester. To investigate this, **3** was desymmetrized using one equivalent of 6-amino-1-hexanol (**Figure S33**) and we find that the amine selectively acted as a nucleophile over the hydroxyl. ^{1}H NMR analysis showed that 40% of the molecules were monosubstituted, and no traces of the hydroxyl-substituted core were observed.

Multifunctional BTA derivatives synthesis:

With the confidence that we could install different sidearms and functionalities on BTA using this activated ester methodology, we moved to create BTA derivatives with different side arms. Monosubstituted **11** was utilized and desymmetrized further, producing **15** with one dodecyl and one hexyl sidearm (**Scheme 5** and **Figure S34–S36**). This reaction resulted in a 60% yield based on ^{1}H NMR analysis and 50% isolated yield. Next, we created a molecule with one hydrophobic sidearm and one reactive functionality (norbornene), which could later be utilized for thiol-ene, norbornene-tetrazine, or ROMP polymerization. From **9**, **16** was made (**Scheme 5 and Figure S37&S38**) in 61% yield by ^{1}H NMR and 44% yield isolated. Important to note that in both of these reaction pathways the starting monosubstituted **9** and **11** are recovered around 10–15% and can be utilized in future reactions; thus, the isolated yield based on recovered starting material approaches 60%.

Knowing that we can create a multifunctional di-substituted derivative, next we wanted to create tri-substituted BTA derivatives. We utilized **12** with two dodecyl side arms and reacted the last activated ester to either 5Nb-2MA or 3-azido-1-propanamine to create functional BTAs **17** and **18** (**Scheme 6**) with orthogonally reactive handles. After an overnight (16–20 hours) reaction in DCM, ^{1}H NMR analysis showed a 100% conversion of **12** to both **17** (**Figures S39&S40**) and **18** (**Figures S41&S42**). The isolated yield (from **12**) for **17** and **18** was 87% and 85%, respectively, while the linear two-step yield (starting from **3**) was 42% and 40%, respectively. This shows that the high fidelity desymmetrization can be expanded to functional handles, and potential can be utilized to attach biological molecules, probes, and effective post-assembly modifications of resultant supramolecular polymers.

Finally, we aimed to create a fully desymmetrized ABC-type BTA in order to test the full desymmetrization efficiency. In three steps, we synthesized BTA **19** (starting from **16**) with a hydrophobic sidearm (hexyl), norbornene sidearm, and azide sidearm (**Scheme 6**) as orthogonal functionalities. After separation **19** was obtained in 85% isolated yield (**Figure S43&S44**). Starting from symmetrical **3** to create **19** the full linear yield of the reaction was 31% by ^{1}H NMR and 24% by mass. This approach doubles

the yield (12%) afforded by already existing desymmetrization routes to create ABC BTA.[18,21] This represents the first linear and general approach towards fully desymmetrized BTAs, and this approach is envisioned to work with a wide variety of amine sidearms due to the high fidelity and mild reaction conditions.

Molecular design and synthesis of polymeric BTA (BTA-PEG20K-BTA)

Next, we moved to explore if the developed methodology could be employed for the rapid and facile creation of polymeric supramolecular macromolecules in addition to the small molecules presented above. Towards this aim, we wanted to employ our new methodology to create a small library of telechelic BTA-PEG-BTA polymers to be used as potential hydrogelators and 3D environments for cell culture. Previous work showed that a hydrophobic spacer is required to protect the BTA amides in an aqueous environment, and BTAs undergo self-assembly via hydrogen bonding and hydrophobic interactions to form long fibrils.[16,20] Previous studies on telechelic BTAs have also shown that a minimum of an eight-carbon hydrophobic spacer was needed for stable hydrogel formation;[10] however, the ability to vary the outer side arm on these hydrogelator architectures has been limited by the previous methodology.

(A)

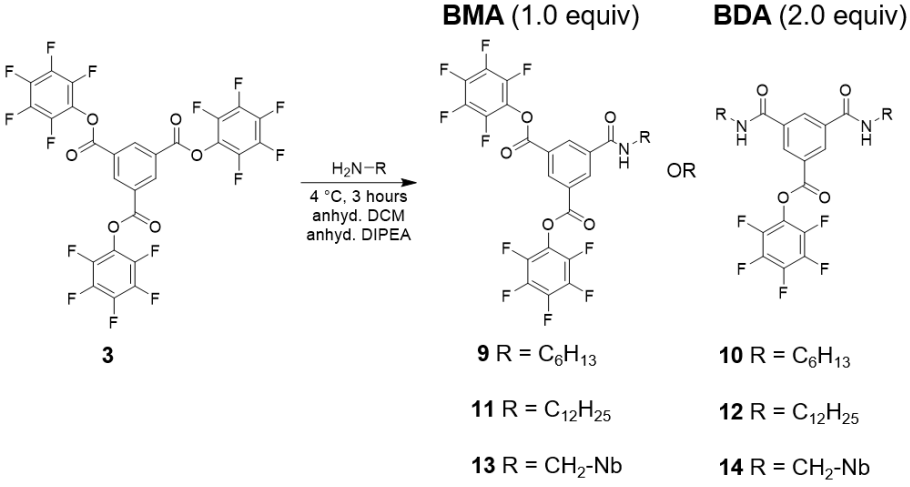

(B)

	Amine nucleophile (R)		
	Hexyl (C_6H_{13})	Dodecyl ($C_{12}H_{25}$)	CH_2-Nb
BMA (%)	49 **(9)**	39 **(11)**	50 **(13)**
BDA (%)	53 **(10)**	56 **(12)**	70 **(14)**

Scheme 4. Desymmetrization of synthon 3. A) Desymmetrization was tolerant to aliphatic amines such as hexylamine (C_6H_{13}), dodecylamine ($C_{12}H_{25}$), and methyl norbornene (CH_2-Nb). B) Reported % yield of BMA and BDA molecules formed during a reaction, derived from ^{1}H NMR integration analysis.

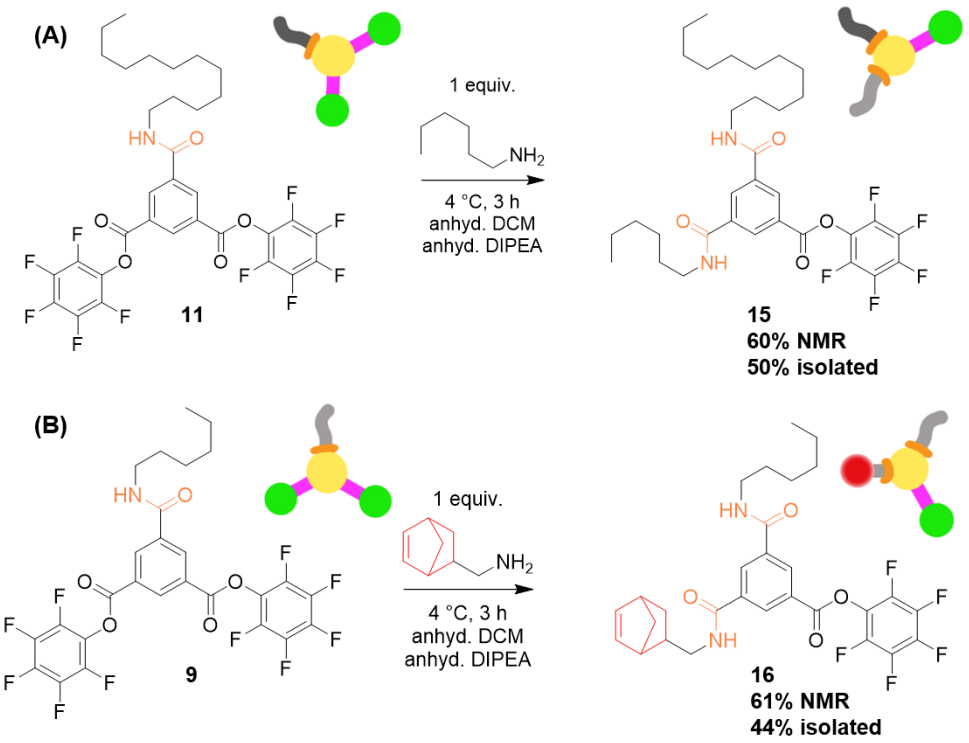

Scheme 5. A) Molecule **15** with dodecyl and hexyl aliphatic side-arms was synthesized by desymmetrizing molecule **11** using hexylamine. Molecule **15** was obtained in 60% yield by ^{1}H NMR integration analysis B) Molecule **16** was synthesized by desymmetrizing molecule **9** using 5-Norbornene-2-methylamine. Molecule **16** was obtained in 61% yield by ^{1}H NMR integration analysis. Norbornene is a light active functionality and offers the potential to be employed later for attaching biological molecules.

In our design, we chose dodecyl as a hydrophobic spacer between BTA and PEG20K and varied the outer sidearms on the BTA. Amine end-functionalized PEG with dodecyl as an internal spacer (bisaminododecane PEG20K, **Figure S45&S46**), was created by conjugating dodecyl diamine to PEG20K diol using carbonyldiimidazole (CDI) chemistry. A small library of BTA hydrogelators (**20**, **21,** and **22**) with C_6 sidearms (**20**), mixed C_6 and C_{12} sidearms (**21**), and C_{12} sidearms (**22**) was generated by coupling bisaminododecane PEG20K to **10**, **15**, and **12** (**Scheme 7**). Important to note that this newly developed methodology not only allowed the rapid variation of outer sidearms on the BTA, but also allowed the creation of macromolecular BTA **21** with mixed outer side arms hexyl (C_6) and dodecyl (C_{12}).

All telechelic architectures were obtained with more than 95% yield, showing the high fidelity of the final pentafluorophenol ester for conjugation to macromolecules. ^{1}H NMR showed that all polymers are pure and have a high degree of functionalization 81%, 67%, and 78% for hydrogelator **20**, **21**, and **22**, respectively (**Figure S47–49**). GPC analysis confirms showed that all hydrogelators have weight average molecular weight around (M_w) around 23 kg/mol with a PDI of 1.2 (**Table S7**). With this new methodology, we were able to make new telechelic BTA

architectures on a multi-gram scale in under two weeks, which indicates the rapid large-scale capability of the designed methodology.

Self-assembly studies

With the small library of telechelic BTA supramolecular macromolecules in hand, we wanted to explore the self-assembly of these materials and their potential use as hydrogelators. Previous studies have shown that, successful BTA assembly in water requires a hydrophobic pocket formation to facilitate amide stacking and stable aggregate formation.[16] Consequently, we initially utilized a Nile red assay to investigate the hydrophobic pocket formation upon assembly. In pure water, Nile red shows very low intensity, and the fluorescence intensity increases in more apolar environments.[40] Self-assembly of BTA has been shown to increase the fluorescence intensity of Nile red owing to the hydrophobic pocket formation.[16,5] In dilute solution, we observed an increase in fluorescence with increasing hydrophobic length on the exterior of the BTA (**Figure 1A**), suggesting an increase in the size and volume of the hydrophobic pocket. The fluorescence intensity increased twice when the hydrophobic length was doubled on a single BTA unit (hydrogelator **20** to **22**). The maximum fluorescence intensity wavelength (λ_{max}) can be indicative of the polarity of the hydrophobic pocket. For all tested concentrations 1 (45 μM), 2 (90 μM), and 5 mg/ml (230 μM) of telechelic BTA hydrogelators (**Figure S50**), the maximum fluorescence intensity stayed constant at 621 nm with a small 4 nm red shift for **22** going from 1mg/ml to 2mg/ml (**Figure 1B**). This result suggests that all hydrogelators adopt a similar

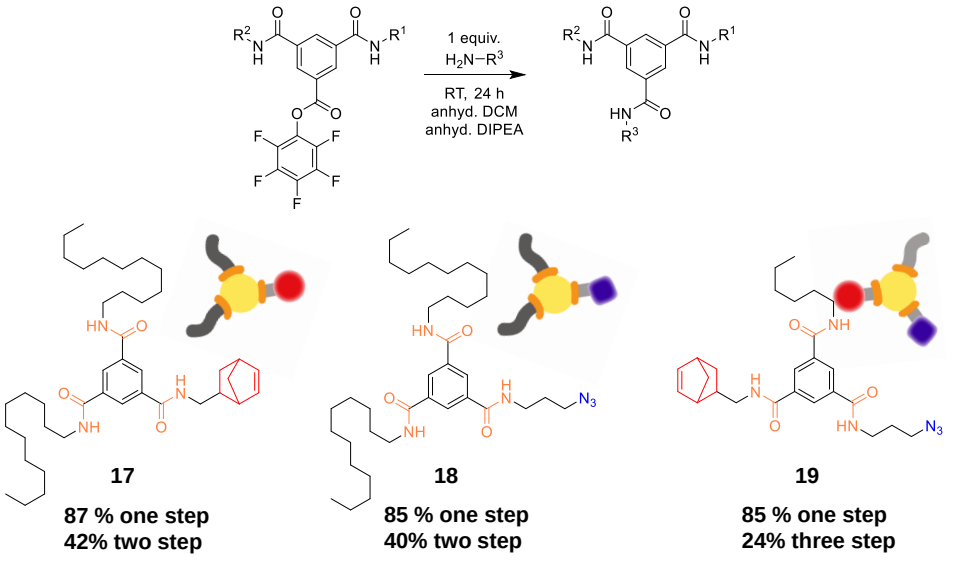

Scheme 6. Final step towards the production of non-symmetric BTAs. Partially desymmetrized BTAs **17** and **18** were synthesized using **12** and attaching methyl norbornene or propyl azide. Fully desymmetrized, ABC type BTA **19** was synthesized by coupling propyl azide to molecule **16**. Such multifunctional azide and norbornene BTAs can be used to functionalize supramolecular fibers or individual BTAs.

polarity hydrophobic environment upon BTA aggregation,[16] with differences mostly in hydrophobic pocket size.

With confidence from the Nile red experiments that the BTAs formed a hydrophobic pocket via aggregation, we moved to investigate the morphology of the aggregates in solution. Cryogenic transmission electron microscopy (cryo-TEM) was employed to investigate the BTA hydrogelator structure in a dilute solution (**Figure 1 C**). Moving up the series, we observed that the fibers became more sheet-like and longer with increasing hydrophobic character on the outside of the polymer. Hydrogelator **20** showed thin fibers between 5–10 nanometers in diameter, **21** showed fibrous sheets with a diameter between 20–60 nanometers, and **22** showed fibrous sheets of diameter around 150 nanometers which consist of nanofibers resting parallel and next to each other. Hydrogelator **20**, **21**, and **22** are a couple of hundred nanometers long. The diluted hydrogel of **22** in water in a similar concentration range as dilute solutions (10mg/ml) showed fibrous sheets of diameter between 40–150 nanometers and several micrometers long (**Figure S51**). All the macromolecular hydrogelators showed successful self-assembly in dilute solution. Furthermore, the self-assembly resulted in the formation of fibrous structures, which can start to mimic ECM fibrous morphology as seen in collagen and fibrin.

Hydrogel formation and critical gelation concentration (CGC)

First, we assessed the ability of the telechelic BTA supramolecular macromolecules to form a hydrogel in water. To this end, we formed 10 % (w/v) hydrogels via a successive (3x) heat/cool procedure. A final heat/cool cycle on a heating plate (80 °C) with slow cooling to 20 °C was employed to facilitate controllable hydrogel formation. Next, we were interested to determine the critical gelation concentration (CGC), via a qualitative vial inversion (no flow under 30 seconds). We found that CGC depends on the hydrophobic length; architectures with more hydrophobic exteriors result in lower CGC. As shown in **Figure S52**, hydrogelator **20** and **22** showed CGC ~5% and ~2.5% (w/v). The difference in CGC indicates the importance of the hydrophobic pocket on the formation of a hydrogel at low concentrations, this two-fold higher CGC is conspicuously mirrored by the two-fold higher Nile red intensity seen above. Taken together, we can conclude dodecyl spacer resulted in larger hydrophobic pocket formation and stable aggregate formation, which provide more stability to hydrogels. Interestingly, the asymmetric hydrogelator **21** showed the lowest CGC of 1.42% (w/v), however, the exact reason remains to be unknown. Such fully desymmetrized architectures are potentially interesting for future studies.

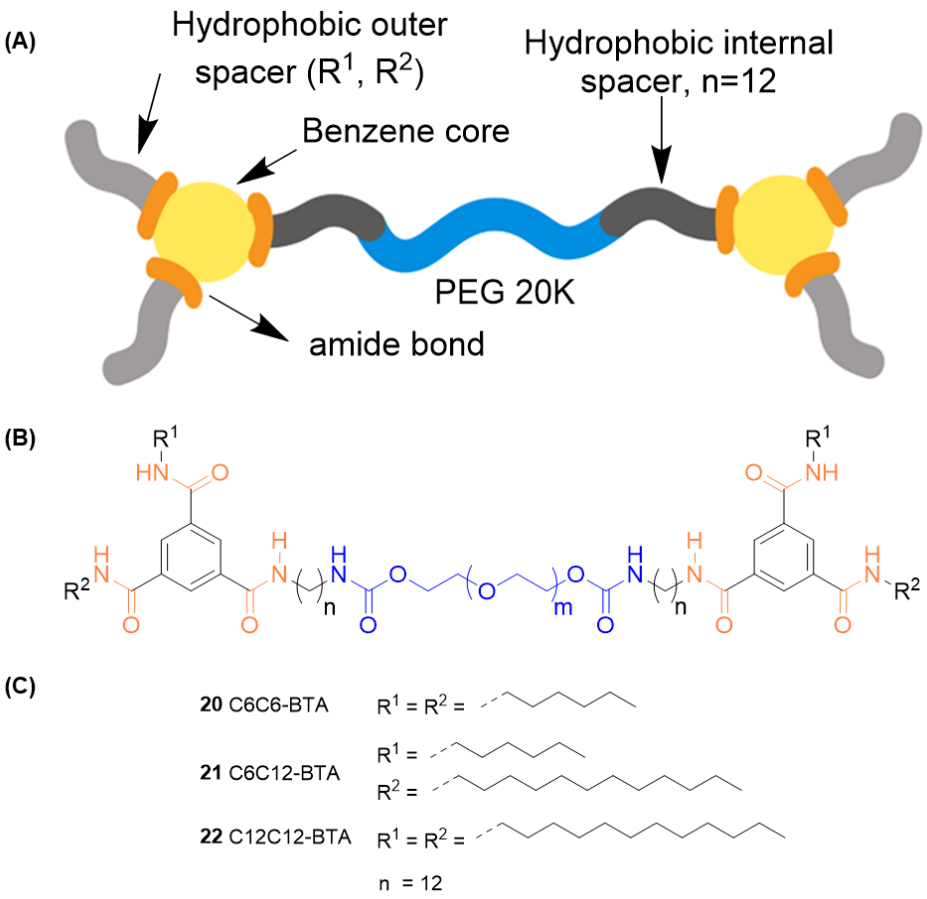

Scheme 7. A) Schematic representation of macromolecular hydrogelators targeted in this study. B) Chemical structure of BTA hydrogelator made by connecting two small molecule BTAs with PEG 20K, and C) Hydrophobic side groups employed to create hydrogelators **20**, **21** and **22**.

Mechanical properties of hydrogels

Next, we set out to investigate the mechanical properties of the resultant hydrogels. First, we qualitatively investigated the flow behavior of the hydrogelators with the vial inversion test. As shown in **Figure 2A&S53**, the hydrogelators flowed (or did not flow) on different timescales, from minutes (**20**) to no flow after 72 hours (**22**). A significant difference in flow behavior suggests that these hydrogels have different viscoelasticity.

In order to investigate the storage moduli and dynamic mechanical properties of these hydrogels, we turned to cone-plate rheology. A frequency sweep was performed at 1% strain, within the linear viscoelastic region. As seen in **Figure S54**, all hydrogelators showed nearly identical equilibrium shear storage moduli around 10,000 Pa. The similar equilibrium storage modulus of these materials would suggest a similar topology or morphology of the hydrogels, as the cross-link density remains relatively constant at a given concentration between the series. Interestingly,

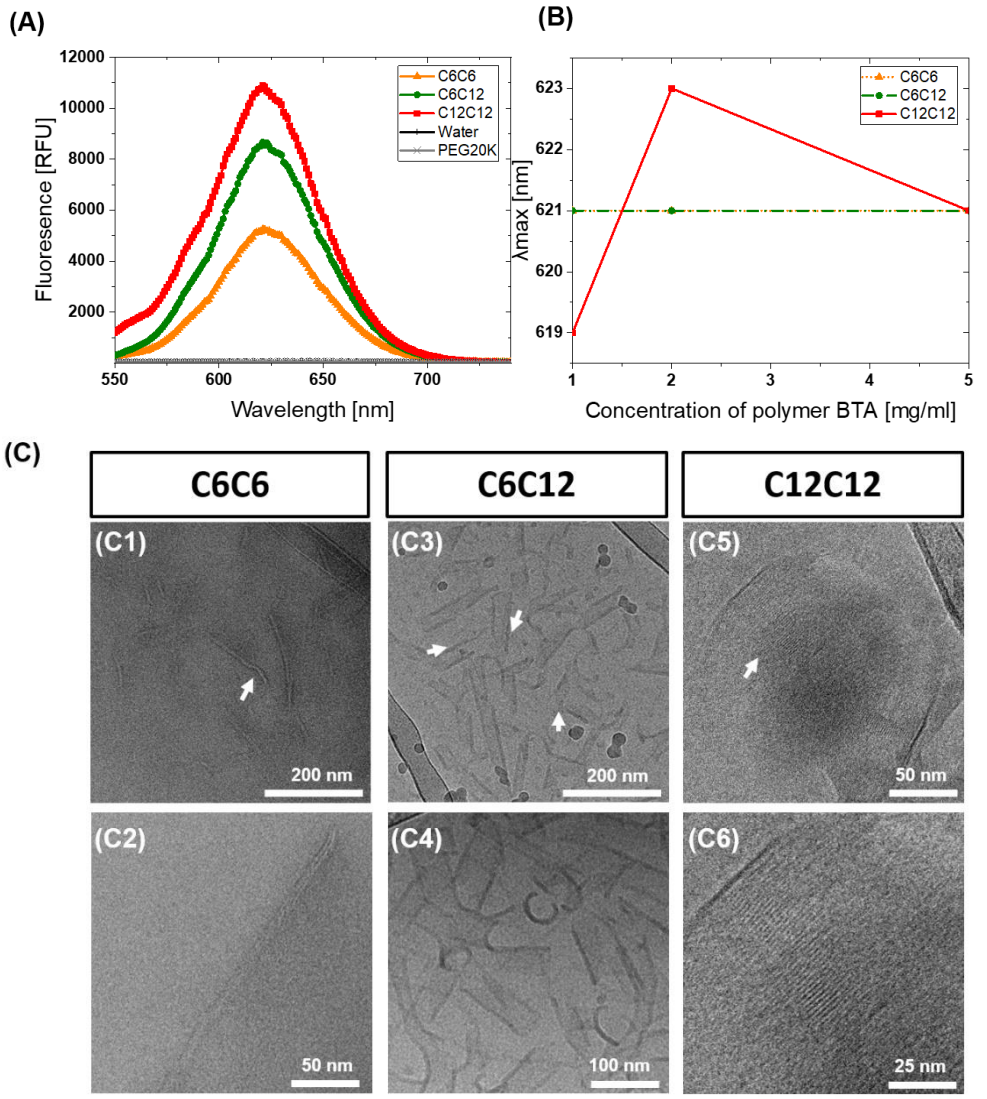

Figure 1. Dilute solution self-assembly studies: A) Nile red encapsulation shows an increase in fluorescence intensity from the C_6 to C_{12} hydrogelators (5 mg/ml, 230 μM), B) The lambda max (λmax) of encapsulated Nile Red at 1, 2, and 5 mg/ml showed minimal changes across the hydrogel series, suggesting a similar strength of the hydrophobic environment. C) cryo-TEM images showing the fibrous self-assembly morphology for hydrogelator **20** and fibrous sheet-like morphology for **21** and **22**.

the viscoelastic properties of the hydrogel changed greatly as a function of the side arms. Hydrogelator **22** showed a storage modulus largely independent of frequency across almost five decades, while hydrogelators **20** and **21** responded dynamically to applied shear; the storage moduli increased from low to high frequency and plateaued (**Figure S54**). While the similar

equilibrium storage moduli indicated a similar internal structure to the hydrogel, the differences in the viscoelastic behavior suggested differences in internal dynamics.

Self-healing and moldability:

Due to the reversibility of supramolecular interactions, we wanted to test the self-healing behavior of these hydrogels. The self-healing behavior was visualized by cutting a macroscopic hydrogel disc in two pieces and then compressing two pieces of hydrogel together. All hydrogelators showed excellent self-healing properties under a few minutes at room temperature (**Figure 2B& S55**). Next, we studied the moldability of hydrogels. The hydrogel was transferred from a round mold to a square mold. For hydrogelator **20**, the hydrogel flowed quickly, under one minute, and filled the square mold (shown in Figure **S55A**). For hydrogelators **21** and **22** (**Figure 2B**), we had to compress the hydrogel using a spatula to take the shape of a square. This suggests the responsive nature of hydrogels to external forces and the ability to adapt to different shapes under stress. Such hydrogels with the ability to take the desired shape may find applications to fill the voids resulting from damaged tissues after injury or cavities after surgical operations.

Self-healing behavior was quantitatively investigated using oscillatory rheology by applying high and low-strain shear rupture cycles. During a strain sweep, hydrogelator **20** behaved like a liquid (G”>G’), and hydrogelator **21** and **22** showed a crossover point around 100% and 20% strain, respectively (**Figure 2C**). The storage moduli recovered 80% and 100% for hydrogelator **21** and **22** under tens of seconds (**Figure 2D**). We also observed that **22** increases slightly in storage modulus after each strain cycle, which perhaps could be due to slippage of material at such high strain or owing to residual stresses. Rapid recovery of storage moduli indicates rapid self-healing behavior, dynamicity, and reversibility of cross-links in BTA hydrogelators.

Cell viability:

Using the newly developed methodology, we were able to create scaleable and tunable fibrous hydrogels which could be considered as suitable ECM mimics. Ultimately, we would like to use this methodology and similar hydrogel architectures for 3D cell culture and tissue engineering applications. Though dilute solutions of BTAs have been used in the presence of cells before[41], BTA materials and hydrogels have only limitedly been investigated for their cytocompatibility[11] and never in 3D encapsulation. Consequently, we wanted to quickly explore cell encapsulation and viability in these materials. Dynamic and viscoelastic matrices have been shown to greatly affect chondrocyte proliferation and cartilage-like matrix production.[42,43] We chose to use chondrocytes (ATDC5) as they are important cells for the investigation of enhanced chondrogenic differentiation and a cell line model to study cartilage tissue regeneration.[44]

ATDC5 could be encapsulated within 10% (w/v) hydrogels via a mixing protocol that leverages the self-healing nature of the hydrogels. To investigate cell viability, we utilized the live/dead staining where cells were stained calcein (green) and ethidium homodimer (red) after four days. The large majority of cells stayed alive within these hydrogels after mixing and over four days

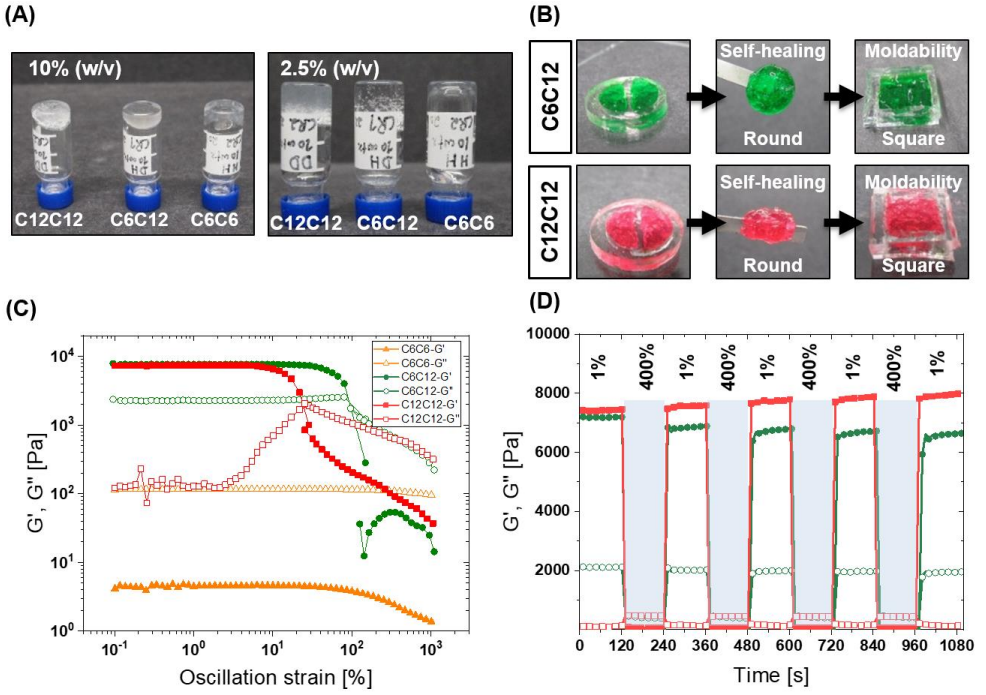

Figure 2. Mechanical properties of hydrogels and viscoelasticity. A) All BTA supramolecular macromolecules form hydrogels at 10% (w/v). Vial inversion test showed exterior hydrophobic dependent critical gelation concentration. B) Hydrogels are self-healing when two cut pieces of hydrogel are pressed against each other. Hydrogels can be remolded into different macroscopic shapes by pressing with spatula, for example round hydrogel can adapt square shape (green C_6C_{12}; red $C_{12}C_{12}$). C) In the strain sweep C_6C_{12} and $C_{12}C_{12}$ are observed to have the same moduli, with a greater linear viscoelastic regime for C_6C_{12}. At this frequency (1 rad/s), C_6C_6 was mostly liquid. D) Hydrogels are self-healing under shear rheology. After rupture, the materials quickly recover to initial moduli in just few seconds. C_6C_{12} is in green and $C_{12}C_{12}$ is in red color. Rheology samples were measured at 10% (w/v).

(Figure 3), and interestingly we observed that cells were able to form multicellular aggregates within hydrogels over four days. These initial cell viability tests show that this methodology and these hydrogelator structures possess no major cytotoxicity concerns. More detailed cell/material characterization is to be performed in the future.

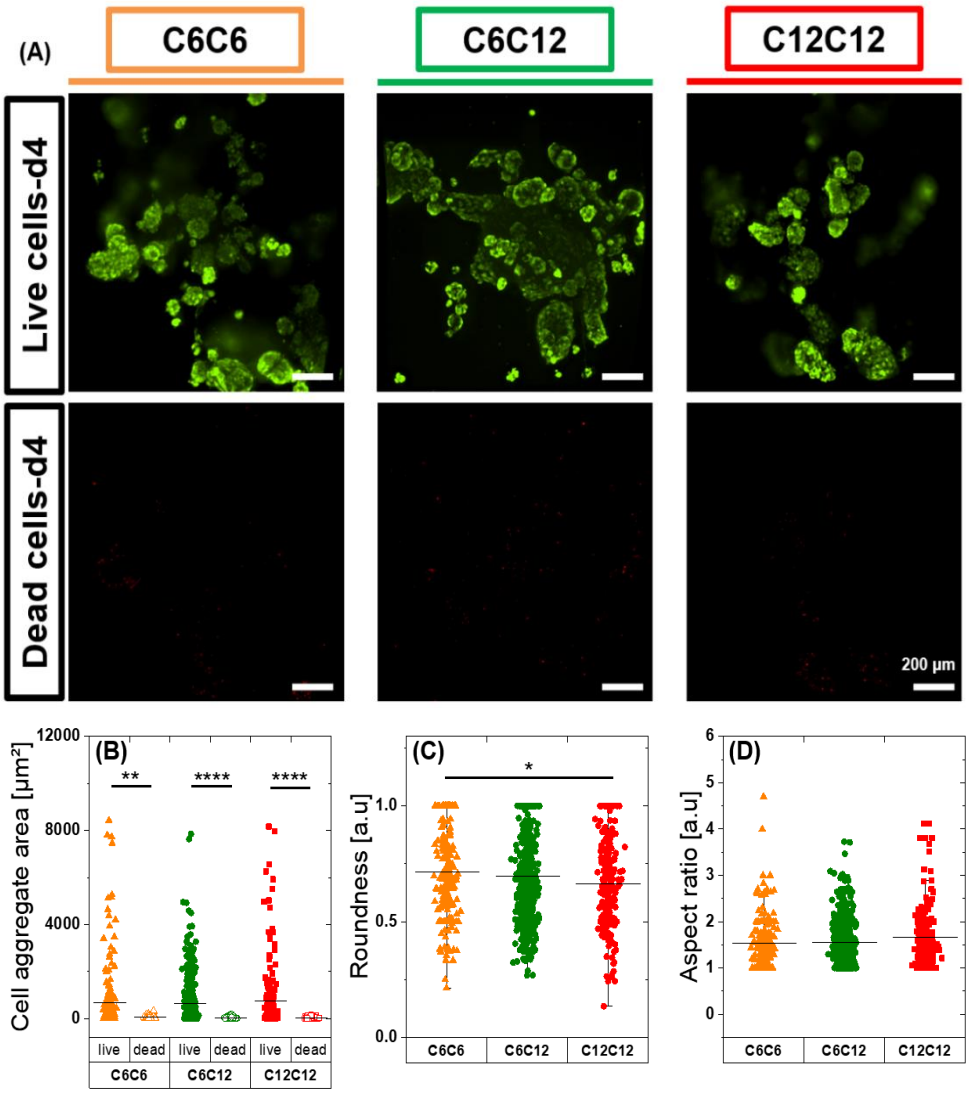

Figure 3. Synthesized BTA supramolecular macromolecules hydrogels show good cytocompatibility. A) Chondrocytes (ATDC5) were encapsulated within gels and stained after 4 days in culture. Green color represents live cells and red color represents dead cells. Scale bar: 200 µm. B–D) Live and dead stack images were flattened and using image J B) cell aggregates area, C) roundness of aggregates, and aspect ratio were calculated. Statistical significance was determined using one-way ANOVA (Origin software) and means comparison were analyzed using Tukey post test. *p <0.05, **p <0.01, ***p <0.001, ****p <0.0001.

Conclusions

In this work, we have developed a new synthetic strategy to create desymmetrized BTA molecules, macromolecules, and ultimately functional materials. We employed an activated ester

desymmetrization methodology, which was economically viable, mild, and fast. We found that BTE-F_5Ph is the most stable activated ester and offers a flexible synthon for the creation of BTA derivatives with different sidearms and several functionalities. The yield for BTA monosubstituted, disubstituted, and trisubstituted derivatives was high and above statistically expected results for almost all reactions. Unlike existing synthetic approaches to BTAs, **3** offers a flexible desymmetrization strategy; intermediates are stable, solid, and do not require protection, starting materials can be recovered, and intermediates can be stored for further multifunctional BTA synthesis.

These BTA monomers offer the potential to be incorporated into a variety of BTA materials via modular mixing e.g., for tuning bioactivity and creation of polymeric BTA hydrogelators. Utilization of some of our desymmetrized BTAs allowed the creation of a small library of telechelic BTAs on a multi-gram scale with a high yield. One of the major advantages this strategy offers is that now BTA functionalized materials can be made with two different external arms on the BTA (i.e., hydrogelator **21**).

The telechelic BTA macromolecules synthesized in this study showed fibrous morphology in a dilute solution, akin to the fibrous assemblies within the native ECM. At higher concentrations, the telechelic BTA macromolecules form stable hydrogels and offer similar equilibrium storage moduli, but show differences in dynamic mechanical properties. Furthermore, these BTA hydrogels are moldable, self-healing, and show good cytocompatibility (chondrocytes).

This methodology is envisioned to be highly tolerant to sensitive functional groups and favors the creation of linear and divergent libraries quickly within the lab. With the ability to create more complex molecules, the ability to create more complex supramolecular polymers becomes more attainable. While we chose to investigate the ability to create ECM-mimicking BTA fibrous hydrogels, this approach should be amenable to numerous applications where BTA serves as a supramolecular motif. With this new scalable strategy, we can confidently explore more complex BTA hydrogels in a variety of tissue engineering applications, and more complex BTA architectures can be accessed for a variety of studies and applications utilizing BTA supramolecular assembly.

References

(1) Aida, T.; Meijer, E. W.; Stupp, S. I. Functional Supramolecular Polymers. *Science.* **2012**, *335* (6070), 813–817. https://doi.org/10.1126/science.1205962.

(2) Goor, O. J. G. M.; Hendrikse, S. I. S.; Dankers, P. Y. W.; Meijer, E. W. From Supramolecular Polymers to Multi-Component Biomaterials. *Chem. Soc. Rev.* **2017**, *46* (21), 6621–6637. https://doi.org/10.1039/C7CS00564D.

(3) Webber, M. J.; Appel, E. A.; Meijer, E. W.; Langer, R. Supramolecular Biomaterials. *Nat. Mater.* **2015**, *15* (1), 13–26. https://doi.org/10.1038/nmat4474.

(4) Sur, S.; Tantakitti, F.; Matson, J. B.; Stupp, S. I. Epitope Topography Controls Bioactivity in Supramolecular Nanofibers. *Biomater. Sci.* **2015**, *3* (3), 520–532. https://doi.org/10.1039/c4bm00326h.

(5) Hendrikse, S. I. S.; Su, L.; Hogervorst, T. P.; Lafleur, R. P. M.; Lou, X.; Van Der Marel, G. A.; Codee, J. D. C.; Meijer, E. W. Elucidating the Ordering in Self-Assembled Glycocalyx Mimicking

Supramolecular Copolymers in Water. *J. Am. Chem. Soc.* **2019**, *141* (35), 13877–13886. https://doi.org/10.1021/jacs.9b06607.

(6) Hendrikse, S. I. S.; Wijnands, S. P. W.; Lafleur, R. P. M.; Pouderoijen, M. J.; Janssen, H. M.; Dankers, P. Y. W.; Meijer, E. W. Controlling and Tuning the Dynamic Nature of Supramolecular Polymers in Aqueous Solutions. *ChemComm* **2017**, *53* (14), 2279–2282. https://doi.org/10.1039/c6cc10046e.

(7) Boekhoven, J.; Stupp, S. I. 25th Anniversary Article: Supramolecular Materials for Regenerative Medicine. *Adv. Mater.* **2014**, *26* (11), 1642–1659. https://doi.org/10.1002/adma.201304606.

(8) Dankers, P. Y. W.; Meijer, E. W. Supramolecular Biomaterials. A Modular Approach towards Tissue Engineering. *Bull. Chem. Soc. Jpn.* **2007**, *80* (11), 2047–2073. https://doi.org/10.1246/bcsj.80.2047.

(9) Vereroudakis, E.; Bantawa, M.; Lafleur, R. P. M.; Parisi, D.; Matsumoto, N. M.; Peeters, J. W.; Del Gado, E.; Meijer, E. W.; Vlassopoulos, D. Competitive Supramolecular Associations Mediate the Viscoelasticity of Binary Hydrogels. *ACS Cent. Sci.* **2020**. https://doi.org/10.1021/acscentsci.0c00279.

(10) Leenders, C. M. A.; Mes, T.; Baker, M. B.; Koenigs, M. M. E.; Besenius, P.; Palmans, A. R. A.; Meijer, E. W. From Supramolecular Polymers to Hydrogel Materials. *Mater. Horiz.* **2014**, *1* (1), 116–120. https://doi.org/10.1039/C3MH00103B.

(11) Varela-aramburu, S.; Morgese, G.; Su, L.; Schoenmakers, S. M. C.; Perrone, M.; Leanza, L.; Perego, C.; Pavan, G. M.; Palmans, A. R. A.; Meijer, E. W. Exploring the Potential of Benzene-1,3,5-Tricarboxamide Supramolecular Polymers as Biomaterials. **2020**. https://doi.org/10.1021/acs.biomac.0c00904.

(12) Cantekin, S.; de Greef, T. F. A.; Palmans, A. R. A. Benzene-1,3,5-Tricarboxamide: A Versatile Ordering Moiety for Supramolecular Chemistry. *Chem. Soc. Rev.* **2012**, *41* (18), 6125–6137. https://doi.org/10.1039/c2cs35156k.

(13) Raynal, M.; Portier, F.; Van Leeuwen, P. W. N. M.; Bouteiller, L. Tunable Asymmetric Catalysis through Ligand Stacking in Chiral Rigid Rods. *J. Am. Chem. Soc.* **2013**, *135* (47), 17687–17690. https://doi.org/10.1021/ja408860s.

(14) Mörl, M.; Steinlein, C.; Kreger, K.; Schmidt, H. W.; Altstädt, V. Improved Compression Properties of Polypropylene Extrusion Foams by Supramolecular Additives. *J. Cell. Plast.* **2018**, *54* (3), 483–498. https://doi.org/10.1177/0021955X17695096.

(15) Straßburger, D.; Stergiou, N.; Urschbach, M.; Yurugi, H.; Spitzer, D.; Schollmeyer, D.; Schmitt, E.; Besenius, P. Mannose-Decorated Multicomponent Supramolecular Polymers Trigger Effective Uptake into Antigen-Presenting Cells. *ChemBioChem* **2018**, *19* (9), 912–916. https://doi.org/10.1002/cbic.201800114.

(16) Leenders, C. M. A.; Albertazzi, L.; Mes, T.; Koenigs, M. M. E.; Palmans, A. R. A.; Meijer, E. W. Supramolecular Polymerization in Water Harnessing Both Hydrophobic Effects and Hydrogen Bond Formation. *ChemComm* **2013**, *49* (19), 1963–1965. https://doi.org/10.1039/c3cc38949a.

(17) Matsumoto, N. M.; Lafleur, R. P. M.; Lou, X.; Shih, K. C.; Wijnands, S. P. W.; Guibert, C.; Van Rosendaal, J. W. A. M.; Voets, I. K.; Palmans, A. R. A.; Lin, Y.; Meijer, E. W. Polymorphism in Benzene-1,3,5-Tricarboxamide Supramolecular Assemblies in Water: A Subtle Trade-off between Structure and Dynamics. *J. Am. Chem. Soc.* **2018**, *140* (41), 13308–13316. https://doi.org/10.1021/jacs.8b07697.

(18) Baker, M. B.; Gosens, R. P. J.; Albertazzi, L.; Matsumoto, N. M.; Palmans, A. R. A.; Meijer, E. W. Exposing Differences in Monomer Exchange Rates of Multicomponent Supramolecular Polymers in Water. *ChemBioChem* **2016**, *17* (3), 207–213. https://doi.org/10.1002/cbic.201500606.

(19) Vandenberg, M. A.; Sahoo, J. K.; Zou, L.; McCarthy, W.; Webber, M. J. Divergent Self-Assembly Pathways to Hierarchically Organized Networks of Isopeptide-Modified Discotics under Kinetic Control. *ACS Nano* **2020**, *14* (5), 5491–5505. https://doi.org/10.1021/acsnano.9b09610.

(20) Besenius, P.; Portale, G.; Bomans, P. H. H.; Janssen, H. M.; Palmans, A. R. A.; Meijer, E. W. Controlling the Growth and Shape of Chiral Supramolecular Polymers in Water. *PNAS* **2010**, *107* (42), 17888–17893. https://doi.org/10.1073/pnas.1009592107/-/DCSupplemental.

(21) Roosma, J.; Mes, T.; Leclère, P.; Palmans, A. R. A.; Meijer, E. W. Supramolecular Materials from Benzene-1,3,5-Tricarboxamide-Based Nanorods. *J. Am. Chem. Soc.* **2008**, *130* (4), 1120–1121. https://doi.org/10.1021/ja0774764.

(22) Albertazzi, L.; Van Der Zwaag, D.; Leenders, C. M. A.; Fitzner, R.; Van Der Hofstad, R. W.; Meijer, E. W. Probing Exchange Pathways in One-Dimensional Aggregates with Super-Resolution Microscopy. *Science.* **2014**, *344* (6183), 491–495. https://doi.org/10.1126/science.1250945.

(23) Stals, P. J. M.; Haveman, J. F.; Palmans, A. R. A.; Schenning, A. P. H. J. The Self-Assembly Properties of a Benzene-1, 3, 5-Tricarboxamide Derivative. *J. Chem. Educ.* **2009**, *86* (2), 230–233.

(24) Gamez, P.; Reedijk, J. 1,3,5-Triazine-Based Synthons in Supramolecular Chemistry. *Eur. J. Inorg. Chem.* **2006**, No. 1, 29–42. https://doi.org/10.1002/ejic.200500672.

(25) Röglin, L.; Lempens, E. H. M.; Meijer, E. W. A Synthetic "Tour de Force": Well-Defined Multivalent and Multimodal Dendritic Structures for Biomedical Applications. *Angew. Chemie - Int. Ed.* **2011**, *50* (1), 102–112. https://doi.org/10.1002/anie.201003968.

(26) Chen, C.; Raymond Dagnino, J.; McCarthy, and J. R. A Convenient Synthetic Method for Trisubstituted S-Triazines. *J. Org. Chem.* **1995**, *60*, 8428–8430.

(27) Baker, M. B.; Ghiviriga, I.; Castellano, R. K. Molecular Multifunctionalization via Electronically Coupled Lactones. https://doi.org/10.1039/c2sc00943a.

(28) Baker, M. B.; Ferreira, R. B.; Tasseroul, J.; Lampkins, A. J.; Abbas, A. Al; Abboud, K. A.; Castellano, R. K. Selective and Sequential Aminolysis of Benzotrifuranone: Synergism of Electronic Effects and Ring Strain Gradient. *JOC* **2016**, No. 81, 9279–9288. https://doi.org/10.1021/acs.joc.6b01867.

(29) Türp, D.; Nguyen, T. T. T.; Baumgarten, M.; Müllen, K. Uniquely Versatile: Nano-Site Defined Materials Based on Polyphenylene Dendrimers. *New J. Chem.* **2012**, *36* (2), 282–298. https://doi.org/10.1039/c1nj20449a.

(30) Das, A.; Theato, P. Activated Ester Containing Polymers: Opportunities and Challenges for the Design of Functional Macromolecules. *Chem. Rev.* **2016**, *116* (3), 1434–1495. https://doi.org/10.1021/acs.chemrev.5b00291.

(31) Engler, A. C.; Chan, J. M. W.; Coady, D. J.; O'Brien, J. M.; Sardon, H.; Nelson, A.; Sanders, D. P.; Yang, Y. Y.; Hedrick, J. L. Accessing New Materials through Polymerization and Modification of a Polycarbonate with a Pendant Activated Ester. *Macromolecules* **2013**, *46* (4), 1283–1290. https://doi.org/10.1021/ma4001258.

(32) He, L.; Szameit, K.; Zhao, H.; Hahn, U.; Theato, P. Postpolymerization Modification Using Less Cytotoxic Activated Ester Polymers for the Synthesis of Biological Active Polymers. *Biomacromolecules* **2014**, *15* (8), 3197–3205. https://doi.org/10.1021/bm500902t.

(33) Katritzky, A. R.; Singh, S. K.; Cai, C.; Bobrov, S. Direct Synthesis of Esters and Amides from Unprotected Hydroxyaromatic and -Aliphatic Carboxylic Acids. *J. Org. Chem.* **2006**, *71* (9), 3364–3374. https://doi.org/10.1021/jo052293q.

(34) Shi, Y.; Liu, X.; Cao, H.; Bie, F.; Han, Y.; Yan, P.; Szostak, R.; Szostak, M.; Liu, C. Conversion of Esters to Thioesters under Mild Conditions. *Org. Biomol. Chem.* **2021**, *19* (13), 2991–2996. https://doi.org/10.1039/d1ob00187f.

(35) Covington, A. K.; Robinson, R. A.; Bates, R. G. The Ionization Constant of m-Nitrophenol from 5 to 50°. *J. Phys. Chem.* **1963**, *67* (12), 2860–2861. https://doi.org/10.1021/j100884a011.

(36) G. F. Allen; And, R. A. R.; Bower, V. E. The Ionization Constant of p-Nitrophenol from 0 to 60°. *J. Phys. Chem.* **1962**, *66* (1), 171–172. https://doi.org/10.1021/ja01851a058.

(37) Gasbarri, C.; Angelini, G. Spectroscopic Investigation of Fluorinated Phenols as PH-Sensitive Probes in Mixed Liposomal Systems. *RSC Adv.* **2014**, *4* (34), 17840–17845. https://doi.org/10.1039/c4ra01507j.

(38) Klykov, O.; Weller, M. G. Quantification of N-Hydroxysuccinimide and N-Hydroxysulfosuccinimide by Hydrophilic Interaction Chromatography (HILIC). *Anal. Methods* **2015**, *7* (15), 6443–6448. https://doi.org/10.1039/c5ay00042d.

(39) D. E. AMES and T. F. GREY. The Synthesis of Some N-Hydroxyimides. *J. Chem. Soc.* **1955**, 631–636. https://doi.org/https://doi.org/10.1039/JR9550000631.

(40) Stuart, M. C. A.; Van De Pas, J. C.; Engberts, J. B. F. N. The Use of Nile Red to Monitor the Aggregation Behavior in Ternary Surfactant-Water-Organic Solvent Systems. *J. Phys. Org. Chem.* **2005**, *18* (9), 929–934. https://doi.org/10.1002/poc.919.

(41) Morgese, G.; de Waal, B. F. M.; Varela-Aramburu, S.; Palmans, A. R. A.; Albertazzi, L.; Meijer, E. W. Anchoring Supramolecular Polymers to Human Red Blood Cells by Combining Dynamic

Covalent and Non-Covalent Chemistries. *Angew. Chemie - Int. Ed.* **2020**, *59* (39), 17229–17233. https://doi.org/10.1002/anie.202006381.

(42) Lee, H.; Gu, L.; Mooney, D. J.; Levenston, M. E.; Chaudhuri, O. Mechanical Confinement Regulates Cartilage Matrix Formation by Chondrocytes. *Nat. Mater.* **2017**, No. 16, 1243–1251. https://doi.org/10.1038/nmat4993.

(43) Richardson, B. M.; Wilcox, D. G.; Randolph, M. A.; Anseth, K. S. Hydrazone Covalent Adaptable Networks Modulate Extracellular Matrix Deposition for Cartilage Tissue Engineering. *Acta Biomater.* **2019**, *83*, 71–82. https://doi.org/10.1016/j.actbio.2018.11.014.

(44) Park, H.; Kim, D.; Lee, K. Y. Interaction-Tailored Cell Aggregates in Alginate Hydrogels for Enhanced Chondrogenic Differentiation. *J. Biomed. Mater. Res. - Part A* **2017**, *105* (1), 42–50. https://doi.org/10.1002/jbm.a.35865.

Supplementary information

Abbreviations:

Dichloromethane (DCM), Tetrahydrofuran (THF), N, N-Diisopropylethylamine (DIPEA), Benezene-1,3,5- tricarbonyl trichloride (BTCl), Dimethyl sulfoxide (DMSO), milligram (mg), milliliter (mL), micromolar (μM)

General:

All chemicals were purchased from commercial sources and used as received unless stated otherwise. 5-Norbornene-2-methylamine (mixture of isomers, TCI Chemicals), N, N-Diisopropylethylamine (DIPEA)solution was dried using sodium hydroxide pellets. The Hexylamine solution was dried using a powder magnesium sulfate drying agent. Dichloromethane (DCM) and Tetrahydrofuran (THF) employed for desymmetrization reactions were ≥99% anhydrous. Thin-layer chromatography (precoated 0.25 mm, 60-F254 silica gel plates from Merck) was used to follow the reactions, and silica gel (40–63 μm, 60 Å from Sigma-Aldrich) flash chromatography was run to isolate the pure compounds.

Nuclear Magnetic Resonance (NMR) analysis and sample preparation.

NMR analysis was performed using a Bruker Ascend 700MHZ NMR Spectrometer for proton and 176MHZ for carbon. The data was analyzed using the TopSpin 3.5 and spectra were calibrated to either chloroform ($CDCl_3$: 7.27ppm) or d_6-DMSO (2.5ppm). for sample preparation, a 2–7 mg sample was dissolved in either deuterated chloroform or deuterated DMSO (roughly 700 μl). Chemical shifts are given in ppm (δ) values relative to the residual solvent. Splitting patterns are labeled as s, singlet; bs, broad singlet, d, doublet; dd, double doublet; t, triplet; q, quartet; p, pentet; m, multiplet, and b stands for broad.

MALDI-TOF:

Matrix-Assisted Laser Desorption/Ionization Time-of-Flight (MALDI TOF)-MS has performed on an Applied Biosystems 4800 MALDI TOF/TOF system in reflector positive mode. α-cyano-4-hydroxycinnamic acid in 50% water / 50% acetonitrile containing 0.1% TFA was used as a matrix. Samples were spotted on the plate and dried in the open air before analyses. Chloroform was used as a solvent in case of low solubility in acetonitrile.

Nile red studies:

For each hydrogelator, three samples with the final concentration of 1 mg/mL, 2mg/mL, and 5mg/mL were prepared. To start with solid polymer was weighed in a glass vial and 50 μl methanol was added to the glass vial for dissolving hydrogelators molecularly so that there is no stacking of BTA units. A little bit of heating is required especially for **17** to fully dissolve. Later, 950 μl of water was added to the glass vial. Heating and cooling cycles were repeated until the solution become transparent and let the BTA molecule age overnight. The next day, 200 μl from

each solution was transferred to a transparent bottom black well plate, and added to it 3.2 µl of Nile red (from a stock solution of 1 mg/10 mL= 315 µM) resulting in a final Nile red concentration of 5 µM. The well plate was incubated for 30 mins in the dark at room temperature and fluorescence emission spectra were recorded.

Cryo-TEM:

All samples were prepared at 10 mg/mL. The polymer was dissolved in 50 µl of methanol and then 950 µl of water was added to the hydrogelator solution. The sample solution was heated until the sample became transparent and was allowed to cool at room and age overnight (16–24 hours) before imaging. The sample vitrification procedure was carried out using an automated vitrification robot (FEI Vitrobot™ Mark IV). Cryo-TEM grids, R2/2 Quantifoil Jena grids, were purchased from Quantifoil Micro Tools GmbH. Before the vitrification procedure (3 µL aliquots, blotting time varied from 3 s to 4 s, -5 mm blotting offset, 100% relative humidity) the grids were surface Glow discharged using a Cressington 208 carbon coater operating at 7 mA for 30 s. The cryo-TEM experiments were performed on an FEI Arctica 200KV microscope. The Arctica is equipped with a FEG operating at 200 kV and the images were recorded using a Falcon III camera.

Hydrogel formation

The solid polymer was weighed in a glass vial and water was added to make the final concentration 10% (w/v). The glass vial was heated until the polymer solution became turbid and vortexed, and then the solution was allowed to cool until it turns into a hydrogel. Heating-cooling cycles were repeated 3x. Subsequently, the hydrogel was placed on the heating plate, and the temperature was raised to 80 °C. Then the temperature was turned off and the hydrogel was cooled to 20 °C.

CGC determination

Starting from 10% (w/v), the hydrogel was diluted to half by adding water and performing a vial inversion test after 24 hours. The vial was inverted and hydrogel flow was observed for under 30 seconds. If hydrogel did not begin to flow after 30 seconds, it was considered a hydrogel, and if the hydrogel flowed earlier then it was not considered a hydrogel.

Macroscopic self-healing and moldability:

The hydrogel was formed as mentioned above ("hydrogel formation" heading) and a few µl of food-grade water-based liquid colorant was added on top of the hydrogel to give hydrogel a color for better visual presentation. Hydrogelator **15**, **16**, and **17** are colored yellow, green, and red. Hydrogels were placed in a round mold, divided into two parts, and then placed together and pressed with the spatula for the self-healing test. Self-healing was determined successful if two pieces of hydrogel merged to give a single hydrogel which is stable and did not fall apart when lifted under forces of gravity. After a few minutes in a closed container under a humid environment, the hydrogels were lifted using the spatula and hydrogelator **21** and **22** can be lifted

successfully and no separation of two pieces of hydrogel occur. Hydrogelator **20** could not since it is a weak hydrogel and started to flow like viscous liquid when handled with a spatula, and lifted under the gravity force. However, hydrogelator **20** does show self-healing.

For moldability, the hydrogel was taken from a round mold, placed in the square mold, and pressed with a spatula a little bit to adjust to a new shape.

Mechanical properties:

Rheological measurements were performed using a DHR-2 rheometer using a 20 mm cone-plate geometry with a 2.002° angle. All measurements were performed at 20 °C. First, the linear viscoelastic region was determined by performing a strain sweep on the 10 wt % hydrogels. We found that storage and loss modulus is independent of strain below 10% strain and that hydrogels from **21** and **22** clearly showed hydrogel dominant behavior (G'>G"), while the hydrogel from **20** showed liquid dominant behavior at this frequency (1 rad/s). A rejuvenation process was carried out to remove any mechanical history within hydrogels. We choose a 400% strain amplitude at a frequency of 1 rad/s. Strain amplitude is well into the non-linear regime of the samples. Following the rejuvenation process, a time sweep at 1% strain was carried out to observe the aging kinetics and allow sample equilibration. Subsequently, a frequency sweep was carried out from 0.01 rad/s to 627 rad/s at 1% oscillation strain followed by oscillatory strain amplitude sweeps 1 to 1000% at an angular frequency of 1 rad/s. For self-healing measurements, a step-strain experiment was carried out, the strain was varied between 400% and 1% (at 1 rad/s) for the rupture and recovery phase of the sample.

Cell encapsulation and viability:

ATDC5 (chondrocytes) were encapsulated in 200 μL BTA hydrogel at a concentration of 5 million (M) cells per mL of hydrogelator. For encapsulation of cells within hydrogels, 100ul of hydrogel was transferred to the well plate and centrifuged to form a uniform layer at the bottom of the 48-well plate (non-treated for cell culture). Cell suspension in 25 μL of media was spread on top of the hydrogel and centrifuged at 80xg for cells to sediment in a hydrogel. After centrifugation, the other 100 μL of the hydrogel was added on top of the hydrogel and gently mixed using a spatula. On top of each hydrogel, 200 μL media was added and the hydrogels were incubated at 37°C. Dulbecco's Modified Eagle's Medium-F12 (DMEM-F12, low glucose) supplemented with 10% (v/v) fetal bovine serum (FBS) and 1% (v/v) P/S) was used in this study.

LIVE/DEAD™ Viability/Cytotoxicity Kit (ThermoFisher SCIENTIFIC) was used for evaluating cell viability. For live-dead staining, the hydrogels were transferred into a 35 mm glass bottom dish (ibidi, Germany), washed with PBS, and a solution of calcein AM (final concentration 1 μM) and ethidium homodimer-1 (final concentration 2 μM) was added to each hydrogel. The hydrogels were incubated for 45-60 minutes in the dark at 37 °C and imaged using an inverted fluorescence microscope (Nikon Eclipse Ti-e) under the conditions of 37 °C and 5% CO_2. Images were analyzed using ImageJ.

Benezene-1,3,5- tricarbonyl trichloride (BTCl) desymmetrization using hexylamine:

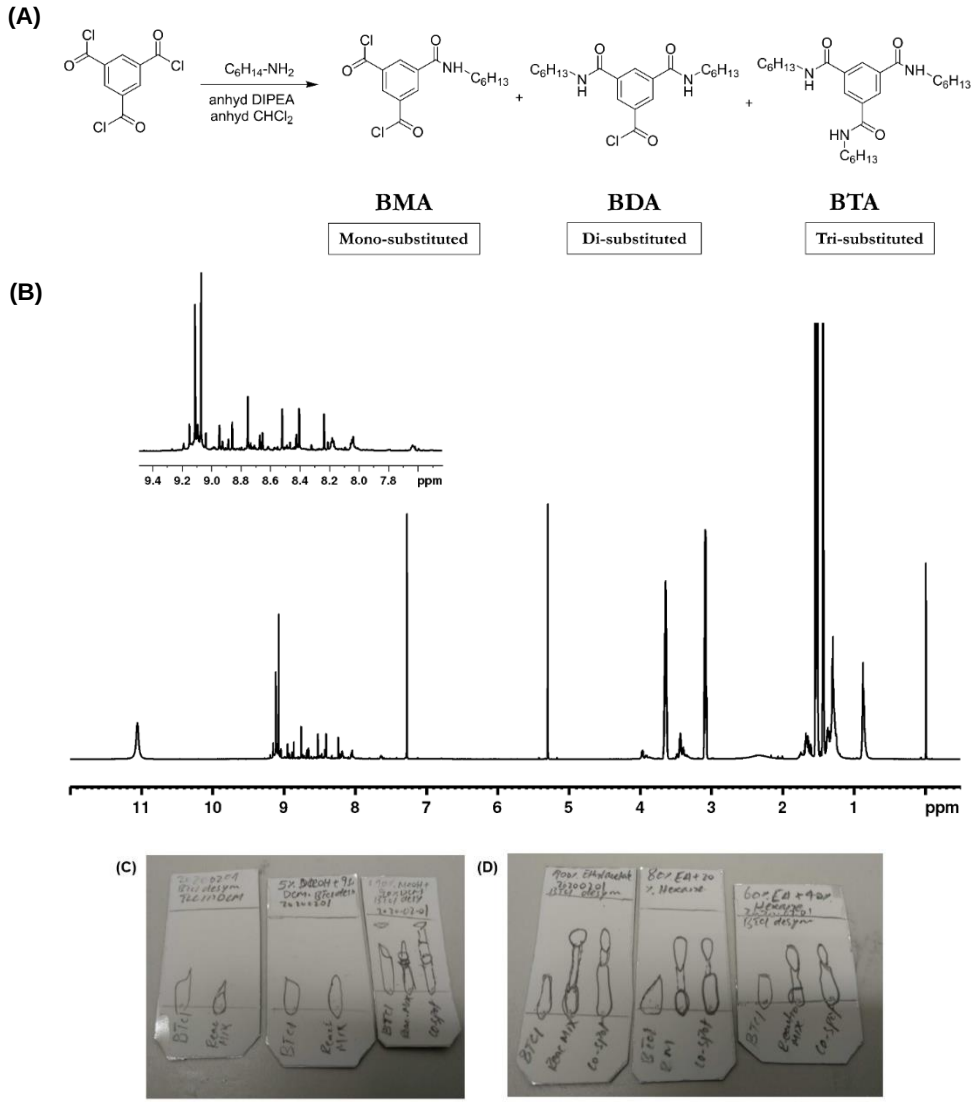

Figure S1. A) BTCl desymmetrization reaction scheme using hexylamine as a model molecule, B) ^{1}H NMR of BTCl desymmetrization using hexylamine. Separation using thin-layer chromatography: C) Left: in DCM, middle: in 5% (v/v) MeOH+95% (v/v) DCM, right: 10% (v/v) MeOH+90% (v/v) DCM. D) Left: in ethyl acetate (EA), middle: in 80% EA (v/v) +20% (v/v) hexane, right: 60% (v/v) EA+40% (v/v) Hexane.

Table S1: Nitrophenol solubility

Solvent	BTCl	$3NO_2PH$	$4NO_2Ph$
DCM	S	NS	NS
Chloroform	S	P	P
THF	S	S	S
DMSO	S	S	S

DCM=Dichloromethane, THF= tetrahydrofuran, DMSO= dimethylsulfoxide, NS=not soluble, P= partially soluble, S= soluble. between 3–5 mg of each compound in 3–4 mL of the solvent.

Synthesis of 1-(3-nitrocyclohexa-1,3-dien-1-yl) 3,5-bis(3-nitrophenyl) benzene-1,3,5-tricarboxylate (1):

In a flame-dried flask, benzene-1,3,5- tricarbonyl trichloride (BTCl, 0.1 g, 0.38 mmol, 1 equiv.) was dissolved in 4 mL of freshly dried THF (over NaOH). First, DIPEA (0.29 g, 2.26 mmol, 6 equiv.) and then 3-nitrophenol ($3NO_2Ph$, 0.26 g, 1.88 mmol, 5 equiv.) were added to the reaction flask under a nitrogen atmosphere. The formation of solid crystals started to appear in just 5 minutes and the reaction solvent color turns light yellow. TLC was obtained after 1 hour of the reaction in DCM and showed three spots with R_f close to 0, at R_f 0.5 (3-nitrophenol) and 0.7 (expected product, **1**). Adding 5% methanol and running TLC moved these spots higher with R_f close to 0 and R_f at 0.6 and 0.9 but no other spot became visible. The reaction mixture was allowed to stir at room temperature for 20 hours and the color of the reaction solvent turned dark yellow. After 20 hours, the stirring was stopped and the volatiles was removed under a vacuum. The crude reaction mixture was purified by repeated crystallization: 1x using ethyl acetate/hexane (50:50) and 2x using ethyl acetate/hexane/THF (40:40:20). Molecule **1** (BTE-$3NO_2Ph$) was obtained as light yellowish solid (0.16 g, 76% yield) and stored under nitrogen atmosphere at room temperature in a desiccator. ^{1}H NMR (700 MHz, d_6-DMSO) δ 9.09 (s, 3H), 8.41 (t, H), 8.24 (dd, H), 7.93 (dd, H), 7.83 (t, H). ^{13}C NMR (176 MHz, d_6-DMSO) 162.75, 150.64, 148.38, 135.48, 130.99, 130.60, 129.06, 121.44, 117.68. The mass of the molecule was not obtained using MALDI-TOF in a positive mode. MS (MALDI-TOF) calcd. for $C_{27}H_{15}N_3O_{12}$ $[M+H]^+$ 574.07, not obtained in reflector positive ion mode.

NOTE: $[M+H]^+$ using MALDI was not obtained, we think perhaps the molecule did not ionize.

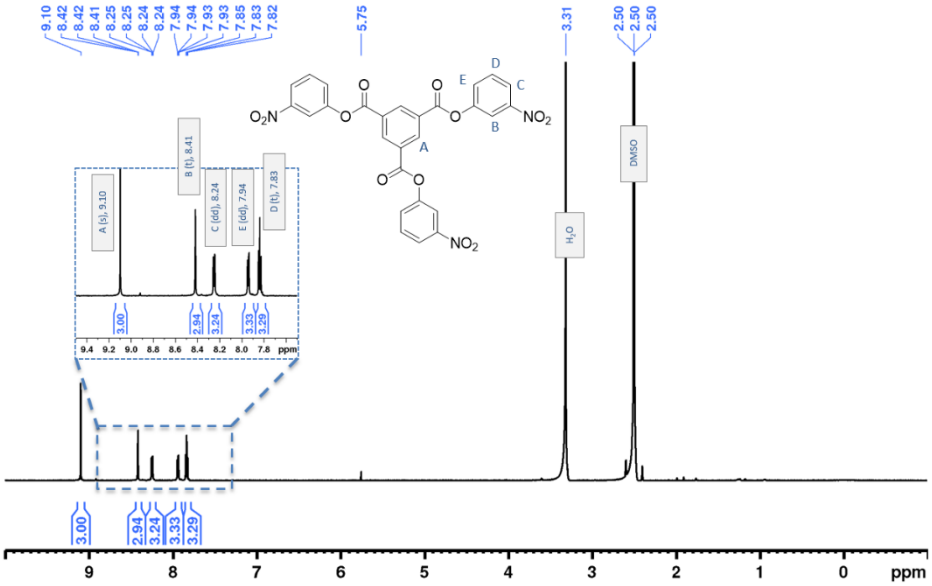

Figure S2. ^{1}H NMR (d_6-DMSO) of BTE-3NO$_2$Ph (molecule **1**)

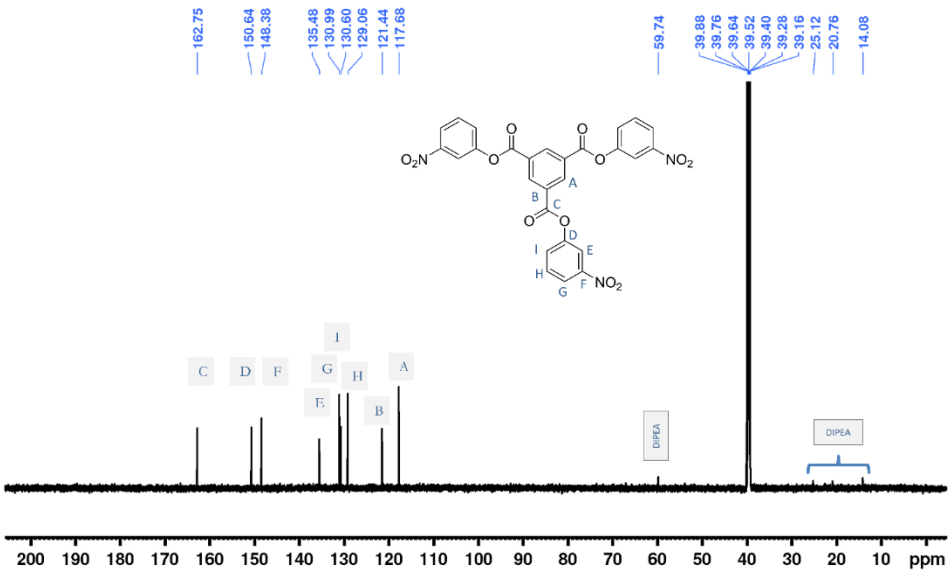

Figure S3. ^{13}C NMR (d_6-DMSO) of BTE-3NO$_2$Ph (molecule **1**)

Synthesis of 1-(4-nitrocyclohexa-1,3-dien-1-yl) 3,5-bis(4-nitrophenyl) benzene-1,3,5-tricarboxylate (2):

Benezene-1,3,5- tricarbonyl trichloride (BTCl) (0.1 g, 0.38 mmol, 1 equiv) was weighed in the dried round bottom flask and DIPEA (0.29 g, 2.26 mmol, 6 equiv) and 4-nitrophenol (3NO2Ph) (0.26 g, 1.88 mmol, 5 equiv) dissolved in 4 mL of freshly dried THF was added to the flask under nitrogen atmosphere through a syringe under stirring. Solid crystals started to appear in the reaction mixture under 5 mins. Thin-layer chromatography (TLC) in DCM showed two spots with R_f close to 0.5 (3-nitrophenol) and at R_f 0.7 (expected product, **2**). When TLC was run by adding 5% methanol and two spots moved higher with R_f values 0.6 and 0.9 and no other spot showed up. The reaction mixture was stirred for 20 hours at room temperature. TLC showed the same spots after 20 hours. The reaction mixture was then vacuum dried and purified by repeated crystallization: 1x using ethyl acetate/ hexane (50:50) and 2x using ethyl acetate/hexane/THF (40:40:20). Molecule **2** (BTE-4NO_2Ph, 0.2 g, 92% yield) was obtained as creamy white/light yellowish solid. ^{1}H NMR (700 MHz, d_6-DMSO) δ 9.08 (s, 3H), 8.40 (d, 3H), 7.75 (d, 3H). ^{13}C NMR (176 MHz, d_6-DMSO) 162.15, 154.95, 145.39, 135.39, 130.42, 125.17, 123.15. MALDI-TOF peak for $C_{27}H_{15}N_3O_{12}$ $[M+H]^+$ 574.07 was not detected in reflector positive ion mode.

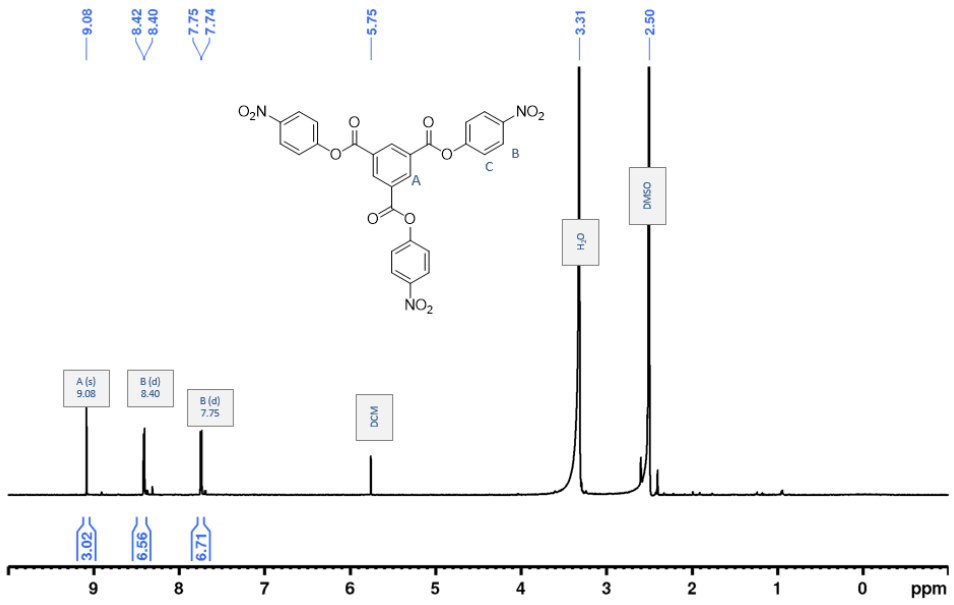

Figure S4. ^{1}H NMR (d_6-DMSO) of **2** (BTE-4NO_2Ph)

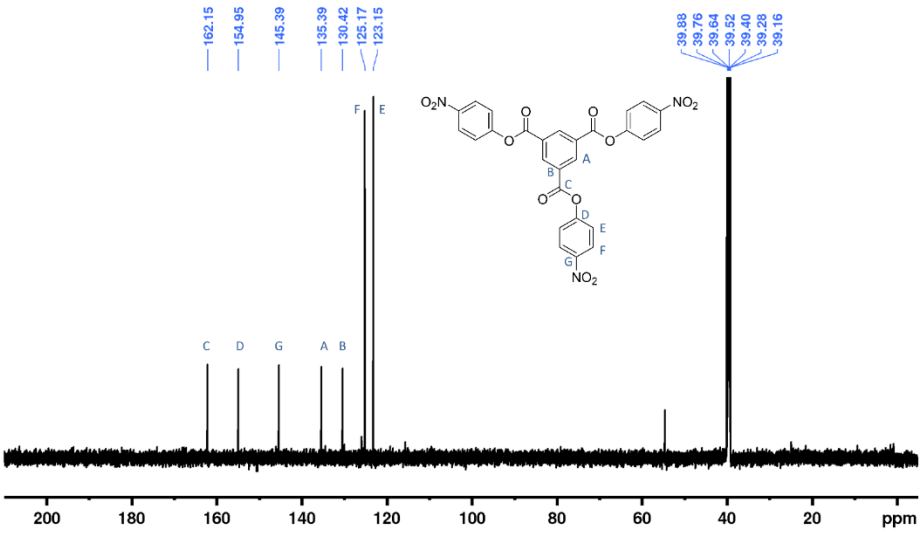

Figure S5. ^{13}C NMR d_6-DMSO of **2** (BTE-4NO2Ph)

Table S2: Alternative workups for purification of molecules 1 and 2 and obtained % yields

Solvent	BTE-3NO$_2$Ph Isolated yield	BTE-4NO$_2$Ph Isolated yield
Hexane:Ethyl acetate (50/50)	Not fully soluble with heating	Not fully soluble with heating
THF:Ethyl acetate (40/60)	26%	N/A
THF:ethyl acetate:hexane (20:40:40)	76%	92%

Synthesis of tris(perfluorophenyl) benzene-1,3,5-tricarboxylate (3):

To a clean and dry 250 mL round bottom flask equipped with a stir bar and under nitrogen was added pentafluorophenol (5.56 g, 30.13 mmol, 4 equiv) followed by anhydrous dichloromethane (DCM, 30 mL), and the reaction solution was stirred until complete dissolution of pentafluorophenol. Subsequently, dry diisopropylethylamine (DIPEA, 3.89 g, 30.13 mmol, 4 equiv) was mixed with anhydrous dichloromethane (20mL) and was added dropwise to the reaction mixture, and then the reaction mixture was placed into an ice bath and allowed to cool. After cooling, 1,3,5, benzene tricarbonyl trichloride (2.0 g, 7.53 mmol, 1 equiv) dissolved in 30

mL of dry DCM and added dropwise to the reaction mixture. The reaction mixture was removed from the ice bath after 30 minutes and allowed to stir at room temperature for 4 hours. TLC (run in DCM) showed two spots at R_f close to zero and at R_f 0.9. The reaction mixture in DCM was passed through a silica bed twice. The solvent (DCM) was removed under reduced pressure, yielding BTE-F_5Ph as pure white solid crystals (4.9 g, 91% yield). ^{1}H NMR (700 MHz, $CDCl_3$) δ 9.29 (s, 3H). ^{13}C NMR (176 MHz, $CDCl_3$) 160.5, 142.1, 140.9, 140.6, 139.5, 139.0, 137.8, 137.5, 129.6, 124.9, HRMS (MALDI-TOF) m/z: $[M+H]^+$ calcd. for $C_{27}H_3O_6F_{15}$, 707.97; found 708.02.

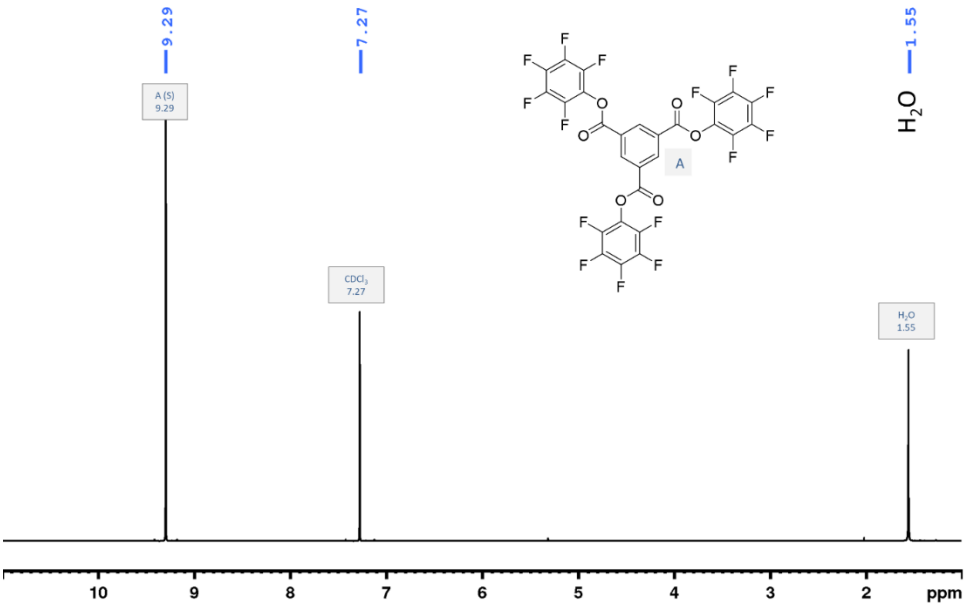

Figure S6. ^{1}H NMR ($CDCl_3$) of BTE-F_5Ph (molecule **3**)

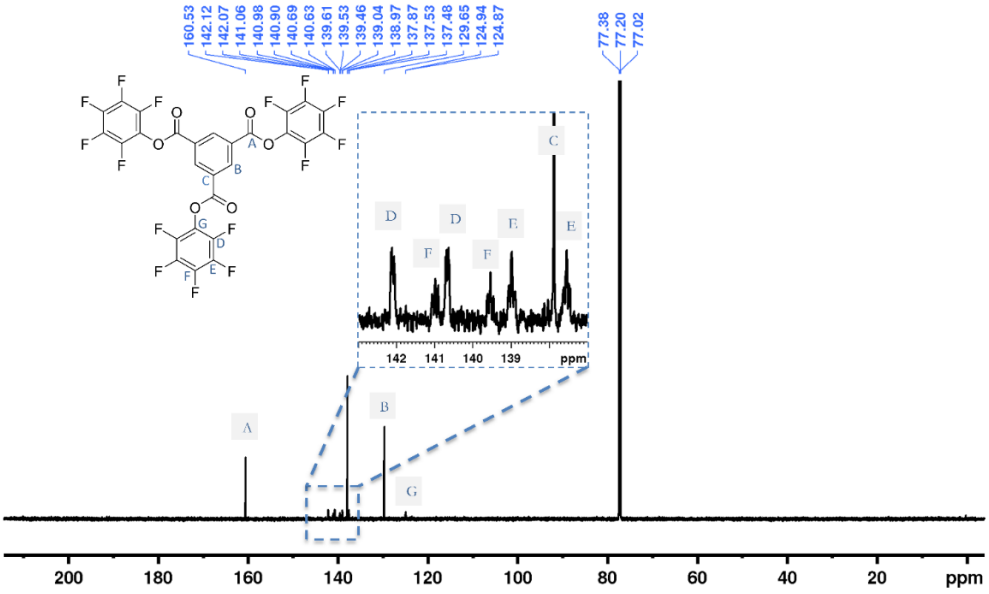

Figure S7. ^{13}C NMR ($CDCl_3$) of BTE-F_5Ph (molecule **3**)

Table S3: Workups for purification of **molecule 3** and obtained % yields

Methods	Solvent	BTE-F5Ph % Yield
Excessive washing of reaction mixture with acetonitrile	Acetonitrile	45%
Crystallization	acetonitrile+hexane/chloroform	60%
Filtration and passing through a bed of silica	Dichloromethane	91%

Table S4: NHS solubility in different organic solvents for the synthesis of molecule 4

Solvents	NHS
DCM	P
Chloroform	P
DMF	S
DMSO	**S**
THF	S

DCM=Dichloromethane, THF= tetrahydrofuran, DMSO= dimethylsulfoxide, DMF= dimethylformamide, NS=not soluble, P= partially soluble, S= soluble. NHS compound 3–5 mg was dissolved roughly in 3–4 mL of the solvent.

Synthesis of tris(2,5-dioxopyrrolidin-1-yl) benzene-1,3,5-tricarboxylate (4):

A 50 mL clean and dry single-neck flask equipped with a stir bar was purged with nitrogen. BTCl (0.1 g, 0.38 mmol, 1 equiv.) was added under a nitrogen atmosphere and the flask was closed with a screw cap. Freshly dried THF (using NaOH pellets) was added to the flask using a cannula and stirred until dissolved. DIPEA (0.39 g, 3 mmol, 8 equiv.) and NHS (0.22 g, 1.88 mmol, 5 equiv.) dissolved in 7mL of anhydrous THF were added drop by drop to the reaction mixture using a syringe. The resulting mixture was stirred for 20 hours and then the volatiles was removed by vacuum. TLC showed two spots at R_f equal to ~0.1 and ~0.4 (**Figure S9**); however, during separation using silica gel flash column chromatography, **4** was not obtained pure and free NHS seems to eluted with **4** (**Figure S10**, ^{1}H NMR collected fractions for R_f 0.4). Crystallization in ethyl acetate: hexane (80:20) provided a greasy solid and the reaction mixture was not fully soluble even in a hot boiling solvent. TLC showed that a greasy solid is not pure. No product crystallization was observed in THF: ethylacetate: hexane (33:33:33).

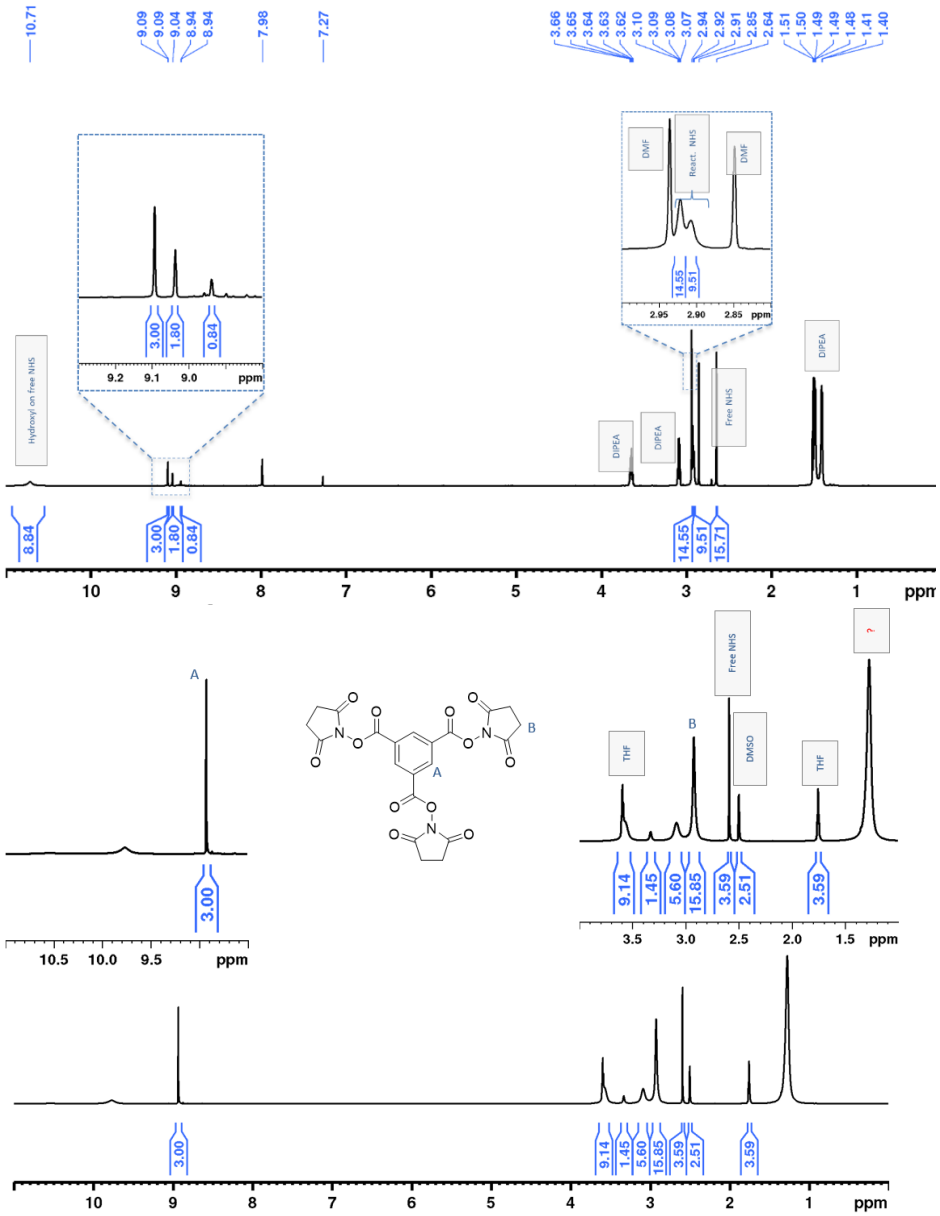

Figure S8. ^{1}H NMR ($CDCl_3$) of reaction mixture when reaction was run in DMF (top) to synthesize **4** (BTE-NHS). Appearance of three peak around 9 ppm suggests that this reaction produced non-symmetric BTE-NHS molecule which is not of interest for this study. ^{1}H NMR (d_6-DMSO) of the reaction mixture when **4** was synthesized in dry THF. Appearance of singlet for aromatic proton "A" indicates formation of symmetrical molecule **4.**

Table S5: BTE-3NO2Ph (1) and BTE-4NO2Ph (2) solubility in different organic solvents

Solvent	BTE-3NO2Ph (1)	BTE-4NO2Ph (2)
Toluene	NS	NS
DMF	P	P
acetonitrile	P	P
DCM	NS	NS
THF	NS	NS
2-propanol	P	P
1,4 dioxane	P	P
Dimethyl carbonate	P	P

NS = not soluble, P = partial solubility, S = fully soluble. Each Nitrophenol compound between 2–5 mg was dissolved in ~4 mL of the solvent.

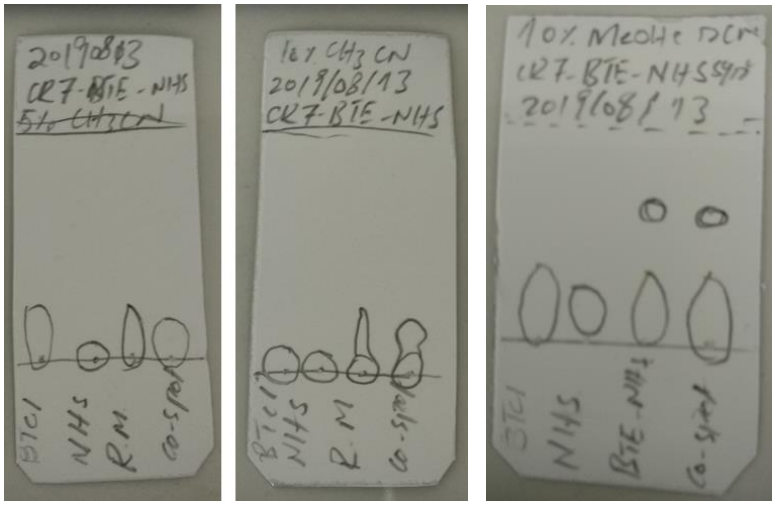

Figure S9. BTE-NHS synthesis in THF: Thin layer chromatography spots for benezene-1,3,5-tricarbonyl trichloride (BTCl), N-Hydroxysuccinimide (NHS) and reaction mixture in (Left) 5% (v/v) CH_3CN+95% (v/v) DCM, (middle) 10% (v/v) CH_3CN+90% (v/v) DCM, and (right) 10% (v/v) CH_3OH+90% (v/v) DCM.

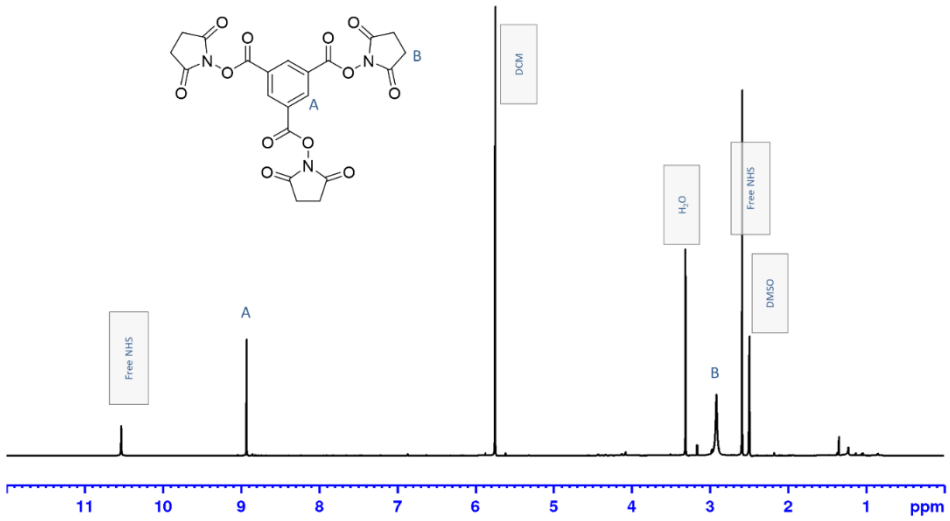

Figure S10. ^{1}H NMR (d_6-DMSO) after flash column chromatography using 10%(v/v) CH_3OH+90%(v/v) DCM showing presence of free NHS. Free NHS appears to be travelling with **4**. We were able to separate reaction mixture spots on TLC as shown above in **figure S9** but **4** was not obtained pure when separated using silica gel flash column chromatography.

Desymmetrization reaction scheme of 1-(3-nitrocyclohexa-1,3-dien-1-yl) 3,5-bis(3-nitrophenyl) benzene-1,3,5-tricarboxylate (1):

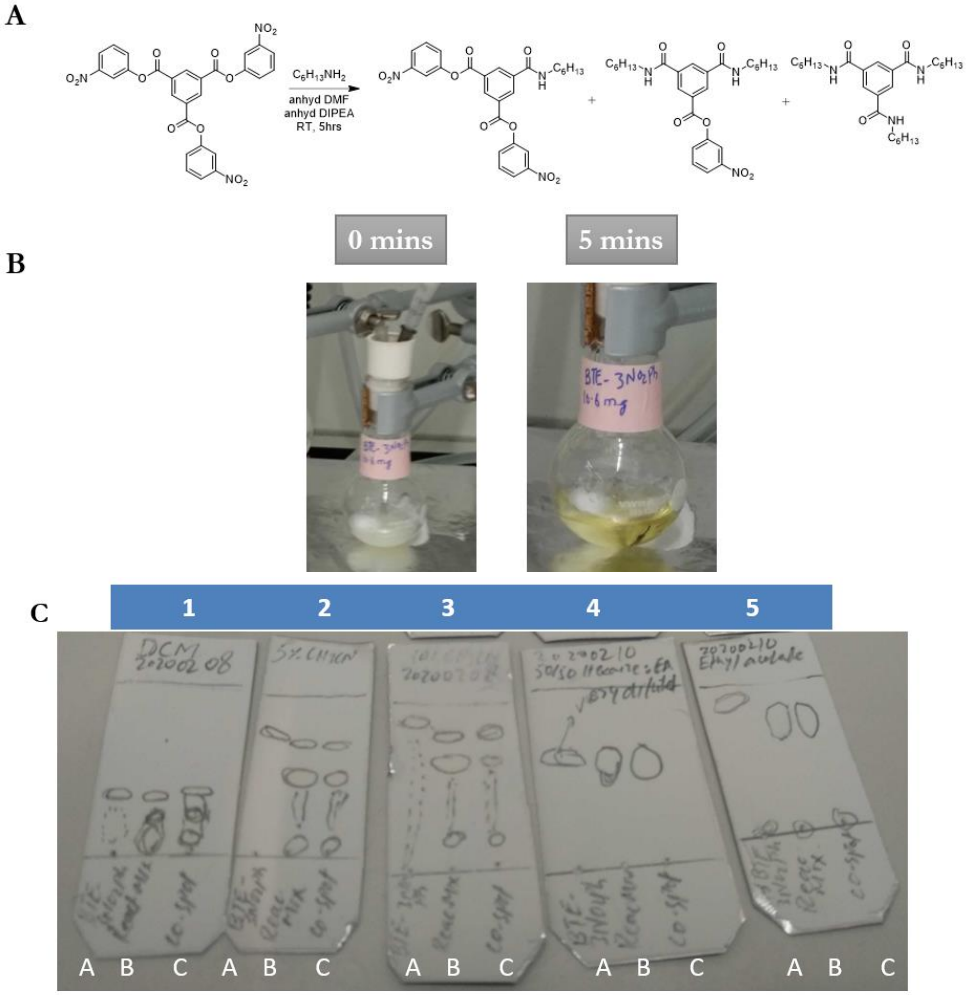

Figure S11. A) Reaction scheme of desymmetrization reaction of molecule **1** using DMF solvent. B) Molecule **1** showed partial solubility in DMF (left), solubility increased, and the reaction solution became clear with the reaction proceeding (right). C) TLC of the reaction mixture in DCM (labeled as 1), in 5%(v/v) CH_3CN+95%(v/v) DCM, 10%(v/v) CH_3CN+90%(v/v) DCM, 50%(v/v) ethylacetate+50%(v/v) hexane, and in the ethyl acetate. Different solvent combinations were used to separate product spots formed during the reaction. Maximum three spots were visible on TLC when using solvent 10%(v/v) CH_3CN+90%(v/v) DCM.

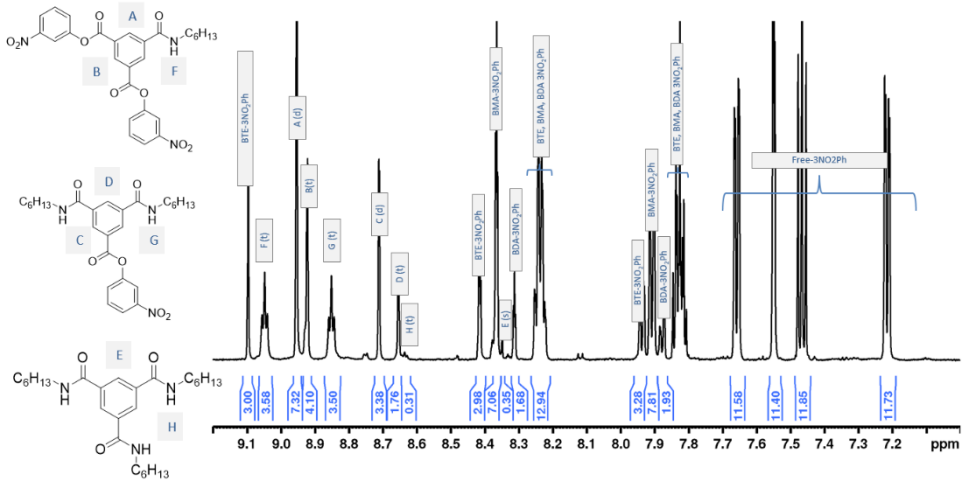

Figure S12. ^{1}H NMR (d_6-DMSO) of reaction mixture of **1** (BTE-3NO$_2$PH) when desymetrized using one equivalent of hexylamine. Different expected molecules (mono-substituted, di-substituted and tri-substituted) peaks are assigned based on chemical environment of proton and ^{1}H NMR peaks integration analysis. Zoomed in area is shown for sake of clarity of the peaks.

Synthesis of molecule 5:

Under nitrogen atmosphere, **1** (20mg, 0.035mmol, 1 equiv.) was dissolved in a dry round bottom flask using 3 mL anhydrous DMF. The color of the reaction mixture was milky white and 1 was not fully soluble in the reaction solvent. DIPEA (12 µl, 0.069 mmol, 2.0 equiv.) and hexylamine (4.6 µl, 0.035 mmol, 1.0 equiv.) were dissolved in 3–4 mL and added drop by drop to the reaction flask using a syringe and under nitrogen atmosphere. The reaction solution was stirred at room temperature for 5 hours. With the reaction proceeding solubility of **1** increases and color of the reaction mixture changes from milky white to light yellow and all the crystals disappeared. TLC of the reaction mixture was taken in different solvent combinations as shown above in **Figure S11** and showed a maximum of three spots with R_f close to 0.1, 0.7, and 0.9 in DCM with 10% (v/v) acetonitrile. After 5 hours of reaction solvent was concentrated *in a vacuo* and molecules were separated using silica gel flash column chromatography. Using eluent dichloromethane with 5% (v/v) acetonitrile, **5** was obtained (6.9 mg, 37% isolated yield). ^{1}H NMR (700 MHz, *d_6*-DMSO) δ 9.03 (t, 1H), 8.94 (d, 2H), 8.91 (t, 1H), 8.35 (dd, 2H), 8.22 (t, 2H), 7.90 (DD, 2H), 7.82 (t, 2H), 3.30 (t, 2H), 1.56 (p, 2H), 1.31 (m, 6H), 0.86 (t, 3H). 13C NMR (176 MHz, *d_6*-DMSO) δ 163.6, 163.1, 150.7, 148.39, 135.9, 133.48, 133.1, 130.98, 129.8, 129.1, 126.2, 121.3, 115,81.

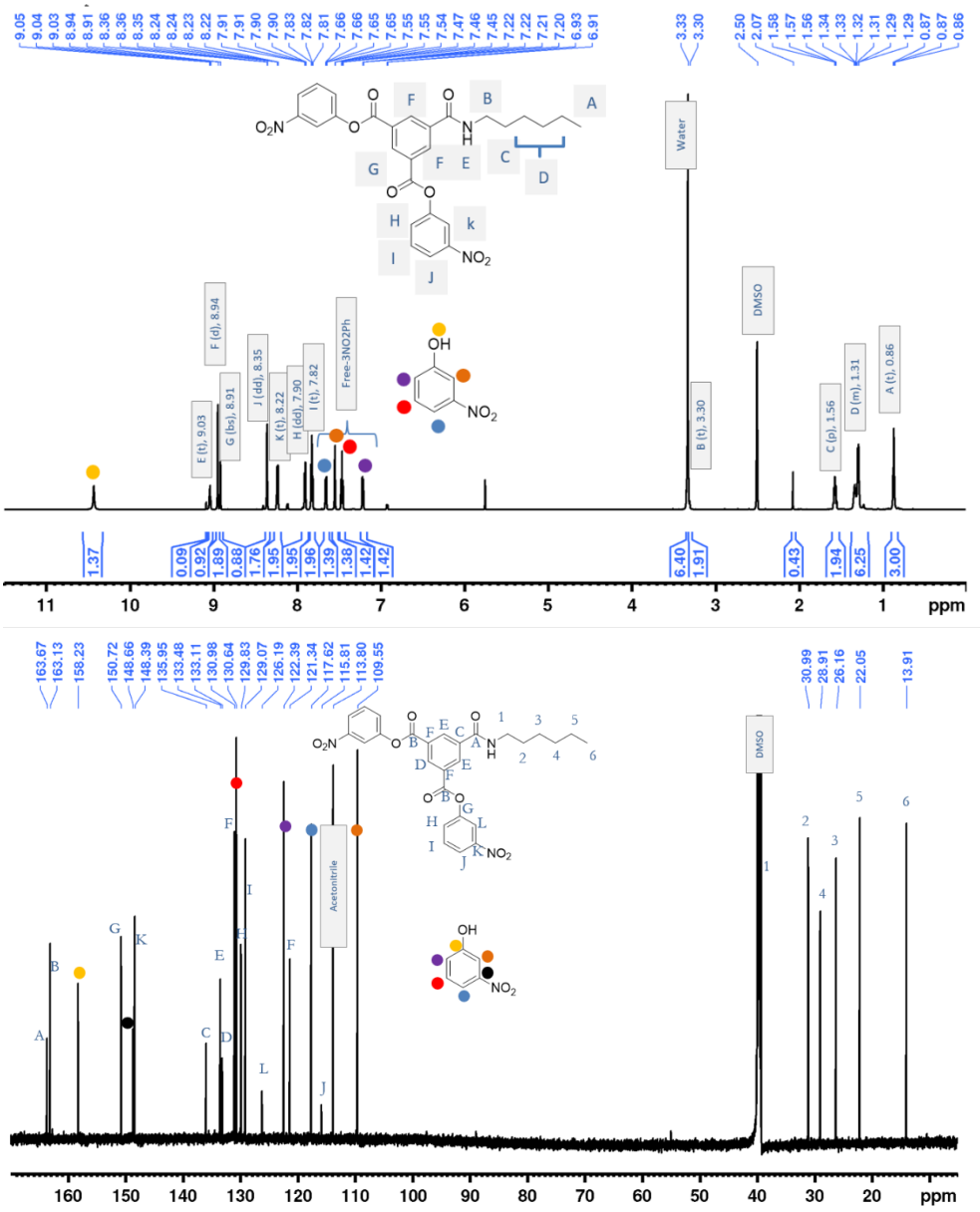

Figure S13. ^{1}H (top) and ^{13}C (bottom) NMR of molecule **5** (BMA-3NO_2Ph). Free 3-nitrophneol which cleaved off from **1** during desymmetrization eluted with **5.** 3-nitrophenol peaks are labeled with color circles.

Synthesis of molecule 7:

Under nitrogen atmosphere, **1** (20mg, 0.035mmol, 1 equiv.) was dissolved in a dry round bottom flask using 5–6 mL anhydrous DMF. The reaction mixture color was milky white and non-transparent and **1** was partially soluble in anhydrous DMF. DIPEA (18 µl, 0.11 mmol, 3 equiv.) and hexylamine (9.2 µl, 0.07 mmol, 2.0 equiv.) were dissolved in 7–8 mL of anhydrous DMF and added drop by drop to the reaction flask using a syringe and at room temperature under nitrogen atmosphere. The reaction mixture was stirred for 5 hours, and the color of the reaction goes from milky white to yellow and clear without any solid crystals. **7** was separated using silica gel flash column chromatography using DCM with 10% (v/v) acetonitrile. ^{1}H NMR (700 MHz, d_6-DMSO) δ 8.85 (t, 2H), 8.71 (d, 1H), 8.65 (t, 2H), 8.31 (t, 1H), 8.22 (dd, 1H), 7.88 (dd, 1H), 7.81 (t, 1H), 3.26 (t, 4H), 1.55 (p, 4H), 1.29 (m, 12H), 0.86 (t, 6H). ^{13}C NMR (176 MHz, d_6-DMSO) δ 164.54, 163.57, 150.81, 148.41, 135.59, 131.48, 130.98, 130.72, 129.08, 129.00, 121.24, 117.57, 31.00, 28.95, 26.16, 22.05, 13.92.

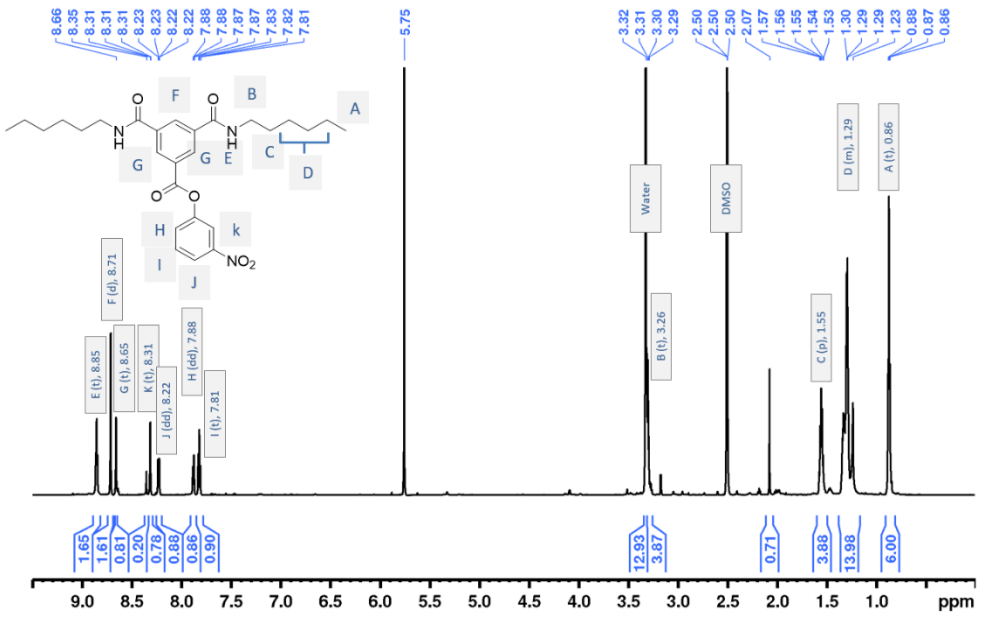

Figure S14A. ^{1}H NMR of molecule **7**

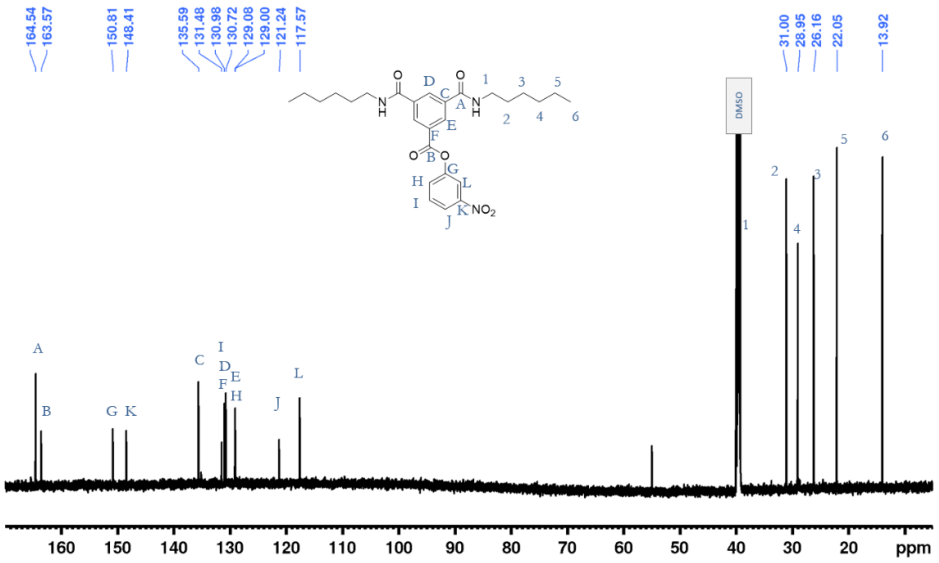

Figure S14B. ^{13}C NMR of molecule **7**

Desymetrization of 1-(4-nitrocyclohexa-1,3-dien-1-yl) 3,5-bis(4-nitrophenyl) benzene-1,3,5-tricarboxylate (2):

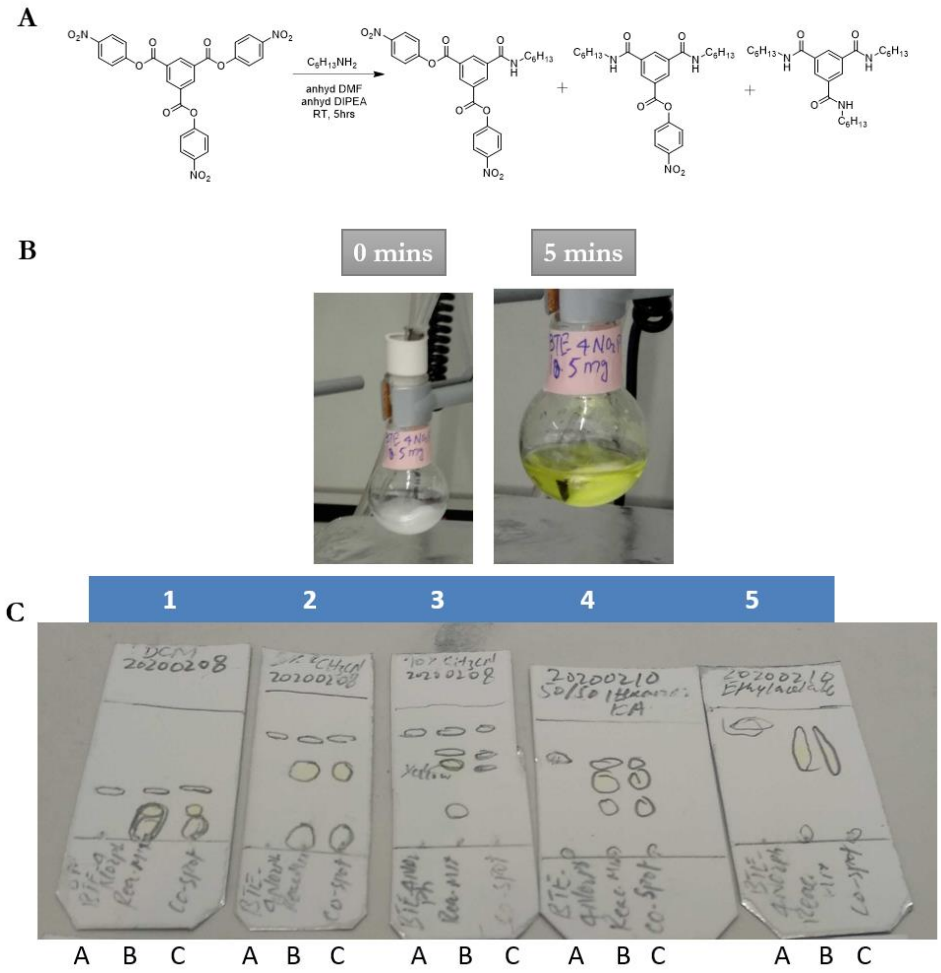

Figure S15. A) Molecule **2** desymmetrization reaction scheme and reaction were run in anhydrous DMF. B) Molecule **2** was partially soluble in DMF (reaction flask at left), and solubility increased and the reaction solution become clear (right reaction flask) with the reaction proceeding. C) TLC of the reaction mixture showed one spot in DCM at Rf 0.3 (TLC labeled as 1) and three spots in DCM with 5% acetonitrile (TLC labeled as 2) at R_f 0, 0.5, and 0.8, and four spots in DCM with 10% acetonitrile (TLC labeled as 3) at R_f 0.3, 0.5, 0.6, 0.9. TLC labeled as 4 was run using DCM with 50% hexane and 50% ethyl acetate. TLC labeled as 5 was run in 100% ethyl acetate.

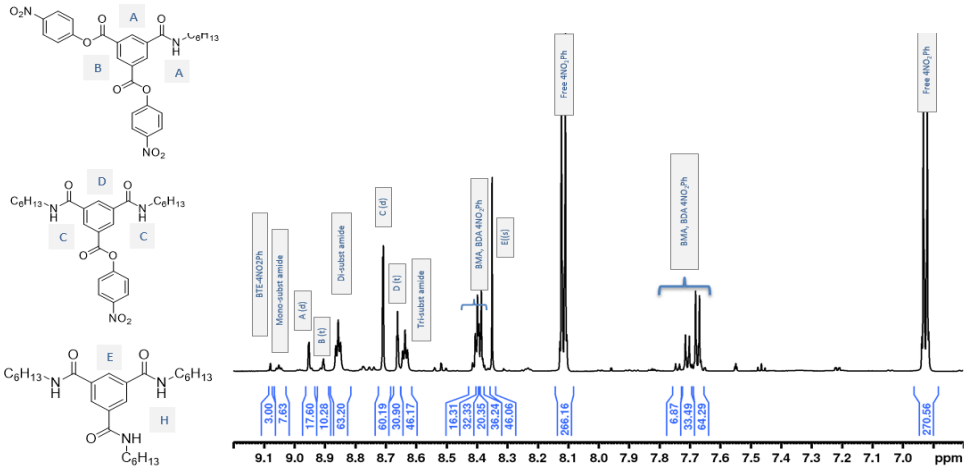

Figure S16. ^{1}H NMR of reaction mixture of BTE-4NO$_2$PH (molecule **2**) desymetrization using hexylamine (2 equiv). Expected molecules (mono-substituted, di-substituted and tri-substituted) peaks are assigned based on ^{1}H NMR peaks integration analysis.

Synthesis of molecule 6:

In a dry round bottom flask, **2** (20mg, 0.035 mmol, 1 equiv.) was dissolved 3–4 mL anhydrous DMF under a nitrogen atmosphere. DIPEA (12 µl, 0.069 mmol, 2.0 equiv.) and hexylamine (4.6 µl, 0.035 mmol, 1.0 equiv.) were dissolved in 3–4 mL and added drop by drop to the reaction flask using a syringe and under nitrogen atmosphere. The color of the reaction mixture was milky white and upon adding DIPEA and hexylamine, the reaction solvent turned yellow, and the reaction mixture was clear without any solid crystals. After 5 hours, the reaction mixture was dried *in vacuo* **6** was separated by silica gel flash column chromatography using DCM with 5% (v/v) acetonitrile. **6** was not obtained as pure and it contains starting materials **2**, free 4-nitrophenol, which can be seen in **Figure S17** ^{1}H NMR spectrum. Molecule **6** was produced in 38% yield from proton ^{1}H NMR peak integration analysis.

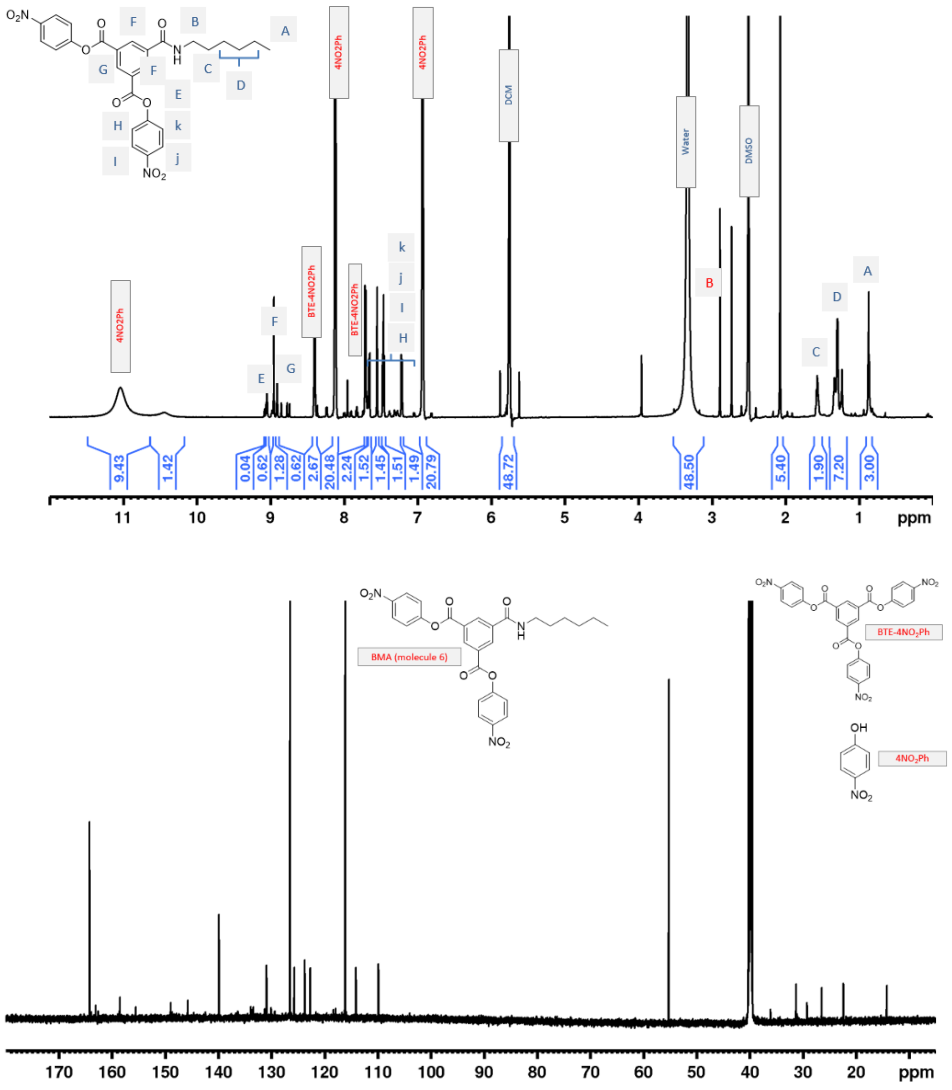

Figure S17. ^{1}H NMR ($CDCl_3$) (top) and C ^{13}NMR (bottom) of **6** (BMA-4NO_2Ph). It contains starting materials BTE-4NO_2Ph and free 4-nitrophenol. All eluted together in flash column chromatography separation.

Synthesis of molecule 8:

In a dry round bottom flask, **2** (20mg, 0.035 mmol, 1 equiv.) was dissolved 5–6 mL anhydrous DMF under a nitrogen atmosphere. DIPEA (18 µl, 0.1 mmol, 3 equiv.) and hexylamine (9.2 µl, 0.07 mmol, 2.0 equiv.) were dissolved in 5–6 mL of anhydrous DMF and added dropwise to the reaction flask under nitrogen atmosphere. After 5 hours, the reaction solvent was dried *in a vacuo.* DCM with 10% (v/v) acetonitrile solvent mixture was used to elute **8** on silica gel flash column chromatography. Molecule **8** was obtained (3 mg, 17% isolated yield). ^{1}H NMR (700 MHz, *d6*-DMSO) δ 8.86 (t, 2H), 8.70 (d, 2H), 8.66 (bs, 1H), 8.39 (d, 2H), 7.68 (d, 2H), 3.29 (t, 4H), 1.54 (p, 4H), 1.39 (m, 12H), 0.87 (t, 6H), ^{13}C NMR (176 MHz, d_6-DMSO) δ 164.54, 163.55, 155.67, 145.65, 135.93, 131.90, 131.00, 129.16, 125.71, 123.71, 31.29, 29.23, 26.44, 22.34, 14.21. Note, Carbon labeled as 1 in the ^{13}C spectrum of the molecule shows up under DMSO peaks.

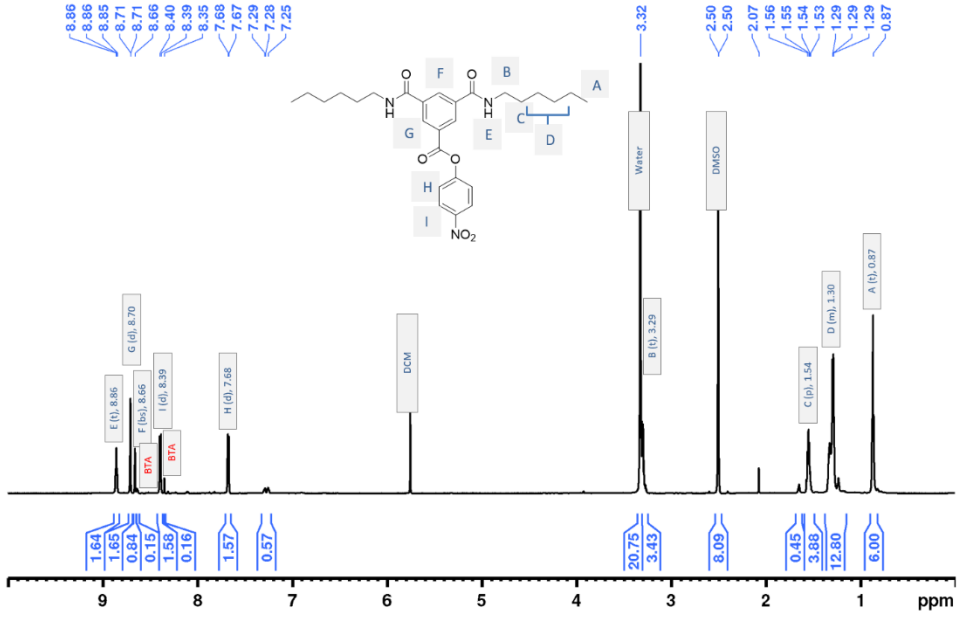

Figure S18A. ^{1}H NMR of molecule **8.** Molecule **8** is around 95% pure and contains around 5% of trisubstited hexylamine derivative labelelled as BTA.

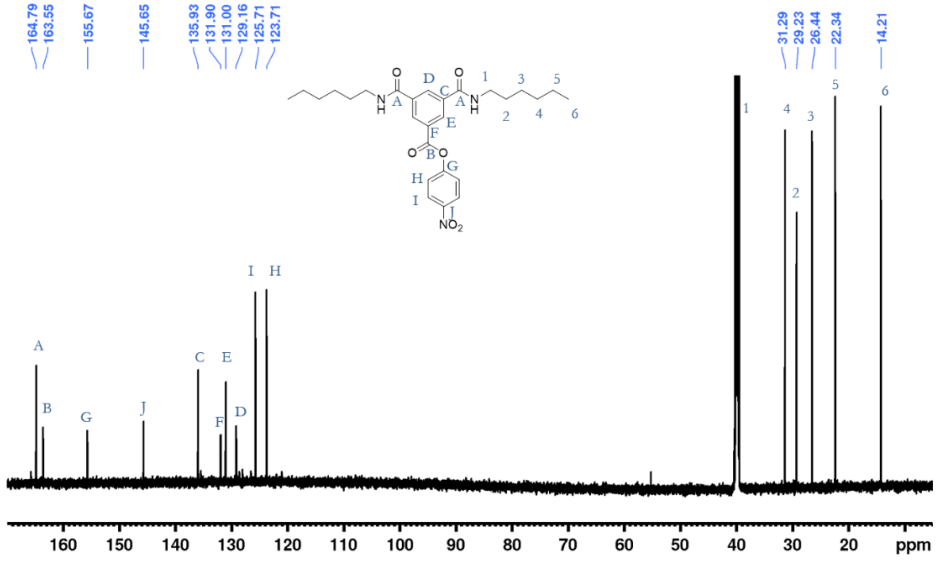

Figure S18B. ^{13}C NMR of molecule **8.**

Desymmetrization of tris(perfluorophenyl) benzene-1,3,5-tricarboxylate (3):

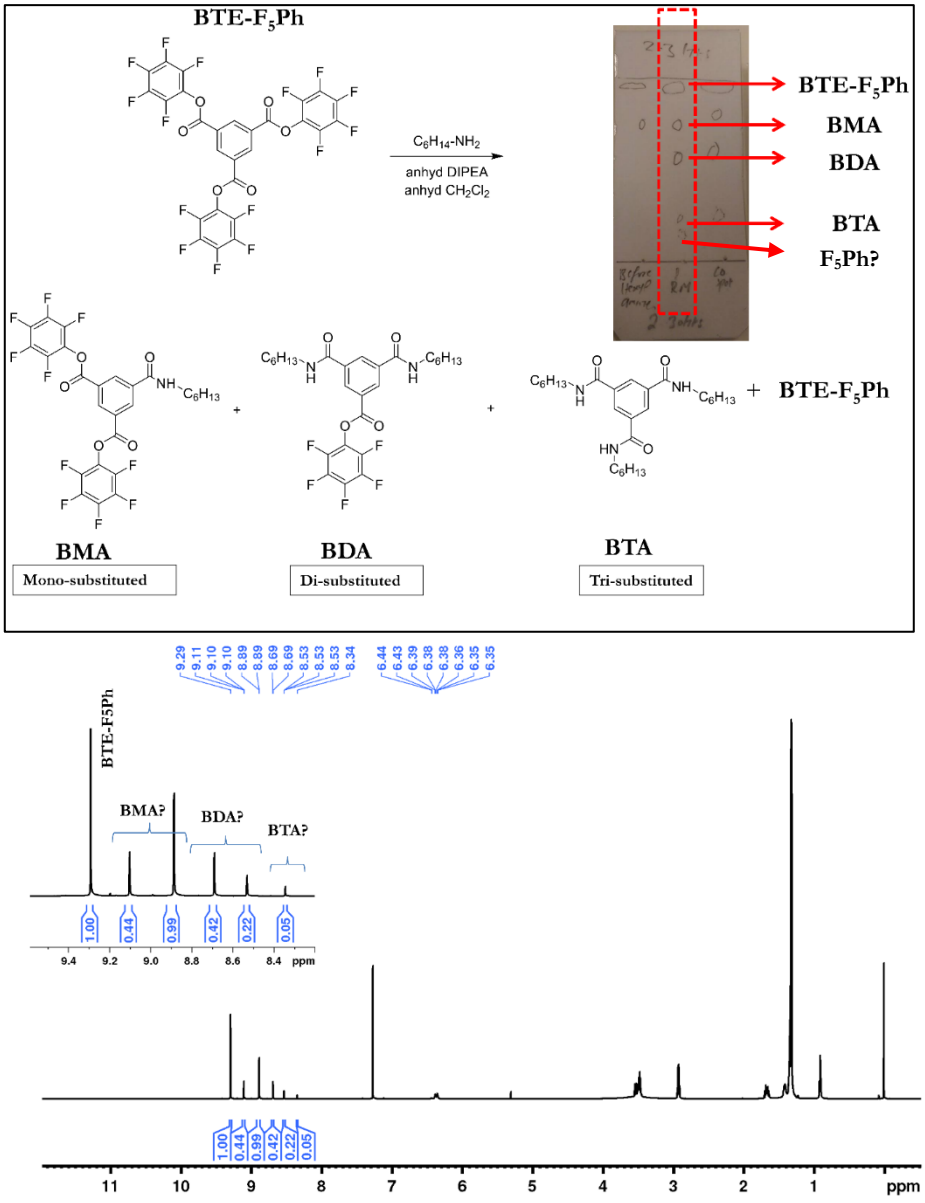

Figure S19. Reaction scheme (top) of desymmetrization of molecule **3** (BTE-F_5PH)**.** Thin layer chromatography showed that there are total of five spots which indicates that there are five molecules in reaction mixture. ^{1}H NMR (bottom) of desymmetrization of molecule 3 (BTE-F5PH) using hexylamine.

Synthesis of molecule 9:

In the dried round bottom flask under nitrogen atmosphere molecule **3** (15 mg, 0.021 mmol, 1 equiv.) was dissolved in 3 mL of anhydrous DCM and the reaction glass flask was placed into a cold dry ice bath in acetone (-78 °C). DIPEA (14.8 µl, 0.085 mmol, 4 equiv.) dissolved in anhydrous DCM was added to the reaction flask. After this, a solution of hexylamine (2.8 µl, 0.021 mmoles, 1.0 equiv.) dissolved in 4 mL anhydrous DCM was added dropwise to the reaction flask under a nitrogen atmosphere. The reaction solution was stirred for 1.5 hours at -78 °C. The reaction solution was concentrated *in vacuo* and purified by silica gel flash column chromatography. Monosubstituted derivative, **9**, was separated using eluent dichloromethane and obtained as a white solid (5.3 mg, 40% isolated yield). ^{1}H NMR (700 MHz, $CDCl_3$) δ 9.1 (t, 1H), 8.88 (d, 2H), 6.5 (t, 1H), 3.54 (dt, 2H), 1.68 (m, 2H), 1.32 (m, 6H), 0.9 (t, 3H). ^{13}C NMR (176 MHz, $CDCl_3$) δ 164.6, 161.1, 137.1, 134.9, 134.6, 128.8, 40.8, 31.6, 29.6, 26.8, 22.7, 14.2. MS (MALDI-TOF) calcd. for $C_{27}H_{17}F_{10}NO_5$: 625.09, found: 626.12 $[M+H]^+$.

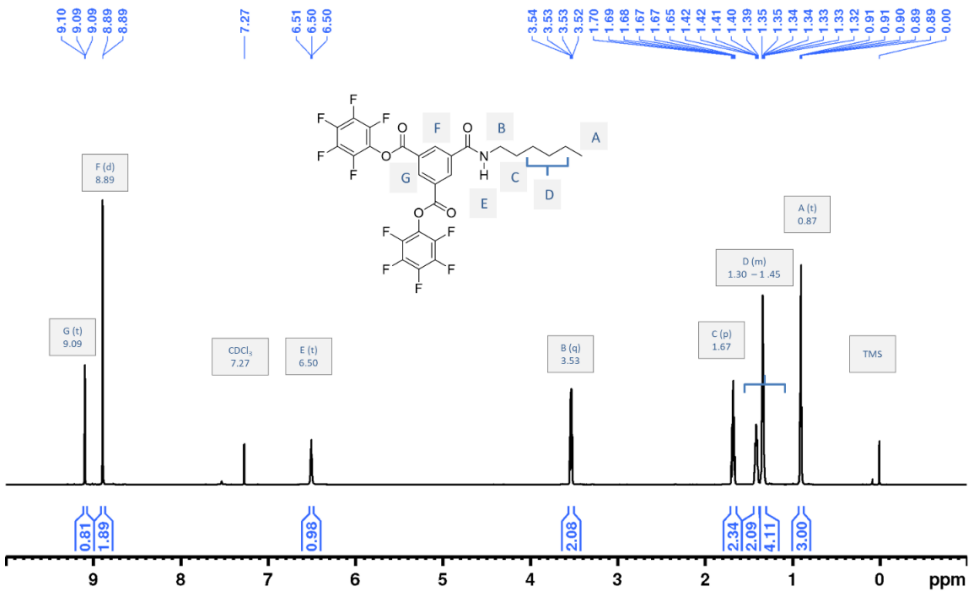

Figure S20. ^{1}H NMR ($CDCl_3$) of molecule **9**

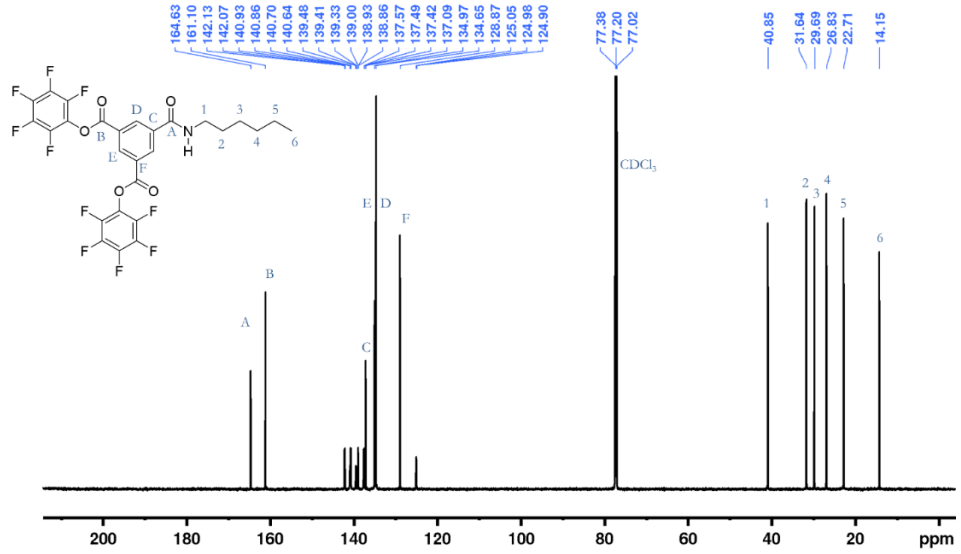

Figure S21. ^{13}C NMR ($CDCl_3$) molecule **9**

Synthesis of molecule 10:

Molecule **3** (15 mg, 0.021 mmol, 1 equiv.) was dissolved in anhydrous DCM (3 mL) under a nitrogen atmosphere and cooled with a dry ice bath to -78°C. Solution of DIPEA (14.7 µl, 0.085 mmol, 4.0 equiv.) in anhydrous DCM (3 mL) was added dropwise to the reaction flask under a nitrogen atmosphere. Subsequently, dry hexylamine (5.6 µl, 0.042 mmol, 2.0 equiv.) solution in anhydrous DCM (3 mL) was added dropwise to the reaction flask and cooled to -78°C in about 15 minutes under a nitrogen atmosphere. The reaction solution was stirred for 1.5 hours at -78°C and concentrated *in vacuo*. The reaction mixture was purified using silica gel flash column chromatography and molecule **10** was separated using eluent 95% by volume DCM and 5% by volume acetonitrile. Molecule **10** was obtained as a white solid in 48 % yield (5.5 mg). ^1H NMR (700 MHz, $CDCl_3$) δ 8.66 (d, 2H), 8.52 (t, 1H), 6.5 (t, 2H), 3.47 (dt, 4H), 1.63 (m, 4H), 1.32 (m, 12H), 0.9 (t, 6H).^{13}C NMR (176 MHz, $CDCl_3$) δ 165.3, 161.7, 136.3, 131.5, 131.4, 128.0, 40.7, 31.6, 29.6, 26.8, 22.7, 14.2. MS (MALDI-TOF), calcd. for $C_{27}H_{31}F_5N_2O_4$: 542.2, found: 543.2 $[M+H]^+$.

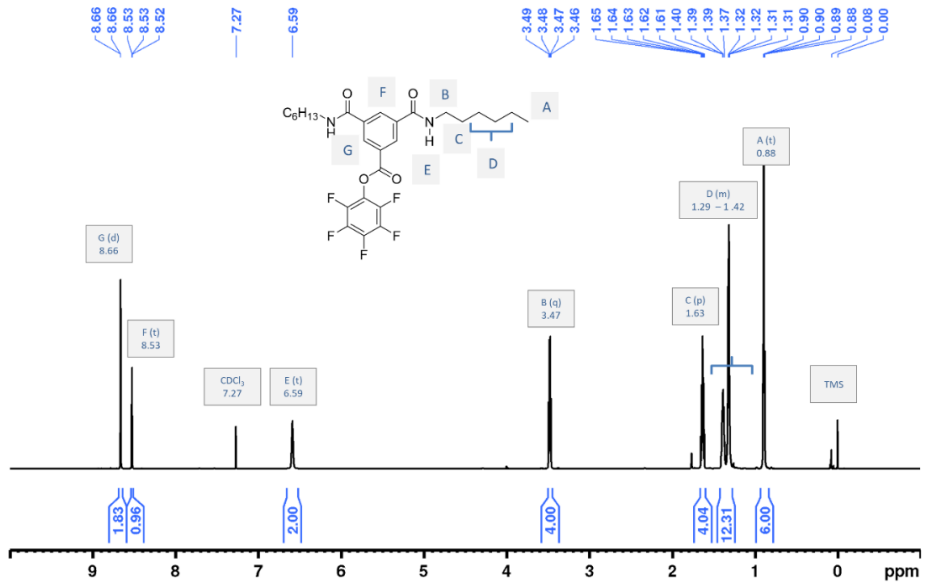

Figure S22. ^{1}H NMR ($CDCl_3$) of molecule **10**

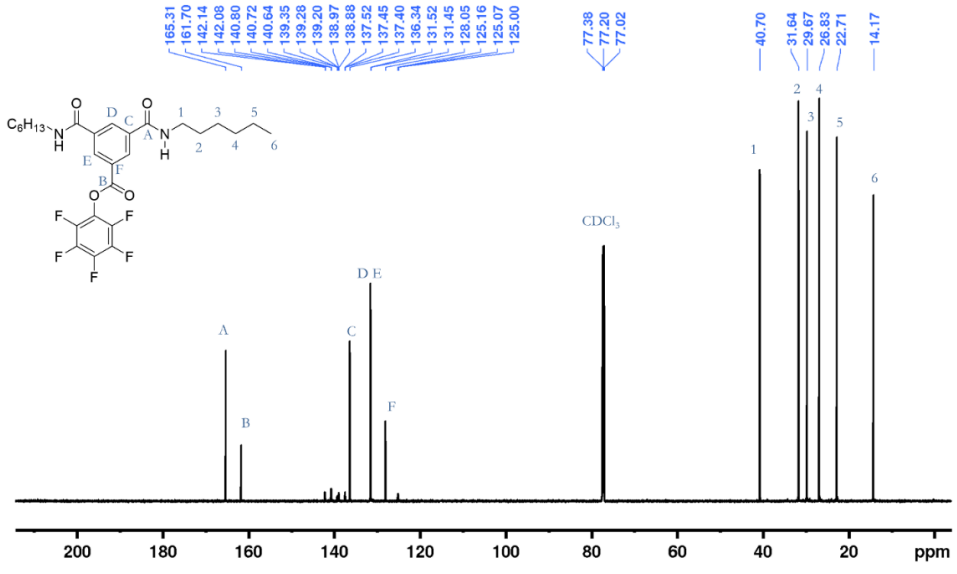

Figure S23. ^{13}C NMR ($CDCl_3$) of molecule **10**

Synthesis of molecule 11:

In a dry round bottom flask, **3** (50 mg, 0.071 mmol, 1 equiv.) was dissolved in 2.5 mL of anhydrous DCM under a nitrogen atmosphere. The temperature of the solution was maintained at 4°C using an ice bath. DIPEA solution (49 µL, 0.28 mmol, 4.0 equiv.) was dissolved in anhydrous 2 mL anhydrous DCM and added to the reaction flask. The reaction solvent color turns yellow. Subsequently, a solution of dodecyl amine (13 mg, 0.07 mmol, 1.0 equiv.) in 3 mL anhydrous DCM was added dropwise to the reaction flask. The reaction was allowed to stir at 4°C and after 2 hours reaction solvent was removed under reduced pressure ^{1}H NMR of the reaction mixture was taken and **11** was produced in 39% yield from proton ^{1}H NMR analysis. Using DCM solvent on silica gel flash column chromatography, **11** was separated. ^{1}H NMR (700 MHz, $CDCl_3$) δ 9.1 (1H, t), 8.88 (2H, d), 6.32 (1H, t), 3.53 (2H, q), 1.68 (2H, m), 1.45–1.26 (18H, m), 0.88 (3H, t). ^{13}C NMR (176 MHz, $CDCl_3$) δ 164.5, 161.1, 137.1, 134.9, 134.6, 128.8, 40.8, 32.08, 29.82, 29.79, 29.76, 29.74, 29.71, 29.51, 29.48, 27.18, 22.85, 14.26. MS (MALDI-TOF) calcd. for $C_{33}H_{29}F_{10}NO_5$: 709.9, observed:710.2 $[M+H]^+$.

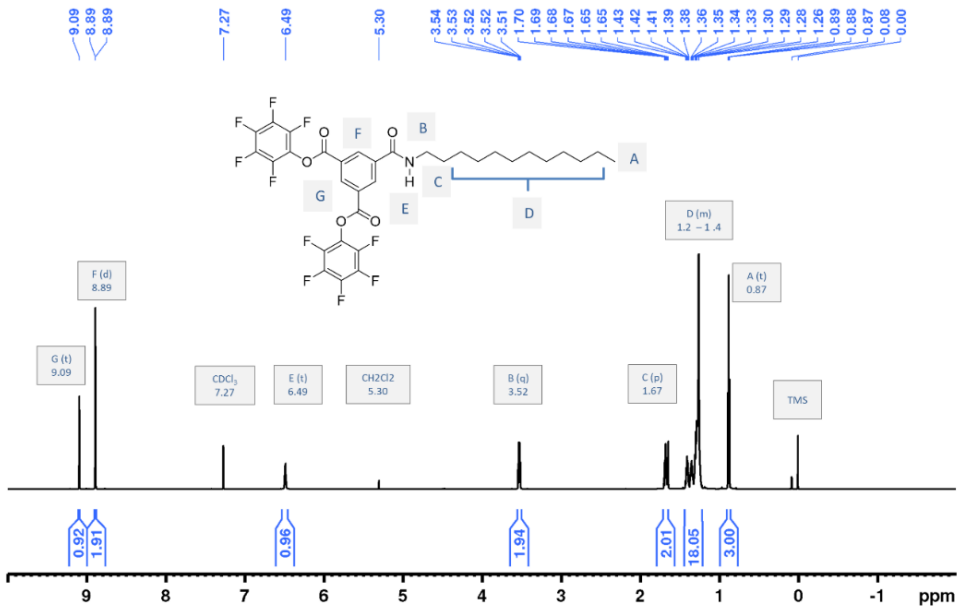

Figure S24. ^{1}H NMR ($CDCl_3$) of molecule **11**

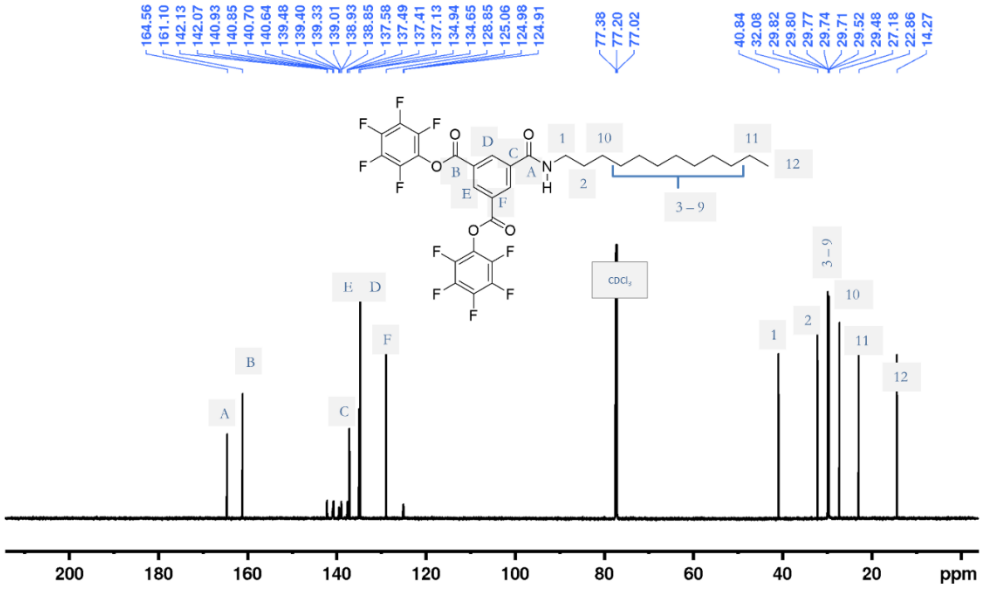

Figure S25. ^{13}C NMR ($CDCl_3$) of molecule **11.**

Synthesis of molecule 12:

In a dry round bottom flask, **3** (1000 mg, 1.4 mmol, 1equiv.) was dissolved in 50 mL of anhydrous DCM under a nitrogen atmosphere. The reaction flask was set into ice cold bath at 4 °C. DIPEA (861 μL, 5.0 mmol, 3.5 equiv.) solution in anhydrous DCM was added dropwise to the reaction flask at 4 °C using a syringe. Once the reaction solution temperature was maintained at 4 °C, dodecylamine (523 mg, 2.8 mmol, 2.0 equiv) in 25 mL anyh DCM was added dropwise to the reaction flask under nitrogen atmosphere and over the time interval of 10–15 minutes. The reaction was stirred for 1.5 hours at 4 °C. The reaction mixture was vacuum dried under reduced pressure and **12** was obtained using eluent DCM with 5% (v/v) acetonitrile in 49% isolated yield (486 mg) as a white powder. ^1H NMR (700 MHz, $CDCl_3$) δ 8.69 (2H, d), 8.51 (1H, t), 6.68 (2H, t), 3.45 (4H, q), 1.61 (4H, m), 1.4–1.2 (36H, m), 0.86 (6H, t). ^{13}C NMR (176 MHz, $CDCl_3$) δ 165.2, 161.7, 136.3, 131.5, 131.4, 128.0, 40.7, 32.08, 29.82, 29.80, 29.77, 29.72, 29.71, 29.52, 29.49, 27.18, 22.86, 14.28. MS (MALDI-TOF), calcd. for $C_{39}H_{55}F_5N_2O_4$: 710.4, found : 711.4 $[M+H]^+$.

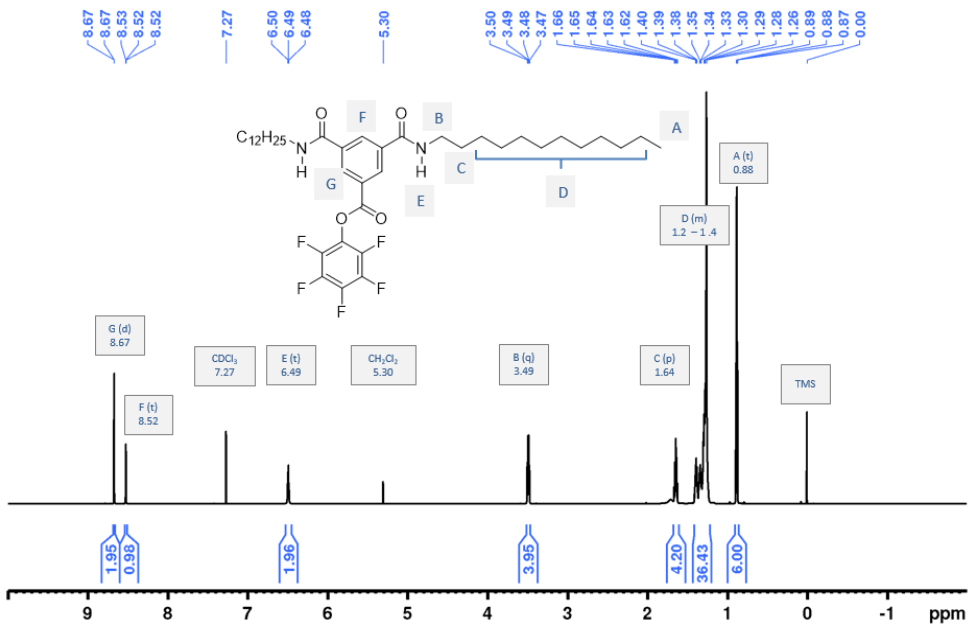

Figure S26. ^{1}H NMR ($CDCl_3$) of molecule **12**

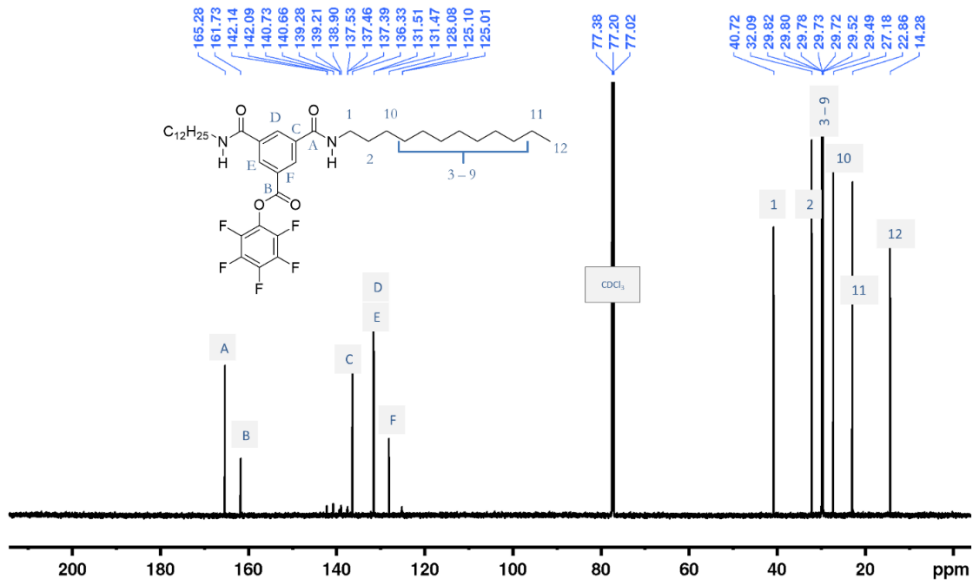

Figure S27. ^{13}C NMR ($CDCl_3$) of molecule **12**

Table S6: Table showing molecules formed in desymmetrization reaction. [a]

	Hydrophobic spacer (R)				
	Hexyl (C_6)		Dodecyl (C_{12})		Norbornene
Reaction conditions	**4°C**	**-78°C**	**4°C**	**-78°C**	**20°C**
% **BMA** (0.5 and 1 mole equiv.)	34% and 48%	32% and 49%	32% and 39%	26% and 42%	N/A
% **BDA** (1 and 2 mole equiv.)	14% and 53%	26% and 65%	28.7% and 56%	26% and 57%	52%

[a]BMA and BDA molecule formation was found to be maximum at an equimolar concentration of aliphatic amines. % of molecules formed reported in the table are derived from ^{1}H NMR peaks integration analysis.

Desymetrization of tris(perfluorophenyl) benzene-1,3,5-tricarboxylate (3) using 5Nb-2MA:

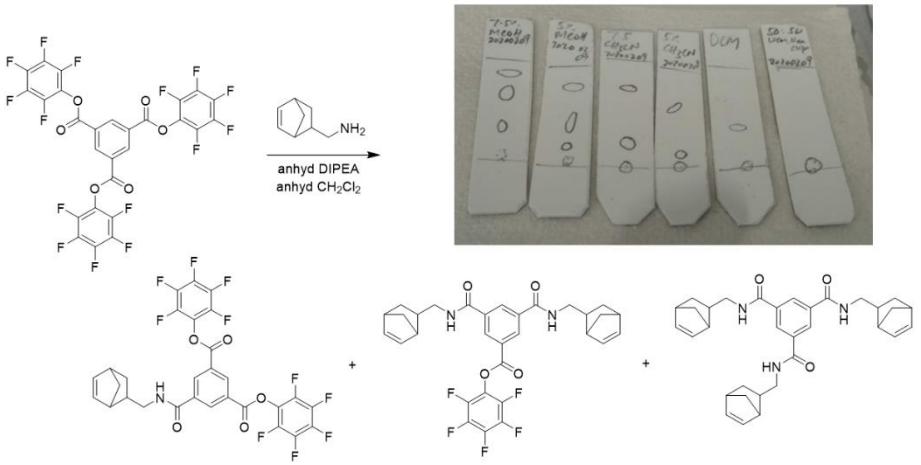

Figure S28. Desymmetrization of molecule **3** using 5-Norbornene-2-methylamine to create molecule **13** (monosubstituted) and **14** (disubstituted) derivatives.

Synthesis of molecule 13:

Under nitrogen atmosphere and in a dry round bottom flask, **3** (20 mg, 0.028 mmol, 1equiv.) was dissolved in 3mL anhydrous DCM. The reaction flask was placed into the ice-cold bath (4 °C) and then DIPEA (9.84 µl, 0.056 mmol, 2.0 equiv.) dissolved in anhydrous DCM was added into the reaction flask. Later, 5Nb-2MA (3.6 µl, 0.028 mmol, 1.0 equiv.), dissolved in anhydrous DCM, was added to the reaction flask drop by drop over 5–10 minutes using a syringe under a nitrogen atmosphere. After addition, the reaction solution was allowed to stir for 2 hours and the formation of **13** was checked by thin layer chromatography shown in **Figure S28**. The excess of DCM was removed *in vacuo* and **13** were separated using silica gel flash chromatography using eluent DCM as a white powder in 40% isolated yield (7.2 mg). ^{1}H NMR and ^{13}C NMR are shown below. ^{1}H NMR (700 MHz, $CDCl_3$) δ 9.10-9.09 (m, 1H, $H_{A\text{-}endo\text{-}exo}$), 8.9 (d, 2H, $H_{B\text{-}exo}$), 8.87 (d, 2H, $H_{B\text{-}endo}$), 6.5 (t, 1H, $H_{C\text{-}exo}$), 6.4 (t, 1H, $H_{C\text{-}endo}$), 6.24(dd, 1H, H_{5endo}), 6.1 (m, 2H, $H_{5,6exo}$), 6.04 (dd, 1H, H_{6endo}), 3.6(m, 2H, H_8), 3.5(m, 2H, H_8), 3.25(m, 2H, H_8), 2.91 (s, 1H, H_1), 2.87 (s, 1H, H_4), 2.7(m, 2H, H_2), 2.43(m, 2H, H_2), 2.35(t, 2H, H_2), 1.94 (m, 2H, H_3), 1.50 (dd, 2H, H_7), 1.43 (bs, 2H, H_7), 1.41-1.33 (m, 2H, H_7), 1.31 (s, 2H, H_7), 1.29(s, 2H, H_7), 1.26 (m, 2H, H_3), 0.69 (ddd, 2H, H_3). ^{13}C NMR (176 MHz, $CDCl_3$) δ 164.4, 161.07, 142.08, 140.8, 140.5, 139.3, 138.8, 138.2, 137.45, 137.2, 137.1, 137.0, 136.2, 134.95, 134.91, 134.65, 134.59, 132.07, 128.8, 124.9, 45.9, 45.2, 44.7, 44.5, 42.6, 41.94, 39.3, 39.00, 31.16, 30.32. MS (MALDI-TOF), calcd. for $C_{29}H_{15}F_{10}NO_5$: 647.08, found : 647.94 $[M+H]^+$.

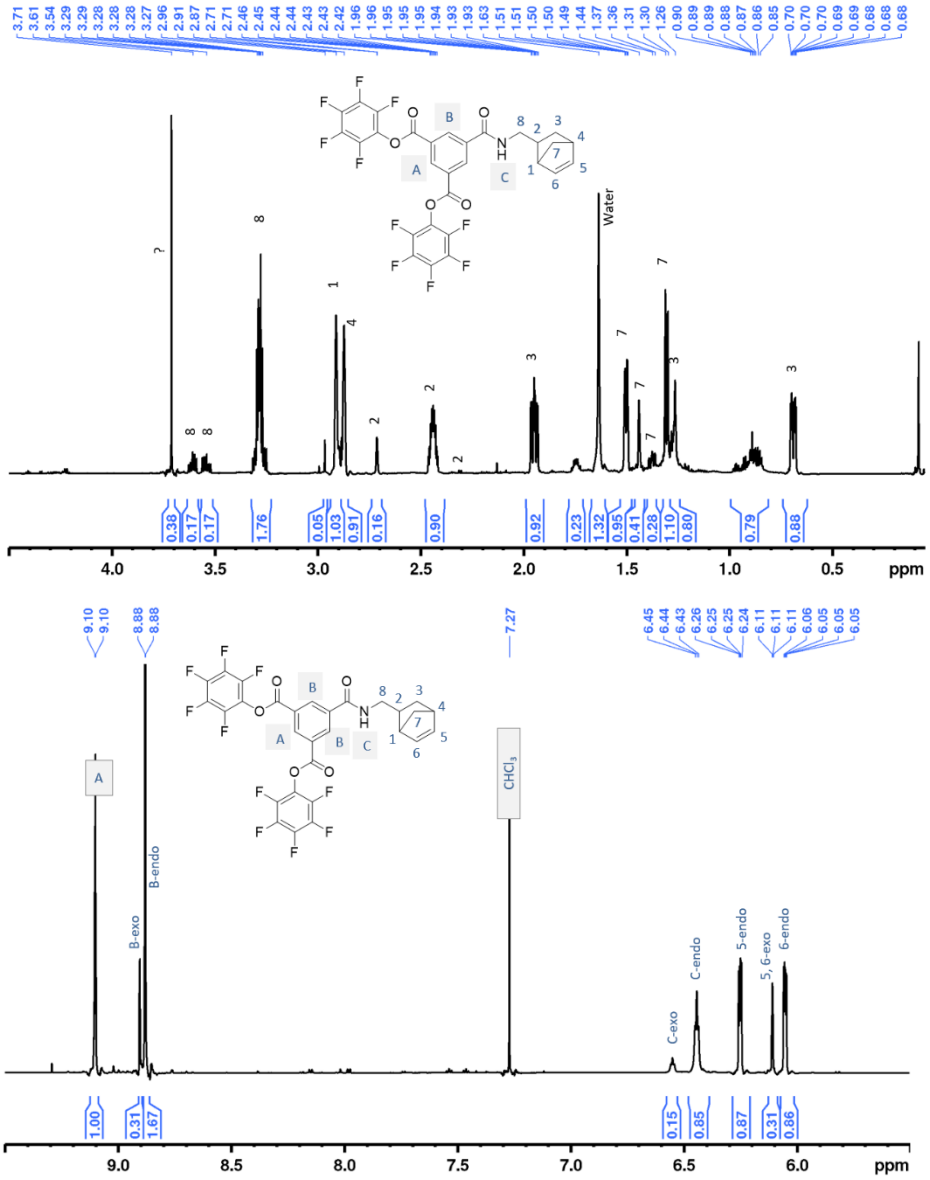

Figure S29. ^{1}H NMR molecule 13.

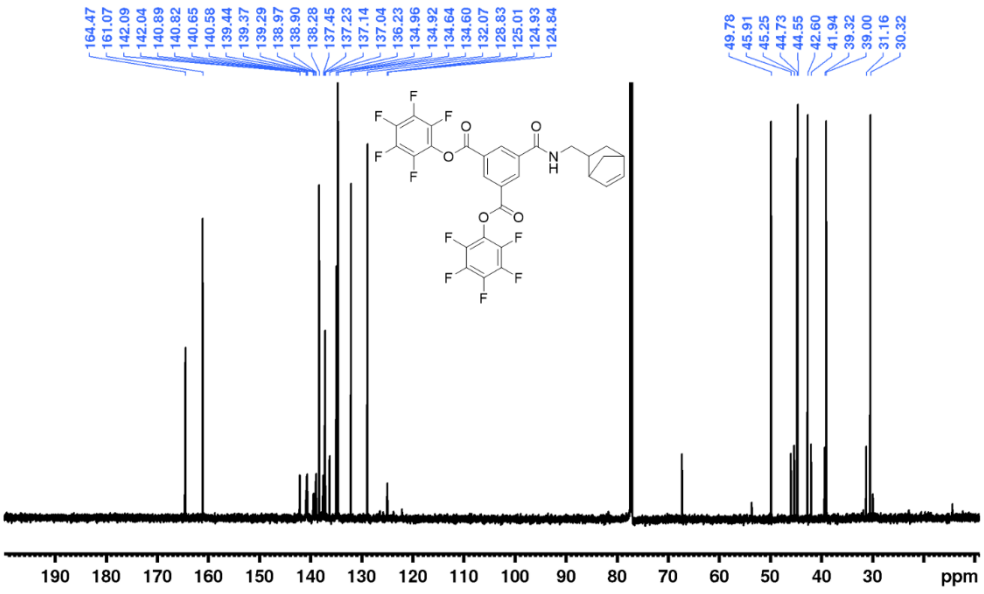

Figure S30. ^{13}C NMR molecule **13**.

Synthesis of molecule 14:

A dry round bottom flask was loaded with molecule **3** (500 mg, 0.71 mmol, 1 equiv.) under a nitrogen atmosphere and dissolved in 40 mL anhydrous DCM. Subsequently, a solution of anhydrous DIPEA (369 µL, 2.11 mmol, 3 equiv.) in 2 mL anhydrous DCM was added to the reaction flask. The reaction flask was set into an ice bath (4 ºC). Solution of 5Nb-2MA (182 µL, 1.41 mmol, 2.0 equiv.) in DCM (25 mL) was added dropwise to the reaction flask for roughly 10 minutes under a nitrogen atmosphere. The reaction was stirred for 2.5 hours at 4 ºC and the reaction mixture was vacuum dried to remove excess solvent. **14** was separated by running flash column chromatography on silica gel using eluent DCM/acetonitrile (92.5/7.5) by volume. **14** was obtained as a white powder (202 mg) in 49% isolated yield and 52% yield based on the recovered starting material. ^{1}H NMR (700 MHz, $CDCl_3$) δ 8.71-8.69 (m, 2H, $H_{Aexo\text{-}exo,\ endo\text{-}exo}$), 8.68-8.65(m, 2H, $H_{Aexo\text{-}end,\ endo\text{-}endo}$), 8.55 (t, 1H, $H_{Bexo\text{-}exo}$), 8.53 (t, 1H, $H_{Bendo\text{-}exo}$), 8.51(t, 1H, $H_{Bendo\text{-}endo}$), 6.5 (t, 1H, H_C), 6.4 (t, H, H_C) 6.24(dd, 1H, $H_{5endo\text{-}endo,\ exo\text{-}exo}$), 6.1 (t, 2H, $H_{5,6\ endo\text{-}exo}$), 6.04 (dd, H, $H_{6endo\text{-}endo,\ exo\text{-}exo}$), 3.58(m, 2H, H_8), 3.51(m, 2H, H_8), 3.25(m, 2H, H_8), 2.90 (bs, 1H, H_1), 2.86 (bs, 1H, H_4), 2.7(m, 2H, H_2), 2.41(m, 2H, H_2), 2.31(t, 2H, H_2), 1.94 (m, 2H, H_3), 1.49 (dd, 2H, H_7), 1.43 (bs, 2H, H_7), 1.41-1.33 (m, 2H, H_7), 1.30 (bs, 2H, H_7), 1.29(bs, 2H, H_7), 1.26 (m, 2H, H_3), 0.67 (ddd, 2H, H_3). ^{13}C NMR (176 MHz, $CDCl_3$) δ 165.13, 161.72, 142.12, 140.63, 139.28, 138.87, 138.80, 138.22, 137.45, 137.19, 136.38, 136.29, 132.11, 131.5, 131.42, 128.12, 125.06, 49.7, 45.8, 44.6, 44.5, 42.6, 41.9, 39.2, 39.0, 31.1, 30.3. MS (MALDI-TOF), calcd. for $C_{31}H_{27}F_5N_2O_4$: 586.19, found : 587.13 $[M+H]^+$.

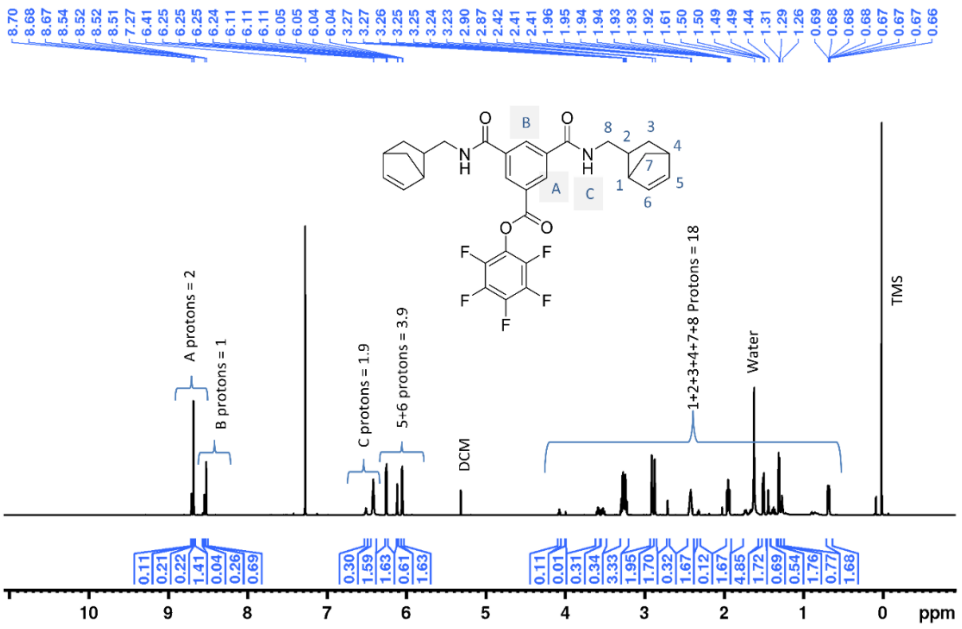

Figure S31: ^{1}H NMR ($CDCl_3$) molecule **14**.

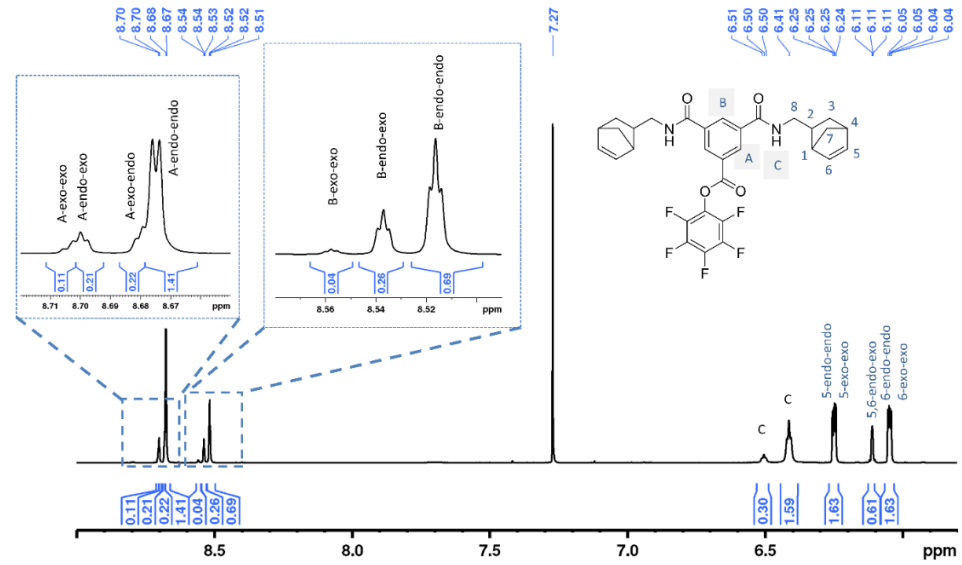

Figure S31A: ^{1}H NMR ($CDCl_3$) **14**, zoomed in from 5.8ppm to 9.0 ppm.

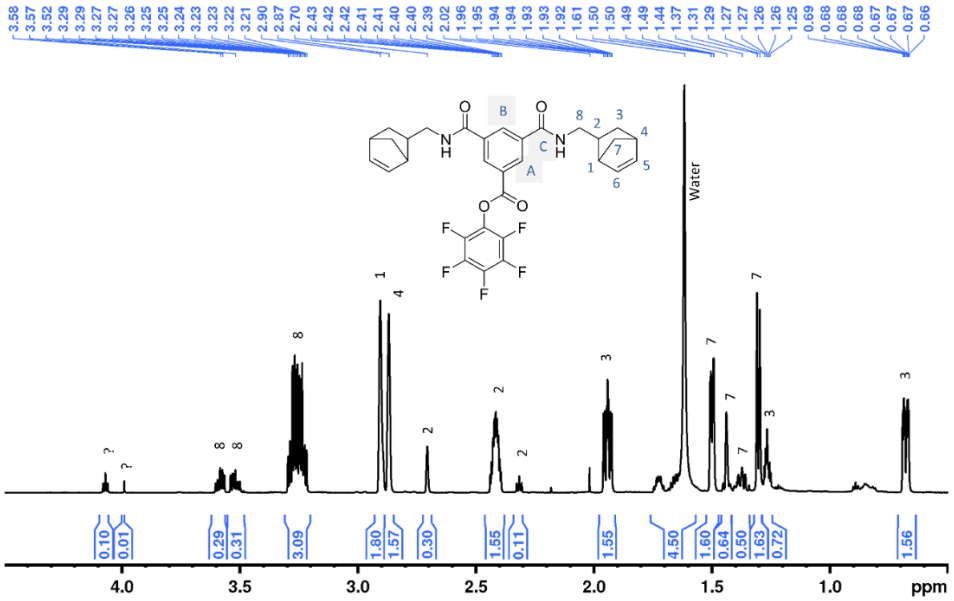

Figure S31B. ^{1}H NMR ($CDCl_3$) **14** molecule, zoomed in from 0.0 ppm to 4.5 ppm.

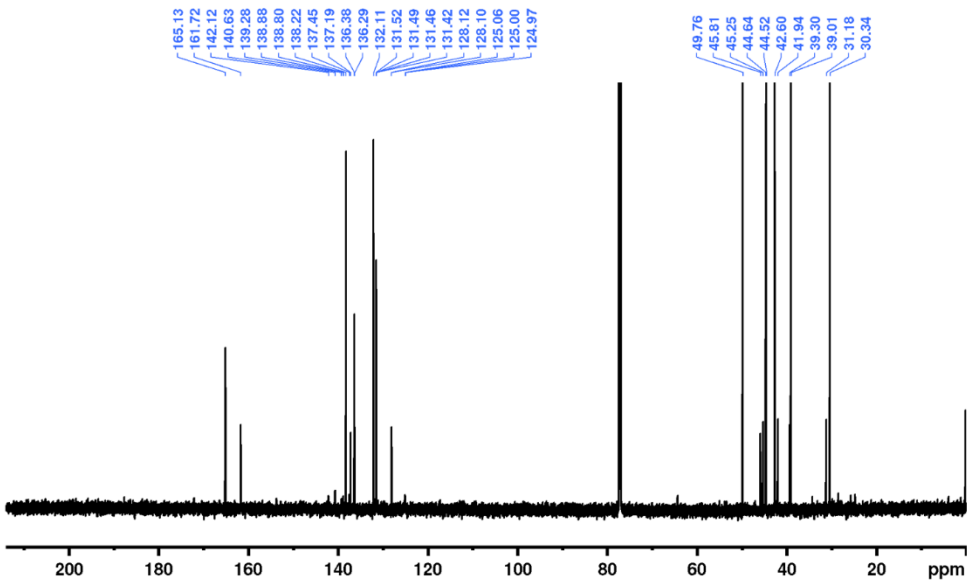

Figure S32. ^{13}C NMR ($CDCl_3$) 14.

Desymmetrization using 6-amino-1-hexanol:

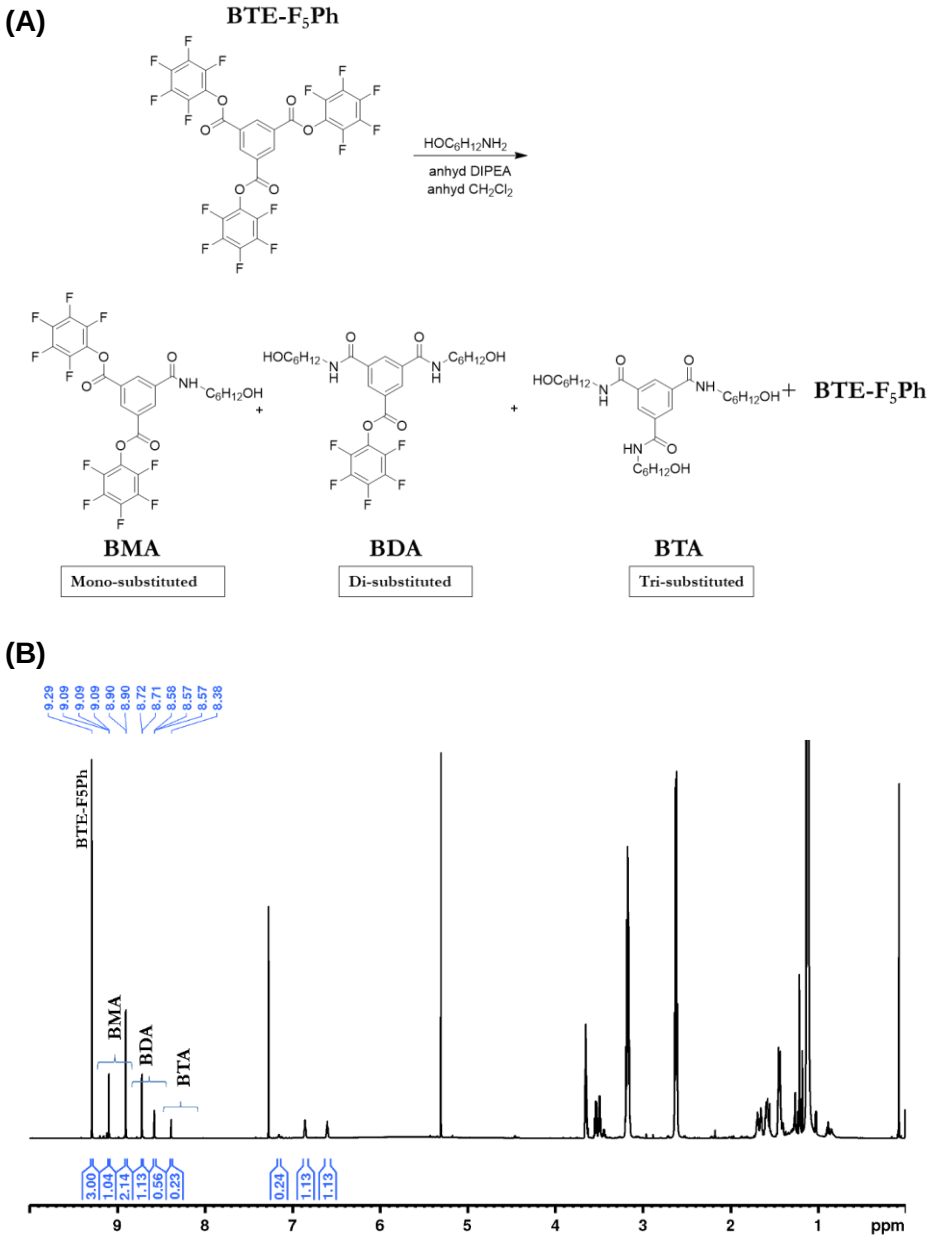

Figure S33. A) Reaction scheme for desymmetrization of molecule **3** using hexylamine alcohol. B) ^{1}H NMR ($CDCl_3$) of reaction mixture. Integration peak analysis indicates that there are total 4 molecules in reaction mixture which based on their peak ppm and peak integration analysis are mono-substituted, di-substituted and tri-substituted and leftover starting molecule **3** (BTE-F_5PH).

Synthesis of molecule 15:

A dry round bottom flask was charged with **11** (20 mg, 0.028 mmol, 1 equiv.) under a nitrogen atmosphere and dissolved in 4mL anhydrous DCM. It was stirred until fully dissolved and then a solution of anhydrous DIPEA (9.8 µL, 0.06 mmol, 2 equiv.) in 2mL anhydrous DCM was added to the flask. The reaction flask was transferred to an ice bath and subsequently, hexylamine (3.7µL, 0.03 mmol, 1.0 equiv.) solution in DCM (3mL) was added dropwise to the reaction flask in 15 minutes under continuous stirring. The reaction mixture was stirred for 1.5 hours and then the reaction mixture was vacuum dried. **15** was separated by running flash column chromatography on silica gel using eluent DCM/acetonitrile (95/5) by volume. **15** was obtained from white powder in 50% (9mg) isolated yield. ^{1}H NMR (700 MHz, $CDCl_3$) δ 8.68 (2H, d), 8.52 (1H, t), 6.43 (2H, t), 3.50 (4H, m), 1.65 (4H, p), 1.43–1.20 (24H, m), 0.93–0.85 (6H, dt). ^{13}C NMR (176 MHz, $CDCl_3$) δ 165.2, 161.7, 136.3, 131.5, 131.4, 128.1, 53.61, 40.72, 32.08, 31.64, 29.82, 29.80, 29.77, 29.72, 29.71, 29.68, 29.52, 29.48, 27.17, 26.83, 22.85, 22.70, 14.28, 14.18. MS (MALDI-TOF), calcd. for $C_{33}H_{43}F_5N_2O_4$: 626.31, found: 627.23 $[M+H]^+$.

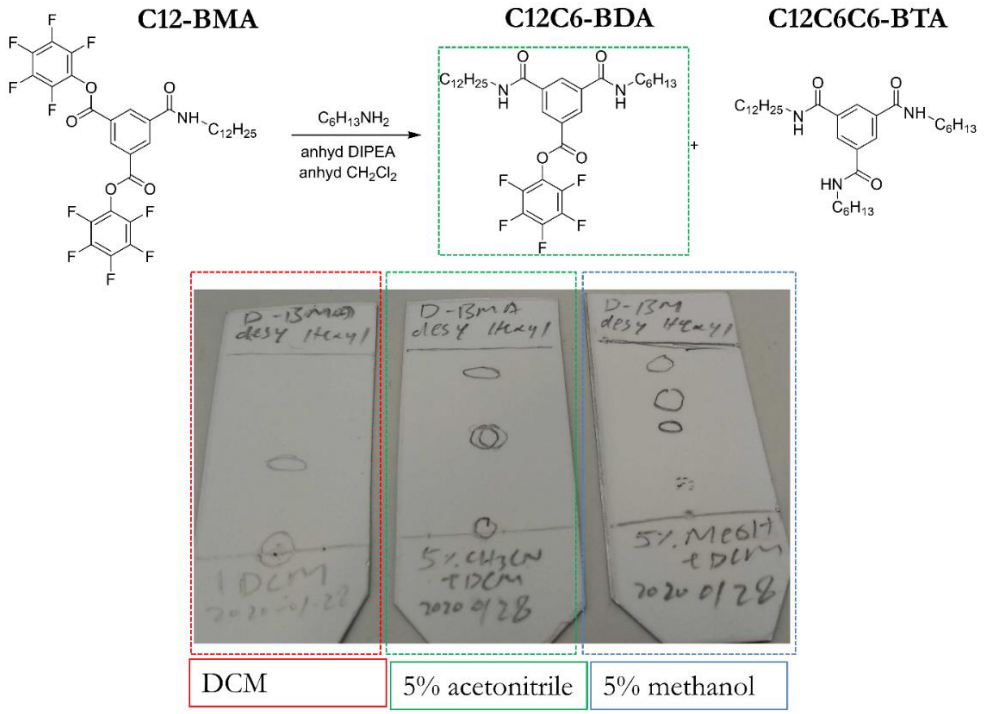

Figure S34. Reaction scheme of synthesis of molecule 15. Using hexylamine, **11** was desymmetrized for creating molecule **15**.

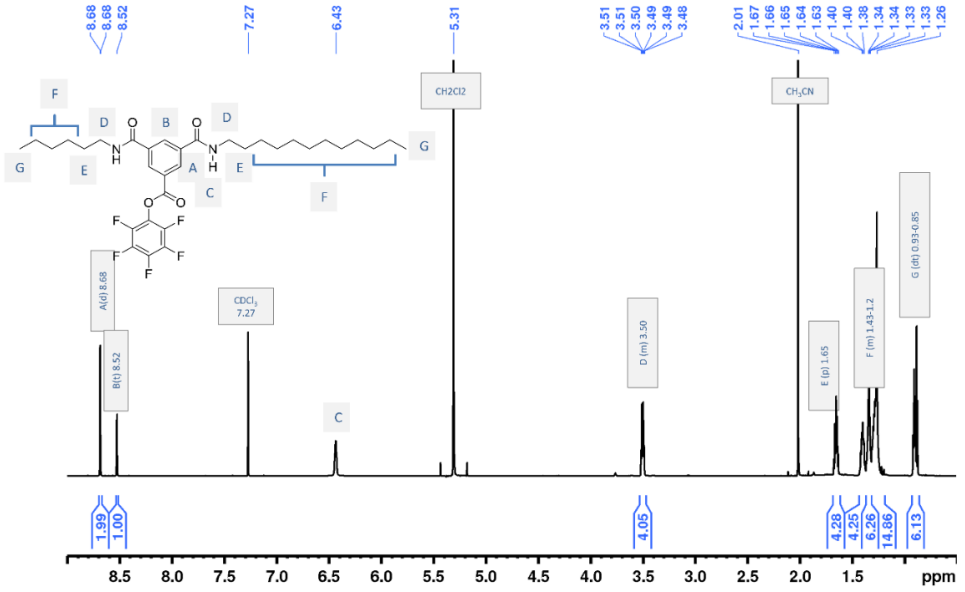

Figure S35. ^{1}H NMR ($CDCl_3$) of **15**

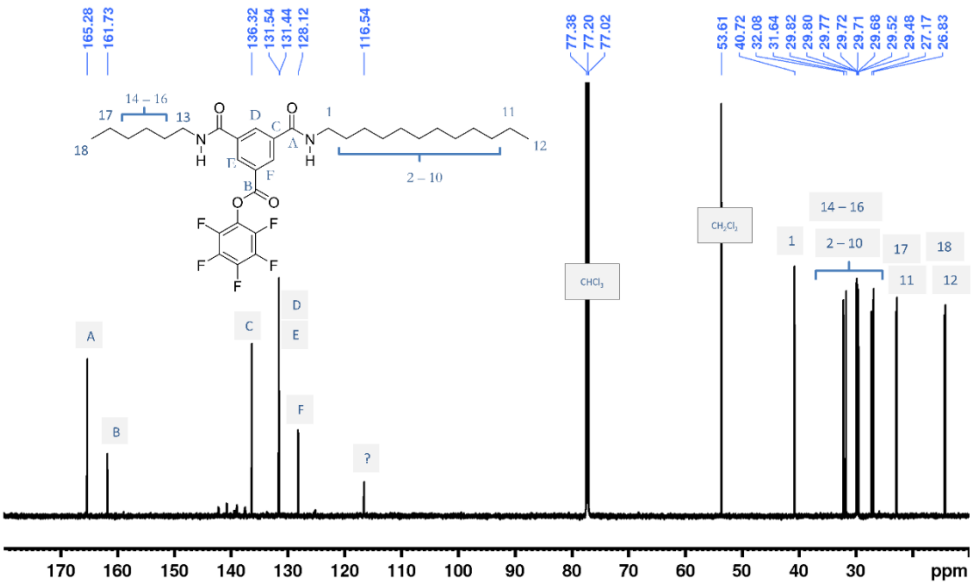

Figure S36. ^{13}C NMR ($CDCl_3$) of molecule **15**

Synthesis of molecule 16:

A dry round bottom flask was added **9** (75 mg, 0.12 mmol, 1equiv.) under a nitrogen atmosphere and dissolved in 6mL anhydrous DCM. Subsequently, a solution of anhydrous DIPEA (27 µL, 0.16 mmol, 0.65 equiv.) in 12mL anhydrous DCM was added to the reaction flask. 5Nb-2MA (11.6 µL, 0.096 mmol, 0.84 equiv.) solution in DCM (6mL) was added dropwise to the reaction flask in 10-15 minutes under an inert atmosphere. After 2 hours of continuous stirring, the reaction mixture was vacuum dried. **16** was separated by running flash column chromatography on silica gel using eluent DCM/acetonitrile (95/5) by volume. **16** was obtained white powder in 44% (30mg) yield. ^{1}H NMR (700 MHz, $CDCl_3$) δ 8.69-8.63 (m, 2H, Ar), 8.55-8.49 (m, H, Ar), 6.68 (t, 1H, H_c), 6.57 (t, 1H, H_c), 6.22(dd, H, H_5), 6.08 (m, 2H, $H_{5,6}$), 6.02(dd, H, H_6), 3.48(q, 2H H_D), 3.22(m, 2H, H_8), 2,89 (bs, H, H_4), 2.85 (bs, H, H_1), 2.68 (m, H, H_{2exo}), 2.39 (m, H, H_{2endo}), 2.01 (bs, 2H, H_7), 1.92 (m, 2H, H_7), 1.7 (m, 2H, H_7), 1.64 (p, 2H, H_E), 1.47 (dd, 2H, H_3), 1.4 (m, 2H, H_F), 1.32(m, 4H, H_G), 0.89 (t, 3H, H_H), 0.65 (dd, 2H, H_3). ^{13}C NMR δ 165.29, 165.24, 161.67, 138.16, 137.16, 136.29, 136.26, 132.09, 131.51, 131.45, 131.40, 128.01, 49.73, 45.79, 45.22, 44.62, 44.49, 42.58, 41.92, 40,67, 39,26, 38.98, 31.60, 31.15, 30.32, 29.63, 26.79, 22.67, 14.13.

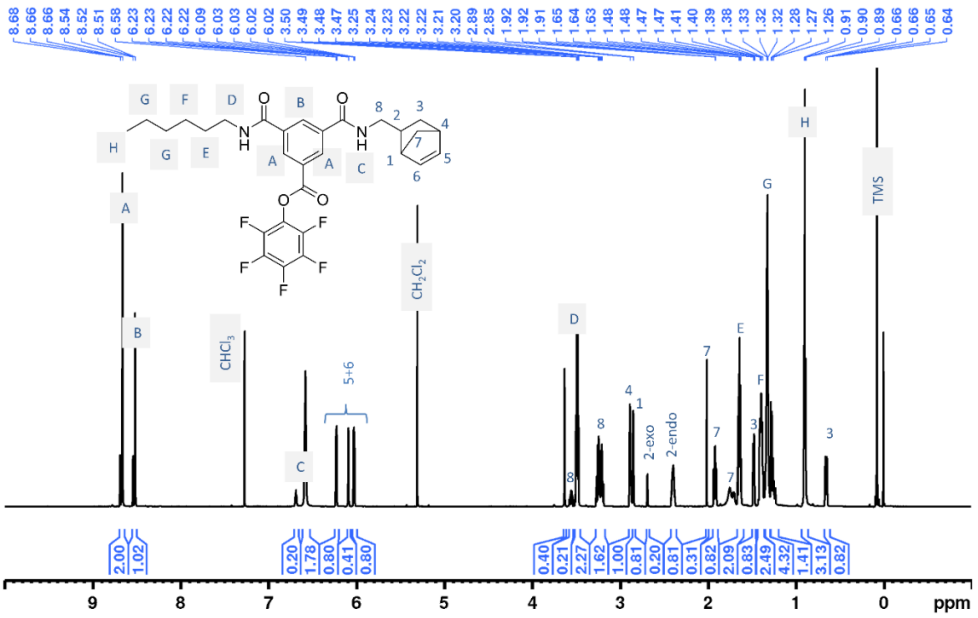

Figure S37. ^{1}H NMR ($CDCl_3$) of molecule **16**

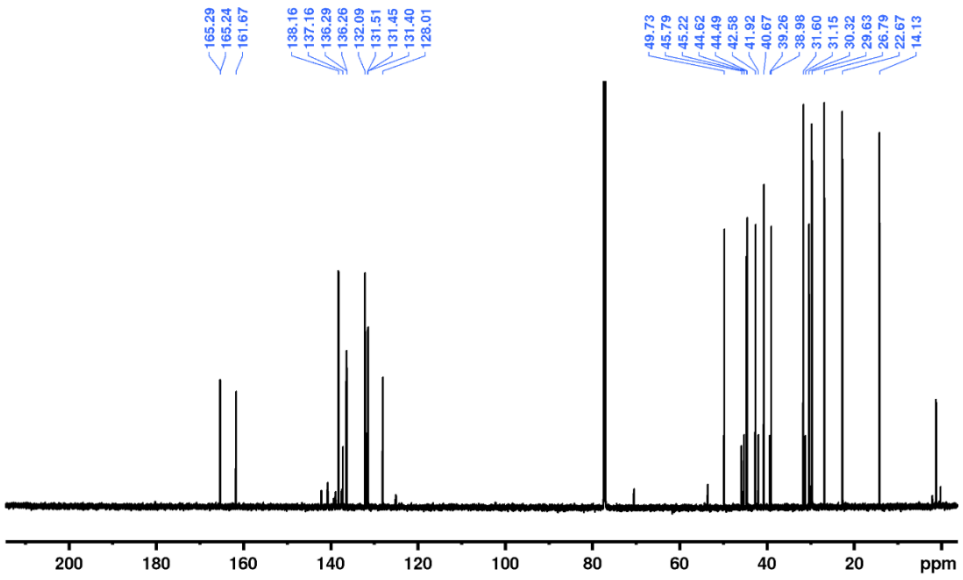

Figure S38. ^{13}C NMR ($CDCl_3$) of molecule **16**

Synthesis of molecule 17

To a clean and dry round, the bottom flask was added **12** (25 mg, 0.035 mmol, 1equiv.) and dissolved in anhydrous dichloromethane (DCM, 4 mL) under an inert atmosphere. To a stirring reaction, the solution was added dry DIPEA (13.5 µL, 0.077 mmol, 2.2 equiv.) and 5Nb-2MA (9.4 µL, 0.074 mmol, 2.1 equiv) solution in anhydrous DCM (3mL) was added to the reaction flask. After overnight stirring excess, DCM was removed *in vacuo* and **17** was obtained via column chromatography using eluent methanol/dichloromethane (5/95) by volume. The isolated yield of the reaction was 87% (20.1 mg). ^{1}H NMR spectrum is shown in **Figure S39**. It was not possible to evaluate the peak splitting pattern for some of the peaks in ^{1}H NMR and we leave all the information in the ^{1}H NMR spectrum. Perhaps that could be already BTA stacking of the molecules in $CDCl_3$.^{13}C NMR δ 166.43, 166.39, 137.90, 137.00, 136.42, 135.56, 135.49, 132.30, 128.03, 127.99, 53.75, 49.69, 45.67, 45.22, 44.48, 44.46, 42.58, 42.04, 41.93, 40.54, 39.21, 38.96, 32.06, 30.34, 29.82, 29.79, 29.74, 29.65,29.50, 27.20, 22.83. MS (MALDI-TOF), calcd. for $C_{41}H_{67}N_3O_3$: 649.52, found: 650.37 $[M+H]^+$.

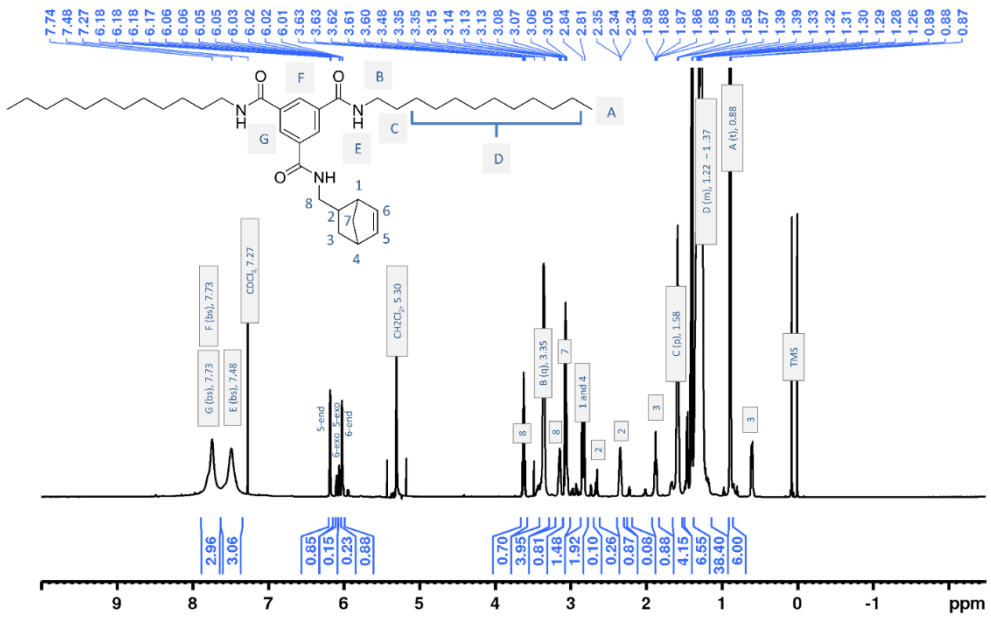

Figure S39. ^{1}H NMR ($CDCl_3$) molecule **17**

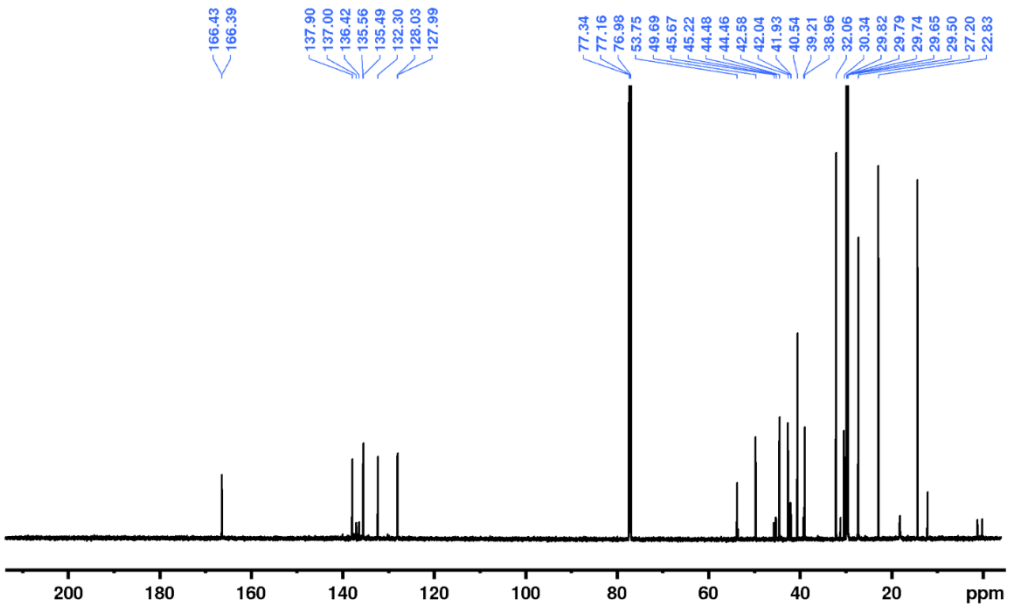

Figure S40. ^{13}C NMR ($CDCl_3$) molecule **17**

Synthesis of molecule 18:

A clean and round bottom flask equipped with a stir bar was charged with **12** (25 mg, 0.035 mmol, 1equiv.) and dissolved in anhydrous dichloromethane (DCM, 4 mL) under an inert atmosphere. The reaction solution was stirred until **12** dissolved and then to a stirring solution was added a solution of DIPEA (13.4 µL, 0.08 mmol, 2.2 equiv) and 3-Azido-1-propanamine (7.2 µL, 0.074 mmol, 2.1 equiv.) in anhydrous DCM (3 mL) was added. After overnight stirring at RT, the reaction mixture was vacuum dried to remove the excess solvent (DCM) and **12** were obtained in 85% yield (19mg) by running flash column chromatography on silica gel using eluent methanol/dichloromethane (5/95) by volume. ^{1}H NMR (700 MHz, $CDCl_3$) δ 7.82 (bs, 2H, Ar), 7.59 (bs, H, Ar), 7.24 (bs, 3H, (C=O)N<u>H</u>), 3.49 (q, 2H,(C=O)NHC<u>H</u>$_2$CH$_2$CH$_2$N$_3$), 3.41 (t, 2H, C<u>H</u>$_2$N$_3$), 3.38 (q, 4H, (C=O)NHC<u>H</u>$_2$), 1.89 (p, 2H, C<u>H</u>$_2$CH$_2$N$_3$), 1.58(p, 4H, (C=O)NHCH$_2$C<u>H</u>$_2$), 1.26–1.43 (m, 36H, aliphatic), 0.88 (t, 6H, aliphatic). ^{13}C NMR (176 MHz, $CDCl_3$) δ 166.7, 166.43, 135.62, 135.26, 127.95, 127.82, 49.38, 40.53, 37.85, 32.07, 29.84, 29.81, 29.76, 29.64, 29.51, 28.92, 27.20, 22.83, 14.26. MS (MALDI-TOF), calcd. for $C_{36}H_{62}N_6O_3$: 626.49, found : 627.43 $[M+H]^+$.

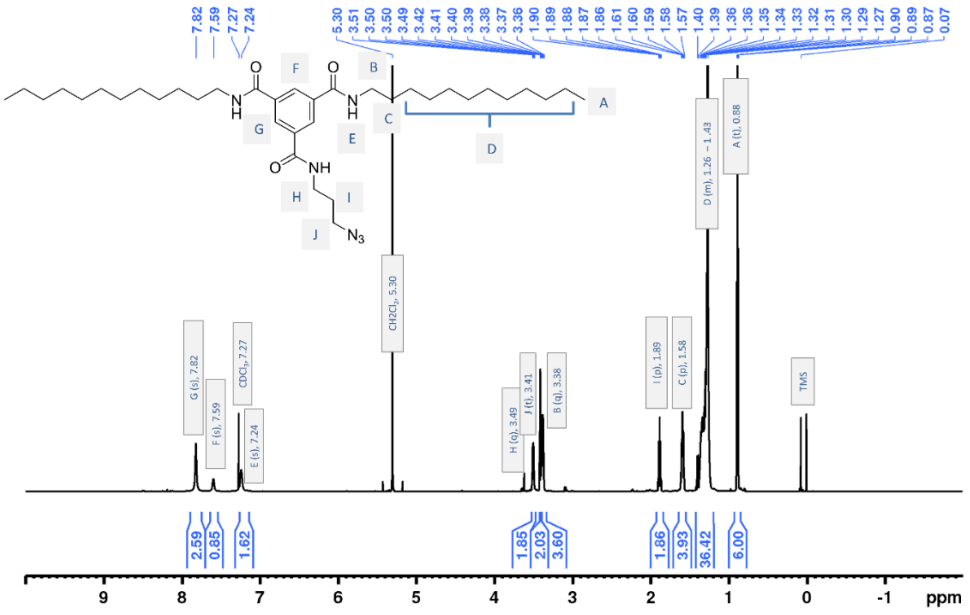

Figure S41. ^{1}H NMR ($CDCl_3$) molecule **18**

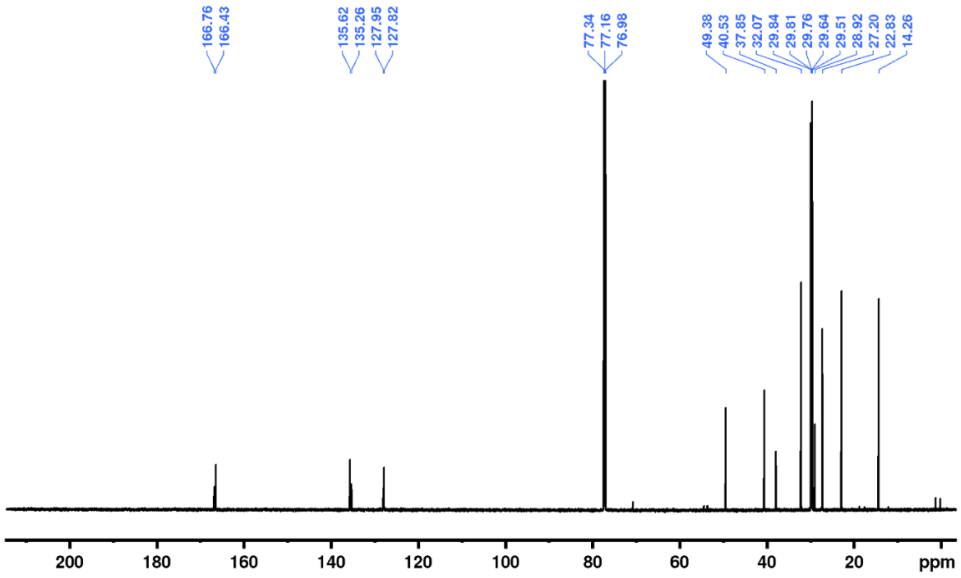

Figure S42. ^{13}C NMR ($CDCl_3$) molecule **18**

Synthesis of molecule 19

A dry round bottom flask was charged with **16** (22 mg, 0.039 mmol) under a nitrogen atmosphere and dissolved in 2mL anhydrous DCM. Subsequently, solution of anhydrous DIPEA (13.4 μL, 0.078 mmol, 2 equiv.) in 2mL anhydrous DCM was added into the reaction flask. Next, 3-Azido-1-propanamine (6.1 μL, 0.062 mmol, 1.6 equiv.) solution in DCM (2 mL) was added to the reaction flask using a glass pipette. The reaction was stirred overnight and then the reaction mixture was vacuum dried to make the reaction solution concentrated. **19** was separated by running flash column chromatography on silica gel using eluent DCM/MeOH (95/7.5) by volume. Molecule **19** was obtained from white powder in 85% (17 mg). ^1H NMR (700 MHz, $CDCl_3$) δ δ 7.73 (bs, 3H, Ar), 7.56 (bs, 1H, H_b), 7.29 (bs, 1H, H_c), 6.20 (dd, 1H, H_{5endo}), 6.12-6.06 (m, 2H, $H_{5,6exo}$), 6.02(dd, H, H_{6endo}), 3.64-3.33(m), 3.20-2.7 (m), 2.65 (bs, H, H_{2exo}), 2.34 (m, H, H_{2endo}), 2.05-1.78 (m), 1.7-1.54 (m), 1.42-1.19 (m), 0.90 (m, 3H, H_H), 0.65 (dd, 2H, H_3). ^{13}C NMR (176 MHz, d_6-DMSO) δ 165.38, 135.1, 134.86, 128.32, 54.91, 40.02, 31.00, 28.99, 26.15, 22.04, 13.91. since we took carbon spectra in *d6*-DMSO which showed septet at 39.52 and several peaks from hexyl, methyl norbornene and propyl hid under d6-DMSO peaks. MS (MALDI-TOF), calcd. for $C_{26}H_{36}N_6O_3$: 480.28, found : 481.21 $[M+H]^+$.

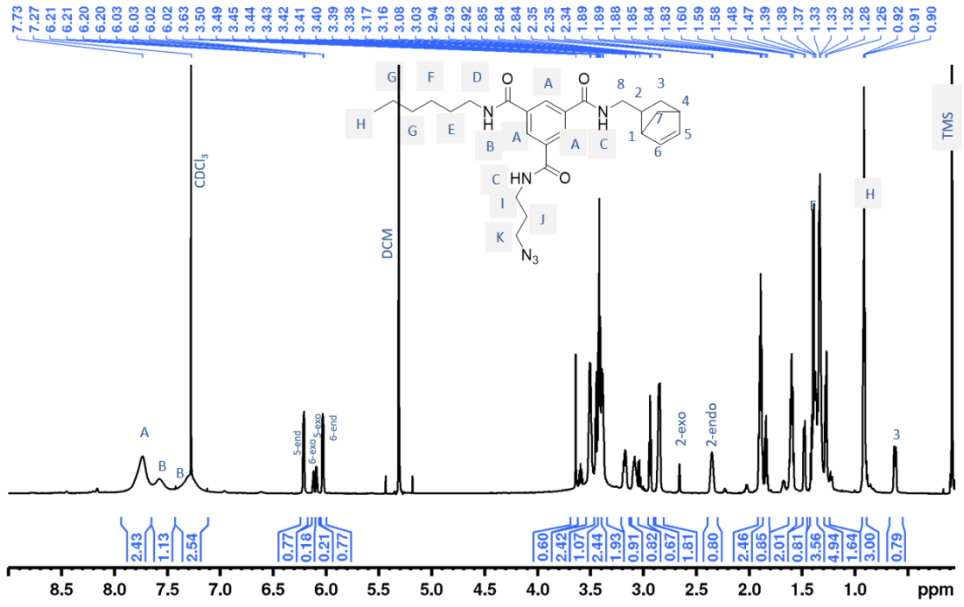

Figure S43. [1]H NMR of molecule **19**

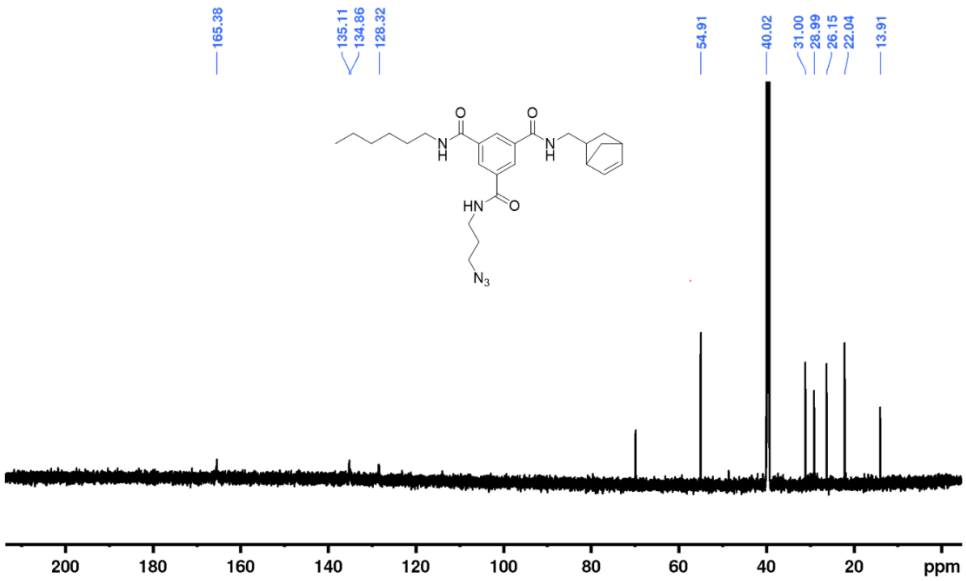

Figure S44. [13]C NMR of molecule **19**

PEG-CDI synthesis:

Bishydroxy PEG (20 kg/mol) was dried via azeotropic distillation using toluene. Dried bishydroxy PEG (30 g, 3 mmol, 1equiv.) dissolve in 100 mL of anhydrous 1,4-dioxane at 37 °C under a nitrogen atmosphere. Vacuum-dried (at 50 °C for 3 hours) carbonyl diimidazole (CDI, 0.08 g, 0.5 mmol, 5 equiv. per OH) dissolved in 30 mL of anhydrous 1,4-dioxane was added to the reaction flask under nitrogen inert atmosphere. The reaction mixture was stirred at 37 °C for 3 hours. The reaction mixture was precipitated out in excess cold diethyl ether twice and dried overnight in rotavap at 40 °C. The product was obtained as a white solid with a 96% (29g) yield. ^{1}H NMR (700 MHz, $CDCl_3$) δ 8.11 (s, 2H, Ar), 7.61 (s, 2H, Ar), 7.40 (s, 2H, Ar), 4.51(t, 4H, $C\underline{H_2}OC{=}O$), 3.79 (t, 4H, $OC\underline{H_2}CH_2$), 3.4 (b, 1772H, $O\text{-}\underline{CH_2CH_2}\text{-}O$). The mass of the polymer is 19313 g/mol with a polydispersity index of 1.1.

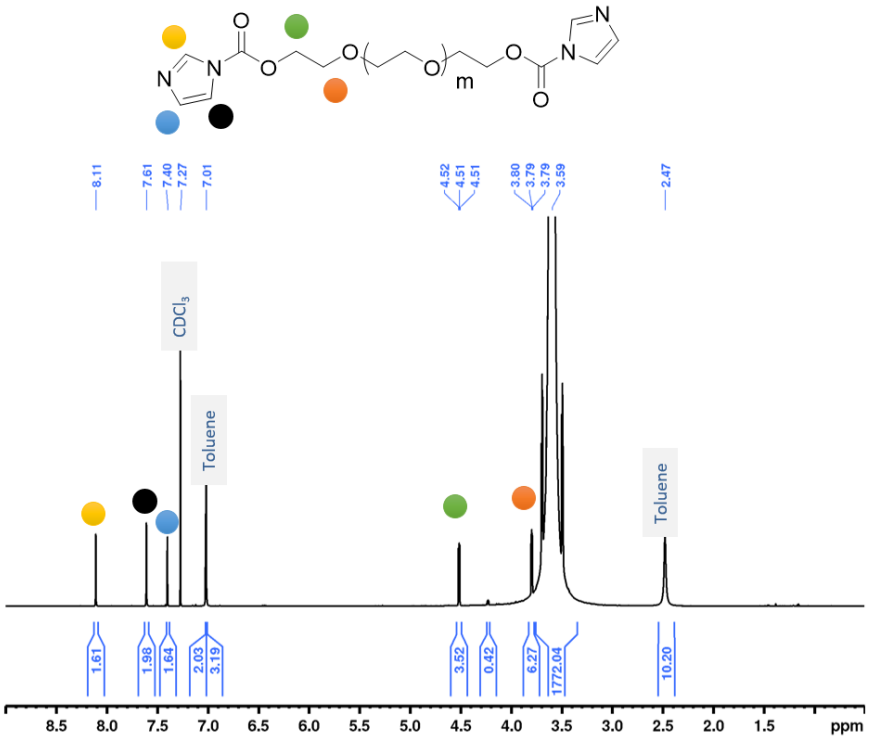

Figure S45. ^{1}H NMR ($CDCl_3$) of PEG-CDI

PEG-Bisamino dodecane synthesis:

PEG-CDI (27 g, 1.34 mmol, 1 equiv.) was vacuum dried at 60 ºC for 3 hours and dissolved in 270 mL anhydrous DMF. The polymer solution was added dropwise to the solution of 1,12 diaminododecane (3.5 g, 19 mmol, 14 equiv.) dissolved in 275 mL of anhydrous DMF and maintained at 70 ºC. The reaction mixture at 70 ºC was stirred for 24 hours under a nitrogen atmosphere. The reaction mixture was concentrated by removing DMF and precipitated in excess cold diethyl ether. The product was again dissolved in DCM and precipitated out in excess cold diethyl ether. The product was obtained as a white solid with a 97% yield. The mass of the polymer is 25760 g/mol with a dispersity index of 1.2. ^{1}H NMR (700 MHz, $CDCl_3$) δ 4.83 (s, 2H, NHC=O), 4.20 (t, 4H, $CH_2OC=O$), 3.7 (b, 1776H, $O(CH_2)_2O$), 3.15 (q, 4H, $C_{H2}NHC=O$), 2.68 (t, 4H, CH_2NH_2), 1.47-1.25 (m, 40H, aliphatic)

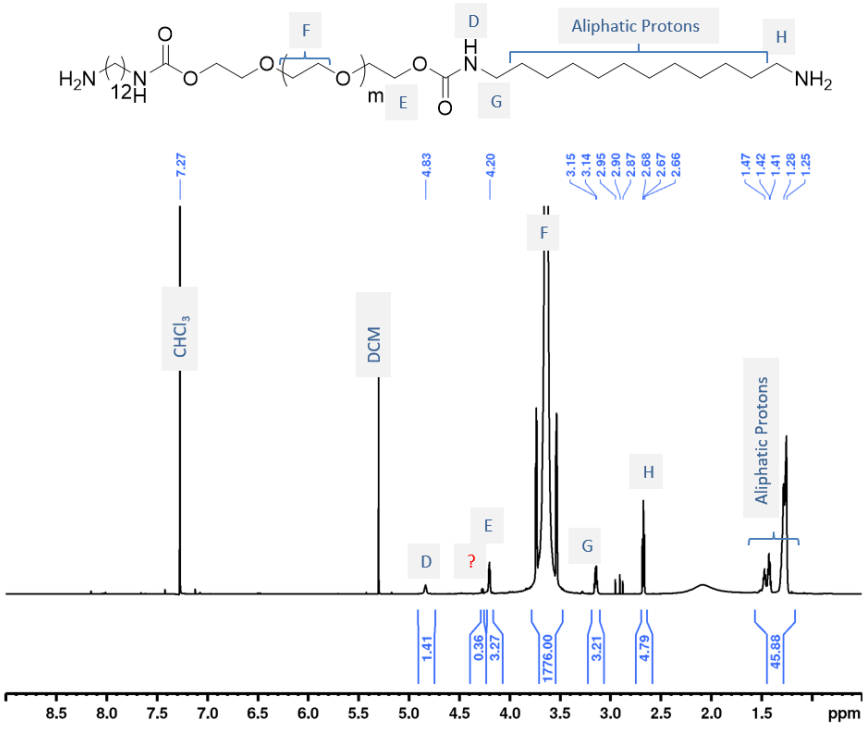

Figure S46. ^{1}H NMR ($CDCl_3$) of bismainodeodecane PEG 20K.

Synthesis of hydrogelator 20

In a dry round bottom flask, **10** (0.2g, 0.34mmol, 1.1equiv) was dissolved in 8mL anhydrous DCM, and DIPEA (0.06g, 0.44 mmol, 1.5 equiv) was added into the reaction flask. Subsequently, PEG bisaminododecane (3.2g, 0.3 mmol, 1 equiv) solution in anhydrous DCM (5–6 ml) was added dropwise to the reaction flask. The reaction mixture was stirred for 40 hours at room temperature (~20°C) under a nitrogen atmosphere. Excess solvent was removed in vacuo and the crude reaction mixture precipitated in excess cold diethyl ether obtaining BTA 1 hydrogelator, as a white powder in 98% yield. The second purification was done by dialyzing the sample in methanol against methanol to remove any unreacted small molecule impurities. Hydrogelator **20** was obtained in 89% yield with a mass of 24344 g/mol and with a polydispersity index of 1.2. ^{1}H NMR (700 MHz, d_6-DMSO) 8.65-8.6 (m, 6H, NH(C=O)), 8.35 (s, 6H, Ar), 7.15 (t, 2H, CH2NH(C=O)O), 4.04-4.0 (t, 4H, NH(C=O)OCH2), 3.5 (bs, 1776H, O-(CH2)2-O), 3.29-3.24 (t, 12H, (C=O)NHCH2), 2.95-2.90 (q, 4H, CH2NH(C=O)O), 1.6-1.14 (mm, 72H, aliphatic), 0.88-084 (t, 12H, CH2CH3, aliphatic).

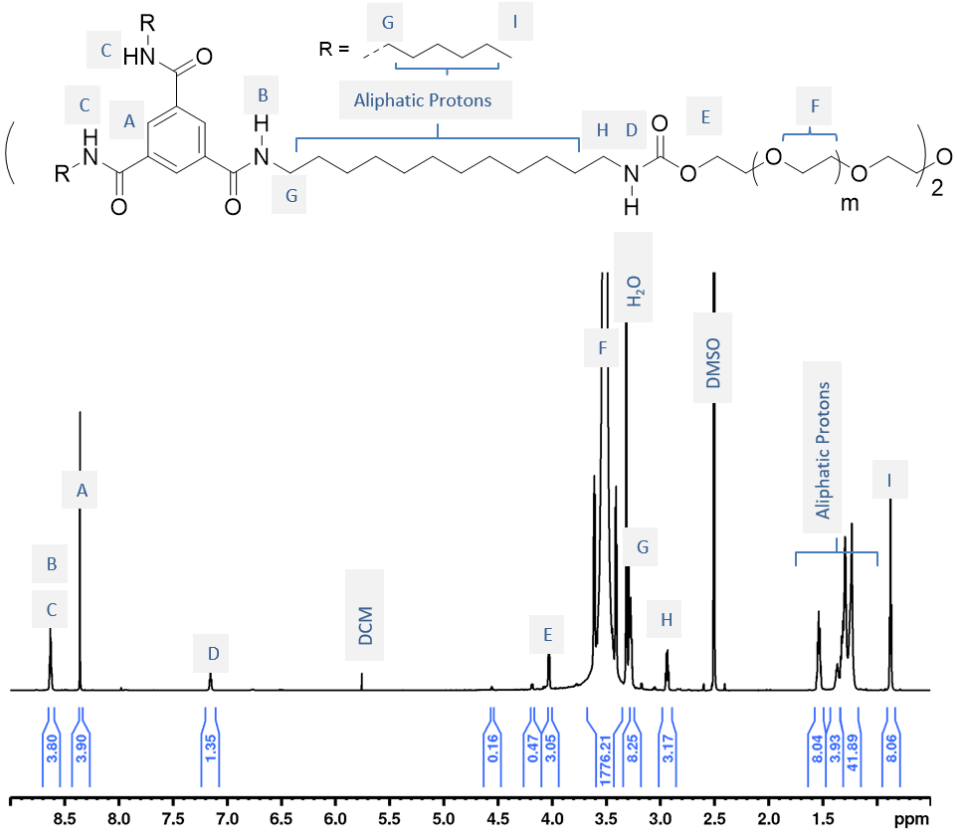

Figure S47. ^{1}H NMR (d_6-DMSO) of hydrogelator **20**

Synthesis of hydrogelator 21

15 (0.03 g, 0.043 mmol, 1.1 equiv.) was dissolved in 3 mL anhydrous DCM, and DIPEA (0.008 g, 0.06 mmol, 1.5 equiv) was added to it. PEG bisaminododecane (0.4 g, 0.04 mmol, 1.0 equiv) was weighed in a dried flask, dissolved in anhydrous DCM (3–4 mL), and added to the flask. The reaction continued to run for 40 hours at 20 °C under an inert atmosphere. The reaction mixture was concentrated using a vacuum and precipitated out using excess cold diethyl ether. The same procedure was repeated twice. The product was dried in a vacuum oven at 45 °C for 3 hours and the white product was obtained with a 75% yield. Hydrogelator **21** was obtained with a mass of 21,207 g/mol with a polydispersity index of 1.2. ^{1}H NMR (700 MHz, d_6-DMSO) 8.65–8.58 (m, 6H, N<u>H</u>(C=O)), 8.36–8.32 (s, 6H, Ar), 7.17–7.12 (t, 2H, $CH_2N\underline{H}(C=O)O$), 4.06–3.99 (t, 4H, $N\underline{H}(C=O)OC\underline{H}_2$), 3.64–3.37 (bs, 1776H, $O\text{-}(C\underline{H}_2)_2\text{-}O$), 3.29–3.24 (m, 12H, $(C=O)NHC\underline{H}_2$), 2.95–2.90 (q, 4H, $C\underline{H}_2NH(C=O)O$), 1.56–1.17 (mm, 76H, aliphatic), 0.88–0.84 (t, 12H, $CH_2C\underline{H}_3$, aliphatic).

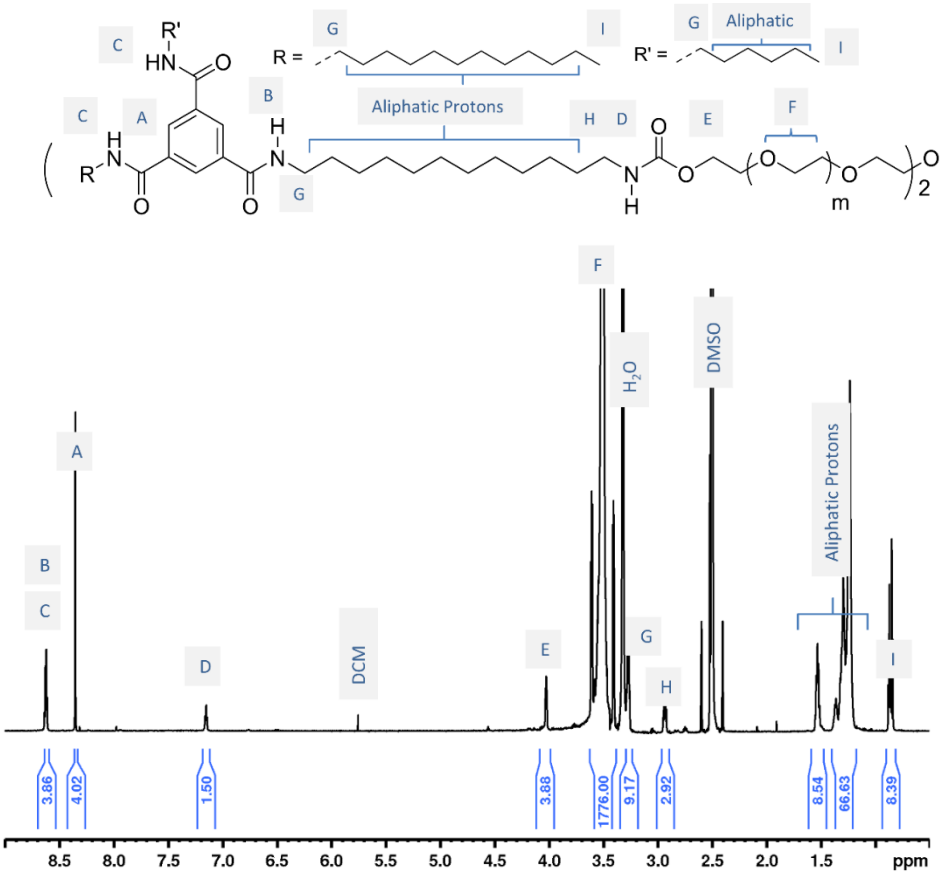

Figure S48. ^{1}H NMR (d_6-DMSO) of hydrogelator **21**

Synthesis of hydrogelator 22

12 (C12C12, 0.23g, 0.32 mmol, 1.1 equiv) was dissolved in 8mL anhydrous DCM, and DIPEA (0.056g, 0.44 mmol, 1.5 equiv.) was added to it. PEG bisaminododecane (3g, 0.29 mmol, 1 equiv) was weighed in a dried flask, dissolved in anhydrous DCM (5-6 ml), and added to the flask. The reaction continued to run for 40 hours at 20°C under an inert atmosphere. The reaction mixture was first purified by precipitation in cold diethyl ether and a pure molecule was obtained in 98% isolated yield as a white powder. Later also sample was dissolved in methanol and dialyzed against methanol for further purification. The pure molecule was obtained in 84% yield. Hydrogelator **22** was obtained in 84% yield with a mass of 23573 g/mol and with a polydispersity index of 1.2. 1H NMR (700 MHz, *d*$_6$-DMSO) 8.65-8.57 (t, 6H, NH(C=O)), 8.38-8.31 (s, 6H, Ar), 7.18-7.10 (t, 2H, CH2NH(C=O)O), 4.06-3.94 (t, 4H, NH(C=O)OCH2), 3.6-3.37 (bs, 1776H, O-(CH2)2-O), 3.29-3.22 (t, 12H, (C=O)NHCH2), 2.96-2.90 (q, 4H, CH2NH(C=O)O), 1.59-1.15 (mm, 120H, aliphatic), 0.88-0.80 (dt, 12H, CH2CH3, aliphatic).

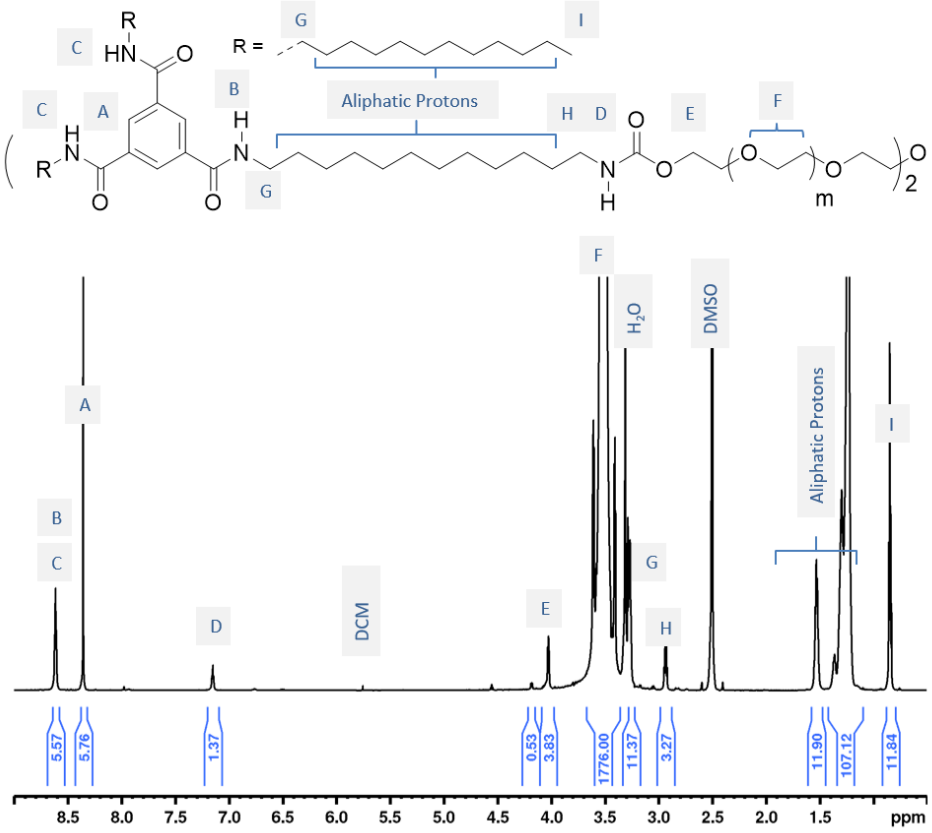

Figure S49. ^{1}H NMR (d_6-DMSO) of hydrogelator **22**

Table S7: Details on molecular weight average for hydrogelator 20, 21, and 22. All the samples were dissolved in DMF at concentrations around 5 mg/mL, and filtered through 0.2 µm filters before being injected into the GPC system for analysis.

Hydrogelator name	M_n (g/mol)	M_w (g/mol)	Đ (M_w/M_n)
20	20039	24344	1.2
21	18146	21207	1.16
22	19500	23573	1.2

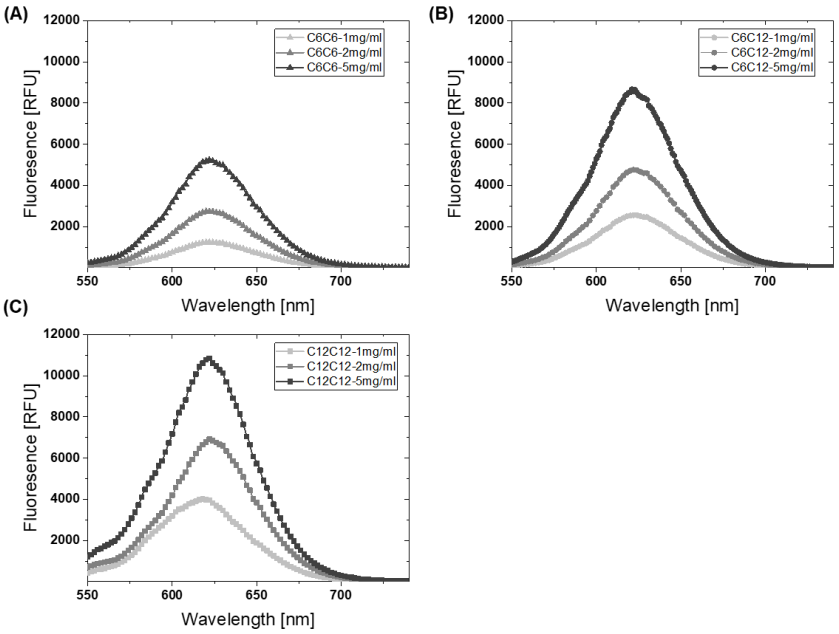

Figure S50. Nile red of hydrogelator 20 (A), 21 (B) and 22 (C) at concentration 1mg/mL, 2mg/mL, and 5mg/mL.

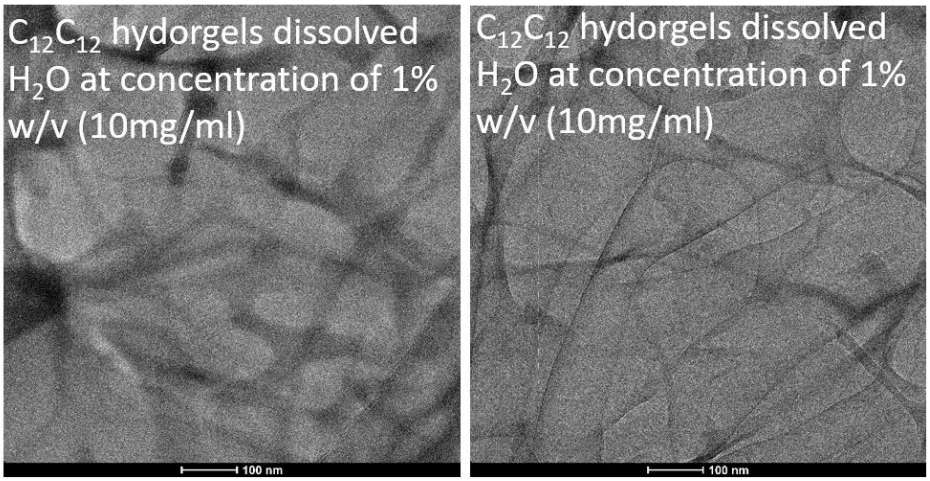

Figure S51. Cryo-TEM image of **22** gel when diluted in water around 10mg/ml.

Critical gelation concentration (CGC):

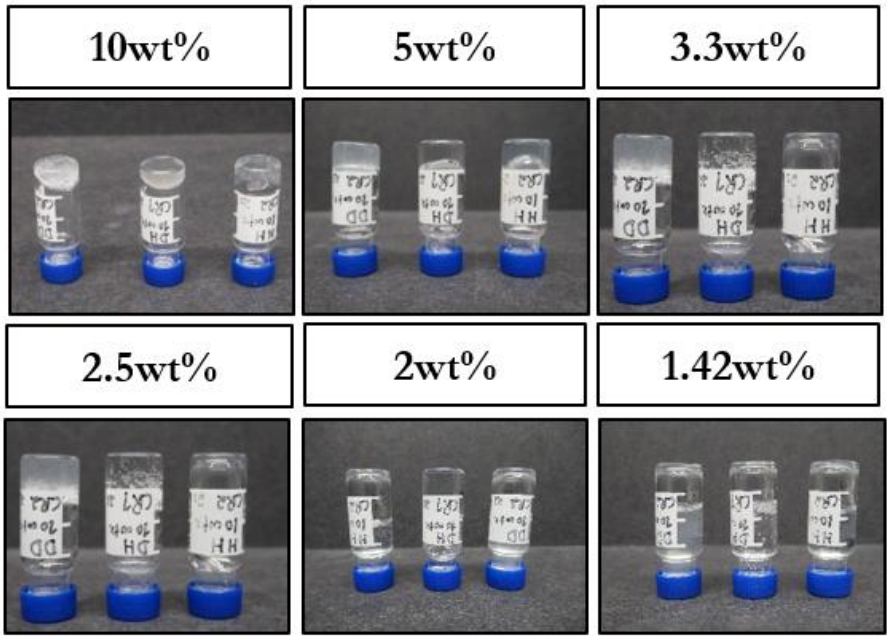

Figure S52. Critical gelation concentration experiment: hydrogelator **20**, **21**, and **22** are labeled as HH, DH, and DD. The hydrogelators **20**, **21**, and **22** showed CGC ~5% (w/v), 1.42%, and ~2.5% (w/v). The vial was inverted at each wt% and observed if the hydrogel will flow or stay stable on top of the inverted vial. Observing or waiting time of the inverted vial to determine CGC was a maximum of 30 seconds.

Vial inversion experiment:

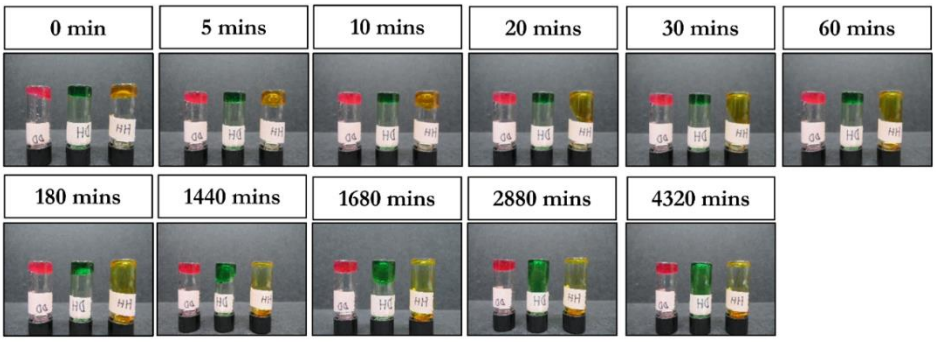

Figure S53. Vial inversion experiment to determine flow behavior of hydrogels at 10% (w/v). Hydrogelator **20**, **21**, and **22** are labeled as HH, DH, and DD. Flow behavior is a qualitative test that provides information on hydrogel viscoelastic behavior. Hydrogelator **20** (HH) roughly started to flow after 20 minutes of vial inversion. A small flow can be seen for hydrogelator **21** after 1680 minutes (28 hours) and hydrogelator **22** did not flow even after 4320 minutes (72 hours).

Mechanical Properties:

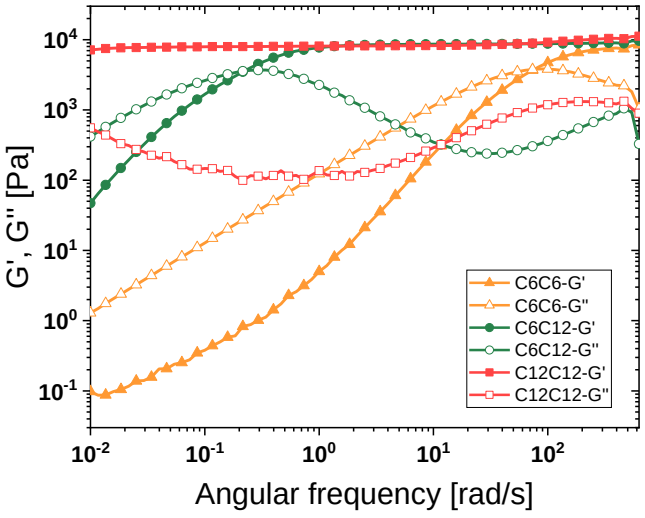

Figure S54. All hydrogelator showed frequency dependent loss moduli (G") which show that hydrogelators are viscoelastic

Self-healing and moldability:

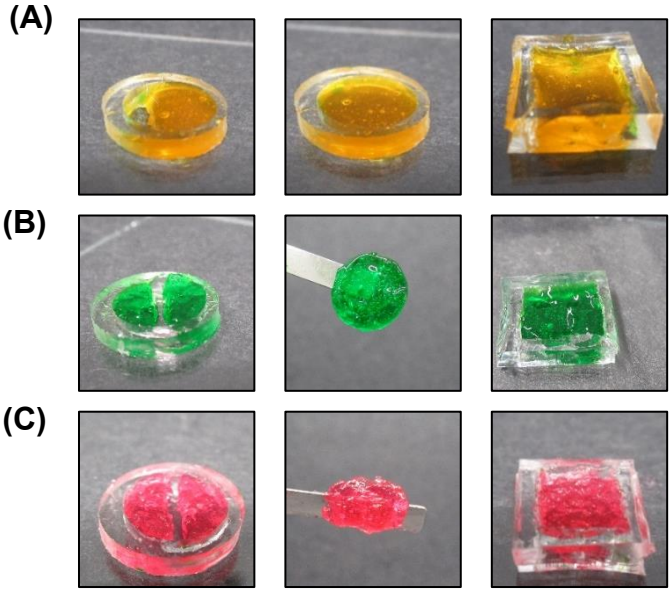

Figure S55. Self-healing and moldability of hydrogelators **20** (orange), **21** (green), and **22** (red). All hydrogelators are self-healing instantaneously when hydrogels pieces are placed and pressed together with spatula. Also, hydrogels are moldable since they can adopt to different mold shapes when subjected to stress.

Chapter VII

Molecular tuning of Benzene-1,3,5-tricarboxamide supramolecular fibrous hydrogel enables unprecedented control over viscoelasticity and creates tunable bioinks for bioprinting

Shahzad Hafeez[1], Agustina Aldana[1], Hans Duimel[2], Clemens van Blitterswijk[1], Lorenzo Moroni[1], Matthew B. Baker[1]

[1] Department of Complex Tissue Regeneration, MERLN Institute for Technology Inspired Regenerative Medicine, Maastricht University, P.O. Box 616, 6200 MD Maastricht, the Netherlands;

[2] Maastricht MultiModal Molecular Imaging Institute, P.O. Box 616, 6200 MD Maastricht, the Netherlands.

A version of this chapter was submitted to **Advanced Materials** and the revised version with the reviewers' feedback and further data analysis has been published in **Advanced Materials** (2023).

Hafeez, S.; Aldana, A.; Duimel, H.; Ruiter, F. A. A.; Decarli, M. C.; Lapointe, V.; van Blitterswijk, C.; Moroni, L.; Baker, M. B. Molecular Tuning of a Benzene-1,3,5-tricarboxamide Supramolecular Fibrous Hydrogel Enables Control over Viscoelasticity and Creates Tunable ECM-mimetic Hydrogels and Bioinks. *Adv. Mater.* **2023**, 2207053. https://doi.org/10.1002/adma.202207053.

Abstract:

Hydrogels are an important class of materials for applications in cell culture and tissue engineering; however, traditional covalent hydrogels lack the native tissue dynamics and hierarchical fibrous structure found in the extracellular matrix. Consequently, there remains a large challenge to engineer functional dynamics in a fibrous hydrogel and recapitulate these native properties. In this study, we report on the molecular tuning of a self-assembling supramolecular benzene-1,3,5-tricarboxamide (BTA) hydrogelator resulting in fibrous hydrogels with accessible viscoelasticity over 5 orders of magnitude, while maintaining a constant equilibrium storage modulus. Using the recently developed synthetic methodology, we created BTA hydrogelators with twelve, sixteen, eighteen, twenty, and twenty-four hydrophobic carbon atoms. All BTA hydrogelators formed hydrogels with fibrillar morphology, akin to the ECM, and all hydrogels were observed to be self-healing, shear-thinning, and injectable. We observed that the hydrophobic endcap carbon length controlled the viscoelasticity and stress relaxation time scales in a logarithmic fashion. Utilizing the shear-thinning and self-healing properties, we found that the BTA supramolecular hydrogels are extrudable, injectable, and can be 3D printed into multiple layers without the need for a supporting bath and secondary cross-linking. These hydrogels showed high cell viability for chondrocytes as observed in a 2D contact assay, bulk 3D hydrogels, and bioprinted hydrogels. This simple molecular tuning by changing hydrophobicity (with just a few carbon atoms) provides precise control of the viscoelasticity and 3D printability in fibrillar hydrogels and could be ported onto other 1D self-assembling structures. The molecular control and design of hydrogel network dynamics can push the field of supramolecular chemistry towards designing new ECM-mimicking hydrogelators for numerous cell culture and tissue engineering applications and give access towards highly biomimetic bioinks for bioprinting.

Introduction:

The natural extracellular matrix (ECM) is a non-cellular component present within all tissues and provides mechanical and biological cues to embedded cells to maintain cell differentiation and development.[1,2,3] The ECM is a fibrillar hydrogel consisting of self-assembled proteins such as collagen, laminin, and fibrin in an aqueous environment. This self-assembly within and between proteins is mainly driven by non-covalent supramolecular interactions and imparts transient and dynamic properties to the ECM.[1,4] Hydrogels are often used in numerous biomaterials applications to mimic this hydrated hydrogel microenvironment around the cell and are considered an ideal material for cell growth and tissue engineering. Though traditional hydrogels allow tuning static mechanical properties and bioactive cues presentation, they lack the dynamicity of native fibril ECM.[5,6] Scientists have responded by designing dynamic hydrogels for applications in cell culture and tissue engineering.[7,8]

Various fibrous hydrogels using self-assembly principles and supramolecular chemistry have been developed.[4,9,10] For example, hydrogels made up of self-assembling peptides, self-assembling peptide amphiphile (PA), low molecular weight hydrogelators (LMWH), and supramolecular self-assembling polymers are prominent areas of research.[9] Self-assembling peptide-based hydrogels have been shown to promote osteogenic[11], neuronal differentiation (in co-culture with astrocytes)[12], and promote enamel regeneration[13]. Similarly, PA nanofibers with RGD have been shown to support the adhesion and migration of fibroblasts[14], osteogenic differentiation of MSCs[15], and induce rapid differentiation of cells into neurons.[16] Ureido-pyrimidone (UPy) an example of supramolecular self-assembling polymers allows tuning bioactivity via modular mixing[17,18] and sustained delivery of growth factors for promoting regeneration of infarct[19,20] and fibrotic tissues.[21] A few recent studies have reported fibrous LMWH BTA[22] and telechelic polymeric BTA hydrogels[23] as biomaterials. While the use of nanofibrillar hydrogels biomaterials is well studied, the control of the dynamics via molecular motion and links to functional properties remains an area less developed.[18,24]

Viscoelasticity has been shown to influence cell spreading[25,26], differentiation[27,28,29,30,31], and mechanochemical pathways (YAP/TAZ).[32] Reversible cross-links dynamics offer a conceptually appealing approach for engineering viscoelasticity by utilizing knowledge of the equilibrium constant K_{eq}, and the forward and reverse rate constants of binding. Utilizing imine-type dynamic covalent chemistry (DCvC), the hydrolysis rate (k_{-1}) has been varied for tuning viscoelasticity [3332343536]. Using pKa differences in phenylboronic acid derivatives[37] and knowledge of boronate ester equilibrium[38], viscoelasticity has also been tuned. Furthermore, the lifetime of supramolecular host-guest complexes, defined by the rate of rupture (k_{off}), has been directly linked to hydrogel viscoelastic properties.[39,40,41,42,43] Tuning viscoelasticity using reversible chemistries mostly has been done in non-fibrillar hydrogel with some recent attempts of tuning viscoelasticity in fibrous hydrogels i.e., in amphiphilic peptides[44], in BTA[45], and in UPy[18] hydrogelators; however, tuning viscoelasticity and stress relaxation across broad timescales in synthetic fibrous hydrogel remains a challenge.

Hydrogel dynamics is not only important for control over cellular behavior but can also be exploited for creating shear-thinning and self-healing materials, which holds great potential for applications in 3D printing and as injectable carriers for cell and drug delivery.[46,47,48] Shear-thinning materials can rupture upon applied shear stress, resulting in a decrease in viscosity and easier to inject, and self-heal to their original mechanical after injection. Reversible covalent and supramolecular chemistries are employed for developing shear-thinning and self-healing hydrogels as injectable carriers and for 3D printing. Dynamic covalent reversible networks, particularly imine type, have been employed successfully as injectable hydrogels[49,35,50] and applications in 3D printing and bioprinting.[36,35] Reversible covalent phenylboronic acid (PBA) derivatives based on hydrogels with shear-thinning and self-healing properties have been shown to be injectable[51]. Host-Guest supramolecular hydrogels with shear-thinning properties have also shown potential in 3D printing.[52,49] Most of the reported shear-thinning and self-healing hydrogels are non-fibrillar, and thus do not mimic the nanostructure seen in the native ECM. Separate studies have reported tuning viscoelasticity in shear-thinning hydrogels[36,53] and tuning 3D printability in short peptide fibril hydrogel[54]; however, development of fibril hydrogels with controlled viscoelasticity, which can be 3D printed, remains desired.

In light of the interesting properties that supramolecular interactions have to offer, we set out to develop supramolecular hydrogel with a fibrous structure and a broad range of viscoelasticity. We aimed to achieve this with benzene-1,3,5-tricarboxamide (BTA) supramolecular moiety, utilizing our newly developed and recently reported desymmetrization strategy.[23] We hypothesized that by simply tuning the hydrophobic length, we could alter the viscoelasticity and stress relaxation timescales of the resultant hydrogels without an appreciable increase in the molecular weight of the polymer. We created a small library of BTA hydrogelators by systematically varying end group carbon length from 6 to 12 carbon units. We were also interested to see if systematic tuning of this hydrophobicity can provide control on shear-thinning, self-healing, and 3D printability. Using shear rheology, we investigated the effect of hydrophobic carbon length on viscoelasticity, stress relaxation timescales, self-healing capacity, and shear-thinning. Furthermore, using an extrusion 3D printer, we investigated the 3D printability and shape fidelity of the resultant constructs. Finally, we validated the cytocompatibility of these newly developed BTA hydrogelators with chondrocytes in dilute solutions, 3D hydrogels, and bioprinted constructs.

Results and Discussion

Molecular design and BTA hydrogelator synthesis

With the aim to study the influence of external hydrophobics on structure and viscoelasticity, we designed a series of telechelic BTA hydrogelator derivatives by varying the length of the external aliphatics (**Figure 1)**. The external hydrophobic aliphatic length was varied from six to eight, ten, and twelve methylene units for systematic investigation. The internal hydrophobic aliphatic spacer of twelve carbon atoms/methylene units was kept constant to align with previous studies.[55]

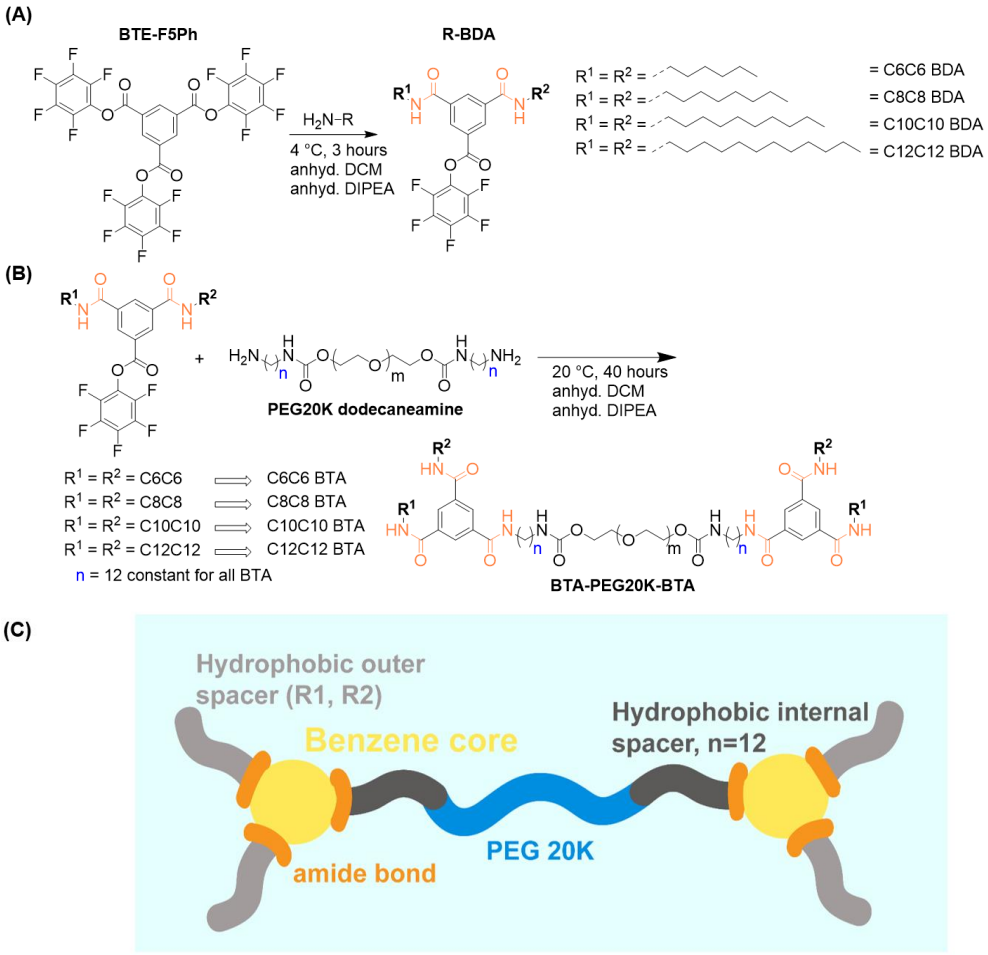

Figure 1. BTA hydrogelator synthesis. A) Reaction scheme for making BTA synthon using benzene-1,3,5-tricarbonyl tripentafluoroester (BTE-F_5PH) by desymmetrization using nucleophilic aliphatic amine. Aliphatic amines were employed with six, eight, ten, and twelve carbon lengths. B) Reaction scheme for polymer BTA hydrogelator synthesis by connecting BTA synthon synthesized in "A" and conjugating it with bisaminododecane PEG20K. The external hydrophobic length is varied from six to eight to ten to twelve for creating a library of hydrogelators. C) Schematic representation of polymer BTA hydrogelator, benzene core is indicated in yellow, amide bonds are shown with orange wedges, hydrophobics are in gray and PEG20K is in blue.

We employed our newly developed desymmetrization strategy, which allowed us to agilely and systematically vary external hydrophobic length from six to twelve carbon/methylene units. Using a symmetrical benzene-1,3,5-tricarbonyl tripentafluoroester (BTE-F_5Ph), we utilized aliphatic amines of six, eight, ten, and twelve carbon atoms to desymmetrized into di-substituted (R-BDA) derivatives (**Figure 1A and Figure S1**). Integration of the ^{1}H NMR spectrum of the crude reaction mixtures showed that R-BDA was produced above statistical yields, in line with previous observations[23]. **C_6C_6-BDA** and **$C_{12}C_{12}$-BDA** were synthesized and characterized

following the procedure reported in our previous study[23] and detailed information on the synthesis and characterization of **C_8C_8-BDA** and **$C_{10}C_{10}$-BDA** can be found in SI (**Figure S2–S5**).

Next, the R-BDA synthon was connected to poly(ethylene glycol) 20K (PEG20K) dodecane amine (**Figure 1B**) for the creation of telechelic BTA hydrogelators **C_6C_6 BTA-PEG-BTA**, **C_8C_8 BTA-PEG-BTA**, **$C_{10}C_{10}$ BTA-PEG-BTA**, and **$C_{12}C_{12}$ BTA-PEG-BTA**. In this study for the sake of simplicity, we will call telechelic BTAs by their short names **C_6C_6 BTA**, **C_8C_8 BTA**, **$C_{10}C_{10}$ BTA**, and **$C_{12}C_{12}$ BTA**, respectively. **C_6C_6 BTA** and **$C_{12}C_{12}$ BTA** were reproduced following the procedure as reported in our recently published work.[23] We extended the series by including and synthesizing **C_8C_8 BTA**, and **$C_{10}C_{10}$ BTA** using the same synthetic strategy.[23] All final hydrogelators were obtained pure (confirmed with proton nuclear magnetic resonance spectroscopy, **Figure S6 &S7**) with a weight average molecular weight ~23000 g/mol and Đ 1.2 (gel permeation chromatography, **Figure S8**). All hydrogelators were obtained in greater than 95% isolated yield. This newly developed methodology allowed us to make all hydrogelators on the multi-gram scale in just two weeks, which shows the synthesis capability and scalability of the approach. More details on ^{1}H NMR characterization and molecular weight analysis can be found in SI (**Figure S6–S8**).

Self-assembly studies in dilute solutions and hydrogel form

With the target polymers in hand, we next wanted to investigate the propensity for self-assembly within the series in water. Since the self-assembly of the BTA-based hydrogelators should create a hydrophobic pocket in aqueous solutions, we turned to Nile Red to obtain information on this molecular environment. Nile red is a solvatochromic dye and its spectrophotometric properties can provide information on the hydrophobic pocket formation and polarity of the hydrophobic pocket in supramolecular systems. As shown previously, Nile red show low fluorescence signal in water, and fluorescence intensity increased in the more apolar solvent[56], and can be used to probe the molecular environment of self-assembled systems in water.[55,57] Nile red shows very low fluorescence intensity in water and Nile Red fluorescence intensity gradually increased with increasing hydrophobic length on the BTA **(Figure S9 E–H)**. The fluorescence intensity increased nearly two-fold as the number of carbon atoms went from 12 to 24 (from 12 carbon atoms for **C_6C_6 BTA** to 24 carbon atoms for **$C_{12}C_{12}$ BTA**). The results suggest that a higher number of carbon atoms created a larger hydrophobic pocket resulting in more Nile red encapsulation, yet the step-wise effect suggests some non-linear changes in the hydrophobic volume within the series. In addition, fluorescence intensity increased mostly linearly with increasing concentration of the hydrogelators in 1–10 mg/ml concentration range (45mM to ~450 mM telechelic BTA (**FigureS9 A–D** for all other BTA). This linear increase suggests no major changes to the self-assembly mode in this range.

Maximum fluorescence intensity wavelength (λ_{max}) provides information about the polarity of the environment [56]. Water showed λ_{max} at 645 nm and blue shifted to around 621 nm for all hydrogelators (**Figure S9 I**). The increase in fluorescence intensity and a similar blue shift in λ_{max}

confirm the hydrophobic pocket formation with similar polarity within the self-assembled structures at these lower concentrations, with a small but notable difference between the <16 and >20 architectures.

Cryo-TEM was employed for investigating the structure of the self-assembly in a dilute solution (dissolved in minimal methanol and self-assembly in water). We found that all the hydrogelators created high-aspect-ratio fibers in a dilute solution, with some differences in the amounts of fiber aggregation. Shown in **Figure 2A and Figure S10**, **C_6C_6** showed a mixed population of thin fibers (10 nm in diameter) and fibrous sheets (width between 20–180 nm); relatively speaking, more fibers were observed compared to sheets. **C_8C_8 BTA** also showed a mixed population of nanosheets ranging from 110–180 nm in width and fibers with a diameter of around 10 nm; here we observed more sheets and fewer fibers. **$C_{10}C_{10}$ BTA** and **$C_{12}C_{12}$ BTA** showed only fibrous sheets of 80–225 nm width. Fibrous sheets contain many flat parallel BTA nanofibers, with an individual nanofiber having a diameter between 1–2 nm. All nanostructures (fibers and sheets) are a few hundred nanometers in length. Larger structures for **$C_{10}C_{10}$ BTA** and **$C_{12}C_{12}$ BTA** under cryo-TEM are also in agreement with the larger hydrophobic pocket formation during Nile red compared to **C_6C_6** and **C_8C_8.** Fibrous sheets of similar length scales (for **C_8C_8**, **$C_{10}C_{10}$**, and **$C_{12}C_{12}$**) were also observed in dilute solutions when samples were prepared only in water using a similar heating-cooling procedure (**Figure S11**). The hydrophobic length influences the structure of the hydrogelator, and hydrogelators are inclined to form 2D fibrous sheet morphology with increasing hydrophobic length.

Next, we employed cryo-SEM for BTA hydrogel structure investigation. All hydrogelators formed hydrogels in water. BTA hydrogelators showed anisotropically aligned fibrous morphology, and fibers were bundled together. Single fibers showed a diameter between 1–2 μm (**Figure 2B and Figure S12**). Interestingly, each fiber was made up of a bundle of fibrils. Unlike the changes in self-assembly seen in dilute solution (Nile Red and cryo-TEM), cryo-SEM showed a very similar fibrous morphology for all hydrogels in the series, likely due to hydrogel formation at higher concentrations.

The BTA hydrogelator structures mimic the dimensions of collagen structures at the nanoscale and micron scales. Collagen fibrils are made up of tropocollagen molecules. A tropocollagen molecule has a diameter of 1.5 nm and a length of 300 nm.[58] The individual BTA nanofibers found in BTA sheets had a diameter of ≈1.5 nm and a length of 150–300 nm, on a similar scale of tropocollagen molecules. BTA hydrogelators nanosheets' width of 20–225 nm matched collagen fibrils diameter of 10–300 nm (**Figure 2**). In addition, a BTA hydrogelator fiber diameter of 1–2 μm (cryo-SEM in hydrogel form, **Figure 2C**) overlapped with a collagen fiber diameter of 1–20 μm.[59,60] Not only does BTA hydrogelator mimic the structural dimensions of

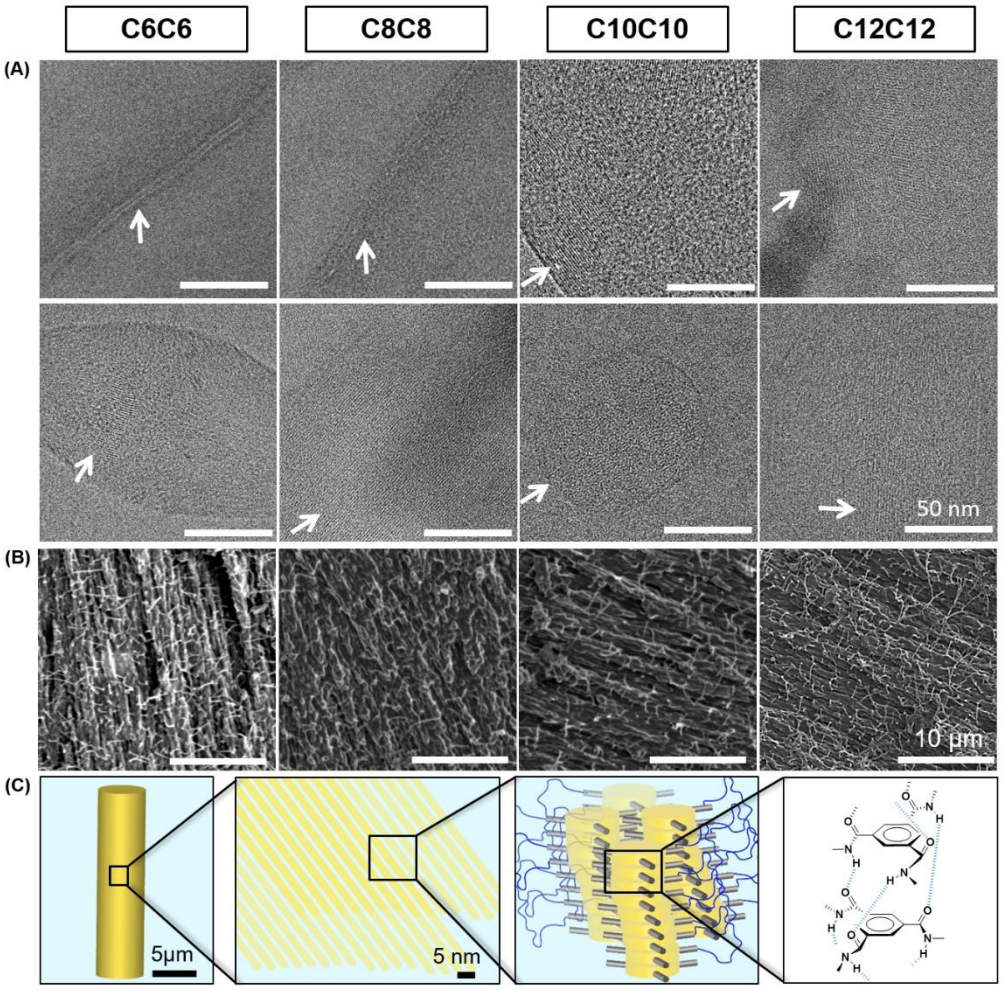

Figure 2. Self-assembly structure evaluation. A) cryo-TEM images of hydrogelators at a concentration 10 mg/ml. All samples were dissolved in minimal methanol and then mixed with water for self-assembly. All hydrogelators showed fibrous sheet-like morphology. **C_6C_6** and **C_8C_8** also showed fiber-like morphology. B) cryo-SEM structure of hydrogels formed in water, all hydrogels showed fibrous morphology. C) Suggested schematics of BTA molecules from micron scale, a micron size fiber which was observed in cryo-SEM (most left panel), nanofiber and nanosheets observed in cryo-TEM (second panel from left), BTA aggregation and hydrophobic pocket formation observed Nile red (third panel from left), BTA molecules in BTA aggregates are held together via 3-fold hydrogen bonding interactions facilitated by hydrophobic interactions (most right panel).

collagen, but also mimicked anisotropically aligned collagen fibers. In short, cryo-TEM and cryo-SEM (vide supra) showed that BTA hydrogelators mimicked the nanoscale and microscale structural aspects and anisotropy of collagen fibrous structure.

Hydrogel formation, critical gelation concentration, vial inversion, and hydrogel structure

The ability of hydrogel formation was initially assessed in water. Solid polymer at 10% (w/v) was dissolved in Milli-Q water by heating (until it becomes turbid) and vortexing. The polymer solution forms a hydrogel upon cooling to room temperature. All of the hydrogelators form self-supporting slightly turbid hydrogels at 10% (w/v) (**Figure 3A)**. Hydrogel formation was also tested in PBS and DMEM and all hydrogelators formed similar hydrogels in these environments.

Next, we assessed critical gelation concentration (CGC). Finding the CGC serves as a qualitative assessment of the hydrogelators to stay stable upon vial inversion. Here, we defined the "hydrogel" as a material that showed no flow within 30 seconds of vial inversion. The CGC was found to be 5.0, 3.3, 2.0, and 1.8 %(w/v) for **C_6C_6**, **C_8C_8**, **$C_{10}C_{10}$**, and **$C_{12}C_{12}$ BTA** (**Figure 3A** and **Figure S13**), respectively. This shows that hydrophobic length has a large influence on CGC, the larger the hydrophobic length, the more gel-like the material at lower concentrations. Trends in critical gelation concentration also explain larger hydrophobic pocket formation for **$C_{10}C_{10}$** and **$C_{12}C_{12}$** compared to **C_6C_6**, and **C_8C_8** observed during Nile red experiment (**Figure S9)**. A larger aliphatic hydrophobic spacer forms a bigger hydrophobic pocket, which provides effective shielding to the BTA core and lowers the CGC.

Then, we assessed the flow behavior of hydrogels via a vial inversion test, which is also a qualitative assessment of hydrogel viscoelastic properties (**Figure S14**). **C_6C_6 BTA** started to flow slowly after the vial inversion and reached the bottom of the glass vial after one hour. **C_8C_8 BTA** began to flow after three hours and almost reached the bottom of the glass vial in 48 hours. Interestingly, **$C_{10}C_{10}$ BTA** and **$C_{12}C_{12}$ BTA** did not flow even after 240 hours (10 days). These results showed that the hydrophobic length has a significant influence on the hydrogel flow behavior; with increasing hydrophobic length on BTA hydrogel changes to more solid-like behavior. This crude experiment also clearly suggests that **C_6C_6 BTA** and **C_8C_8 BTA** are more viscoelastic compared to **$C_{10}C_{10}$ BTA** and **$C_{12}C_{12}$ BTA**.

Hydrogels show highly tunable viscoelasticity at a constant storage modulus

To obtain more insight into the flow differences observed in the vial inversion test, the storage moduli and viscoelasticity of the hydrogel series were investigated using shear rheology. All mechanical characterization of hydrogels was carried out at 10% (w/v) in water. In determining the linear viscoelastic regime, we observed a decrease in rupture strain with an increase in hydrophobic length; however, at 1% strain all samples were within the linear regime (**Figure S15**). When running the frequency sweep, we observed that all hydrogelators have identical high-frequency equilibrium storage modulus of around 10,000 Pa (**Figure 3B and 3C**). Interestingly, the high-frequency equilibrium storage modulus was found to be independent of hydrophobic length. The basic theory of transient networks (by Green and Tobolosky) predicts a high-frequency storage modulus directly related to the number density of elastically effective chains (ν) [61].

$$G_\infty = \nu kT \qquad (1)$$

Where ν is the number density of elastically effective chains, k is the Boltzmann constant, T is the temperature, G_∞ is directly related to the mesoscopic structure, which is determined by structural arrangement in self-assembled amphiphilic molecules. This similar high-frequency storage modulus suggests similar cross-link density and similar hydrogels internal structure,[62] supported by the similarities in the cryo-TEM and cryo-SEM (vide supra) structures.

Frequency sweeps indicated that all of the hydrogelators are viscoelastic (**Figures 3B and 3C)**. The crossover point between loss moduli and storage moduli shifted to a higher frequency with decreasing hydrophobic length forming a more dynamic hydrogel. Yet, the moving of crossover point to higher frequency followed a very regular trend over 5 decades of frequencies, roughly moving almost two decades going from **$C_{12}C_{12}$ BTA (at 0.0005 rad/s) to $C_{10}C_{10}$ BTA (at 0.021 rad/s)** to **C_8C_8 BTA (1.1 rad/s)** to **C_6C_6 BTA 1 (~85 rad/s).** The **$C_{12}C_{12}$ BTA** showed a rubbery plateau region across 5 decades and showed a crossover point relatively in the lower frequency range forming a less dynamic hydrogel compared to other BTAs. Increasing hydrophobic length to enhance elastic properties has also been utilized for wormlike micelles and pseudo-Gemini surfactants (vide infra).[63] Frequency sweep results coupled with similar high-frequency storage modulus suggest that exchange dynamics of BTA are directly responsible for BTA hydrogel dynamics.

We were intrigued by this regularity with carbon chain length and investigated **C_6C_{12} BTA** (made in **chapter V**) hydrogelator with hexyl and dodecyl sidearms. Importantly, this is an asymmetrical molecule unlike others reported in this study and would also answer if the number of carbon atoms determines viscoelastic crossover points or symmetry of the BTA molecule influences viscoelastic properties. Ideally, if the number of carbon atoms is dictating crossover frequencies/viscoelastic properties, there should be one decade shift for **C_6C_{12} BTA** on the angular frequency axis relative to either **C_8C_8 BTA** (to the left) or **$C_{10}C_{10}$ BTA** (to the right). Satisfyingly, the **C_6C_{12} BTA** showed a crossover point at 0.25 rad/s (**Figure 3C, S16**) which is almost one decade shift to the right and left when compared to **$C_{10}C_{10}$ BTA** and **C_8C_8BTA**, respectively. Observing viscoelastic response and such defined crossover frequencies suggests the dynamic nature of BTA cross-links and distinct exchange dynamics for each BTA hydrogelator.

Tan delta (G"/G') provides information about stress dissipation capacity. Tan delta was highest for **C_6C_6 BTA** at 0.1rad/s and 1.0 rad/s and decreased with an increasing number of carbon atoms on BTA (**Figure S16 A–C)**. A decreasing tan delta shows a decrease in the dynamicity or stress dissipation capacity of hydrogels from **C_6C_6** to **$C_{12}C_{12}$ BTA** (**Figure S16 C)**. Maxima in loss moduli and Minima in the Tan delta curve describe a relaxation process (**Figure S16 A–B,** shown with arrows**)** and both shifted to the lower angular frequency with an increasing number of carbon atoms, indicating BTA exchange dynamics at the origin of this relaxation mode, since longer hydrophobic would decrease the kinetics of exchange dynamics between BTA fibers[64] resulting in the less dynamic and slow relaxing hydrogel.

Hydrogels with tunable stress relaxation

Early attempts to fit the frequency sweep data with single Maxwell elements (using **equations S1 and S2** in supporting information) resulted in poor fitting for loss moduli (see **Figure S17–S21**) on frequency sweep data, except for **C_6C_6**, suggesting a second mode of relaxation in these hydrogels. Then, the data was fit for two Maxwell elements in parallel (**Figure S17–S21**), which lead to considerably better curve fitting for storage and loss moduli. The fitting using the two modes of relaxation resulted in average relaxation times of 0.01, 0.9, 36, and 2250 s for **C_6C_6**, **C_8C_8**, **$C_{10}C_{10}$**, and **$C_{12}C_{12}$ BTAs**, respectively (**Figure S22**). The stress relaxation time for the **C_6C_{12} BTA** is 2.7 s (**Figure S24**), nicely fitting in this stepwise trend. The two-mode Maxwell curve fit indicated a fast relaxation process (ranging from 0.005–0.01 s) with a relatively small contribution (maximum 10%) to the average stress relaxation times. Such fast relaxation times have been attributed to polymer chains motion in dynamic hydrogels.[33]

Then, we moved to investigate stress relaxation times with a step strain test using rheology. The **C_6C_6 BTA** relaxed in a fraction of a second, the **C_8C_8 BTA** around 10 seconds, the **$C_{10}C_{10}$ BTA** approximately in a few hundred seconds, and the **$C_{12}C_{12}$ BTA** relaxed approximately 90% after roughly 4000 seconds (**Figure 3D**). Still, in line with the series, the **C_6C_{12} BTA** took roughly around 40 seconds to fully relax the stress (**Figure 3D**). The stress relaxation profile shifted to longer stress relaxation times with an increasing number of carbon atoms from **C_6C_6 BTA** to **$C_{12}C_{12}$ BTA**. Supramolecular materials may have more than one molecular mechanism of stress relaxation, which can be better predicted with the generalized Maxwell model or Maxwell-Weichert model for n-elements in parallel for viscoelastic fluids (shown in **equation S3 in SI)**.[27] Curve fitting using the generalized Maxwell model for two Maxwell elements in parallel (**equation 3 and Figure S23 in SI)** resulted in an average stress relaxation time of 0.04, 1, 48, 1300 seconds for **C_6C_6 BTA, C_8C_8 BTA, $C_{10}C_{10}$ BTA,** and **$C_{12}C_{12}$ BTA**, respectively; the stress relaxation time for **C_6C_{12} BTA** was 5 s (**Figure 3E and S24**). Curve fitting for a single Maxwell element also resulted in similar stress relaxation times (**Figure S24**) indicating one mode is mainly responsible for stress relaxation and minimal contribution from the second mode of relaxation (in line with frequency sweep curve fitting and contribution of modes). Satisfyingly, the stress relaxation times obtained from the step strain test are consistent with the results obtained from frequency sweep data (**Figure 3E**) with the exception of **$C_{12}C_{12}$** showing a relatively shorter average stress relaxation time in step strain compared to oscillatory shear (frequency sweep). Taken together, molecular tuning of hydrophobicity on the exterior of the BTA by varying only a few carbon atoms on the BTA hydrogelator with a Mw 23,000 molecule, stress relaxation can be controlled over 5 orders of magnitude in the fibrous hydrogel. Stress relaxation curves obtained in BTA hydrogels are similar to stress relaxation curves of tissues such as the brain[29], peripheral nerve[65], muscle[33], liver[66,67], and articular cartilage[68].

Supramolecular self-assembled systems are dynamic and supramolecular assembly undergoes continuous dissociations and associations of supramolecular complexes, or depolymerization and polymerization of supramolecular polymers. Relaxation time in supramolecular structures is referred to as structural relaxation time (τ_{str}), resulting from the constant breaking and reforming

of supramolecular structures. Structural relaxation time in supramolecular systems provides information about the kinetics and exchange dynamics of supramolecular structure. Structural relaxation time in self-assembled (colloidal systems or worm-like micelles) has been correlated to activation energy (Ea) and binding time (A) of hydrophobic monomers within a self-assembled micelle as shown with **equation 2.**[69,70]

$$Stress\ relaxation/strcutural\ (\tau_{str}) = Ae^{\frac{E_a}{kT}} \qquad (\mathbf{2})$$

Ea is the activation energy required for breaking up a given cross-linking point or self-assembling connection, A is the fastest possible break-up time of the hydrophobic monomer, and T is temperature.

In wormlike micelles, activation energy (Ea) required for a hydrophobic chain to be taken out of hydrophobic assembly into an aqueous/polar environment is 1.2 kT per CH_2 group.[70] In our library, we find surprising agreement with this previously established theory. According to this theory, adding four additional CH_2 groups increases the relaxation time (τ_{str}) by a factor of ~100. We observed that adding four CH_2 groups on a single BTA molecule leads to an increase in stress relaxation by a factor of ~100. Using equation **2**, the activation energy required for BTA molecules to exit the hydrophobic assembly core is between 1–1.2 kT per CH_2 group. The activation energy required for a hydrophobic chain to exit in BTA self-assembled structure is in agreement with previously reported wormlike micelles.[70,71,72,73] This alignment again reinforces the concept of slower BTA exchange dynamics for the BTA hydrogelator with a larger number of carbon atoms on the BTA exterior.

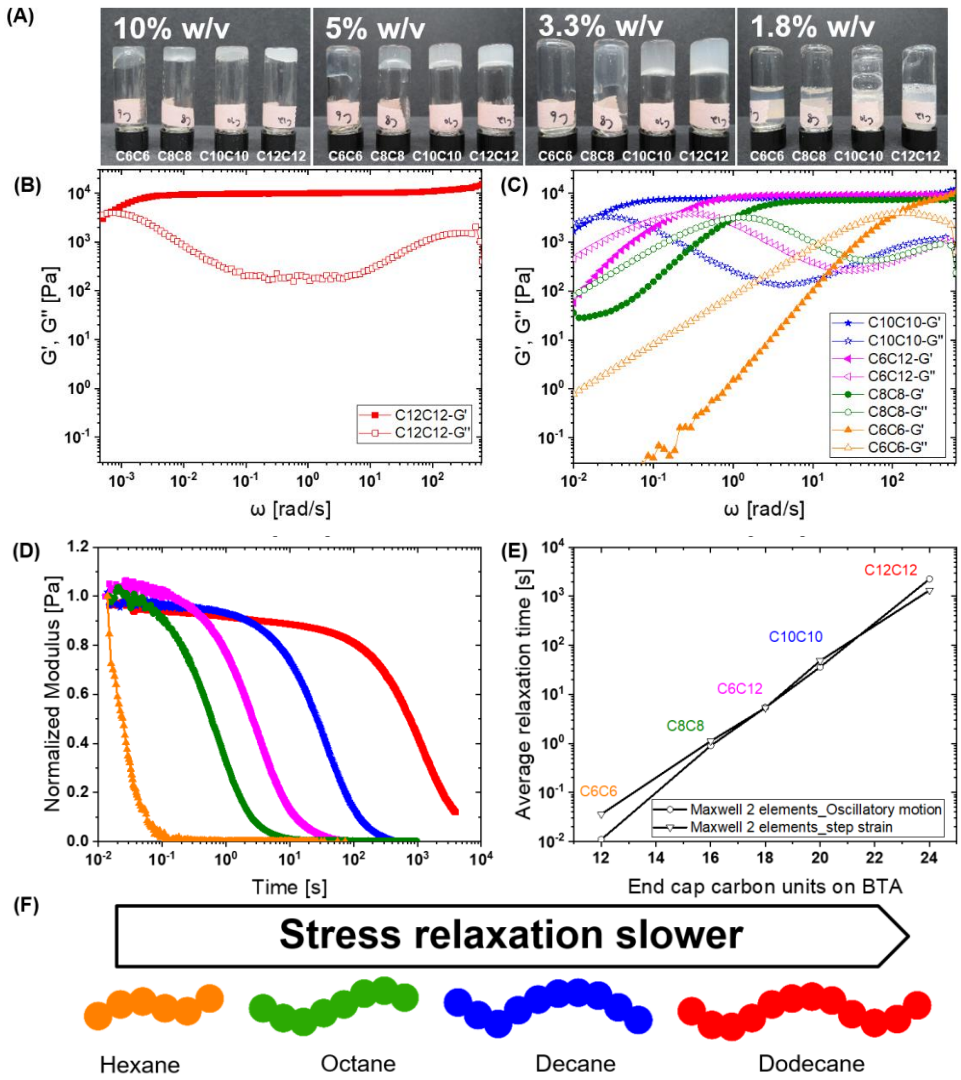

Figure 3. Hydrogel formation, viscoelasticity, and stress relaxation: A) All hydrogelator form hydrogels in water, and critical gelation concentration (CGC) decreases with decreasing carbon length. CGC for **C_6C_6**, **C_8C_8**, **$C_{10}C_{10}$**, and **$C_{12}C_{12}$** BTA was 5% (w/v), 3.3% (w/v), 2% (w/v), and 1.8% (w/v) respectively. B–C) Frequency sweep of hydrogelators at 1% strain. All hydrogelators showed the same equilibrium storage moduli. Each hydrogelator showed a cross-over point between loss moduli and storage moduli at a different angular frequency. **$C_{12}C_{12}$** showed a crossover point around 0.0005 rad/s. The cross-over point moved to a higher angular frequency with decreasing end-cap carbon length with the **C_6C_6** BTA crossover point appearing around 100 rad/s. Moving of crossover point to higher angular frequencies indicates faster dynamics of the BTA hydrogelator. The frequency sweep for **C_6C_{12}** showed a crossover point between **$C_{10}C_{10}$** and **C_8C_8** suggesting that viscoelasticity can be tuned on a broad range spectrum by varying end-cap carbon length via non-symmetric BTAs. D) The stress relaxation profile for different hydrogelators obtained from the step strain experiment by applying a constant 1% strain. E) Stress relaxation times are determined by fitting the generalized Maxwell model of viscoelasticity. Hydrogels were made in Milli-Q water at 10% (w/v) for all viscoelasticity measurements. F) Schematic representation of carbon atoms in a single hydrophobic group and arrow shows the trend in stress relaxation.

An increase in temperature enhances the dynamicity and viscoelasticity of hydrogels

Next, we investigated the hydrogel's viscoelasticity at 37 ºC, more relevant for cell culture. All BTA hydrogels showed a high-frequency storage modulus similar to 20 ºC indicating similar crosslink density (**Figure S25**). In contrast, the terminal region or crossover angular frequencies (rad/s) between G' and G" moved one order of magnitude to the right on the angular frequency axis (rad/s), which shows hydrogels are more dynamic at 37 ºC (**Figure S25 B**). Supramolecular systems are known to have faster dissociation/association and depolymerization/polymerization kinetics with an increase in temperature [74], and the shift of viscoelastic spectra with temperature is well established. Our results also align with previously reported hydrogen/deuterium (H/D) exchange dynamics of small supramolecular BTAs determined using mass spectrometry, where H/D molecular exchange becomes faster with increasing temperature (40 ºC, 50 ºC, and 55 ºC) compared to room temperature (20 ºC)[64]. Overall, these results showed that control over BTA supramolecular dynamics can be achieved by varying temperature without changing the high-frequency storage modulus.

Then, we fit the frequency sweep data using two Maxwell elements at 37 ºC. The Maxwell model for two elements resulted in average stress relaxation times of 0.01, 0.2, 6.3, and 360 seconds for **C_6C_6, C_8C_8, $C_{10}C_{10}$, and $C_{12}C_{12}$**, respectively. **C_6C_{12}** showed an average relaxation time of 0.6 seconds (**Figure S26**). We noticed that with nearly doubling the temperature (20 ºC to 37 ºC), most hydrogelator relaxed almost 6x faster. We were curious if this will match when **equation 2** is solved for an increase in temperature from 20 ºC to 37 ºC. Surprisingly, the solution of **equation 2** shows a factor of 6.4x faster/slower stress relaxation when the temperature is increased/decreased from 20 ºC to 37 ºC and vice versa. These results show that an increase in temperature can result in faster relaxing hydrogels.

Hydrogel preparation in DMEM did not alter viscoelasticity and stress relaxation

Having established the viscoelasticity of these hydrogels in water, we next explored hydrogel's viscoelasticity in Dulbecco's Modified Eagle Medium/Nutrient Mixture F-12 (DMEM/F-12). DMEM/F-12 is a basal medium for many cell types and contains amino acids, vitamins, and ions, which could potentially influence supramolecular interactions and resulting viscoelastic properties. We, therefore, investigated **C_8C_8, $C_{10}C_{10}$, and $C_{12}C_{12}$** viscoelastic properties in DMEM/F-12. We found that DMEM/F-12 did not affect equilibrium storage moduli and hydrogelators (**C_8C_8, $C_{10}C_{10}$, and $C_{12}C_{12}$**) showed surprisingly similar crossover frequencies (rad/s) to water (**Figure S27)**. We fit the data for two Maxwell elements, which resulted in similar stress relaxation times compared to water (**Figure S28)**. Overall, these results suggest viscoelasticity and stress relaxation timescales are well maintained when hydrogels are prepared in DMEM/F-12.

BTA hydrogelators are self-healing, shear-thinning, and injectable

Supramolecular interactions are reversible and can result in self-healing behavior within hydrogels. We first investigated the dynamicity and reversibility of hydrogelators with a visual qualitative self-healing test. Hydrogels were formed in a round mold, cut into two pieces, and pressed against each other using a spatula (**Figure 4A and Figure S29**) except **C_6C_6 BTA** hydrogel, which is liquid as it flowed and showed self-healing. Qualitatively all hydrogelators showed self-healing in under just 1 minute. **C_8C_8 BTA $C_{10}C_{10}$ BTA** showed a more homogenous and compact self-healing interface, while **$C_{12}C_{12}$** hydrogel had a somewhat granular texture and a little less compact and inhomogeneous self-healing interface. All hydrogels could be lifted using a spatula and were found to be stable, except **C_6C_6 BTA,** which started to flow when lifted using the spatula. In order to investigate the self-healing behavior of hydrogels more quantitatively, step strain shear rupture self-healing cycles were carried out (**Figure 4B**). Hydrogels recovered almost 100% in the recovery phase (low strain, 1% strain) under a few seconds demonstrating the self-healing behavior of the hydrogel, which was reproducible over several cycles.

Next, we investigated shear-thinning using continuous flow sweep (**Figure S30 E**). A decrease in viscosity was observed with increasing shear rate; however, the exuding of hydrogel during the experiment at the high shear rate was observed, which makes the data less representative at high shear rates. Then, we confirmed hydrogel shear-thinning using frequency sweep which showed that complex viscosity decreases with increasing angular frequency (**Figure 4C Figure S30 D**). Complex viscosity decreased with applied angular frequency strain and all hydrogelators flowed very similarly under higher shear rates, suggesting similar flow behavior of ruptured networks.

After confirming shear-thinning behavior, the BTA hydrogelators (shown in **Figure S30 A–C**) injectability was investigated. All BTA hydrogelators were injectable using 20G (internal diameter =0.603 mm) at 10% (w/v). **C_8C_8 BTA** resulted in continuous smooth fiber compared to other BTA hydrogelators; however, it took more force (qualitatively). Next, injectability was tested at a low hydrogelator concentration, 5% (w/v) using 20G and 22G (internal diameter =0.41 mm). While all hydrogelators could be injected, **$C_{10}C_{10}$** and **$C_{12}C_{12}$** injected fibers were more stable compared to **C_8C_8 BTA**.

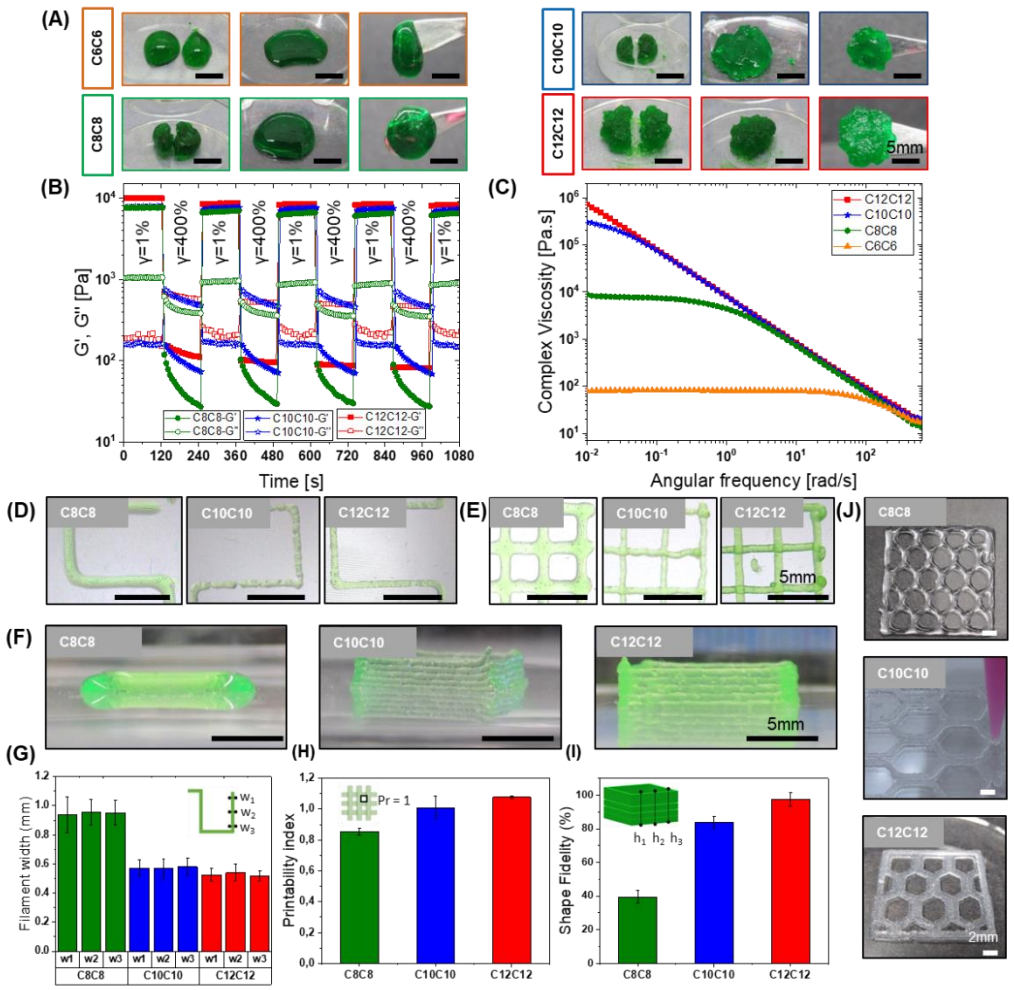

Figure 4. Self-healing, shear-thinning, and 3D printing of BTA hydrogels: A) All hydrogelators showed self-healing; each hydrogel was cut into two pieces and then the pieces were placed together and pressed with a spatula. B) Self-healing of hydrogels at room temperature under alternating strain. Gels recovered to their initial moduli in just a few seconds. C) Complex viscosity decreases with increasing angular frequency showing that gels are shear-thinning assuming COX-MERZ transformation holds. D) Single filament extruding for measuring diameter uniformity. E) Grid-like structure was printed for evaluating pore geometry. F) Multiple layer structure was printed and **$C_{10}C_{10}$** and **$C_{12}C_{12}$** maintained multilayer structure, while **C_8C_8** could not carry the weight of the extra layers on the first layer and deform post-printing. G) Filament width or diameter of extruded filament in "D" measured at three different locations, diameters (w1, w2, and w3) are identical showing filament homogeneity for all hydrogelators. **$C_{10}C_{10}$** and **$C_{12}C_{12}$** showed filament diameters around 500 μm considerably smaller than **C_8C_8**, which is around 1000 μm. H) Printability index calculated from grid-like structure geometry printed in "C". Ideal rectangular pore shape is defined with printability index = 1 and **$C_{10}C_{10}$** and **$C_{12}C_{12}$** showed printability index close to 1. I) Shape fidelity was determined by comparing the height of computer designed structure to the post-printing height printed in "F". **$C_{10}C_{10}$** and **$C_{12}C_{12}$** retained above 80% of their height compared to **C_8C_8**, which is around 40%. J) Printing of hexagon structures, using different hydrogelators at 10% w/v, C10C10, and C12C12 hydrogel resulted in better hexagon shape printing compared to **C_8C_8**.

We then investigated the hydrogelators ability to adapt to different shapes by placing them into different molds. The moldability of hydrogels showed the hydrogelator's ability to adapt to different shapes, which can find application to fill in cavities for example during surgeries. All hydrogelators, when placed in different molds and pressed with a spatula, adapted the shape of the new mold (**Figure S31**). For **C_6C_6 BTA**, pressing with the spatula was not required since it would flow and take the shape of the mold. Adapting the shape of the mold in response to applied stresses visually showed that hydrogels were viscoelastic fluids and could dissipate applied stresses by taking the shape of the new mold.

Self-healing, shear-thinning, injectability, and moldability within BTA hydrogelators likely are because of reversibility and dynamics of supramolecular interactions. Self-healing and shear-thinning properties in supramolecular systems have been associated with their transient and dynamic interactions [59]. When injected through a syringe, supramolecular interactions dissociate (shear-thinning) and re-associate within seconds (self-healing) after injection [39,75]. Transient dynamics have been engineered by tuning non-covalent interactions[21,76] and host-guest supramolecular interactions [77,52,78] for designing injectable hydrogels. Injectability and moldability within our materials are interesting properties and could find a use for delivering cells, and drugs and for filling surgery cavities via injection.

BTA hydrogelator offers control on 3D printability and retained bulk anisotropic structure

Shear-thinning and self-healing properties also make them a strong candidate to be explored for 3D printing applications and investigate the hydrophobic length effect on printability. We were encouraged by our rheological and handling observations to try extrusion-based 3D printing for the developed hydrogels (**Figure 4D–J and Figure S31–33**). We chose to investigate printing with **C_8C_8BTA**, **$C_{10}C_{10}$ BTA**, and **$C_{12}C_{12}$ BTA at** 10 % (w/v), since at these concentrations the **C_6C_6BTA** does not retain its shape (see injectability studies). We started extruding a single fiber and found that the shape fidelity of the extruded fiber is better for the **$C_{10}C_{10}$ BTA** and **$C_{12}C_{12}$ BTA** compared to the **C_8C_8 BTA** (**Figure 4D and 4G**). Next, we calculated the printability index (PI) by printing and quantifying a square grid-like structure (**Figure 4E**). The printability index is a measure of printing accuracy and a perfect square has a PI of 1[79]. We printed a square grid pattern for determining the PI. We find PI roughly equal to 1 for **$C_{10}C_{10}$ BTA** and **$C_{12}C_{12}$ BTA** confirming good printing accuracy of extruded fibers; however, for **C_8C_8 BTA** printability index was 0.8, which can be attributed to the spreading of **C_8C_8 BTA** extruded fiber (**Figure 4H**).

Then, we were interested to investigate if hydrogelators allow the printing of multilayer self-supporting structures. This free-standing print has been a challenge for materials based on non-covalent and supramolecular interactions; however, close tuning of the properties of the material should enable free-standing prints. We printed 5 layers of a hollow cube structure for each hydrogelator (**Figure 4F**) and interestingly **$C_{10}C_{10}$ BTA** and **$C_{12}C_{12}$ BTA** showed excellent shape fidelity. To obtain more quantitative information on structural accuracy, a percentage shape

fidelity was calculated by dividing the as-printed height (H_P) by the designed height (H_H). Shape fidelity for **$C_{12}C_{12}$ BTA** and **$C_{10}C_{10}$ BTA** was close to 100% and 90%, respectively, while shape fidelity for **C_8C_8 BTA** decreased to 40% (**Figure 4I**).

Then, we also extruded a few complex hexagon-like structures, which could be printed successfully with **C_8C_8 BTA**, **$C_{10}C_{10}$ BTA, and $C_{12}C_{12}$ BTA** hydrogelators (**Figure 4J**), showing the flexibility of hydrogelators to be 3D printed into somewhat complex shapes.

These printing experiments suggested that the hydrophobic length has a significant influence on the stability of 3D fabricated structures and there is a critical threshold for hydrogels to be stable post-extrusion. In terms of the molecular picture, this suggests that the addition of a few carbon atoms keeps the speed of self-healing, and limits creep, while still allowing the hydrogelator to be suitably shear thinning for printing.

Shear-thinning hydrogels based on supramolecular chemistry (host-guest) have been 3D printed before; however, hydrogel requires either UV[52,78] or ionic[80] crosslinking post-printing for stability since supramolecular interactions are weak. BTA hydrogels allow being printed as multilayer constructs without introducing extra covalent crosslinks or changing pH.

Furthermore, BTA hydrogels retained bulk anisotropic fibril structure post extrusion. **$C_{10}C_{10}$ BTA** and **$C_{12}C_{12}$ BTA** showed anisotropic fibril morphology post extrusion, while **C_8C_8 BTA** and **C_6C_6 BTA** showed more planar surface with ridges on the surface (**Figure S34**). Different morphology of **C_8C_8 BTA** and **C_6C_6 BTA** post extrusion could be attributed to different surface fracture patterns i.e., a surface crack appeared parallel to the ice crystal, and fibers remain hidden under the surface. Short peptide[54], supramolecular polypeptide DNA[81], and peptide amphiphile-based supramolecular hydrogels[80] have been printed before with fibril morphology; however, there are no reports of the broad range of viscoelasticity and stress relaxation tuning in 3D printable fibril supramolecular hydrogels. In addition, BTA hydrogels remain the only purely synthetic supramolecular fibril hydrogel with tunable broad-range viscoelasticity, which offers tunable 3D printing.

Cell viability

After establishing mechanical properties and tunable 3D printing, we wanted to investigate the cytocompatibility of newly developed BTA hydrogels to explore their use as bioinks and platform biomaterials. We choose to run initial viability experiments with chondrocytes since dynamic hydrogels are shown to affect positively chondrocytes proliferation and cartilage-like matrix production[28,34]. Live-dead assay after 4 days of encapsulation showed that a large number of chondrocytes stayed alive within BTA hydrogels (**Figure 5A**). Quantitatively, the live and dead projection areas of the ATDC5 cell aggregates were calculated using image J. Live-cell multicellular aggregates showed a mean area value greatly higher compared to dead cells (**Figure 5B**) and all hydrogelators showed greater than 90% of the average area of live cells, except **C_6C_6 BTA**, which showed 82% live cells area (**Figure S35A**). We calculated live and dead cell areas, since single-cell counting was not feasible owing to multicellular aggregate formation.

Interestingly, chondrocytes formed multicellular aggregates within all BTA hydrogels. Supramolecular dynamic hydrogels have been shown to support spheroid fusion within hydrogels and fusion behavior has been credited to viscous properties, which allow cells to remodel their microenvironment in the absence of protease.[82] BTA hydrogels are viscoelastic (as discussed above) and multicellular aggregate formation can be attributed to the viscous and dynamic properties of BTA hydrogel. We also observed some erosion of hydrogel over 4 days of culture, which likely can be due to the dynamic nature of BTA supramolecular interactions.

In addition, we assessed cell viability in a two-dimensional (2D) setup by exposing cultured cells on tissue culture plastic to dilute solutions (100 μg/mL) of BTA hydrogelators for investigating cytotoxicity at low concentrations (in solution form). In addition, we were interested to understand if the presence of a BTA hydrogelator in solution form would negatively affect the spreading morphology of ATDC5. The addition of supramolecular BTA hydrogelator solutions did not affect cells negatively and only a few dead cells were spotted (**Figure 5C**). Similar to tissue culture plastic control (without any BTA hydrogelator solution), cells continuously proliferated and covered ~70–80% area of the well plate by day 4 (**Figure 5C**). ATDC5 cells also showed spreading morphology similar to tissue culture plastic (**Figure S35C**) and the BTA hydrogelator solution did not change cell morphology. Live and dead cell areas were calculated using Image J and greater than 95% of the average area of cells was found to be composed of live cells (**Figure 5D and Figure S35B**). Live and dead cells were also counted using image J to analyze particle function and greater than 95% of cells were alive.

Bioprintability

After successful 3D printing and cell viability, we were interested to see if the BTA hydrogelators would be suitable as a bioink. In order to enable 3D printing with live cells (bioprinting), the bioink material must be printable with cells mixed in and allow cell survivability post-printing process. Chondrocytes (ATDC5) were encapsulated in **C_8C_8 BTA**, **$C_{10}C_{10}$ BTA,** and **$C_{12}C_{12}$ BTA** hydrogelators and bioprinted into grid-like structures using a 22G needle (**Figure S36A**). Cell viability was monitored after 2 hours and 24 hours of bioprinting via live/dead staining. All tested hydrogelator showed viability above 90% after 24 hours (**Figure S5E**). We further observed that cells were largely single cells right after printing and cell aggregation was observed after 24 hours of bioprinting (**Figure S36**). This indicates that hydrogels allow cellular interactions, likely due to the dynamic nature of interactions in BTA hydrogel.

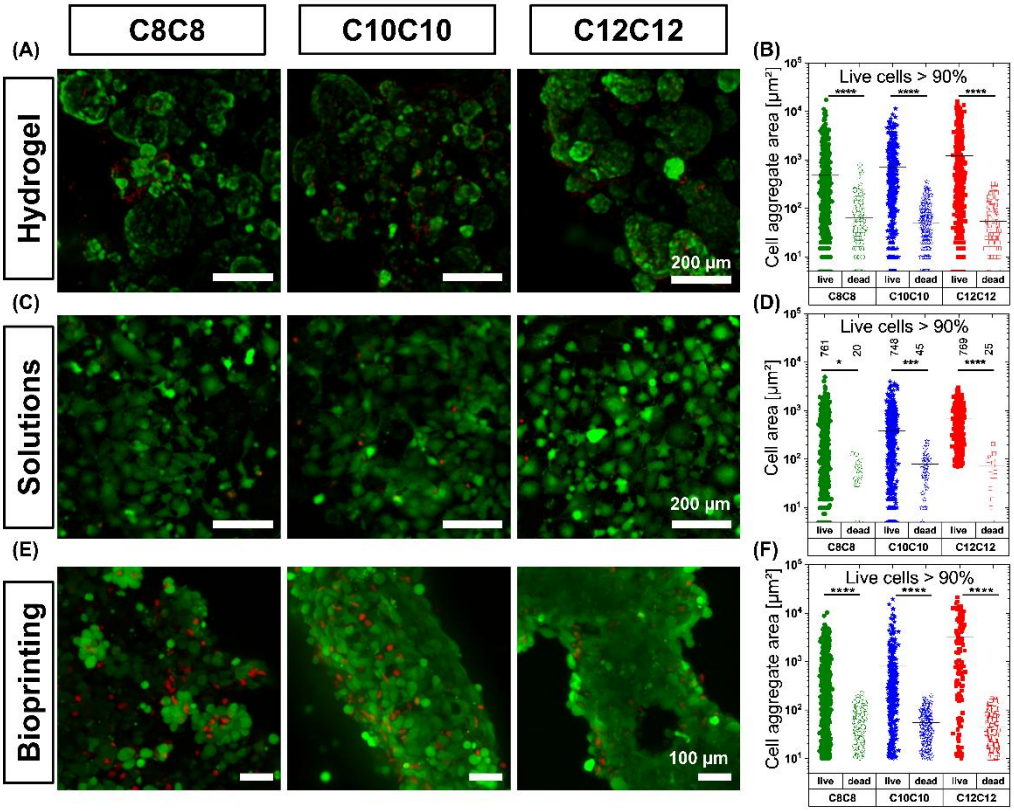

Figure 5. Chondrocytes cell viability in 3D and 2D. A) showing live and dead chondrocytes (ATDC5) encapsulated within hydrogels after 4 days. Live-dead image of $\mathbf{C_{12}C_{12}}$ was adapted from **chapter VI**. B) Live and dead cell area of multiple cellular aggregates within gels (3D), quantification of single cell area was not possible since chondrocytes form multicellular aggregates, each point on the graph represents an area of an aggregate calculated using image J and a number on the top represents a number of counted cellular aggregates. C) Live-dead images of cells cultured on tissue culture plastic and exposed to a dilute solution of BTA hydrogelators at a concentration of 100 µg/ml. D) Quantification of single cell area cultured on tissue culture plastic and exposed to dilute solutions. E) Live-dead images of bioprinted chondrocytes (ATDC5) after 24 hours in culture. F) Live-dead area of multicellular chondrocyte aggregates in bioprinted constructs, like in panel "D" the area of multicellular aggregate was calculated and each point on the graph shows an area of aggregate. The live cell average area is higher than dead cells in all culture conditions. Grubbs outlier test with a significance level of 0.01 was performed on B, D, and F to remove the outliers. The statistical analysis of live and dead cell areas was conducted using one-way ANOVA, with Tukey's post-hoc test for comparisons. The software OriginLab was used for the analysis, and the level of significance was set at *P < 0.05, **P < 0.005, ***P < 0.0005, and ****P < 0.0001. A total of 20-800 cell aggregates or single cells were examined during the analysis.

Conclusion

In this work, we have synthesized a library of BTA hydrogelators by changing external hydrophobic length with above 90% yields and on the multi-gram scale. All telechelic BTA hydrogelators showed fibrous morphology in dilute solution and hydrogel state, on a similar dimensional scale to native ECM (collagen). All hydrogelators formed stable hydrogel at 10% w/v and showed similar high-frequency storage modulus. Changing the total number of carbon atoms from 12 (**C_6C_6**) to 24 (**$C_{12}C_{12}$**) on the BTA end group allowed tuning viscoelasticity and stress relaxation over 5 orders of magnitude within fibril hydrogel. Increasing hydrophobic length resulted in reduced viscoelasticity and increased average stress relaxation times. This can be explained by the existing theory and methodology of the self-assembling theory of self-assembling worm-like micelles. All hydrogel showed shear-thinning, self-healing, and injectable properties. **C_8C_8**, **$C_{10}C_{10}$**, and **$C_{12}C_{12}$** can be 3D printed, and hydrophobic carbon length exhibited a marked effect on the shape fidelity of 3D printed constructs post-printing. Chondrocytes exhibited good cell viability in bulk and bioprinted hydrogels. This study shows BTA hydrogels 3D bioprinting for the very first time and introduces BTA hydrogels as a promising candidate in the list of dynamic ECM mimicking bioinks. In summary, this study represents a step forward in designing and developing synthetic fibril supramolecular hydrogels with unprecedented control over viscoelasticity and tunable bioinks. Our approach teaches a conceptual methodology for the creation of dynamic supramolecular hydrogels with controlled viscoelasticity and 3D printability. We anticipate that this methodology can thus be translated into other supramolecular structures such as bis-urea, UPy, and peptide amphiphile.

Experimental section

Self-assembly studies using Nile red and cryo-TEM

The solutions of hydrogelators (**C_6C_6 BTA**, **C_8C_8 BTA**, **$C_{10}C_{10}$ BTA,** and **$C_{12}C_{12}$ BTA**) at a concentration of 1mg/ml, 2mg/ml, and 5mg/ml were prepared. The desired amount of hydrogelator was molecularly dissolved in ~50 μL methanol with vortexing and heating using a heat gun (mostly required for **$C_{10}C_{10}$ BTA** and **$C_{12}C_{12}$ BTA**). Water (milli-Q) was added to the methanol solution and the total amount of solution was adjusted to 1000 μL. Next, the BTA solution was heated, vortexed, and cooled. The same procedure was repeated a minimum of twice and a maximum of thrice to ensure no precipitation or aggregation of BTA and that the BTA solution is transparent. During the last step, the BTA solution was controlled and cooled to ~20°C from the heating plate maintained at 80°C. The solution was aged overnight (16–24 hours) before self-assembly studies. Next, we transferred 200 μL of the BTA solution to a well plate and 3.2 μL of Nile red solution was added. The Nile red final concentration was adjusted to 5μM. The samples were incubated on the orbital shaker for and in the dark for 30 minutes and then fluorescence spectra were recorded.

For cryo-TEM, the same procedure was repeated and the samples were prepared at 10mg/ml. The sample vitrification procedure was followed as reported in **chapter V** and samples were imaged using FEI Arctica 200KV microscope.

Hydrogel formation

The desired amount of hydrogelator was weighed in the glass vial and Milli-Q water (rheology) or in DMEM with 1% Penicillin-Streptomycin (P/S). The final concentration of the hydrogelator was adjusted to 10% w/v. BTA polymer was heated using a heat gun until ~80 °C and the solution becomes opaque (above the LCST of the PEG20K). The heating solution was vortexed for dissolving the BTA polymer uniformly. The same procedure was repeated twice. Subsequently, the hydrogel mixture was centrifuged at 2000g for five minutes for water vapors and polymer residues to sit at the bottom of the glass vial. Next, the hydrogel mixture was placed on a heating plate set to 80°C (using a controlled thermometer knob), the temperature was turned off and the hydrogel mixture was cooled to room temperature (~20°C).

Rheology

Rheological measurements were performed using a DHR-2 rheometer using a 20 mm cone-plate geometry with a 2.002° angle. All measurements were performed at room temperature (20 °C). A rejuvenation process was carried out to remove any mechanical history within hydrogels. We choose a 400% strain amplitude at a frequency of 1 rad/s. Strain amplitude is well into the non-linear regime of the samples. Following the rejuvenation process, a time sweep at 1% strain was carried out to observe aging kinetics and let the sample equilibrate. Subsequently, a frequency sweep was carried out from 0.01 rad/s to 627 rad/s at 1% oscillation strain followed by oscillatory strain amplitude sweeps 1 to 1000% at an angular frequency of 1 rad/s. A time sweep at 1% strain was conducted until the sample reached the equilibrium storage modulus. Then, a step strain stress relaxation experiment was conducted under 1% strain for 1000 seconds. Followed by stress relaxation, a self-healing test was performed. Step strain cycles of 400% and 1% strain were applied for 120 seconds for rupturing the hydrogel network and watching for recovery of storage and loss moduli.

Moldability and self-healing

The hydrogel was made at 10% (w/v) following the standard procedure described above in the hydrogels-making section. A few microliters of the green food dye were added to give green color for good visibility. The hydrogel was introduced in the hexagonal mold and then switched (using a spatula) to a round-to-star-to-heart-shaped mold. During each turn, the hydrogel was compressed with a spatula for adjusting to the desired shape.

Injectability

For injectability, the hydrogel was introduced into the syringe using the spatula and then injected using 20 gauge and 22 gauge stainless steel needles.

3D printability

To investigate printability, we used the BioX bioprinter (CellInk, Sweden). All printing was performed at room temperature. Conical plastic needles (VIEWEG GmbH, Germany) were fixed to 3 mL syringes with different needle diameters as follows (ID = inner diameter): 20 G (ID = 0.58 mm) and 22 G (ID = 0.41 mm). The minimum pressure applied depends on the hydrogel, which was 60, 110, and 90 kPa for C8, C10, and C12, respectively. The infill density was set to 100% and the distance from the needle to the print surface was optimized so that the leading edge of the flow was in line with the needle. Printability tests were carried out using a plastic Petri dish as the printing surface. All blends had two drops of green food dye added during the mixing process for better post-print visualization. We then imaged each print (20-megapixel camera) and used ImageProPlus (MediaCybernetic, USA) software to threshold images and measure dimensions.

Filament uniformity

The first test conducted was to print a single layer, continuous strand of material following a path designed using 3D Builder (Microsoft®). An image of the printed structure was analyzed in ImageProPlus where the width of the strand was measured at multiple locations and averaged.

Layer stacking

A 5-layered hollow cube was designed in 3D Builder (Microsoft®) and printed using the optimized parameters found earlier. Three structures of each hydrogel were printed. Images were then obtained as before and analyzed using ImageProPlus to find the height of each cube. The printing fidelity was then calculated by comparing the printed height hi (mm) to the design height h (mm), to obtain a percentage shape fidelity for each sample using the following formula.

$$\%Shapefidelity = \frac{|hi-h|\times 100}{h}$$

Pore geometry

Other parameter investigated to show the printing accuracy of BTA hydrogels was the printability index (Pr), which was proposed by Ouyang et al.[83]. This parameter compares the pore geometry, considering square holes as an ideal condition for regular grid printed structures (Pr = 1). However, in an under-gelation condition, the extruded filament would demonstrate a more liquid-like state and the upper layer would fuse with the lower layer, thus creating approximately circular holes. They defined the ink printability (Pr) based on square shape using the following formula.

$$Pr = \frac{L^2}{16\times A}$$

where L means perimeter and A means area. To determine the Pr value of each printing parameter combination, images of printed structures were analyzed in ImageProPlus software to determine the perimeter and area of interconnected channels (n=5).

ATDC5 chondrocytes cell culture

ATDC5 were cultured at 37 °C in Dulbecco's modified eagle medium (DMEM-F12) with 10% fetal bovine serum, and 1% penicillin/streptomycin. Cells were placed in the humidified incubator at 37 °C and 5% CO_2. Cells were given a fresh cell culture medium every other day and harvested when reached 85% confluency.

Cell encapsulation in BTA hydrogel

Chondrocytes (ATDC5) were encapsulated in BTA hydrogel at a concentration of 5 million (M) cells per mL of hydrogelator. The hydrogel was made in DMEM-F12+1%P/S for cell studies. For encapsulation of cells within a hydrogel, hydrogels (200µl) were divided into two wells (48-well plate, non-adherent), and centrifuged for five minutes at 2000g to make a uniform layer at the bottom of the well plate. Cell suspension in 50ul volume was spread on top of the hydrogel, waited for 5-10 minutes for hydrogel to soak up the media, and centrifuged at 80g for one minute. The centrifugation step was done to help cells settle in the hydrogel. The second layer of the hydrogel from another well was added on top of the first hydrogel layer with cells and again centrifuged at 80g for one minute. After centrifugation, the hydrogel was folded from the edge to the center multiple times and let it relax for cells to spread evenly. The moldability of the hydrogels allows folding and stress-relaxing properties to allow the flow of the hydrogel. To ensure good cell encapsulation and that cells are well spread throughout the hydrogel, the hydrogel was cut gently into many pieces using the spatula and then pieces were placed together for self-healing. Self-healing is surprisingly fast and it just takes a maximum of 10 minutes for self-healing of the hydrogel. Cell culture media was added (500 ul per well) and hydrogels were incubated in the incubator maintained at 37 °C with 5% CO_2.

Cell seeding on tissue culture plastic for BTA dilute solution cell viability studies

We seeded 5000 cells per well in a 24-well plate treated for cell adhesion. The cell-cultured well plate was incubated at 37 °C in the humidified incubator overnight for cell attachment. The next day, BTA dilute solution at a final concentration of 100 µg/ml in cell culture media was added on top of the cells. The well plate was again placed back in the incubator and cell viability (Live/dead) was investigated after 4 days of exposure to BTA dilute solutions.

Live-dead cell viability assay

Cell viability was assessed using the LIVE/DEAD™ Viability/Cytotoxicity Kit (Thermo Fisher Scientific). Cell cultured hydrogels were transferred 35 mm glass-bottom dish (ibidi, Germany), gently washed with PBS, and a solution of 1 µM calcein AM and 2 µM ethidium homodimer-1 in PBS was added and hydrogel was immersed. The hydrogels were incubated (in the dark) for ~45 minutes in 37°C incubators with 5% CO_2. The solution of calcein and ethidium homodimer

was removed and gently washed with PBS. Hydrogels were imaged using an inverted fluorescence microscope (Nikon Eclipse Ti-e).

For cells cultured on tissue culture plastic and exposed to BTA dilute solution, media was removed gently from the well plate, and live/dead solution (as prepared above) was added to the well plate and incubated at 37°C incubators with 5% CO_2 in the dark for 45 minutes. Live/dad solution was removed, cells were washed with PBS (1x), and imaged using an inverted fluorescence microscope (Nikon Eclipse Ti-e).

Bioprinting

Cells were encapsulated in the hydrogels as described in the cell encapsulation procedure. Hydrogels were transferred to a 3 mL syringe and bioprinted using a 22G conical nozzle with the BioX bioprinter in an in-built cleanroom environment. The grid-like structure was designed in the BioX software using a basic shape of 10 mm x 10 mm and an infill of 20%, resulting in four layers grid structure. The applied pressure was 60 kPa for C8 and 90 kPa for C10 and C12; while the printing speed was 3 mm per second for all samples. Once the constructs were printed in μ-Dish 35 mm high Glass Bottom dish, DMEM media was added to each dish, and 3D printed constructs were cultured at 37°C and 5% CO2.

Statistical Analysis

The statistical analysis was conducted utilizing Origin-Lab 2022 software. One-way ANOVA with Tukey's post-hoc test was used to determine significant differences.

References

(1) Mouw, J. K.; Ou, G.; Weaver, V. M. Extracellular Matrix Assembly: A Multiscale Deconstruction. *Nat. Rev. Mol. Cell Biol.* **2014**, *15* (12), 771–785. https://doi.org/10.1038/nrm3902.

(2) Daley, W. P.; Peters, S. B.; Larsen, M. Extracellular Matrix Dynamics in Development and Regenerative Medicine. *J. Cell Sci.* **2008**, *121* (3), 255–264. https://doi.org/10.1242/jcs.006064.

(3) Frantz, C.; Stewart, K. M.; Weaver, V. M. The Extracellular Matrix at a Glance. *J. Cell Sci.* **2010**, *123* (24), 4195–4200. https://doi.org/10.1242/jcs.023820.

(4) Goor, O. J. G. M.; Hendrikse, S. I. S.; Dankers, P. Y. W.; Meijer, E. W. From Supramolecular Polymers to Multi-Component Biomaterials. *Chem. Soc. Rev.* **2017**, *46* (21), 6621–6637. https://doi.org/10.1039/C7CS00564D.

(5) Rosales, A. M.; Anseth, K. S. The Design of Reversible Hydrogels to Capture Extracellular Matrix Dynamics. *Nat. Rev. Mater.* **2016**, *1*, 1–15. https://doi.org/10.1038/natrevmats.2015.12.

(6) Ooi, H. W.; Hafeez, S.; Van Blitterswijk, C. A.; Moroni, L.; Baker, M. B. Hydrogels That Listen to Cells: A Review of Cell-Responsive Strategies in Biomaterial Design for Tissue Regeneration. *Mater. Horizons* **2017**, *4* (6), 1020–1040. https://doi.org/10.1039/c7mh00373k.

(7) Wojtecki, R. J.; Meador, M. A.; Rowan, S. J. Using the Dynamic Bond to Access Macroscopically Responsive Structurally Dynamic Polymers. *Nat. Mater.* **2011**, *10* (1), 14–27. https://doi.org/10.1038/nmat2891.

(8) Webber, M. J.; Tibbitt, M. W. Dynamic and Reconfigurable Materials from Reversible Network Interactions. *Nat. Rev. Mater.* **2022**, *0123456789*. https://doi.org/10.1038/s41578-021-00412-x.

(9) Webber, M. J.; Appel, E. A.; Meijer, E. W.; Langer, R. Supramolecular Biomaterials. *Nat. Mater.* **2015**, *15* (1), 13–26. https://doi.org/10.1038/nmat4474.

(10) Gough, J. E.; Saiani, A.; Miller, A. F. Peptide Hydrogels: Mimicking the Extracellular Matrix. *Bioinspired, Biomim. Nanobiomaterials* **2012**, *1* (1), 4–12. https://doi.org/10.1680/bbn.11.00007.

(11) Horii, A.; Wang, X.; Gelain, F.; Zhang, S. Biological Designer Self-Assembling Peptide Nanofiber Scaffolds Significantly Enhance Osteoblast Proliferation, Differentiation and 3-D Migration. *PLoS One* **2007**, *2* (2), 1–9. https://doi.org/10.1371/journal.pone.0000190.

(12) Shi, W.; Huang, C. J.; Xu, X. D.; Jin, G. H.; Huang, R. Q.; Huang, J. F.; Chen, Y. N.; Ju, S. Q.; Wang, Y.; Shi, Y. W.; Qin, J. B.; Zhang, Y. Q.; Liu, Q. Q.; Wang, X. B.; Zhang, X. H.; Chen, J. Transplantation of RADA16-BDNF Peptide Scaffold with Human Umbilical Cord Mesenchymal Stem Cells Forced with CXCR4 and Activated Astrocytes for Repair of Traumatic Brain Injury. *Acta Biomater.* **2016**, *45*, 247–261. https://doi.org/10.1016/j.actbio.2016.09.001.

(13) Brunton, P. A.; Davies, R. P. W.; Burke, J. L.; Smith, A.; Aggeli, A.; Brookes, S. J.; Kirkham, J. Treatment of Early Caries Lesions Using Biomimetic Self-Assembling Peptides-A Clinical Safety Trial. *Br. Dent. J.* **2013**, *215* (4), 1–6. https://doi.org/10.1038/sj.bdj.2013.741.

(14) Sur, S.; Matson, J. B.; Webber, M. J.; Newcomb, C. J.; Stupp, S. I. Photodynamic Control of Bioactivity in a Nanofiber Matrix. *ACS Nano* **2012**, *6* (12), 10776–10785. https://doi.org/10.1021/nn304101x.

(15) Webber, M. J.; Tongers, J.; Renault, M. A.; Roncalli, J. G.; Losordo, D. W.; Stupp, S. I. Development of Bioactive Peptide Amphiphiles for Therapeutic Cell Delivery. *Acta Biomater.* **2010**, *6* (1), 3–11. https://doi.org/10.1016/j.actbio.2009.07.031.

(16) Silva, G. A.; Czeisler, C.; Niece, K. L.; Beniash, E.; Harrington, D. A.; Kessler, J. A.; Stupp, S. I. Selective Differentiation of Neural Progenitor Cells by High-Epitope Density Nanofibers. *Science (80-.).* **2004**, *303* (5662), 1352–1355. https://doi.org/10.1126/science.1093783.

(17) Dankers, P. Y. W.; Harmsen, M. C.; Brouwer, L. A.; Van Luyn, M. J. A.; Meijer, E. W. A Modular and Supramolecular Approach to Bioactive Scaffolds for Tissue Engineering. *Nat. Mater.* **2005**, *4* (7), 568–574. https://doi.org/10.1038/nmat1418.

(18) Diba, M.; Spaans, S.; Hendrikse, S. I. S.; Bastings, M. M. C.; Schotman, M. J. G.; van Sprang, J. F.; Wu, D. J.; Hoeben, F. J. M.; Janssen, H. M.; Dankers, P. Y. W. Engineering the Dynamics of Cell Adhesion Cues in Supramolecular Hydrogels for Facile Control over Cell Encapsulation and Behavior. *Adv. Mater.* **2021**, *33* (37), 2008111. https://doi.org/10.1002/adma.202008111.

(19) Bastings, M. M. C.; Koudstaal, S.; Kieltyka, R. E.; Nakano, Y.; Sluijter, J. P. G.; Meijer, E. W.; Chamuleau, S. A. J.; Dankers, P. Y. W. A Fast PH-Switchable and Self-Healing Supramolecular Hydrogel Carrier for Guided , Local Catheter Injection in the Infarcted Myocardium. **2014**, 70–78. https://doi.org/10.1002/adhm.201300076.

(20) Koudstaal, S.; Bastings, M. M. C.; Feyen, D. A. M.; Waring, C. D.; Nadal-ginard, B.; Doevendans, P. A.; Ellison, G. M.; Chamuleau, S. A. J. Sustained Delivery of Insulin-Like Growth Factor-1 / Hepatocyte Growth Factor Stimulates Endogenous Cardiac Repair in the Chronic Infarcted Pig Heart. **2014**, 232–241. https://doi.org/10.1007/s12265-013-9518-4.

(21) Dankers, P. Y. W.; Hermans, T. M.; Baughman, T. W.; Kamikawa, Y.; Kieltyka, R. E.; Bastings, M. M. C.; Janssen, H. M.; Sommerdijk, N. A. J. M.; Larsen, A.; Van Luyn, M. J. A.; Bosman, A. W.; Popa, E. R.; Fytas, G.; Meijer, E. W. Hierarchical Formation of Supramolecular Transient Networks in Water: A Modular Injectable Delivery System. *Adv. Mater.* **2012**, *24* (20), 2703–2709. https://doi.org/10.1002/adma.201104072.

(22) Varela-aramburu, S.; Morgese, G.; Su, L.; Schoenmakers, S. M. C.; Perrone, M.; Leanza, L.; Perego, C.; Pavan, G. M.; Palmans, A. R. A.; Meijer, E. W. Exploring the Potential of Benzene-1,3,5-Tricarboxamide Supramolecular Polymers as Biomaterials. *Biomacromolecules* **2020**, *21* (10), 4105–4115. https://doi.org/10.1021/acs.biomac.0c00904.

(23) Hafeez, S.; Ooi, H. W.; Suylen, D.; Duimel, H.; Hackeng, T. M.; van Blitterswijk, C.; Baker, M. B. Desymmetrization via Activated Esters Enables Rapid Synthesis of Multifunctional Benzene-1,3,5-Tricarboxamides and Creation of Supramolecular Hydrogelators. *J. Am. Chem. Soc.* **2022**, *144* (9), 4057–4070. https://doi.org/10.1021/jacs.1c12685.

(24) Álvarez, Z.; Kolberg-Edelbrock, A. N.; Sasselli, I. R.; Ortega, J. A.; Qiu, R.; Syrgiannis, Z.; Mirau, P. A.; Chen, F.; Chin, S. M.; Weigand, S.; Kiskinis, E.; Stupp, S. I. Bioactive Scaffolds with Enhanced Supramolecular Motion Promote Recovery from Spinal Cord Injury. *Science (80-.).* **2021**, *374* (6569), 848–856. https://doi.org/10.1126/SCIENCE.ABH3602.

(25) Chaudhuri, O.; Gu, L.; Darnell, M.; Klumpers, D.; Bencherif, S. A.; Weaver, J. C.; Huebsch, N.;

Mooney, D. J. Substrate Stress Relaxation Regulates Cell Spreading. *Nat. Commun.* **2015**, *6*, 6364. https://doi.org/10.1038/ncomms7365.

(26) Sacco, P.; Baj, G.; Asaro, F.; Marsich, E.; Donati, I. Substrate Dissipation Energy Regulates Cell Adhesion and Spreading. *Adv. Funct. Mater.* **2020**, *2001977*, 2001977. https://doi.org/10.1002/adfm.202001977.

(27) Chaudhuri, O.; Gu, L.; Klumpers, D.; Darnell, M.; Bencherif, S. A.; Weaver, J. C.; Huebsch, N.; Lee, H. P.; Lippens, E.; Duda, G. N.; Mooney, D. J. Hydrogels with Tunable Stress Relaxation Regulate Stem Cell Fate and Activity. *Nat. Mater.* **2016**, *15* (3), 326–334. https://doi.org/10.1038/nmat4489.

(28) Lee, H. P.; Gu, L.; Mooney, D. J.; Levenston, M. E.; Chaudhuri, O. Mechanical Confinement Regulates Cartilage Matrix Formation by Chondrocytes. *Nat. Mater.* **2017**, *16* (12), 1243–1251. https://doi.org/10.1038/nmat4993.

(29) Chaudhuri, O.; Cooper-White, J.; Janmey, P. A.; Mooney, D. J.; Shenoy, V. B. Effects of Extracellular Matrix Viscoelasticity on Cellular Behaviour. *Nature*. 2020, pp 535–546. https://doi.org/10.1038/s41586-020-2612-2.

(30) Cameron, A. R.; Frith, J. E.; Cooper-White, J. J. The Influence of Substrate Creep on Mesenchymal Stem Cell Behaviour and Phenotype. *Biomaterials* **2011**, *32* (26), 5979–5993. https://doi.org/10.1016/j.biomaterials.2011.04.003.

(31) Charrier, E. E.; Pogoda, K.; Wells, R. G.; Janmey, P. A. Control of Cell Morphology and Differentiation by Substrates with Independently Tunable Elasticity and Viscous Dissipation. *Nat. Commun.* **2018**, *9* (1), 449. https://doi.org/10.1038/s41467-018-02906-9.

(32) Lou, J.; Stowers, R.; Nam, S.; Xia, Y.; Chaudhuri, O. Stress Relaxing Hyaluronic Acid-Collagen Hydrogels Promote Cell Spreading, Fiber Remodeling, and Focal Adhesion Formation in 3D Cell Culture. *Biomaterials* **2018**, *154*, 213–222. https://doi.org/10.1016/j.biomaterials.2017.11.004.

(33) McKinnon, D. D.; Domaille, D. W.; Cha, J. N.; Anseth, K. S. Biophysically Defined and Cytocompatible Covalently Adaptable Networks as Viscoelastic 3d Cell Culture Systems. *Adv. Mater.* **2014**, *26* (6), 865–872. https://doi.org/10.1002/adma.201303680.

(34) Richardson, B. M.; Wilcox, D. G.; Randolph, M. A.; Anseth, K. S. Hydrazone Covalent Adaptable Networks Modulate Extracellular Matrix Deposition for Cartilage Tissue Engineering. *Acta Biomater.* **2019**, *83*, 71–82. https://doi.org/10.1016/j.actbio.2018.11.014.

(35) Hafeez, S.; Ooi, H.; Morgan, F.; Mota, C.; Dettin, M.; van Blitterswijk, C.; Moroni, L.; Baker, M. Viscoelastic Oxidized Alginates with Reversible Imine Type Crosslinks: Self-Healing, Injectable, and Bioprintable Hydrogels. *Gels* **2018**, *4* (4), 85. https://doi.org/10.3390/gels4040085.

(36) Morgan, F. L. C.; Fernández-Pérez, J.; Moroni, L.; Baker, M. B. Tuning Hydrogels by Mixing Dynamic Cross-Linkers: Enabling Cell-Instructive Hydrogels and Advanced Bioinks. *Adv. Healthc. Mater.* **2022**, *11* (1), 2101576. https://doi.org/10.1002/adhm.202101576.

(37) Yesilyurt, V.; Ayoob, A. M.; Appel, E. A.; Borenstein, J. T.; Langer, R.; Anderson, D. G. Mixed Reversible Covalent Crosslink Kinetics Enable Precise, Hierarchical Mechanical Tuning of Hydrogel Networks. *Adv. Mater.* **2017**, *29* (19), 1605947–1605947. https://doi.org/10.1002/adma.201605947.

(38) Marozas, I. A.; Anseth, K. S.; Cooper-White, J. J. Adaptable Boronate Ester Hydrogels with Tunable Viscoelastic Spectra to Probe Timescale Dependent Mechanotransduction. *Biomaterials* **2019**, *223*, 119430. https://doi.org/10.1016/j.biomaterials.2019.119430.

(39) Mantooth, S. M.; Munoz-Robles, B. G.; Webber, M. J. Dynamic Hydrogels from Host–Guest Supramolecular Interactions. *Macromol. Biosci.* **2019**, *19* (1), 1–12. https://doi.org/10.1002/mabi.201800281.

(40) Appel, E. A.; del Barrio, J.; Loh, X. J.; Scherman, O. A. Supramolecular Polymeric Hydrogels. *Chem. Soc. Rev.* **2012**, *41* (18), 6195–6214. https://doi.org/10.1039/c2cs35264h.

(41) Lim, J. Y. C.; Lin, Q.; Xue, K.; Loh, X. J. Recent Advances in Supramolecular Hydrogels for Biomedical Applications. *Mater. Today Adv.* **2019**, *3*, 100021. https://doi.org/10.1016/j.mtadv.2019.100021.

(42) Zou, L.; Braegelman, A. S.; Webber, M. J. Dynamic Supramolecular Hydrogels Spanning an Unprecedented Range of Host-Guest Affinity. *ACS Appl. Mater. Interfaces* **2019**, *11* (6), 5695–5700. https://doi.org/10.1021/acsami.8b22151.

(43) Loebel, C.; Seliktar, D.; Burdick, J. A.; Ayoub, A.; Simaan-Yameen, H.; Kossover, O.; Galarraga, J.

H. Tailoring Supramolecular Guest–Host Hydrogel Viscoelasticity with Covalent Fibrinogen Double Networks. *J. Mater. Chem. B* **2019**, 17–19. https://doi.org/10.1039/c8tb02593b.

(44) Lin, Y. A.; Kang, M.; Chen, W. C.; Ou, Y. C.; Cheetham, A. G.; Wu, P. H.; Wirtz, D.; Loverde, S. M.; Cui, H. Isomeric Control of the Mechanical Properties of Supramolecular Filament Hydrogels. *Biomater. Sci.* **2018**, *6* (1), 216–224. https://doi.org/10.1039/c7bm00722a.

(45) Vereroudakis, E.; Bantawa, M.; Lafleur, R. P. M.; Parisi, D.; Matsumoto, N. M.; Peeters, J. W.; Del Gado, E.; Meijer, E. W.; Vlassopoulos, D. Competitive Supramolecular Associations Mediate the Viscoelasticity of Binary Hydrogels. *ACS Cent. Sci.* **2020**, *6*, 1401–1411. https://doi.org/10.1021/acscentsci.0c00279.

(46) Correa, S.; Grosskopf, A. K.; Lopez Hernandez, H.; Chan, D.; Yu, A. C.; Stapleton, L. M.; Appel, E. A. Translational Applications of Hydrogels. *Chem. Rev.* **2021**, *121* (18), 11385–11457. https://doi.org/10.1021/acs.chemrev.0c01177.

(47) Morgan, F. L. C.; Moroni, L.; Baker, M. B. Dynamic Bioinks to Advance Bioprinting. *Adv. Healthc. Mater.* **2020**, *9* (15), 1901798. https://doi.org/10.1002/adhm.201901798.

(48) Lopez Hernandez, H.; Souza, J. W.; Appel, E. A. A Quantitative Description for Designing the Extrudability of Shear-Thinning Physical Hydrogels. *Macromol. Biosci.* **2021**, *21* (2). https://doi.org/10.1002/mabi.202000295.

(49) Lou, J.; Liu, F.; Lindsay, C. D.; Chaudhuri, O.; Heilshorn, S. C.; Xia, Y. Dynamic Hyaluronan Hydrogels with Temporally Modulated High Injectability and Stability Using a Biocompatible Catalyst. *Adv. Mater.* **2018**, *30* (22), 1–6. https://doi.org/10.1002/adma.201705215.

(50) Wang, H.; Zhu, D.; Paul, A.; Cai, L.; Enejder, A.; Yang, F.; Heilshorn, S. C. Covalently Adaptable Elastin-Like Protein–Hyaluronic Acid (ELP–HA) Hybrid Hydrogels with Secondary Thermoresponsive Crosslinking for Injectable Stem Cell Delivery. *Adv. Funct. Mater.* **2017**, *27* (28), 1–11. https://doi.org/10.1002/adfm.201605609.

(51) Yesilyurt, V.; Webber, M. J.; Appel, E. A.; Godwin, C.; Langer, R.; Anderson, D. G. Injectable Self-Healing Glucose-Responsive Hydrogels with PH-Regulated Mechanical Properties. **2016**, 86–91. https://doi.org/10.1002/adma.201502902.

(52) Highley, C. B.; Rodell, C. B.; Burdick, J. A. Direct 3D Printing of Shear-Thinning Hydrogels into Self- Healing Hydrogels. *Adv. Mater.* **2015**, *27*, 5075–5079.

(53) Daniel E Shumer, N. J. N. N. P. S. Shear-Thinning Supramolecular Hydrogels with Secondary Autonomous Covalent Crosslinking to Modulate Viscoelastic Properties In Vivo. *Physiol. Behav.* **2017**, *176* (12), 139–148. https://doi.org/10.1002/adfm.201403550.Shear-Thinning.

(54) Susapto, H. H.; Alhattab, D.; Abdelrahman, S.; Khan, Z.; Alshehri, S.; Kahin, K.; Ge, R.; Moretti, M.; Emwas, A. H.; Hauser, C. A. E. Ultrashort Peptide Bioinks Support Automated Printing of Large-Scale Constructs Assuring Long-Term Survival of Printed Tissue Constructs. *Nano Lett.* **2021**, *21* (7), 2719–2729. https://doi.org/10.1021/acs.nanolett.0c04426.

(55) Hendrikse, S. I. S.; Su, L.; Hogervorst, T. P.; Lafleur, R. P. M.; Lou, X.; Van Der Marel, G. A.; Codee, J. D. C.; Meijer, E. W. Elucidating the Ordering in Self-Assembled Glycocalyx Mimicking Supramolecular Copolymers in Water. *J. Am. Chem. Soc.* **2019**, *141* (35), 13877–13886. https://doi.org/10.1021/jacs.9b06607.

(56) Leenders, C. M. A.; Albertazzi, L.; Mes, T.; Koenigs, M. M. E.; Palmans, A. R. A.; Meijer, E. W. Supramolecular Polymerization in Water Harnessing Both Hydrophobic Effects and Hydrogen Bond Formation. *ChemComm* **2013**, *49* (19), 1963–1965. https://doi.org/10.1039/c3cc38949a.

(57) Stuart, M. C. A.; Van De Pas, J. C.; Engberts, J. B. F. N. The Use of Nile Red to Monitor the Aggregation Behavior in Ternary Surfactant-Water-Organic Solvent Systems. *J. Phys. Org. Chem.* **2005**, *18* (9), 929–934. https://doi.org/10.1002/poc.919.

(58) Buehler, M. J. Nature Designs Tough Collagen: Explaining the Nanostructure of Collagen Fibrils. *Proc. Natl. Acad. Sci. U. S. A.* **2006**, *103* (33), 12285–12290. https://doi.org/10.1073/pnas.0603216103.

(59) Christiansen, D. L.; Huang, E. K.; Silver, F. H. Assembly of Type I Collagen: Fusion of Fibril Subunits and the Influence of Fibril Diameter on Mechanical Properties. *Matrix Biol.* **2000**, *19* (5), 409–420. https://doi.org/10.1016/S0945-053X(00)00089-5.

(60) Doillon, C. J.; Dunn, M. G.; Bender, E.; Silver, F. H. Collagen Fiber Formation in Repair Tissue: Development of Strength and Toughness. *Collagen Res. ReI* **1985**, *5* (6), 481–492. https://doi.org/10.1016/S0174-173X(85)80002-9.

(61) Denkova, A. G.; Mendes, E.; Coppens, M.-O. Rheology of Worm-like Micelles Composed of Tri-Block Copolymer in the Limit of Slow Dynamics. *J. Rheol. (N. Y. N. Y).* **2009**, *53* (5), 1087–1100. https://doi.org/10.1122/1.3190170.

(62) Leenders, C. M. A.; Mes, T.; Baker, M. B.; Koenigs, M. M. E.; Besenius, P.; Palmans, A. R. A.; Meijer, E. W. From Supramolecular Polymers to Hydrogel Materials. *Mater. Horiz.* **2014**, *1* (1), 116–120. https://doi.org/10.1039/C3MH00103B.

(63) Feng, Y.; Chu, Z. PH-Tunable Wormlike Micelles Based on an Ultra-Long-Chain "Pseudo" Gemini Surfactant. *Soft Matter* **2015**, *11* (23), 4614–4620. https://doi.org/10.1039/c5sm00677e.

(64) Lou, X.; Lafleur, R. P. M.; Leenders, C. M. A.; Schoenmakers, S. M. C.; Matsumoto, N. M.; Baker, M. B.; van Dongen, J. L. J.; Palmans, A. R. A.; Meijer, E. W. Dynamic Diversity of Synthetic Supramolecular Polymers in Water as Revealed by Hydrogen/Deuterium Exchange. *Nat. Commun.* **2017**, *8* (May), 15420. https://doi.org/10.1038/ncomms15420.

(65) Wall, E. J.; Kwan, M. K.; Rydevik, B. L. Stress Relaxation of a Peripheral Nerve. *J. Hand Surg. Am.* **1991**, *16* (5), 859–863. https://doi.org/10.1016/S0363-5023(10)80149-2.

(66) Liu, Z.; Bilston, L. E. Large Deformation Shear Properties of Liver Tissue. *Biorheology* **2002**, *39* (6), 735–742.

(67) Liu, Z.; Bilston, L. On the Viscoelastic Character of Liver Tissue: Experiments and Modelling of the Linear Behaviour. *Biorheology* **2000**, *37* (3), 191–201.

(68) Desrochers, J.; Amrein, M. W.; Matyas, J. R. Viscoelasticity of the Articular Cartilage Surface in Early Osteoarthritis. *Osteoarthr. Cartil.* **2012**, *20* (5), 413–421. https://doi.org/10.1016/j.joca.2012.01.011.

(69) Cates, M. E. Reptation of Living Polymers: Dynamics of Entangled Polymers in the Presence of Reversible Chain-Scission Reactions. *Macromolecules* **1987**, *20* (9), 2289–2296. https://doi.org/10.1021/ma00175a038.

(70) Malo de Molina, P.; Gradzielski, M. Gels Obtained by Colloidal Self-Assembly of Amphiphilic Molecules. *Gels* **2017**, *3* (3), 30. https://doi.org/10.3390/gels3030030.

(71) Du, C.; Zhang, X. N.; Sun, T. L.; Du, M.; Zheng, Q.; Wu, Z. L. Hydrogen-Bond Association-Mediated Dynamics and Viscoelastic Properties of Tough Supramolecular Hydrogels. *Macromolecules* **2021**, *54* (9), 4313–4325. https://doi.org/10.1021/ACS.MACROMOL.1C00152/ASSET/IMAGES/MEDIUM/MA1C00152_M005.GIF.

(72) Appel, E. A.; Forster, R. A.; Koutsioubas, A.; Toprakcioglu, C.; Scherman, O. A. Activation Energies Control the Macroscopic Properties of Physically Cross-Linked Materials. *Angew. Chemie - Int. Ed.* **2014**, *53* (38), 10038–10043. https://doi.org/10.1002/ANIE.201403192.

(73) Drozdov, A. D.; Christiansen, J. de C. Structure–Property Relations in Linear Viscoelasticity of Supramolecular Hydrogels. *RSC Adv.* **2021**, *11* (28), 16860–16880. https://doi.org/10.1039/D1RA02749B.

(74) Seiffert, S.; Sprakel, J. Physical Chemistry of Supramolecular Polymer Networks. *Chem. Soc. Rev* **2012**, *41*, 909–930. https://doi.org/10.1039/c1cs15191f.

(75) Feliciano, A. J.; van Blitterswijk, C.; Moroni, L.; Baker, M. B. Realizing Tissue Integration with Supramolecular Hydrogels. *Acta Biomater.* **2021**, *124*, 1–14. https://doi.org/10.1016/j.actbio.2021.01.034.

(76) Parisi-Amon, A.; Mulyasasmita, W.; Chung, C.; Heilshorn, S. C. Protein-Engineered Injectable Hydrogel to Improve Retention of Transplanted Adipose-Derived Stem Cells. *Adv. Healthc. Mater.* **2013**, *2* (3), 428–432. https://doi.org/10.1002/adhm.201200293.

(77) Rodell, C. B.; Kaminski, A. L.; Burdick, J. A. Rational Design of Network Properties in Guest-Host Assembled and Shear-Thinning Hyaluronic Acid Hydrogels. *Biomacromolecules* **2013**, *14* (11), 4125–4134. https://doi.org/10.1021/bm401280z.

(78) Loebel, C.; Rodell, C. B.; Chen, M. H.; Burdick, J. A. Shear-Thinning and Self-Healing Hydrogels as Injectable Therapeutics and for 3D-Printing. *Nat. Protoc.* **2017**, *12* (8), 1521–1541. https://doi.org/10.1038/nprot.2017.053.

(79) Schwab, A.; Levato, R.; D'Este, M.; Piluso, S.; Eglin, D.; Malda, J. Printability and Shape Fidelity of Bioinks in 3D Bioprinting. *Chemical Reviews*. 2020, pp 11028–11055. https://doi.org/10.1021/acs.chemrev.0c00084.

(80) Sather, N. A.; Sai, H.; Sasselli, I. R.; Sato, K.; Ji, W.; Synatschke, C. V.; Zambrotta, R. T.; Edelbrock,

J. F.; Kohlmeyer, R. R.; Hardin, J. O.; Berrigan, J. D.; Durstock, M. F.; Mirau, P.; Stupp, S. I. 3D Printing of Supramolecular Polymer Hydrogels with Hierarchical Structure. *Small* **2021**, *17* (5), 1–14. https://doi.org/10.1002/smll.202005743.

(81) Li, C.; Faulkner-Jones, A.; Dun, A. R.; Jin, J.; Chen, P.; Xing, Y.; Yang, Z.; Li, Z.; Shu, W.; Liu, D.; Duncan, R. R. Rapid Formation of a Supramolecular Polypeptide-DNA Hydrogel for in Situ Three-Dimensional Multilayer Bioprinting. *Angew. Chemie - Int. Ed.* **2015**, *54* (13), 3957–3961. https://doi.org/10.1002/anie.201411383.

(82) Daly, A. C.; Davidson, M. D.; Burdick, J. A. 3D Bioprinting of High Cell-Density Heterogeneous Tissue Models through Spheroid Fusion within Self-Healing Hydrogels. *Nat. Commun.* **2021**, *12* (1), 1–13. https://doi.org/10.1038/s41467-021-21029-2.

(83) Ouyang, L.; Yao, R.; Zhao, Y.; Sun, W. Effect of Bioink Properties on Printability and Cell Viability for 3D Bioplotting of Embryonic Stem Cells. *Biofabrication* **2016**, *8* (3), 035020. https://doi.org/10.1088/1758-5090/8/3/035020.

Supporting information

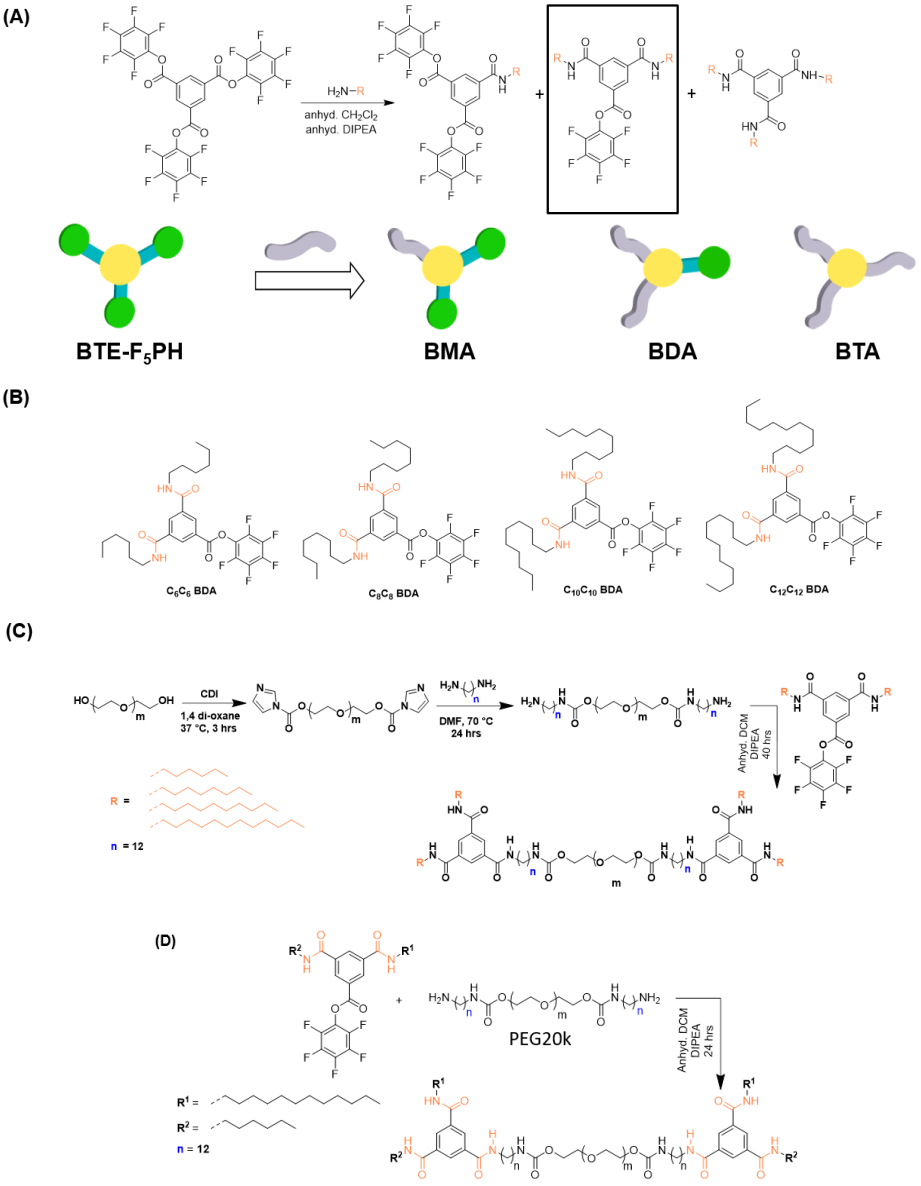

Figure S1. BTA hydrogelator structure and schematics. A) Benzene-1,3,5-tricarbonyl tripentafluoroester (BTE-F_5PH) desymmetrization scheme and schematics to create BTA synthon molecule. B) List of BDA molecules produced to be used as synthon to produce BTA hydrogelator. C) Chemical reaction scheme to produce BTA hydrogelators **C_6C_6 BTA, C_8C_8 BTA, $C_{10}C_{10}$ BTA, $C_{12}C_{12}$ BTA**. D) Synthetic chemical reaction scheme for hydrogelator **C_6C_{12} BTA.**

BTE-F5PH synthesis

BTE-F_5Ph was resynthesized according to our recently reported study[1] and proton and carbon NMR were matches for the purity check of the molecules[1].

C_8C_8 BDA precursor synthesis

BTE-F_5Ph (0.5g, 2.1 mmol, 1equiv.) was dissolved in 35 mL of anhydrous DCM in a dried reaction flask under a nitrogen atmosphere. DIPEA (369 µL, 2.1 mmol, 1equiv.) solution in 25 mL anhydrous DCM was added to the reaction flask. The reaction flask was set in the ice water bath and the reaction mixture was cooled to 4 °C. Octylamine (0.2 g, 1.4 mmol, 0.67 equiv) in 25 mL anhydrous DCM was added dropwise to the reaction flask under a nitrogen atmosphere. The reaction stirred for 1.5 hours at 4°C. The reaction mixture was vacuum dried under reduced pressure and C_8C_8 BDA was isolated on silica gel using eluent DCM/acetonitrile (95/5). ^{1}H NMR yield of the reaction mixture was 51% and the isolated yield was 45% (189 mg). ^{1}H NMR (700 MHz, $CDCl_3$) δ 8.65 (d, 2H), 8.52 (t, 1H), 6.63 (t, 2H), 3.47 (q, 4H), 1.63 (p, 4H), 1.39-1.25 (m, 20H), 0.87 (t, 6H). ^{13}C NMR (176 MHz, $CDCl_3$) δ 165.4, 161.6, 136.2, 131.5, 131.4, 128.0, 40.7, 31.9, 29.64, 29.39, 29.31, 27.12, 22.76, 14.2.

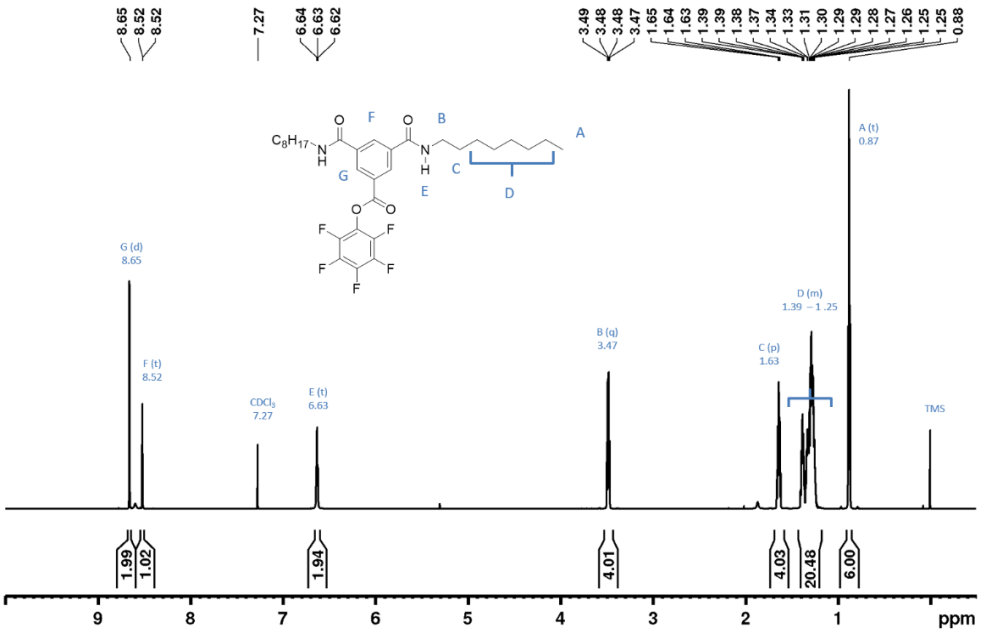

Figure S2. ^{1}H NMR of **C8C8 BDA**

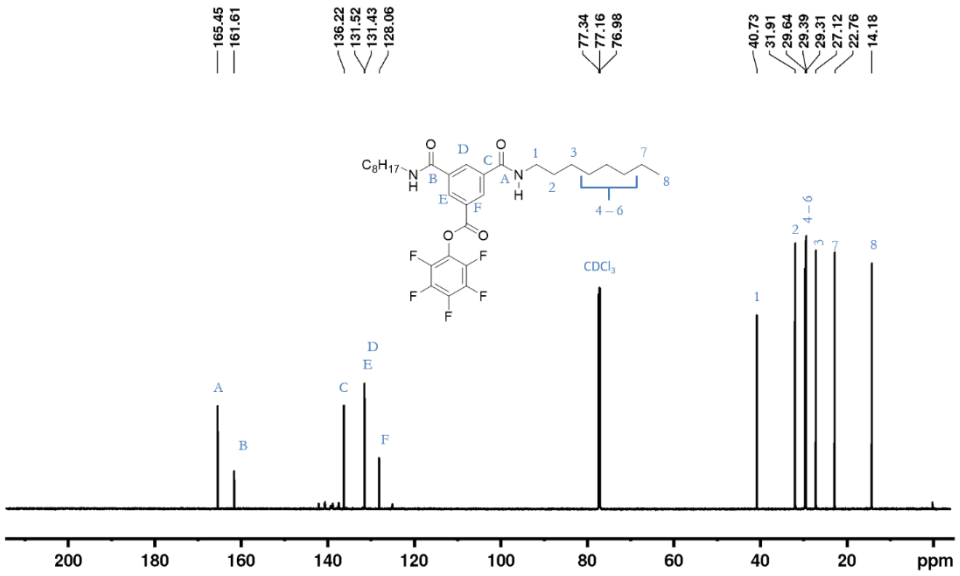

Figure S3. ^{13}C NMR of molecule ***C_8C_8 BDA***

$C_{10}C_{10}$ BDA precursor synthesis

BTE-F_5Ph (0.5g, 2.1 mmol, 1equiv.) was dissolved in 35 mL of anhydrous DCM under a nitrogen atmosphere and placed into an ice bath (4°C) followed by dropwise addition of DIPEA (369 µL, 2.1 mmol, 1equiv.) dissolved in 25 mL anhydrous DCM. Following this, decylamine (0.22g, 1.4 mmol, 0.67 equiv) dissolved in 25 mL anhydrous DCM was added dropwise (slowly over 10-15 minutes) to the reaction flask under a nitrogen atmosphere. The reaction solution was stirred for 1.5 hours at 4°C and then the reaction mixture was vacuum dried under reduced pressure to remove excess of DCM. $C_{10}C_{10}$ BDA was separated using silica gel column chromatography using eluent DCM/acetonitrile (95/5). ^{1}H NMR reaction yield was 50% and the isolated yield 43 (201 mg). ^{1}H NMR (700 MHz, $CDCl_3$) δ 8.66 (d, 2H), 8.52 (t, 1H), 6.59 (t, 2H), 3.47 (q, 4H), 1.62 (m, 4H), 1.28-1.39 (m, 28H), 0.88 (t, 6H). ^{13}C NMR (176 MHz, $CDCl_3$) δ 165.3, 161.6, 136.2, 131.5, 131.4, 128.0, 40.7, 32.01, 29.68, 29.66, 29.43, 27.13, 22.80, 14.22.

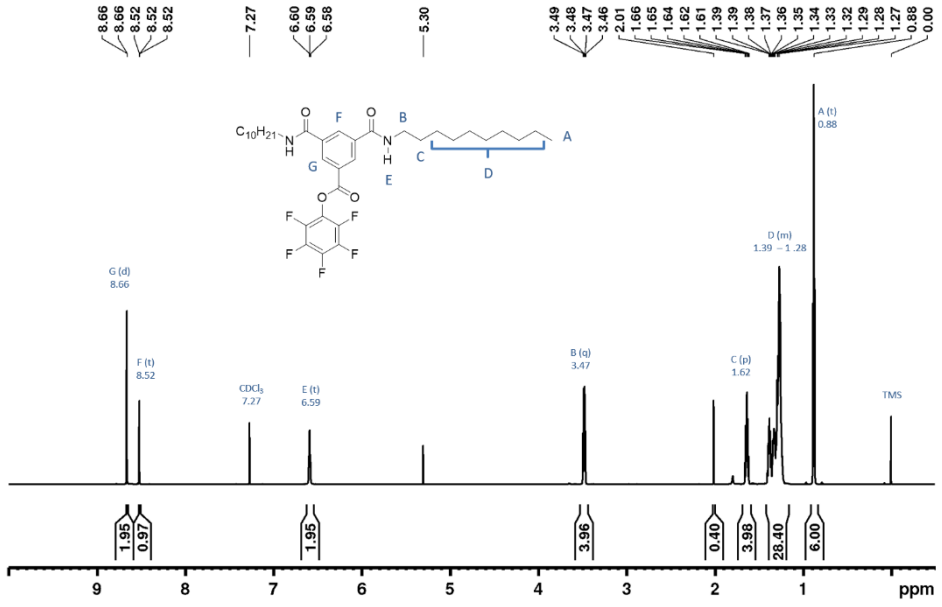

Figure S4. ^{1}H NMR of molecule *$C_{10}C_{10}$ BDA*

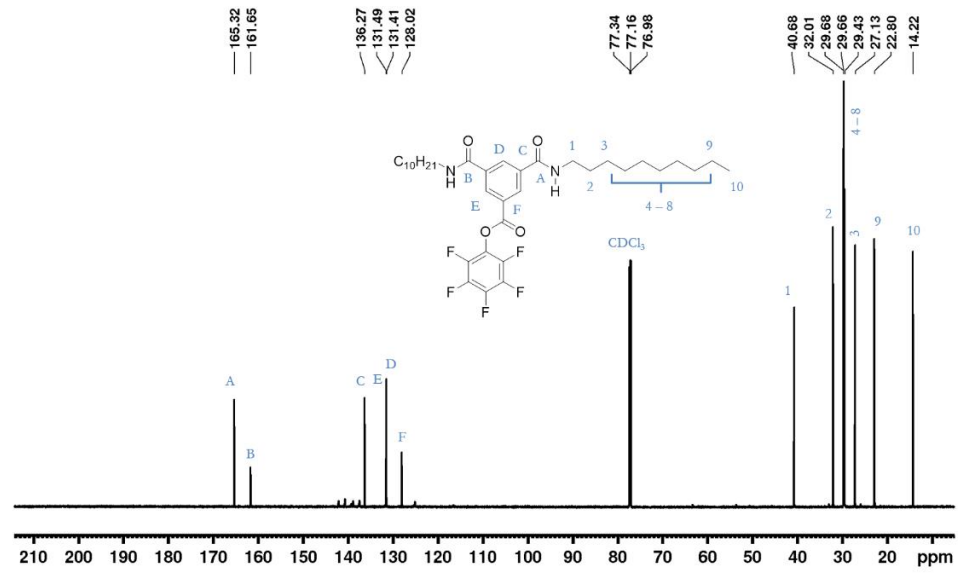

Figure S5. ^{13}C NMR of molecule *$C_{10}C_{10}$ BDA*

C_6C_6 and $C_{12}C_{12}$ BDA precursor synthesis (references to the synthesis article)

C_6C_6 and **$C_{12}C_{12}$** were synthesized according to our recently reported procedure and ^{1}H NMR and ^{13}C NMR were matched[1].

C_6C_6 and $C_{12}C_{12}$ BTA hydrogelator synthesis

C_6C_6 BTA and **$C_{12}C_{12}$ BTA** hydrogelator were synthesized as described in our recently published work[1].

C_8C_8 BTA hydrogelator synthesis

C_8C_8 BDA (0.2g, 0.3 mmol 1.1equiv) was dissolved in 8mL anhydrous DCM, and DIPEA (0.052g, 0.44 mmol, 1.5 equiv) was added to it. PEG20K bisaminododecane (2.8g, 0.3 mmol, 1 equiv) was weighed in a dried flask, dissolved in anhydrous DCM (5-6 ml), and added to the flask. The reaction continued to run for 40 hours at 20 ºC under a nitrogen-inert atmosphere. The reaction mixture was first purified by precipitation in cold diethyl ether and a pure molecule was obtained in 97% isolated yield as a white powder. Later also sample was dissolved in methanol and dialyzed against methanol for 3 days. The pure molecule was obtained in 96% isolated yield. ^{1}H NMR (700 MHz, $(CD_3)_2SO$) 8.65-8.58 (t, 6H, NH(C=O)), 8.37-8.34 (s, 6H, Ar), 7.16-7.11 (t, 2H, CH2NH(C=O)O), 4.03-4.00 (t, 4H, NH(C=O)OCH2), 3.59-3.42 (bs, 1776H, O-(CH2)2-O), 3.29-3.23 (t, 12H, (C=O)NHCH2), 2.95-2.90 (q, 4H, CH2NH(C=O)O), 1.57-1.15 (mm, 88H, aliphatic), 0.88-0.80 (dt, 12H, CH2CH3, aliphatic).

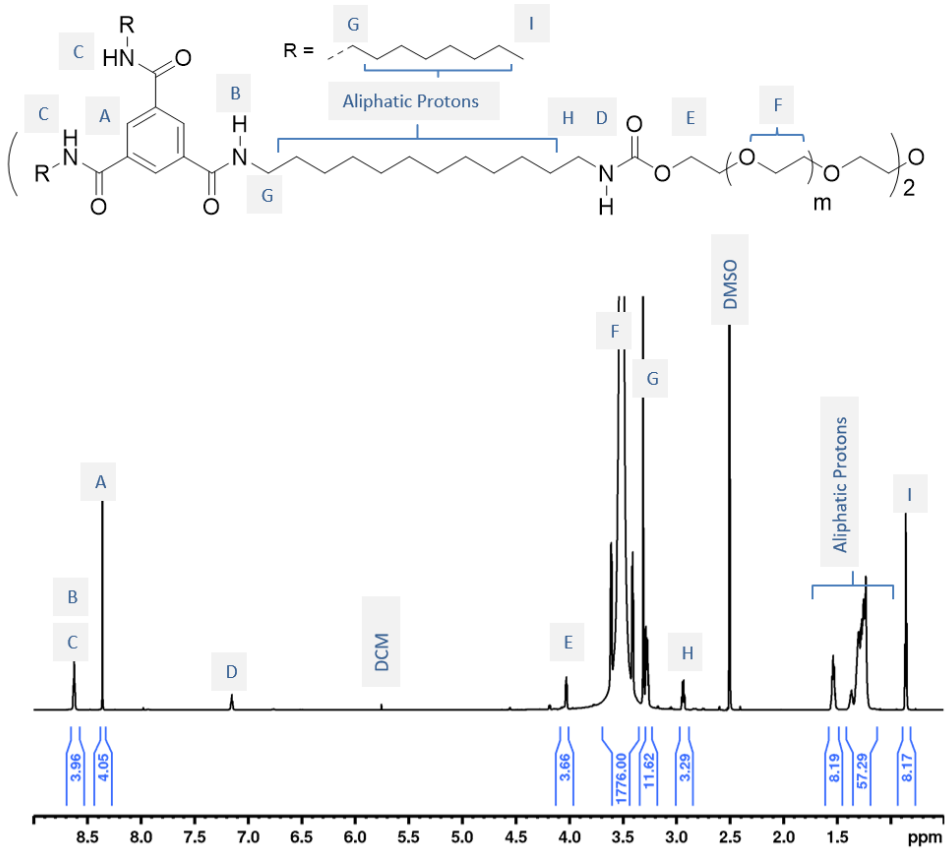

Figure S6. ^{1}H NMR of *C_8C_8 BTA*

$C_{10}C_{10}$ BTA hydrogelator synthesis

$C_{10}C_{10}$ BDA (0.2g, 0.3 mmol 1.1 equiv) was dissolved in 8mL anhydrous DCM, and DIPEA (0.052g, 0.4 mmol, 1.5 equiv) was added to it. PEG bisaminododecane (2.8g, 0.3 mmol, 1 equiv) was weighed in a dried flask, dissolved in anhydrous DCM (5-6 ml), and added to the reaction flask. The reaction was allowed to run for 40 hours at room temperature (~20°C) under an inert atmosphere. The reaction mixture was concentrated in a minimal amount of DCM and precipitated in cold diethyl ether and obtained in 98% yield as a white powder. Subsequently, the hydrogelator was dissolved in methanol and dialyzed against methanol for 3 days. The pure molecule was obtained in 80% yield. ^{1}H NMR (700 MHz, $(CD_3)_2SO$) 8.63-8.59 (t, 6H, NH(C=O)), 8.36-8.33 (s, 6H, Ar), 7.18-7.12 (t, 2H, CH2NH(C=O)O), 4.00-4.00 (t, 4H, NH(C=O)OCH2), 3.56-3.44 (bs, 1776H, O-(CH2)2-O), 3.31-3.30 (t, 12H, (C=O)NHCH2), 2.96-2.90 (q, 4H, CH2NH(C=O)O), 1.58-1.15 (mm, 104H, aliphatic), 0.87-0.80 (dt, 12H, CH2CH3, aliphatic).

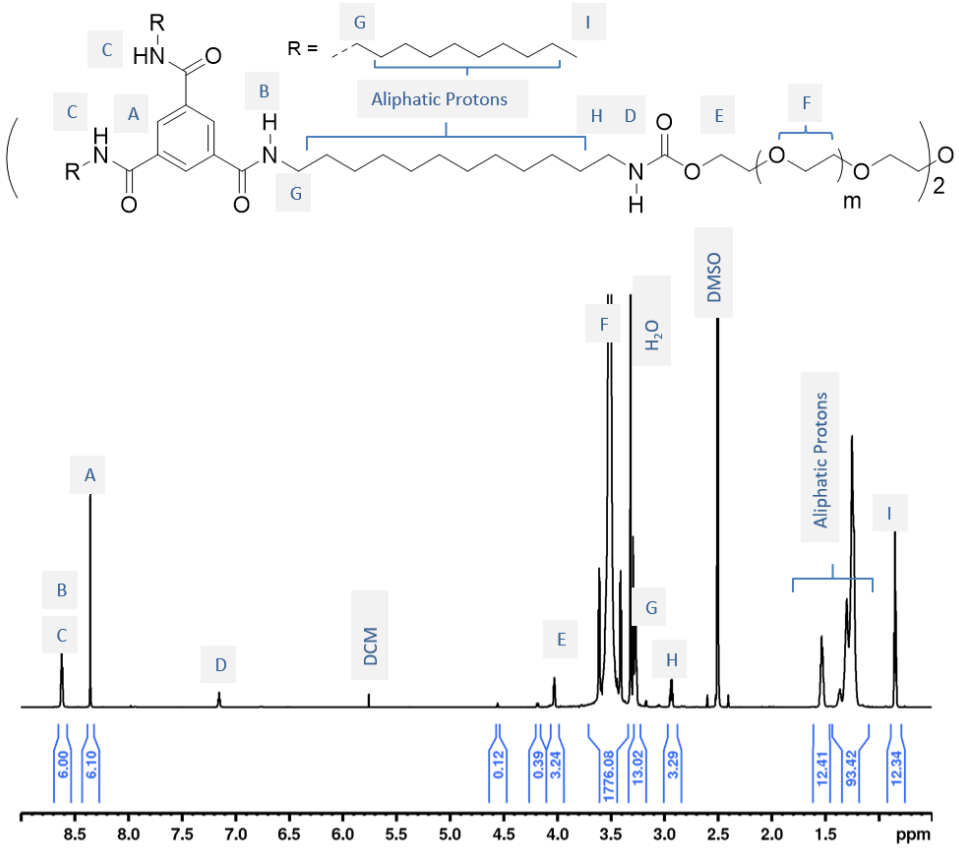

Figure S7. ^{1}H NMR of *$C_{10}C_{10}$ BTA*

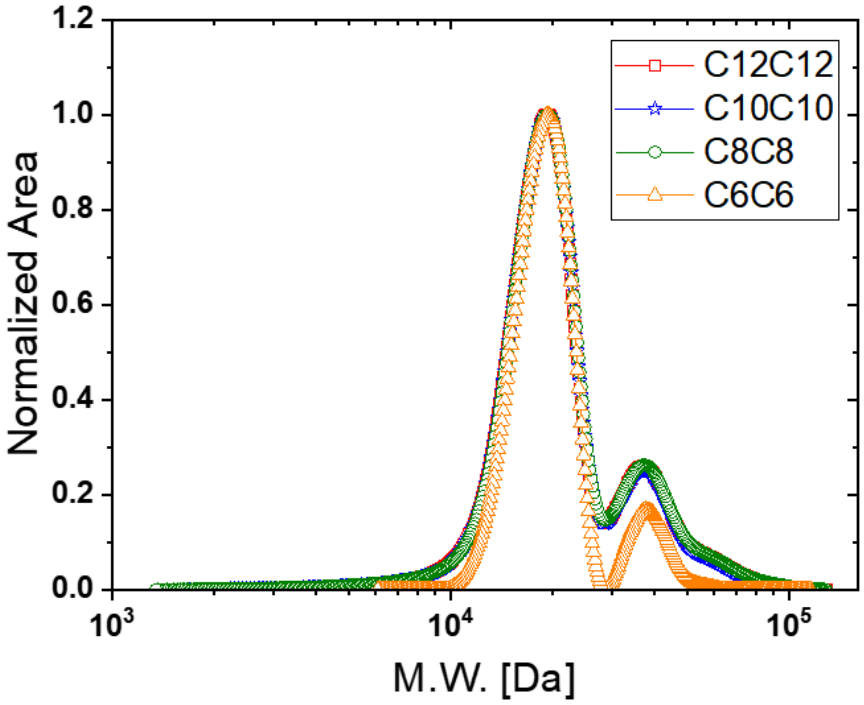

Figure S8. GPC graph using DMF eluent and RI detector. Molecular masses show two peak tops around 19,000 and 37,000 g/mol. All hydrogelator showed average molecular weight of around 23,000 g/mol with Đ of 1.2.

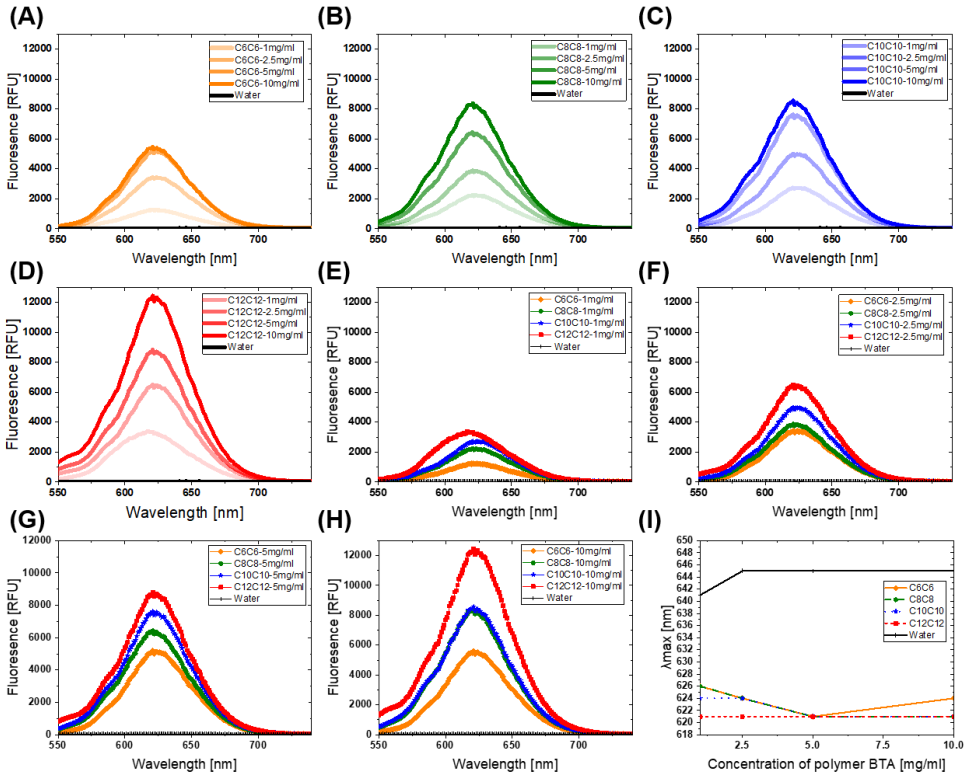

Figure S9. Hydrophobic pocket formation study via solvatochromic Nile red dye. A), B), C), and D) for C6C6, C8C8, C10C10 and C12C12 BTA hydrogelators. Each hydrogelator was tested at 1 mg/ml, 2.5 mg/ml, 5 mg/ml and 10 mg/ml. Fluorescence signal increases with increasing BTA hydrogelator concentration, indication of more Nile red capture in hydrophobic core. E), F), G), and H) comparison of C6C6, C8C8, C10C10 and C12C12 BTA hydrogelators at concentration of 1mg/ml, 2.5mg/ml, 5mg/ml and 10mg/ml. Nile red fluorescence emission spectrum of water is shown with black color line. Nile red in water showed very low fluorescence intensity signal. An increase in fluorescence intensity for the hydrogelators compared to water showed the presence of hydrophobic pocket. Increase in fluorescence intensity with increasing hydrophobic length indicates larger hydrophobic pocket formation. I) All samples showed very similar maximum fluorescence intensity indicating hydrophobic pocket of similar polarity.

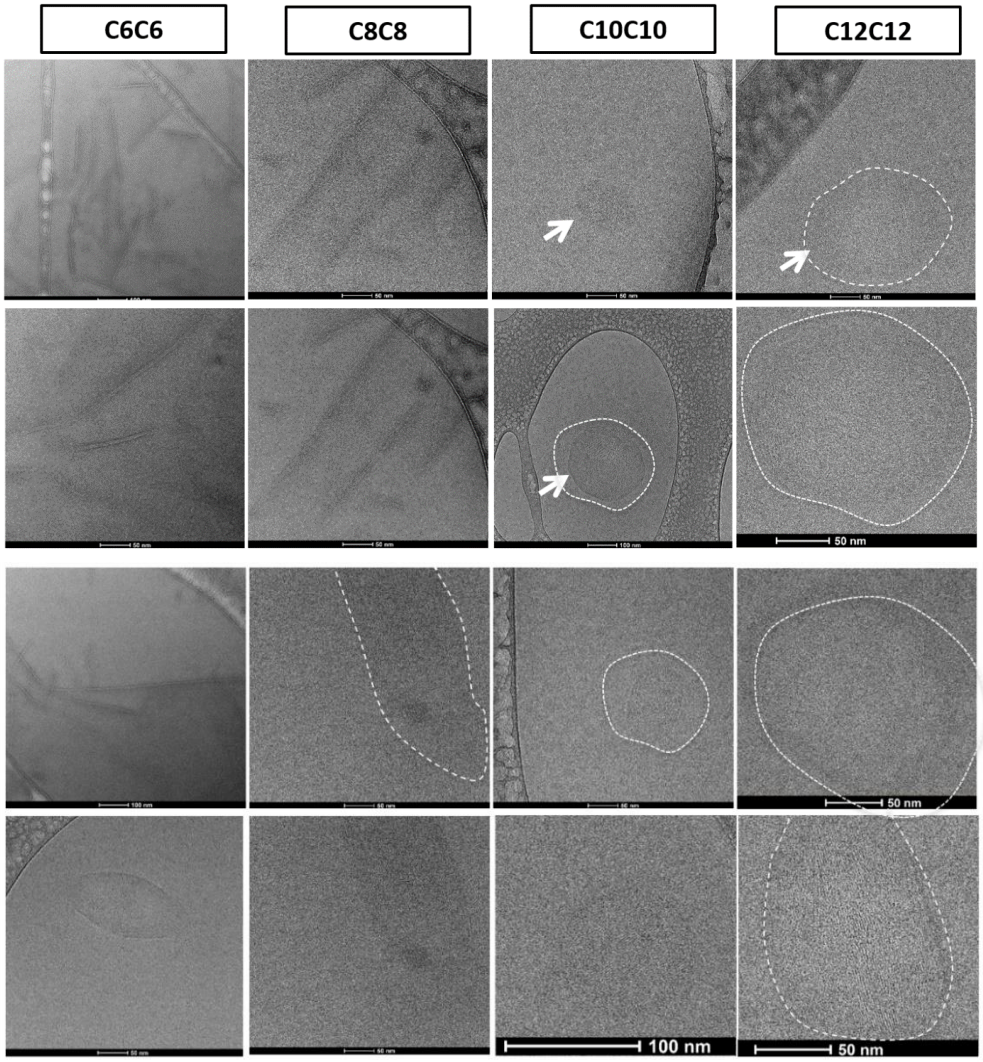

Figure S10. Self-assembly studies using cryo-TEM. All BTA hydrogelators showed fibrous morphology. C6C6 BTA and C8C8 BTA showed fiber-like and sheet-like morphology while C10C10 BTA and C12C12 BTA showed fibrous sheet-like morphology. All hydrogels were dissolved in minimal methanol, self-assembled in water, and investigated after overnight aging at room temperature.

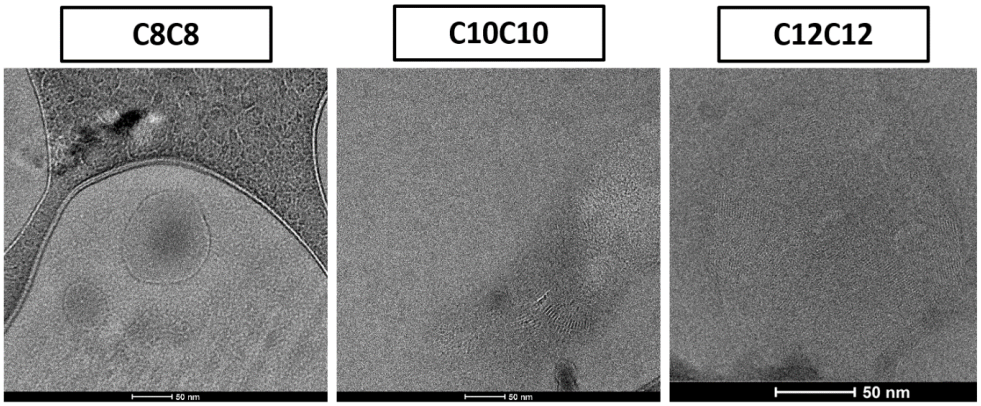

Figure S11. Self-assembly studies using cryo-TEM. BTA hydrogelators samples were prepared in water only. We quickly investigated BTA hydrogelator samples prepared only in water. C8C8 BTA, C10C10 BTA and C12C12 BTA showed fibrous sheet-like morphology.

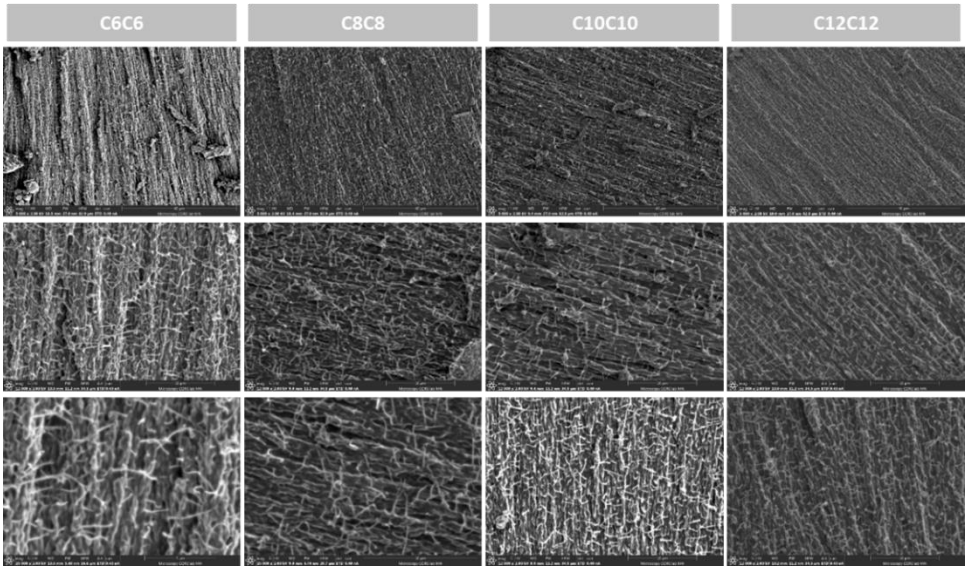

Figure S12. Self-assembly studies using cryo-SEM. All BTA hydrogelators showed anisotropically aligned fibrous morphology.

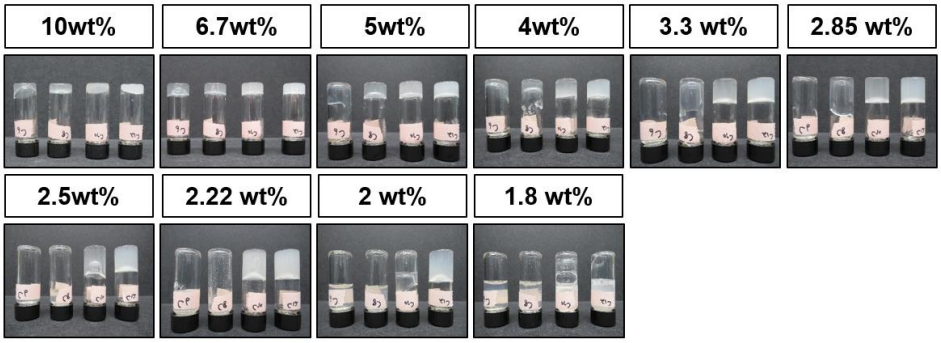

Figure S13: Critical gelation concentration. Hydrogels were made at 10% (w/v) and diluted to find out critical gelation concentration (CGC). CGC was found to be 5% (w/v), 3.3% (w/v), 2% (w/v) and 1.8% (w/v) for C6C6, C8C8, C10C10, and C12C12 BTA hydrogelator.

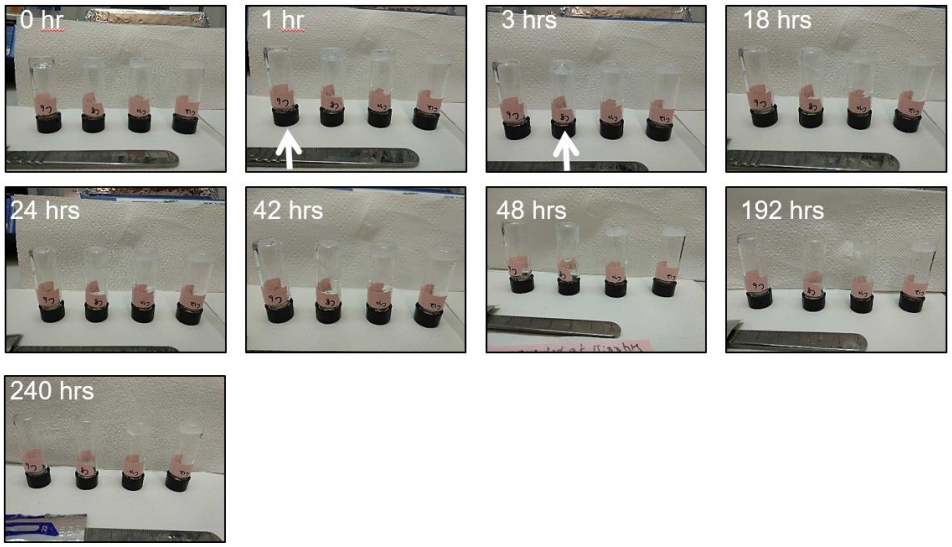

Figure S14. Vial inversion experiment. Vial inversion experiment showing flow behavior of hydrogels. The vial inversion test is a quick way to show the qualitative viscoelasticity of hydrogel. The time that a hydrogel starts to flow after a vial inversion depends on the end cap carbon length or hydrophobic length on BTA. Larger The larger the endcap carbon length on BTA the longer it takes for a hydrogel to flow. C6C6 BTAhydrogelator reached to the bottom of the vial in one hour and the C8C8 BTA hydrogelator started to flow after 3 hours and reached ¾ in 48 hours. C10C10 BTA and C12C12 BTA did not flow even after 240 hours (10 days), indicating that gels are more solid than C8C8 and C6C6 BTA hydrogelator.

Strain sweep

First, we determine rupture strain and linear viscoelastic region. Rupture strain decreases with increasing hydrophobic length; Rupture strains of ~90%, 42%, and 25% were observed for C8C8, C10C10, and C12C12 BTAs (Figure S15). C6C6 BTA behaved as a liquid at an investigated angular frequency of 10 rad/s. All BTA hydrogelators showed a yielding point (onset of the decrease in storage modulus) of 5–10% strain before rupture strain. BTA hydrogelators showed strain-independent storage modulus before the yielding point.

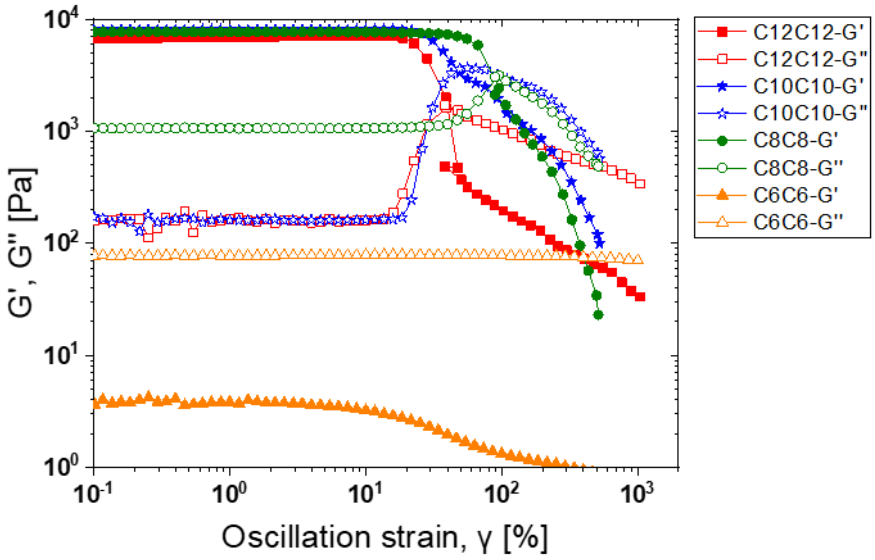

Figure S15. Oscillation strain sweep for C6C6 BTA, C8C8 BTA, C10C10 BTA, and C12C12 BTA hydrogelators.

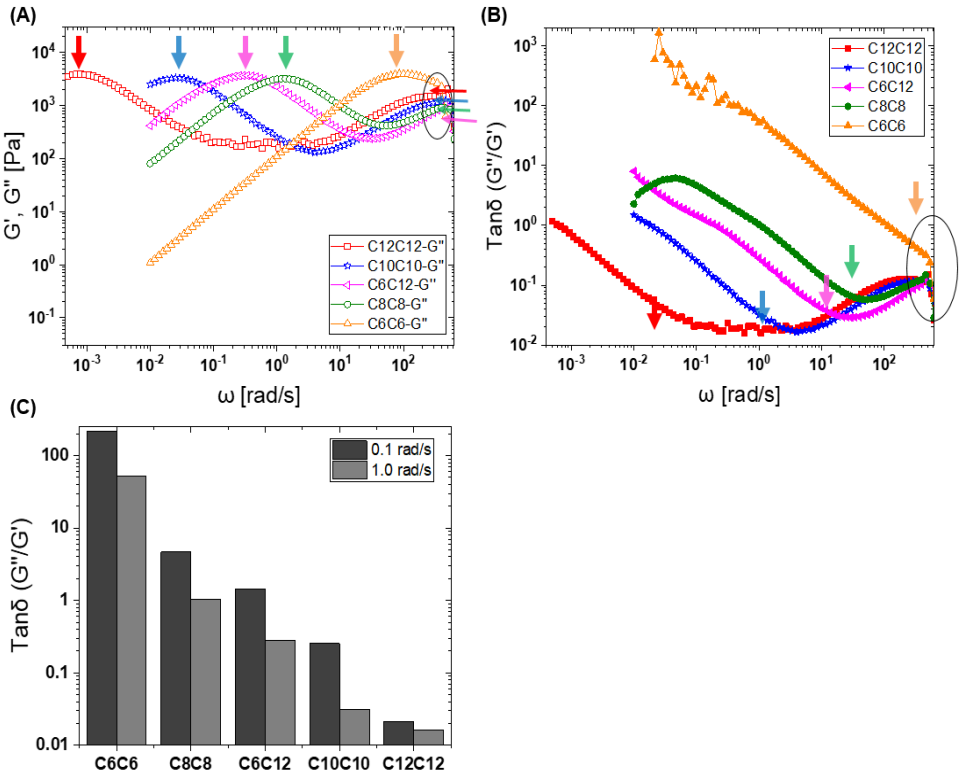

Figure S16. Viscoelastic properties: A) loss moduli plotted for hydrogelators; all hydrogelators showed two maximum in loss moduli besides C6C6 which has only one, B) Tan delta for all hydrogelators; arrows show minima in tan delta, which shows relaxation frequency, C) Tan delta at 0.1 rad/s and 1.0 rad/s; Tan delta decreases with increasing the end cap carbon length.

Hydrogels with tunable stress relaxation

A crossover point between loss moduli and storage moduli is a characteristic of Maxwellian viscoelastic fluids. This characteristic frequency showing a crossover point is directly correlated to a dissipation time scale. Using the Maxwell model for viscoelastic fluids as shown in **equations 1** and **2**, stress relaxation times can be calculated. Maxwell's model consists of an elastic component (spring) connected in series with a viscous component (dashpot).

$$G'(\omega) = G\infty \sum_{i=1}^{n} \frac{fi\omega^2\tau_i^2}{1+\omega^2\tau_i^2} \qquad (S1)$$

$$G''(\omega) = G\infty \sum_{i=1}^{n} \frac{fi\omega\tau_i}{1+\omega^2\tau_i^2} \qquad (S2)$$

Where G_∞ is the equilibrium modulus, ω is the angular frequency and τ is stress relaxation time. Frequency sweep obtained data when fit into equations 1 and 2 for one Maxwell element (**Figure S17–S22**). Using equations 1 and 2 for single Maxwell elements, curve fitting was poor for loss moduli for all hydrogelators and resulted in improved curve fitting for two Maxwell elements in parallel (**Figure S17–S22**). As shown in **Figure S23,** stress relaxation times were similar for one and two Maxwell elements, which suggests that there is one dominant mode of stress relaxation and the second mode is present but the contribution in stress relaxation is relatively small.

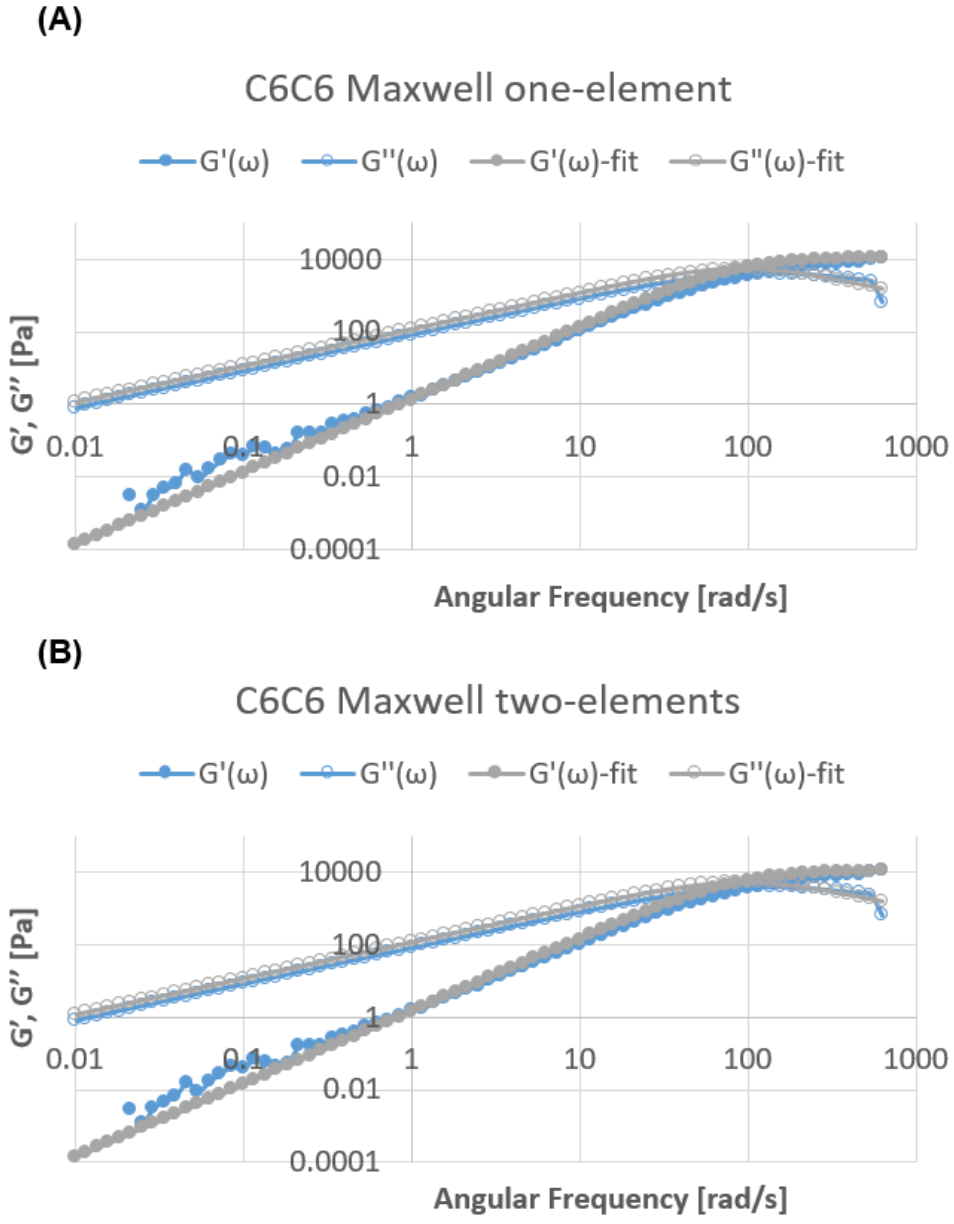

Figure S17. Maxwell model fitting for one A) and two Maxwell elements B) on frequency sweep data for ***C_6C_6 BTA*** hydrogelator.

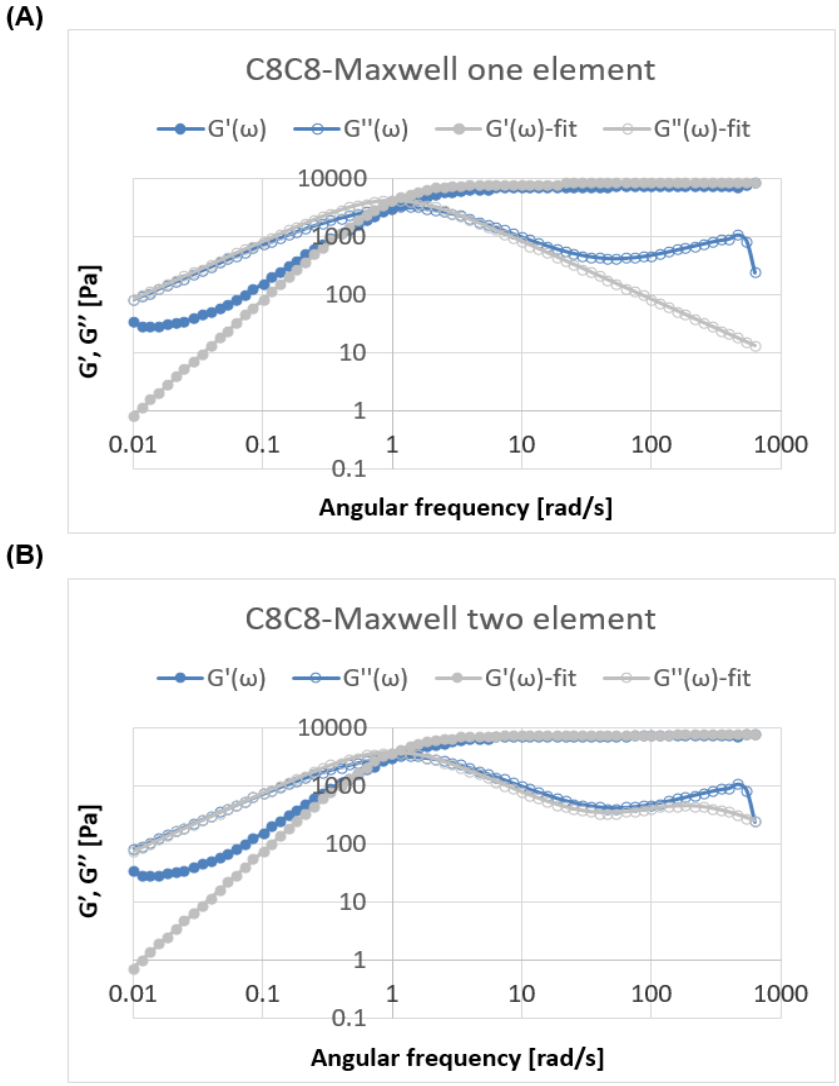

Figure S18. Maxwell model fitting for one A) and two Maxwell elements B) on frequency sweep data for ***C_8C_8 BTA*** hydrogelator.

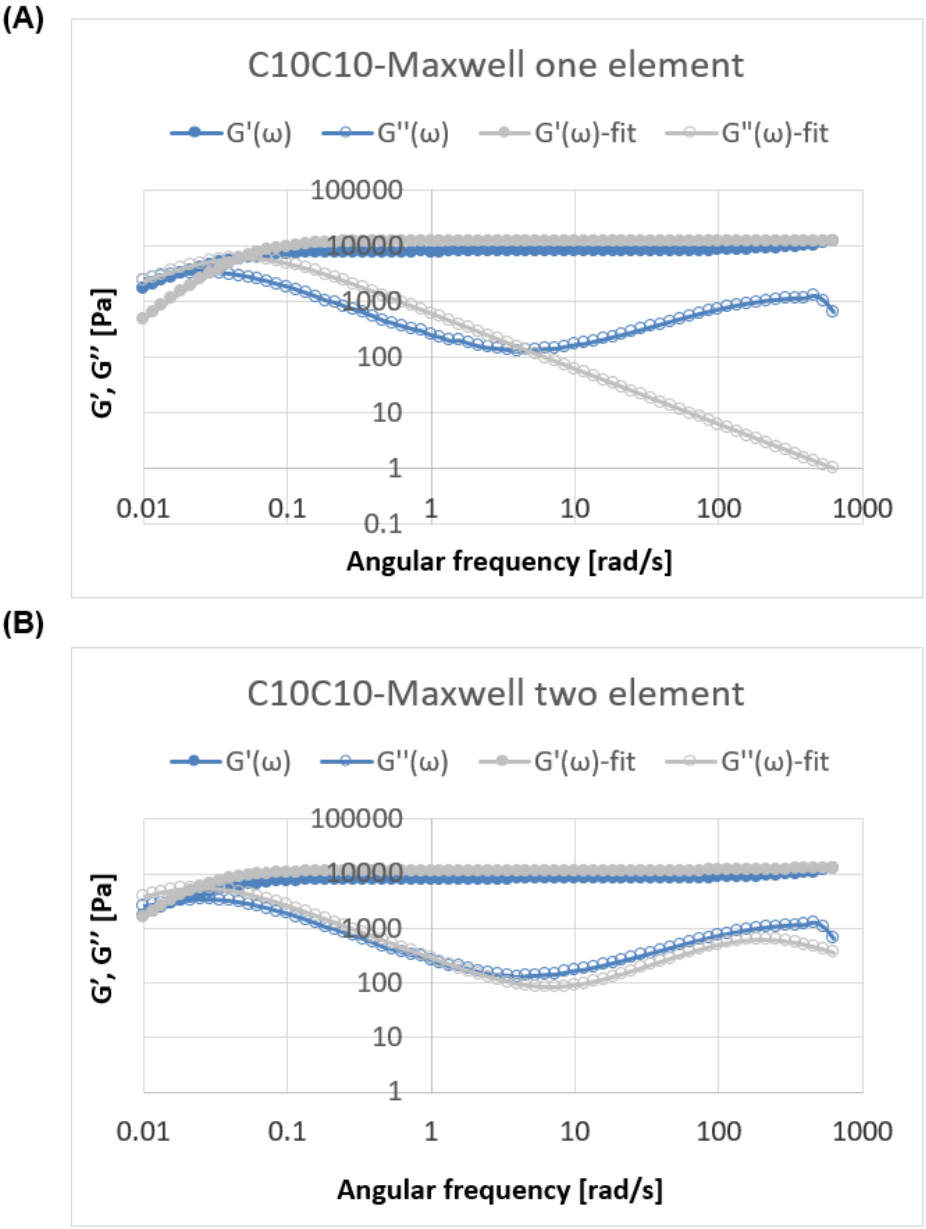

Figure S19. Maxwell model fitting for one A) and two Maxwell elements B) on frequency sweep data for ***$C_{10}C_{10}$ BTA*** hydrogelator.

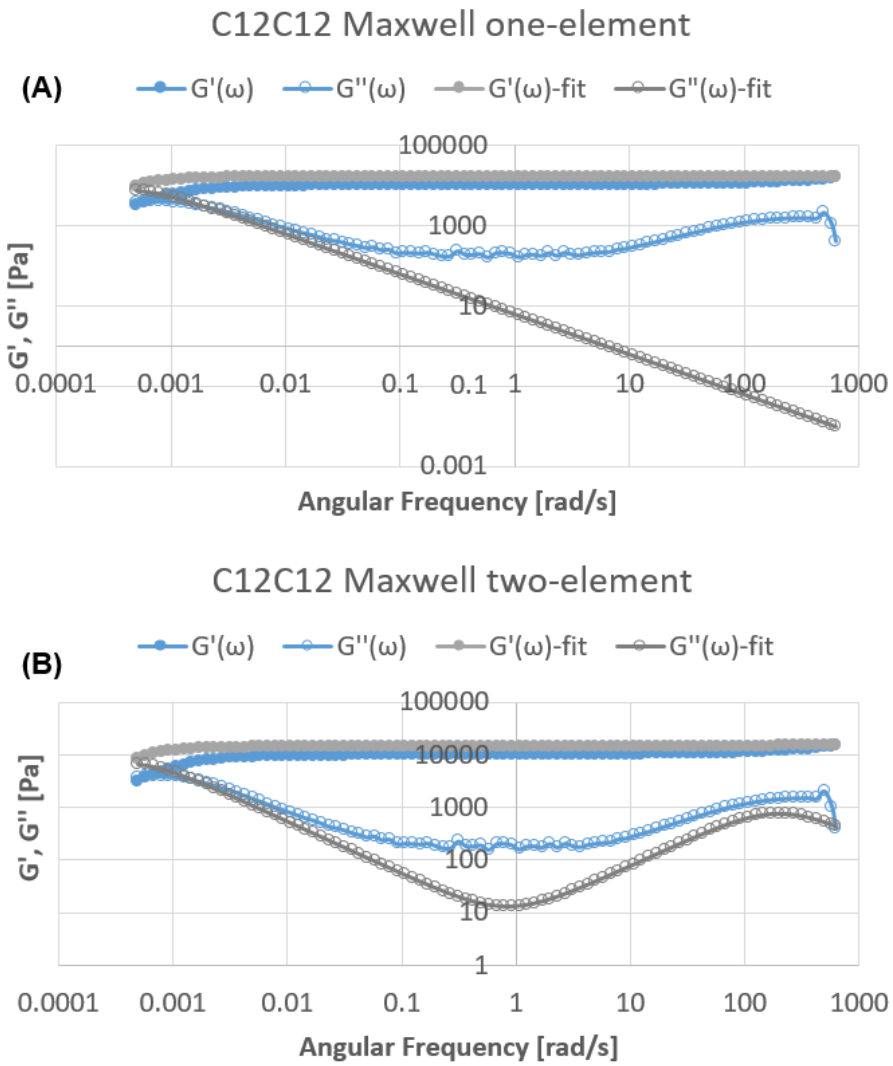

Figure S20. Maxwell model fitting for one A) and two Maxwell elements B) on frequency sweep data for ***$C_{12}C_{12}$ BTA*** hydrogelator.

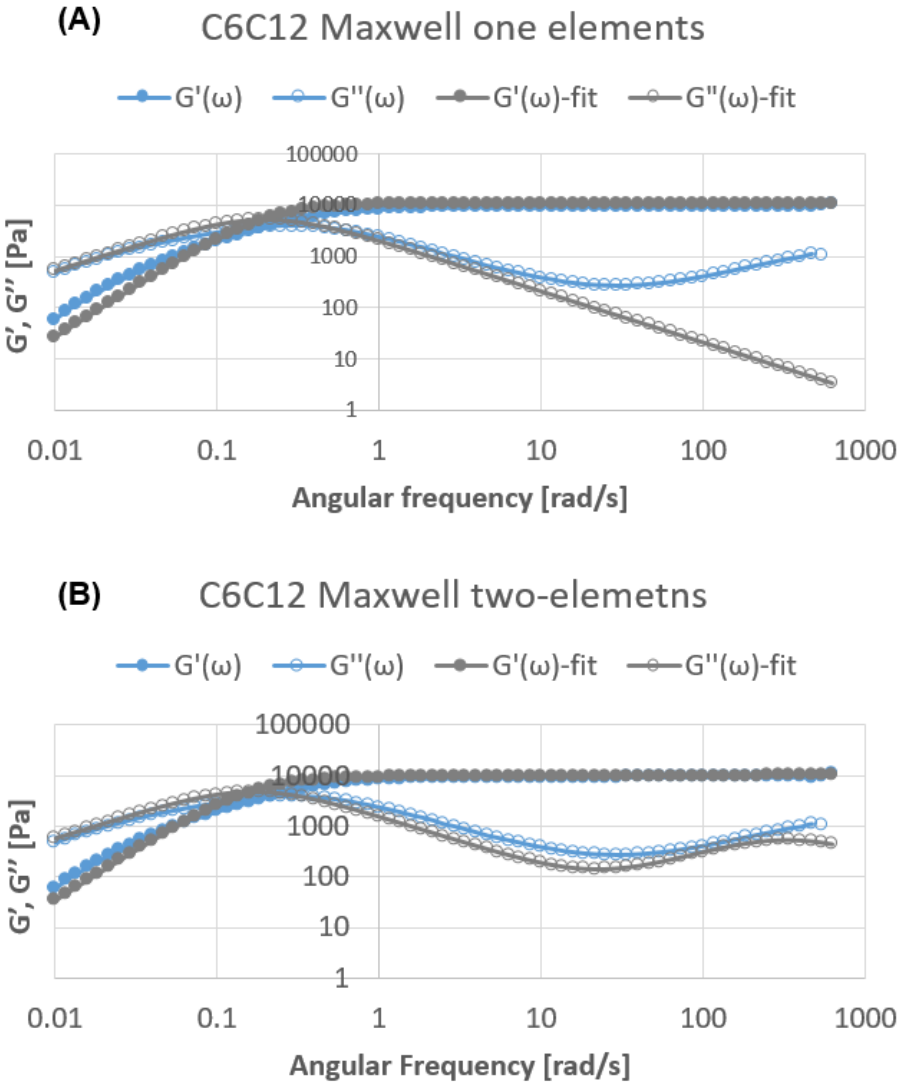

Figure S21. Maxwell model fitting for one A) and two Maxwell elements B) on frequency sweep data for ***C_6C_{12} BTA*** hydrogelator.

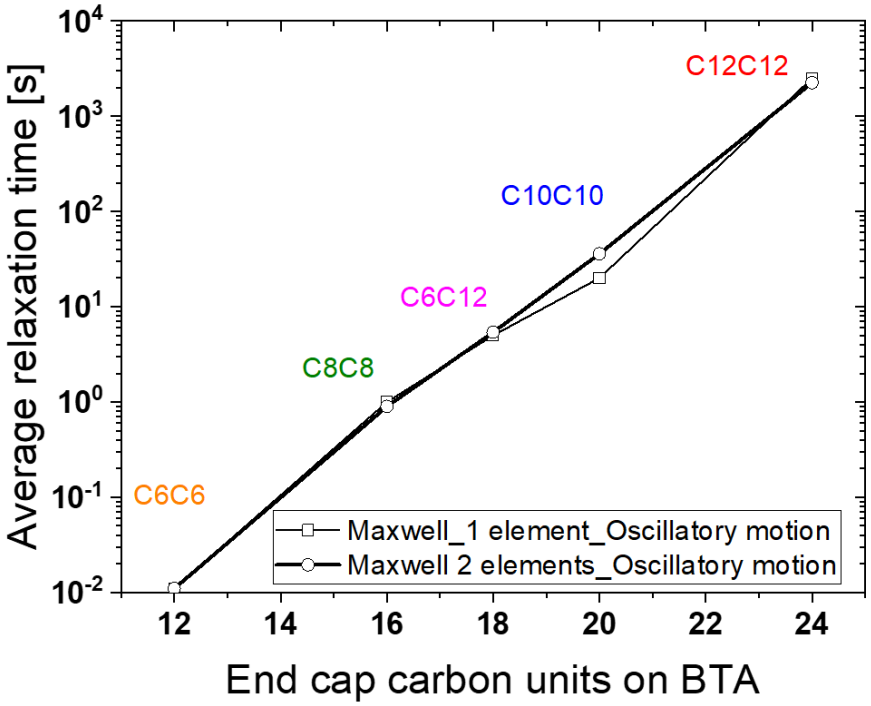

Figure S22. Average stress relaxation times calculated by applying one and two Maxwell elements on BTA hydrogelators.

Stress relaxation from step strain experiment

Data was also fit into Maxwell Model of viscoelastic fluids for single Maxwell elements and two Maxwell elements in parallel. Stress relaxation times were obtained by fitting step strain data into equation S3.

$$Generalized\ Maxwell\ model\ G(t) = \sum_n G_n e^{\frac{-t}{\tau_n}} \qquad (S3)$$

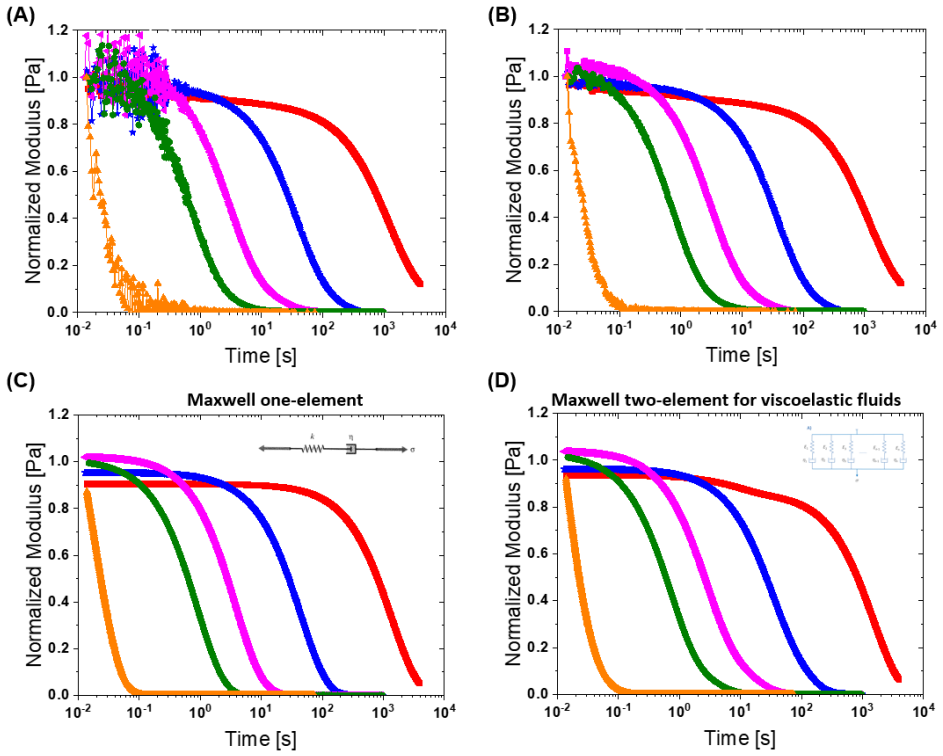

Figure S23. A) Stress relaxation data from shear rheology step strain experiment where constant strain of 1% was applied. B) Data was smoothed using adjacent point average smoothing function in origin and 10 adjacent data points were averaged. C) Stress relaxation profiles from fitting data into Maxwell model of viscoelastic fluids for single Maxwell elements, (D) Stress relaxation profiles obtained by fitting data into generalized Maxwell model of viscoelastic fluids or Maxwell-Wiechert model of viscoelastic fluids for two Maxwell elements in parallel.

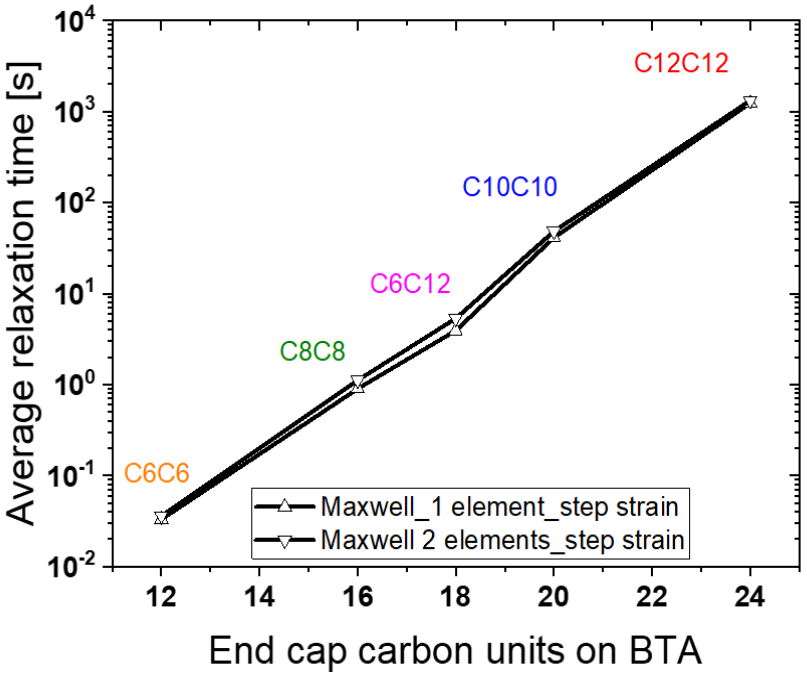

Figure S24. Stress relaxation times determined from step strain experiment using one and two Maxwell elements in parallel for viscoelastic fluids.

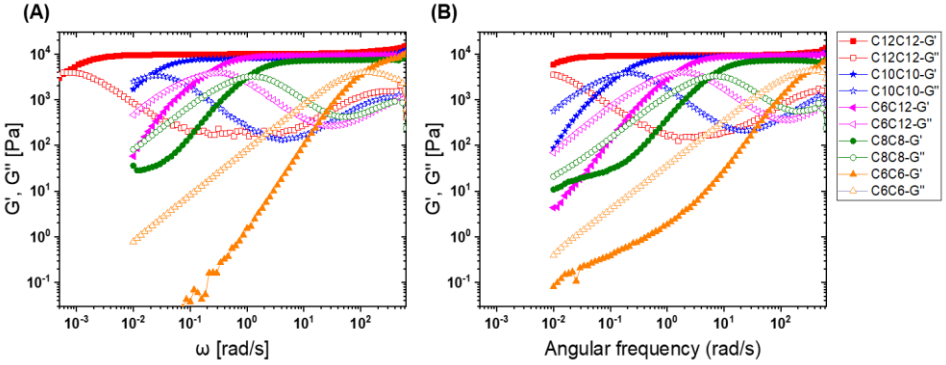

Figure S25. Frequency sweep. A) Angular Frequency sweep of C6C6, C8C8, C10C10, C12C12, and C6C12 at 20 ºC. All hydrogelators showed similar equilibrium storage moduli and the crossover point between loss moduli and storage moduli moved to the higher angular frequency with decreasing endcap carbon length on BTA, which indicates that the viscoelasticity of hydrogels is increasing with decreasing endcap carbon length on BTA. B) Frequency sweep of hydrogelator at 37 ºC. Almost one-decade shift to the higher angular frequency with an increase in temperature from 20 ºC to 37 ºC indicates faster hydrogel dynamics at 37 ºC.

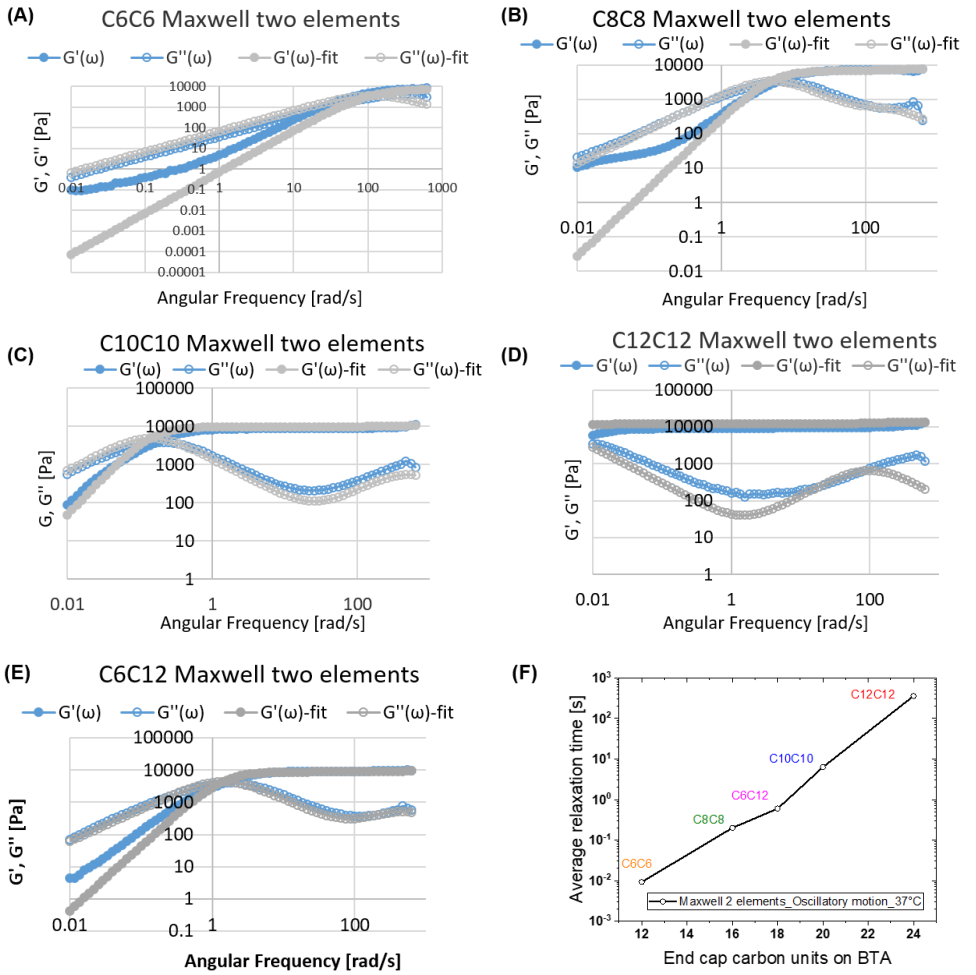

Figure S26. Frequency sweep of A) C6C6, B) C8C8, C) C10C10, D) C12C12, and E) C6C12 **BTAs** at 37 ºC. Blue represents the original data and grey represents when the data were fit to two Maxwell elements in parallel. F) Stress relaxation times obtained from A), B), C), D), and E) upon fitting data to two Maxwell elements in parallel. Hydrogels at 37 ºC also show logarithmic stress relaxation increase with increasing carbon length on BTA.

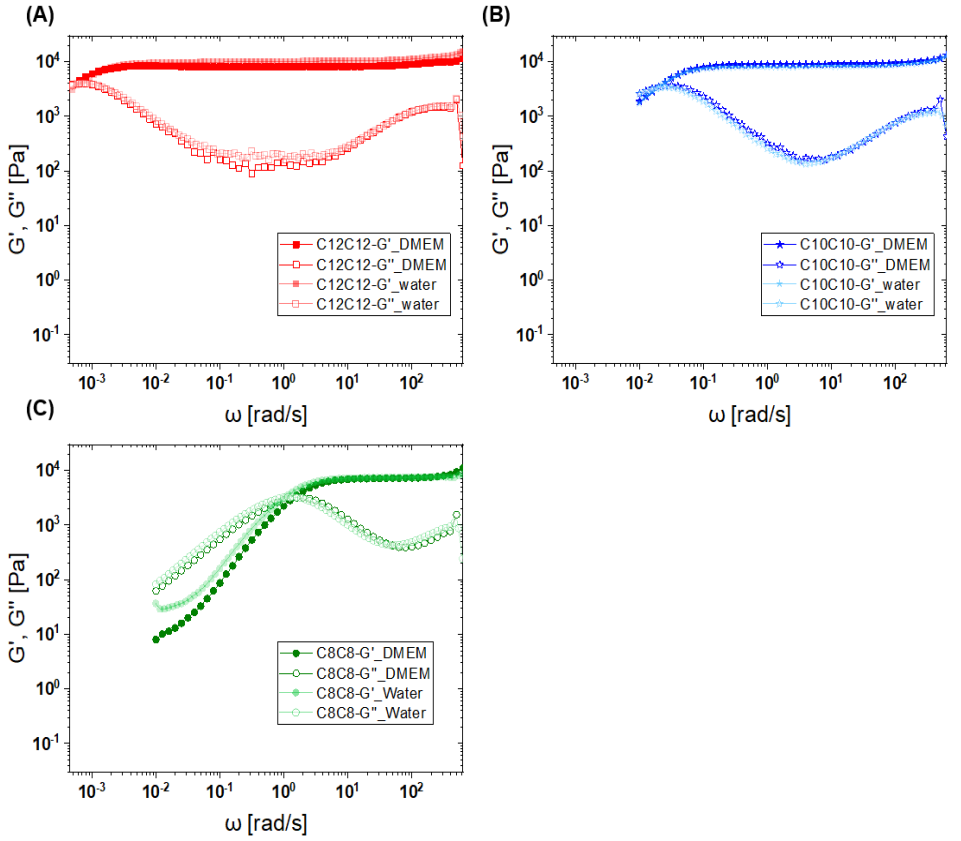

Figure S27. Frequency sweep comparison in Milli-Q water versus in DMEM: A), B) and C) for C12C12 BTA, C10C10 BTA, C8C8 BTA in Dulbecco's Modified Eagle Medium (DMEM) and in Milli-Q water. Frequency sweeps overlapped and showed no difference in storage moduli and angular frequency crossover points indicating hydrogel dynamics are not affected when hydrogels were prepared in DMEM compared to Milli-Q water.

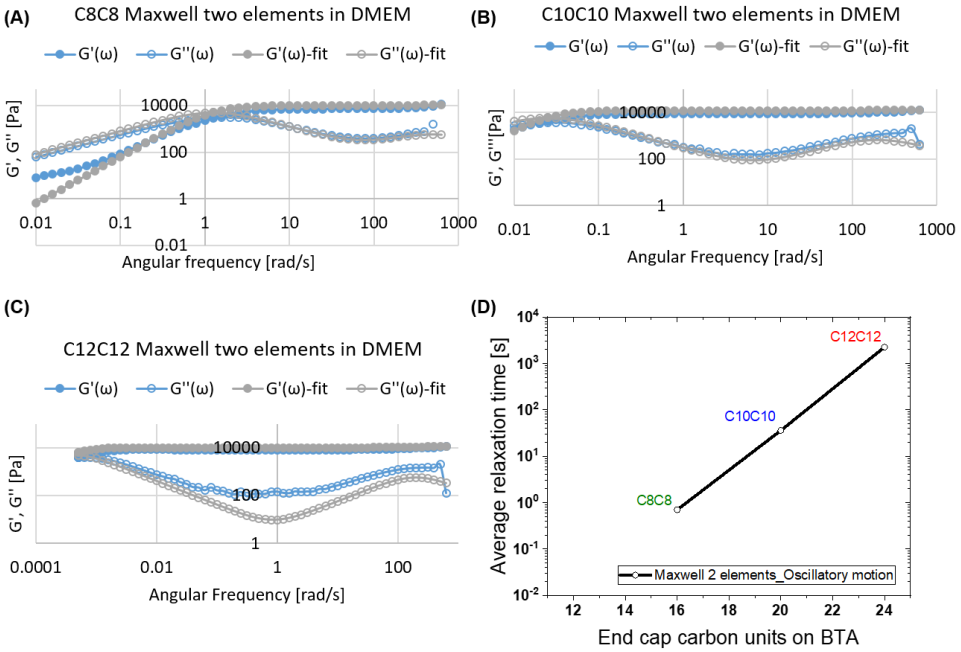

Figure S28. Frequency sweep of A) C8C8, B) C10C10, and C) C12C12 in DMEM. Blue color represents the original data and grey color represents the when the data was fit to two Maxwell elements in parallel. D) Stress relaxation times obtained when the data was fit to two Maxwell elements in parallel.

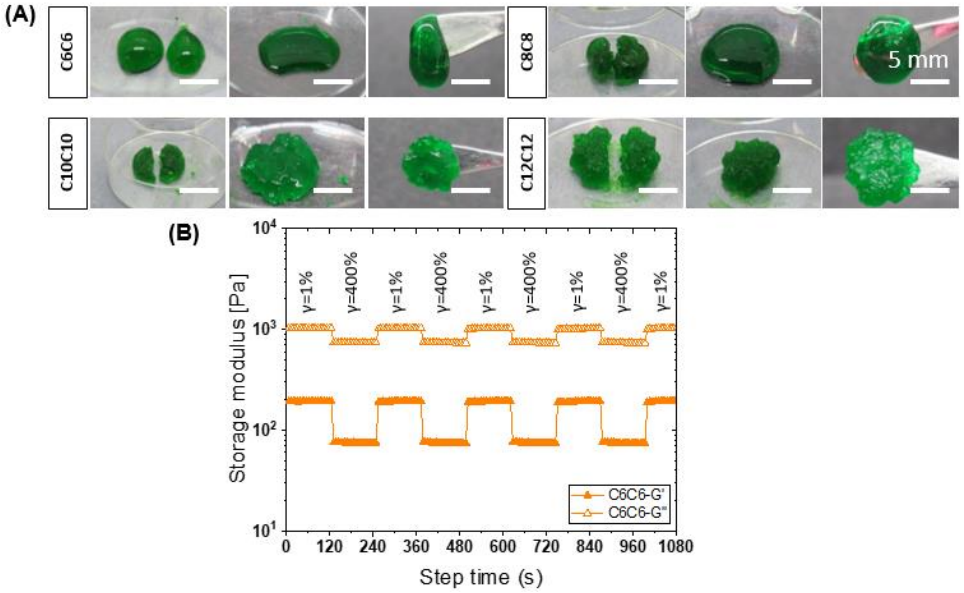

Figure S29. Self-healing of hydrogels. A) macroscopic self-healing with cutting a hydrogel in two pieces and then pressing two pieces of the hydrogel together, B) self-healing of hydrogels in step strain experiment, hydrogel was ruptured with 400% strain and recover under 1% strain. All hydrogelators recovered to their initial moduli under few seconds after each rupture cycle.

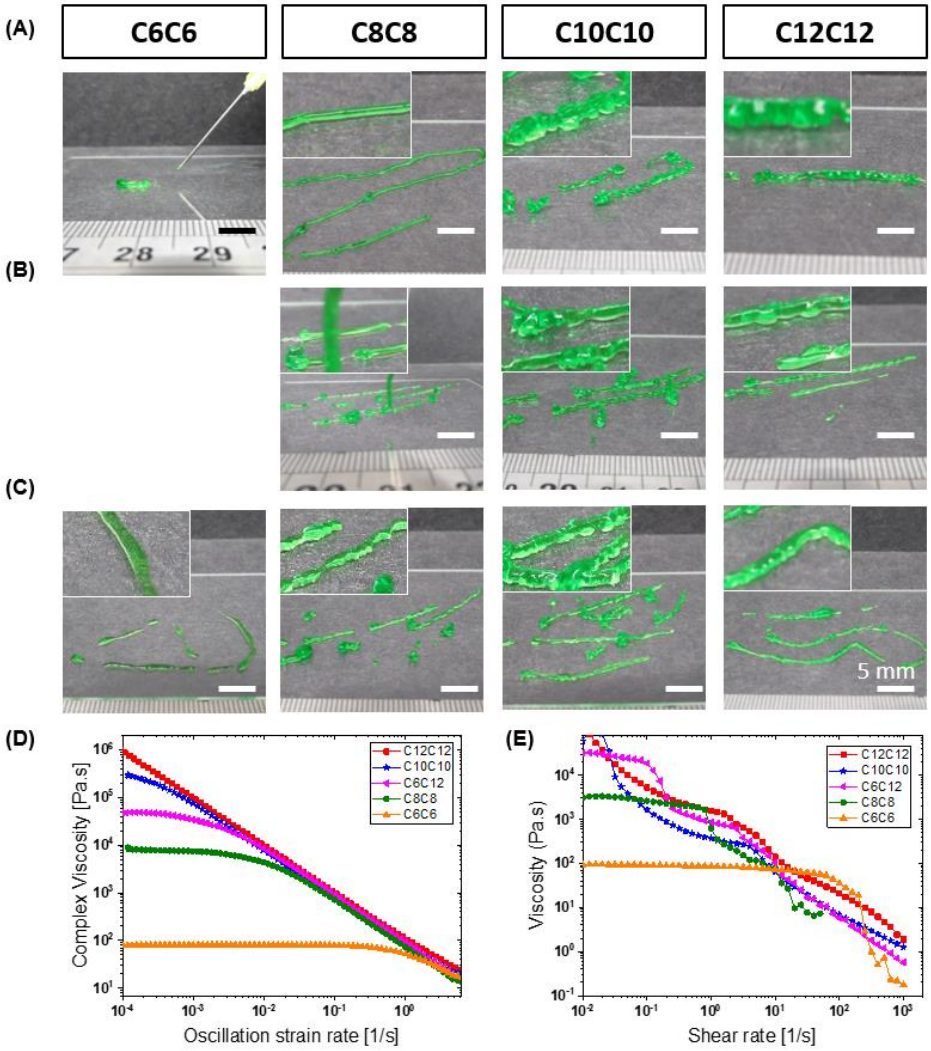

Figure S30. The injectability of hydrogelators. A) 10% (w/v) using 20G, C8C8 resulted in smooth fiber compared to all other hydrogelators. B) 5% (w/v) using 20G, all hydrogelators are injectable, and extruded hydrogel fibers are softer and more fragile compared to 10% (w/v). C) 5% (w/v) using 22G, all hydrogels showed injectability. D) Flow sweep curve shows viscosity decreases as we increased the shear rate. This decrease in viscosity when subjected to shear stress is a demonstration of the shear-thinning behavior of the hydrogels. E) In this continuous flow sweep experiment, the shear rate was increased continuously, and hydrogel started to break and exude out of cone-plate (at some places) geometry for all hydrogelator with increasing shear rate. Therefore, reported viscosity values might not be 100% true and only be used for looking at the trend in viscosity with increasing shear rate for demonstrating that hydrogels are shear-thinning.

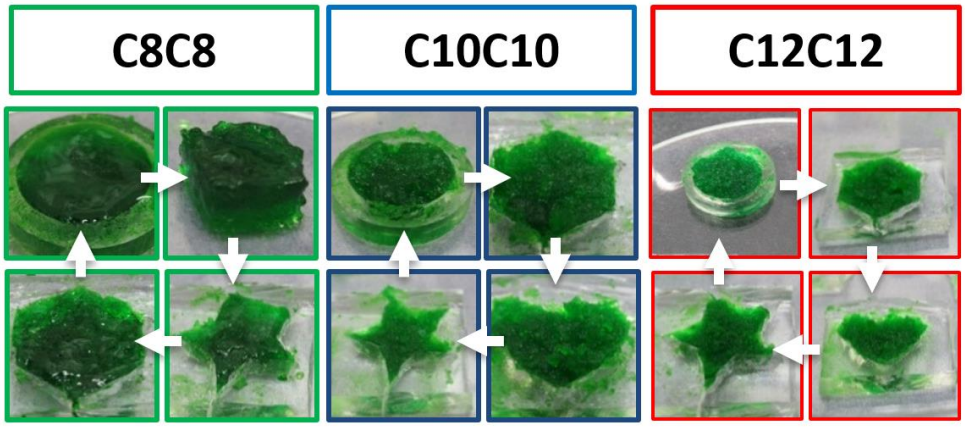

Figure S31. Moldability of BTA hydrogelators. Hydrogels are moldable into different shapes; from round to square to hexagon to star shape. Adaptability into different shapes shows stress dissipation capacity of hydrogels to adopt to different shapes and responsiveness to applied stresses.

3D printing

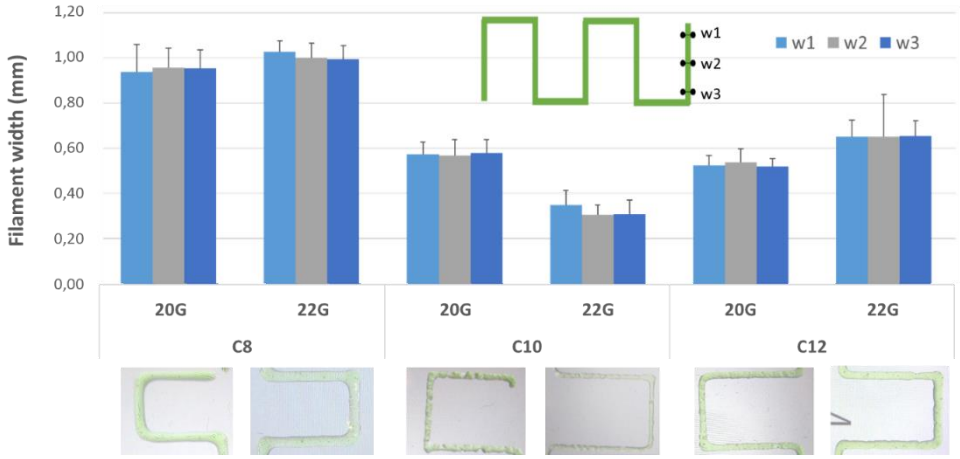

Figure S32. C8C8 BTA, C10C10 BTA, and C12C12 BTA hydrogels were printed into continuous zigzag strand filament shapes in order to determine the filament width using 20 gauge (internal diameter =0.603 mm) and 22 gauge (internal diameter =0.41 mm).

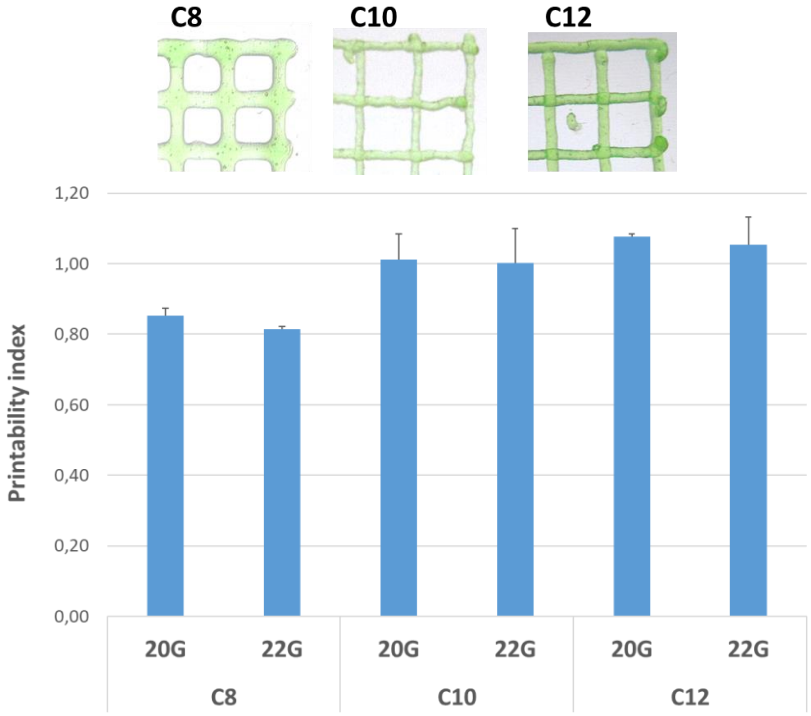

Figure S33. C8C8 BTA, C10C10 BTA, and C12C12 BTA hydrogels were printed in grid-like structure for determining printability index.

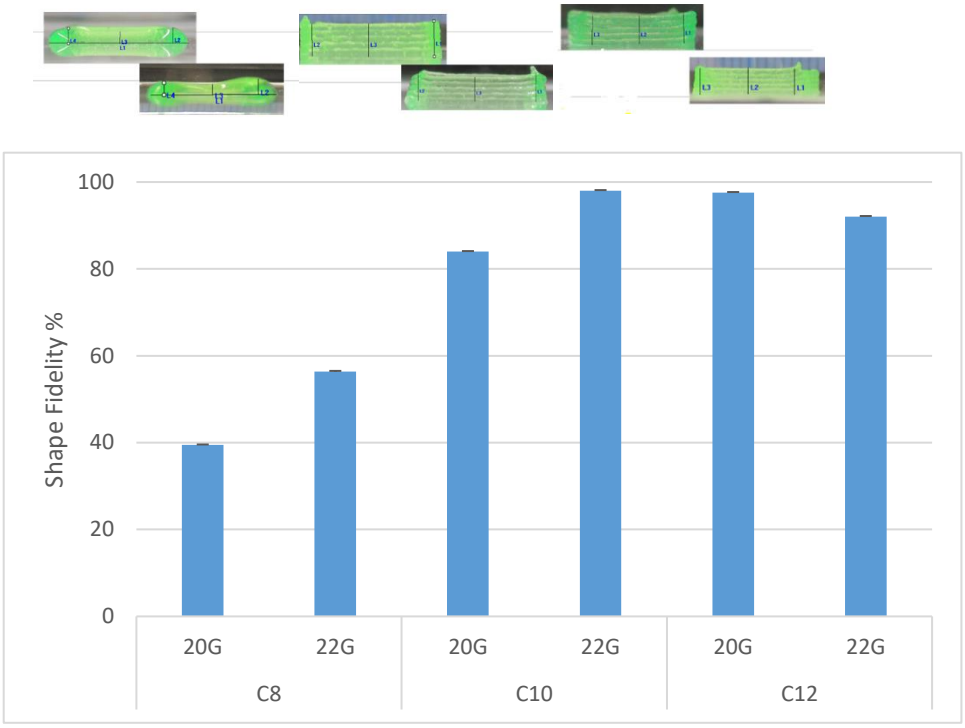

Figure S34. C8C8 BTA, C10C10 BTA and C12C12 BTA hydrogels were printed in as hollow cubes for determining structure shape fidelity. We printed 5-layers hollow cube and compared printed height to theoretical height for determining shape fidelity. C10C10 BTA and C12C12 BTA retained above 80% of their height compared to C8C8 BTA, which retained around 40% of theoretical printed height.

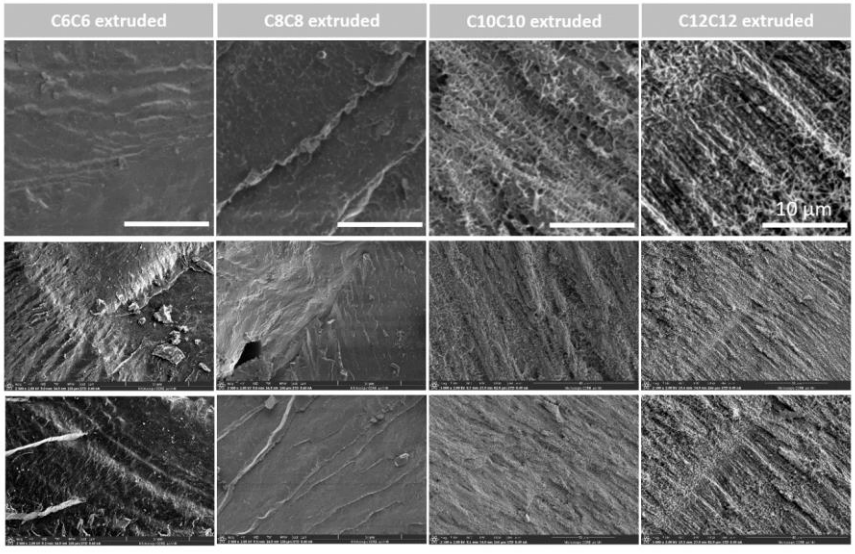

Figure S35. Cryo-SEM structure post extrusion. Structure of hydrogels after extruding through 22 gauge (0.413 µm) stainless steel needle.

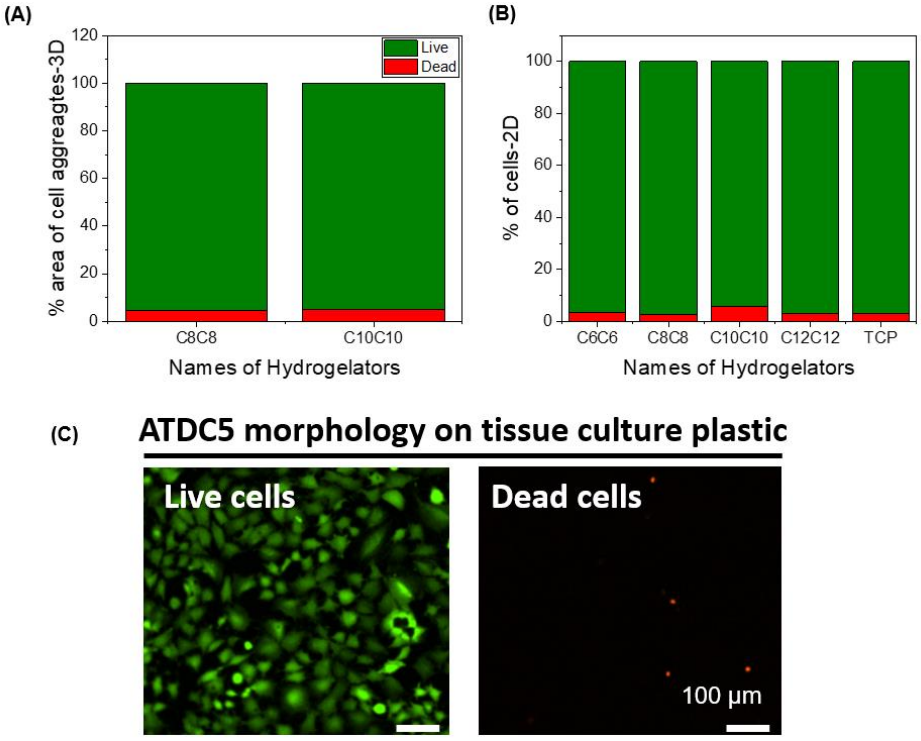

Figure S36. Live-dead cell quantification. A) % area of ATDC5 live cells aggregates when cells were encapsulated in hydrogelators. Greater than 300 cell aggregates were measured for live and dead cells and then % of live and dead cells determined. B) % area of live-dead cells cultured on tissue culture plastic (2D) and exposed to dilute solutions of hydrogelators. Green color bar represents % of live cells and red color bar represents % of dead cells. For both 2D and 3D, greater than 85% cells were alive after 4 days in culture. Mostly live cells were found and greater than 700 live cells area was counted and averaged. C) ATDC5 cells exhibited spreading morphology on tissue culture plastic. Tissue culture plastic was used as a control for comparing cell morphology to conditions where cultured ATDC5 were exposed to dilute solutions of BTA hydrogelators.

Bioprinting

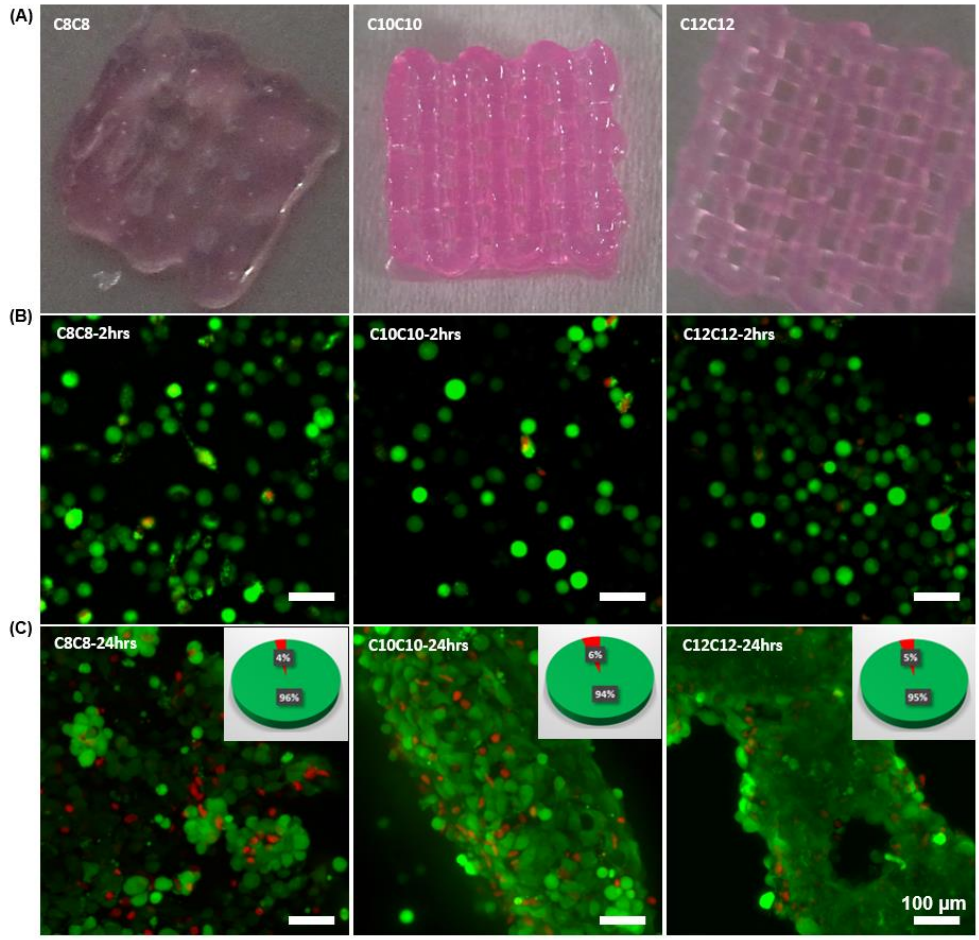

Figure S37. Cell viability in 3D printed grid structures. A) Bioprinting of grid structures, three to six layers were printed for each hydrogelator, B) Live-dead images of encapsulated chondrocytes (ATDC5) after roughly 2 hours in culture and C) live-dead image after 24 hours in culture, images show Z stack of extruded fiber under a microscope. Cell aggregation was observed in all hydrogelators. The inset graph shows the percentage of live and dead cell areas. The green color represents live cells, and the red color represents dead cells.

Chapter VIII

Covalent cross-linking of a supramolecular assembly creates tough, fibrous hydrogels and bioinks

Shahzad Hafeez[1], Monize Caiado Decarli[1], Agustina Aldana[1], Mahsa Ebrahimi[2], Floor A.A. Ruiter[1,3], Hans Duimel[3], Clemens van Blitterswijk[1], Louis M. Pitet[2], Lorenzo Moroni[1], Matthew B. Baker[1]

[1] Department of Complex Tissue Regeneration, MERLN Institute for Technology-Inspired Regenerative Medicine, Maastricht University, P.O. Box 616, 6200 MD Maastricht, the Netherlands;

[2] Advanced Functional Polymers Group, Department of Chemistry, Institute for Materials Research (IMO), Hasselt University, Martelarenlaan 42, 3500, Hasselt, Belgium

[3] Department of Cell Biology–Inspired Tissue Engineering, MERLN Institute for Technology-Inspired Regenerative Medicine, Maastricht University, P.O. Box 616, 6200 MD Maastricht, The Netherlands;

[4] Maastricht MultiModal Molecular Imaging Institute, P.O. Box 616, 6200 MD Maastricht, the Netherlands.

A version of this chapter was submitted to **Advanced Materials** and the revised version with new edits and further data analysis has been published in **Advanced Materials** (2023).

Hafeez, S.; Decarli, M. C.; Aldana, A.; Ebrahimi, M.; Ruiter, F. A. A.; Duimel, H.; van Blitterswijk, C.; Pitet, L. M.; Moroni, L.; Baker, M. B. In Situ Covalent Reinforcement of a Benzene-1,3,5-Tricarboxamide Supramolecular Polymer Enables Biomimetic, Tough, and Fibrous Hydrogels and Bioinks. *Adv. Mater.* **2023**, *2301242*, 1–18. https://doi.org/10.1002/adma.202301242.

Abstract

Conventional synthetic hydrogels often lack the load-bearing capacity and mechanical properties of native biopolymers, such as cartilage. In some natural tissues, like cartilage, toughness is often imparted via the combination of fibrous non-covalent self-assembly with covalent bond formation. The controlled combination of supramolecular fibers and covalent interactions remains difficult to engineer, yet could provide a clear strategy for advanced biomaterials. Here, a synthetic supramolecular/covalent strategy is investigated for creating a tough hydrogel that embodies the hierarchical fibril architecture of native tissues. A benzene-1,3,5-tricarboxamide (BTA) based hydrogelator was developed with synthetically addressable norbornene handles, which self-assembled across multiple length scales to form a fibrillar and viscoelastic hydrogel. Inspired by collagen's covalent cross-linking of fibrils, we fine-tuned the mechanical properties such as toughness, stiffness, and strength of the hydrogels by covalent inter- and intra-fiber cross-links. At over 90% water, the hydrogels withstood up to 550% tensile strain, 90% compressive strain, and dissipated energy with recoverable hysteresis. The norbornene BTA hydrogels were shear-thinning, and could be 3D bioprinted with good shape fidelity. The fabricated structures were further toughened by introducing covalent cross-linking. These materials enabled the bioprinting of hMSC spheroids and differentiation/maturation into chondrogenic tissue. Collectively, our findings highlight that the conjunction of self-assembly and covalent cross-linking of supramolecular fibers offers a potentially powerful strategy for the bottom-up design of dynamic, yet tough, synthetic hydrogels and bioinks.

Introduction

Tissues such as cartilage, muscles, tendons, and ligaments exhibit remarkable toughness, elasticity, and fast recovery[1], especially when compared to synthetic soft biomaterials. The exceptional mechanical properties of many tissues are often attributed to the hierarchical fibril macromolecular structure across multiple length scales. An excellent example of this hierarchical structure is collagen, the backbone of many tough tissues. Collagen fibrils are composed of a self-assembled structure of tropocollagen, mainly driven by non-covalent interactions. These supramolecular fibrils are further stabilized by intra- and intermolecular covalent cross-links (via aldol condensation and aldimine cross-links).[2] Theoretical and molecular modeling studies suggest that intermolecular hydrogen-bonding interactions and permanent cross-links between the collagen fibrils are mainly responsible for the impressive mechanical properties and toughness of collagen.[3] This supramolecular/covalent strategy is not only seen in collagen. Other examples include the self-assembly of tropoelastin into fibrous elastin, driven by lysine forming bi-functional and tetra-functional cross-links,[4,5] and α-actinin forming cross-links between actin filaments.[6] While this conjunction of supramolecular assembly and covalent reinforcement is widely observed in natural systems, it is much less explored in synthetic materials.

Hydrogels mimic many aspects of soft tissues and offer the potential to be used as instructive biomaterials and structural implants, among many other biomedical applications. Yet, the applications of hydrogels are often limited by their mechanical properties, especially mechanical toughness. To overcome this limitation, several synthetic strategies for forming tough hydrogels are emerging and include double networks[7,8,9], dual cross-linking (covalent bonds and H-bonding)[10], conjoined networks[11], sacrificial H-bonding interactions[12,13], force-triggered reactive strand extension[14], and dense entanglements.[15,16] Most strategies for tough hydrogels reported in the literature have homogenous mesh-like structures. In contrast, nature has extensively utilized one-dimensional (1D) supramolecular polymers, such as tropocollagen, microtubules, and actin filaments as powerful structural motifs for strong and tough tissues. In synthetic hydrogel design, little attention has been paid to mimicking the synergy of 1D self-assembly and covalent fixation as seen in nature. The Stupp group has introduced cross-links in a 1D supramolecular peptide amphiphile[17,18]; however, these hydrogels are soft (shear moduli ~1000 Pa) and toughness has not been investigated. Burdick and coworkers also reported a tough hydrogel through tandem supramolecular and covalent cross-linking; however, the hydrogel is made up of a double network and lacks 1D self-assembly[19]. Despite these major advances, the tuning of toughness utilizing nature's synergy of self-assembly and covalent cross-linking in synthetic fibrous hydrogels remains a challenge.

Supramolecular and dynamic hydrogels are attractive candidates for three-dimensional (3D) printing with living cells[20], due to the benefits of being biomimetic, mechanically tunable, self-healing, and shear-thinning. The 3D bioprinting of hydrogels has been used to fabricate complex tissue-like structures such as heart valves[21,22], vascular networks[23,24,25,26], corneal domes[27], and kidneys.[28] Yet, balancing the dynamics of a hydrogel with stability and toughness has created

additional challenges toward bioprinting complex 3D life-like structures. Consequently, most of the bioinks developed are only marginally suited for extrusion bioprinting since they are highly viscous liquids[29], can sediment cells at the bottom of ink cartridges, block the nozzle owing to fast UV cross-linking[30], involve large pH shifts (for collagen hydrogels), or have supraphysiological levels of calcium ions (e.g., for alginate bioinks). Shear-thinning hydrogels have clearly been shown to increase cell viability during bioprinting,[31] and this property has been rationally designed using dynamic covalent bonds[32,33], and supramolecular host-guest interactions.[34–36] Recent reports showed the engineering of shear-thinning behavior in 1D peptide amphiphile[37] and short peptide bioinks;[38] however, designing a synthetic biomimetic bioink with 1D self-assembled fibers that possess both shear-thinning and remarkable toughness remains a formidable challenge.

To create a biomimetic, tough, and processable hydrogel, we took inspiration from nature's conjunction of self-assembly and covalent reinforcement. We designed a benzene-1,3,5-tricarboxamide (BTA) hydrogelator with norbornene (NB) functional handles that we surmised could self-assemble into 1D fibrils. We hypothesized that these biomimetic supramolecular assemblies could be fixed/cross-linked, ultimately leading to a tough hydrogel via intra- and inter-fiber cross-links. Via rheology and mechanical testing (compression and tensile), we discovered that the toughness, stiffness, and strength of the hydrogels could be tuned in biomimetic regions. Ultimately, this supramolecular-co-covalent strategy allowed the creation of remarkably tough 3D bioinks, which were explored for 3D printing of an *in vitro* cartilage tissue model.

Results and Discussion

Molecular design and NB BTA synthesis

We designed the norbornene BTA (NB BTA) macromonomer by introducing norbornene functionalities on the two outer ends of a telechelic BTA polyethylene glycol macromonomer (**Figure 1a**). The hydrophobic nature of the norbornene, in combination with a dodecane internal spacer,[39] was envisioned to provide a hydrophobic pocket upon self-assembly, while the poly(ethylene glycol) (20 kg/mol, PEG20K) would provide good water miscibility. The unsaturated norbornene would also serve as a functional handle on the macromonomer, enabling functionalization using the thiol-ene reaction. With a previously reported desymmetrization strategy[40], the di-norbornene BTA synthon was readily obtained by desymmetrizing benzene-1,3,5-tricarbonyl tripentafluoroester (BTE-F_5Ph) with two equivalents of 5-norbornene 2-methylamine (5NB-2MA) (**Figure S1**). The target NB BTA macromonomer was synthesized by covalently connecting two di-norbornene BTA synthon molecules to dodecane amine-terminated polyethylene glycol (20 kg/mol, PEG20K) (**Figure S1**). We

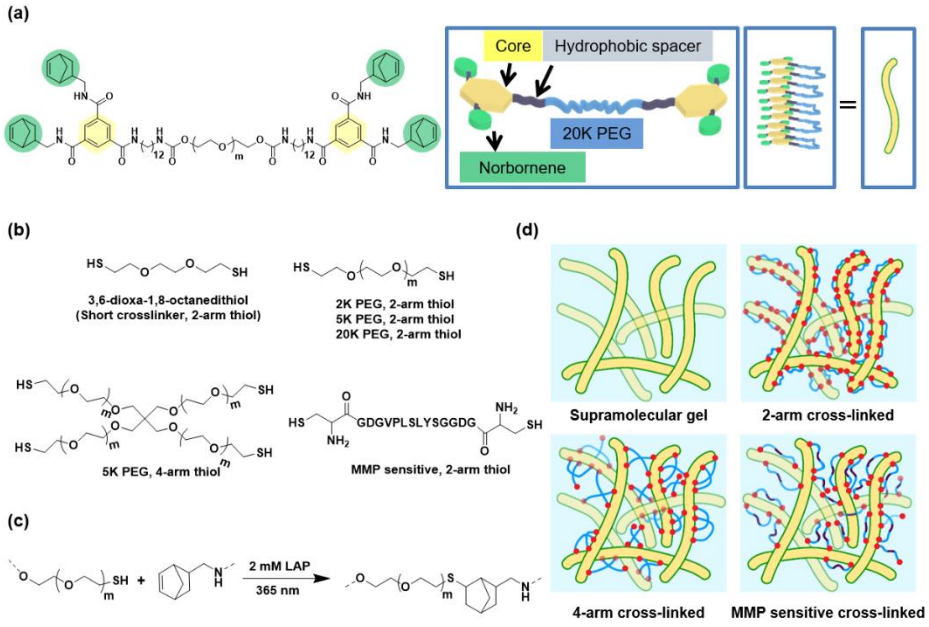

Figure 1. Molecular structures of NB BTA and cross-linkers employed in the study. a) Chemical structure of norbornene functionalized NB BTA hydrogelator. Cartoon representation of NB BTA hydrogelator, proposed stacking of NB BTA molecules (middle) to form a fibril (right). b) Thiol cross-linkers utilized for cross-linking supramolecular assemblies. c) Reaction scheme for thiol-ene chemistry of norbornene and thiol. d) Schematic of the supramolecular hydrogel network (top left), after cross-linking with a short 2-arm thiol cross-linker (top right), 4-arm thiol cross-linker (bottom left), and MMP sensitive 2-arm thiol cross-linker (bottom right).

successfully synthesized the pure macromonomer (^{1}H NMR in **Figure S2**) with an average molecular weight of ~23 kg/mol and dispersity of 1.2 (*Đ*, hydrogel permeation chromatography, **Figure S3**). Schematics of the NB BTA macromonomer, self-assembly, thiol-ene chemistry, and inter- and intra-fiber cross-linking using different thiol cross-linkers are shown in **Figure 1 b–d.**

NB BTA aggregates to form fibrillar morphology

The self-assembly of the NB BTA macromonomer was first investigated in an aqueous environment by dissolution in a minimal amount of methanol and assembly via injection into water. Utilizing the solvatochromic dye Nile Red[41] as a reporter, we observed an increase in fluorescence, consistent with the formation of a hydrophobic pocket.[42] The fluorescence intensity increased with increasing hydrogelator concentration from 1, 2, and 5 mg/ml, which suggested an increasing volume of hydrophobic pocket (**Figure 2a**). These fluorescence intensity wavelengths (λ_{max}, ~620 nm) remained constant for all tested concentrations and was blue-shifted compared to a PEG20K solution in water (**Figure S4**). The blue shift suggests a non-polar environment, and the similar λ_{max} pointed to a consistent strength of the hydrophobic pocket at all concentrations. These observations are in line with previously reported 1D fibrous

BTA structures with aliphatic hydrophobic spacers, and gave us confidence that we had a well-behaved supramolecular assembly within a range of accessible concentrations.[40]

In order to gain structural information on this self-assembly, we investigated the self-assembled NB BTA macromonomer (at 10 mg/mL) with cryo-transmission electron microscopy (cryo-TEM). Cryo-TEM revealed NB BTA superstructures, the size of which presumably points to the formation of bundled, parallel nanofibers in samples that had been aged between 16–24 hours (**Figure 2c and Figure S5**). A single nanofiber measured approximately 1.5 nm in diameter, and the bundles varied between 15–60 nm in diameter. Next, an aged sample was examined after 30 days (5 mg/ml, **Figure 2e**). Immediately apparent are the high-aspect-ratio fibers formed in these samples. The NB BTA showed fiber bundles with diameters of 5 nm and 15–50 nm, and the fingerprint-like bundles transitioned to well-defined fibers. The length of the nanofibers varied between a couple of hundred nanometers to a micrometer. Aging the samples further did not provide significant differences, as similar dimensions were observed after 270 days (**Figure S6**).

The self-assembled NB BTA retained the hydrophobic pocket and fibrillar morphology after cross-linking

Having established hydrophobic formation and fibrous morphology, we next tested if the self-assembled NB BTA structures underwent major changes to the hydrophobic pocket after being subjected to cross-linking conditions (2 mM LAP photoinitiator, 365 nm UV light and ~1 mW/cm^2 for 1–4 minutes). Using a short (8-atoms) di-thiol cross-linker, we cross-linked a dilute solution of the macromonomer. This cross-linked NB BTA displayed similar Nile Red fluorescence to the non-crosslinked controls both in intensity and λ_{max} (**Figure 2b**). Neither red nor blue shift was detected, which suggests that the polarity of the hydrophobic pocket was not majorly affected by the cross-linking reaction. The fixed supramolecular assemblies were further probed by cryo-TEM to examine any potential structural changes after the covalent cross-linking. No changes were observed in the structure or fibrillar morphology on the micron and 10s of nm scale. (**Figure 2d and Figure S5**). With this knowledge in hand, we subsequently pursued uncovering the potential of these macromonomers as hydrogel materials.

Formation and cross-linking of hydrogels from supramolecular NB BTA

We investigated the ability of the NB BTA macromonomer to form hydrogels in water at different concentrations (2.5, 5.0, 7.5, and 10% w/v). Hydrogel formation was confirmed at all tested concentrations via the vial inversion test (**Figure S7**). The lower-concentration hydrogels were qualitatively soft and fragile with increasing stiffness upon increasing concentration. The NB BTA hydrogels were subsequently cross-linked with a short di-thiol. After equilibration at room temperature for ~2 hours, the hydrogels were cross-linked using a photoinitiator and UV-light (LAP, 365 nm for 30–60 seconds, **Figure 3a,b**, **Figure S7**). Immediately we noticed that all concentrations transitioned from fragile samples to remarkably tough and stretchable (**Movies S1–S4**). These qualitative changes suggested successful cross-linking.

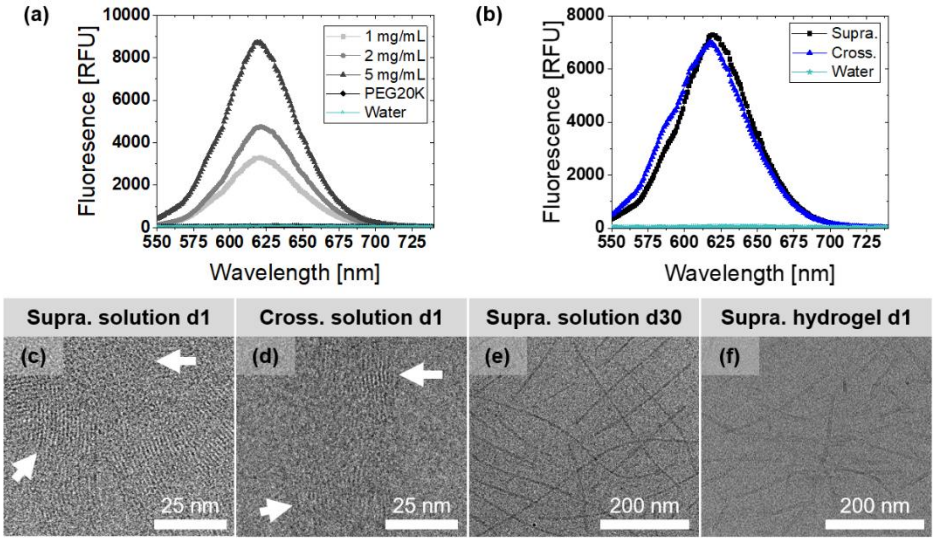

Figure 2. Self-assembly studies. a) Nile red fluorescence as a function of NB BTA concentration in water. b) Nile red fluorescence for cross-linked versus non-cross-linked (supramolecular) NB BTA solution at 5 mg/ml. c) Nanofibres of NB BTA at 10 mg/mL as observed via cryo-TEM. d) the supramolecular structure is still observed after exposure to UV light (365 nm at ~1 mW/cm2) for cross-linking. e) Supramolecular fibers in dilute solutions at 5 mg/mL aged for 30 days showed nanofibre bundles with a diameter of around 5 nm. f) A dissolved supramolecular hydrogel (to 5 mg/ml) also showed bundles of fibrils around 10–15 nm in diameter.

We then further investigated the macroscopic properties of the 5% (w/v) hydrogel before and after cross-linking with the short di-thiol at 1:1 ratio of [NB]:[thiol] (**Figure 3**). While both the non-crosslinked and cross-linked hydrogels were compressible, the cross-linked hydrogel showed immediate recovery upon removing the force (**Figure 3c,d**). The supramolecular hydrogel could be cut easily using a spatula and sharp blade (**Figure 3e,g**) while the cross-linked hydrogel required substantially more effort and was only severed after several cycles of aggressive cutting (**Figure 3f,h and Movie S5**). The cross-linked hydrogel resisted a considerable load when compressed with a spatula before cracking (**Figure S8**), while the supramolecular-only hydrogel was much more fragile. Furthermore, the supramolecular hydrogels (pre-crosslinking) were able to be extruded into uniform filament shapes (**Figure 3i,k**), indicative of good injectability and potential for 3D printing. After cross-linking, the originally weak filament could then be extended to 4.5 times (i.e., 450% strain) its original length before breaking (**Figure 3j,l and Movie S6**).

The NB BTA hydrogel exhibited fibrous morphology

Next, the internal structure of the supramolecular hydrogel before and after cross-linking was probed using cryo-TEM and cryo-SEM. One supramolecular hydrogel was diluted (a 5% w/v hydrogel diluted to 5 mg/ml) for cryo-TEM, which revealed fibers with a diameter of around 15 nm and lengths of several hundreds of nanometers (**Figure 2f and Figure S9**). These diluted

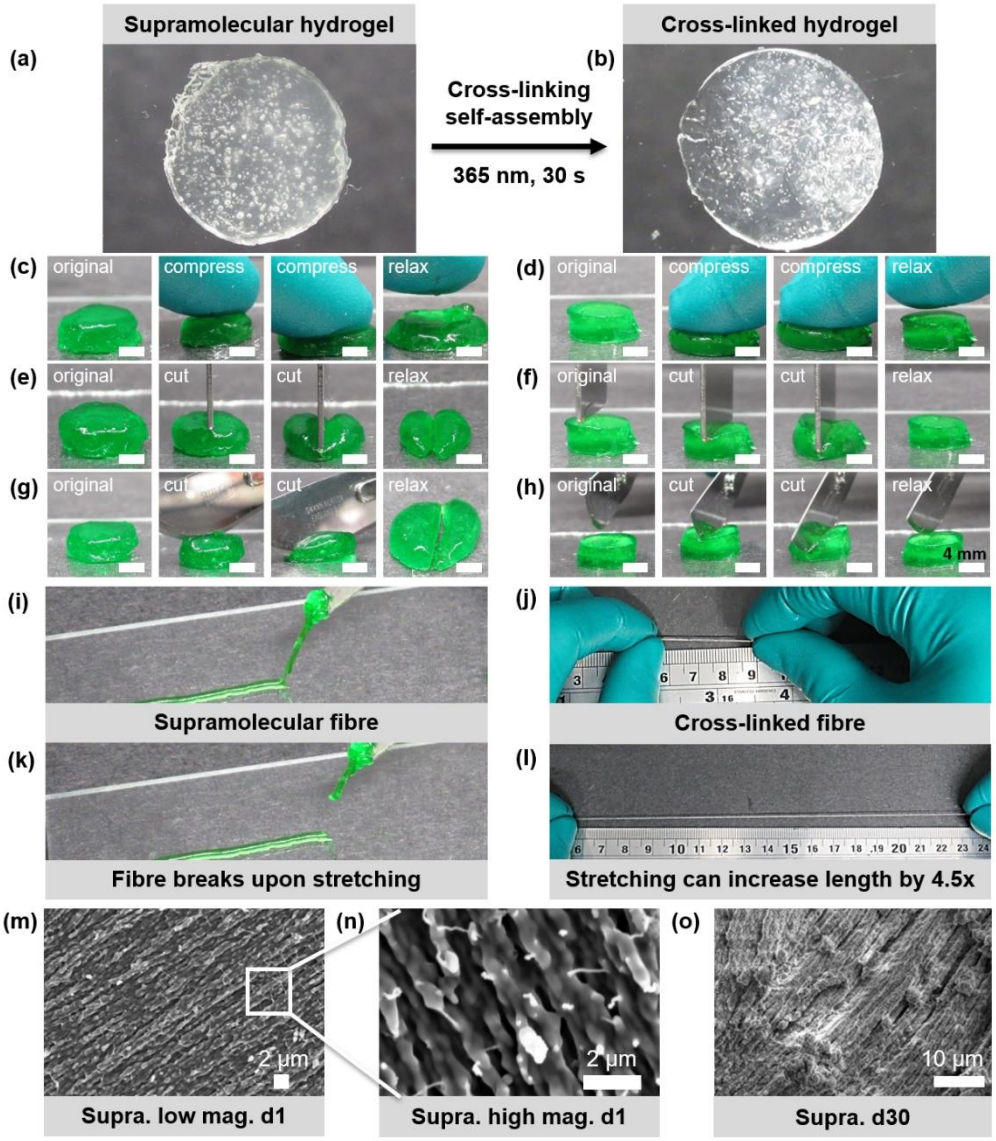

Figure 3. Cross-linking of the supramolecular hydrogel leads to strong, tough, and stretchable hydrogels. a, g) Optical image of NB BTA hydrogel at 5% (w/v) before (a) and after (b) cross-linking. c–h) Optical images of supramolecular and cross-linked hydrogel under extreme compression (c vs d), cutting using spatula (e vs f), and cutting using sharp blade (g vs h). i–l) Stretching of extruded supramolecular (i and k) and cross-linked filament (j and l). Supramolecular filament broke while cross-linked can be stretched to 4.5× of its original length. m–o) The supramolecular hydrogel (50 mg/ml) showed anisotropic fibril morphology via cryo-SEM at low (m) and high (n) magnification, and the hydrogel aged for 30 days (o) showed aligned bundle of fibres.

supramolecular hydrogel structures closely resembled the aged supramolecular solutions seen in the dilute solution studies (*vide supra*). The bulk hydrogel microstructure was visualized using

cryo-SEM. The supramolecular hydrogel (5% w/v in water) showed bundles of fibers that appeared to be parallel (i.e., anisotropically aligned) (**Figure 3 m,n** and **Figure S10**). The supramolecular hydrogel retained this anisotropic alignment and bundled fibril morphology in a sample aged for 30 days at room temperature (**Figure 3o and Figure S11**).

Tuning of the mechanical properties via concentration and cross-linker type

With ample evidence for the impressive change in mechanical properties, and the conservation of supramolecular structure before/after cross-linking, we turned to the mechanical fine-tuning of these hydrogels. We hypothesized that mechanical tuning could be simply achieved via polymer concentration (2.5% to 10% w/v). Investigated with shear rheology (**Figure 4a**), the hydrogels possessed a rather large linear viscoelastic regime up to about 30% strain (**Figure S12**). The storage moduli increased monotonically with increasing polymer concentration, consistent with increased physical interactions between the fibers. Yet notably, the viscoelasticity diminished with increasing concentration. The crossover points during a frequency sweep, which reflects the dynamic nature of the supramolecular interactions, decreased from 34 rad/s for 2.5% to 0.25 rad/s and 0.01 rad/s for 5% and 10% NB BTA hydrogels, respectively (**Figure 4a and Figure S12**).

After knowing the effect of concentration on the mechanical properties, we wished to explore the mechanical properties of cross-linked hydrogels. The *in situ* thiol-ene cross-linking was performed on the rheometer. Using a short thiol cross-linker in a 1:1 [NB]:[thiol] ratio, all formulations (2.5–10%) cross-linked quickly as indicated via a sharp rise in the storage modulus (below 10 seconds, 365 nm and ~10 mW/cm^2 at 1% strain and 10 rad/s, **Figure 4b**). Under these conditions, the 2.5% (w/v) hydrogel was initially a viscous liquid, but gelled rapidly after cross-linking; its storage modulus increased 10-fold to 1 kPa. A two-fold increase in storage modulus was observed for 5% (w/v) and 10% (w/v) formulations, with final values of 7 kPa and 15 kPa, respectively. Looking into the cross-linked hydrogels further, they showed a plateau storage modulus across almost 4 orders of angular frequency, indicative of their elastic nature. Of considerable note, the plateau moduli for the cross-linked hydrogels are nearly identical to the high-frequency equilibrium storage modulus for the non-cross-linked hydrogels (**Figure 4a,c and Figure S12**). This equilibrium storage modulus is generally considered to be the modulus outside of the timescale of materials dynamics and is the modulus representative of the structure of the network. Observing identical moduli before and after cross-linking suggests that the network/structure stayed largely the same; it appeared that the cross-linking mainly shuts down the dynamics and does not alter the network topology heavily. Additionally, we also observed that the cross-linking does not change the self-assembled nanostructure when comparing cryo-TEM images (in dilute solution; *vide supra*, **Figure 2 and Figure S5**).

Subsequently, the molar ratio of the thiol cross-linker (0.25, 0.5, 1, and 2 equivalents) was explored as a handle to tune the mechanics of the hydrogel at a constant polymer concentration (5% w/v). All formulations were initially viscoelastic (**Figure S13**). However, the equilibrium storage moduli varied with the molar ratio of the thiol cross-linker: from ~4 kPa for the lowest

and highest (0.25 and 2.0, respectively) molar equivalents, to ~8 kPa for 1 molar equivalent. Upon cross-linking the hydrogels followed the common trend in traditional covalent hydrogels of an increase in storage modulus with an increasing degree of cross-linking, until equimolar ratios, followed by a drop once the cross-linker is in excess; however, this trend was also observed in the pre-cross-linked samples. All of the hydrogels transitioned to being dominantly elastic after cross-linking (**Figure 4d and Figure S13**), and the equilibrium storage modulus of each formulation remained constant, again suggesting that the cross-linking did not significantly change the underlying hydrogel's network.

To probe the effect of cross-linking on the storage modulus, topologically more complex cross-linkers were employed. We compared 5K-PEG-4-arm and 2K-PEG-2-arm variants, keeping the arm length roughly constant. We observed that the 4-arm PEG cross-linked slowly when compared to the 2-arm PEG during rheology. However, both exhibited a similar storage modulus of 4.5 kPa. The similar storage moduli between the two samples indicated that the extra topological cross-link in the 5K-PEG-4arm did not contribute significantly to the modulus of the hydrogel (**Figure 4e** and **Figure S14**) at low strains. This again suggests that the covalent network topology does not appreciably influence the storage modulus at low strains, prompting us to further investigate the effect of cross-linker length on mechanical properties.

We then proceeded to explore the molecular length of the cross-linker and its influence on mechanical properties. In principle, a shorter cross-linker would preferentially form interfiber connections, while longer cross-linkers could form more interfiber cross-links. The hydrogels were cross-linked using di-thiols of varying lengths: short, 2K-PEG-2-arm, 5K-PEG-2-arm, and 20K-PEG-2-arm. The molar ratio (1:1 of [NB]:[thiol]) and concentration (5% w/v) were kept constant in all cases. Each sample showed elastic behavior after cross-linking, and marginal changes in the mechanical properties were observed as a function of length. A delayed speed of cross-linking was observed with an increasing molar mass of the cross-linker, and the moduli of the hydrogels dropped stepwise from ~8 kPa for the short thiol cross-linker to 4 kPa for the 20K-PEG-2-arm cross-linker (**Figure S15**). The experiments do not support an increase in inter-fiber cross-linking with the higher lengths, yet do show that the mechanical properties are slightly perturbed by larger polymers. Again, the supramolecular hydrogels (before cross-linking) displayed similar equilibrium storage moduli to the cross-linked hydrogels(**Figure S15a–c**). These results further reinforced the observation that the shear moduli of the hydrogel formulations are not dependent on the covalent cross-linker as much as the initial supramolecular network formed.

If the stress on the network is not transferred to the covalent bonds until high strains, the cross-linker length series may be interesting for large deformations. We did start to observe a relative trend in the strain at break, increasing with increasing cross-linker length. The shorter cross-linkers showed a gel-to-sol transition between 200 to 400% strain, while the longer cross-linkers could withstand up to 500% strain on the rheometer (**Figure S15e**). Since shear rheology becomes less accurate at high strains, we explored the mechanics in more depth with tensile testing. During uniaxial extension, the failure strain increased with increasing cross-linker length:

~225% for short, 425% for 2K-PEG, and 550% for 5K-PEG (**Figure 4g–i**). Unfortunately, the 20K-PEG sample could not withstand the handling forces required to reliably fix the sample in the grips. Considering that the pre-cross-linked supramolecular hydrogel stretched very little (and could not withstand loading on the tensile tester), connecting the self-assembled structures through molecular bridges resulted in tunable stretchability correlated with the cross-linker length. We also observed that the tensile modulus was dependent on the cross-linker length with ~25 kPa for the short cross-linker and ~5 kPa for both the 2K-PEG and 5K-PEG (**Figure S16**). Work of extension was around ~30 kJ/m^3 for short and 2K-PEG cross-linkers, and ~55 kJ/m^3 for PEG5K cross-linker indicating that the longer cross-linker resulted in relatively higher strain energy at the breakpoint (**Figure S16**).

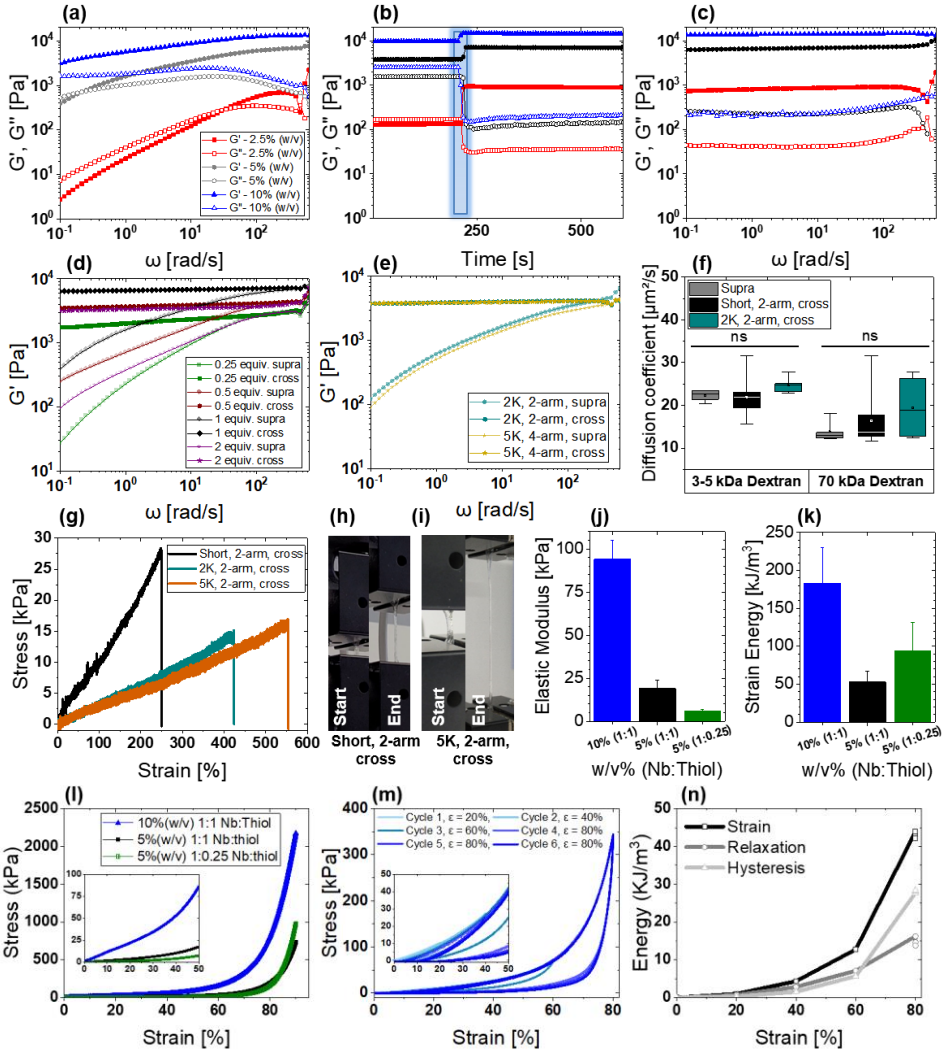

Figure 4. Mechanical properties of hydrogels before and after cross-linking. a) Supramolecular hydrogel storage moduli (G', filled symbols) and loss moduli (G", open symbols) as a function of angular frequency at 2.5%, 5%, and 10% (w/v) NB BTA. b) Evolution of (G', filled symbols) and loss moduli (G", open symbols) over time for cross-linking of the supramolecular hydrogel when exposed to a UV-light source. c) Storage moduli (G', filled symbols) and loss moduli (G", open symbols) as a function of the angular frequency of the cross-linked gels. d,e) Storage moduli as a function of the angular frequency of uncross-linked and cross-linked hydrogels using different mole equivalents of short di-thiol crosslinker (d) and using 2arm versus 4arm cross-linkers (e). f) Diffusion coefficients of supramolecular and cross-linked hydrogels using short di-thiol and PEG2K cross-linker remain similar before and after cross-linking. g–i) Stress-strain curves of the cross-linked hydrogels during a tensile test (g), and optical images of the short (h) and PEG 5K (i) hydrogels during the test. j,k) Elastic modulus (j) and strain energy (k) calculated from the compression tests. l) Compression stress-strain curves of the cross-linked hydrogels until 90% strain loaded at 1 mm/min. m) Compression stress-strain curves for ramped cyclic loading of the 10% (w/v, 1:1 NB/thiol) cross-linked hydrogel of varying strain loaded at 1 mm/min and released at 0.2 mm/min. The same sample was reloaded immediately for the next cycle without any waiting time. n, strain energy, relaxation energy and hysteresis energy calculated for each cycle in the graph (m).

Next, we wished to investigate these supramolecular/covalent hydrogels further using compression testing, in order to understand their ability to withstand the compression forces found in many load-bearing tissues. We first tested the supramolecular hydrogel, since this was precluded from the tensile testing. A 10% w/v supramolecular hydrogel was observed to have an elastic compressive modulus of 7 kPa, while the strength and strain energy at 90% strain was 327 kPa and 30.49 kJ/m^3, respectively (**Figure S17**). Then, after cross-linking (short di-thiol, 1:1 ratio), this same sample exhibited a ~10-fold increase in elastic compressive modulus (90 kPa), a ~7-fold increase in strength (~2 MPa), and a ~6-fold increase in strain energy (180 kJ/m^3, **Figure 4j,k,l,** and **Figure S17**). We also investigated the cross-linked hydrogel (using the short di-thiol) at 5% w/v with a 1:1 and 1:0.25 ratio of [NB]:[thiol] in order to probe both the effect of concentration and cross-link density. The elastic moduli were 20 kPa and 5 kPa and the compressive strengths were ~0.5 MPa and ~1 MPa for the 5% 1:1 and 1:0.25 hydrogels, respectively (**Figure 4j,k,l**). These results indicated the ability to tune the compressive moduli as a function of both the concentration of the macromonomer and the concentration of the cross-linker. Important for tissue engineering applications, these elastic moduli (between 5–90 kPa) fall within the range observed for various native tissues,[43] and the compressive strengths (~0.5–2.5 MPa) are within in the range of biological tissues such as cartilage[44] and the human Annulus Fibrosus.[45]

During these compression tests, we noticed that the supramolecular hydrogels exhibited pseudoplastic deformation (**Figure S17**, shown for 10% w/v), while none of the cross-linked hydrogels fractured even under 90% compression (**Figure 4l**). Visually, we observed elastic recovery rates corresponding to their moduli and cross-link density after these compression tests. Near instantaneous recovery was observed for the 10% (w/v, 1:1 [NB]:[thiol]), while the 5% (w/v, 1:1 [NB]:[thiol]) recovered ~ 93% of its original height in under 2 minutes and the 5% (w/v, 1:0.25 [NB]:[thiol]) recovered greater than 90% of its height in 20–30 minutes. This elastic recovery behavior can be expected since the covalent cross-links store energy elastically, and the elastic recovery can be enhanced with the increasing number of covalent cross-links.[7]

Seeing this clear trend in elastic recovery after the compression test, the combination of supramolecular and covalent cross-links was investigated for their ability to effectively dissipate energy reversibly. Performing cyclic loading from 20–80% strain revealed that the 10% 1:1 ratio hydrogel had enhanced hysteresis (area between loading and unloading curves) with increased strain, consistent with an effective dissipation mechanism. The loading cycle curves matched well, demonstrating elastic recovery and no appreciable change in the elastic modulus was observed (**Figure 4m)**. Interestingly, during a constant strain of 80% in three consecutive cycles without any lapse time, the maximum stress and strain energy remains the same (**Figure 4n**) and no softening was observed[46], which usually occurs in classical double networks[19] and hybrid hydrogels.[7] The data suggested that the supramolecular interactions are disrupted with the applied strain, yet were able to rapidly and reversibly recover without rupturing covalent bonds. Furthermore, while individual molecules may pull out of fibers during high strain, fibril sliding (like in collagen fibrillar sliding[1]) could also contribute significantly to energy dissipation. During

this energy-dissipating rearrangement of the supramolecular polymers and network, the covalent bonds resist deformation by storing elastic energy and enabling elastic recovery. Using the above-proposed mechanism, we could also rationalize the bimodal stress-strain response observed during compression: a compliant response at low strains and a stiff response at higher strains like the load-bearing soft collagenous tissues.[47]

The supramolecular and cross-linked hydrogels showed similar diffusion coefficients

So far, our experiments have suggested that the topology of the underlying supramolecular hydrogel network after cross-linking is not noticeable at low deformation, yet is only discernible upon the application of larger amounts of force or strain. To further understand the nanoscale structure before and after cross-linking, we surmised that the diffusion coefficient should also remain relatively constant if there are no significant changes to the low-strain moduli. We turned to fluorescence recovery after photobleaching (FRAP) experiments with two different dextrans sizes (3-5 and 70 kDa) to probe this hypothesis. No significant difference in diffusion coefficient was observed between the supramolecular NB BTA hydrogel and those samples cross-linked with short di-thiol or 2K-PEG (**Figure 4f and Figure S18**). We did observe the normal decrease in diffusion coefficient as a function of the dextran size. Our observations differ from traditional covalent hydrogels in which network density and topology typically influence the diffusion coefficient of analytes[48]; however, our strategy closely mimics Nature's approach of cross-linking semi-flexible bundles of fibers with an open porous network without appreciable changes in the open structure.[49] Our results point to a similar mechanism in these synthetic supramolecular/covalent materials. Altering the topology and connectivity of the network on a molecular level is only seen at higher forces and strains, yet still allows the free diffusion of analytes throughout the sample.

The supramolecular and cross-linked hydrogels are self-healing

With a biomimetic and tough hydrogel in hand, we then proceeded to investigate the self-healing capability of the NB BTA hydrogels. Mainly, could the supramolecular self-assembly still impart self-healing, and what were the limits when subjected to covalent bond formation? Furthermore, self-healing is an important property required for hydrogels to quickly reform the network and maintain shape fidelity in a variety of applications from reprocessable materials, to injectability and 3D printing. The supramolecular NB BTA hydrogels (5% and 10% w/v) showed self-healing in under 2 minutes after cutting into two pieces and then pressing firmly together (**Figure S19**). More quantitatively, the self-healing of the networks was investigated using shear rheology and determined to be within a few seconds (**Figure 5a and Figure S19**).

We subsequently determined the ability of hydrogels cross-linked with short di-thiols to self-heal after 2 and 24 hours (5% w/v with di-thiol 0.5, 1, and 2 equivalents, **Figure S20 and 21**). The hydrogels were cut into two pieces, which were then manually re-joined. While the 1-mole equivalent provided little resistance to separation (**Movie S8)**, the 2-mole equivalents (**Movie**

S9) provided relatively more resistance. The sample with 0.5-mole equivalents offered the most resistance and required repeated mechanical stretching to separate the two pieces (**Movie S7**). A similar trend was observed for longer time points; however, the self-healing was slightly more pronounced after 24 hours and required more force to disrupt cohesion. The self-healing behavior of the cross-linked sample can be attributed to the reversible supramolecular associations of NB BTAs; however, it is worth noting that all samples eventually broke at the original defect. The samples with 0.5 and 2 molar equivalents likely showed better self-healing due to fewer covalent cross-links and more mobility of the supramolecular macromonomers within the hydrogel.

Finally, we investigated the self-healing of the hydrogels using shear rheology of cross-linked hydrogels at 2.5%, 5%, and 10% (w/v) with an equimolar amount of short cross-linker (1:1 [NB]:[thiol]). In contrast to qualitative self-healing, the shear rheology showed near-instantaneous self-healing/recovery. We also tested the longer cross-links (2K-PEG-2-arm, 5K-PEG-2-arm, and 20K-PEG-2-arm) and found rapid self-healing (**Figure S22**). In line with previous experiments, we find that self-healing kinetics on the rheometer do not translate well into macroscopic self-healing of hydrogel monoliths.

The NB BTA supramolecular hydrogels exhibited shear-thinning properties

Shear-thinning behavior is highly beneficial to engineers in hydrogels for injectability and bioprinting. The NB BTA hydrogel at 10% and 5% (w/v) shows almost a linear decrease in complex viscosity with increasing shear rate and reached 30 Pa s and 8 Pa s, respectively, at shear rates of 6 Hz (**Figure 5b and Figure S23**). A continuous flow sweep also showed a continuous decrease in viscosity with an increasing shear rate (**Figure S23**). These rapid shear-thinning properties can be attributed to fast exchange rates (i.e., low lifetimes) of NB BTA molecules between fibers. This shear-thinning and self-healing forecasted a promising potential for these hydrogels in injectable and 3D bioprinting applications.

The NB BTA hydrogel is injectable and creates anisotropically aligned fibers after injection and cross-linking

Knowing that the NB BTA hydrogel exhibits good self-healing and shear-thinning, we next moved to investigate the injectability of the hydrogel and the post-injection hydrogel morphology. For both the 5% and 10% (w/v) hydrogels, manual injection with a 22-gauge needle led to the extrusion of continuous filaments with good shape fidelity (**Figure S23 and Movie S5**). Overall, the 5% hydrogel provided easier injection (less pressure) and more continuous fiber formation upon injection compared to the 10%. These hydrogels can also be shaped upon injection; we were capable of extruding different institute names (BIOMATT, MERLN, CTR) by hand (**Figure S23**).

The micron-scale structural features of the extruded hydrogels were investigated after injection and before/after cross-linking using cryo-SEM. The extruded supramolecular hydrogels showed anisotropically aligned bundles of fibers that were more compact and strongly bundled when

compared to the non-extruded supramolecular hydrogel (*vide infra*, **Figure 5e, and Figure S10**). After cross-linking, the fiber bundles were slightly distorted, yet were largely retained as in previous experiments. Of note, during the sample preparation for cryo-SEM, the cross-linked hydrogel took a large amount of force to break, which could result in the observed non-uniform and distorted structures (**Figure 5f and Figure S10**).

The NB BTA can be used as a biomaterial ink for the 3D printing of a cartilage structure

After establishing that syringe-extruded hydrogel retained an aligned bundle morphology, hydrogels at 5% and 7.5% (w/v) were tested for 3D printing using pressure-based extrusion. The hydrogel at 5% (w/v) displayed more continuous and uniform filaments compared to the 7.5% (w/v) hydrogel. The applied pressure to extrude 5% was 90 kPa compared to the 200 kPa required for 7.5% (w/v) using a 22 gauge conical nozzle, while the field knows that high pressures can impact cell viability.[33] Correspondingly, hydrogels at 5% (w/v) were used for 3D printing of a single filament, a grid-like structure, 6 layers of a hollow cube, a hexagonal structure, and then 8 layers of a circular hollow tube (**Figure 5g–i**). All of the structures were printed with uniform filaments and retained their shapes post-printing. Subsequently, a solid-tissue-like structure was printed, namely a 3D model of a human meniscus. The meniscus was chosen given the hydrogel's toughness and fast elastic recovery. A meniscus cartilage model (meniscus shape, 15 x 17 mm, 6 layers, and rectilinear infill pattern) was 3D printed (using the 5% (w/v)) into several meniscus shapes (**Figure 5 j, k and Figure S24**); in all cases, the hydrogel printed easily, the transitions from thick to thin edges were made smoothly, and the hydrogel shape remained stable post-printing.

Next, we investigated the effect of cross-linking on the resolution, retention of fine structural details, and mechanical robustness during printing. A meniscus was 3D printed using the 5% (w/v) hydrogel with the short di-thiol cross-linker. The hydrogel was cross-linked by irradiation using 365 nm UV-light from 30–60 seconds between each layer (**Figure 5l,m and Figure S25**). The 3D printed and cross-linked hydrogels retained fine details of the 3D cartilage model when compared to the supramolecular hydrogel (*vide supra*). To demonstrate toughness, the printed cartilage model was placed between two glass plates, and a student weighing 60 kg was placed on the plates for 30 seconds repeatedly (three times). After unloading, we observed that the hydrogel did not break and recovered more than 90% of its original height within 5 minutes (**Figure 5p–r**).

Tissues and especially tissue interfaces are rarely uniform. They often possess spatial gradients of mechanical properties; for example, the stiffness increases in cartilage tissue from the superficial soft zone to the calcified deep zone.[43] In line with this reality, we wondered if this platform could enable zonal gradients by printing using a layer-by-layer approach. Utilizing the self-healing capacity of our hydrogels, along with the knowledge that the equilibrium storage modulus can be tuned by changing cross-linker mole equivalents (*vide supra*), we aimed to create

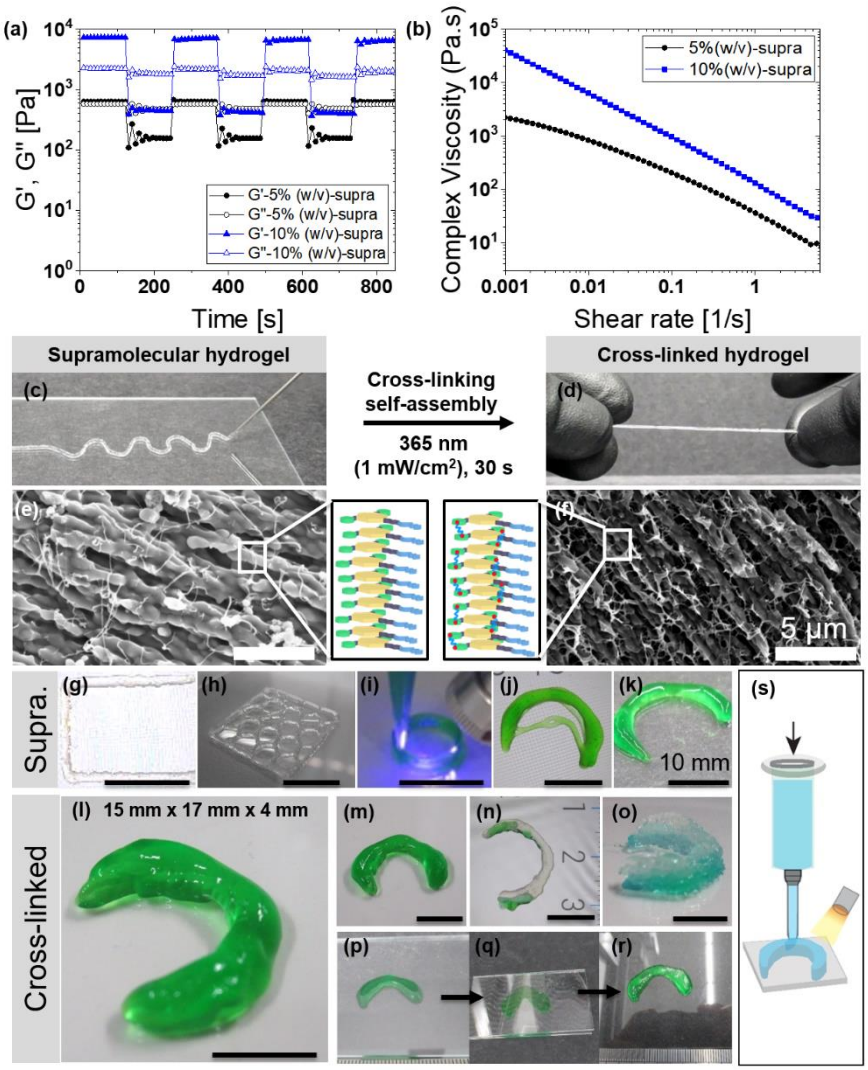

Figure 5. Shear-thinning, self-healing, injectability and 3D printability of NB BTA hydrogel. a) a self-healing rheology test showed recovery of the storage modulus before and after rupturing the gel network indicating rapid self-healing behaviour. b) Decrease in complex viscosity with increasing shear rate showed shear-thinning behaviour of the hydrogels. c) Extruding of supramolecular hydrogel (5% w/v) into a continuous uniform fibre with 1 equivalent short thiol crosslinker and 2mM LAP photoinitiator. Extruded fibre was crosslinked using 365 nm UV-light. d) Cross-linked fibre was observed to be strong and stretchable. e, f) Cryo-SEM images of non-crosslinked (e) and crosslinked (f) hydrogels after extruding through 22 gauge syringe showed fibril morphology before and after crosslinking. g–i) Supramolecular hydrogel extruded into single filament (g), hexagonal (h), and hollow tube structures (i). j, k) Hollow (j) and solid (k) Meniscus cartilage model 3D printed using supramolecular hydrogel. l,m, Meniscus cartilage model printed with 5% hydrogel, then crosslinked after printing each layer. n, o) Cartilage model printed with 5% hydrogel with inks with different equivalents of thiol crosslinker. Green ink (top part in n and bottom part in o) has 1:1 ratio of NB to thiol and clear ink (bottom part in n and top part in o) has 1:0.5 ratio of NB to thiol. p–r) Meniscus cartilage model recovery before (left) and after (right) 60 kg of weight exerted three times. s) Schematic of 3D printing of cartilage model using extruding printer.

a prototype of a zonal construct. Toward this aim, we created a NB BTA cartilage model with two different moduli by varying the short thiol cross-linker ratio while keeping the NB BTA 5% (w/v) constant. The different biomaterial inks were deposited at different sites on the cartilage model to show that the inks can be deposited spatially with desired mechanical properties. The printed gradient was then cross-linked as a single solid entity without any discontinuities or cracks (**Figure 5n,o**).

Cross-linking with matrix metalloproteinases (MMPs) enzyme-sensitive cross-linkers enables a degradable and dynamic hydrogel

So far, all the hydrogel formulations created within this study result in biomimetic, but not biodegradable constructs. An appealing approach would be to create a degradable cross-linker, which can impart cell-responsive degradability to the hydrogel. Consequently, we moved to develop cross-linked hydrogels using an MMP-sensitive di-thiol cross-linker. We used a CGDG-VPLSLYSG-GDGC cross-linker, which is susceptible to degradation upon exposure to MMP2 and MMP9 enzymes. This peptide cross-linker led to successful hydrogel formation, and we first studied the hydrogel degradation using type IV collagenase in DMEM (comprised of MMP-2 and MMP-9). The hydrogel with the MMP-sensitive cross-linker degraded within 10 days (100% mass loss), while even after 20 days, the non-degradable hydrogels was a maximum of 10% weight loss; a hydrogel cross-linked using a 1:1 ratio of MMP-sensitive:non-degradable cross-linkers exhibited approximately 20% mass loss. We further observed that degradation was delayed when the media had fetal bovine serum (FBS, 10% by volume, **Figure S26**), perhaps due to reduced activity of MMP2 and MMP9 in the presence of FBS. Taken together, these findings show that the incorporation of MMP sensitive cross-linker into the NB BTA hydrogels leads to a reversibly dynamic hydrogel for creating a reversibly dynamic hydrogel, of which degradation rate can be partially controlled via the mixing of cross-linker types.

The NB BTA hydrogels maintained cell viability in bulk, after injection, and during bioprinting

To evaluate the bioprintability of the NB BTA hydrogels, relevant to tissue engineering applications, we determined the cell viability of printed cell-laden hydrogels. Towards this aim, we chose to work with ATDC5 chondrocytes, a widely studied cell type for cartilage tissue engineering and cartilage-like matrix production. ATDC5s were encapsulated within the NB BTA hydrogels (5% w/v) and cell viability was observed in the supramolecular hydrogel before and after cross-linking (1:1 NB/thiol, schematically shown in **Figure 6a**). After 2 hours, the hydrogels were stained with calcein-AM (green=live cell) and ethidium homodimer (red=dead cell) to determine cell viability. Quantification of the cells showed that >80% of cells were alive after 2 h in both the supramolecular and cross-linked hydrogel (**Figure 6b,c, and Figure S27**). Similar cell viability (>80% by numbers and >90% of the total cell area) between the supramolecular and cross-linked samples demonstrated that exposure to the cross-linking conditions did not detrimentally affect the cell viability.

Many studies have shown that shear-thinning and self-healing hydrogels protect cells from shear stresses during injection and extrusion bioprinting,[31,32,50] so we investigated the NB BTA hydrogel as a potential injectable cell carrier. ATDC5 cell-laden hydrogels (4% w/v) were extruded manually (using hand pressure) through a 22 gauge syringe (ID=0.41 mm, schematically shown in **Figure 6a**) and cell viability was determined before and after cross-linking. We observed that >80% via cell counting and >90% via cell area were alive before and after cross-linking; this result suggested that cells remained highly viable in the NB BTA hydrogel after extrusion and the post-extrusion cross-linking did not decrease cell viability (**Figure 6d,e, and Figure S27**).

After demonstrating that the NB BTA hydrogel was a suitable carrier for cell viability and extrusion, we investigated bioprinting of a complex meniscus shape. Bioprinting (4% w/v) the same meniscus shape as above, yet now using ATDC5 chondrocytes, allowed the determination of cell viability by staining with a live-dead assay at day 1, 5, and 11. We observed that the cells remained highly viable (green color: live cells) through day 11 (**Figure 6 g–j**), providing confidence to pursue further bioprinting studies with this material.

The NB BTA hydrogel supported primary cartilage-specific proteins in a bioprinted construct

Finally, we studied the potential of the biomimetic and tough NB BTA hydrogel with controlled degradability for the differentiation of human mesenchymal stem cells (hMSCs) towards the chondrogenic lineage in a bioprinted scaffold. Here we chose to use hMSCs spheroids (mini tissue blocks, schematically shown in **Figure 6f**) as they are a promising platform for chondrogenic differentiation and have widespread therapeutic potential. Uniform hMSC spheroids were produced using a micro-molded non-adhesive agarose hydrogel, then the produced spheroids were bioprinted in the 4% w/v NB BTA hydrogel in a meniscus shape. In this study, we chose to study a partially (half MMP sensitive and half short di-thiol cross-linker) and non-degradable (fully short di-thiol) cross-linked hydrogel in order to study the degradation capabilities of the bioprinted constructs. The spheroids remained stable and maintained their near-spherical morphology in both hydrogels; however, we did observe some elongation of the spheroids in the fully short di-thiol hydrogel, likely due to shear forces during extrusion (**Figure 6l and Figure S29**). The bioprinted constructs were cultured under both basic and chondrogenic differentiation conditions through day 28. The short di-thiol cross-linked hydrogel stayed stable for 28 days in both the basic and chondrogenic media cultures at 37 °C; however, the hydrogel partially cross-linked with MMP-sensitive cross-linkers degraded in 14 days in the chondrogenic differentiation media and 21 days in the basic media (**Figure 6o and Figure S29,30**). Degradation of these MMP-sensitive constructs in the presence of hMSCs spheroids indicated that the hMSCs were actively secreting MMP2 and MMP9 enzymes.

We then investigated the cartilage-specific protein production, i.e., collagen II in the surviving constructs. The presence of collagen II was observed clearly after day 28 in culture and indicated

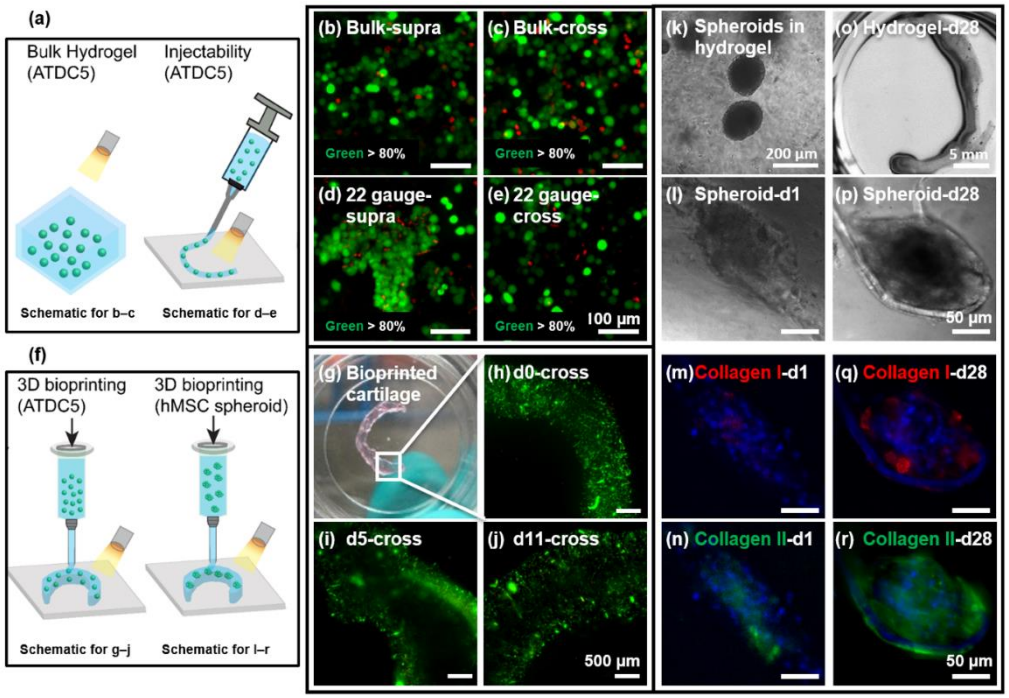

Figure 6. Cell viability after injectability and in 3D bioprinted hydrogels. a) Schematics representing bulk hydrogel and injectability method employed for cell viability in b–e. b, c) Live-dead images of ATDC5 chondrocytes in supramolecular and cross-linked hydrogel after 2 hours. Green colour represents live cell and red colour represents dead cell. d, e) Live-dead images of ATDC5 chondrocytes in after injectability through 22 gauge after 2 hours of injection. f) schematics representing 3D bioprinting of chondrocytes and hMSC spheroids employed in g–j and l–r, respectively. g) Visual image of NB BTA hydrogel bioprinted cartilage construct. Cartilage model was printed using 22 gauge and with ATDC5 encapsulated. h–j) live-dead images of cartilage model from day 0 until day 11. k) hMSC spheroids retains spherical morphology after mixing in NB BTA hydrogel. l–n) hMSC spheroid image (l) and immunostaining for collagen I (m) and collagen II (n) after 1 day of culture in hydrogel. n, macroscopic hydrogel (crosslinked using short di-thiol) picture after 28 days in culture under chondrogenic differentiation conditions. p–r) hMSC spheroid image (p) and immunostaining for collagen I (q) and collagen II (r) after 28 days of culture in hydrogel.

the *in vitro* maturation and chondrogenic differentiation of the hMSCs (**Figure 6n–r and Figure S31**). We also observed a small amount of collagen I after day 28 in culture, usually on the outer edge of the spheroids **Figure 6m,q**. In the negative control sample (after 28 days in basic medium), immunostaining did not show collagen II, and a limited amount of collagen I was observed (**Figure S31)**. Overall, these results showed that the hMSC spheroids successfully produced collagen II, a cartilage-specific ECM protein, in the bioprinted NB BTA hydrogel scaffolds, and that the spheroids stayed stable and functional in the bioprinted constructs.

Outlook

Nature has extensively utilized the synergistic effect of combining 1D supramolecular fibril assembly with covalent cross-linking for designing materials with unique mechanical properties.

Our findings suggest this ubiquitous, yet overlooked, strategy may be highly relevant in the design of synthetic biomaterials. Herein, we designed a synthetic hydrogel that combined the synergism of supramolecular assembly (first step) and covalent cross-linking (second step). The hydrogel mimicked the fibrous architecture of the native ECM, and the cross-linking of 1D supramolecular assemblies allowed tuning of the mechanical properties without affecting the fibrous morphology or diffusion of sample analytes through the material. Notably, the hydrogel platform allowed for tuning of the stiffness (5–100 kPa), toughness (50–180 kJ/m^3), and strength (0.5–2 Mpa) of the hydrogels. The NB BTA hydrogel also exhibited room temperature recovery during ramped cyclic loading tests (between 20–80% strain), and no softening was observed. These NB BTA hydrogels were highly stretchable to ~550% strain and exhibited excellent shear-thinning, self-healing, and injectable properties. The reversible self-assembly in the supramolecular hydrogel enabled extrusion and 3D bioprinting, while the thiol-ene modification offered instantaneous cross-linking to retain sharp features on the printed construct. The supramolecular hydrogel can be 3D printed in many types of shapes ranging from a single filament to a complex cartilage model with good shape fidelity, with and without secondary cross-linking. Furthermore, the NB BTA hydrogel allowed the 3D printing of gradient, yet cohesive, structures with distinct mechanical properties such as stiffness and toughness, and can remove the need to print different materials with different cross-linking mechanisms for each bioink. While tough supramolecular hydrogels have been reported before, this is the first synthetic 1D fibrillar and tough supramolecular hydrogel with the capacity to be bioprinted into complex 3D structures. The NB BTA hydrogel exhibited excellent biocompatibility with chondrocytes (ATDC5) and supported hMSC differentiation to produce cartilage-specific proteins. In addition, just like in the natural ECM, we were able to engineer cell-mediated matrix degradation and remodelability by cross-linking with MMP cleavable peptide cross-linker.

Our approach opens up a conceptual framework to tailor supramolecular interactions for the design of nanoscale architecture, followed by covalently (but reversible or degradable) fixing the hierarchical structure. This strategy provides access to supramolecular assemblies for obtaining biomaterials with desired structures and mechanical properties previously unattainable by only supramolecular or covalent network strategies. Our approach thus can be generalized to build a 1D fibrous structure with a given set of structure-property relationships and can be expanded not only into the design of hydrogels within bioinks and biomaterials but also in numerous other applications where strength and structure are needed. For example, this approach can likely be generalized to other supramolecular polymers and allows access to harnessing the specificity and reversibility of supramolecular interactions to design novel materials with unique architectures, multiple functionalities, and mechanical properties. Specific to bioinks, the design of modular inks with controlled structure, tunable mechanical properties, and 3D bioprinting for creating spatiotemporal mechanical and biological gradients will be an exciting, challenging, and essential future step.

Methods

Materials

All chemicals were purchased from Sigma-Aldrich unless otherwise stated. Bicyclo[2.2.1]hept-5-en-2-ylmethanamine, also known as, 5-Norbornene-2-methylamine, a mixture of isomers, was purchased from TCI Chemicals. Silica gel (precoated 0.25 mm, 60-F254) was purchased from Merck. N, N-Diisopropylethylamine (DIPEA) used in the desymmetrization reaction was dried using sodium hydroxide pellets.

Synthesis of bis-norbornyl amide mono-pentafluoroester BTA precursor (perfluorophenyl 3,5-bis((bicyclo[2.2.1]hept-5-en-2-ylmethyl)carbamoyl)benzoate

The bis-norbornyl amide mono-pentafluorphenyl ester was synthesized according to our previously published protocol and reproduced for this study.[40] In a dry, round-bottom flask, maintained under a nitrogen atmosphere tris(perfluorophenyl) benzene-1,3,5-tricarboxylate (510 mg, 2.2 mmol, 1 equiv.) was dissolved in 40 mL anhydrous dichloromethane (DCM). The above solution was cooled in a water-ice bath for 20 minutes and then a solution of anhydrous N, N-diisopropylethylamine (DIPEA) (376 μL, 2.2 mmol, 1 equiv.) in 18 mL anhydrous DCM was added into the reaction flask. Next, a solution of bicyclo[2.2.1]hept-5-en-2-ylmethanamine (186 μL, 1.45 mmol, 0.67 equiv.) in DCM (36 mL) was added drop-wise to the reaction flask in approximately 20 minutes under nitrogen atmosphere. The reaction was stirred for 2 hours at 4 ºC, after which the reaction mixture was vacuum-dried to remove excess solvent. The precursor molecule (perfluorophenyl 3,5-bis((bicyclo[2.2.1]hept-5-en-2-ylmethyl)carbamoyl)benzoate) (from crude) was separated on silica gel using eluent DCM/acetonitrile (92.5/7.5) by volume. The product was obtained as a white powder in a 52% (222 mg) isolated yield, and the ^{1}H NMR matched the previous report.[40]

PEG20K-bisamino dodecane synthesis

PEG-bisamino dodecane was resynthesized according to our previously published protocol[40]. Briefly, in the first step CDI activated PEG20K was synthesized by using bishydroxy PEG20K and carbonyldiimidazole (CDI). In the second step, the polymer solution was added dropwise to the excess solution of 1,12 diaminododecane for creating PEG20K-Bisamino dodecane. The final polymer was precipitated in excess diethyl ether and characterized using ^{1}H NMR.

NB BTA macromonomer synthesis and characterization

In a dry, round-bottom flask, the BTA precursor (perfluorophenyl 3,5-bis((bicyclo[2.2.1]hept-5-en-2-ylmethyl)carbamoyl)benzoate) (0.25 g, 0.43 mmol, 1.1 equiv) was dissolved in 10 mL anhydrous DCM and DIPEA (101 μL, 0.6 mmol, 1.5 equiv) was added into the reaction flask. Subsequently, PEG bisaminododecane (4 g, 0.4 mmol, 1 equiv.) solution, dissolved in anhydrous DCM (10 ml) by vigorous stirring, was added dropwise to the reaction flask. The reaction mixture was stirred for 40 hours at room temperature (~20 °C) under a nitrogen atmosphere.

Excess solvent was removed *in vacuo* and the crude reaction mixture was precipitated in excess cold diethyl ether twice and NB BTA macromolecule was obtained as a white powder in 98% yield (3.9 g). A second purification was done by dialyzing the sample in methanol against methanol to remove any unreacted small molecule impurities and the target compound was NB BTA obtained in 93% yield (2.8 g out of 3 g). Gel permeation chromatography (GPC) analysis showed a molecular weight of around 23000 g/mol with a Đ of 1.2. ^{1}H NMR shows that macromonomer is pure. H ^{1}NMR and GPC characterizations are shown in **Figures S2 & 3.**

Self-assembly studies sample preparation for Nile red and cryo-TEM

NB BTA (1 mg, 2 mg, and 5 mg) was weighed and dissolved in 50–100 μL methanol with the help of heating using a heat gun. The NB BTA solution in methanol was either injected into water or water was added to the methanol solution, and the final volume of the solution was adjusted to 1000 μL (1 mL). The solution was heated (until it become opaque using a heat gun) and vortexed. The same procedure was repeated two times and then the NB BTA solution was placed on a heating plate maintained at 80 °C. The temperature was turned off for gradual cooling of the NB BTA solution to room temperature. The NB BTA solution was aged overnight (16–20 hours) at room temperature before investigating Nile Red and cryo-TEM studies.

For cross-linking NB BTA self-assemblies, NB BTA at 5 mg/mL was dissolved in 50–100 μL and then the total volume was adjusted to 900 μL. A similar heating, vortexing, and cooling procedure was repeated as above for supramolecular solutions. After overnight (16–20 hours) aging of NB BTA solution at room temperature, LAP photoinitiator and cross-linker solutions in Milli Q water were added and the total volume was adjusted to 1000 ul. LAP final concentration was 2mM and NB to thiol was in a 1:1 equimolar ratio to the number of norbornene groups. The solution was cross-linked in a 365 nm UV oven at ~1mW/cm^2 for 1–4 minutes.

Nile red

For Nile red studies, a 200 μl sample was taken from the solutions prepared above for supramolecular assemblies at 1 mg/mL, 2 mg/mL, and 5 mg/mL, and 3 μL Nile red solution (from a stock solution of 315 μM) was added to adjust final Nile red concentration to 5 μM. The samples, protected from light, were left at RT for a minimum of 30 minutes and fluorescence was recorded using a ClarioStar plate reader (BMG LabTech) nm) at excitation wavelength 500 nm and emission wavelength 550–740 nm.

Similarly, for the cross-linked sample at 5 mg/mL, after exposure to UV, 3 μL Nile red solution was added to 200 μl of NB BTA solution prepared above and incubated for a minimum of 30 minutes. Nile red final concentration was 5 μM. The supramolecular NB BTA sample without a cross-linker was used as a control and also has a Nile red final concentration of 5 μM.

Cryo-TEM

NB BTA sample was prepared either at 5 mg/ml or 10 mg/ml in water as described above in the self-assembly sample preparation section. The cryo-TEM experiments were performed on a FEI Technai 20. The grid preparation, sample vitrification, and imaging procedure was performed as described in the study[40].

Cryo-SEM

Hydrogel samples were made in water at 4% and 5% (wt) using the heating-cooling procedure described below in the hydrogel formation section. We used high-pressure freezer planchettes to embed the hydrogel sample and the hydrogel sample was cooled in liquid Ethane (−18 °C). Very quickly, the sample was transferred to liquid nitrogen (-196 °C) and freeze-fractured by pulling the planchettes inside the liquid nitrogen bath. Using a vacuum cryo-transfer shuttle of the SCIOS system, the specimen carrier was transferred to the CRYO-SEM (SCIOS from FEI) and cooled to −187 °C. The sample was sputter-coated using an in-built platinum coater. The cryo-scanning electron microscope was operated at an accelerating voltage of 2 kV.

Hydrogel formation

NB BTA hydrogelator as solid polymer was weighed and added in a clear glass vial (size of 2–4 mL) and milli-Q water was added to adjust concentration to either 2.5% w/v, 5% w/v, and 10% w/v. Briefly, for 5% w/v, 10 mg of NB BTA hydrogelator was weighed in a glass vial and 200 µl of water was added and heated until the solution become opaque, due to the lower critical solution temperature (LCST ~80 ºC) of the PEG20K. Next, opaque solutions were vortexed. The same procedure was repeated twice. The hydrogel was centrifuged at 2000 g for around 10 minutes to ensure any residues on the glass walls settled down at the bottom of the glass vial. In the last step, the gel was cooled with a controlled decrease in temperature: the hydrogel mixture was placed on a heating plate set to 80 ºC and the temperature was turned off and the hydrogel gradually cooled to lab temperature set to ~20 °C.

For cross-linked hydrogels, the hydrogel was made initially at a higher concentration and aged overnight. The next day photoinitiator (LAP) and short thiol cross-linker solution were added to adjust the final concentration to 2.5%, 5%, and 10% w/v. For example, for 5% w/v and 1:1 ratio of norbornene to thiol for a short cross-linker, 10 mg were dissolved in 125 µL water (4 mM, 8% w/v initial concentration,) and the hydrogel was made with the above-described procedure heating, vortexing, and aging overnight. Then 25 µL of 38 mM of short thiol cross-linker, 25 µL of 16 mM of LAP photoinitiator solution, and 25 µL of Milli-Q water was added to adjust the final concentration of hydrogelator to 2.4 mM (5% w/v), LAP to 2 mM and short thiol final concentration to 4.7 mM. The hydrogel was broken and thoroughly mixed with the LAP and cross-linker solutions and the hydrogel was then equilibrated between 1–3 hours before cross-linking for uniform distribution of cross-linker.

For 2K, 5K, and 20K PEG di-thiol cross-linkers, the same above procedure was repeated and for equimolar concentration, the required mass of the cross-linker was weighed; for example, 2.1 mg 2K di-thiol was weighed and to which 50 μL milli-Q water and 25 μL of 16 mM of LAP photoinitiator solution was added for adjusting concentration (mM) values as described above. The rest of the procedure was the same for making a hydrogel. For MMP-sensitive hydrogels, the cross-linker CGDGVPLS↓LYSGGDGC was used. The peptide cross-linker 1.4 mg was dissolved in 50 μL Mili-Q water and 25 μL of 16 mM of LAP photoinitiator solution. For different ratios of NB to thiol, mole equivalents and the concentration of cross-linkers were adjusted accordingly.

Rheology

Rheological measurements were performed using a DHR-2 rheometer (TA instruments). We used 20 mm cone-plate geometry with a 2.002° angle. All measurements were performed at room temperature (~20 °C). For removing any mechanical history, a rejuvenation protocol was performed, which was composed of strain amplitude sweep until 400–1000% strain (at frequency 1 rad/s) for rupturing the network followed by time sweep (at 1% strain) for observing aging kinetics. Oscillatory strain amplitude sweeps from 1 to 1000% were carried out at an angular frequency of 1 rad/s. A frequency sweep was performed at 1% oscillation strain ranging from 0.1 rad/s to 627 rad/s. Self-healing measurements, in the first step, the hydrogel network was ruptured at 400% strain followed by the recovery phase at 1% strain. A minimum of 3 cycles were done for the self-healing test. Cross-linking of hydrogel was performed in a time sweep at 1% strain and 10 rad/s using UV light intensity of approximately ~10 mW/cm^2.

Uniaxial compression tests

All uniaxial compressive tests were performed at room temperature using the Shimadzu AGSX universal mechanical testing instrument equipped with a 500 N load cell. Hydrogel specimens for mechanical testing were prepared using cylindrical-shaped PDMS molds with a diameter of 10 mm and height of 2 mm or a diameter of 8 mm and height of 3 mm. The round PDMS mold was placed inside 12 well plates and then the mold was filled with hydrogel using a spatula. The well plate was covered with the lid and centrifuged at 3000g to remove any possible trapped air bubbles. The well plate lid was covered with parafilm and stored overnight in the fridge at 4 ºC before testing to avoid any water evaporation A preload force of 0.01–0.2 N was applied to ensure good contact between hydrogel and compression plate. Each sample was deformed to 90% strain at a constant strain rate of 1 mm min^{-1}. Cross-linked hydrogel tests were carried out in triplicate and supramolecular gel at 5% w/v and 10% was done in duplicate. Elastic modulus was calculated as the slope of the stress-strain curve between either 0–10% or 0–20% strain region since correlation stays linear.

Cyclic compression tests

To characterize the mechanical behavior of the materials in the loading condition close to the working conditions and to evaluate the reversible behavior of hydrogels and their ability to recover, besides the compression measurements, multiple cyclic loading-unloading compression experiments were performed using the Shimadzu AGSX universal mechanical testing instrument equipped with a 500 N load cell. The specimens were compressed to 20% of the initial height in the first cycle at a deformation speed of 1 mm min^{-1} and then released immediately at the velocity of 0.2 mm min^{-1}. Then, the strain progressively increased to 40, 60 and 80 % in the following cycles. Moreover, three cycles of compression were applied from 0% to 80% strain. Strain energy and relaxation energy were calculated from the areas under the curve and

Uniaxial tensile tests

All uniaxial tensile tests were performed at room temperature using the Shimadzu AGSX universal mechanical testing instrument equipped with a 500 N load cell. Hydrogel samples were prepared in dog bone PMMA molds (dimensions L= 26 mm, W= 2 mm, D= 4 mm). All the tensile tests were repeated at least 3 times and each hydrogel was stretched at a strain rate of 5 mm min^{-1} until failure.

Fluorescence recovery after photobleaching (FRAP)

Hydrogels of 200 uL in volume were prepared in 4-chamber 35 mm glass-bottom dishes (D35C4-20-0-N, Cellvis), 1 mL of FITC-labelled dextran solution (3-5 or 70 kDa at 0.1 mg/mL, Sigma-Aldrich, FD4-250MG and 46945-100MG-F) was added and incubated overnight at 4°C in the dark. Fluorescent recovery after photobleaching (FRAP) imaging was performed on a Leica TCS SP8 STED using the FRAP modules of Leica Application Suite X software (LAS X FRAP). FRAP bleaching was performed on a z-height of 40 μm in each hydrogel. Parameters were set as followed: bleaching point of 60 μm diameter, pre/post bleaching laser at 5%/ 488 nm/ 800 gain, and a time per frame of 0.223 sec. After 5 frames pre-bleach (1.2 sec), samples were bleached for 90 frames (21.2 sec), and fluorescent recovery was gathered for 400 frames post-bleaching (110.5 sec). ROI data were extracted in Fiji ImageJ-win64. Area and mean grey values were obtained for the bleach, total and background ROIs. The obtained values were imported in the open-source application FrapBot[51] to obtain the $\tau_{1/2}$ (half-time) of the fluorescent recovery curve. Obtained $\tau_{1/2}$ was used to calculate the diffusion coefficients by the Soumpasis equation, with D=diffusion coefficient, r=radius of the bleaching area, and $\tau_{1/2}$=the halftime of recovery (eq. 1). Statistical analysis was performed in GraphPad Prism 8.2.0, one-way ANOVA.

$$D = 0.224 * \left(\frac{r^2}{\tau_{\frac{1}{2}}}\right) \qquad \text{eq. 1}$$

3D printing

NB BTA hydrogels, without photoinitiator, at a final concentration of 5% w/v was tested. To investigate printability, we used the extrusion-based BioX bioprinter (CellInk, Sweden). All printing was performed at room temperature. Conical plastic needles (VIEWEG GmbH, Germany) were fixed to 3 mL syringes with 22 gauge nozzle diameter (ID = 0.41 mm). The pressure applied to form a continuous filament depends on the hydrogel formulation, which was around 90 kPa. The infill density was set to 100% and the distance from the needle to the print surface was optimized so that the leading edge of the flow was in line with the needle. In order to explore the printability of NB BTA hydrogels, 4 structures were printed: (a zigzag path, 10 mm in width and 32 mm in length), a 3-layer hollow cube (10 mm in width and length and 2 mm in height), grid-like structures (two layers 10 x 10 grid, 15 mm in width and length), and 3D meniscus (10.8 mm x 8.9 mm x 1.4 mm). Printability tests were carried out using a plastic petri dish as the printing surface. We then imaged each print (16-megapixel camera) and used ImageProPlus (MediaCybernetic, USA) software to threshold images and measure dimensions.

Degradation mass loss studies

The cross-linked hydrogel was made following the procedure mentioned in the hydrogel formation section above. Hydrogel cross-linked with short di-thiol (1:1 ratio of NB to thiol), MMP sensitive di-thiol (1:1 ratio of NB to thiol), and cross-linked with the 0.5-mole equivalent of short thiol and the 0.5-mole equivalent of MMP sensitive thiol cross-linker was made. Degradation was studied in DMEM media without FBS and with 10% FBS. Degradation media has 200 ng/ml of type IV collagenase (MMP-2 and MMP-9) until day 3 and then increased to 500ng/ml from day 3 to day 20. Collagenase IV concentration was increased for accelerating degradation since hydrogel barely degraded until day 3 in 200ng/ml collagenase IV. The hydrogel was taken out of the media, and extra water on the surface was cleaned with tissues and then the wet weight of the hydrogel was recorded at days 1, 2, 3, 4, 7, 10, 13, 20. Data for each sample is normalized to day 1 for calculating mass loss percentage (%) or degradation over 20 days. The mass loss % of the hydrogel was quantified using the following equation.

$$Massloss(\%) = \frac{m_i - m_1}{m_1} \qquad \text{eq. 2}$$

Where m_i is the wet mass at a specific time point and m_1 is the wet mass of the gel after 24 hours in DMEM.

ATDC5 chondrocytes cell culture

ATDC5 was cultured at 37 °C in a humidified incubator with 5% CO2. Chondrocytes cell culture media for ATDC5 expansion consists of Gibco® DMEM/F-12 (1:1) no glutamine, and 10% fetal bovine serum, and 1% P/S. ATDC5 were passaged at 75–80% confluent. Using 0.05% trypsin-EDTA cells were detached and washed with PBS. Cells were re-suspended in the required amount of chondrocyte cell culture media for encapsulation in hydrogels.

ATDC5 cell encapsulation in NB BTA hydrogel and bioink preparation

Chondrocytes (RIKEN cell bank, Japan) were encapsulated in NB BTA hydrogel at a concentration of 5 million (M) cells per mL of hydrogelator. For cell culture studies, the hydrogel was prepared in DMEM/F-12 (1:1) with 1% Penicillin-Streptomycin (P/S) at an initial concentration of 8% w/v following the method described in the hydrogel-making section above. The next day cell suspension was added to adjust the final concentration to 4% w/v for supramolecular hydrogel. For cross-linked hydrogel, LAP photoinitiator, cross-linker solution, and the cell suspension were added to adjust the final concentration to 4% w/v. For example, NB BTA was dissolved in 375 μL DMEM (with 1% P/S) at the initial concentration of 8% w/v (4mM). The next day, short thiol 75 μL of 38 mM and 75 μL of 16 mM LAP solution was added and mixed by breaking the hydrogel. After equilibration, a time of ~2 hours of cell suspension in 225 μL was mixed in hydrogel using the self-healing method described below. For mixing cell suspension in the hydrogel, a uniform hydrogel layer covering an entire surface area of the well plate (48-well plate, non-adherent) was made by centrifugation at 2000g. Cell suspension in DMEM was uniformly spread on top of the hydrogel, and another layer of the same hydrogel was added on top of the previous layer. After a waiting time of 5–10 minutes when two layers are self-healed, the gel was broken gently into small pieces using a spatula and put the pieces together to ensure uniform cell distribution. After a waiting time of ~30 minutes in a sterile flow hood, which allows sufficient self-healing of small pieces of hydrogel, in presence of cell suspension, the hydrogel was transferred to a 3mL sterile syringe for injectability and bioprinting. Thiol to NB was in 1:1 ratios and the short thiol final concentration was 4 mM, NB-BTA final concentration was 2 mM. The LAP photoinitiator's final concentration was 2mM.

Cell culture conditions and production of hMSC spheroids

Human mesenchymal stromal cells (hMSC, 8F3543, Lonza) were expanded in alpha MEM medium with GlutaMAX (32561-029, Gibco) supplemented with 10% (v/v) of fetal bovine serum (FBS, F7524, Sigma-Aldrich) by culturing 3,000 cells/cm^2 until they reached 70% of confluence up to passage 5, at 37° C under a 5% CO_2 atmosphere. The microwell array insert used to produce hMSC spheroids was previously described.[52] Briefly, 5×10^5 cells were seeded in each microwell array to obtain 164 spheroids containing an average of 3,048 cells each. The cells were cultured in these arrays (37° C, 5 % CO_2 atmosphere) until day 5 to form highly spherical spheroids. The culture medium was refreshed every 48 hours.

MSC spheroids encapsulation for Bioink preparation

The hMSC spheroids were collected from the microwell array inserts, washed twice with PBS, and mixed into the hydrogel. Two types of hydrogel were used for encapsulation spheroids; a hydrogel cross-linked fully with short thiol and a 0.5-short:0.5MMP hydrogel which is partially cross-linked with short thiol (0.5-mole equivalent) and partially with MMP sensitive cross-linker (0.5-mole equivalent). Around 2,500 hMSCs spheroids were mixed per milliliter of hydrogel,

giving a total cell suspension of around 7.6×10^6 cells/mL encapsulated. A similar procedure of bioink preparation was repeated for short thiol cross-linker as described above for chondrocytes.

For a 0.5-short:0.5MMP hydrogel volume of 750 μL, 30 mg NB BTA polymer was dissolved in 375 μL of MEM (1% P/S) at an initial concentration of 8% w/v (4mM), and hydrogel was aged overnight. The next day, 38 μL of short and 38 μL of MMP sensitive cross-linker, each with an initial concentration of 38mM, and 75 μL of LAP with 16mM initial concentrations were mixed in the hydrogel by breaking the hydrogel. After an equilibration time of ~1 hour, MSC spheroids suspension in 225 μL DMEM was mixed with hydrogel with described steps above in the procedure of bioink preparation for chondrocytes. Each cross-linker, NB BTA polymer, and LAP has a final concentration of 2mM in the hydrogel.

Injectability

The ATDC5-laden hydrogel was transferred to a sterile 3 mL syringe and then injected through a 22 gauge conical needle. Hydrogels were cross-linked using UV light at ~1 mW/cm² between 30–60 seconds.

Bioprinting

After MSC spheroids were encapsulated within hydrogels, 3D meniscus structures (stl file, 10.8 mm x 8.9 mm x 1.4 mm) were printed using the BioX extrusion printer (CellInk, Sweden). All printing was performed at room temperature. Conical plastic needles (VIEWEG GmbH, Germany) were fixed to 3 mL syringes with 22 gauge nozzle diameter (ID = 0.41 mm). The pressure applied to form a continuous filament was 90 kPa. The infill density was set to 100% and the distance from the needle to the print surface was optimized so that the leading edge of the flow was in line with the needle.

Morphological analysis of spheroids after mixing and bioprinting process over 28 days

To evaluate the impact of the bioprinting and spheroid encapsulation inside the hydrogel cross-linked with short thiol cross-linker and 0.5-short and 0.5-MMP sensitive cross-linkers, bioprinted constructs were cultured for up to 28 days in alpha MEM basic medium and chondrogenic differentiation medium. Images of the constructs were taken using an optical microscope (Eclipse Ti-E Nikon, Japan) after the bioink preparation step, and on days 3, 7, 14, 21, and 28 after bioprinting.

Chondrogenic differentiation performed on bioprinted constructs

First, the validation of hMSCs used in this work for chondrogenic differentiation was confirmed according to published protocol by Penick et al., 2005.[53] Then, spheroid-based bioprinted constructs were differentiated for 28 days in a post-bioprinting process as previously described Decarli et al., 2022, using a chondrogenic culture medium initially defined by Johnstone et al. 1998[54] with some modifications.

Cell viability (live/dead)

LIVE/DEAD® Viability/Cytotoxicity Kit from Thermofisher (Netherlands) was used for evaluating cell viability. ATDC5 cultured hydrogels were transferred to a glass-bottom well plate, and a solution of calcein-AM (final concentration 1 μM) and ethidium homodimer-1 (EthD-1, final concentration 2 μM) was added to cover the whole hydrogel. The hydrogels were incubated for 45 minutes in the dark at 37 °C and imaged using an inverted fluorescence microscope (Nikon Eclipse TI-E microscope, Japan). Live and dead cell area was quantified using image J. At places where cells were clumped together and formed aggregates they were counted as one cell in ImageJ analysis, and this could affect the ratio between live and dead cell numbers. To overcome this we calculated the area of live and dead cells.

Immunochemical analysis

Immunohistochemical analysis was performed to determine the presence of collagen types I, II, and F-actin. The assays were performed in fixed samples containing the whole bioprinted constructs. Due to the complex composition of the spheroid-based constructs, some modifications were implemented in the immunostaining procedure to ensure efficient stain penetration throughout the sample, as previously described (Decarli et al., 2022). Briefly, the primary antibodies anti-mouse collagen-I (Abcam 6308), and anti-rabbit collagen-II (Abcam 34712) diluted to 1:200 were used. The samples were also incubated with secondary antibodies (1:500), phalloidin (1:100), and DAPI DNA dye (1:100). The samples were then analyzed on a glass slide using a fluorescence microscope (Nikon Eclipse TI-E microscope, Japan).

References

(1) Wegst, U. G. K.; Bai, H.; Saiz, E.; Tomsia, A. P.; Ritchie, R. O. Bioinspired Structural Materials. *Nat. Mater.* **2015**, *14* (1), 23–36. https://doi.org/10.1038/nmat4089.

(2) Kang, A. H.; Gross, J. Relationship between the Intra and Intermolecular Cross-Links of Collagen. *Proc. Natl. Acad. Sci. U. S. A.* **1970**, *67* (3), 1307–1314. https://doi.org/10.1073/pnas.67.3.1307.

(3) Buehler, M. J. Nature Designs Tough Collagen: Explaining the Nanostructure of Collagen Fibrils. *Proc. Natl. Acad. Sci. U. S. A.* **2006**, *103* (33), 12285–12290. https://doi.org/10.1073/pnas.0603216103.

(4) Eyre, D. R.; Paz, M. A.; Gallop, P. M. Cross-Linking in Collagen and Elastin. *Annu. Rev. Biochem.* **1983**, *53*, 717–748. https://doi.org/10.1146/annurev.biochem.53.1.717.

(5) Ozsvar, J.; Yang, C.; Cain, S. A.; Baldock, C.; Tarakanova, A.; Weiss, A. S. Tropoelastin and Elastin Assembly. *Front. Bioeng. Biotechnol.* **2021**, *9* (February), 1–11. https://doi.org/10.3389/fbioe.2021.643110.

(6) Djinović-Carugo, K.; Young, P.; Gautel, M.; Saraste, M. Molecular Basis for Cross-Linking of Actin Filaments: Structure of the α-Actinin Rod. *Cell* **1999**, *98* (4), 537–546. https://doi.org/10.1016/S0092-8674(00)81981-9.

(7) Sun, J. Y.; Zhao, X.; Illeperuma, W. R. K.; Chaudhuri, O.; Oh, K. H.; Mooney, D. J.; Vlassak, J. J.; Suo, Z. Highly Stretchable and Tough Hydrogels. *Nature* **2012**, *489* (7414), 133–136. https://doi.org/10.1038/nature11409.

(8) Hong, S.; Sycks, D.; Chan, H. F.; Lin, S.; Lopez, G. P.; Guilak, F.; Leong, K. W.; Zhao, X. 3D Printing of Highly Stretchable and Tough Hydrogels into Complex, Cellularized Structures. *Adv. Mater.* **2015**, *27* (27), 4035–4040. https://doi.org/10.1002/adma.201501099.

(9) Gong, J. P.; Katsuyama, Y.; Kurokawa, T.; Osada, Y. Double-Network Hydrogels with Extremely High Mechanical Strength. *Adv. Mater.* **2003**, *15* (14), 1155–1158.

https://doi.org/10.1002/adma.200304907.

(10) Hu, X.; Vatankhah-Varnoosfaderani, M.; Zhou, J.; Li, Q.; Sheiko, S. S. Weak Hydrogen Bonding Enables Hard, Strong, Tough, and Elastic Hydrogels. *Adv. Mater.* **2015**, *27* (43), 6899–6905. https://doi.org/10.1002/adma.201503724.

(11) Xu, L.; Wang, C.; Cui, Y.; Li, A.; Qiao, Y.; Qiu, D. Conjoined-Network Rendered Stiff and Tough Hydrogels from Biogenic Molecules. *Sci. Adv.* **2019**, *5* (2), eaau3442. https://doi.org/10.1126/sciadv.aau3442.

(12) Han, Z.; Wang, P.; Lu, Y.; Jia, Z.; Qu, S.; Yang, W. A Versatile Hydrogel Network–Repairing Strategy Achieved by the Covalent-like Hydrogen Bond Interaction. *Sci. Adv.* **2022**, *8* (8), 5066. https://doi.org/10.1126/sciadv.abl5066.

(13) Guo, M.; Pitet, L. M.; Wyss, H. M.; Vos, M.; Dankers, P. Y. W.; Meijer, E. W. Tough Stimuli-Responsive Supramolecular Hydrogels with Hydrogen-Bonding Network Junctions. *J. Am. Chem. Soc.* **2014**, *136* (19), 6969–6977. https://doi.org/10.1021/ja500205v.

(14) Wang, Z.; Zheng, X.; Ouchi, T.; Kouznetsova, T. B.; Beech, H. K.; Av-Ron, S.; Matsuda, T.; Bowser, B. H.; Wang, S.; Johnson, J. A.; Kalow, J. A.; Olsen, B. D.; Gong, J. P.; Rubinstein, M.; Craig, S. L. Toughening Hydrogels through Force-Triggered Chemical Reactions That Lengthen Polymer Strands. *Science (80-.).* **2021**, *374* (6564), 193. https://doi.org/10.1126/science.abg2689.

(15) Kim, J.; Zhang, G.; Shi, M.; Suo, Z. Fracture, Fatigue, and Friction of Polymers in Which Entanglements Greatly Outnumber Cross-Links. *Science (80).* **2021**, *374* (6564), 212–216. https://doi.org/10.1126/science.abg6320.

(16) Norioka, C.; Inamoto, Y.; Hajime, C.; Kawamura, A.; Miyata, T. A Universal Method to Easily Design Tough and Stretchable Hydrogels. *NPG Asia Mater.* **2021**, *13* (1). https://doi.org/10.1038/s41427-021-00302-2.

(17) Freeman, R.; Han, M.; Álvarez, Z.; Lewis, J. A.; Wester, J. R.; Stephanopoulos, N.; McClendon, M. T.; Lynsky, C.; Godbe, J. M.; Sangji, H.; Luijten, E.; Stupp, S. I. Reversible Self-Assembly of Superstructured Networks. *Science (80).* **2018**, *362* (6416), 808–813. https://doi.org/10.1126/science.aat6141.

(18) Edelbrock, A. N.; Clemons, T. D.; Chin, S. M.; W Roan, J. J.; Bruckner, E. P.; Álvarez, Z.; Edelbrock, J. F.; Wek, K. S.; Stupp, S. I.; Edelbrock, A. N.; Stupp, S. I.; Clemons, T. D.; Álvarez, Z.; Edelbrock, J. F.; Chin, S. M.; W Roan, J. J.; Bruckner, E. P.; Wek, K. S. Superstructured Biomaterials Formed by Exchange Dynamics and Host–Guest Interactions in Supramolecular Polymers. *Adv. Sci.* **2021**, *8* (8), 2004042. https://doi.org/10.1002/ADVS.202004042.

(19) Rodell, C. B.; Dusaj, N. N.; Highley, C. B.; Burdick, J. A. Injectable and Cytocompatible Tough Double-Network Hydrogels through Tandem Supramolecular and Covalent Crosslinking. *Adv. Mater.* **2016**, *28* (38), 8419–8424. https://doi.org/10.1002/adma.201602268.

(20) Morgan, F. L. C.; Moroni, L.; Baker, M. B. Dynamic Bioinks to Advance Bioprinting. *Adv. Healthc. Mater.* **2020**, *9* (15), 1901798. https://doi.org/10.1002/adhm.201901798.

(21) Lee, A.; Hudson, A. R.; Shiwarski, D. J.; Tashman, J. W.; Hinton, T. J.; Yerneni, S.; Bliley, J. M.; Campbell, P. G.; Feinberg, A. W. 3D Bioprinting of Collagen to Rebuild Components of the Human Heart. *Science (80).* **2019**, *365* (6452), 482–487. https://doi.org/10.1126/science.aav9051.

(22) Hockaday, L. A.; Kang, K. H.; Colangelo, N. W.; Cheung, P. Y. C.; Duan, B.; Malone, E.; Wu, J.; Girardi, L. N.; Bonassar, L. J.; Lipson, H.; Chu, C. C.; Butcher, J. T. Rapid 3D Printing of Anatomically Accurate and Mechanically Heterogeneous Aortic Valve Hydrogel Scaffolds. *Biofabrication* **2012**, *4* (3), 1758–5082. https://doi.org/10.1088/1758-5082/4/3/035005.

(23) Kolesky, D. B.; Truby, R. L.; Gladman, A. S.; Busbee, T. A.; Homan, K. A.; Lewis, J. A. 3D Bioprinting of Vascularized, Heterogeneous Cell-Laden Tissue Constructs. *Adv. Mater.* **2014**, *26* (19), 3124–3130. https://doi.org/10.1002/adma.201305506.

(24) Grigoryan, B.; Paulsen, S. J.; Corbett, D. C.; Sazer, D. W.; Fortin, C. L.; Zaita, A. J.; Greenfield, P. T.; Calafat, N. J.; Gounley, J. P.; Ta, A. H.; Johansson, F.; Randles, A.; Rosenkrantz, J. E.; Louis-Rosenberg, J. D.; Galie, P. A.; Stevens, K. R.; Miller, J. S. Multivascular Networks and Functional Intravascular Topologies within Biocompatible Hydrogels. *Science (80).* **2019**, *364* (6439), 458–464. https://doi.org/10.1126/science.aav9750.

(25) Skylar-Scott, M. A.; Uzel, S. G. M.; Nam, L. L.; Ahrens, J. H.; Truby, R. L.; Damaraju, S.; Lewis, J. A. Biomanufacturing of Organ-Specific Tissues with High Cellular Density and Embedded Vascular Channels. *Sci. Adv.* **2019**, *5* (9), eaaw2459. https://doi.org/10.1126/sciadv.aaw2459.

(26) Ghanizadeh Tabriz, A.; Hermida, M. A.; Leslie, N. R.; Shu, W. Three-Dimensional Bioprinting of Complex Cell Laden Alginate Hydrogel Structures. *Biofabrication* **2015**, *7*, 045012. https://doi.org/10.1088/1758-5090/7/4/045012.

(27) Hull, S. M.; Lindsay, C. D.; Brunel, L. G.; Shiwarski, D. J.; Tashman, J. W.; Roth, J. G.; Myung, D.; Feinberg, A. W.; Heilshorn, S. C. 3D Bioprinting Using UNIversal Orthogonal Network (UNION) Bioinks. *Adv. Funct. Mater.* **2020**, *2007983*, 1–11. https://doi.org/10.1002/adfm.202007983.

(28) Bakht, S. M.; Gomez-Florit, M.; Lamers, T.; Reis, R. L.; Domingues, R. M. A.; Gomes, M. E. 3D Bioprinting of Miniaturized Tissues Embedded in Self-Assembled Nanoparticle-Based Fibrillar Platforms. *Adv. Funct. Mater.* **2021**, *2104245*, 2104245. https://doi.org/10.1002/adfm.202104245.

(29) Ouyang, L.; Armstrong, J. P. K.; Lin, Y.; Wojciechowski, J. P.; Lee-Reeves, C.; Hachim, D.; Zhou, K.; Burdick, J. A.; Stevens, M. M. Expanding and Optimizing 3D Bioprinting Capabilities Using Complementary Network Bioinks. *Sci. Adv.* **2020**, *6* (38), 1–14. https://doi.org/10.1126/sciadv.abc5529.

(30) Aldana, A. A.; Houben, S.; Moroni, L.; Baker, M. B.; Pitet, L. M. Trends in Double Networks as Bioprintable and Injectable Hydrogel Scaffolds for Tissue Regeneration. *ACS Biomater. Sci. Eng.* **2021**, *7* (9), 4077–4101. https://doi.org/10.1021/acsbiomaterials.0c01749.

(31) Wang, H.; Zhu, D.; Paul, A.; Cai, L.; Enejder, A.; Yang, F.; Heilshorn, S. C. Covalently Adaptable Elastin-Like Protein–Hyaluronic Acid (ELP–HA) Hybrid Hydrogels with Secondary Thermoresponsive Crosslinking for Injectable Stem Cell Delivery. *Adv. Funct. Mater.* **2017**, *27* (28), 1–11. https://doi.org/10.1002/adfm.201605609.

(32) Lou, J.; Liu, F.; Lindsay, C. D.; Chaudhuri, O.; Heilshorn, S. C.; Xia, Y. Dynamic Hyaluronan Hydrogels with Temporally Modulated High Injectability and Stability Using a Biocompatible Catalyst. *Adv. Mater.* **2018**, *30* (22), 1–6. https://doi.org/10.1002/adma.201705215.

(33) Hafeez, S.; Ooi, H.; Morgan, F.; Mota, C.; Dettin, M.; van Blitterswijk, C.; Moroni, L.; Baker, M. Viscoelastic Oxidized Alginates with Reversible Imine Type Crosslinks: Self-Healing, Injectable, and Bioprintable Hydrogels. *Gels* **2018**, *4* (4), 85. https://doi.org/10.3390/gels4040085.

(34) Highley, C. B.; Rodell, C. B.; Burdick, J. A. Direct 3D Printing of Shear-Thinning Hydrogels into Self- Healing Hydrogels. *Adv. Mater.* **2015**, *27*, 5075–5079.

(35) Loebel, C.; Rodell, C. B.; Chen, M. H.; Burdick, J. A. Shear-Thinning and Self-Healing Hydrogels as Injectable Therapeutics and for 3D-Printing. *Nat. Protoc.* **2017**, *12* (8), 1521–1541. https://doi.org/10.1038/nprot.2017.053.

(36) Rodell, C. B.; Kaminski, A. L.; Burdick, J. A. Rational Design of Network Properties in Guest-Host Assembled and Shear-Thinning Hyaluronic Acid Hydrogels. *Biomacromolecules* **2013**, *14* (11), 4125–4134. https://doi.org/10.1021/bm401280z.

(37) Sather, N. A.; Sai, H.; Sasselli, I. R.; Sato, K.; Ji, W.; Synatschke, C. V.; Zambrotta, R. T.; Edelbrock, J. F.; Kohlmeyer, R. R.; Hardin, J. O.; Berrigan, J. D.; Durstock, M. F.; Mirau, P.; Stupp, S. I. 3D Printing of Supramolecular Polymer Hydrogels with Hierarchical Structure. *Small* **2021**, *17* (5), 1–14. https://doi.org/10.1002/smll.202005743.

(38) Susapto, H. H.; Alhattab, D.; Abdelrahman, S.; Khan, Z.; Alshehri, S.; Kahin, K.; Ge, R.; Moretti, M.; Emwas, A. H.; Hauser, C. A. E. Ultrashort Peptide Bioinks Support Automated Printing of Large-Scale Constructs Assuring Long-Term Survival of Printed Tissue Constructs. *Nano Lett.* **2021**, *21* (7), 2719–2729. https://doi.org/10.1021/acs.nanolett.0c04426.

(39) Leenders, C. M. A.; Mes, T.; Baker, M. B.; Koenigs, M. M. E.; Besenius, P.; Palmans, A. R. A.; Meijer, E. W. From Supramolecular Polymers to Hydrogel Materials. *Mater. Horiz.* **2014**, *1* (1), 116–120. https://doi.org/10.1039/C3MH00103B.

(40) Hafeez, S.; Ooi, H. W.; Suylen, D.; Duimel, H.; Hackeng, T. M.; van Blitterswijk, C.; Baker, M. B. Desymmetrization via Activated Esters Enables Rapid Synthesis of Multifunctional Benzene-1,3,5-Tricarboxamides and Creation of Supramolecular Hydrogelators. *J. Am. Chem. Soc.* **2022**, *144* (9), 4057–4070. https://doi.org/10.1021/jacs.1c12685.

(41) Stuart, M. C. A.; Van De Pas, J. C.; Engberts, J. B. F. N. The Use of Nile Red to Monitor the Aggregation Behavior in Ternary Surfactant-Water-Organic Solvent Systems. *J. Phys. Org. Chem.* **2005**, *18* (9), 929–934. https://doi.org/10.1002/poc.919.

(42) Leenders, C. M. A.; Baker, M. B.; Pijpers, I. A. B.; Lafleur, R. P. M.; Albertazzi, L.; Palmans, A. R. A.; Meijer, E. W. Supramolecular Polymerisation in Water; Elucidating the Role of Hydrophobic and Hydrogen-Bond Interactions. *Soft Matter* **2016**, *12* (11), 2887–2893.

https://doi.org/10.1039/c5sm02843d.

(43) Guimarães, C. F.; Gasperini, L.; Marques, A. P.; Reis, R. L. The Stiffness of Living Tissues and Its Implications for Tissue Engineering. *Nat. Rev. Mater.* **2020**, *5* (5), 351–370. https://doi.org/10.1038/s41578-019-0169-1.

(44) Slivka, M. A.; Leatherbury, N. C.; Kieswetter, K.; Niederauer, G. G. Porous, Resorbable, Fiber-Reinforced Scaffolds Tailored for Articular Cartilage Repair. *Tissue Eng.* **2001**, *7* (6), 767–780. https://doi.org/10.1089/107632701753337717.

(45) O'Connell, G. D.; Sen, S.; Elliott, D. M. Human Annulus Fibrosus Material Properties from Biaxial Testing and Constitutive Modeling Are Altered with Degeneration. *Biomech. Model. Mechanobiol.* **2012**, *11* (3–4), 493–503. https://doi.org/10.1007/s10237-011-0328-9.

(46) Schmoller, K. M.; Bausch, A. R. Similar Nonlinear Mechanical Responses in Hard and Soft Materials. *Nat. Mater.* **2013**, *12* (4), 278–281. https://doi.org/10.1038/nmat3603.

(47) Stella, J. A.; D'Amore, A.; Wagner, W. R.; Sacks, M. S. On the Biomechanical Function of Scaffolds for Engineering Load-Bearing Soft Tissues. *Acta Biomater.* **2010**, *6* (7), 2365–2381. https://doi.org/10.1016/j.actbio.2010.01.001.

(48) Axpe, E.; Chan, D.; Offeddu, G. S.; Chang, Y.; Merida, D.; Hernandez, H. L.; Appel, E. A. A Multiscale Model for Solute Diffusion in Hydrogels. *Macromolecules* **2019**, *52* (18), 6889–6897. https://doi.org/10.1021/acs.macromol.9b00753.

(49) Schoenmakers, D. C.; Rowan, A. E.; Kouwer, P. H. J. Crosslinking of Fibrous Hydrogels. *Nat. Commun.* **2018**, *9* (1), 1–8. https://doi.org/10.1038/s41467-018-04508-x.

(50) Marquardt, L. M.; Doulames, V. M.; Wang, A. T.; Dubbin, K.; Suhar, R. A.; Kratochvil, M. J.; Medress, Z. A.; Plant, G. W.; Heilshorn, S. C. Designer, Injectable Gels to Prevent Transplanted Schwann Cell Loss during Spinal Cord Injury Therapy. *Sci. Adv.* **2020**, *6* (14), 1–16. https://doi.org/10.1126/sciadv.aaz1039.

(51) Kohze, R.; Dieteren, C. E. J.; Koopman, W. J. H.; Brock, R.; Schmidt, S. Frapbot: An Open-Source Application for FRAP Data. *Cytom. Part A* **2017**, *91* (8), 810–814. https://doi.org/10.1002/cyto.a.23172.

(52) Decarli, M. C.; de Castro, M. V.; Nogueira, J. A.; Nagahara, M. H. T.; Westin, C. B.; de Oliveira, A. L. R.; Silva, J. V. L.; Moroni, L.; Mota, C.; Moraes, Â. M. Development of a Device Useful to Reproducibly Produce Large Quantities of Viable and Uniform Stem Cell Spheroids with Controlled Diameters. *Mater. Sci. Eng. C* **2022**, 112685. https://doi.org/10.1016/j.msec.2022.112685.

(53) Penick, K. J.; Solchaga, L. A.; Welter, J. F. High-Throughput Aggregate Culture System to Assess the Chondrogenic Potential of Mesenchymal Stem Cells. *Biotechniques* **2005**, *39* (5), 687–690. https://doi.org/10.2144/000112009.

(54) Johnstone, B.; Hering, T. M.; Caplan, A. I.; Goldberg, V. M.; Yoo, J. U. In Vitro Chondrogenesis of Bone Marrow-Derived Mesenchymal Progenitor Cells. *Exp. Cell Res.* **1998**, *238* (1), 265–272. https://doi.org/10.1006/excr.1997.3858.

Supplementary Figures

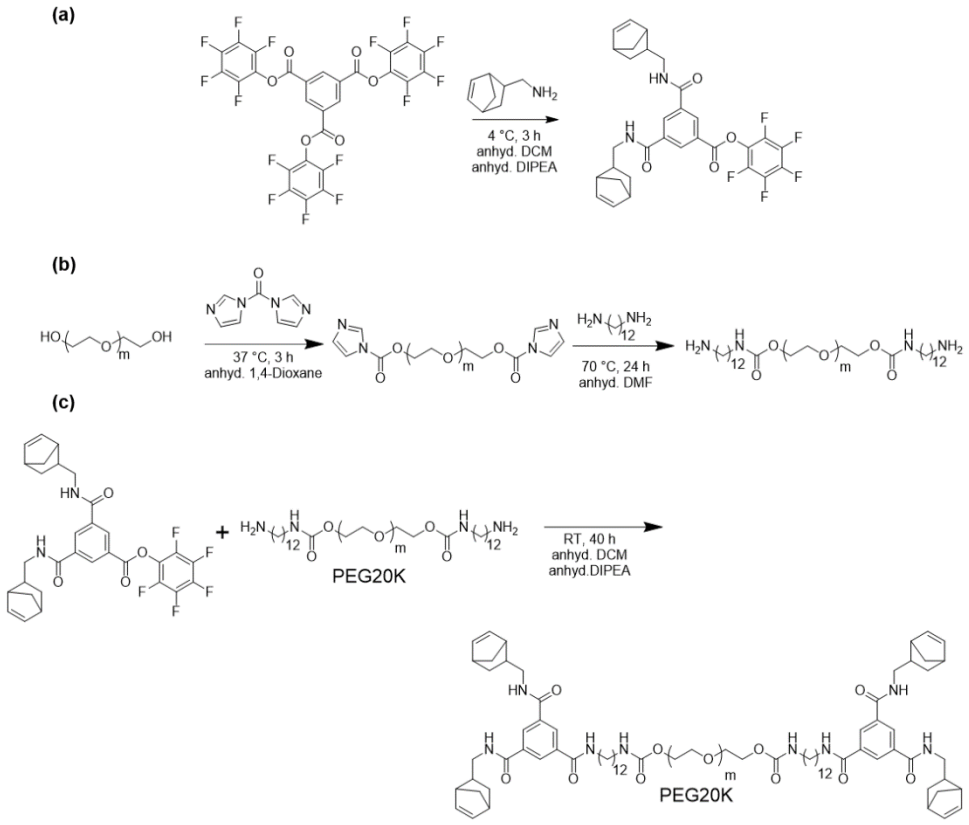

Figure S1. a) Tris(perfluorophenyl) benzene-1,3,5-tricarboxylate desymmetrization using 5-Norbornene-2-methylamine molecule for creating Nb BTA precursor molecule. b) Reaction scheme showing PEG bismaino dodecane synthesis. c) Reaction scheme demonstrating NB BTA hydrogelator synthesis.

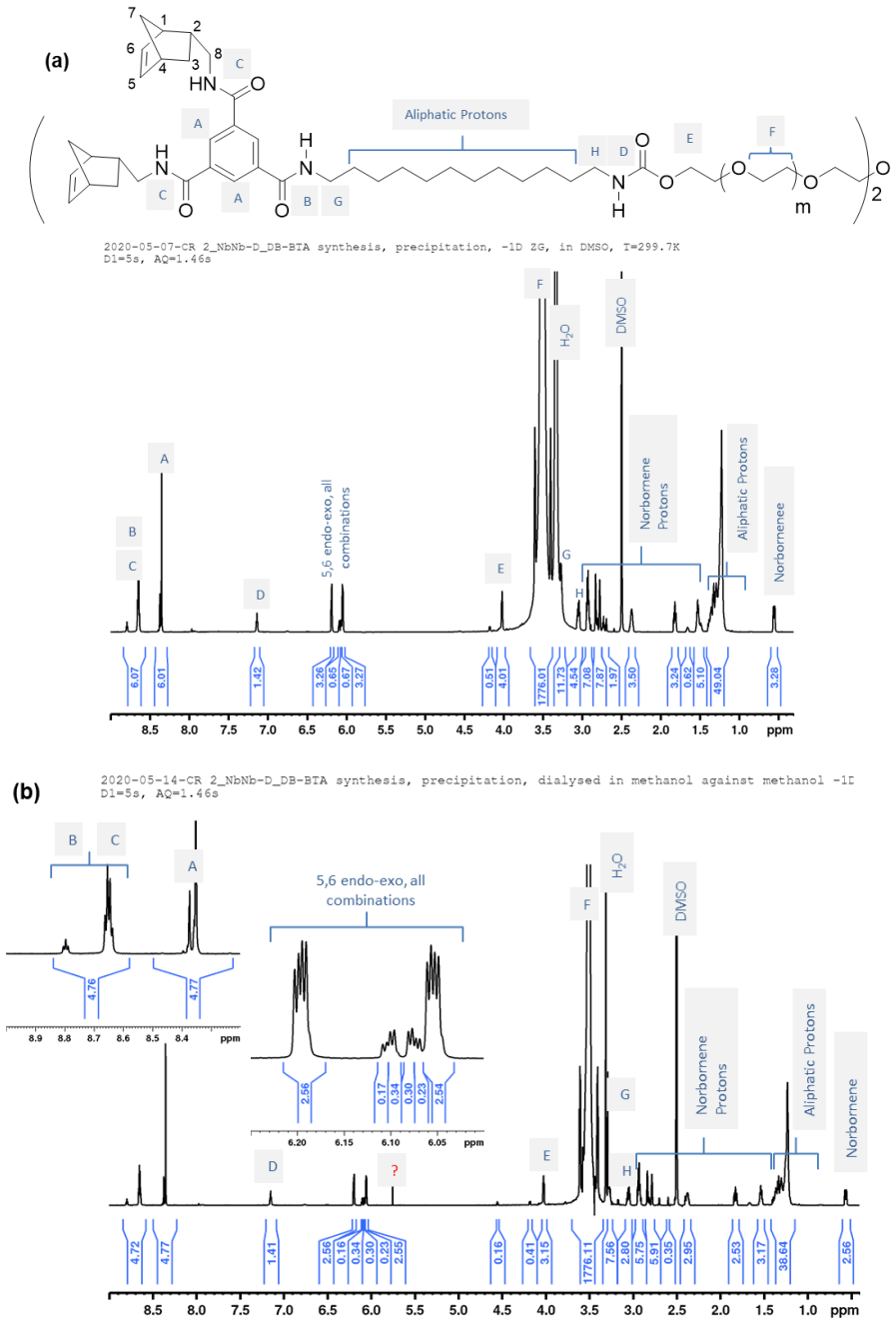

Figure S2. a) ^{1}H NMR analysis after purification in diethyl ether. b) ^{1}H NMR analysis after second purification when dialysing in methanol against methanol.

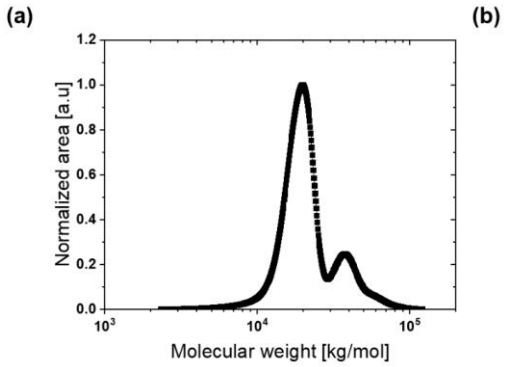

Average Mw	Đ
23532 kg/mol	1.2

Figure S3. a) Gel permeation chromatography (GPC) graph shows molecular weight distribution during gel permeation chromatography (GPC). GPC graph shows a peak around 20 kg/mol and 40 kg/mol. The peak around 40 kg/mol could be due to chain extension during synthesis of amine functionalized PEG 20K. b) average molecular weight of 23532 g/mol with polydispersity index (Đ)of 1.2.

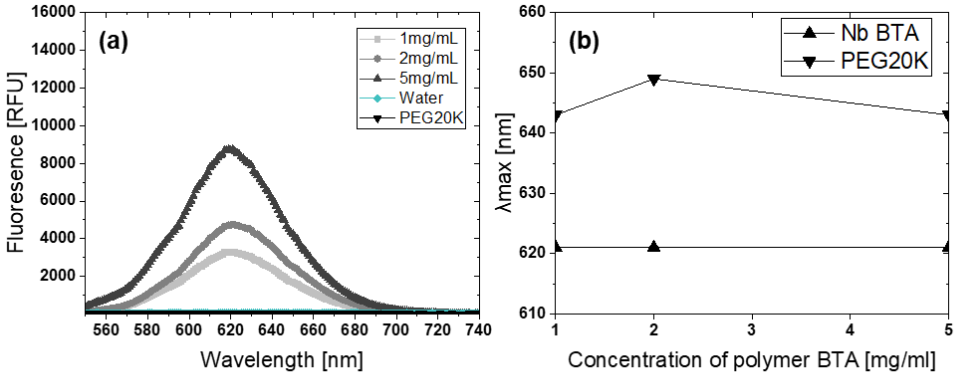

Figure S4. a) Nile red at different concentrations of Nb BTA hydrogelator. b) λmax for different concentrations of Nb BTA in dilute solutions at given concentrations.

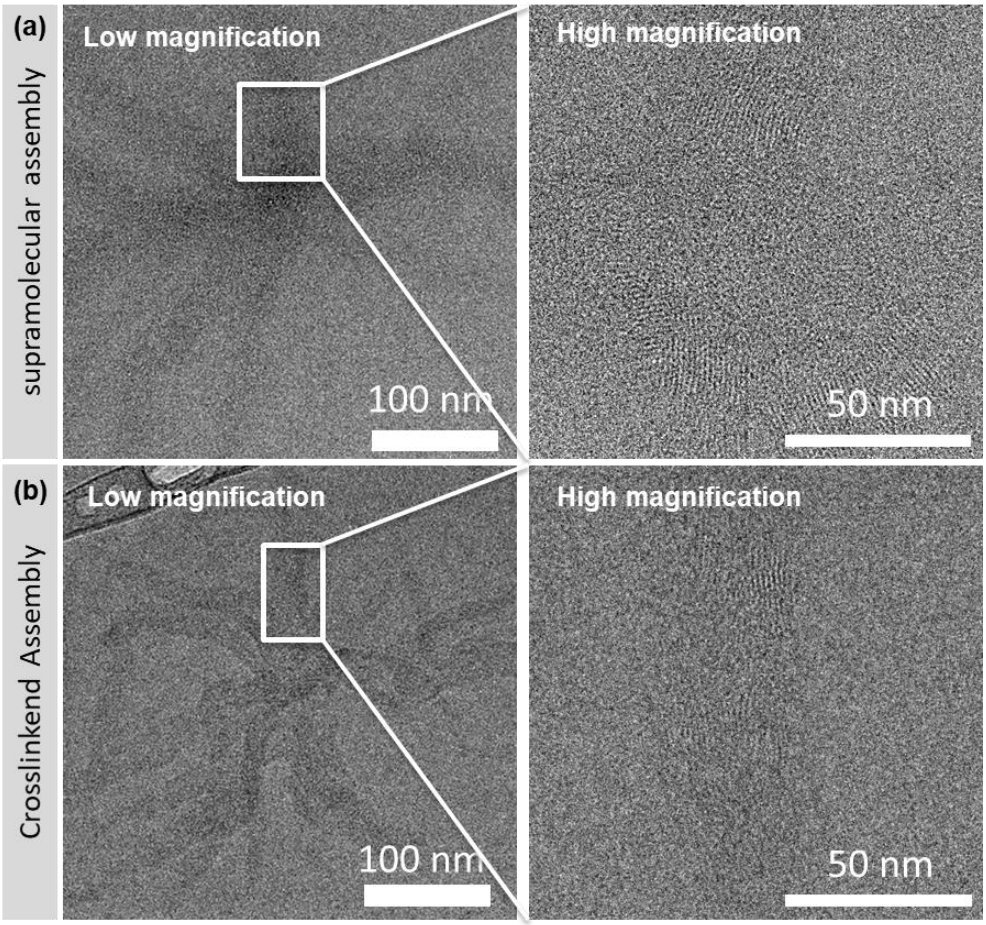

Figure S5. a) Supramolecular self-assembly at 10 mg/ml. b) Cross-linked self-assembly at 10 mg/ml aged for 16–24 hours.

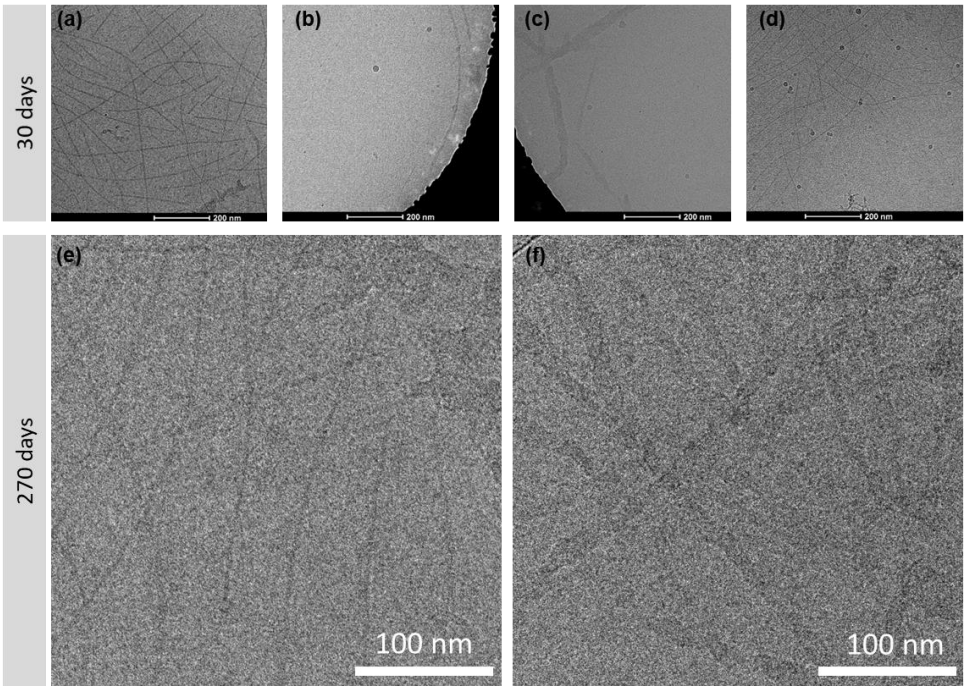

Figure S6. a–d) Supramolecular self-assembly aged for 30 days, shows fibrils around 5 nm and 15 nm. e,f) Sample aged for 270 days (~9 months) also shows bundle of fibrils. The sample is dilute solution at concentration of 5mg/ml.

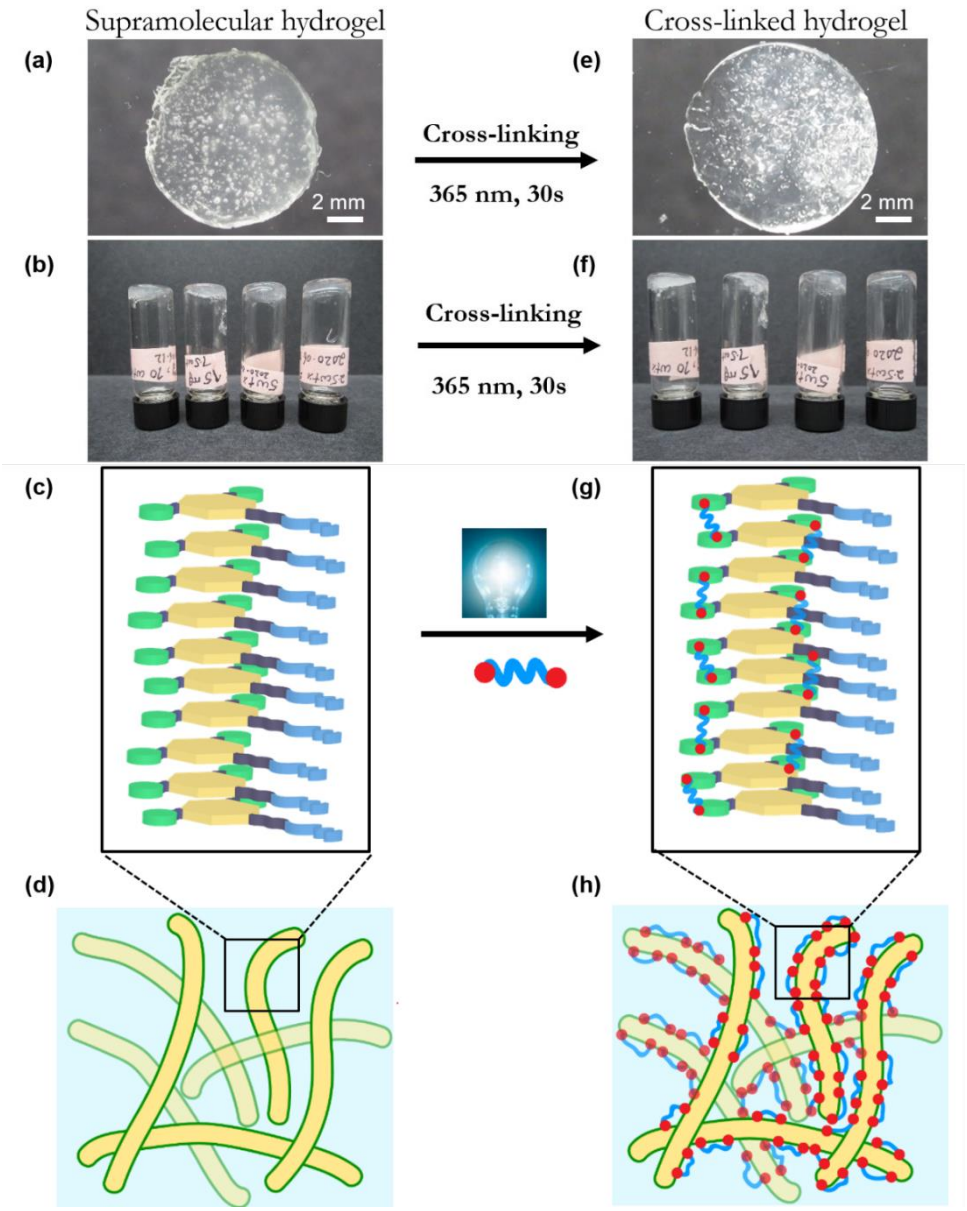

Figure S7. a,e) Supramolecular hydrogel (a) on the left of the arrow and cross-linked hydrogel (e) on the right of arrows. b,f) On the left are vials with 10% w/v, 7.5% w/v, and 5% w/v and 2.5% w/v supramolecular hydrogel (b) and on the right of arrow are cross-linked hydrogel (f) after cross-linking. c,g) Schematic self-assembly of supramolecular (c) cross-linked (g) BTA single nanofiber using short dithiol crosslinker. d,h) Supramolecular (d) cross-linked (h) hydrogel network schematics.

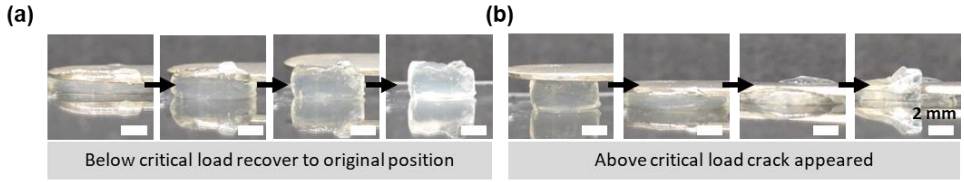

Figure S8. a, Cross-linked hydrogel recover to original position below critical load and b, crack started to appear after a critical load along spatula edge.

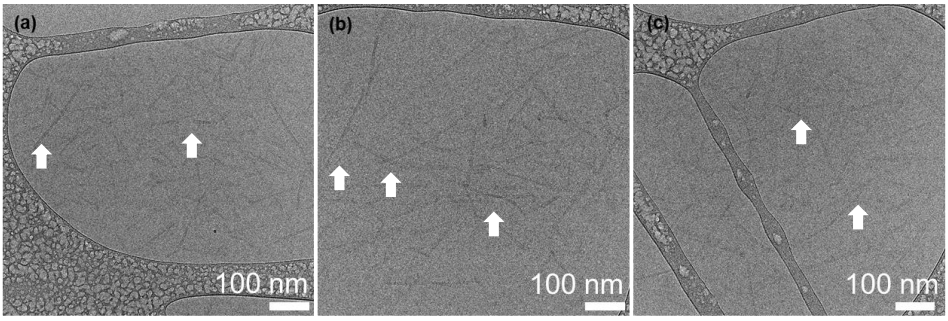

Figure S9. a–c) Supramolecular hydrogel was made at 5 w/v % and then after overnight ageing, diluted to 0.5 w/v %, similar concentration to dilute solution condition (5mg/ml) for cryo-TEM sample preparation. Cryo-TEM showed that dissolved hydrogels possess fibrillar morphology.

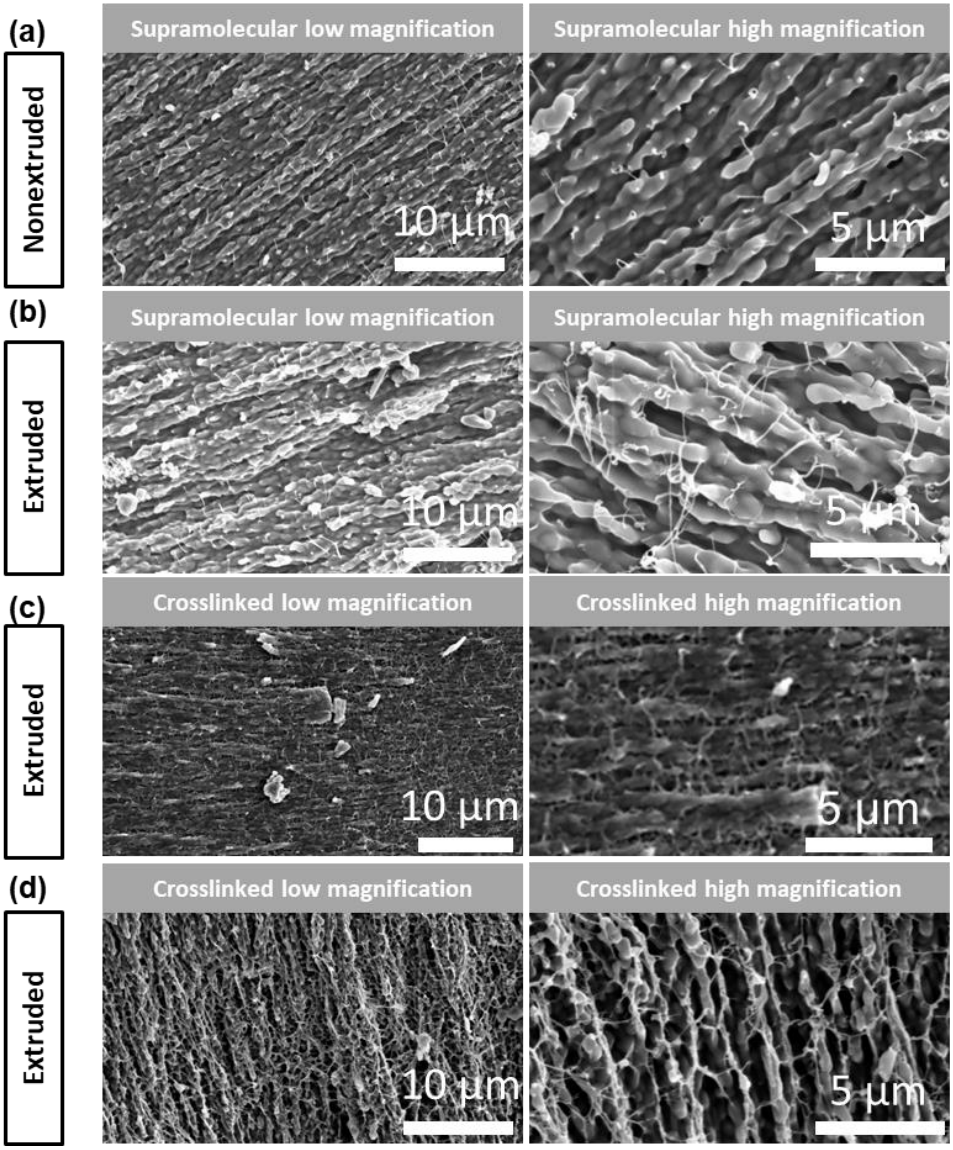

Figure S10. a) Supramolecular bulk hydrogel. b) Supramolecular extruded hydrogel. c,d) Cross-linked post extruding hydrogel imaged within 24 hours of cross-linking (c) and after roughly 3 months of storing at room temperature (d). Hydrogel in "d" was stored at room temperature in glass vial and we noticed that hydrogel was dryish before preparing sample for cryo-SEM. A little twisting in fibers could also be due to drying of hydrogel.

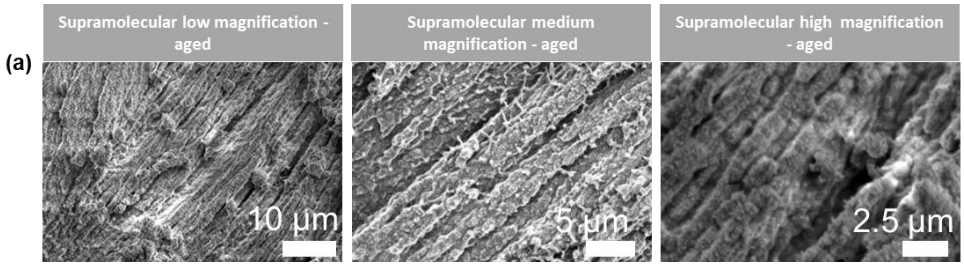

Figure S11. a) Supramolecular hydrogels aged for a month (30 days) retain fiber bundle morphology.

Tuning mechanical properties using network topology

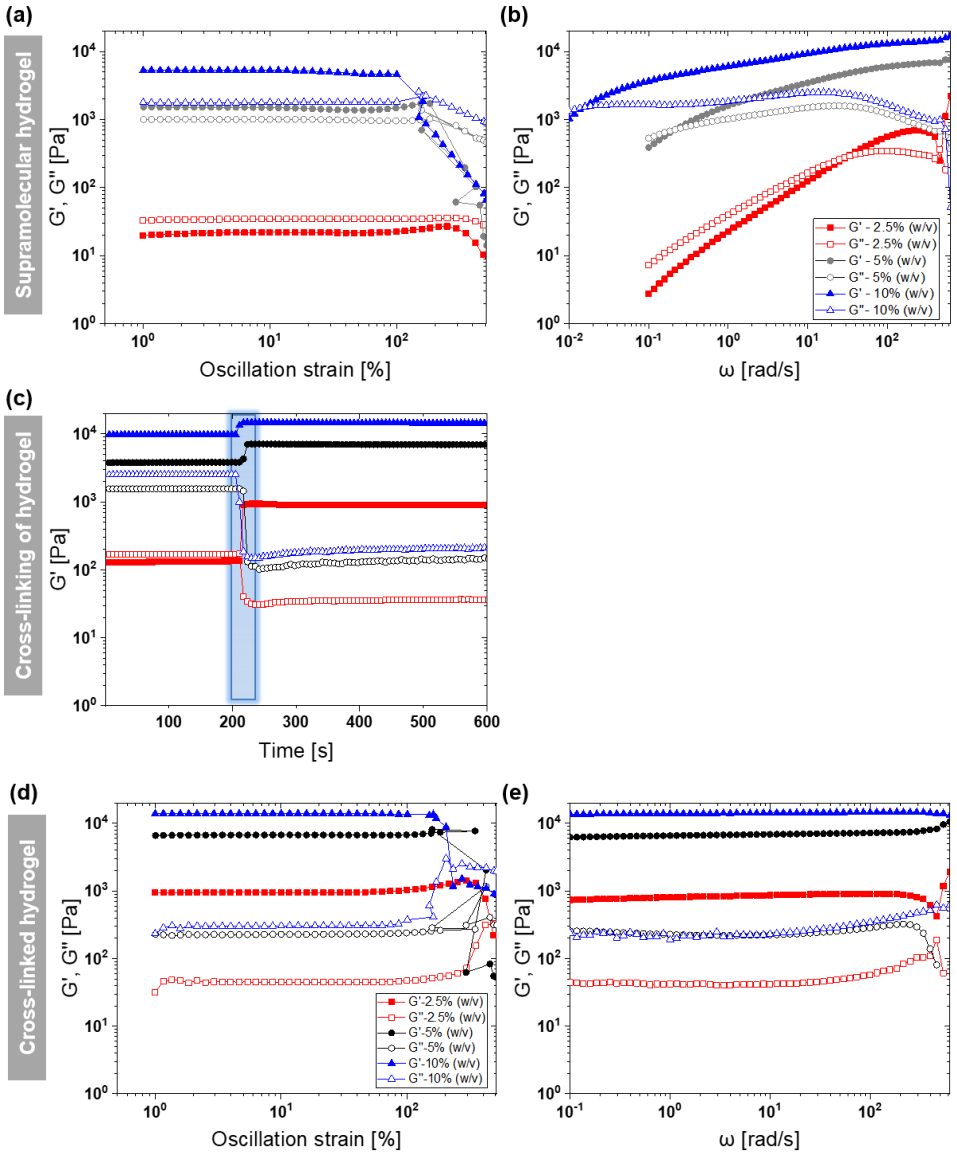

Figure S12. a) Strain sweep for supramolecular hydrogel for 2.5%, 5% and 10% w/v. b) Angular frequency sweep for 2.5%, 5% and 10% w/v. supramolecular hydrogel. c) Cross-linking of supramolecular hydrogel by exposing to UV light. d) Cross-linked hydrogel strain sweep for 2.5%, 5% and 10% w/v. e) Angular frequency sweep for 2.5%, 5% and 10% w/v for cross-linked hydrogel.

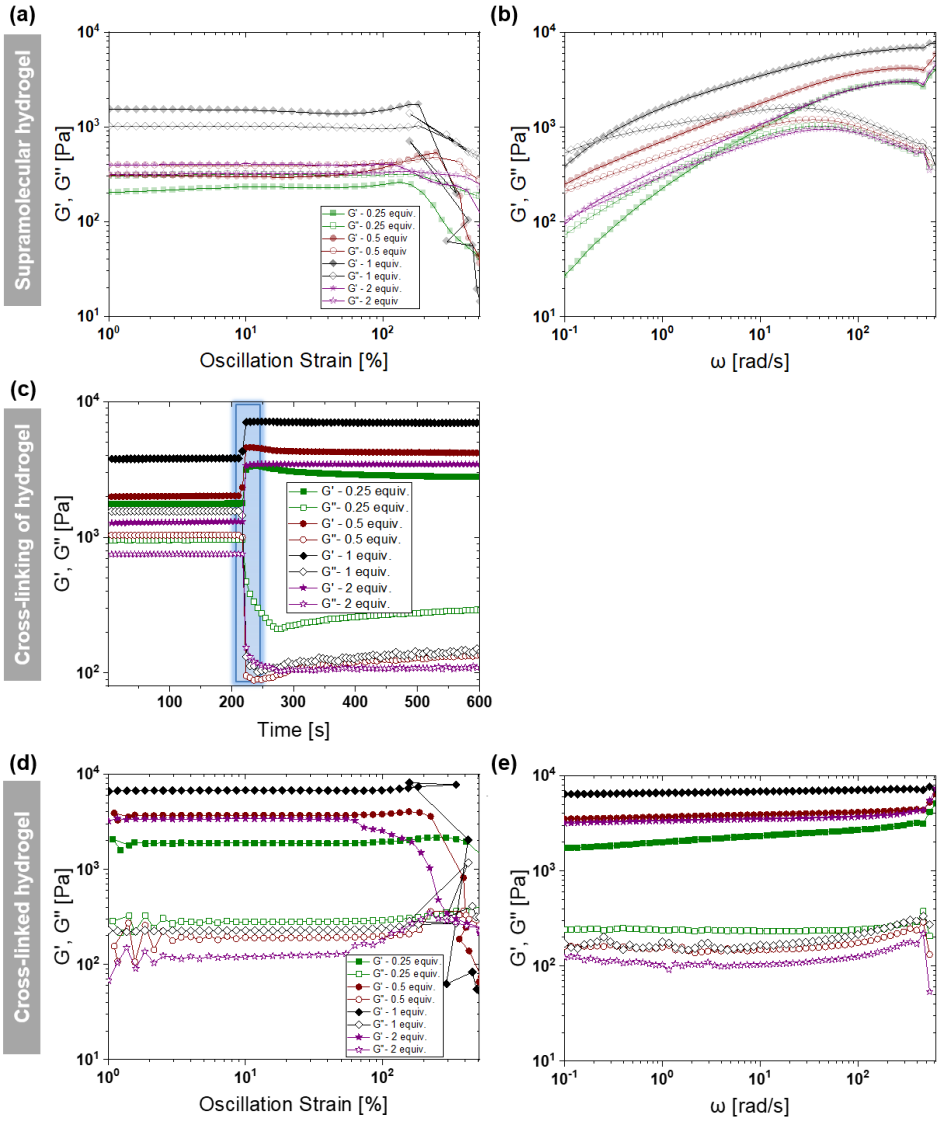

Figure S13. a) Strain sweep for supramolecular hydrogel for 2.5%, 5% and 10% w/v. b) Angular frequency sweep for 2.5%, 5% and 10% w/v for supramolecular hydrogel. c) Cross-linking of Nb BTA hydrogel using short thiol crossl-inker at different mole equivalents. d) Cross-linked hydrogel strain sweep for 2.5%, 5% and 10% w/v. e) Angular frequency sweep for 2.5%, 5% and 10% w/v for cross-linked hydrogel.

Network topology of cross-linker can also affect mechanical properties owing to step growth nature of norbornene thiol-ene cross-linking. We cross-linked using 5K-PEG-4arm thiol and 2K-PEG-2arm thiol for comparison such that each PEG arm would have a length of around 1K. All hydrogels were investigated using shear rheology at a constant 5% w/v and 1:1 Nb/thiol ratio. Supramolecular hydrogels were viscoelastic, showed a crossover point at a similar angular frequency, and exhibited very similar equilibrium storage modulus. When cross-linking, 2 arm cross-linker showed fast cross-linking compared to the 4-arm. Cross-linked hydrogels for 5K-PEG-4arm and 2K-PEG-arm showed plateau storage modulus of around 4500 Pa independent of frequency. Taking into consideration the theoretical number of bonds, 5K-PEG-4arm should show higher storage modulus compared to 2K-PEG-2arm since two 2arm PEG chains are covalently attached to make 4-arm PEG cross-linker resulting in one extra cross-link per two new cross-links formed. Apparently, extra cross-link between PEG chains for 4-arm does not contribute to storage modulus since we observed similar storage modulus for both cross-linkers, which potentially can suggest that only new formed bonds during thiolene chemistry contributed to storage modulus.

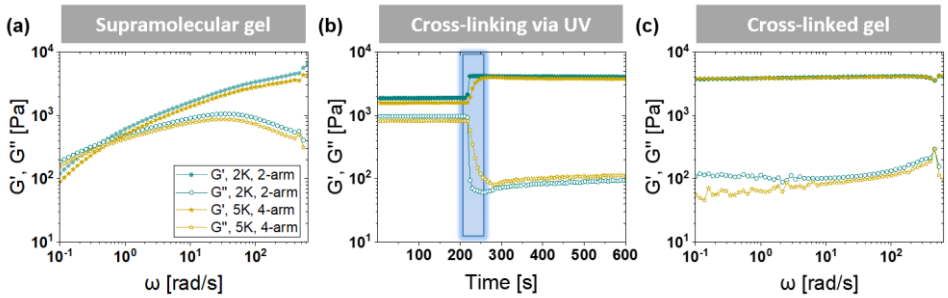

Figure S14. a) Angular frequency sweep using 2K 2-arm and 5K 4-arm thiol cross-linker before cross-linking. Supramolecular hydrogel showed a crossover point between G' and G", typical of viscoelastic materials. b) Cross-linking of BTA hydrogel using 365 nm UV light at 10 mW/cm^2. c) Cross-linked hydrogel frequency sweep showed G' and G" independent of angular frequency. All hydrogels were investigated at constant 5% w/v and 1:1 Nb/thiol ratio.

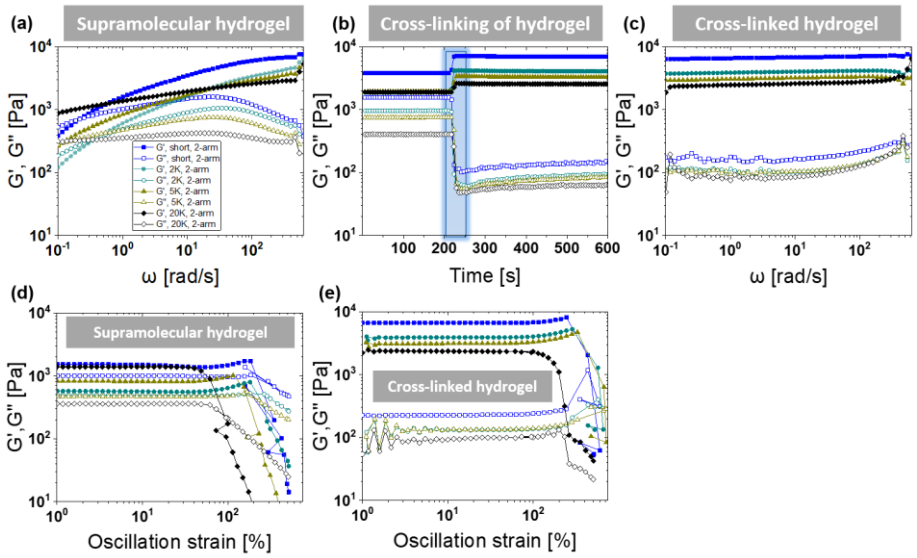

(f)

Strain at break	Short	PEG2K	PEG5K	PEG20K
Supramolecular	200 – 300%	200 – 300%	200 – 300%	~100%
Cross-linked	300 – 400%	300 – 400%	400 – 500%	>500%

Figure S15. a) Angular frequency sweep at 5% w/v using 2-arm thiol cross-linker of different molecular lengths b) Cross-linking of BTA hydrogel using short dithiol cross-linker of different molecular lengths. c) Frequency sweep for cross-linked hydrogel at constant 5% w/v. d) Supramolecular hydrogel strain sweep. e) cross-linked hydrogel strain sweep. f) Table shows the values of strain at break for different cross-linkers.

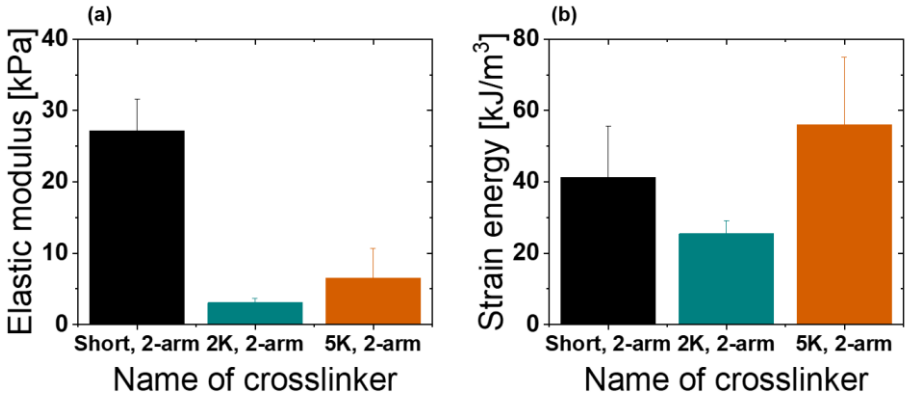

Figure S16. a) Elastic modulus calculated from tensile stress-strain curve between 0–20% tensile strain for hydrogels cross-linked using short, 2K and 5K dithiol cross-linker and at 5% (w/v, 1:1 Nb/thiol). b) resulting strain energy when the sample was cross-linked and stretched to rupture during tensile testing.

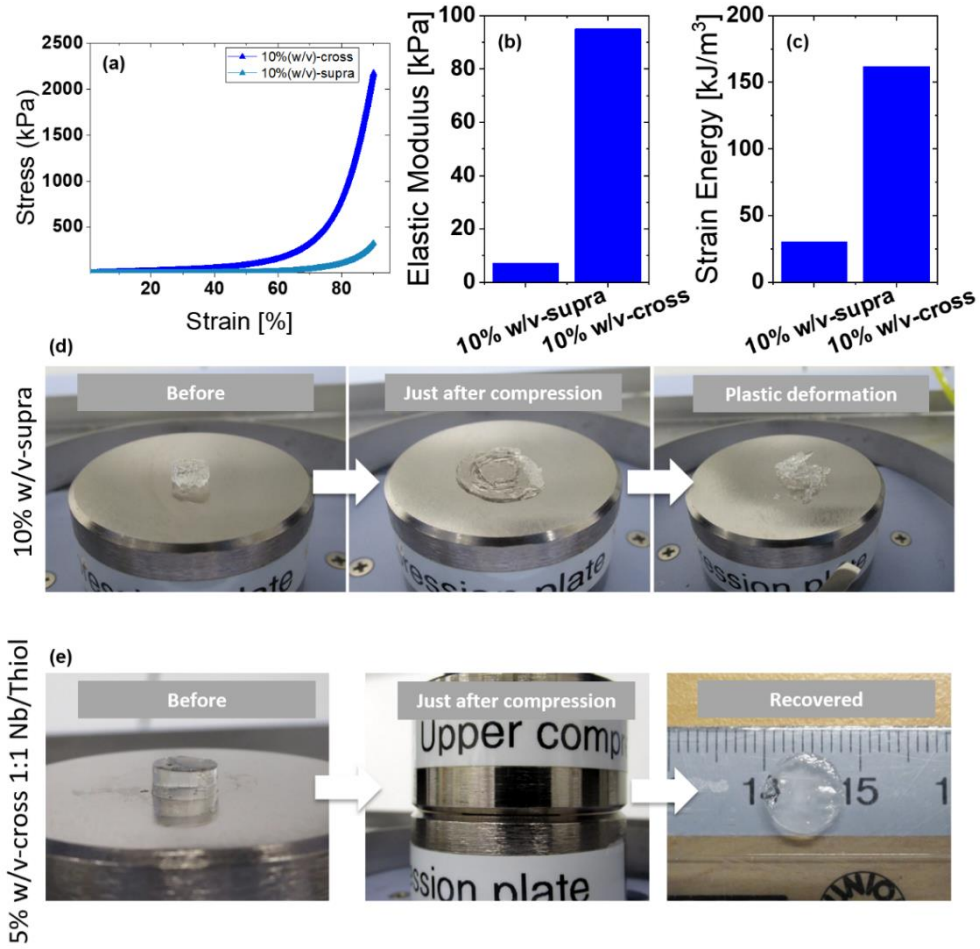

Figure S17. a) Stress-strain curve of 10% supramolecular and 10% w/v (1:1 Nb/thiol) cross-linked hydrogel during compression test. b) Representative sample elastic moduli (between 0–20% of compressive strain) for supramolecular versus crosslinked hydrogel. c) Resulting strain energy when compressed until 90% strain for supramolecaulr and crosslinked hydrogel. d) Optical images of hydrogel before and after compression for 10% w/v supramolecular hydrogels showing pseudo plastic deformation. e) Crosslinked hydrogel using short dithiol crosslinker at 5% w/v (1:1 Nb/thiol) before and after compress, demonstrating elastic recovery in crosslinked supramolecular hydrogel.

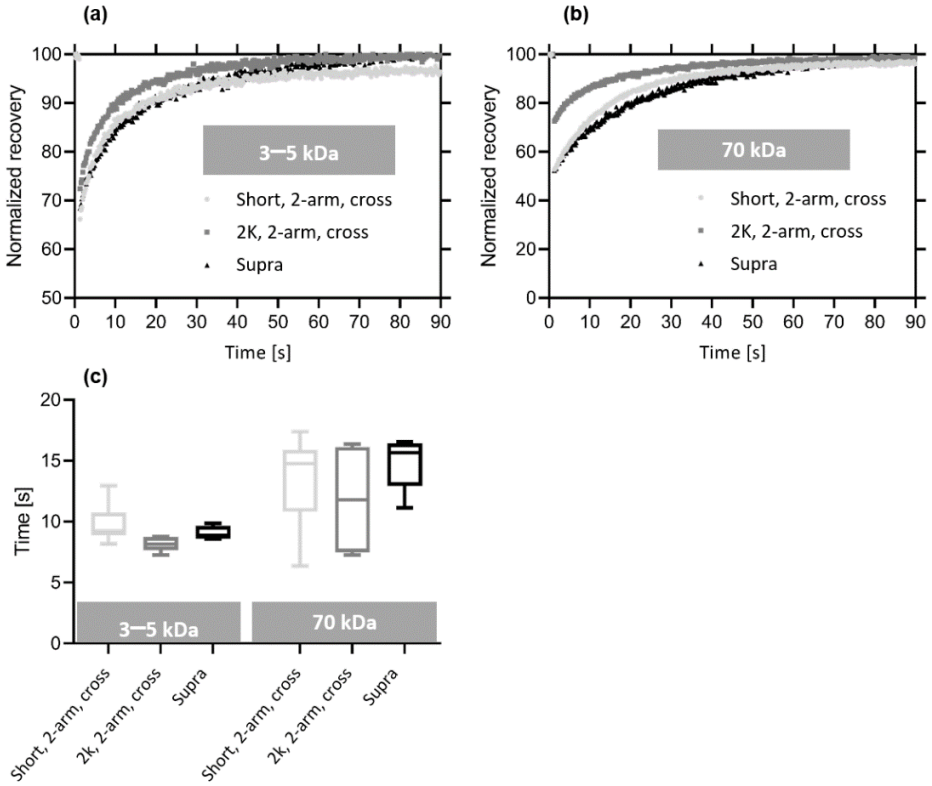

Figure S18. a) FRAP recovery curves using fluorescently labelled dextran of 3–5 kDa and b) 70 kDa hydrogels cross-linked using short and 2K crosslinkers and c) Calculated recovery half time from recovery profiles above. No significant differences were found between samples.

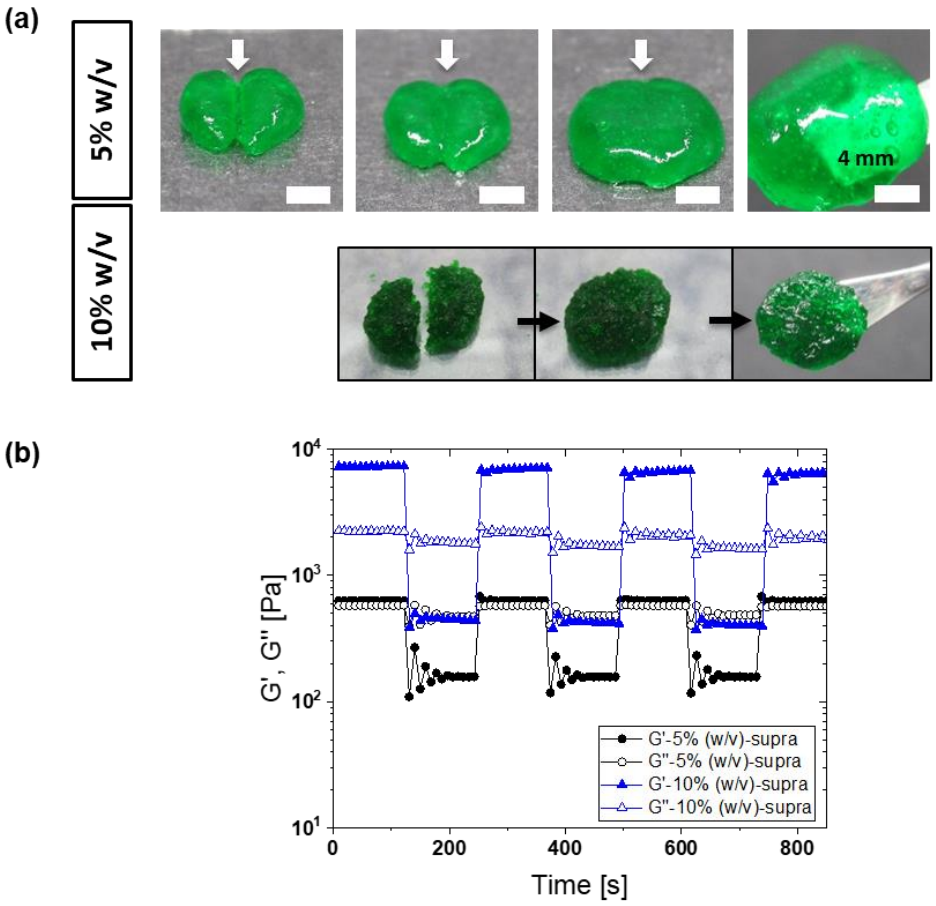

Figure S19. a) Self-healing of supramolecular hydrogel at 5% w/v and 10% w/v shown by optical images and b) using shear rheology shear rupture self-healing cycles.

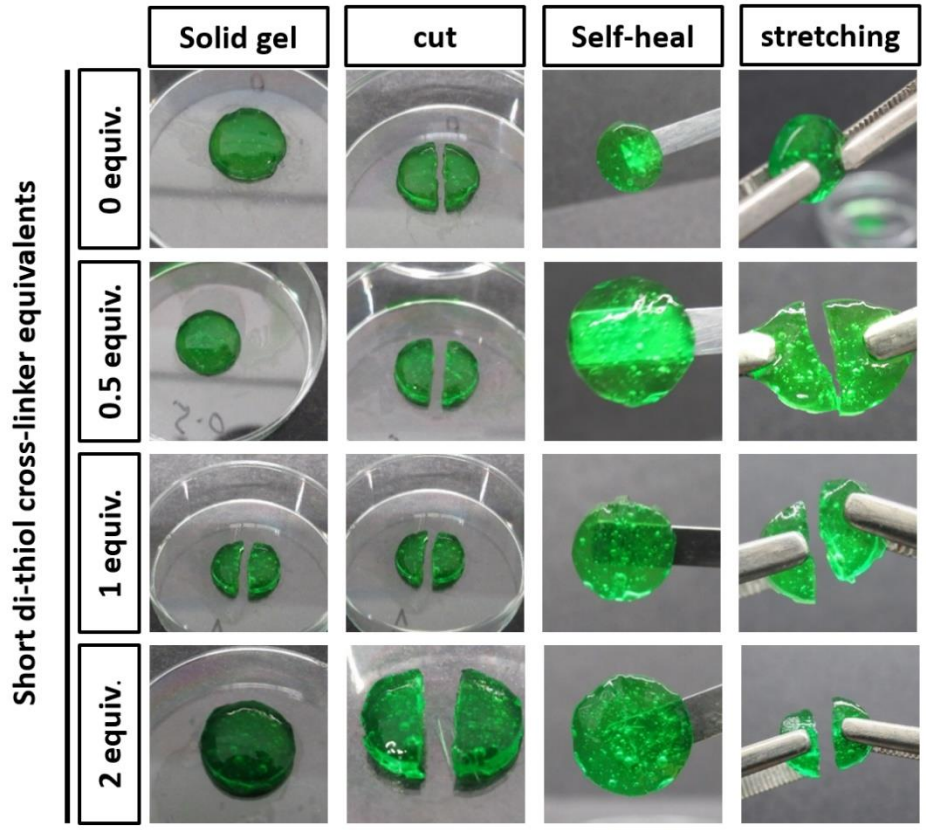

Figure S20. Visual self-healing behavior of cross-linked hydrogel using different mole equivalents of short 2-arm thiol cross-linker after 2 hours. Hydrogel cut into two pieces and then rejoined back into disk shape. All hydrogel self-healed and offer resistance to stretch before coming apart; however, 0.5 mole equivalents hydrogel offer relatively more resistance compared to all other hydrogels.

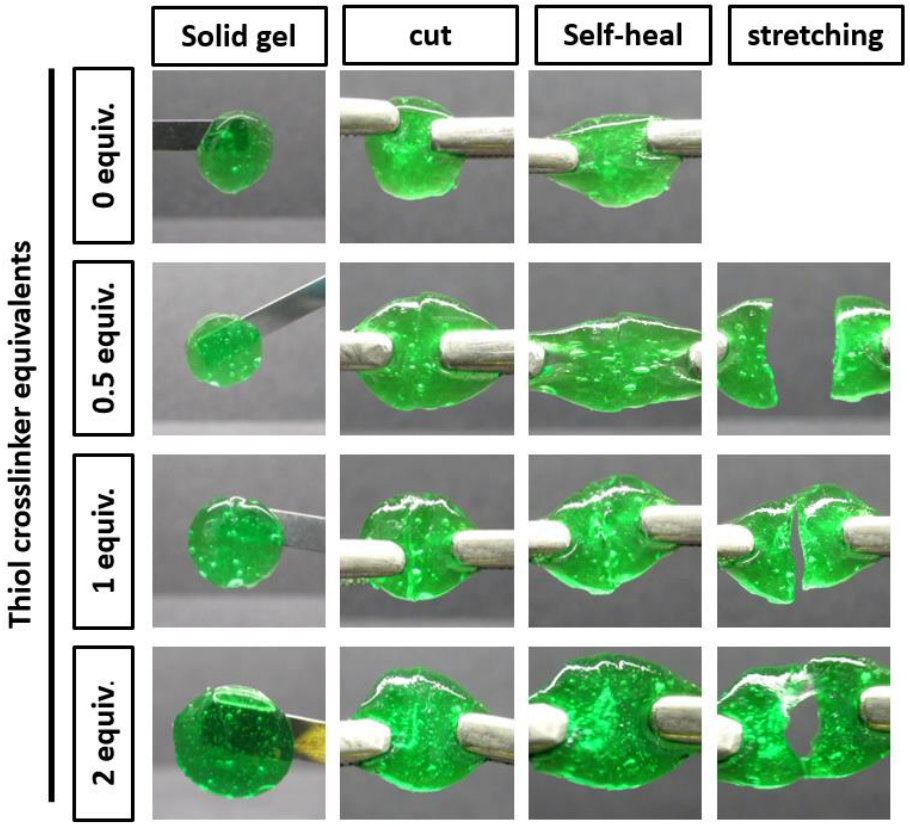

Figure S21. Visual self-healing behavior of crosslinked hydrogel after 24 hours. Each hydrogel cut into two pieces and then put them back together. All hydrogel self-heal nicely and offer slight stretch. Compared to others, 0.5 mole and 2 mole equivalents offer more stretch and more resistance before separation of rejoined pieces.

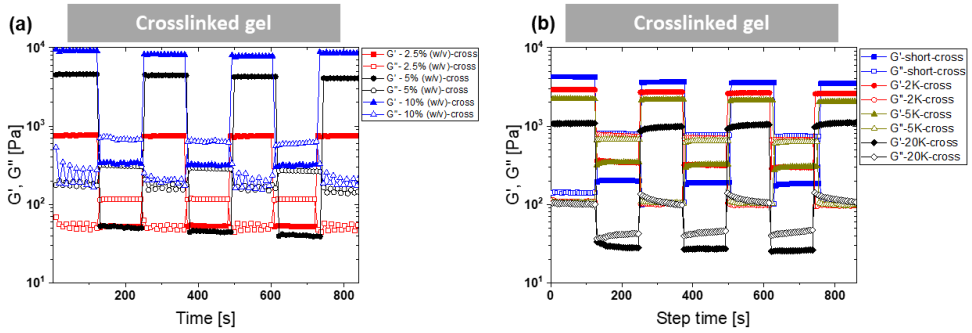

Figure S22. a) Shear rheology of hydrogels crosslinked using short dithiol crosslinker at 2.5% w/v, 5% w/v and 10% w/v at equimolar (1:1) ratio of thiol to norbornene. b) Self-healing behavior of crosslinked hydrogel crosslinked using short, PEG2K, PEG5K, and PEG20K dithiol crosslinker at equimolar ratio of NB to thiol.

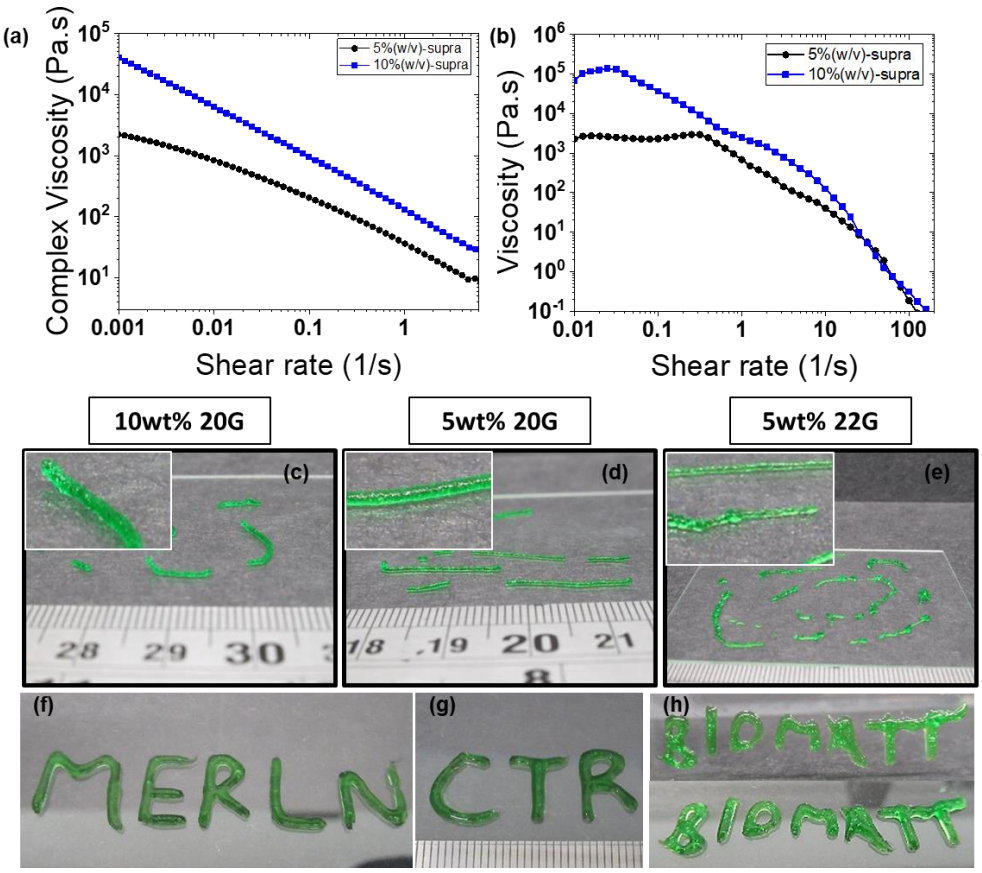

Figure S23. Shear-thinning and extruding of hydrogel: a) A decrease in complex viscosity as a function of shear rate. b) decrease in viscosity as a function of shear rate indicating shear-thinning behavior of hydrogels. c–e) Extruding of hydrogel using 22 gauge needle into a single filament. f–h) Different logos of institutes were extruded using by applying pressure manually with hand shows flexibility of the ink to adapt different shapes.

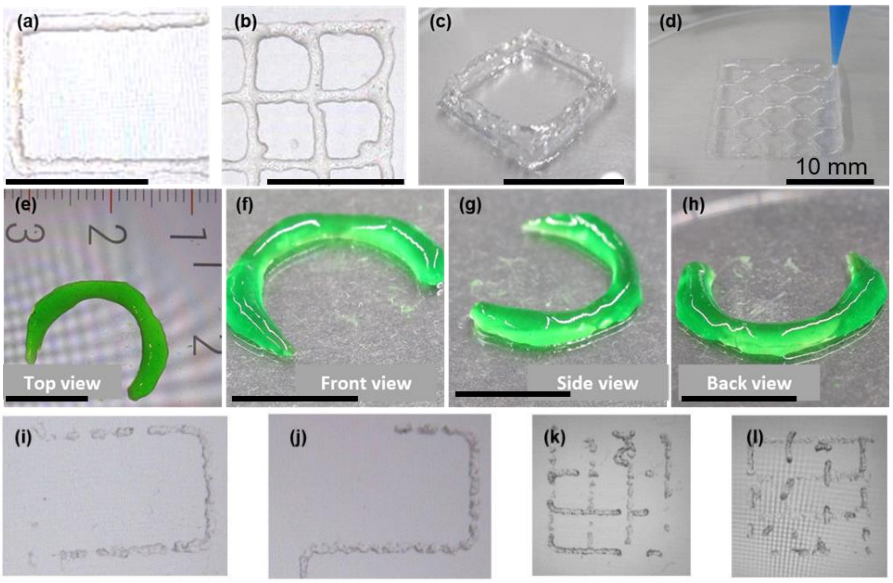

Figure S24. a) 3D printing of supramolecular hydrogel (non-crosslinked) into a single uniform filament. b) 3D printing of grid likes structure, c) 3D printing of 6-layer cube structure. d) 3D printing of 2-layer hexagonal structure. e–h) supramolecular hydrogel (non-crosslinked) printed into cartilage model. a–h) utilized 5% (w/v) of the hydrogel. i–j) filament printing and **k–l)** square grid-like pattern printing using 7.5% (w/v) Nb BTA hydrogel.

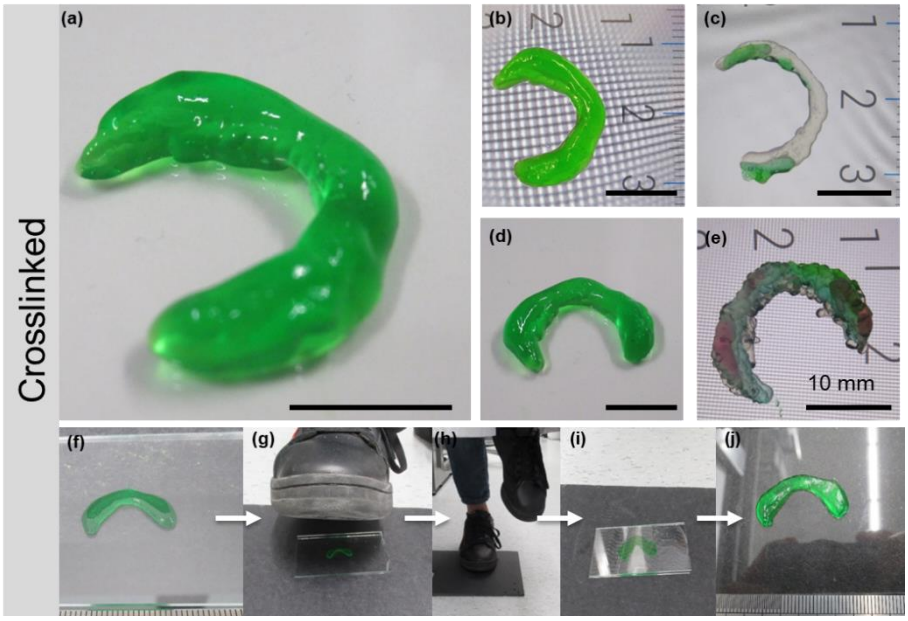

Figure S25. a–c) Layer by layer 3D printing of supramolecular hydrogel into cartilage model and then crosslinking to print a final cartilage model. d–e) 3D printing of two inks with different mechanical properties. White ink (bottom part) has 1:0.5 ratio of Nb to thiol and green ink (top part) has 1:1 ratio of Nb to thiol. f–j) Cartilage model recovery after 60 kg of weight exerted three times.

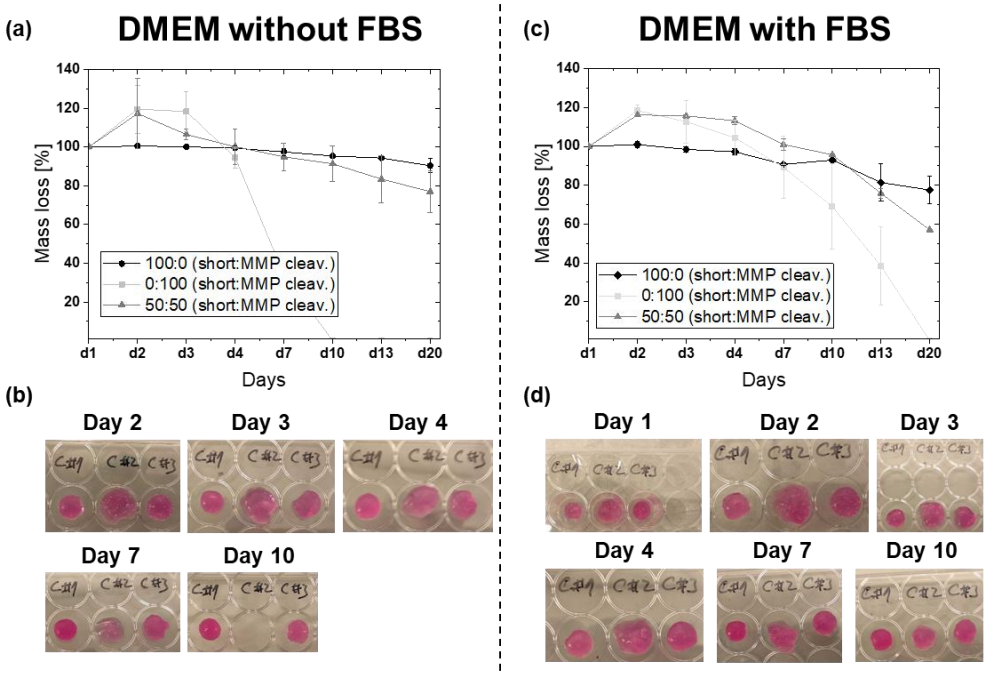

Figure S26. Degradation of hydrogel. a) Mass loss in DMEM without FBS. b) Optical images of hydrogel during degradation study. C#1 shows a hydrogel crosslinked with short dithiol crosslinker, C#2 is a hydrogel crosslinked with MMP sensitive crosslinker, and C#3 is a hydrogel crosslinked with 0.5 mole equivalent of short thiol and 0.5 mole equivalent of MMP sensitive crosslinker. c) Mass loss in DMEM with FBS. d) Optical images of hydrogel during degradation study in DMEM with FBDS. C#1, C C#2, and C#3 represents the same conditions as in the "b".0.5-mole

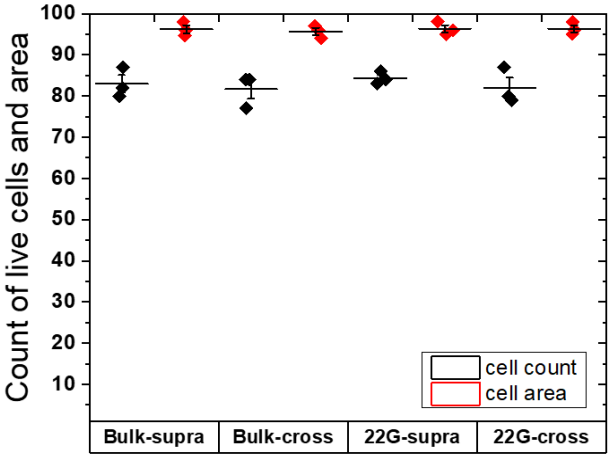

Figure S27. ATDC5 chondrocytes viability using live-dead assay. ATDC5 displayed greater than 80% viability in supramolecular and crosslinked hydrogel before and post injection using 22 gauge needle.

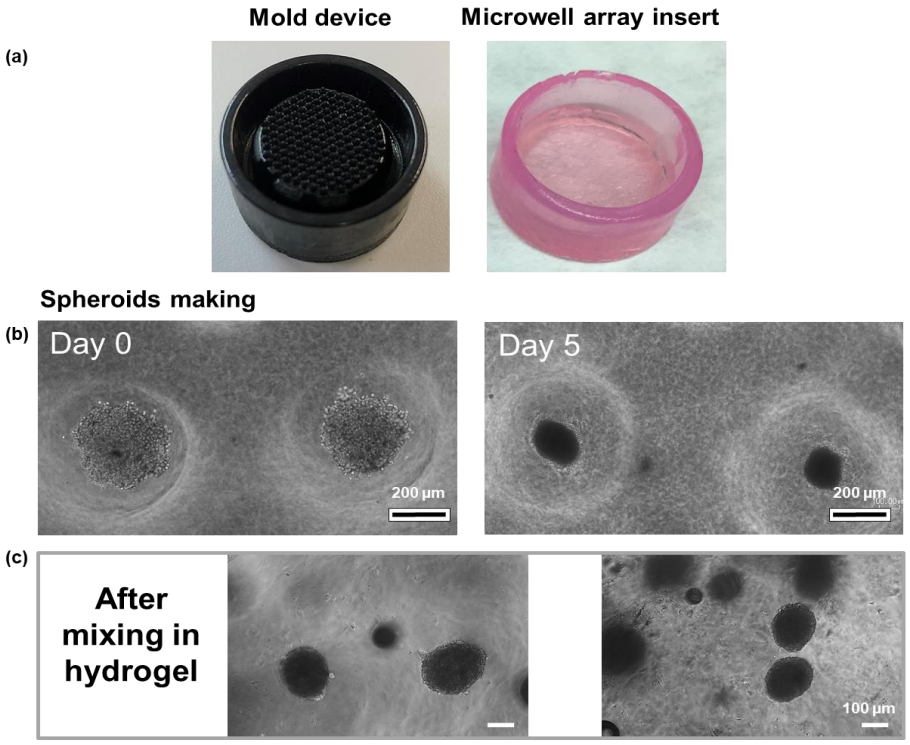

Figure S28. Spheroid formation and morphology of hMSC spheroids after mixing in hydrogel. a) Spheroid formation device making using mold. b) Spheroids making in the device, left panel at day 0 and right panel at day 5. c) Spheroids morphology after mixing in BTA hydrogel and before bioprinting.

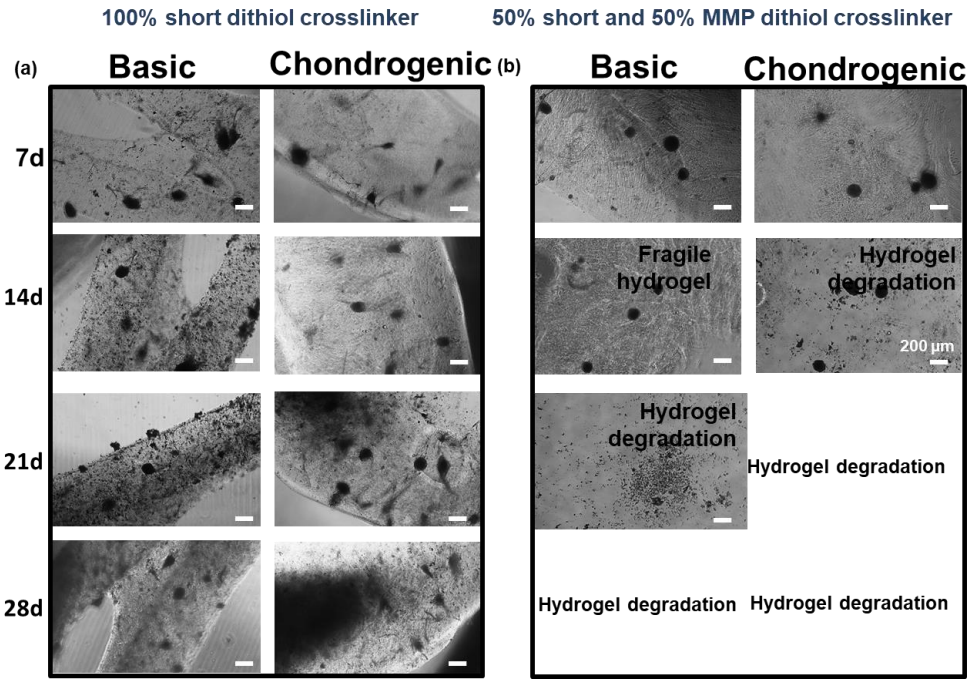

Figure S29. Bioprinted constructs on 7, 14, 21 and 28 days after bioprinting. a, Hydrogel crosslinked using short dithiol crosslinker. Hydrogel was stable until day 28 and could be lifted under both basic and chondrogenic media conditions. b, Hydrogel crosslinked using 50% (0.5 mole equivalent) of short dithiol and 50% (0.5 mole equivalent) of MMP cleavable dithiol crosslinker. Hydrogel degraded in 14 days under basic media conditions and in 21 days in chondrogenic differentiation media.

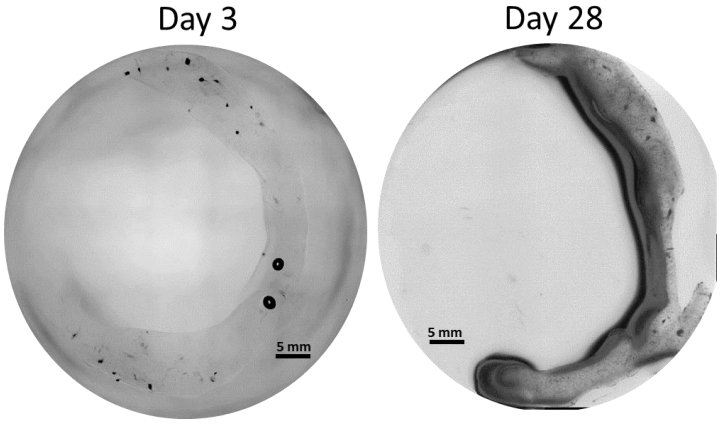

Figure S30. Bioprinted hydrogel stability and shape fidelity. Hydrogel crosslinked using short dithiol crosslinker stays stable until day 28.

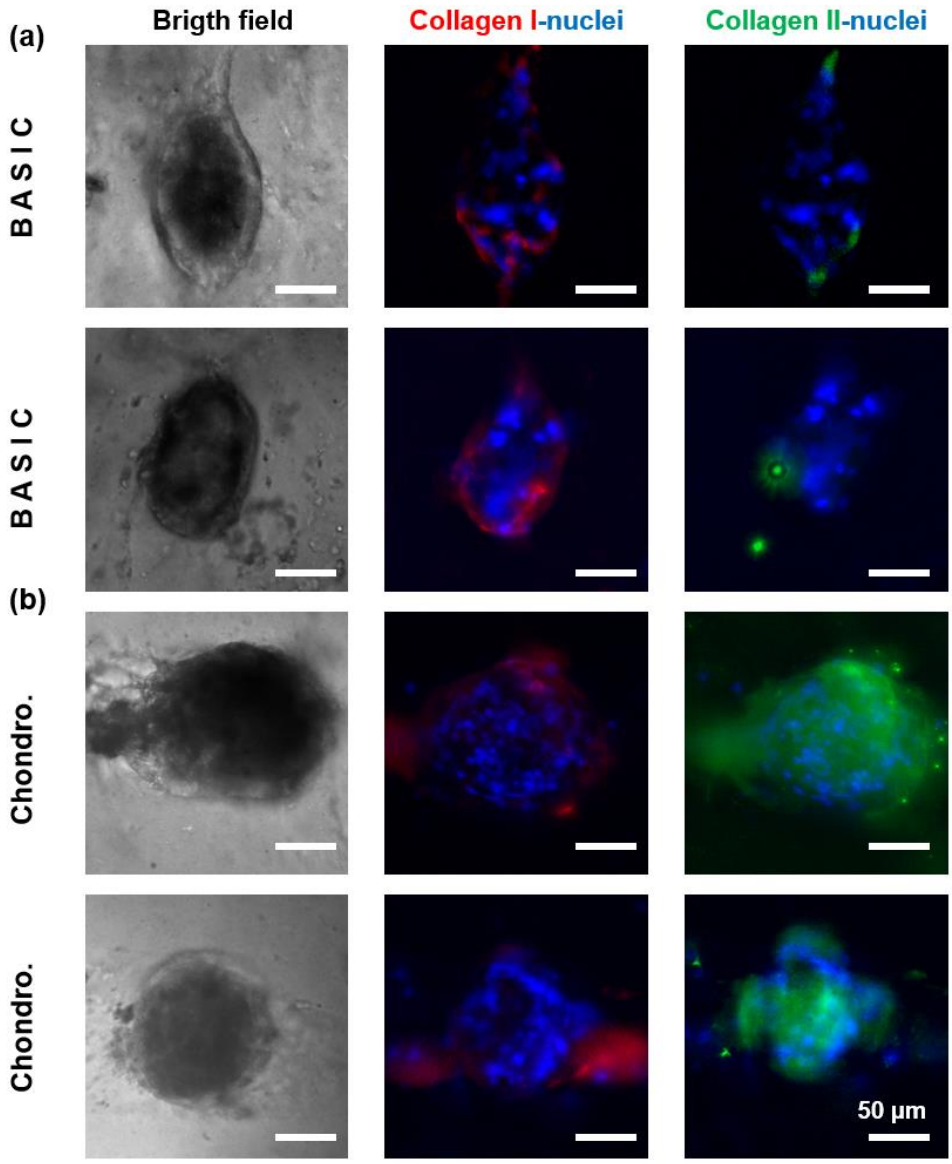

Figure S31. Cartilage-specific ECM production in bioprinted hydrogel. Hydrogel was crosslinked using short dithiol and cartilage-specific ECM produced and investigated at 28 days by immunostaining. a, b, Collagen I (red), collagen II (green), and nuclei (blue) stainings after 28 days of differentiation under basic (a) and chondrogenic (b) differentiation media.

Chapter IX

Discussion of dynamic hydrogels and bioinks

Shahzad Hafeez[1] Clemens van Blitterswijk[1], Lorenzo Moroni[1], Matthew B. Baker[1,]

[1] Department of Complex Tissue Regeneration, MERLN Institute for Technology-Inspired Regenerative Medicine, Maastricht University, P.O. Box 616, 6200 MD Maastricht, the Netherlands

The work described in this thesis fits within the field of biomaterials for tissue engineering with a particular focus on developing dynamic hydrogels and bioinks. The overarching goal of the thesis was to develop and investigate dynamic hydrogels for applications in cell culture and bioinks for 3D bioprinting. Unlike traditional static hydrogels, a dynamic hydrogel has the potential to mimic the dynamicity, viscoelasticity, and structure of the natural extracellular matrix (ECM) and tissues. We developed and investigated hydrogels based on dynamic covalent chemistry (DC_VC) and supramolecular chemistry for applications in cell culture and tissue engineering. More emphasis was given to supramolecular hydrogels based on benzene-1,3,5-tricarboxamides (BTAs), owing to the potential of BTA assemblies to mimic fibril morphology and the freedom to tune dynamics.

In this chapter, we start discussing hydrogels as biomaterials for tissue engineering and why they are suitable materials for cell culture and tissue engineering. Then we move our discussion to why we need dynamicity in hydrogels for applications in cell culture, tissue engineering, and advanced bioinks. We discussed different chemistries and strategies designed and developed for tuning viscoelasticity and 3D bioprinting and then discussed our contributions.

Hydrogels for cell culture

Typically, cells are cultured on flat stiff materials such as polystyrene and glass. Cells cultured in these environments tend to display flattened shapes, abnormal polarization, and loss of differentiated phenotypes. These culture conditions are very stiff compared to the relatively soft ECM microenvironment in which a cell resides in the body. This makes these matrices physiologically irrelevant and culture systems that better mimic the mechanical and biological milieu are needed to mimic the complex native ECM microenvironment. The ECM on average also contains more than 75% water, making it essentially a hydrogel. Scientists have responded by developing natural and synthetic hydrogels to recapitulate the ECM.

Hydrogels are considered one of the most promising materials for cell culture owing to their ability to mimic the hydrated environment of the native ECM and provide freedom to engineer mechanical, compositional, and structural complexity into cell culture systems. In early studies, several hydrogel systems have been employed in answering a fundamental question on cell-materials interactions. Hydrogels enabled answering if the matrix elasticity directs stem cell lineage. Using polyacrylamide hydrogels, Engler et al., demonstrated that matrix stiffness can specify lineage specification. For example, they discovered that soft matrices mimicking the brain are neurogenic, stiffer matrices mimicking muscle are myogenic, and rather rigid matrices mimicking collagenous bone are osteogenic.[1,2] While elastic hydrogels allowed for answering fundamental questions and enhanced understanding of cell-matrix interactions on 2D matrices; however, they do not mimic non-linear time-dependent properties of native ECM and tissues. Additionally, cells in native tissues reside in a 3D environment and cells can migrate, spread, and form cell aggregates; however, a cell in elastic hydrogel often stays rounded. This led scientists to look beyond tuning stiffness and the development of new dynamic hydrogels for cells to actively remodel their microenvironment and for correct deposition of ECM.

Dynamic hydrogels with tunable viscoelasticity

In the early days, dynamic hydrogels were made by introducing hydrolytically degradable cross-links such as ester bonds.[3,4,5] Hydrolytically degradable hydrogels are useful for the release of drug molecules and for cell growth and spreading; however, these hydrogels showed bulk and uncontrolled degradation and complicated the mechanical properties and dynamics that influence cell behavior. This stimulated scientists to design a new set of hydrogels where degradation can be locally controlled by a cell-released enzyme. A new set of synthetic hydrogels with peptide cross-links with cleavage sites for cell-secreted matrix metalloproteinases were developed. Protease-degradable hydrogels enhanced understanding of cellular migration, remodeling, and tissue formation.[6,7] The design of a protease-sensitive hydrogel provided a powerful tool to understand cell-ECM interactions for controlling cell function; however, engineering controlled viscoelasticity for matching cellular timescale remains a challenge.

The emergence of viscoelastic hydrogels enabled an understanding of viscoelastic time scales influence on cell behavior. Several approaches have been utilized for engineering viscoelasticity within hydrogels. Viscoelastic polyacrylamide hydrogels with incomplete crosslinking were developed which allowed viscous behavior and creep in materials.[8] Polyacrylamide viscoelastic hydrogels have been made by either varying the ratio of acrylamide and bisacrylamide or by introducing unbound linear acrylamide polymer chains in crosslinked polyacrylamide hydrogel network.[9] Viscoelasticity in ionically crosslinked alginate hydrogels has been tuned using alginate of low, medium, and high molecular weight.[10,11] Viscoelasticity has also been tuned in hydrogels by grafting polyethylene glycol and then ionically cross-linking[12] and by forming interpenetrating networks of alginate and collagen and cross-linked with the combination of ionic and covalent cross-linking. [13]

Dynamic covalent chemistry has played a greater role in developing dynamic and viscoelastic hydrogels. Dynamic covalent chemistry enabled us to rationally tune dynamicity and viscoelasticity by utilizing the equilibrium constant (K_{eq}) and forward rate constant (k_1) and reverse rate constant (k_{-1}). Dynamic covalent hydrogels based on dynamic covalent bonds such as hydrazone[14,15–19,20,21,22], semicarbazone[20], oxime[20,18], boronate esters[23,24,25,26,27] and thioester exchange[28] are developed.

Besides dynamic covalent chemistry, supramolecular chemistry also offers an appealing approach for tuning viscoelasticity in hydrogels. For example, by combining host molecules such as cyclodextrin[29–31,32,33] and cucurbit[7]uril[34,35] with complementary guest molecules, hydrogels with various degrees of viscoelasticity have been made. Recent studies show the utilization of hydrogen bonding and hydrophobic interactions for tuning viscoelasticity within supramolecular and fibrillar hydrogels such as UPy[36] and BTA[37].

Dynamic hydrogels as bioinks for 3D bioprinting

3D bioprinting is a powerful and straightforward technique for the creation of complex and intricate 3D tissues. Many bioprinting techniques are developed with the final aim to create a functional tissue; however, we will discuss extrusion bioprinting in this section. First, we will focus on the requirements of a bioink for extrusion bioprinting and discuss the progress in the development of bioinks. Extrusion bioprinting involves continuous extrusion and deposition of filaments. Some important properties that require consideration for the application of bioinks for 3D bioprinting include viscosity, gelation kinetics, shear-thinning, self-healing, viscoelasticity, biodegradation, cytocompatibility, and biocompatibility. An ideal bioink should allow bioprinting with the required mechanical properties while maintaining good cytocompatibility and should steer cell phenotype for correct and healthy tissue formation.

Traditional bioinks have focused heavily on low-viscosity bioinks to avoid excessive shear stress during the extrusion. Several bioinks composed of natural polymers (alginate[38,39,40,41], hyaluronic acid[42], gelatin[43,44], collagen[45], fibrin[46], agarose[47], and decellularized extracellular matrices[48]) and synthetic polymers (polyvinyl alcohol[49] and PEG hydrogels[50]) have been developed. However, shape retention after printing remains poor. Sacrificial bioinks have also been employed for the bioprinting of low-viscosity bioinks. In recent years freeform reversible embedding of suspended hydrogels (FRESH) printing has been developed for overcoming shape retention limitations, especially for arches and projections[51]. Other notable bioink strategies include thermal and photo-triggered tandem gelation[52], 3D bioprinting capabilities using complementary thermo-reversible gelatin network bioinks[53], and 3D bioprinting using universal orthogonal network (UNION) bioinks.[54] While we have more generalizable strategies on the horizon, the controlled dynamicity and viscoelasticity within these hydrogels largely remain missing.

Bioprinting of hydrogel with controlled dynamicity and with good shape retention has been considered mutually exclusive, and this conundrum has led to the development of shear-thinning hydrogels. Shear-thinning is a decrease in the viscosity of material upon application of shear stress or shear rate. In recent years granular hydrogels (jammed hydrogel microparticles) are 3D bioprinted owing to their shear-thinning properties[55,56] while maintaining their near original mechanical properties post-printing with good cytocompatibility[57] and spheroids formation.[58] Recent studies have also shown successful 4D bioprinting of micro-flake microparticle hydrogels while maintaining good cytocompatibility.[59] Though granular hydrogels possess shear-thinning and dynamicity; systematic studies are missing on the bioprinting of granular hydrogels with controlled dynamicity and viscoelasticity.

Dynamic covalent chemistry (DCvC) offers a more appealing approach for designing dynamic hydrogels with shear-thinning and controlled viscoelasticity. Dynamic covalent chemistry allows correlating molecular parameters directly to macroscopic properties; for example, the hydrogel's stiffness directly relates to the equilibrium constant (K_{eq}), the hydrogel's self-healing directly relates to the forward rate constant (k_1), and the hydrogel's shear-thinning and stress relaxation directly relates to the reverse rate constant (k_{-1}). A dynamic covalent network of phenylboronic

acids and glucose-like complexes was developed. The initial selection of phenylboronic acid with characteristic pK_a and systematic variation in pH allowed control over viscoelasticity. These hydrogels were injectable and showed tissue biocompatibility upon subcutaneous injection.[25] Bioprinting studies with phenylboronic acids-diol complexes remain unexplored. Imine-based hydrazone dynamic covalent chemistry has been utilized for developing bioinks with controlled viscoelasticity in dynamic and shear-thinning networks. Lattice shape structures were 3D printed with good shape retention; however, bioprinting was not shown.[60] An injectable hydrogel using hydrazone dynamic covalent chemistry with thermoresponsive engineered elastin-like protein (ELP) was also developed. This hydrogel protects hMSC during injection and the ELP secondary network allowed tuning of the stiffness and stability of hydrogel. Though injection of hMSCs using clinically relevant gauge was shown, bioprinting of multilayer construct remained unreported.[21] Polysaccharides-based bioink made of the acyl hydrazone and Schiff base reaction has been successfully bioprinted and chondrocytes maintained chondrogenic phenotype in these hydrogels.[61] In our group, we have developed an imine-type dynamic bioink. The selection of imine-type cross-links (oxime, semicarbazone, and hydrazone) with appropriate K_{eq} allowed tuning the viscoelasticity of these bioinks. All cross-links demonstrated injectability; however, only hydrazone allowed bioprinting. Chondrocytes showed good viability in bioprinted hydrogels.[20] In the follow-up from our group, Morgan et al. demonstrated that modular mixing of slow (oxime) and fast (hydrazone) dynamic covalent chemistries allowed tuning viscoelasticity and controlling the cell behavior of these hydrogels. Cell spreading within extruded bioinks can be controlled from round to spreading morphology which has been attributed to the dynamicity and stress relaxation capability of these hydrogels.[18]

Another exciting chemistry for the development of dynamic bioinks is supramolecular chemistry. Just like dynamic covalent chemistry, the association, and dissociation in supramolecular monomers can be rationally tuned for engineering dynamicity and viscoelasticity within bioinks. Supramolecular chemistry uses non-covalent interactions such as hydrogen bonds, metal chelation, hydrophobic interactions, and van der Waals interactions for the creation of rationally designed hydrogels and bioinks. What makes supramolecular interactions special and appealing is that they are very specific, reversible, and directional.[62] The first supramolecular hydrogel bioink was based on polypeptide-DNA complexation. Cells remained functional in the 3D bioprinted constructs.[63] Widely explored examples of supramolecular bioinks have been based on β-cyclodextrin and adamantane host-guest chemistry. The dynamic nature of β-cyclodextrin and adamantane interactions imparted properties such as shear-thinning, self-healing, and viscoelasticity within these hydrogels. Bioprinted structures were produced by printing a shear-thinning hydrogel into a self-healing hydrogel.[64] The bioprinted structures did not show stability and required secondary stabilization.[65] Self-assembling short peptides have also been employed to create supramolecular bioinks. Lysine-containing hexapeptides have been shown to support embryonic stem cell culture and adipogenic differentiation of hMSC in hydrogel droplets.[66] However, no large structures were bioprinted and reports on viscoelasticity are absent. Ultrashort tetrapeptides are another class of bioinks; these have been 3D printed into structures of a few centimeters in scale. Cells printed in these hydrogels remained viable (above

90%) for 24 days of culture.[67] Reports on viscoelasticity are not found for these bioinks. Peptide amphiphile inks have also been printed into 3D structures with nanoscale and bulk alignment.[68] In these bioinks, myoblasts showed good viability after 7 days of bioprinting. Other examples of supramolecular bioinks include pseudo-polyrotaxane structures (PEG side chains grafted onto chitosan and threaded with α-CD) dually cross-linked using β-glycerophosphate. Bioprinted fibroblasts showed higher levels of Paxillin, and N-cadherin in these hydrogels on day 14 as compared to day 3.[69]

Our efforts of tuning viscoelasticity in hydrogels and bioinks

In pursuit of developing advanced bioinks with controlled viscoelasticity, we worked on developing bioinks made of imine-type dynamic covalent chemistry and BTA supramolecular chemistry.

Dynamic networks are essential for tuning viscoelasticity and bioprinting

In **Chapter IV,** we presented our work on the tuning of viscoelasticity and bioprinting using reversible imine-type cross-links. Utilizing knowledge of K_{eq} of small molecules from literature, we developed a series of imine-type (oxime, semicarbazone, and hydrazone) dynamic hydrogels. Storage modulus and viscoelasticity followed the expected trend of K_{eq}. For example, oxime (3000 Pa) with the highest K_{eq} showed the highest modulus followed by semicarbazone (500 Pa) and hydrazone (200 Pa). Hydrazone exhibited the highest viscoelasticity compared to semicarbazone and oxime. Human dermal fibroblasts (HDF) displayed spreading morphology in hydrazone hydrogel in contrast to less spreading morphologies in semicarbazone and oxime hydrogels. The dynamic nature of hydrazone cross-link enables the 3D printing of smooth fibers and life-like vascular structures. Chondrocytes (ATDC5) demonstrated high cell viability in the bioprinted hydrazone bioink. In summary, we demonstrated that imine-type dynamic covalent chemistry offers great potential for tuning viscoelasticity in bioinks.

Though we were able to show tuning of viscoelasticity and bioprinting using imine-type dynamic covalent chemistry hydrogels, detailed studies on cell spreading and differentiation remain to be performed. These studies will help to find a suitable range of viscoelasticity for different tissues. This would enable answering the questions of which tissue cells like more or less dynamicity. Neuronal cell outgrowth, hMSCs spheroid formation, maturation, and embryonic and pluripotent stem cell organoids formation and growth will be interesting areas to explore.

Modular mixing is a promising platform for tuning viscoelasticity (stress relaxation) and spheroid formation in supramolecular fibrous hydrogels

In **Chapter V,** we tackled the challenge of tuning viscoelasticity in supramolecular fibrous hydrogels for recapitulating the ECM's dynamicity and fibrous structure. Next, we showed for the very first time that the viscoelasticity and dynamics of supramolecular interactions can be

leveraged for influencing cell aggregation and spheroid formation. In this chapter, we utilized the modular mixing of BTA architectures with slow and fast exchange dynamics. Stable hydrogels with controlled viscoelasticity were formed when BTA architectures were copolymerized in various ratios. Stress relaxation times within these hydrogels can be tuned from under a second to several thousands of seconds. Chondrocyte ATDC5 and human dermal fibroblast exhibited >80% viability. Neuronal cells (PC12 and dorsal root ganglion, DRG) showed out-growth within these hydrogels. ATDC5 formed cellular aggregates and human mesenchymal stem cells (hMSCs) formed spheroids within these hydrogels. Importantly, we discovered that cellular aggregation was driven by viscoelasticity and dynamicity of hydrogels: fast and more compact aggregates/spheroids were observed for hydrogels with greater viscoelasticity. These hydrogels can be a useful platform for growing spheroids which are mini-blocks for growing larger tissues and finding applications in drug testing.

This is an interesting set of hydrogels with some unique mechanical properties. Cadherin expression and lineage commitment of hMSCs spheroids as a function of the dynamicity of hydrogel would be the next steps to explore with these hydrogels. Since the brain is a stress-relaxing tissue, investigation of neuronal cells with BTA hydrogel of controlled stress relaxation would allow a better understanding of stress relaxation's influence on neuronal cell growth.

Simple synthetic strategies are essential for the upscale synthesis of multifunctional multicomponent supramolecular macromonomers

In **chapter V**, we have presented BTA-based supramolecular materials that mimic the fibrous morphology and viscoelasticity found in the natural ECM. However, large-scale synthesis of complex and multifunctional BTA hydrogelators is required. Existing desymmetrization strategies have been limited in upscaling and purification of multifunctional BTAs[70,71,72]. To address this challenge, in **chapter VI**, we have developed a new desymmetrization based on activated ester coupling of a symmetric synthon. We developed a small library of benzene core-based activated triesters (BTE) synthons and discovered that a benzene-1,3,5-tripentafluorophenol triester (BTE-F_5Ph) allowed for successful desymmetrization and the production of multifunctional BTAs in good yield and with high reaction fidelity. This novel desymmetrization route has allowed for the quick synthesis of a small library of BTA monomers with hydrophobic and/or orthogonal reactive handles. We have successfully extended this desymmetrization strategy for creating polymeric BTA hydrogelators. Cryo-TEM revealed that newly synthesized polymeric BTA hydrogelators undergo aggregation and created fibers and fibrous sheets-like structures. We tuned the mechanical properties of the BTA hydrogelator by changing the hydrophobic arm on the BTA molecule. Chondrocytes showed high cytocompatibility within these hydrogels. Possible large-scale synthesis with the fibrous structure indicates the potential of these hydrogelators for cell culture and tissue engineering applications as synthetic ECM.

Though we have shown the power and flexibility of this approach, this newly developed desymmetrization strategy offers immense potential for creating a diverse range of BTAs which

then can be utilized for creating more complex polymeric BTA architectures. For example, other click chemistry and dynamic covalent chemistry can be installed on BTA arms which then can be utilized for crosslinking BTA assemblies or bioactivation of BTA scaffolds. Dynamic covalent chemistry can also be utilized to enhance mechanical properties and tune viscoelasticity, dynamicity,shear-thinning, and self-healing capacity within BTA hydrogels for 3D bioprinting applications. Other potential areas to explore will be installing saccharides and peptides for mimicking glycans and the bioactivity of the natural ECM.

Molecular tuning of supramolecular interactions creates hydrogel networks with controlled viscoelasticity

Tuning viscoelasticity across a broad range of fibrous hydrogels remains a challenge. Utilizing the desymmetrization strategies developed in **chapter VI**, we created a library of supramolecular BTA hydrogelators in **chapter VII** with fibrous structure and controlled viscoelasticity. We varied the hydrophobic carbon length on the BTA from twelve to sixteen, eighteen, twenty, and twenty-four. All hydrogelators self-assembled into fibrous structures and formed hydrogels in water. We discovered that the carbon length on the BTA determines the viscoelasticity and stress relaxation of the hydrogels in a logarithmic fashion. These hydrogels were self-healing, shear-thinning, and injectable. Additionally, these hydrogels were 3D printable into multilayer structures. Chondrocytes showed high cell viability in 2D contact assay, in bulk 3D hydrogels, and in bioprinted 3D hydrogels. This simple molecular tuning enables precise control over viscoelasticity and 3D printability and provides a more generalized strategy that can be ported to other supramolecular systems, such as UPy, peptide amphiphiles, and bolaamphiphiles.

Though these hydrogels showed controlled viscoelasticity in fibrous hydrogels, it is hard to utilize them for longer cell culture duration. Owing to the dynamic nature of interactions, these hydrogels tended to degrade over time during cell culture. However, we have seen cell aggregation in these hydrogels during cell viability studies and these hydrogels offer a potential way to make cell aggregates in a controlled physiologically relevant environment for tissue engineering and drug testing applications. On controlling dynamicity for *in vitro* cell culture applications, one way to tune dynamicity would be to design a hydrogelator with bioorthogonal reactive chemistries for introducing cross-links. Another way could be to tune dynamics by introducing additional covalent cross-links for stability; for example, combining with polyethylene diacrylate (PEGDA) or other polymer solutions, which can provide a secondary stabilizing mechanism without affecting fibrous morphology. Cell-adhesion studies also remain missing in these hydrogels to find out the effect of viscoelastic timescales on cell spreading. Perhaps future studies can focus on introducing cell-adhesion peptides (i.e., RGD) for investigating cell morphology on top (2D) and within hydrogels (3D). Importantly, *in vivo* studies are needed where these hydrogels can be injected into cavities and tissue formation could be investigated. *In vivo,* studies will enable us to answer if the dynamic hydrogels promote tissue formation and how fast or slow is the erosion of these hydrogels *in vivo* compared to *in vitro*. This will be essential information to steer the future direction of dynamic hydrogels.

Covalent cross-linking of a supramolecular assembly creates tough, fibrous hydrogels and bioinks

Tissues such as cartilage and muscle in the human body are dynamic, yet tough. Hydrogels developed in **chapter VII** are dynamic, yet lack toughness. To create tough hydrogels, we took inspiration from collagen structure which is abundantly found in tough tissues such as cartilage. Simulation studies have attributed this toughness in collagen to the combination of fibrous non-covalent self-assembly with covalent bond formation, yet this remains difficult to engineer in synthetic hydrogels. We introduced a supramolecular/covalent strategy to create tough hydrogels with a fibrous structure. We developed a BTA-based hydrogelator with norbornene (NB-BTA) handles, which can undergo thiol-ene chemistry to generate covalent cross-links. The NB-BTA hydrogelator is self-assembled at a nanoscale and microscale, resulting in fibrillar and viscoelastic hydrogels. Then, just like covalent cross-links in collagen, we tuned the mechanical properties such as toughness, strength, and stiffness by covalent inter- and intra- fiber cross-links. The hydrogels showed maximum strength around 2 MPa without breaking at 90% strain and withstood 550% tensile strain and recovered to their original strength after multiple hysteresis cycles. We discovered that the NB-BTA hydrogel was shear-thinning, self-healing, and could be 3D bioprinted into complex life-like structures. The 3D bioprinted structures could be further toughened and strengthened by covalent cross-linking of the fibrous assemblies. Further, we have shown that hMSC spheroids differentiated into chondrogenic-like tissue in these hydrogels. Together, we have shown that the combination of self-assembly and covalent cross-linking of supramolecular fibers offers a potentially effective method for the bottom-up creation of dynamic, yet robust, synthetic hydrogels and bioinks.

With this hydrogel system we have demonstrated *in vitro* chondrogenic tissue formation; however, many interesting studies remain unexplored and would be interesting for future applications. For example, owing to the injectable properties and freedom of tuning mechanical properties, this hydrogel can be injected to fill in tissue cavities and the mechanical properties can be adjusted to match the requirement of different tissues. Additionally, we have demonstrated that this hydrogel can be made degradable by cross-linking with a protease-sensitive di-thiol crosslinker. Such selective degradation in tough hydrogels would be useful for the creation of tough yet degradable hydrogels for successful new healthy tissue formation. One step further would be matching the degradation rate of hydrogels with new tissue formation.

Another exciting area of research is the investigation of interactions of cells with hierarchically organized supramolecular materials. The NB-BTA is a hierarchical material and is an interesting candidate for investigating supramolecular material-cell interaction owing to tunable dynamicity and ability to bioactivate NB-BTA hydrogel. Preliminary work was carried out on the bioactivation of NB-BTA hydrogels and the investigation of cell attachment. While bioactivation of the NB-BTA hydrogel was accomplished with the cysteine RGD peptide (CGGGRGDS). We observed human umbilical vein endothelial cells (HUVECs) cell attachment and some spreading on these hydrogels (**Figure S1**). Then we studied the attachment and spreading of

hMSCs on these hydrogels using either 250 nM or 500 nM RGD concentration. HMSCs showed attachment and also a small spreading was observed (**Figure S2**). These observations were made on the bright field and perhaps the staining of the cell will allow a better understanding of the extent of spreading and morphology of hMSCs on NB-BTA hydrogels.

Next, we hypothesized that changing spacer length between RGD and cysteine (C) amino acids might influence cell attachment and cell spreading. Spacer length will increase the distance of RGD from the hydrogel hydrophobic core. We employed cysteine RGD with a spacer length of 3, 9, and 15 amino acids. RGD with spacer length of 3 amino acids (C-GGG-RGDS, labeled as short), 9 amino acids (C-GGSGGSGGG-RGDS, labeled as the medium), and 15 amino acids (C-GGSGGSGGSGGSGGG-RGDS, labeled as long) for investigation of the spacer length affect on cell spreading. ATDC5 chondrocytes were studied for cell attachment and spreading studies. We observed aggregate formation on all hydrogels after 72 hours of culture (**Figure S3**). Some cell spreading at the boundary of cell aggregate was observed for RGD with a short spacer length and some thin protrusions were also observed for RGD with a long spacer length. However, no conclusion can be drawn from preliminary cell studies on cell spreading. Perhaps, adhesion-dependent cells such as hMSCs and fibroblasts will be a good model to study cell attachment and cell spreading as a function of spacer length for future studies. Additionally, step by step, changes in the dynamicity of hydrogel would allow the decoupling effect of the dynamicity of hydrogel networks from spacer length (in other words dynamicity/mobility of RGD peptide on hydrogel surface). In this current design of Nb-BTA hydrogel, cysteine RGD is conjugated to a hydrophobic core since Norborne also acts as a hydrophobic core for the effective stacking of BTA monomers. The RGD conjugation to the hydrophilic region might be more interesting to explore cell attachment and spreading.

Strain stiffening is an increase in storage modulus above a critical threshold strain. Many components of ECM such as collagen and fibrin exhibit strain-stiffening behavior. We observed some strain stiffening in some of the formulations; however, the shortage of time does not allow us to probe this further. The author would suggest probing strain stiffening behavior further. For example, wt% of hydrogel, aging of hydrogel or dilute solution before cross-linking, and cross-linking of hydrogel with inorganic nanomaterials would be interesting areas to explore for investigation of strain stiffening behavior in these hydrogels.

Viscoelasticity tuning: future challenges and opportunities

Living tissues and the ECM exhibit dynamicity and viscoelasticity.[73,74] However, a big challenge remains in the better understanding of viscoelastic times scales of tissues; for example, only a few studies have reported on the viscoelastic time scales of different tissues[73,75–77]. Currently, the field is lacking extensive studies on the comparison of viscoelastic time scales of different tissues with a comparison between healthy versus diseased, during development versus young, and young versus old. Additionally, the comparison should be made across different species for

example human versus sheep and sheep versus rat. On recording these time scales, different measurement techniques are used, for example, compression testing, rheology, nanoindentation, and particle tracking microrheology for a different set of materials. This makes the comparison of relaxation time scales across different techniques and different materials difficult. General guidelines on recording and reporting stress relaxation time scales will enable a fair comparison across different techniques and different materials. This will enhance our understanding of viscoelastic time scales across different species and different tissues. Furthermore, these time scales will help in a better choice of materials for investigating cellular responses.

The last decade has seen an increase in the number of studies demonstrating viscoelasticity influencing cell spreading and differentiation. However, contradicting results also have been shown on 2D hydrogels, which have been demonstrated to viscoplastic deformation alginate and collagen hydrogels. More work is needed first in measuring the viscoelasticity and viscoplasticity of tissues and then decoupling viscoelasticity and viscoplasticity to influence cell behavior *in vitro*. At this moment, it is unclear how viscoplasticity and viscoelasticity are related and how cell perceives information from such matrices. For example, cells can permanently deform viscoplastic matrix, which will complicate the mechanical response of materials. Additionally, one needs to be careful about the prediction of results from cellular studies considering cells could deform hydrogels permanently (viscoplasticity). Time-dependent mechanical response of viscoelastic and viscoplastic materials overtimes also remains unexplored. Furthermore, understanding of viscoelasticity in 3D culture remains limited. Now with the spheroids and organoids model on the rise, it is important to investigate the influence of viscoelastic time scales on the formation and maturation of organoids. However, decoupling viscoelasticity from viscoplasticity and other factors such as porosity, diffusion, and topography/orientation will be critical for a better understanding of the role of viscoelasticity on tissue maturation and growth.

A range of chemistries including ionic, covalent, dynamic covalent, and supramolecular chemistries have been investigated for tuning viscoelasticity within hydrogels. These viscoelastic hydrogels have enhanced our understanding of cell-material interactions. There are still many challenges to be addressed. For example, most dynamic hydrogels are prone to dissolution, which affect the stiffness and stress relaxation of these materials. Long-term mechanical properties of dynamic hydrogels remain to be understood and how significantly this can affect cellular response also remains unclear. Engineering a broad range of viscoelasticity in hydrogels and linking them to molecular parameters remains a challenge. Viscoelasticity across three orders of magnitude has been demonstrated using hydrazone dynamic covalent bond; however, this study used organic catalyst in higher several hundred mM concentration, and cell studies are missing[78]. Viscoelasticity tuning in boronic acid hydrogels[24] has also been linked to a molecular parameter such as pK_a; however, viscoelasticity has been tuned by the change in pH which likely going to decrease the cytocompatibility of these hydrogels. New strategies are needed for engineering a broad range of viscoelasticity by either utilizing molecular design or biocompatible stimulus for the development of compatible viscoelastic hydrogels. Dynamic covalent

chemistries also offer some disadvantages; for example, dynamic chemistries can also undergo side reactions with the media and cells; for example, boronic acid hydrogels can be sensitive to glucose in the media, imine-type dynamic chemistries can be sensitive to amines, and thioester can be sensitive to free thiols in the media. Enzyme-based dynamic chemistries can be susceptible to uncontrolled release of enzymatic degradation. Controlling hydrogel dynamics with light can allow the selective change in dynamics and investigate cellular responses without releasing any by-products[79–82]. In particular, chemical motifs sensitive to visible light and infrared would be suitable to avoid any side effects of UV light. The development of hydrogels with multiple-wavelength orthogonal photochemistry will be an interesting area to explore.

Other native features that remain largely missing in current dynamic hydrogels are spatiotemporal control of mechanical and viscoelastic properties. Most chemistries employed are irreversible.[83,84] Reversible chemistries based on light have the potential of tuning mechanical properties reversibly. Some studies have shown the tuning stiffening and softening of matrices using light-based chemistries. For example, photodegradation and photoinitiated crosslinking reactions have been utilized for tuning the softening[85] and stiffening[86] of the hydrogels. However, tuning a wide range of stiffness and viscoelasticity remains challenging, and biorthogonal and light-based dynamic covalent chemistries offer future opportunities to address these challenges.[82,87] Additionally, light-based reversible chemistries could allow local viscoelasticity tuning without affecting bulk hydrogel properties.

Force-dependent hydrogel systems offer interesting future opportunities[88,89–92]. For example, collagen offers force-dependent stress relaxation and stress stiffening. Future dynamic hydrogels should envision designing hydrogels where cell-applied forces can be utilized for changes in material mechanical properties (stress relaxation and strain stiffening) and release of drug or growth factors[88,91]. This would require designing new mechanical bonds which are responsive to stresses in the range applied by cells (nanonewton to piconewton). For designing such hydrogels natural ECM could be the source of inspiration; for example, supramolecular proteins in natural ECM are self-assembled via weak non-covalent interactions and possess fibril morphology. These complexes of weak non-covalent interactions in proteins not only exhibit stress relaxation (slip bonds), but also strengthen when multiple weak interactions work together (catch bonds)[93]. Supramolecular chemistry has already shown potential and offers a large toolbox for designing a material with non-linear and force-responsive properties.

Bioinks development: future challenges and opportunities

Despite advances in designing dynamic hydrogel networks, there remain challenges and opportunities for better design of bioinks. The field is still lacking rational design of dynamic bioinks with tailorable mechanical and bioprinting properties. Dynamic chemistries offer the advantages of recapitulating ECM dynamicity and non-linear mechanical properties; however, the very same dynamic nature also makes the hydrogel unpredictable once under a physiological

environment and in contact with cell culture media. For example, the infinite swelling of dynamic hydrogels results in erosion and creep of bioprinted constructs. Some recent studies have tackled this with secondary covalent crosslinking for prolonging cell culture times on the expanse of reduced dynamicity. The rational design of dynamic bioinks required knowledge of dynamicity from cell-specific ECM or specific tissue. For example, some tissues might need a more dynamic environment than other cell types for their maturation. More systematic studies on tissue either using rheology, mechanical testing, or atomic force microscopy are required for a better understanding of the level of dynamicity required for correct tissue formation. With this knowledge in hand, a better selection can be made on the choice of dynamic chemistry.

Spatiotemporal control over mechanical properties remains still challenging to control in bioinks. Tissues have gradients of mechanical properties, which can be addressed by the bioprinting of different bioinks with different mechanical properties. Tissues' mechanical properties also evolve during maturation and tissue formation; for example, cell-ECM interactions transition to cell-cell interactions. This would suggest a low level of dynamicity at an earlier stage and a higher level of dynamicity at a later stage. Advanced bioinks can be designed which offer a low level of dynamicity at an earlier stage and in response to stimuli higher level of dynamicity can be achieved. For example, in such cases, light-based chemistries can be employed which are photolabile (nitrobenzyl) for achieving a higher level of dynamicity. Photoreversible chemistry (photoreversible dimerization of coumarin) potentially could also be used for controlling the dynamicity of bioink. Other stimuli such as enzyme and pH changes can also be employed; however, they could lead to complex responses of cell behavior.

The ECM is stimuli-responsive and multifunctional material and serves as the best motivation for the design of advanced bioink with stimuli-responsive and multifunctional bioinks. Stimuli responsiveness already have been engineered using enzyme, pH, and magnetic field.[94] Enzymatic responsiveness potentially can be leveraged further for fine control over hydrogel behavior. For example, chemical moieties and cross-linkers, which are responsive to specific enzymes, can be incorporated for control over tuning mechanical and biological (growth factor release) properties. Orthogonal chemistries are also interesting for incorporating stimuli-responsiveness. The DeForest group created cross-linkers that successfully replicated Boolean logic operators YES/OR/AND.[95] These chemistries offer great insights for the translation of such feedback loops in more advanced bioinks for releasing drugs/biomolecules and for tuning mechanical and dynamic properties.

Four-dimensional (4D) living cell bioprinting has emerged as a powerful technique and involves time as 4th dimension in 3D bioprinted constructs. 4D bioprinting involves creating motion in 3D bioprinted constructs. Recent studies have successfully shown 4D bioprinting using micro-flake granular hydrogels. This study shows various complex 3D to 4D shape morphing in 3D printed constructs with and without cells; 4D cartilage-like tissue formation has been shown in these hydrogels.[59] Another recent example includes the 4D printing of extrudable and degradable PEG microgel scaffolds for multidimensional cell culture. For spatiotemporal control over scaffolds properties (evolution of void spaces over time), semi-orthogonal chemistries (amide,

thioester, and ester) were utilized in logic gated manner.[96] Other recent examples include the 4D printing of biocompatible nanocomposite hydrogel based on anisotropic ferromagnetic nanoparticles in soft PEG hydrogels.[97] These hydrogels allowed control over movement, rotation, and deflection in 4D-printed scaffolds. 4D bioprinting is still an emerging area of research and various stimuli such as pH, temperature, ionic strength, glucose, and enzymes can be tailored in 3D bioprinted hydrogel networks for creating motion in 3D bioprinted hydrogels.

Biomimicry of hierarchical fibrous structures with controlled dynamics remains largely missing in current bioinks. Though there exist several natural fibrous hydrogels, translation to rationally designed bioinks remains yet limited. Recent strategies have focused on engineering approaches such as electrospinning for the creation of fibrous hydrogels crosslinked with hydrazone dynamic linkages[98], though this hydrogel has not been investigated for 3D bioprinting. Another approach has focused on creating micro-strands from pre-crosslinked bulk hydrogels by sizing through a grid with an aperture of 40–100 μm. This hydrogel exhibited shear-thinning and shear recovery behavior required for extrusion bioink.[99] Besides engineering approaches supramolecular chemistry could offer bottom-up and rationally designed fibrous bioinks. Short peptides[67] and peptides amphiphiles[68] supramolecular fibrous bioinks have been reported recently. BTA-based bioinks are developed in this thesis. UPy hydrogels are injectable[100]; however, clear examples demonstrating bioprinting remain to be reported. Bisurea bolaamphiphile and polyisocyanates are other well-known supramolecular systems that remain open yet for translation to bioinks.

Supramolecular chemistry is a great design tool for overcoming some of the challenges described above for designing future bioinks. Future challenges such as stimuli-responsive, multifunctional, spatiotemporal control, and 4D bioprinting can easily be addressed in dynamic hydrogels using supramolecular chemistry principles. For example, specificity and responsiveness of supramolecular interactions can be utilized for creating hydrogels that are responsive to a specific stimulus. For multifunctionality, supramolecular monomers with various functional handles can be made and copolymerized for designing multicomponent bioinks, which are multifunctional. Using the same principle of copolymerization or modular mixing and self-healing capacity of supramolecular hydrogels, supramolecular bioinks with spatiotemporal gradients of mechanical properties and biological cues can be developed and bioprinted. Some of the recent studies have demonstrated some of these concepts in supramolecular materials, which can be ported into the future design of bioinks.[101,102] Supramolecular chemistry is also very best suited for 4D bioprinting, since supramolecular interactions or in general supramolecular materials can be made sensitive to the different stimuli (pH, temperature, glucose, and enzyme, etc.,) and orthogonal chemistries can be installed on supramolecular handles for creating motions in 3D bioprinted constructs. The work from Stupp's lab on supramolecular–covalent hybrid polymers for light-activated mechanical actuation offers a good starting point for the design of new supramolecular dynamic bioinks.[103]

References

(1) Engler, A.; Bacakova, L.; Newman, C.; Hategan, A.; Griffin, M.; Discher, D. Substrate Compliance versus Ligand Density in Cell on Gel Responses. *Biophys. J.* **2004**, *86* (1 I), 617–628. https://doi.org/10.1016/S0006-3495(04)74140-5.

(2) Engler, A. J.; Sen, S.; Sweeney, H. L.; Discher, D. E. Matrix Elasticity Directs Stem Cell Lineage Specification. *Cell* **2006**, *126* (4), 677–689. https://doi.org/10.1016/j.cell.2006.06.044.

(3) Lin, C. C.; Anseth, K. S. PEG Hydrogels for the Controlled Release of Biomolecules in Regenerative Medicine. *Pharm. Res.* **2009**, *26* (3), 631–643. https://doi.org/10.1007/S11095-008-9801-2.

(4) Thiele, J.; Ma, Y.; C Bruekers, S. M.; Ma, S.; S Huck, W. T.; Thiele, J.; Ma, Y.; C Bruekers, S. M.; S Huck, W. T.; Ma, S. 25th Anniversary Article: Designer Hydrogels for Cell Cultures: A Materials Selection Guide. *Adv. Mater.* **2014**, *26* (1), 125–148. https://doi.org/10.1002/ADMA.201302958.

(5) Zustiak, S. P.; Leach, J. B. Hydrolytically Degradable Poly(Ethylene Glycol) Hydrogel Scaffolds with Tunable Degradation and Mechanical Properties. *Biomacromolecules* **2010**, *11* (5), 1348–1357. https://doi.org/10.1021/BM100137Q/SUPPL_FILE/BM100137Q_SI_001.PDF.

(6) Lutolf, M. P.; Lauer-Fields, J. L.; Schmoekel, H. G.; Metters, A. T.; Weber, F. E.; Fields, G. B.; Hubbell, J. A. Synthetic Matrix Metalloproteinase-Sensitive Hydrogels for the Conduction of Tissue Regeneration: Engineering Cell-Invasion Characteristics. *Proc. Natl. Acad. Sci. U. S. A.* **2003**, *100* (9), 5413–5418. https://doi.org/10.1073/pnas.0737381100.

(7) Lutolf, M. P.; Raeber, G. P.; Zisch, A. H.; Tirelli, N.; Hubbell, J. A. Cell-Responsive Synthetic Hydrogels. *Adv. Mater.* **2003**, *15* (11), 888–892. https://doi.org/10.1002/ADMA.200304621.

(8) Cameron, A. R.; Frith, J. E.; Cooper-White, J. J. The Influence of Substrate Creep on Mesenchymal Stem Cell Behaviour and Phenotype. *Biomaterials* **2011**, *32* (26), 5979–5993. https://doi.org/10.1016/j.biomaterials.2011.04.003.

(9) Charrier, E. E.; Pogoda, K.; Wells, R. G.; Janmey, P. A. Control of Cell Morphology and Differentiation by Substrates with Independently Tunable Elasticity and Viscous Dissipation. *Nat. Commun.* **2018**, *9* (1), 449. https://doi.org/10.1038/s41467-018-02906-9.

(10) Chaudhuri, O.; Gu, L.; Klumpers, D.; Darnell, M.; Bencherif, S. A.; Weaver, J. C.; Huebsch, N.; Lee, H. P.; Lippens, E.; Duda, G. N.; Mooney, D. J. Hydrogels with Tunable Stress Relaxation Regulate Stem Cell Fate and Activity. *Nat. Mater.* **2016**, *15* (3), 326–334. https://doi.org/10.1038/nmat4489.

(11) Zhao, X.; Huebsch, N.; Mooney, D. J.; Suo, Z. Stress-Relaxation Behavior in Gels with Ionic and Covalent Crosslinks. In *Journal of Applied Physics*; 2010; Vol. 107, p 063509. https://doi.org/10.1063/1.3343265.

(12) Nam, S.; Stowers, R.; Lou, J.; Xia, Y.; Chaudhuri, O. Varying PEG Density to Control Stress Relaxation in Alginate-PEG Hydrogels for 3D Cell Culture Studies. *Biomaterials* **2019**, *200* (September 2018), 15–24. https://doi.org/10.1016/j.biomaterials.2019.02.004.

(13) Vining, K. H.; Stafford, A.; Mooney, D. J. Sequential Modes of Crosslinking Tune Viscoelasticity of Cell-Instructive Hydrogels. *Biomaterials* **2019**, *188*, 187–197. https://doi.org/10.1016/J.BIOMATERIALS.2018.10.013.

(14) McKinnon, D. D.; Domaille, D. W.; Cha, J. N.; Anseth, K. S. Biophysically Defined and Cytocompatible Covalently Adaptable Networks as Viscoelastic 3d Cell Culture Systems. *Adv. Mater.* **2014**, *26* (6), 865–872. https://doi.org/10.1002/adma.201303680.

(15) McKinnon, D. D.; Domaille, D. W.; Cha, J. N.; Anseth, K. S. Bis-Aliphatic Hydrazone-Linked Hydrogels Form Most Rapidly at Physiological PH: Identifying the Origin of Hydrogel Properties with Small Molecule Kinetic Studies. *Chem. Mater.* **2014**, *26* (7), 2382–2387. https://doi.org/10.1021/cm5007789.

(16) Richardson, B. M.; Wilcox, D. G.; Randolph, M. A.; Anseth, K. S. Hydrazone Covalent Adaptable Networks Modulate Extracellular Matrix Deposition for Cartilage Tissue Engineering. *Acta Biomater.* **2019**, *83*, 71–82. https://doi.org/10.1016/j.actbio.2018.11.014.

(17) Richardson, B. M.; Walker, C. J.; MacDougall, L. J.; Hoye, J. W.; Randolph, M. A.; Bryant, S. J.; Anseth, K. S. Viscoelasticity of Hydrazone Crosslinked Poly(Ethylene Glycol) Hydrogels Directs Chondrocyte Morphology during Mechanical Deformation. *Biomater. Sci.* **2020**, *8* (14), 3804–3811.

https://doi.org/10.1039/D0BM00860E.

(18) Morgan, F. L. C.; Fernández-Pérez, J.; Moroni, L.; Baker, M. B. Tuning Hydrogels by Mixing Dynamic Cross-Linkers: Enabling Cell-Instructive Hydrogels and Advanced Bioinks. *Adv. Healthc. Mater.* **2022**, *11* (1), 2101576. https://doi.org/10.1002/adhm.202101576.

(19) Lou, J.; Liu, F.; Lindsay, C. D.; Chaudhuri, O.; Heilshorn, S. C.; Xia, Y. Dynamic Hyaluronan Hydrogels with Temporally Modulated High Injectability and Stability Using a Biocompatible Catalyst. *Adv. Mater.* **2018**, *30* (22), 1–6. https://doi.org/10.1002/adma.201705215.

(20) Hafeez, S.; Ooi, H.; Morgan, F.; Mota, C.; Dettin, M.; van Blitterswijk, C.; Moroni, L.; Baker, M. Viscoelastic Oxidized Alginates with Reversible Imine Type Crosslinks: Self-Healing, Injectable, and Bioprintable Hydrogels. *Gels* **2018**, *4* (4), 85. https://doi.org/10.3390/gels4040085.

(21) Wang, H.; Zhu, D.; Paul, A.; Cai, L.; Enejder, A.; Yang, F.; Heilshorn, S. C. Covalently Adaptable Elastin-Like Protein–Hyaluronic Acid (ELP–HA) Hybrid Hydrogels with Secondary Thermoresponsive Crosslinking for Injectable Stem Cell Delivery. *Adv. Funct. Mater.* **2017**, *27* (28), 1–11. https://doi.org/10.1002/adfm.201605609.

(22) Lou, J.; Stowers, R.; Nam, S.; Xia, Y.; Chaudhuri, O. Stress Relaxing Hyaluronic Acid-Collagen Hydrogels Promote Cell Spreading, Fiber Remodeling, and Focal Adhesion Formation in 3D Cell Culture. *Biomaterials* **2018**, *154*, 213–222. https://doi.org/10.1016/j.biomaterials.2017.11.004.

(23) Marozas, I. A.; Anseth, K. S.; Cooper-White, J. J. Adaptable Boronate Ester Hydrogels with Tunable Viscoelastic Spectra to Probe Timescale Dependent Mechanotransduction. *Biomaterials* **2019**, *223*, 119430. https://doi.org/10.1016/j.biomaterials.2019.119430.

(24) Yesilyurt, V.; Ayoob, A. M.; Appel, E. A.; Borenstein, J. T.; Langer, R.; Anderson, D. G. Mixed Reversible Covalent Crosslink Kinetics Enable Precise, Hierarchical Mechanical Tuning of Hydrogel Networks. *Adv. Mater.* **2017**, *29* (19), 1605947–1605947. https://doi.org/10.1002/adma.201605947.

(25) Yesilyurt, V.; Webber, M. J.; Appel, E. A.; Godwin, C.; Langer, R.; Anderson, D. G. Injectable Self-Healing Glucose-Responsive Hydrogels with PH-Regulated Mechanical Properties. *Adv. Mater.* **2016**, *28* (1), 86–91. https://doi.org/10.1002/adma.201502902.

(26) Tang, S.; Ma, H.; Tu, H.-C.; Wang, H.-R.; Lin, P.-C.; Anseth, K. S.; Tang, S.; Ma, H.; Anseth, K. S.; Tu, H.; Wang, H.; Lin, P. Adaptable Fast Relaxing Boronate-Based Hydrogels for Probing Cell–Matrix Interactions. *Adv. Sci.* **2018**, *5* (9), 1800638. https://doi.org/10.1002/ADVS.201800638.

(27) Marco-Dufort, B.; Iten, R.; Tibbitt, M. W. Linking Molecular Behavior to Macroscopic Properties in Ideal Dynamic Covalent Networks. *J. Am. Chem. Soc.* **2020**, *142* (36), 15371–15385. https://doi.org/10.1021/jacs.0c06192.

(28) Carberry, B. J.; Rao, V. V; Anseth, K. S. Phototunable Viscoelasticity in Hydrogels Through Thioester Exchange. *Ann. Biomed. Eng.* **2020**, *48* (7), 2053–2063. https://doi.org/10.1007/s10439-020-02460-w.

(29) Chen, X.; Dong, C.; Wei, K.; Yao, Y.; Feng, Q.; Zhang, K.; Han, F.; Mak, A. F. T.; Li, B.; Bian, L. Supramolecular Hydrogels Cross-Linked by Preassembled Host–Guest PEG Cross-Linkers Resist Excessive, Ultrafast, and Non-Resting Cyclic Compression. *NPG Asia Mater.* **2018**, *10* (8), 788–799. https://doi.org/10.1038/s41427-018-0071-0.

(30) Loebel, C.; Rodell, C. B.; Chen, M. H.; Burdick, J. A. Shear-Thinning and Self-Healing Hydrogels as Injectable Therapeutics and for 3D-Printing. *Nat. Protoc.* **2017**, *12* (8), 1521–1541. https://doi.org/10.1038/nprot.2017.053.

(31) Rodell, C. B.; Kaminski, A. L.; Burdick, J. A. Rational Design of Network Properties in Guest-Host Assembled and Shear-Thinning Hyaluronic Acid Hydrogels. *Biomacromolecules* **2013**, *14* (11), 4125–4134. https://doi.org/10.1021/bm401280z.

(32) Hui, E.; Gimeno, K. I.; Guan, G.; Caliari, S. R. Spatiotemporal Control of Viscoelasticity in Phototunable Hyaluronic Acid Hydrogels. **2019**. https://doi.org/10.1021/acs.biomac.9b00965.

(33) Loebel, C.; Seliktar, D.; Burdick, J. A.; Ayoub, A.; Simaan-Yameen, H.; Kossover, O.; Galarraga, J. H. Tailoring Supramolecular Guest–Host Hydrogel Viscoelasticity with Covalent Fibrinogen Double Networks. *J. Mater. Chem. B* **2019**, 17–19. https://doi.org/10.1039/c8tb02593b.

(34) Williams, P. E.; Walsh-Korb, Z.; Jones, S. T.; Lan, Y.; Scherman, O. A. Stress Dissipation in Cucurbit[8]Uril Ternary Complex Small Molecule Adhesives. *Langmuir* **2018**, *34* (44), 13104–13109. https://doi.org/10.1021/acs.langmuir.8b00894.

(35) Zou, L.; Braegelman, A. S.; Webber, M. J. Dynamic Supramolecular Hydrogels Spanning an

Unprecedented Range of Host-Guest Affinity. *ACS Appl. Mater. Interfaces* **2019**, *11* (6), 5695–5700. https://doi.org/10.1021/acsami.8b22151.

(36) Diba, M.; Spaans, S.; Hendrikse, S. I. S.; Bastings, M. M. C.; Schotman, M. J. G.; van Sprang, J. F.; Wu, D. J.; Hoeben, F. J. M.; Janssen, H. M.; Dankers, P. Y. W. Engineering the Dynamics of Cell Adhesion Cues in Supramolecular Hydrogels for Facile Control over Cell Encapsulation and Behavior. *Adv. Mater.* **2021**, *33* (37), 2008111. https://doi.org/10.1002/adma.202008111.

(37) Vereroudakis, E.; Bantawa, M.; Lafleur, R. P. M.; Parisi, D.; Matsumoto, N. M.; Peeters, J. W.; Del Gado, E.; Meijer, E. W.; Vlassopoulos, D. Competitive Supramolecular Associations Mediate the Viscoelasticity of Binary Hydrogels. *ACS Cent. Sci.* **2020**, *6*, 1401–1411. https://doi.org/10.1021/acscentsci.0c00279.

(38) Ooi, H. W.; Mota, C.; Tessa Ten Cate, A.; Calore, A.; Moroni, L.; Baker, M. B. Thiol-Ene Alginate Hydrogels as Versatile Bioinks for Bioprinting. *Biomacromolecules* **2018**, *19* (8), 3390–3400. https://doi.org/10.1021/acs.biomac.8b00696.

(39) Tabriz, A. G.; Hermida, M. A.; Leslie, N. R.; Shu, W. Three-Dimensional Bioprinting of Complex Cell Laden Alginate Hydrogel Structures. *Biofabrication* **2015**, *7* (4), 045012. https://doi.org/10.1088/1758-5090/7/4/045012.

(40) Ivanovska, J.; Zehnder, T.; Lennert, P.; Sarker, B.; Boccaccini, A. R.; Hartmann, A.; Schneider-Stock, R.; Detsch, R. Biofabrication of 3D Alginate-Based Hydrogel for Cancer Research: Comparison of Cell Spreading, Viability, and Adhesion Characteristics of Colorectal HCT116 Tumor Cells. *Tissue Eng. Part C Methods* **2016**, *22* (7), 708–715. https://doi.org/10.1089/ten.tec.2015.0452.

(41) Habib, A.; Sathish, V.; Mallik, S.; Khoda, B. 3D Printability of Alginate-Carboxymethyl Cellulose Hydrogel. *Mater. 2018, Vol. 11, Page 454* **2018**, *11* (3), 454. https://doi.org/10.3390/MA11030454.

(42) Su, W. Y.; Chen, Y. C.; Lin, F. H. Injectable Oxidized Hyaluronic Acid/Adipic Acid Dihydrazide Hydrogel for Nucleus Pulposus Regeneration. *Acta Biomater.* **2010**, *6* (8), 3044–3055. https://doi.org/10.1016/j.actbio.2010.02.037.

(43) Zehnder, T.; Boccaccini, A. R.; Detsch, R. Evaluation of an Alginate–Gelatine Crosslinked Hydrogel for Bioplotting. *Biofabrication* **2015**, *7*, 25001. https://doi.org/10.1088/1758-5090/7/2/025001.

(44) Bertassoni, L. E.; Cardoso, J. C.; Manoharan, V.; Cristino, A. L.; Bhise, N. S.; Araujo, W. A.; Zorlutuna, P.; Vrana, N. E.; Ghaemmaghami, A. M.; Dokmeci, M. R.; Khademhosseini, A. Direct-Write Bioprinting of Cell-Laden Methacrylated Gelatin Hydrogels. *Biofabrication* **2014**, *6* (2), 024105. https://doi.org/10.1088/1758-5082/6/2/024105.

(45) Diamantides, N.; Dugopolski, C.; Blahut, E.; Kennedy, S.; Bonassar, L. J. High Density Cell Seeding Affects the Rheology and Printability of Collagen Bioinks. *Biofabrication* **2019**, *11* (4). https://doi.org/10.1088/1758-5090/AB3524.

(46) Han, J.; Kim, D. S.; Jang, H.; Kim, H. R.; Kang, H. W. Bioprinting of Three-Dimensional Dentin-Pulp Complex with Local Differentiation of Human Dental Pulp Stem Cells. *J. Tissue Eng.* **2019**, *10*. https://doi.org/10.1177/2041731419845849.

(47) Daly, A. C.; Critchley, S. E.; Rencsok, E. M.; Kelly, D. J. A Comparison of Different Bioinks for 3D Bioprinting of Fibrocartilage and Hyaline Cartilage. *Biofabrication* **2016**, *8* (4). https://doi.org/10.1088/1758-5090/8/4/045002.

(48) Kim, M. K.; Jeong, W.; Lee, S. M.; Kim, J. B.; Jin, S.; Kang, H. W. Decellularized Extracellular Matrix-Based Bio-Ink with Enhanced 3D Printability and Mechanical Properties. *Biofabrication* **2020**, *12* (2). https://doi.org/10.1088/1758-5090/AB5D80.

(49) Setayeshmehr, M.; Hafeez, S.; van Blitterswijk, C.; Moroni, L.; Mota, C.; Baker, M. B. Bioprinting Via a Dual-Gel Bioink Based on Poly(Vinyl Alcohol) and Solubilized Extracellular Matrix towards Cartilage Engineering. *Int. J. Mol. Sci. 2021, Vol. 22, Page 3901* **2021**, *22* (8), 3901. https://doi.org/10.3390/IJMS22083901.

(50) Piluso, S.; Skvortsov, G. A.; Altunbek, M.; Afghah, F.; Khani, N.; Koc, B.; Patterson, J. 3D Bioprinting of Molecularly Engineered PEG-Based Hydrogels Utilizing Gelatin Fragments. *Biofabrication* **2021**, *13* (4), 045008. https://doi.org/10.1088/1758-5090/AC0FF0.

(51) Lee, A.; Hudson, A. R.; Shiwarski, D. J.; Tashman, J. W.; Hinton, T. J.; Yerneni, S.; Bliley, J. M.; Campbell, P. G.; Feinberg, A. W. 3D Bioprinting of Collagen to Rebuild Components of the Human Heart. *Science (80-.).* **2019**, *365* (6452), 482–487. https://doi.org/10.1126/science.aav9051.

(52) Kesti, M.; Müller, M.; Becher, J.; Schnabelrauch, M.; D'Este, M.; Eglin, D.; Zenobi-Wong, M. A Versatile Bioink for Three-Dimensional Printing of Cellular Scaffolds Based on Thermally and Photo-Triggered Tandem Gelation. *Acta Biomater.* **2015**, *11* (1), 162–172. https://doi.org/10.1016/J.ACTBIO.2014.09.033.

(53) Ouyang, L.; Armstrong, J. P. K.; Lin, Y.; Wojciechowski, J. P.; Lee-Reeves, C.; Hachim, D.; Zhou, K.; Burdick, J. A.; Stevens, M. M. Expanding and Optimizing 3D Bioprinting Capabilities Using Complementary Network Bioinks. *Sci. Adv.* **2020**, *6* (38), 1–14. https://doi.org/10.1126/sciadv.abc5529.

(54) Hull, S. M.; Lindsay, C. D.; Brunel, L. G.; Shiwarski, D. J.; Tashman, J. W.; Roth, J. G.; Myung, D.; Feinberg, A. W.; Heilshorn, S. C. 3D Bioprinting Using UNIversal Orthogonal Network (UNION) Bioinks. *Adv. Funct. Mater.* **2020**, *2007983*, 1–11. https://doi.org/10.1002/adfm.202007983.

(55) Riley, L.; Schirmer, L.; Segura, T. Granular Hydrogels: Emergent Properties of Jammed Hydrogel Microparticles and Their Applications in Tissue Repair and Regeneration. *Current Opinion in Biotechnology*. Elsevier Current Trends December 1, 2019, pp 1–8. https://doi.org/10.1016/j.copbio.2018.11.001.

(56) Daly, A. C.; Riley, L.; Segura, T.; Burdick, J. A. Hydrogel Microparticles for Biomedical Applications. *Nat. Rev. Mater. 2019 51* **2019**, *5* (1), 20–43. https://doi.org/10.1038/s41578-019-0148-6.

(57) Highley, C. B.; Song, K. H.; Daly, A. C.; Burdick, J. A. Jammed Microgel Inks for 3D Printing Applications. *Adv. Sci.* **2019**, *6* (1), 1801076. https://doi.org/10.1002/advs.201801076.

(58) Zhang, H.; Cong, Y.; Osi, A. R.; Zhou, Y.; Huang, F.; Zaccaria, R. P.; Chen, J.; Wang, R.; Fu, J. Direct 3D Printed Biomimetic Scaffolds Based on Hydrogel Microparticles for Cell Spheroid Growth. *Adv. Funct. Mater.* **2020**, *30* (13), 1910573. https://doi.org/10.1002/ADFM.201910573.

(59) Ding, A.; Jeon, O.; Cleveland, D.; Gasvoda, K. L.; Wells, D.; Lee, S. J.; Alsberg, E. Jammed Micro-Flake Hydrogel for Four-Dimensional Living Cell Bioprinting. *Advanced Materials*. 2022, p 2109394. https://doi.org/10.1002/adma.202109394.

(60) Wang, L. L.; Highley, C. B.; Yeh, Y. C.; Galarraga, J. H.; Uman, S.; Burdick, J. A. Three-Dimensional Extrusion Bioprinting of Single- and Double-Network Hydrogels Containing Dynamic Covalent Crosslinks. *J. Biomed. Mater. Res. - Part A* **2018**, *106* (4), 865–875. https://doi.org/10.1002/jbm.a.36323.

(61) Kim, S. W.; Kim, D. Y.; Roh, H. H.; Kim, H. S.; Lee, J. W.; Lee, K. Y. Three-Dimensional Bioprinting of Cell-Laden Constructs Using Polysaccharide-Based Self-Healing Hydrogels. *Biomacromolecules* **2019**, *20* (5), 1860–1866. https://doi.org/10.1021/acs.biomac.8b01589.

(62) Webber, M. J.; Appel, E. A.; Meijer, E. W.; Langer, R. Supramolecular Biomaterials. *Nat. Mater.* **2015**, *15* (1), 13–26. https://doi.org/10.1038/nmat4474.

(63) Li, C.; Faulkner-Jones, A.; Dun, A. R.; Jin, J.; Chen, P.; Xing, Y.; Yang, Z.; Li, Z.; Shu, W.; Liu, D.; Duncan, R. R. Rapid Formation of a Supramolecular Polypeptide-DNA Hydrogel for in Situ Three-Dimensional Multilayer Bioprinting. *Angew. Chemie - Int. Ed.* **2015**, *54* (13), 3957–3961. https://doi.org/10.1002/anie.201411383.

(64) Highley, C. B.; Rodell, C. B.; Burdick, J. A. Direct 3D Printing of Shear-Thinning Hydrogels into Self- Healing Hydrogels. *Adv. Mater.* **2015**, *27*, 5075–5079.

(65) Ouyang, L.; Highley, C. B.; Rodell, C. B.; Sun, W.; Burdick, J. A. 3D Printing of Shear-Thinning Hyaluronic Acid Hydrogels with Secondary Cross-Linking. *ACS Biomater. Sci. Eng.* **2016**, *2* (10), 1743–1751. https://doi.org/10.1021/ACSBIOMATERIALS.6B00158/ASSET/IMAGES/LARGE/AB-2016-00158E_0008.JPEG.

(66) Loo, Y.; Lakshmanan, A.; Ni, M.; Toh, L. L.; Wang, S.; Hauser, C. A. E. Peptide Bioink: Self-Assembling Nanofibrous Scaffolds for Three-Dimensional Organotypic Cultures. *Nano Lett.* **2015**, *15* (10), 6919–6925. https://doi.org/10.1021/acs.nanolett.5b02859.

(67) Susapto, H. H.; Alhattab, D.; Abdelrahman, S.; Khan, Z.; Alshehri, S.; Kahin, K.; Ge, R.; Moretti, M.; Emwas, A. H.; Hauser, C. A. E. Ultrashort Peptide Bioinks Support Automated Printing of Large-Scale Constructs Assuring Long-Term Survival of Printed Tissue Constructs. *Nano Lett.* **2021**, *21* (7), 2719–2729. https://doi.org/10.1021/acs.nanolett.0c04426.

(68) Sather, N. A.; Sai, H.; Sasselli, I. R.; Sato, K.; Ji, W.; Synatschke, C. V.; Zambrotta, R. T.; Edelbrock, J. F.; Kohlmeyer, R. R.; Hardin, J. O.; Berrigan, J. D.; Durstock, M. F.; Mirau, P.; Stupp, S. I. 3D

Printing of Supramolecular Polymer Hydrogels with Hierarchical Structure. *Small* **2021**, *17* (5), 1–14. https://doi.org/10.1002/smll.202005743.

(69) Hu, T.; Cui, X.; Zhu, M.; Wu, M.; Tian, Y.; Yao, B.; Song, W.; Niu, Z.; Huang, S.; Fu, X. 3D-Printable Supramolecular Hydrogels with Shear-Thinning Property: Fabricating Strength Tunable Bioink via Dual Crosslinking. *Bioact. Mater.* **2020**, *5* (4), 808–818. https://doi.org/10.1016/j.bioactmat.2020.06.001.

(70) Roosma, J.; Mes, T.; Leclère, P.; Palmans, A. R. A.; Meijer, E. W. Supramolecular Materials from Benzene-1,3,5-Tricarboxamide-Based Nanorods. *J. Am. Chem. Soc.* **2008**, *130* (4), 1120–1121. https://doi.org/10.1021/ja0774764.

(71) Leenders, C. M. A.; Mes, T.; Baker, M. B.; Koenigs, M. M. E.; Besenius, P.; Palmans, A. R. A.; Meijer, E. W. From Supramolecular Polymers to Hydrogel Materials. *Mater. Horiz.* **2014**, *1* (1), 116–120. https://doi.org/10.1039/C3MH00103B.

(72) Baker, M. B.; Gosens, R. P. J.; Albertazzi, L.; Matsumoto, N. M.; Palmans, A. R. A.; Meijer, E. W. Exposing Differences in Monomer Exchange Rates of Multicomponent Supramolecular Polymers in Water. *ChemBioChem* **2016**, *17* (3), 207–213. https://doi.org/10.1002/cbic.201500606.

(73) Chaudhuri, O.; Cooper-White, J.; Janmey, P. A.; Mooney, D. J.; Shenoy, V. B. Effects of Extracellular Matrix Viscoelasticity on Cellular Behaviour. *Nature*. 2020, pp 535–546. https://doi.org/10.1038/s41586-020-2612-2.

(74) Tang, S.; Richardson, B. M.; Anseth, K. S. Dynamic Covalent Hydrogels as Biomaterials to Mimic the Viscoelasticity of Soft Tissues. *Prog. Mater. Sci.* **2021**, *120* (July 2020), 100738. https://doi.org/10.1016/j.pmatsci.2020.100738.

(75) Desrochers, J.; Amrein, M. W.; Matyas, J. R. Viscoelasticity of the Articular Cartilage Surface in Early Osteoarthritis. *Osteoarthr. Cartil.* **2012**, *20* (5), 413–421. https://doi.org/10.1016/j.joca.2012.01.011.

(76) Liu, Z.; Bilston, L. E. Large Deformation Shear Properties of Liver Tissue. *Biorheology* **2002**, *39* (6), 735–742.

(77) Liu, Z.; Bilston, L. On the Viscoelastic Character of Liver Tissue: Experiments and Modelling of the Linear Behaviour. *Biorheology* **2000**, *37* (3), 191–201.

(78) Lou, J.; Friedowitz, S.; Will, K.; Qin, J.; Xia, Y.; Lou, J.; Will, K.; Xia, Y.; Friedowitz, S.; Qin, J. Predictably Engineering the Viscoelastic Behavior of Dynamic Hydrogels via Correlation with Molecular Parameters. *Adv. Mater.* **2021**, *33* (51), 2104460. https://doi.org/10.1002/ADMA.202104460.

(79) Wang, C.; Zhang, P.; Xiao, W.; Zhao, J.; Shi, M.; Wei, H.; Deng, Z.; Guo, B.; Zheng, Z.; Yu, Y. Visible-Light-Assisted Multimechanism Design for One-Step Engineering Tough Hydrogels in Seconds. *Nat. Commun.* **2020**, *11* (1), 1–9. https://doi.org/10.1038/s41467-020-18145-w.

(80) Rapp, T. L.; DeForest, C. A. Visible Light-Responsive Dynamic Biomaterials: Going Deeper and Triggering More. *Advanced Healthcare Materials*. John Wiley & Sons, Ltd April 1, 2020, p 1901553. https://doi.org/10.1002/adhm.201901553.

(81) Rapp, T. L.; DeForest, C. A. Tricolor Visible Wavelength-Selective Photodegradable Hydrogels. *ChemRxiv* **2022**, *10.26434/c.*

(82) Accardo, J. V; Kalow, J. A. Reversibly Tuning Hydrogel Stiffness through Photocontrolled Dynamic Covalent Crosslinks. *Chem. Sci.* **2018**, *9* (27), 5987–5993. https://doi.org/10.1039/c8sc02093k.

(83) Guvendiren, M.; Burdick, J. A. Stiffening Hydrogels to Probe Short- and Long-Term Cellular Responses to Dynamic Mechanics. *Nat. Commun.* **2012**, *3*. https://doi.org/10.1038/ncomms1792.

(84) Liu, H. Y.; Greene, T.; Lin, T. Y.; Dawes, C. S.; Korc, M.; Lin, C. C. Enzyme-Mediated Stiffening Hydrogels for Probing Activation of Pancreatic Stellate Cells. *Acta Biomater.* **2017**, *48*, 258–269. https://doi.org/10.1016/j.actbio.2016.10.027.

(85) Rosales, A. M.; Vega, S. L.; DelRio, F. W.; Burdick, J. A.; Anseth, K. S. Hydrogels with Reversible Mechanics to Probe Dynamic Cell Microenvironments. *Angew. Chemie - Int. Ed.* **2017**, *56* (40), 12132–12136. https://doi.org/10.1002/anie.201705684.

(86) Günay, K. A.; Ceccato, T. L.; Silver, J. S.; Bannister, K. L.; Bednarski, O. J.; Leinwand, L. A.; Anseth, K. S. PEG–Anthracene Hydrogels as an On-Demand Stiffening Matrix to Study Mechanobiology. *Angew. Chemie - Int. Ed.* **2019**, *58* (29), 9912–9916. https://doi.org/10.1002/anie.201901989.

(87) Liu, L.; Shadish, J. A.; Arakawa, C. K.; Shi, K.; Davis, J.; DeForest, C. A. Cyclic Stiffness Modulation of Cell-Laden Protein–Polymer Hydrogels in Response to User-Specified Stimuli Including Light. *Adv. Biosyst.* **2018**, *2* (12), 1–9. https://doi.org/10.1002/adbi.201800240.

(88) Stejskalová, A.; Oliva, N.; England, F. J.; Almquist, B. D. Biologically Inspired, Cell-Selective Release of Aptamer-Trapped Growth Factors by Traction Forces. *Adv. Mater.* **2019**, *31* (7). https://doi.org/10.1002/adma.201806380.

(89) Chen, Y.; Mellot, G.; Van Luijk, D.; Creton, C.; Sijbesma, R. P. Mechanochemical Tools for Polymer Materials. *Chemical Society Reviews*. 2021, pp 4100–4140. https://doi.org/10.1039/d0cs00940g.

(90) Abi Ghanem, M.; Basu, A.; Behrou, R.; Boechler, N.; Boydston, A. J.; Craig, S. L.; Lin, Y.; Lynde, B. E.; Nelson, A.; Shen, H.; Storti, D. W. The Role of Polymer Mechanochemistry in Responsive Materials and Additive Manufacturing. *Nat. Rev. Mater.* https://doi.org/10.1038/s41578-020-00249-w.

(91) Huo, S.; Zhao, P.; Shi, Z.; Zou, M.; Yang, X.; Warszawik, E.; Loznik, M.; Göstl, R.; Herrmann, A. Mechanochemical Bond Scission for the Activation of Drugs. *Nat. Chem. 2021 132* **2021**, *13* (2), 131–139. https://doi.org/10.1038/s41557-020-00624-8.

(92) Li, J.; Nagamani, C.; Moore, J. S. Polymer Mechanochemistry: From Destructive to Productive. **2015**. https://doi.org/10.1021/acs.accounts.5b00184.

(93) Mulla, Y.; Avellaneda, M. J.; Roland, A.; Baldauf, L.; Jung, W.; Kim, T.; Tans, S. J.; Koenderink, G. H. Weak Catch Bonds Make Strong Networks. *Nat. Mater.* **2022**, *21* (9), 1019–1023. https://doi.org/10.1038/s41563-022-01288-0.

(94) Mota, C.; Camarero-Espinosa, S.; Baker, M. B.; Wieringa, P.; Moroni, L. Bioprinting: From Tissue and Organ Development to in Vitro Models. *Chemical Reviews*. 2020, pp 10547–10607. https://doi.org/10.1021/acs.chemrev.9b00789.

(95) Badeau, B. A.; Comerford, M. P.; Arakawa, C. K.; Shadish, J. A.; Deforest, C. A. Engineered Modular Biomaterial Logic Gates for Environmentally Triggered Therapeutic Delivery. *Nat. Chem. 2018 103* **2018**, *10* (3), 251–258. https://doi.org/10.1038/nchem.2917.

(96) Miksch, C. E.; Skillin, N. P.; Kirkpatrick, B. E.; Hach, G. K.; Rao, V. V.; White, T. J.; Anseth, K. S. 4D Printing of Extrudable and Degradable Poly(Ethylene Glycol) Microgel Scaffolds for Multidimensional Cell Culture. *Small* **2022**, 2200951. https://doi.org/10.1002/SMLL.202200951.

(97) Kuhnt, T.; Camarero-Espinosa, S.; Takhsha Ghahfarokhi, M.; Arreguín, M.; Cabassi, R.; Albertini, F.; Nieto, D.; Baker, M. B.; Moroni, L. 4D Printed Shape Morphing Biocompatible Materials Based on Anisotropic Ferromagnetic Nanoparticles. *Adv. Funct. Mater.* **2022**. https://doi.org/10.1002/ADFM.202202539.

(98) Davidson, M. D.; Ban, E.; Schoonen, A. C. M.; Lee, M. H.; D'Este, M.; Shenoy, V. B.; Burdick, J. A. Mechanochemical Adhesion and Plasticity in Multifiber Hydrogel Networks. *Adv. Mater.* **2019**, 1905719. https://doi.org/10.1002/adma.201905719.

(99) Kessel, B.; Lee, M.; Bonato, A.; Tinguely, Y.; Tosoratti, E.; Zenobi-Wong, M. 3D Bioprinting of Macroporous Materials Based on Entangled Hydrogel Microstrands. *Adv. Sci.* **2020**, *7* (18), 1–13. https://doi.org/10.1002/advs.202001419.

(100) Dankers, P. Y. W.; Hermans, T. M.; Baughman, T. W.; Kamikawa, Y.; Kieltyka, R. E.; Bastings, M. M. C.; Janssen, H. M.; Sommerdijk, N. A. J. M.; Larsen, A.; Van Luyn, M. J. A.; Bosman, A. W.; Popa, E. R.; Fytas, G.; Meijer, E. W. Hierarchical Formation of Supramolecular Transient Networks in Water: A Modular Injectable Delivery System. *Adv. Mater.* **2012**, *24* (20), 2703–2709. https://doi.org/10.1002/adma.201104072.

(101) Albertazzi, L.; Martinez-Veracoechea, F. J.; Leenders, C. M. A.; Voets, I. K.; Frenkel, D.; Meijer, E. W. Spatiotemporal Control and Superselectivity in Supramolecular Polymers Using Multivalency. *Proc. Natl. Acad. Sci.* **2013**, *110* (30), 12203–12208. https://doi.org/10.1073/pnas.1303109110.

(102) Kamperman, T.; Koerselman, M.; Kelder, C.; Hendriks, J.; Crispim, J. F.; de Peuter, X.; Dijkstra, P. J.; Karperien, M.; Leijten, J. Spatiotemporal Material Functionalization via Competitive Supramolecular Complexation of Avidin and Biotin Analogs. *Nat. Commun.* **2019**, *10* (1), 1–11. https://doi.org/10.1038/s41467-019-12390-4.

(103) Li, C.; Iscen, A.; Sai, H.; Sato, K.; Sather, N. A.; Chin, S. M.; Álvarez, Z.; Palmer, L. C.; Schatz, G. C.; Stupp, S. I. Supramolecular–Covalent Hybrid Polymers for Light-Activated Mechanical

Actuation. *Nat. Mater. 2020 198* **2020**, *19* (8), 900–909. https://doi.org/10.1038/s41563-020-0707-7.

Supplementary information

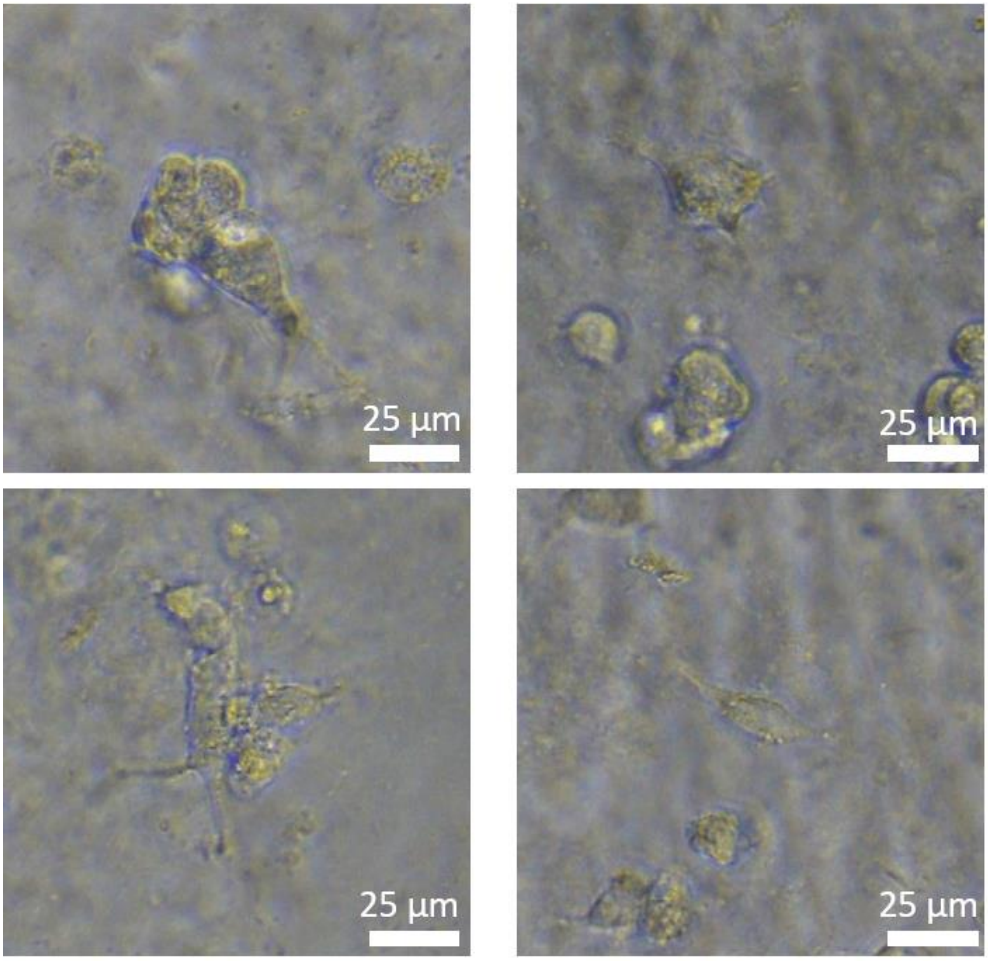

Figure S1. Human umbilical vein endothelial cells (HUVECs) demonstrate displayed attachment and some spreading cells were also observed on NB-BTA hydrogels after 24 hours of cell culture. NB-BTA hydrogels were made at 5% (w/v) and functionalized with cysteine RGD (C-GGG-RGDS) at a final concentration of 250 nM.

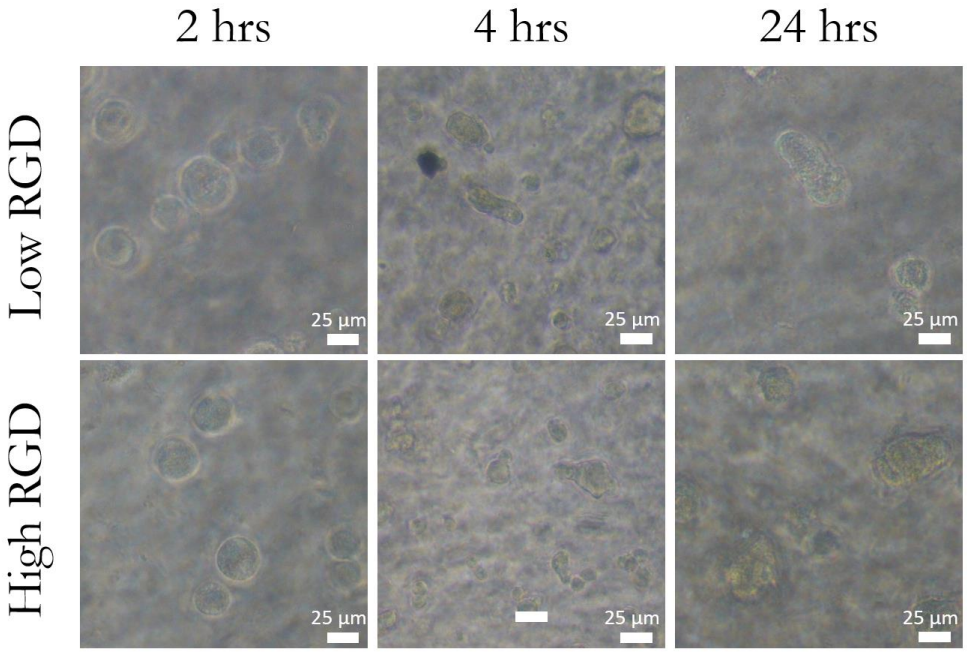

Figure S2. Human mesenchymal stem cells (HMSCs) demonstrate attachment and little spreading after 24 hours of culture on NB-BTA hydrogels. No increased spreading was observed when RGD concentration was doubled. Cysteine RGD (C-GGG-RGDS) was used at 250 nM (low RGD) and 500 nM (high RGD) concentrations. Hydrogel final concentration was 3.3% (w/v).

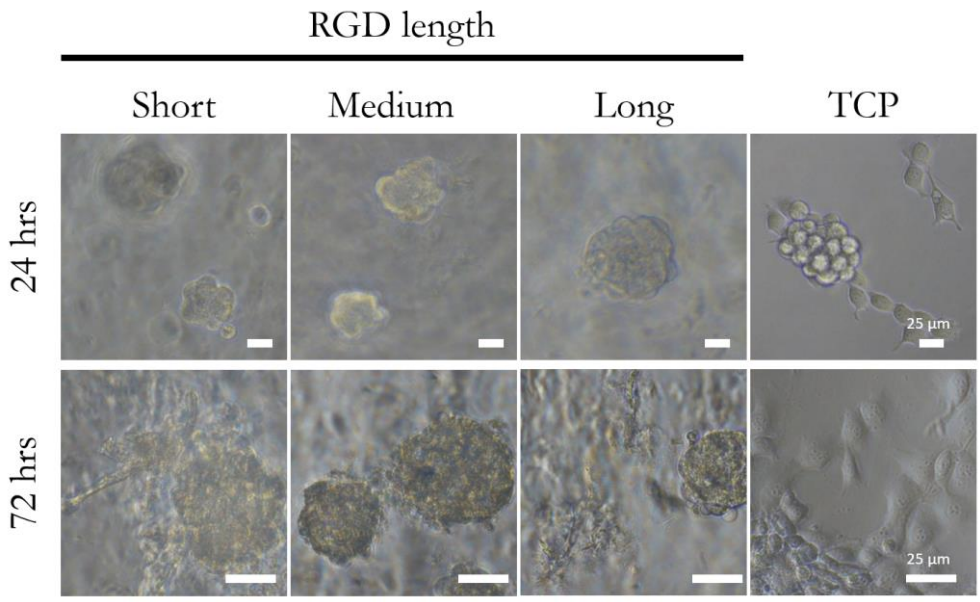

Figure S3. ATDC5 chondrocytes were seeded on NB-BTA hydrogels. NB-BTA hydrogel was functionalized with short (C-GGG-RGDS), medium (C-GGSGGSGGG-RGDS), and long (C-GGSGGSGGSGGSGGG-RGDS) RGD after 24 hours and 72 hours of cell culture. A little spreading, after 72 hours, on the edge of the cell aggregate was observed on the hydrogel functionalized with short RGD. Cell aggregates were also observed for medium and long RGD. Some very thin elongated cells were observed on long RGD hydrogel however, staining and imaging of fixed cells would provide a more accurate morphology of the cells. Cells cultured on tissue culture plastic (TCP) showed spreading morphology.

Chapter X

Valorization

Shahzad Hafeez[1] Clemens van Blitterswijk[1], Lorenzo Moroni[1], Matthew B. Baker[1,]

[1] Department of Complex Tissue Regeneration, MERLN Institute for Technology-Inspired Regenerative Medicine, Maastricht University, P.O. Box 616, 6200 MD Maastricht, the Netherlands;

In this chapter, we discuss the need for bioink development and why 3D bioprinting of soluble bioinks can be a possible solution to defective tissues or organs. Then, we discussed which bioink products are available in the market and how the research done in this thesis could be commercialized.

Why bioinks and 3D bioprinting are needed

Organ and tissue transplantation has been successful in bridging the gap between life and death. Transplantation medicine might be crucial for a healthy life; however, worldwide rising cases of end-stage failure of many organs including the heart, liver, and kidney might hamper this possibility. According to a study, in the US alone, there were approximately 95,000 patients on the waiting list in the year 2006 and over 6300 deaths were recorded of the patients on the waiting list[1]. According to a new survey, 76% of patients failed to receive transplants[2].

For instance, the incidence of renal failure is between 140 and 160 million per year in the US and Canada, whereas the supply of organs from deceased donors (DCD) is between 20 and 22 per million per year[1]. In the US, the cost of dialysis over four years is three times that of a kidney transplant. Canada spent nearly Can$100000 per year for Canadians on dialysis with chronic kidney diseases (CKD) and Can$32 billion per year for patients with CKD but not on dialysis[3]. A European study found that kidney transplantation resulted in a 2 million euro savings for 1000 individuals[1]. Heart failure affects more than 64 million people worldwide which not only resulted in poor quality of life but also adds social and economic burden on the healthcare system[4]. According to a 2013 national survey by the American Heart Association, the direct and indirect expenditures associated with HF in the USA would more than double, from $20.9 billion in 2012 to $53.1 billion in 2030[5]. Cirrhosis is the end-stage chronic liver disease (CLD) and is the 11th leading cause of death worldwide[6]. More than 160 million people were impacted by CLD in 2017[7], and around 1.32 million died as a result[6]. Transplantation of the liver remains only an option for end-stage liver diseases and on average 15% of the CLD patients died while awaiting the transplant[8]. Germany experienced a severe organ shortage in 2011; there were 1191 liver transplants performed and 1792 new patients were added to the waiting list[9]. Bone is another organ that can fracture due to sports injuries, traffic accidents, and osteoporosis[10]. Delayed bone healing or non-unions exist when the repair is not complete. Non-unions can occur because of failure of biology, failure of the host (comorbidities and other diseases such as diabetes or vascular disease), and failure of mechanics[11]. Total fragility fractures of 3.3 million are expected in EU6 (France, Germany, Italy, Spain, UK, and Sweden) by 2030 resulting in an annual fracture-related cost of €48 billion[12]. Average direct costs of treatment for long bone non-union have been reported as follows: Canada, $11,800; the USA $11,333; the UK £ 29,204[11]. There could also be indirect costs to each patient for example either via loss of earnings or through additional social care. This huge socio-economic cost demands an optimal and innovative solution to diseased tissues and the shortage of organs for benefitting humankind at large.

Tissue engineering offers a potential solution to overcome the challenges of treating defective tissues and organ transplantation[13,14,15]. Tissue engineering is a technique that combines cells,

materials, and biochemical molecules intending to maintain, restore or augment the function of injured tissue or organs[16]. Current challenges of tissue engineering include a lack of biomaterials with appropriate mechanical properties for correct tissue formation and the creation of a three-dimensional (3D) complex architecture of native tissues using biomaterials and cells in the lab. This can be achieved via 3D bioprinting. 3D bioprinting is an additive manufacturing technique that utilized bioink combined with cells and biological growth factors to create 3D complex biological constructs with living cells.

The bioink is defined as a material formulation with biological molecules and cells that can be processed using bioprinting technology[17]. Hydrogels are typical materials that are used as bioinks since they mimic the hydrated environment of ECM and allow tuning of mechanical and rheological properties required for correct tissue formation and 3D bioprinting [17–19]. With the development of new dynamic chemistries, hydrogels with reversible and dynamic bonds have been developed which advances the field of 3D bioprinting[20]. 3D bioprinting has the potential to revolutionize medicine and healthcare by providing on-demand and patient-specific solutions to diseased tissue or replacing artificial organs. However, achieving this milestone requires an immense amount of research for finding bioinks with appropriate mechanical and rheological properties and detailed biochemical analysis of gene and protein formation in bioprinted constructs.

Research trends in 3D bioprinting:

Figure 1 shows the exponential increase in the number of publications on bioprinting and according to Santoni et al., a total of 9314 science articles were published from 2000 to 2020 which includes 7574 original research articles and 1740 review papers. A total of 79% of published articles were published after 2014. Importantly, 61% (4620 out of 7574) of research articles and 74% (1288 out of 1740) of research reviews have been published since 2016, which indicates exponential growth of research activities on bioprinting[21].

Market analysis of 3D bioprinting

The global bioprinting market was estimated to be worth USD 586.13 million in 2019 and is projected to reach USD 1,949.94 million by 2025, representing a compound annual growth rate (CAGR) of 21.91% for the duration between 2020 and 2025.[21] Research and Markets reported that global bioprinting market was USD 1.3 billion in 2022 and is projected to reach USD 3.3 billion by 2027 [22]. According to Market Research Future (MRF) report on the 3D bioprinting market by technology, material, application, and end-user, the 3D bioprinting market size value was USD 1.9 billion in 2022 and revenue forecast for 2030 is USD 5.1 billion with compound

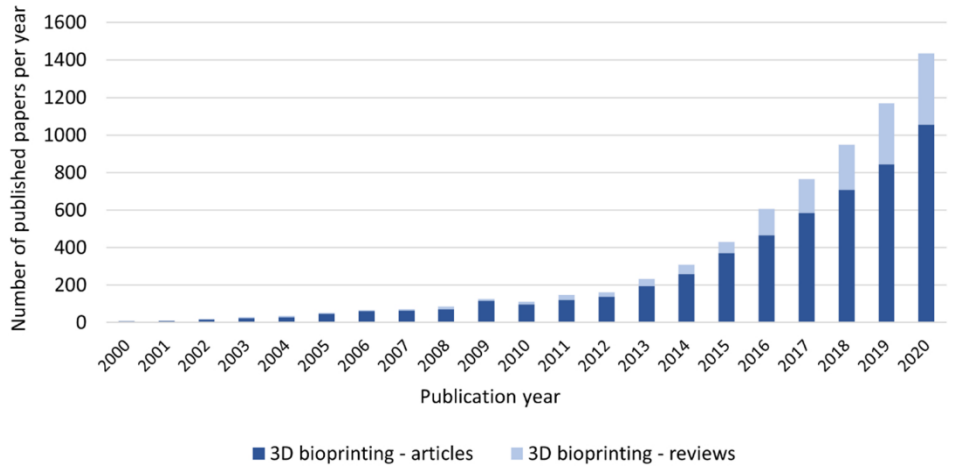

Figure 1. The graph shows the number of publications on 3D bioprinting. Original research articles are shown in blue and reviews are indicated in light blue color [11].

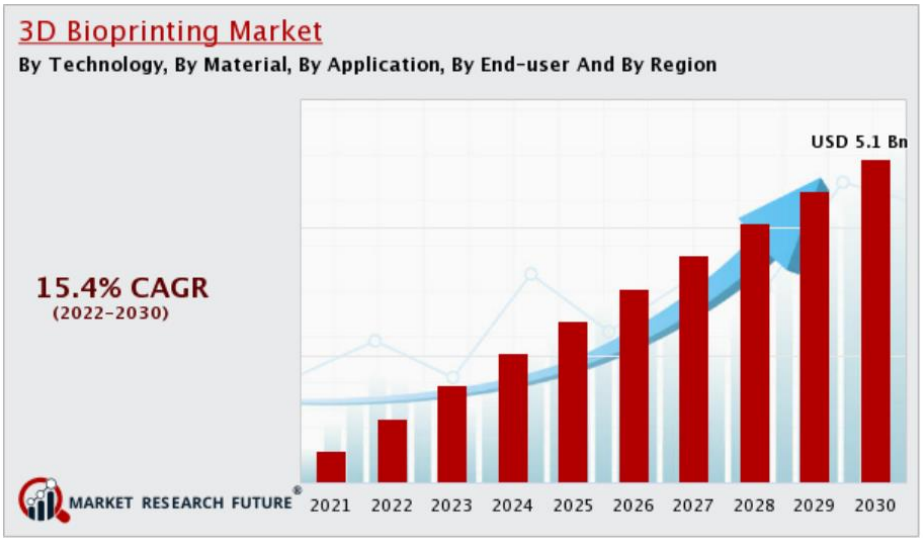

Figure 2. The graph displays the 3D bioprinting market forecast by technology, material, application, and ends user. The 3D bioprinting market is forecasted to reach USD 5.1 billion by 2030. The graph has been taken from Market Research Future website (https://www.marketresearchfuture.com).

annual growth rate (CAGR) of 15.4%[23] (**Figure 2**). A report of the 3D bioprinting market by component, technology, application, and end-user by Precedence Research indicates that the market was worth USD 1.8 billion in 2021 and is projected to reach USD 8.3 billion by 2030, with a CAGR of 18.51% from 2022 to 2030[24].

Market Analysis of bioinks

The global bioinks market generated USD 115.7 million in revenue in 2021, and it is anticipated that this market will grow at a CAGR of 18.6% to reach USD 738.2 million by the end of 2032. **Figure 3** demonstrates the global bioink market of USD 134.2 million[25]. In 2021, sales of bioinks represented an 8.9% revenue share of the worldwide 3D bioprinting market [25].

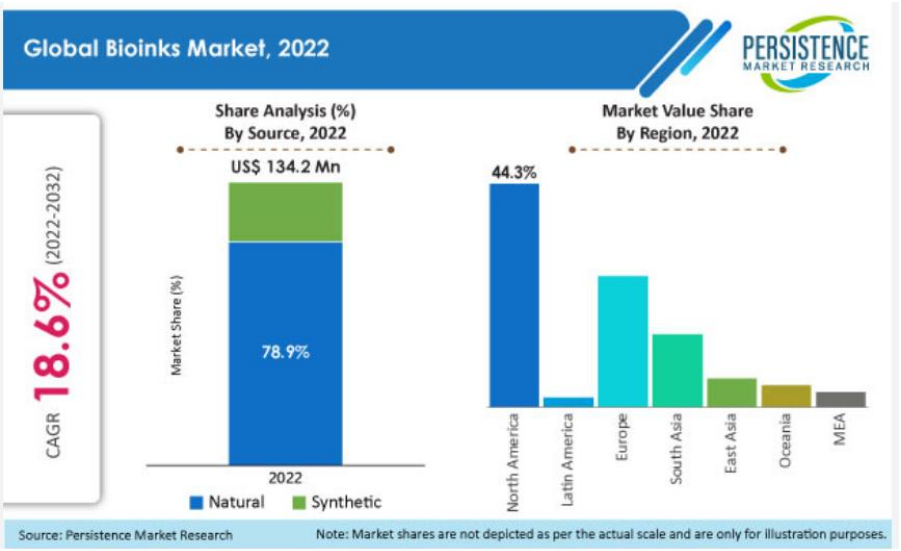

Figure 3. The graph demonstrates that the global bioink market in 2022 of USD 134.2 million.

Existing bioinks

A bioink is a hydrogel polymer. Bioinks can be made from either natural or synthetic polymers. Natural polymers are widely employed due to their natural abundance and excellent biodegradability and biocompatibility. Mainly alginate, collagen, gelatin, hyaluronic acid, and agarose are commonly used natural polymers in bioinks applications. Protein-based materials such as collagen and gelatin contain cell binding sites and other polymers such as hyaluronic acid and alginate can be functionalized with cell binding sites for bioactivity to promote cell attachment, which is desirable for controlling cell spreading and differentiation. The reproducibility of mechanical and biological properties of natural bioink could be challenging due to batch-to-batch variability.

Synthetic bioinks offer the advantage of tunable mechanical and chemical properties. PEG acrylates are purely synthetic bioinks, which have been developed. PEG hydrogels with matrix metalloproteinases (MMP) cleavable crosslinkers have also been developed, which provides mimics biodegradability. Several bioinks have been designed using a combination of natural polymers and synthetic cross-links for better tuning of mechanical and biological properties.

Natural polymers offer the freedom to be modified and cross-linked easily using synthetic cross-links.

In **Table 1**, we have listed existing bioinks with their strengths and weaknesses to provide an overview of different types of bioinks available either in the market or developed in the lab.

Table 2: Bioinks developed, companies selling commercial bioinks, and bioinks strengths and weaknesses.

Bioink	Owned by	Strength	Weakness
Peg-acrylates	Not owned (Sigma, Merck, Advanced BioMatrix, etc.)	Fully synthetic, well-established, cheap(ish)	No stress-relaxation or ability for cells to remodel, low viscosity, high network density, use of UV light
Gel-MA	Not owned (Merck, Sigma, CellInk, Allevi) Ali Khademhussini,	Biodegradable, well-established biocompatibility	Cannot tune biochemistry and mechanical properties independently, low-tunability, uncontrolled degradation, non-degradable kinetic chains, Use of UV-light
Collagen Bioinks	Not owned (CellInk, Advanced BioMatrix, ALLEVI, Humabiologics)	Biocompatible Biomimetic	Largely extracted from an animal source Not reproducible Required pH changes
rhCollagen	CollPlant Holdings	Plant-based technology to produce recombinant human type I collagen (rhCollagen). Biomimetic, similar to collagen I Free of pathogens and no foreign body response Cell binding domains enabled by perfect triple helix enhance cellular attachment Controlled mechanical properties	Costly Difficult to tune the range of mechanics and stress relaxation Expensive
Methacrylated Hyaluronic Acid	Not owned (Allevi, CellInk, Advanced BioMatrix,	Tunable stiffness	No stress relaxation No remodeling by cells Non-specific interactions by cells
Methacrylated Alginate	Advanced BioMatrix	Tunable stiffness Tunable bioactivity No specific interactions with cells	No stress relaxation No remodeling by cells

Alginate-Nanocrystals	CellInk	Established market share, established in multiple cell lines, RGD and laminin conjugated for bioactivity	Not modular, non-degradable, relatively expensive ($179 for 3mL, one use)
Ghost	Burdick Lab	Good publications and visibility Tunable viscoelasticity by secondary cross-links	No company formed yet. Limited and weak mechanical properties.
Peptide self-assembly	BioGelX	Fibrous structure	Poor mechanical properties, expensive ($350 for 4 mL, one use)
MMP cleavable PEG systems	Not owned	Tunable initial mechanical properties Tunable degradation of the hydrogel	The local cellular environment is different than the bulk Difficult to control dynamic mechanical properties and stress relaxation Local and bulk degradation
VitroINK, Xeno-free tunable bioink	The Well Bioscience Inc.	No UV, no temperature/pH curing, or chemical crosslinking Tunable bioactivity with either RGD or IKVAV or YIGSR peptides or with Matrix Metalloproteinases (MMP)	Limited tunability of mechanical properties

Table 1 discussed leading players including Cellink, BiogelX, Allevi, The Well Bioscience Inc, and CollPlant, which focused on developing and commercializing bioinks for 3D biofabrication. Some companies, for example, CollPlant Holdings have aimed to design a universal bioink and commercial product is driving technological advancement. Most bioinks allowed tuning stiffness and introduction of bioactivity. However, tuning of stress relaxation in ECM mimetic fibrous hydrogel is missing. Peptide-based fibrous bioinks have been developed by BioGelX and The Well Bioscience Inc.; however, these hydrogels exhibited poor mechanical properties and no stress relaxation tuning has been shown. We took on the challenge of developing bioinks with tunable stress relaxation and controlled fibrous structure utilizing dynamic covalent chemistry and supramolecular chemistry.

Bioinks developed in this thesis

Bioinks in this thesis were developed using dynamic covalent and supramolecular synthetic chemistries (**Table 2**).

Table 3: list of bioinks developed in this thesis with their unique advantages and disadvantages

Bioink	Owned by	Strength	Weakness
Alginate with imine type crosslinks (our systems)	Chapter IV of this thesis	Commercially and cheaply available cross-linkers; Mechanical properties tunable; Different cell adhesion molecule presentations are possible	Scale-up would be difficult; Unlimited swelling might be an issue
Supramolecular BTA hydrogels (Our system)	Chapter VII of this thesis	Tunable viscoelasticity and stress relaxation across 5 orders of magnitude; ECM (collagen) mimicking the fibrous structure in synthetic bioink	Longer than 10 days cell culture not possible; Erosion in cell culture media
Supramolecular Norbornene BTA hydrogel (our system)	Chapter VIII of this thesis	Tunable stiffness and stress relaxation; Tunable toughness ECM mimicking the fibrous structure; Longer cell culture is possible; Can be made MMP degradable	Use of UV light for cross-linking

Applicability of bioinks developed in this thesis

In this thesis research, we described the development of dynamic bioinks based on dynamic covalent and supramolecular chemistry. Owing to the increasing worldwide demand for organ replacement and tissue regeneration, there is a growing need for advanced bioinks for 3D bioprinting for replacing damaged organs or tissues with healthy and functional organs and tissues. Advanced bioinks require good control of mechanical properties post-printing for healthy tissue formation e.g., stiffness, viscoelasticity, and stress relaxation. In addition, rheological properties such as shear-thinning (decrease in viscosity upon application of shear strain) and self-healing (ability to repair broken bonds and achieve mechanical properties similar to before bioprinting) are important during and after 3D bioprinting. Therefore, we took on the challenge of developing bioinks with controlled mechanical and rheological properties.

Bioinks using dynamic covalent chemistry

In **chapter IV**, we developed a series of dynamic covalent hydrogels for their applicability as bioinks. We employed imine-type cross-links with a range of equilibrium constants (K_{eq}). Using

imine-type dynamic crosslinkers and oxidized alginate with aldehyde groups, we created alginate-based oxime, semicarbazone, and hydrazone dynamic hydrogels. We demonstrated that storage moduli can be tuned in the range of soft tissues (500–3000 Pa). We showed that all of the hydrogels were extrudable through a 25 G needle; however, semicarbazone and hydrazone demonstrated better extrudability compared to oxime. Semicarbazone and hydrazone displayed macroscopic self-healing. We demonstrated ATDC5 chondrocytes and human dermal fibroblasts exhibited good cell viability with these hydrogels. Hydrazone showed excellent 3D bioprinting and ATDC5 chondrocytes demonstrated good biocompatibility within hydrazone hydrogel. Excellent bioprintability and biocompatibility using hydrazone hydrogel showed that hydrazone hydrogel can be the future bioink used in the lab for investigating bioprintability and functional tissue formation with cell types that are more clinically relevant such as mesenchymal stem cells (MSCs) and induced pluripotent stem cells (iPSCs).

We envision providing customized formulations in dry powder form and the user has to follow a protocol for preparing a hydrazone bioink. For example, the user has to dissolve alginate and cross-linker in the calculated amount of cell culture media. Once dissolved, the alginate solution, cross-linker solution, and cell suspension can be mixed to prepare a bioink. After a waiting time of 15–45 minutes, the bioink is ready to be bioprinted into a defined shape.

Bioinks using supramolecular chemistry

Developing dynamic bioinks with controlled fibrous structures and mechanical properties remains a challenge. Supramolecular chemistry can enable the creation of bioinks that are dynamic yet biomimetic e.g., mimic the fibrous structure of proteins in the extracellular matrix (ECM). Supramolecular bioinks can also offer shear-thinning and self-healing properties owing to supramolecular transient interactions. For designing bioinks that are dynamic yet fibrous, we chose to develop bioinks using benzene, 1,3,5-benzene tricarboxamide (BTA). BTA has been known to undergo self-assembly via a combination of hydrogen bonding and hydrophobic interactions, resulting in one-dimensional (1D) fibers of a few nanometers in diameter and micrometer-scale long. Yet, the translation of BTA hydrogelator for bioink development with controlled mechanical properties has not been explored.

In **chapter VII** of this thesis, we developed a series of BTA hydrogelators bioinks with controlled mechanical properties. We simply altered the hydrophobic length (12, 16, 18, 20, and 24) on the exterior of benzene-1,3,5-tricarboxamide (BTA), which resulted in the modulation of viscoelasticity over 5 orders of magnitude in fibrous hydrogels. Interestingly, all hydrogelators demonstrated a similar equilibrium storage modulus. ATDC5 chondrocytes and human mesenchymal stem cells (hMSCs) displayed good cell viability within BTA hydrogels. BTA hydrogelators with 16, 20, and 24 carbon atoms length demonstrated shear-thinning, self-healing, and 3D printing into multi-layers structures. We showed that increasing carbon length on BTA provides better stability and shape fidelity to 3D-printed BTA structures. ATDC5 chondrocytes displayed high cell viability in bioprinted constructs. BTA hydrogelator bioinks

developed in **chapter VII** highlight the importance of the molecular design of hydrogel network for accessing the wide range of viscoelasticity in biomimetic fibrous bioinks for bioprinting.

In **chapter VIII** of the thesis, we developed an improved version of the bioink by replacing hydrophobic on the exterior of the BTA with norbornene (NB). The design of this bioink was inspired by nature's use of covalent reinforcement of self-assembled structures for designing tough tissues. NB BTA can undergo thiol-ene chemistry and could enable intra- and inter-fiber crosslinking. NB BTA self-assembles and forms a fibrillar and viscoelastic hydrogel. We demonstrated that cross-linking of self-assembly by intra- and inter-fiber enables tuning stiffness, strength, and toughness of the hydrogel. NB BTA hydrogels were extrudable, shear-thinning, and self-healing. NB BTA ink showed excellent 3D printability with good shape fidelity and enabled toughening of 3D printed structures by covalent cross-linking. hMSCs spheroids were mixed with NB BTA ink for preparation of NB BTA bioink and bioprinted into cartilage structure. hMSCs spheroids successfully produced cartilage tissue within bioprinted NB BTA constructs. The ability of hMSCs to produce cartilage tissue in NB-BTA hydrogelator makes NB BTA a promising bioink. There are already a few existing fibrous bioinks[26,27] and tough hydrogels[28]; however, tuning toughness within the synthetic biomimetic fibrillar bioink remains a formidable challenge that we addressed by developing NB BTA bioink. Unlike existing bioinks, such as gelatin and Matrigel, NB BTA bioink has been made using fully synthetic components and provides better control over the tuning of dynamics and toughness in synthetic bioink.

We envision providing NB BTA hydrogelator kits for laboratories to conduct their research in the areas of tissue engineering and bioprinting. The NB BTA hydrogelator kit will contain NB BTA hydrogelator powder, cross-linker solution, and appropriate cell culture media for making hydrogels out of the NB BTA hydrogelator. For Bioprinting and extrusion applications, the NB BTA kit will contain a bioprinting syringe and an appropriate needle size for successful bioprinting. Collaboration with other companies can also be considered for the distribution of NB BTA kits for example such companies could be CellInk, Advanced BioMatrix, and Allevi.

We aim to provide NB BTA hydrogelator for a range of applications including cell culture, organoid growth, and drug screening for increasing the commercial potential of the NB BTA bioink. Investigation with other cell types will help establish protocols with a variety of cell types, which is beneficial for enhancing the commercialization potential of the NB BTA bioink. For example, NB BTA hydrogels can be investigated with cells from tough and fibrous tissues such as tendons and muscles. Additional research on coating two-dimensional (2D) polystyrene culture dishes or creating 2D substrates of NB BTA for investigation of cell differentiation will also enhance the commercial value of the NB BTA bioink.

Patents

The research carried out in **chapter IV** has produced a patent entitled "Bioinks", which has been filed in Europe and US.

The research carried out in **chapter VIII** has resulted in the patent application of "Injectable tough and viscoelastic BTA hydrogel". The european search report found our claims to be new and inventive.

References

(1) Abouna, G. M. Organ Shortage Crisis: Problems and Possible Solutions. *Transplant. Proc.* **2008**, *40* (1), 34–38. https://doi.org/10.1016/j.transproceed.2007.11.067.

(2) Lewis, A.; Koukoura, A.; Tsianos, G. I.; Gargavanis, A. A.; Nielsen, A. A.; Vassiliadis, E. Organ Donation in the US and Europe: The Supply vs Demand Imbalance. *Transplant. Rev.* **2021**, *35* (2), 100585. https://doi.org/10.1016/J.TRRE.2020.100585.

(3) Manns, B.; Hemmelgarn, B.; Tonelli, M.; Au, F.; So, H.; Weaver, R.; Quinn, A. E.; Klarenbach, S. The Cost of Care for People With Chronic Kidney Disease. *Can. J. Kidney Heal. Dis.* **2019**, *6*. https://doi.org/10.1177/2054358119835521.

(4) Savarese, G.; Becher, P. M.; Lund, L. H.; Seferovic, P.; Rosano, G. M. C.; Coats, A. J. S. Global Burden of Heart Failure: A Comprehensive and Updated Review of Epidemiology. *Cardiovasc. Res.* **2023**, *118* (17), 3272–3287. https://doi.org/10.1093/cvr/cvac013.

(5) Heidenreich, P. A.; Albert, N. M.; Allen, L. A.; Bluemke, D. A.; Butler, J.; Fonarow, G. C.; Ikonomidis, J. S.; Khavjou, O.; Konstam, M. A.; Maddox, T. M.; Nichol, G.; Pham, M.; Piña, I. L.; Trogdon, J. G. Forecasting the Impact of Heart Failure in the United States a Policy Statement from the American Heart Association. *Circ. Hear. Fail.* **2013**, *6* (3), 606–619. https://doi.org/10.1161/HHF.0b013e318291329a.

(6) Cheemerla, S.; Balakrishnan, M. Global Epidemiology of Chronic Liver Disease. *Clin. Liver Dis.* **2021**, *17* (5), 365–370. https://doi.org/10.1002/cld.1061.

(7) Ye, F.; Zhai, M.; Long, J.; Gong, Y.; Ren, C.; Zhang, D.; Lin, X.; Liu, S. The Burden of Liver Cirrhosis in Mortality: Results from the Global Burden of Disease Study. *Front. Public Heal.* **2022**, *10*. https://doi.org/10.3389/fpubh.2022.909455.

(8) Arulraj, R.; Neuberger, J. Liver Transplantation: Filling the Gap between Supply and Demand. *Clin. Med. J. R. Coll. Physicians London* **2011**, *11* (2), 194–198. https://doi.org/10.7861/clinmedicine.11-2-194.

(9) Manns, M. P. Liver Cirrhosis, Transplantation and Organ Shortage. *Dtsch. Arztebl. Int.* **2013**, *110* (6), 83–84. https://doi.org/10.3238/arztebl.2013.0083.

(10) Svedbom, A.; Hernlund, E.; Ivergård, M.; Compston, J.; Cooper, C.; Stenmark, J.; McCloskey, E. V.; Jönsson, B.; Kanis, J. A. Osteoporosis in the European Union: A Compendium of Country-Specific Reports. *Arch. Osteoporos.* **2013**, *8* (1–2). https://doi.org/10.1007/s11657-013-0137-0.

(11) Nandra, R.; Grover, L.; Porter, K. Fracture Non-Union Epidemiology and Treatment. *Trauma* **2016**, *18* (1), 3–11. https://doi.org/10.1177/1460408615591625.

(12) Borgström, F.; Karlsson, L.; Ortsäter, G.; Norton, N.; Halbout, P.; Cooper, C.; Lorentzon, M.; McCloskey, E. V.; Harvey, N. C.; Javaid, M. K.; Kanis, J. A.; Reginster, J. Y.; Ferrari, S. Fragility Fractures in Europe: Burden, Management and Opportunities. *Arch. Osteoporos.* **2020**, *15* (1). https://doi.org/10.1007/s11657-020-0706-y.

(13) Vacanti, C. A.; Vacanti, J. P. Functional Organ Replacement, The New Technology of Tissue Engineering. *Surg. Technol. Int.* **1991**, *I*, 43–49.

(14) Vacanti, C. The History of Tissue Engineering. *J. Cell. Mol. Med.* **2006**, *1* (3), 569–576. https://doi.org/10.2755/jcmm010.003.20.

(15) Langer, R.; Vacanti, J. P. Tissue Engineering. *Science (80-.).* **1993**, *260* (5110), 920–926. https://doi.org/10.1126/science.8493529.

(16) Khademhosseini, A.; Langer, R. A Decade of Progress in Tissue Engineering. *Nat. Protoc. 2016 1110* **2016**, *11* (10), 1775–1781. https://doi.org/10.1038/nprot.2016.123.

(17) Moroni, L.; Boland, T.; Burdick, J. A.; De Maria, C.; Derby, B.; Forgacs, G.; Groll, J.; Li, Q.; Malda, J.; Mironov, V. A.; Mota, C.; Nakamura, M.; Shu, W.; Takeuchi, S.; Woodfield, T. B. F.; Xu, T.; Yoo, J. J.; Vozzi, G. Biofabrication: A Guide to Technology and Terminology. *Trends Biotechnol.* **2018**, *36* (4), 384–402. https://doi.org/10.1016/j.tibtech.2017.10.015.

(18) Moroni, L.; Burdick, J. A.; Highley, C.; Lee, S. J.; Morimoto, Y.; Takeuchi, S.; Yoo, J. J. Biofabrication Strategies for 3D in Vitro Models and Regenerative Medicine. *Nat. Rev. Mater.* **2018**, *3*, 21–37. https://doi.org/10.1038/s41578-018-0006-y.

(19) Mota, C.; Camarero-Espinosa, S.; Baker, M. B.; Wieringa, P.; Moroni, L. Bioprinting: From Tissue and Organ Development to in Vitro Models. *Chemical Reviews*. 2020, pp 10547–10607. https://doi.org/10.1021/acs.chemrev.9b00789.

(20) Morgan, F. L. C.; Moroni, L.; Baker, M. B. Dynamic Bioinks to Advance Bioprinting. *Adv. Healthc. Mater.* **2020**, *9* (15), 1901798. https://doi.org/10.1002/adhm.201901798.

(21) Santoni, S.; Gugliandolo, S. G.; Sponchioni, M.; Moscatelli, D.; Colosimo, B. M. 3D Bioprinting: Current Status and Trends—a Guide to the Literature and Industrial Practice. *Bio-Design Manuf.* **2022**, *5* (1), 14–42. https://doi.org/10.1007/s42242-021-00165-0.

(22) *3D Bioprinting Market by Component (3D Bioprinters (Microextrusion, Inkjet, Laser, Magnetic), Bioink (Natural, Synthetic, Hybrid)), Material(Hydrogel, Living Cells), Application (Research, Clinical), End user (Biopharma, Academia) - Global Forecast to 202*. https://www.researchandmarkets.com/reports/4846742/3d-bioprinting-market-by-component-3d (accessed 2023-01-15).

(23) *3D Bioprinting Market Size*. https://www.marketresearchfuture.com/reports/3d-bioprinting-market-869 (accessed 2023-01-17).

(24) *3D Bioprinting Market Size, Trends, Growth, Report 2030*. https://www.precedenceresearch.com/3d-bioprinting-market (accessed 2023-01-17).

(25) *Market Study on Bioinks: Demand for Natural Bioinks to Remain Incredibly High*. https://www.persistencemarketresearch.com/market-research/bioinks-market.asp (accessed 2023-01-17).

(26) Susapto, H. H.; Alhattab, D.; Abdelrahman, S.; Khan, Z.; Alshehri, S.; Kahin, K.; Ge, R.; Moretti, M.; Emwas, A. H.; Hauser, C. A. E. Ultrashort Peptide Bioinks Support Automated Printing of Large-Scale Constructs Assuring Long-Term Survival of Printed Tissue Constructs. *Nano Lett.* **2021**, *21* (7), 2719–2729. https://doi.org/10.1021/acs.nanolett.0c04426.

(27) Sather, N. A.; Sai, H.; Sasselli, I. R.; Sato, K.; Ji, W.; Synatschke, C. V.; Zambrotta, R. T.; Edelbrock, J. F.; Kohlmeyer, R. R.; Hardin, J. O.; Berrigan, J. D.; Durstock, M. F.; Mirau, P.; Stupp, S. I. 3D Printing of Supramolecular Polymer Hydrogels with Hierarchical Structure. *Small* **2021**, *17* (5), 1–14. https://doi.org/10.1002/smll.202005743.

(28) Rodell, C. B.; Dusaj, N. N.; Highley, C. B.; Burdick, J. A. Injectable and Cytocompatible Tough Double-Network Hydrogels through Tandem Supramolecular and Covalent Crosslinking. *Adv. Mater.* **2016**, *28* (38), 8419–8424. https://doi.org/10.1002/adma.201602268.

Summary

The development of advanced and dynamic hydrogels and bioinks with extracellular matrix (ECM) biomimicry is needed for understanding cellular response to dynamic networks with controlled viscoelasticity and biomimetic fibrous structure. This thesis investigates dynamic covalent chemistry and supramolecular chemistry for creating hydrogels that recapitulate extracellular matrix (ECM) viscoelasticity, stress relaxation, and fibrillar structure. Unlike the ECM, traditional hydrogels are elastic and allowed controlling stiffness. However, the ECM is dynamic and possesses time-dependent properties of viscoelasticity and stress relaxation. Therefore, we investigated dynamic and reversible chemistries for the creation of synthetic analogs of the ECM with controlled dynamicity, viscoelasticity, and structure. We also investigated newly developed dynamic hydrogels 3D bioprinting for the creation of complex life-like structures.

Utilizing imine-type dynamic covalent chemistry (DCvC) in **chapter IV**, we discovered that cross-links with distinct K_{eq} can be used for tuning viscoelasticity. We found that hydrazone has higher viscoelasticity compared to semicarbazone and oxime. Viscoelasticity had an impact on cell morphology, with fibroblasts displaying a round shape in oxime hydrogels as opposed to a spreading shape in hydrazone hydrogels. Similarly, we also found that the reversibility of hydrazone cross-links imparts self-healing and enables 3D bioprinting of complex life-like structures.

Then, we realized that ECM is a supramolecular and self-assembled fibrous structure with controlled viscoelasticity and dynamicity. Utilizing modular mixing/copolymerization of benzene-1,3,5-tricarboxamide (BTA) monomers (**chapter V**) with fast and slow exchange dynamics, we tuned viscoelasticity and stress relaxation in fibrous structure in the range of soft tissues. Fibroblasts and chondrocytes displayed high cell viability and neuronal cells (PC12) and dorsal root ganglion (DRG) could grow within fibrous and dynamic hydrogels. Interestingly, chondrocytes and human mesenchymal stem cells (hMSCs) formed cell aggregates, and more compact spheroids were observed for hMSCs. We attributed the spheroid formation ability of hMSCs within these hydrogels to the dynamicity and viscous properties of the hydrogel. While discovering more about ECM, we found that not only ECM is multicomponent but also ECM is multifunctional. Creating multifunctionality in ECM mimetic structure is desired and supramolecular chemistry offers a biomimetic and modular approach to creating multifunctional ECM for emulating the complexity of ECM. BTA is inspiring due to its one-dimensional (1D) fiber structure; however, large-scale synthesis of multifunctional BTA is the bottleneck. In **chapter VI**, we developed a new desymmetrization strategy that enables the creation of multifunctional and upscale synthesis of BTA architectures and macromonomers. A small library of benzene-1,3,5-activated esters was created and found that benzene-1,3,5-pentafluorophenol

tri-ester (BTE-F5Ph) enabled effective desymmetrization and synthesis of BTA with hydrophobic spacers and reactive handles (azide and norbornene). We utilized the desymmetrization strategy for the creation of telechelic polymeric BTA macromolecules. We discovered that BTA macromolecules form fibrous hydrogels and mechanical properties can be tuned by altering the hydrophobic handles attached on the BTA. Next, after observing some interesting trends in the viscoelastic properties of newly developed BTA fibrous hydrogel, we hypothesize that the length of hydrophobics could dictate the viscoelastic properties of BTA hydrogel. We created a telechelic BTA macromonomer with twelve, sixteen, eighteen, twenty, and twenty-four carbon atoms on the exterior of BTA (**chapter VII**). All macromonomers formed fibrous hydrogels with similar equilibrium storage modulus. We discovered that hydrogels with more than 5 orders of magnitude viscoelasticity can be made by altering the hydrophobic length from twelve to twenty-four. BTA hydrogels were extrudable, and the shape fidelity of 3D printed constructs was greatly improved with the increasing number of carbon atoms. Bioprinted chondrocytes showed high cell viability within BTA hydrogels. This straightforward method of adding or removing a few carbon atoms on BTA overcomes the long-standing challenge of tuning broad-range viscoelasticity in the fibrous hydrogel. Next, we were inspired by the conjunction of self-assembly and covalent fixation of collagen which is believed to be responsible for the toughness and strength of the collagen protein. We proposed a supramolecular/covalent strategy to achieve remarkable mechanical properties. BTA with norbornene (NB) (NB BTA) functionality was made that self-assembles into the fibrillar structure and forms a fibrous hydrogel with controlled viscoelasticity (**chapter VIII**). Intra- and inter-fiber crosslinks were introduced for tuning the hydrogel's stiffness, strength, and toughness. NB-BTA hydrogel was extremely tough, demonstrated recoverable hysteresis, and can withstand 90% compressive strain, and 550% tensile strain. Shear-thinning and self-healing properties of NB-BTA hydrogel enabled 3D printing of a cartilage-like structure. Human mesenchymal stem cell spheroids produced collagen II in bioprinted NB-BTA hydrogel, which strongly shows the development of chondrogenic tissue in bioprinted NB-BTA hydrogel.

In the future, the creation of multifunctional supramolecular monomers with controlled molecular dynamics will be of great interest for achieving next-level control of ECM dynamicity and biomimicry. In addition, molecular control of supramolecular dynamics will enable the development of advanced bioinks with spatiotemporal control of mechanical and biological properties.

Scientific Activities

Experimental articles in peer-reviewed international journals

S. Hafeez, M.C. Decarli, A. Aldana, M. Ebrahimi, F.A.A. Ruiter, H Duimel, C.V. Blitterswijk, L.M. Pitet, L. Moroni, M. B. Baker**,** Covalent cross-linking of a supramolecular assembly creates tough, fibrous hydrogels and bioinks, **Advanced Materials**, (accepted)

S. Hafeez, A. Aldana, H Duimel, F.A.A. Ruiter, M.C. Decarli, V.L.S LaPointe, C. V. Blitterswijk, L. Moroni, M. B. Baker, Molecular tuning of a benzene-1,3,5-tricarboxamide supramolecular fibrous hydrogel enables control over viscoelasticity and creates tunable ECM-mimetic hydrogels and bioinks, **Advanced Materials**, (2023) 202207053

S. Hafeez, F.R. Passanha, A. J Feliciano, F.A.A. Ruiter, A. Malheiro, R. P. M. Lafleur, N. M. Matsumoto, C.V. Blitterswijk, L. Moroni, P. Wieringa, V.L.S LaPointe, M. B. Baker, Modular mixing of benzene-1, 3, 5-tricarboxamide supramolecular hydrogelators allows tunable biomimetic hydrogels for control of cell aggregation in 3D, **Biomaterials Science**, 10 (2022) 4740.

S. Hafeez, H. W. Ooi, D. Suylen, H. Duimel, T. Hackeng, C. V. Blitterswijk, L. Moroni, M. B. Baker, Desymmetrization via activated esters facilitates the creation of multifunctional 1,3,5-benzene tricarboxamide monomer and dynamic supramolecular hydrogels as synthetic extracellular matrix mimics, **Journal of the American Chemical Society**, 144 (2022) 4057.

S. Hafeez, H. Ooi, F. Morgan, C. Mota, M. Dettin, C. V. Blitterswijk, L. Moroni, M. B. Baker, Viscoelastic oxidized alginates with reversible imine type crosslinks: Self-Healing, injectable, and bioprintable hydrogels, **Gels**, 4 (2018) 85.

Review articles in peer-reviewed international journals

S. Hafeez, C. V. Blitterswijk, L. Moroni, M. B. Baker, Extracellular mimicking dynamic bioinks. Manuscript in preparation.

H. W. Ooi, **S. Hafeez**, C. V. Blitterswijk, L. Moroni, M. B. Baker, Hydrogels that listen to cells: a review of cell-responsive strategies in biomaterial design for tissue regeneration, **Materials Horizons**, 4 (2017)1020.

Contribution towards other research works during PhD

R. Wang, F. Damanik, T. Kuhnt, A. Jaminon, **S. Hafeez**, H. Liu, H. Ippel, P.J. Dijkstra, N. Bouvy, L. Schurgers, A. T. ten Cate, A. Dias, L. Moroni, M. B. Baker, Biodegradable Poly(Ester) Urethane Acrylate Resins for Digital Light Processing: From Polymer Synthesis to 3D Printed Tissue Engineering Constructs. **Advanced Healthcare Materials**, 2202648 (2023), 1–13.

T. Yao, T. V. Neun, R. Rivero, C. Powell, R. Carrazzone, L. Kessels, P. Wieringa, **S. Hafeez**, T. Wolfs, L. Moroni, J. Matson, M. Baker, Electrospun Scaffolds Functionalized with a Hydrogen Sulfide Donor Stimulate Angiogenesis. **ACS Applied Materials & Interfaces**, 14 (2022) 28628.

M. Setayeshmehr, **S. Hafeez**, C. V. Blitterswijk, L. Moroni, C. Mota, M. B. Baker, Bioprinting via a dual-gel bioink based on polyvinyl alcohol and solubilized extracellular matrix towards cartilage engineering, **International journal of molecular sciences**, 22 (2021) 3901.

Patent applications

BIOINKS (18205041.9 - 1107)

Injectable Tough and Viscoelastic BTA hydrogel (Filed in November 2021)

Scientific Communications

Oral Presentations

S. Hafeez, A. Aldana, M. Ebrahimi, H. Duimel, C. V. Blitterswijk, L. M. Pitet, M. B. Baker, Molecular engineering of supramolecular interactions for developing biomimetic hydrogels for biofabrication of soft and tough tissues, 6th TERMIS World Congress, November 15–19, 2021, Maastricht, the Netherlands.

S. Hafeez, A. Aldana, C. V. Blitterswijk, M. B. Baker, Supramolecular engineering for creating ECM mimicking dynamic BTA hydrogels with controlled viscoelasticity for cell culture and biofabrication, European Society for Biomaterials, September 5–9, 2021, Porto, Portugal.

S. Hafeez, A. Aldana, A. Feliciano, R. P. M. Lafleur, N. M. Matsumoto, L. Moroni, C. V. Blitterswijk, E. W. Meijer, M. B. Baker, BTA-based supramolecular hydrogels for tissue engineering and biofabrication, CHAINS 2020, The Dutch Chemistry Conference, December 8–9, 2020, Veldhoven, the Netherlands.

S. Hafeez, A. Aldana, A. Feliciano, R. P. M. Lafleur, N. M. Matsumoto, L. Moroni, C.V. Blitterswijk, E. W. Meijer, M. B. Baker, Tuning supramolecular dynamics to capture ECM viscoelasticity and fibrous structure, 11th World Biomaterials Congress, December 11–16, 2020, Glasgow, Scotland.

S. Hafeez, A. Feliciano, R. P. M. Lafleur, N. M. Matsumoto, L. Moroni, C.V. Blitterswijk, E. W. Meijer, M. B. Baker, Extracellular mimicking BTA supramolecular synthetic viscoelastic hydrogels for chondrocytes culture, ACS National Meeting, 22–26 March 2020, Philadelphia, USA, physical presentation canceled because of COVID-19 pandemic. The online presentation is available on the ACS SciMeetings Platform.

S. Hafeez, A. Feliciano, R. P. M. Lafleur, N. M. Matsumoto, L. Moroni, C.V. Blitterswijk, E. W. Meijer, M. B. Baker, Supramolecular viscoelastic hydrogels as artificial extracellular matrix (ECM), MERLN PhD Symposium, December 6, 2019, Maastricht, the Netherlands.

S. Hafeez, A. Feliciano, R. P. M. Lafleur, N. M. Matsumoto, L. Moroni, C.V. Blitterswijk, E. W. Meijer, M. B. Baker, Evaluating and designing BTA supramolecular hydrogels as a viscoelastic extracellular matrix for cell culture, MRS Spring Meeting, April 22–26, 2019, Phoenix, USA.

S. Hafeez, H. W. Ooi, F. L. C. Morgan, R. P. M. Lafleur, N. M. Matsumoto, C. Mota, L. Moroni, C. V. Blitterswijk, E. W. Meijer, M. B. Baker, Viscoelastic hydrogels as 3D cell culture systems, CHAINS 2018, December 3–5, 2018, Veldhoven, the Netherlands.

S. Hafeez, N. M. Matsumoto, C. V. Blitterswijk, E. W. Meijer, M. B. Baker, BTAs supramolecular hydrogelators as extracellular matrices for tissue engineering, European Society for Biomaterials, September 9–13, 2018, Maastricht, the Netherlands.

S. Hafeez, N. M. Matsumoto, E. W. Meijer, M. B. Baker, BTA Supramolecular hydrogels as extracellular matrices for tissue engineering applications. MERLN PhD Symposium, December 7, 2018, Maastricht, Netherlands.

Poster Presentations

S. Hafeez, A. Feliciano, R. P. M. Lafleur, N. M. Matsumoto, L. Moroni, C. V. Blitterswijk, E. W. Meijer, M. B. Baker, Supramolecular Viscoelastic Hydrogels as Artificial ECM, CHAINS 2019, The Dutch Chemistry Conference, December 10–11, 2019, Veldhoven, the Netherlands.

S. Hafeez, A. Feliciano, R. P. M. Lafleur, N. M. Matsumoto, L. Moroni, C. V. Blitterswijk, E. W. Meijer, M. B. Baker, Extracellular mimicking BTA supramolecular synthetic hydrogels for chondrocyte culture, European Society for Biomaterials, September 9–13, 2019, Dresden, Germany.

S. Hafeez, N. M. Matsumoto, C. V. Blitterswijk, E. W. Meijer, M. B. Baker, BTA supramolecular hydrogels as a dynamic extracellular matrix for chondrocyte culture, 5th TERMIS World Congress, September 4–7, 2018, Kyoto, Japan.

S. Hafeez, N. M. Matsumoto, E. W. Meijer, M. B. Baker, BTA supramolecular hydrogels as a dynamic extracellular matrix for chondrocytes expansion. Bioinspired and Biomimetic Hydrogels, April 15–18, 2018, Gladbach, Germany.

S. Hafeez, N. M. Matsumoto, E. W. Meijer, M. B. Baker, Supramolecular hydrogels as extracellular matrices for tissue engineering applications. ICMS Outreach Symposium, February 1–2, 2018, Eindhoven, the Netherlands.

S. Hafeez, N. M. Matsumoto, E. W. Meijer, M. B. Baker, BTA Supramolecular hydrogels as extracellular matrices for tissue engineering applications. MERLN PhD Symposium, December 7, 2018, Maastricht, Netherlands.

Education Activities

Tutoring

CH2001 — Organic chemistry — Bachelor Maastricht Science Program (2021)
CH2001 — Organic chemistry — Bachelor Maastricht Science Program (2019)
CH2001 — Organic chemistry — Bachelor Maastricht Science Program (2018)
CH2001 — Organic chemistry — Bachelor Maastricht Science Program (2017)

Supervision

Louis Boylan (Master's student, 2020) — An investigation of the Mechanical Properties and Cell Supporting Potential of Oxidized Alginate Hydrogels Crosslinked with Dynamic Covalent Imine Type Chemistry.

Louis's thesis won the 1st place in Pfizer Prijzen voor Life Sciences 2020 in the whole Netherlands.

Mohsen Setayeshmehr (Visiting PhD student, 2018) — Bioprinting Via a Dual-Gel Bioink Based on Poly(Vinyl Alcohol) and Solubilized Extracellular Matrix towards Cartilage Engineering

Work with Mohsen resulted in a publication that was published in the International Journal of Molecular Sciences.

Marlish Ratnakumar (Bachelor student, 2018) — Polyethylene glycol acrylate synthesis

Awards

Award from the MERLN PhD Symposium for best rapid-fire presentation 2018.

Universiteitsfonds Limburg/Swol and EXCALIBUR regenerative medicine fund: As a PhD student along with a team of 4 other colleagues, won a total of €10,000 for developing a chemistry app "CHEMERA" for the gamification of chemistry.

TASR Labs among six winning teams in the sustainable idea: Development of the CHEMERA app for gamification of chemistry made it to the sustainable idea at "Feel the Chemistry, Little Big Talks 2020" Brightlands Campus.

Acknowledgments

I was in 12th grade when I read about Dr. Mohammad Abdus Salam's struggle to get an education and then become a Nobel laureate in Physics, that was the moment that I decided to do science and make a difference. After my bachelor's of engineering education from Pakistan and my master's education from Germany, I decided to carry out a PhD. With the encouragement of Prof. Aldo. R. Boccaccini, Dr. Evi Lippens, and Dr. Taimoor Hassan Qazi I joined MERLN Institute as a PhD student under the supervision of Prof. Clemens van Blitterswijk, Prof. Lorenzo Moroni, and Prof. Matthew Baker. With no real prior knowledge of organic synthesis and being very passionate and a little crazy, I decided to make new biomaterials using dynamic covalent chemistry and supramolecular chemistry. After almost 5-years of hard work, I have accomplished this goal and made some unique dynamic biomaterials.

First and foremost, I would like to thank my promotors; Clemens and Lorenzo. Clemens, thank you for accepting me and putting your trust in me to work on the ERC project. I know you have been very busy and I only wished that I could learn more from your entrepreneurial experience. Lorenzo thank you also for putting your trust in me and hiring me to work at MERLN. Lorenzo, I would like to thank you for your continuous support and very creative scientific feedback, and excitement about the new chemistries. Thank you also for making the CTR department feel at home. I always admire how reachable and calm you are at work.

Next, I would like to thank my co-promotor; Matt, who has directly supervised me during the last 5 years of my life. Thank you for teaching me organic chemistry and the for the confidence that I could learn and make organic molecules. If it was not for the synthesis of dynamic and supramolecular hydrogel, I would not have known that I could make such complex molecules in the lab. Thank you for challenging me on many occasions and especially when many many attempts of BTA separation failed. Thank you for the excitement and motivation through the ups and downs of my PhD. Thank you for being creative, for the space and freedom, for helping me think through the design of new chemistries, and for letting me dream and create molecules.

I would also like to thank other principal investigators at MELRN including Vanessa Lapointe, Paul Wieringa, Carlos Mota, and Jurica Bauer for their valuable feedback on my research. I would also like to thank Louis Pitet for allowing me to do some mechanical testing at Hasselt University. I would like to thank all the lab managers including Eva Gubbins, Marloes Kamphuis, Timo Rademakers, and Denis van Beurdenfor constantly striving to provide a working environment in the lab. I would also like to thank MERLN managers including Dennie Hebels, Romina Gentier, and Angelique Dijk for providing support with data management, general support, and office-related matters, respectively.

One of the earliest people I met at MERLN was Huey Wen (a postdoc and polymer chemist in the CTR group). Thank you for getting me started in the organic chemistry lab and thank you for your friendly personality and random jokes in the lab. Huey Wen, you always provided

support and advice during the early days of my PhD. You are a brilliant chemist and I wish you all the success at your current job at Thermo Fisher Scientific. I would like to thank many other scientists for their advice and feedback on my research, especially during my early years of PhD including Tobias Kuhnt, Sandra Camarero-Espinosa, Ravi Sinha, Rong Wang, David Gomez, and Jip Zonderland.

Several other group members, I enjoyed working with and would like to thank: Agustina Aldana, thank you for the help with the 3D printing of supramolecular hydrogels, I bet was not easy but turned out to be fun. Floor Ruiter, thank you for your help with FRAP experiments and data interpretation. Also, I appreciate you convincing me to enjoy life outside the lab from time to time. Francis, thank you for your help with rheology experiments of dynamic covalent hydrogels, and data analysis and for showing me how to use a rheometer. Tony, thank you for the help with the rheology of modularly mixed hydrogels. It was fun sharing the chemical hood with you and I enjoyed your jokes about Beyoncé. I get to know a lot about American culture and life from you. Ivo, we did not work a lot together, but I like your Jokes in the lab and your light-mindedness. Fiona Rosaleen Passanha, thank you for your help with culturing of millions of mesenchymal stem cells, and thank you for helping me with the critical experiments to finish. I like your generous behavior and willingness to help your colleagues. Monize Caiado Decarli thank you for creating spheroids of mesenchymal stem cells for culturing in BTA dynamic hydrogels. Thank you for being reachable and I like bioprinting discussions with you. I know they can go on for hours! Your help was critical in spheroids bioprinting in BTA tough hydrogels. Rebeca Rivero, we did some experiments together with endothelial cells in dynamic hydrogels, sad that they did not work out fully but thanks for providing endothelial cells and the positive energy that you put into these experiments. Also, thanks for telling me more about your dogs. I hope that you are doing great at your current job at Mosa Meat. Mahsa Ebrahimi, thank you for your help with mechanical testing. I like doing those experiments with you and discussing Iranian food and culture with you. I hope that women get their rights soon in Iran. Afonso Malheiro, I enjoyed working with you and exploring neurite growth in dynamic hydrogels. Thank you for your help with neurite growth experiments and for teaching me PC 12 cell culture. I would like to thank my master's student, Louis Boylan. You have done some good quality research and made us proud by winning the Pfizer prize 2020.

I would like to thank many other colleagues and friends with whom I have crossed paths at CTR and MERLN. Maria Camara Torres, you were also among the first few people I made the connection at MERLN. Thank you for your company, I enjoyed the time-to-time random discussions with you. Rabeil and Tianyu, I enjoyed the time spent with you on TERMIS, Japan. Thank you for taking me to Nara city, otherwise, I will not have had the chance to see 8th-century old temples and so many deers. Vahid Ansari, you are a wonderful person and an amazing cook, thank you for cooking Iranian food for me. Pinak Samal and Jay Samal, you both are very good scientists and I like getting food with you from Lezzet Grill and discussions on political issues between India and Pakistan. Mohsen and Sami, I like traveling with you to Liege and climbing the Montagne de Bueren was fun. Aygul Zengin you are a very hardworking

scientist, thank you for offering help whenever I needed the most. I like collaborating with you and your attitude toward science. I wish you all the best in finishing up your PhD thesis. Yousra Alaoui Selsouli, I like all the cultural and political discussions with you. Said, thank you for introducing me to the keto diet and telling me all the benefits of it. I remember getting drinks and laughing at your jokes on the bank of the Maas River. Shivesh and Claudia, you are a very nice couple, and I enjoyed the discussion with you over many topics including science, biking, and politics. Shivesh, also thanks for arranging cricket days. Filipa Teixeira Castro thank you for the company during my last days at MERLN. You are a passionate and hardworking scientist and I wish you the best of luck with your PhD. I would like to thank many other colleagues with whom I have crossed paths at MERN: Erik Vrij, Urnaa Tuvshindorj, Clarissa Tomasina, Adam Stel, Julia Fernandez Perez, Andrea Roberto Calore, Kenny van Kampen, David Koper, Tristan Bodet, Amit Chandrakar, Gabriele Addario, Jiaping Li, Victor Galvan, Jasia King, Vijayaganapathy Vaithilingam, Daniel Pereira, Omar Paulino Da Silva Filho, Gozde Sahin, Maria Oliveira, and Martijn Kern. I like talking and discussing science with all of you.

I would like to thank my friend; Shujaat, it was a coincidence that we met but we became really good friends. Thank you for cheering and for all the funny jokes. Ahmad, thank you for visiting me during COVID, I enjoyed cooking all the Pakistani food and talking about philosophy and history. Lily, thank you for your friendship and for introducing me to Paulo Coelho, and for all the meaningful conversation over dinner. Wish you the best of luck with your time in Japan. Hannah Schwarz thank you for being a kind person and arranging food events and helping us socialize at the house. Jacob Mather, thank you for being chill at the house, my ears have witnessed how good of a guitarist you have become over the years. I wish you good luck with your dream of opening a restaurant and the guitarist of the restaurant. Danish, you have been a great friend and a very hardworking man. It was sad that you had to move back to Pakistan, but I am glad that you are doing great there. Michael Nickenig, I also had a great time sharing a house with you and you have been a genuinely kind young man. I wish you all the luck with your future endeavors.

I would like to say special thanks to my parents who have made sure I can get the best education. Dad, I know how much you loved me and how proud you would have been to see your son get a doctorate. I am sure you are up there and very proud of me. I miss you and always wish that I could spend more time with you. Mom, I am grateful for the sacrifices that you made to ensure I can complete my education and realize my dreams. Thank you for all your prayers and for raising me as an honest person. Special thanks to my wife, Aqsa. Thank you for being patient and supportive during these challenging years of my life. Also, special thanks to my siblings, who have supported me throughout my education and made me laugh during stressful times. I wish you all the best in life.

I would like to thank our collaborators from the Technical University of Eindhoven. Professor Bert Meijer, thank you for providing BTAs for cell culture studies. Nic, thank you for making the initial set of BTA hydrogelators for me to get started with culturing cells in BTA hydrogel. Rene, thank you for your help with providing BTA material and always being helpful and

answering questions on BTA hydrogels. I would also like to thank our collaborators from the University of Padua, Italy. Monica Dettin, thank you for providing a set of RGD peptides for the bioactivation of dynamic hydrogels.

Last but not least, I would like to thank my thesis assessment committee, Prof. Dr. Tilman Hackeng, Prof. Dr. Romano Orru, Prof. Dr. Bert Meijer (Eindhoven University of Technology), and Prof. Dr. Sarah Heilshorn (Stanford University). Thank you for reading my thesis and for providing critical feedback and valuable assessment. Additionally, I would like to express my deep gratitude to Assoc. Prof. Dr. Sabine van Rijt and Prof. Dr. Roman Truckenmüller for their generous commitment to serving on my defense committee. I greatly appreciate your time.

Biography

Shahzad was born on 6th February 1991. He earned his bachelor's in materials engineering from the University of Engineering and Technology in Lahore, Pakistan. He took first place and won two gold medals. Then he studied a master's program "Advanced Materials and Processes" from Friedrich-Alexander-Universität Erlangen-Nürnberg (FAU), Germany. He carried out his master's thesis at Julius Wolff Institute, Charite, Berlin in collaboration with the Institute of Biomaterials, FAU, Germany. Under the supervision of Dr. Taimoor, Dr. Evi Lippens, and Prof. Aldo R Boccaccini, he worked on investigating stem cell interactions with different bioactive glass particles and developed stress-relaxing and degradable alginate-bioglass composite hydrogel. While reading more he understood the importance of extracellular matrix (ECM) dynamicity and the supramolecular nature of ECM proteins. In December 2016, under the supervision of Prof. Clemens van Blitterswijk, Prof. Lorenzo Moroni, and Asst. Prof. Matthew Baker, Shahzad started as a PhD student at MERLN Institute, Maastricht University, the Netherlands. Using dynamic covalent and supramolecular chemistry, he created hydrogels that can mimic the dynamicity, viscoelasticity, and fibrous structure of ECM proteins. Furthermore, he developed several bioinks for 3D bioprinting using imine-type dynamic covalent chemistry and BTA supramolecular chemistry. He strongly believes that organic chemistry, in general, and dynamic covalent and supramolecular chemistry, in particular, have a vital role to play in the creation of advanced biomaterials, bioinks, and biomedical products.